NONDESTRUCTIVE MEASUREMENT SCIENCE AT NASA LANGLEY

Advancing The State-Of-The-Art Providing A Quantitative Science Base And Technology Transfer For Materials/Structures Characterization

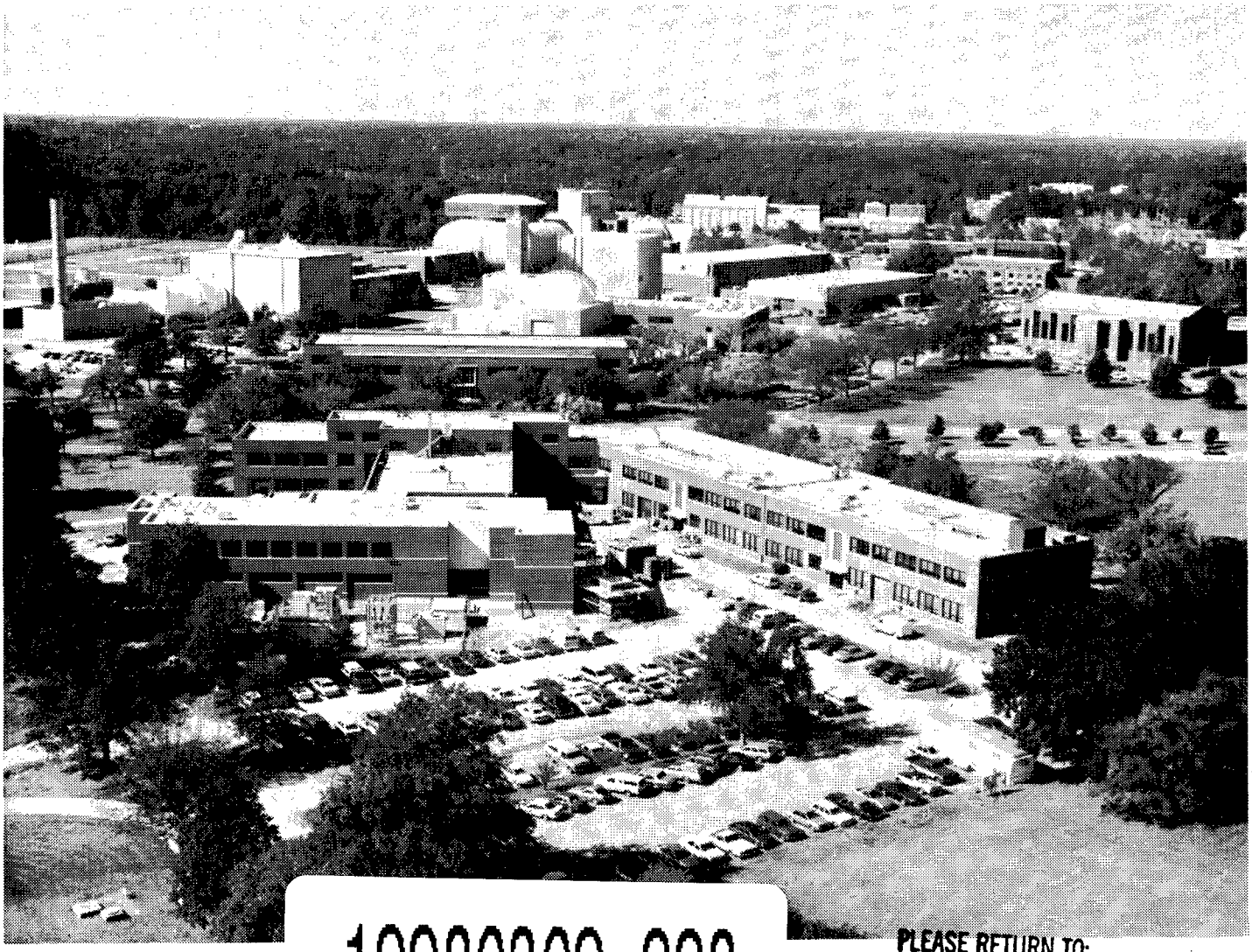

NASA

National Aeronautics and Space Administration

Langley Research Center
Hampton, Virginia 23665-5225

Accession Number: 3688

Publication Date: Jun 01, 1989

Title: NDE Research At Nondestructive Measurement Science At NASA Langley

Corporate Author Or Publisher: NASA Langley Research Center, Hampton, VA 23665-5225

Report Prepared for: NASA, Langley Research Center, Hampton, VA 23665-5225

Comments on Document: This document contains technical papers representative of the research performed at the NASA Langley Nondestructive Measurement Science Branch Laboratories.

Descriptors, Keywords: NDE Aerospace SRM Solid Rocket Motor Fiber Optics Metal Material Superconducting Polymer Composite Thermal Sensor Development

Pages: 00250

Cataloged Date: Aug 14, 1992

Document Type: HC

Number of Copies In Library: 000001

Record ID: 24537

NDE RESEARCH AT
NONDESTRUCTIVE MEASUREMENT SCIENCE BRANCH
INSTRUMENT RESEARCH DIVISION
NASA LANGLEY RESEARCH CENTER
HAMPTON, VIRGINIA 23665-5225
June 1989

A collection of recent papers and papers for which we have significant requests

This document contains technical papers representative of the research performed at the NASA Langley Nondestructive Measurement Science Branch Laboratories. The focus of the program is to advance the science base for NDE resulting in improved quantitative information necessary to assess the safe, economical performance of materials and structures. The program is divided into groups consisting of: Composites, Metals, Advanced Sensors, Remote Sensors, and NDE Imaging. The respective group leaders are: Drs. Eric I. Madaras, Min Namkung, William P. Winfree, Robert S. Rogowski, and Patrick H. Johnston. Dr. Joseph S. Heyman is the program manager with Dr. Eric Madaras as the Assistant Branch Head and Mr. Bobby G. Batten, Director for Planning and Coordination. The multidisciplines associated with this activity are: physics, chemistry, mathematics, materials science, electronics engineering, and computer science. The technologies represented by our staff include: ultrasonics, nonlinear acoustics, thermal acoustics and diffusion, magnetics, fiber optics, and x-ray tomography. We have a strong commitment to transfer technology out of the laboratory to practical applications and welcome interactions with other government, university, and industry centers. Please feel free to contact any of the staff at (804) 864-4970 for more detailed information that is included in this document. We are also initiating an industrial/university consortium to focus on critical aerospace NDE generic problems and welcome cooperation with interested organizations.

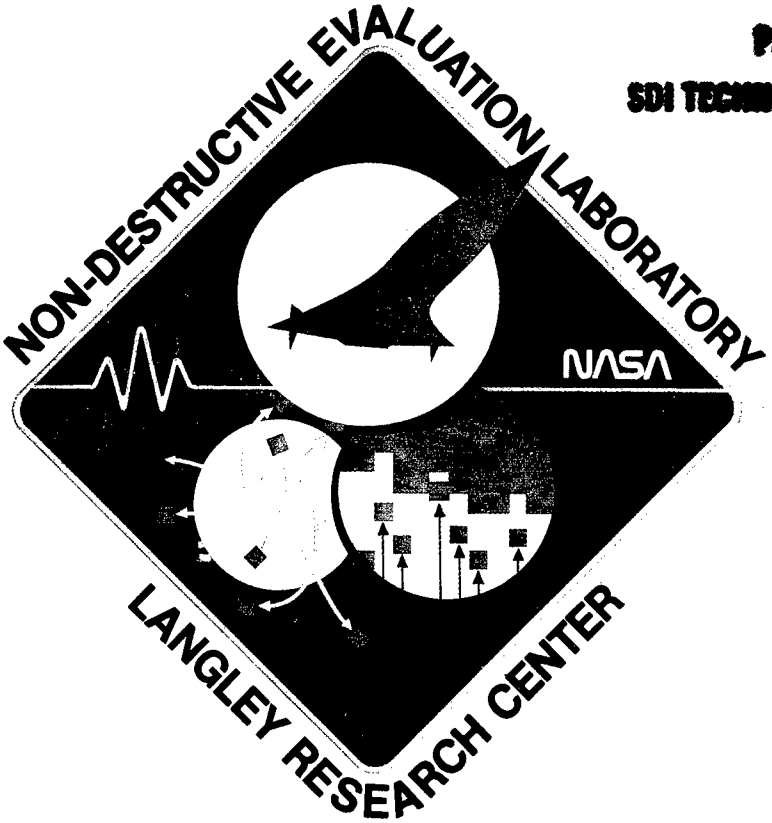

[redacted]

NDE RESEARCH AT LaRC

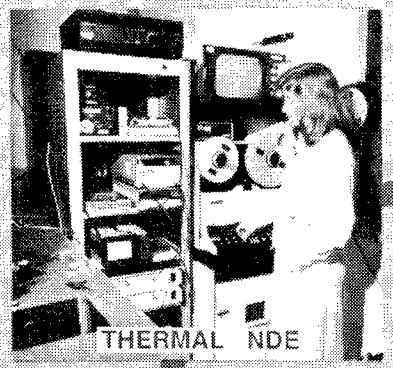
THERMAL NDE

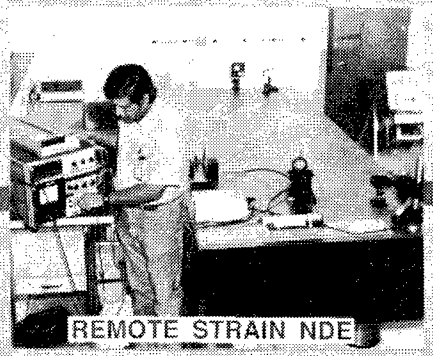
REMOTE STRAIN NDE

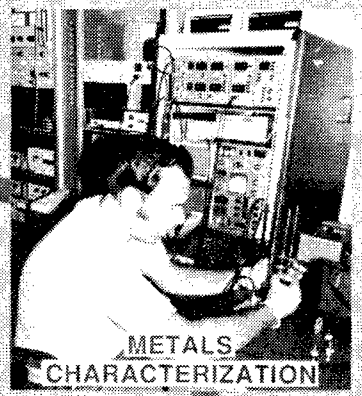
METALS CHARACTERIZATION

LIFE PREDICTION THROUGH ADVANCED NDE MEASUREMENT SCIENCE


COMPOSITES CURE MONITOR

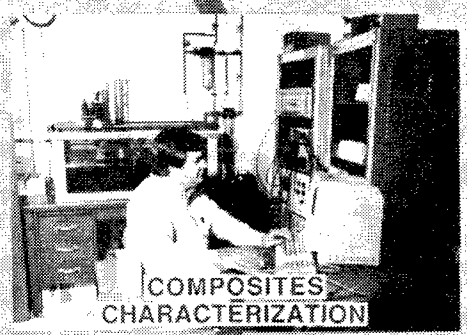
COMPOSITES CHARACTERIZATION


IMPACT DAMAGE NDE

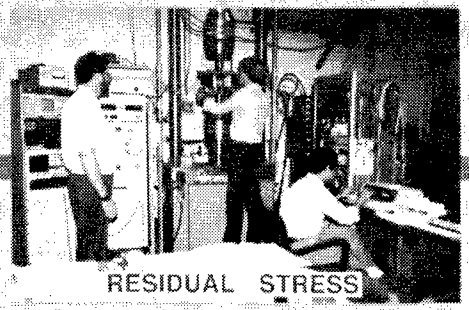
RESIDUAL STRESS


TECHNOLOGY TRANSFER

INDEX

c. Detection of Temper Embrittlement in Steel by Magnetoacoustic Emission Technique
Min Namkung, William T. Yost, John L. Grainger, and Peter W. Kushnick
Review of Progress in Quantitative NDE, August 1-5, 1988

d. Effects of Microstructure of Ferromagnetic Alloys on Magnetoacoustic Emission
Min Namkung, William T. Yost, D. Utrata, John L. Grainger, and Peter W. Kushnick
IEEE Sonics and Ultrasonics Symposium, October 2-5, 1988

e. Effects of Grain Boundary Characteristics of Steel on Magnetoacoustic Emission Spectra
Min Namkung, William T. Yost, D. Utrata, John L. Grainger, and Peter W. Kushnick
Materials Research Society, November 28-December, 1988

f. Review of Magnetoacoustic Residual Stress Measurement Technique for Iron-Like Ferromagnetic Alloys
Min Namkung, D. Utrata, P. Langlois, Peter W. Kushnick, and John L. Grainger
Review of Progress in Quantitative NDE, August 1-5, 1988

g. Requirements for Science in NDE
Joseph S. Heyman

h. Ultrasonic Pulsed Phase Locked Loop Interferometer for Bolt Load Measurements
Sidney G. Allison and C. Gerald Clendenin

i. The Use of Ultrasonic Harmonic Generation to Determine Crack Opening Conditions in Compact Tension Specimens
William T. Yost, Min Namkung, and Sidney G. Allison
Review of Progress in Quantitative NDE, vol. 7B, 1987, pp. 1525-1529.

V. CHARACTERIZATION OF SUPERCONDUCTING MATERIALS

a. Ultrasonic Attenuation Measurements on $LuBa_2Cu_3O_7$ and $HoBa_2Cu_3O_7$
Keun J. Sun, Moises Levy, Bimal K. Sarma, H. C. Ku, H. D. Yang, R. N. Shelton, R. W. McCallum, and P. Klavins
Modern Physics Letters B, July 1987.

b. Ultrasonic-Attenuation Measurements in Single-Phased $YBa_2Cu_3O_7$
M-F. Xu, H-P. Baum, A. Schenstrom, Bimal K. Sarma, Moises Levy, Keun J. Sun, L. E. Toth, S. A. Wolf, and D. U. Gubser
Physical Review B, 37-7, March 1988

c. Relaxation Behavior of Ultrasonic Attenuation in $YBa_2Cu_3O_7$
Keun J. Sun, William P. Winfree, M-F. Xu, Bimal K. Sarma, M. Levy, R. Caton, and R. Selim
IEEE Transactions on Magnetics

d. Frequency-Dependent Ultrasonic Attenuation of $YBa_2Cu_3O_7$
Keun J. Sun, William P. Winfree, M-F. Xu, Bimal K. Sarma, M. Levy, R. Caton and R. Selim
Physical Review B, 38-16, December 1988

VI. CHARACTERIZATION OF POLYMER COMPOSITES

a. Temperature Dependence of the Ultrasonic Properties of AS4/Lexan and XAS/Lexan Composite
Barry T. Smith

b. Detection of Bondline Delaminations in Multilayer Structures With Lossy Components
Eric I. Madaras, William P. Winfree, Barry T. Smith, and Joseph S. Heyman
1987 IEEE Ultrasonics Symposium, October 13-16, 1987

c. An Investigation of the Relationship Between Contrast and Azimuthal Angle for Imaging Porosity in Graphite/Epoxy Composites With Ultrasonic Polar Backscatter
S. M. Handley, James G. Miller, and Eric I. Madaras
1988 IEEE Ultrasonics Symposium, October 2-5, 1988

d. Effects of Bleeder Cloth Impressions on the Use of Polar Backscatter to Detect Porosity
S. M. Handley, James G. Miller, and Eric I. Madaras
1988 Review of Progress in Quantitative NDE, July 31-August 5, 1988

e. Characterization of Porosity in Graphite/Epoxy Composite Laminates With Polar Backscatter and Frequency Dependent Attenuation
S. M. Handley, M. S. Hughes, James G. Miller, and Eric I. Madaras
1987 Ultrasonics Symposium

f. Tensile Stress Acoustic Constants of Unidirectional Graphite/Epoxy Composites
William H. Prosser
Journal of Reinforced Plastics and Composites, to be published

g. Surface Generation and Detection of Coupled Fiber-Matrix Mode Acoustic Wave Propagation in Fiber-Reinforced Composites
William T. Yost and John H. Cantrell
Review of Progress in Quantitative NDE, vol. 5B

h. Detection of Fiber Damage in Graphite Epoxy Composite Using Current Injection and Magnetic Field Mapping
Travis N. Blalock and William T. Yost
Review of Progress in Quantitative NDE, vol. 5B

i. Removal of Dominant Reverberations From Ultrasonic Time-Records of Layered Material by Digital Predictive Deconvolution
Doron Kishoni

j. Ultrasonic Correlator Versus Signal Averager as a Signal to Noise Enhancement Instrument
Doron Kishoni and Benjamin E. Pietsch

VII. THERMAL NDE

a. Contrast Enhancement Through Source Impedance Control in the Thermal NDE
Christopher S. Welch
Review of Progress in Quantitative NDE, vol. 7A

b. A Numerical Grid Generation Scheme for Thermal Simulations in Laminated Structures
Patricia H. James, Christopher S. Welch, and William P. Winfree

c. Thermographic Detection of Delaminations in Laminated Structures
William P. Winfree, Christopher S. Welch, P. H. James, and Elliott Cramer

d. Thermal Diffusivity Measurements in Carbon-Carbon
D. Michele Heath and William P. Winfree

e. Remote Noncontacting Measurements of Heat Transfer Coefficients for Detection of Boundary Layer Transition in Wind Tunnel Tests
D. Michele Heath, William P. Winfree, Debra L. Carraway and Joseph S. Heyman
ICIASF 1987, Williamsburg, Virginia, June 22-25, 1987

VIII. SENSOR DEVELOPMENT

a. Using a Large Aperture, Phase Insensitive Array Transducer to Improve Ultrasonic Detection of Disbonds at a Rough Interface
Eric I. Madaras
1988 Review of Progress in Quantitative NDE

b. Modeling the Pulse-Echo Response of a Two-Dimensional Phase-Insensitive Array for NDE of Layered Media
Patrick H. Johnston and Eric I. Madaras
1988 IEEE Ultrasonics Symposium

c. Determination of the Absolute Sensitivity of Damped MHz Range Ultrasonic Transducers
Pamela D. Hanna, William T. Yost and John H. Cantrell

d. Effects of Diffraction on the Membrane Response of the Submersible Electrostatic Acoustic Transducer
Pamela D. Hanna and William T. Yost

IX. GENERAL

a. Anisotropy of the Ultrasonic Backscatter of Myocardial Tissue: II. Measurements in Vivo
Eric I. Madaras, J. Perez, B. E. Sobel, J. G. Mottley and James G. Miller
J. Acoust. Soc. Am. 83(2) February 1988

I. INTRODUCTION

NDE In Aerospace - Requirements For Science, Sensors And Sense

Joseph S. Heyman
NASA - Langley Research Center
Hampton, VA 23665

Abstract

Nondestructive Evaluation (NDE) is the technology of measurement, analysis, and prediction of the state of material systems, for safety, reliability and mission assurance. It is an old technology yet still in its infancy. The opportunities for research and application are great and the shortfall in technology demands national attention. Those of us in the field are witnessing an awakening of the engineering and management awareness to the importance of NDE. This is an exciting and dynamic time. In this paper, we shall review aspects of aerospace NDE and discuss recent advances. The measurement focus will be on ultrasonics with generous case examples. Problem solutions to be highlighted include critical stress in fasteners, residual stress in steel, NDE in laminated composites, three dimensional NDE laminography and solid rocket motor (SRM) NDE.

Introduction

The modern laboratory has taken a quantum leap in the past decade reflecting the changes that have occurred in electronics and measurement science. The usual scene of the scientist gently adjusting a knob on a precision device to obtain a experimental measurement has been replaced. The new image is that of a glowing computer display with the scientist tapping away on a keyboard with a strange anatomically incorrect mouse running over the desktop!

Instrumentation and technology in the field has also taken advantage of the advances. NDE instrumentation has matured and today represents a capability barely perceived only a few decades ago. Entire waveforms are digitized and stored

for analysis or processed on the fly presenting time or frequency domain information.

Although conventional NDE has been quite successful, it is generally based on correlative relationships which can be complex and multifaceted. The complexity of modern NDE arises from four main factors - quantitative measurement science, physical models for computational analysis, realistic interfacing with engineering decisions, and direct access to management priorities. The first two of these factors deal with measurement and its interpretation while the last two involve the decision process. All four components are necessary to achieve reliable standards, life prediction capability, extended safe economic life, and enhanced reliability with smart systems.

However, with all the technical advances, most of the standard NDE acceptance or rejection criteria are still based on physical measurements that have not changed in 30 years. For example, the information in the standard "C"- scan of today is hardly different from one of the 1960's. Although it may contain more levels of information, the image is still based on the simple assumption that acoustic waves interact with the sample and reveal "important" properties.

In practice, such assumptions have been effective for finding defects such as delaminations, porosity, or inclusions for simple geometries of uniform materials. However, for complex samples the simple interpretation of this data may be hazardous unless the sample is flat, parallel and homogeneous. Perhaps the greatest need in NDE today, as decades ago, is the integration of materials science and measurement science resulting in an improved interpretation of data.

Although improvements in the technology are key to advancing the interpretation of NDE data, the last two factors are also important concerning the integration of NDE with engineering and management priorities. That may prove to be the most

difficult challenge. The cost savings attributable to NDE should be made visible, including the complex areas of safety and reliability. Simply stated, NDE must improve its communication skills and change its image from the red ink side of the ledger.

This paper shall address recent advances in the four factors of NDE. Physical models of acoustic propagation are presented that have led to the development of new measurement technologies advancing our ability to assure that materials and structures will perform as designed. In addition, a brief discussion is given of current research for future mission needs such as smart structures that sense their own health. Such advances permit new projects to integrate "design for inspection" into their plans bringing NDE into engineering and management priorities.

The Need For Science

An important focus in modern ultrasonic NDE is the development of meaningful physical models of critical measurements which are necessary to fully interpret data. Models require a clear statement of the underlying simplifying assumptions and the relevant interactions between the acoustic wave and the media. The most useful models can generally be inverted to determine the physical properties or geometry of the tested item. Furthermore, models can be part of a closed computational loop to verify the model, apply corrections to the model or lead to an alternate interpretation of the data often resulting in a different perspective.

Measurements must be quantitative rather than qualitative and have led to a new emerging science of NDE with the acronym QNDE. Significantly, by measuring real physical properties, QNDE has advanced from a detection process to one of evaluation. It is critical to understand the underlying physics of the observed effects. For example, in an ultrasonic scan, the measured signal strength may decrease raising questions about variations in physical properties that may affect the performance of the material. The analysis is not trivial and involves a broad

understanding of the measurement interaction physics, materials science, and the projected use environment of the material.

The measured signal decrease, perhaps, is caused by an increase in attenuation of the material. Attenuation is caused by absorption (conversion to heat), by scattering (reradiation of the wave), by refraction (coherent redirection of the wave), and by mode conversion (changes in propagation mode). Most of these processes are frequency dependent which makes the analysis more complex. Absorption, for example, can often vary linearly with frequency, as a square power, or as the fourth power. In addition, as the acoustic intensity of the wave increases, such as at the focus of a transducer, nonlinear effects lead to harmonic generation and the formation of shock waves, both of which effect attenuation. Such nonlinear interactions can significantly alter the requirements for both measurement as well as analysis of the data.

In addition, there are critical situations involving attenuation-like phenomena; these situations are not uncommon and require a high level of expertise to analyze correctly. For example, the decrease in signal strength may have nothing to do with real attenuation. It can be caused by an artifact of the measurement process itself. Most transducers which convert acoustic waves into an electrical signals, are larger than a wavelength. Furthermore, most transducers are phase sensitive and measure the integral of pressure over their face. Therefore, if one part of the transducer "sees" a wave of different phase than another part of that transducer, the result will be phase cancellation. This usually results in a measurement error appearing as a signal reduction. Such phase cancellation occurs in materials of nonplanar geometry, with velocity anisotropy, or with inhomogenity. Unless one is measuring parallel, homogeneous isotropic solids with normal incidence of perfect plane waves, this can be serious!

Clearly, velocity variations in a sample require a different interpretation than absorption variations. If only simple measurements are taken, one cannot differentiate the two phenomena resulting in a measurement anomaly. NDE must not be a study of anomalies, but rather a scientific analysis of material properties. Simple measurements and analysis are not adequate for complex situations.

The interpretation of NDE measurements requires a professional discipline equal to any of those in aerospace technology today. QNDE is multidisciplinary integrating expertise in science and engineering that bridge the traditional technologies. Several examples follow that illustrate these directions.

Fastener Stress

The ultrasonic bolt monitor is an excellent example of an application of acoustics to an engineering problem. The scientific foundation of the concept matured over the past 20 years[1-3] and resulted in many experimental concepts, some developed by this author[4-6], based on the nonlinear theory of sound propagation in stressed media.

The basic problem is to insure that critical fasteners achieve proper preload needed to perform their design function. Torque is the common bolt preload procedure. Unfortunately, torque is directly related to preload through friction which cannot be accurately controlled. Friction varies with lubricant, surface finish, geometry, and material. Therefore, torqued fasteners are only loaded to a limiting accuracy which at best is on the order of $\pm$ 20%. Often, the accuracy is no better than a factor of 2.

Physical models show that a fastener under stress elongates and experiences a decrease in sonic velocity (depending on the propagation parameters). Therefore, if a sound wave travels along the axis of a fastener, it experiences an increase in round-trip-time or total phase shift. The amount of change depends on the bolt's length, it's second and third order elastic constants, and the applied stress.

The following analysis is simplified and condensed to be included in this overview. The model is based on the non-Hookean relationship for stress (s) and strain (e) and moduli (M_i) as

$$s = M_2 e + M_3 e^2 + M_4 e^3 + \ldots \quad (1)$$

For small strains, $s = M'(e)\, e = (M_2 + M_3 e)\, e$ (2)

The ultrasonic velocity is related to this expression as:

$V^2 = M'(e) / r = (M_2 + M_3 e) / r$; where r is the density. (3)

Therefore, the change in velocity with strain is related to the higher order elastic moduli through the relationship

$dV / d e = (1/ 2V) (M_3 / r)$. (4)

Equation 4 indicates that the sonic velocity depends on stress through the second and third order elastic constants. Although early researchers expected the elongation to dominate the measurement, velocity effects are greater than incremental length effects. This further illustrates the importance of developing good physical models of the measurement in order to correctly interpret the results.

For the geometry of a typical fastener, our models show that the change in phase length, ø, during stress is $(\Delta ø/ø) = (\Delta l / l - \Delta v / v)$, where v is the velocity and l the length of the bolt. A pulsed phase locked loop (P2L2) instrument[7] was used to reduce the uncertainty in the measurement. Broadband pulse techniques were also examined, but placed limiting demands on the finish and geometry of the bolts and could not achieve parts per 10 million resolution. The P2L2 locks to a given total phase shift in the sample by modifying its internal reference frequency from which the output tone burst is derived. Changes in the sample length or sound velocity cause changes in the operating frequency of the instrument thus maintaining a

constant total phase shift. The instrument produces a measurement of normalized frequency change ($\Delta F / F$) = - ($\Delta t / t$), where t is the round trip time.

Figure 1 shows data obtained with the P2L2 bolt monitor applied to the Space Shuttle's landing wheel fasteners. A variety of lubricants were used for this test to demonstrate the effect of small changes in friction. The x's are data obtained with torque measurements, while the o's are the ultrasonic P2L2 frequency data. Note that even in the presence of frictional variations, the ultrasonic bolt monitor can correctly achieve the desired preload, in contrast to the significant errors produced by torque.

In other experiments, finite element models were run to calculate the stress distribution along the acoustic propagation path of a typical bolt geometry to evaluate the effect of nonuniform loads and incomplete loaded lengths. The effect of unloaded length was shown[7] to significantly change the calibration as predicted by the model. Knowing the effective load length permitted calibrations and/or corrections for nearly all fasteners tested.

Further models of stressed solids were developed and resulted in an ability to measure stress profiles in beams under 3 point bending[8]. In addition, tests on fasteners under bending loads were able to identify the direction and magnitude of the bending to assess the safety of the joint.

Residual Stress

Residual stress is a "silent" killer of materials and can lead to failure at external loads far below those predicted based on strength. The real load seen by the material is a combination of the applied load and the internal stresses caused by this phenomena.

The basis of residual stress is complex, as the size scale changes from a structures point of view to an atomistic point of view. The addition of a single atom in a lattice produces lattice strain and a site of distortion. Lattice slip planes and other dislocations can lead to significant microstresses acting as initiation sites for material failure. On a larger scale, grain boundaries can be distorted by inclusions as well as by plastic deformation resulting in internal stresses. On a structural scale, this can lead to macroresidual stress having definite direction.

The basic measurement of residual stresses is X-ray diffraction determining the interatomic spacing. This, however, characterizes the strain existing on the surface of the material. A recent development, first reported by LaRC at the DOT workshop on residual stress in 1981, has resulted in the ability to measure residual stress in ferrous materials. The development of a physical model led to a series of experiments that link the material stress state to it's magnetic domain behavior and determines the amplitude of the tensile or compressive stress.

The experimental results[9] are explained by a model[10] relating magnetic derivative changes in the acoustic velocity to the initial stress state. As shown in fig. 2, during magnetization, the domains pass from their initial state to one of perfect alignment with the field. Fig.2a indicates the unstressed magnetization derivative, while Fig. 2b) indicates tensile, and Fig. 2 c) shows compression loading.

Since the initial unmagnetized domain state is influenced by the existing state of stress, measurements of the derivative path followed during magnetization determine the initial state of stress. Ultrasonic velocity is strongly affected by the 90° domain wall motion and is used to measure the domain growth and alignment during the magnetization process. For longitudinal waves propagating parallel to the magnetization axis, a decrease in velocity indicates a compressive stress.

Fig. 3 shows the magnetic derivative of a sample of rail steel having 0.68% carbon concentration. The velocity is plotted as a fractional change in frequency shift which is equal to the fractional change in transit time. The data shows the velocity relationship for applied stress ranging from +240 MPa to - 240 MPa.

An application of this technique to determine residual rather than applied stress is shown in fig. 4 for a bar measured with surface acoustic waves before and after plastic deformation. The upper surface of the bar (surface A) developed compressive residual stresses while the under surface (surface B) became tensile. The figure shows that the two surfaces were nearly identical prior to deformation (both slightly tensile) and, as expected, developed residual stresses of opposite signs after plasticity.

Composites NDE

Another area requiring QNDE is composite materials which represent a great advancement for structures with better weight to strength ratio, improved fatigue characteristics, controlled directional strength, and increased stiffness. However, composites also represent a challenge for NDE brought on by their anisotropy, their laminated structure, and their internal inhomogenity.

Some of these problems may be minimized by performing phase insensitive measurements to eliminate an artifact present in most ultrasonic measurements of complex materials. The artifact arises from complex acoustic fields detected with conventional phase sensitive piezoelectric transducers. Physical models of conventional transducers predict up to 100% measurement errors and experimental results verify the magnitude of the problem[11]. The difference in directivity[12] between a phase insensitive and a conventional transducer is shown in fig. 5 . The amplitude variation with incident angle causes measurement artifacts which can result in serious interpretation errors using conventional transducers.

These errors are especially significant in composite materials, and can limit the interpretation of practical measurements, except for the grossest of material variables. For example, fatigue damage in graphite - epoxy composites is difficult to measure with conventional ultrasonics until delaminations or macro-interlaminar cracking form. However, measurements obtained with an acoustoelectric power sensitive transducer fabricated from CdS measure the progressive increase in attenuation accompanying fatigue in a (0^2 / 90^2) symmetric composite material[13]. These measurements were obtained in the frequency domain using a swept tone burst frequency source as an ultrasonic driver and a power detector receiver used in a transmission mode.

3-Dimensional laminography

Although through transmission C-scans have proven successful for composites, there are many instances where volumetric information is needed. For example, it is necessary to know the ply location of a composite delamination to predict its effect on bending loads. That is determined by measuring the entire acoustic reflection time domain response from an interrogating wave and reconstructing each lamina from the interface reflections. Then each lamina can be examined to assess its response to external loads.

The accuracy of the measurement is improved by correcting for the acoustic attenuation and scattering losses which occur along the propagation path. Each lamina is modeled to include attenuation and impedance discontinuities. The models are a starting input in a self- consistent calculation accounting for all experimental input and measured backscattered energy. That process generates a corrected laminography slice[14] which is helpful for defect criticality calculations. In addition, deconvolution filters[15] remove transducer and electronics coloration of the data providing a best measurement estimate.

Bondline NDE in Solid Rocket Motors

A final application of physical models in NDE, is the multilayered case of the solid rocket motor (SRM). The motor geometry consists of a steel external case 1.3 cm. thick with internal layers of insulation, bonding layers, and fuel. The acoustic properties of the insulation and fuel are similar to that of dense rubber. A nondestructive measurement is needed to assess the internal bond layers of the various materials. Conventional pulse-echo applied to the case results in acoustic ringing in the steel that complicates detection of internal bond delaminations.

To further examine the problem, a model of the SRM was developed to analyze the propagation of acoustic energy in the structure. The model includes the acoustic velocity, frequency dependent attenuation, densities, and geometries of each of the many SRM layers. Fig. 6 shows the reflection coefficient thus calculated which includes the superposition of all the interfaces including model delaminations between various layers. The buried bondlines are evident only at narrow frequency bands corresponding to resonances.

Thus, measurements made with a broadband system are compromised by the returning energy that does not contain bondline information . Only acoustic energy near the composite resonances is sensitive to the bond condition. This modeling information resulted in the design of an acoustic system with significantly improved sensitivity and specificity to bondline conditions.

The Future of NDE

Fundamental scientific advances in our understanding of physical acoustics and materials science are needed to bridge the most important gap facing NDE. That gap currently splits NDE from its most ambitious and necessary goal - linking physical measurements to engineering property requirements.

For example, one of the most important properties of a material is its strength. How is that measured today? Samples are broken. How is fatigue toughness determined? Samples are fatigued. How is impact strength determined? Sample are impacted. Our current understanding of physical measurements and materials science is incomplete and cannot, without question, provide conclusive data to characterize those needed engineering properties nondestructively. Building a bridge between QNDE and material engineering performance, is one of the most important directions for NDE research.

That bridge is needed to change program management perception of NDE. When NDE steps up to the challenge of providing real engineering data about structural and material performance, it will join the ranks of the other technologies. Until that time, it will be held in the status of a special "art", without appreciation of its full potential. The future of NDE science is bright with the technology dynamically evolving. The entire field is seeing an upsurge that will result in improved safety, economy, and reliability through integration of QNDE with design.

References

1) Hughes, D. S. and Kelly, J. L., "Second Order Elastic Deformation Of Solids," Phys. Rev. 92, pp 1145 - 1149 (1953).

2) Thurston, R. N., and Brugger, K., " Third Order Elastic Constants And The Velocity Of Small Amplitude Elastic Waves In Homogeneously Stressed Media," Phys. Rev. 133, p A1604-A1610, (1964).

3) Cantrell, J. H., " Anharmonic Properties Of Solids From Measurements Of The Stress Acoustic Constant," J. of Testing and Evaluation, 10, pp 223-229 (1982).

4) Heyman, Joseph S., "A CW Ultrasonic Bolt-strain Monitor," Experimental Mechanics, 17, pp 183-187, (1977).

5) Heyman, Joseph S., " Pseudo Continuoous Wave Instrument," United States Patent 4,117,731 (1978).

6) Heyman, Joseph S., and Chern, E. J., " Ultrasonic Measurement of Axial Stress," Journal Of Testing And Evaluation, 10, pp202-211, (1982).

7) Heyman, Joseph S.; "Pulsed Phase Locked Loop Strain Monitor,"United States Patent 4,363,242 (1982)

8) Heyman, Joseph S. and Issler, W., "Ultrasonic Mapping Of Internal Stresses," IEEE Ultrasonics Symposium Proceedings, (1982).

9) Namkung, M. and Heyman, Joseph S., " Residual Stress Characterization With A Magnetic/Ultrasonic Technique," IEEE Ultrasonics Symposium Proceedings, 84CH2112-1, pp 950-954, (1984).

10) Namkung, M., Utrata, D., Allison, S.G., and Heyman, Joseph S., "Magnetoacoustic Stress Measurement In Railroad Rail Steel," Reviews Of Progress In Quantitative NDE, D. Thompson and D. Cheminti, eds., 5A,pp1481-1487,(1985).

11) Heyman, Joseph S., "Phase Insensitive Acoustoelectric Transducer," J. Acoust. Soc. Am., 64, (1978).

12) Heyman, Joseph S. and Cantrell, John H., " Application Of A Phase Insensitive Receiver To Material Measurements," IEEE Ultrasonics Symposium Proceedings, #77CH1264-1SU, (1977).

13) Cantrell, J.H., Winfree, W. P., and Heyman, Joseph S., "Profiles Of Fatigue Damage In Graphite / Epoxy Composites From Ultrasonic Transmission Power Spectra," *Recent Advances In Composites In The United States And Japan*, ASTM STP 864, J.R. Vinson and M. Taya, Eds., pp 197-206, (1985).

14) Kishoni, D. and Heyman, Joseph S., "Energy Shadowing Correction Of Ultrasonic Pulse-Echo Records By Digital Signal Processing," Reviews Of Progress In Quantitative NDE, D. Thompson and D. Cheminti, eds., 5A, pp 767-780(1986).

15) Kishoni, D., "Application Of Digital Signal Pulse Shaping By Least Squares Method To Ultrasonic Signals In Composites," Reviews Of Progress In Quantitative NDE, D. Thompson and D. Cheminti, eds., 5A, pp781-787, (1986).

Figure Captions

Figure 1) Comparison between the P2L2 ultrasonic bolt monitor and a conventional torque system for achieving critical fastener preload. Different lubricants were used to simulate a variation in friction common to bolting operations.

Figure 2) Magnetic domain model of the effects of stress on the saturation path taken by a sample during magnetization (H) increasing to the right. a) Zero stress; b) Tension; c) Compression. The 90° domain walls have a significant effect on the ultrasonic velocity.

Figure 3). Results of the fractional frequency shift measurements made in railroad steel for different stress levels as a function of magnetization, B.

Figure 4). Before (circles) and after (squares) plastic deformation magnetoacoustic measurements using surface acoustic waves to evaluate the residual stress in a bar.

Figure 5) Directivity of the phase insensitive transducer compared with a conventional piezoelectric transducer.

Figure 6). The ultrasonic frequency spectral reflection coefficient of the SRM geometry. This model shows that acoustic information about the buried bondlines is contained in only a narrow band of frequencies.

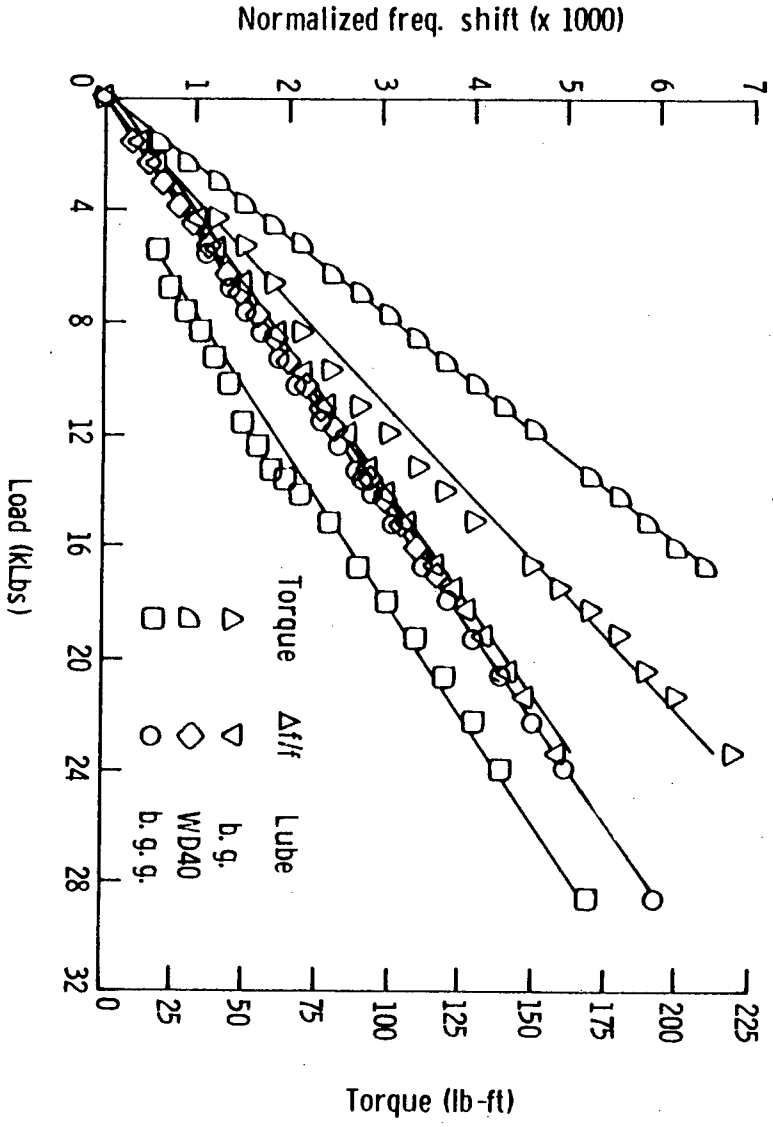
Normalized freq. shift (x 1000)
0
1
2
3
4
5
6
7
Load (KLbs)
0
4
8
12
16
20
24
28
32
Torque (lb-ft)
0
25
50
75
100
125
150
175
200
225
Torque
Δf/f
Lube
b.g.
WD40
b.g.g.

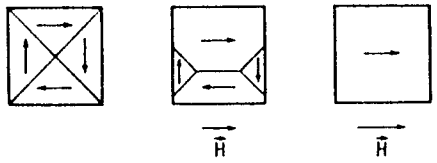

(a)

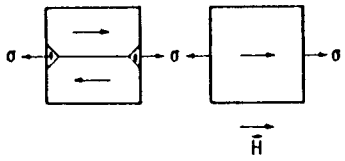

(b)

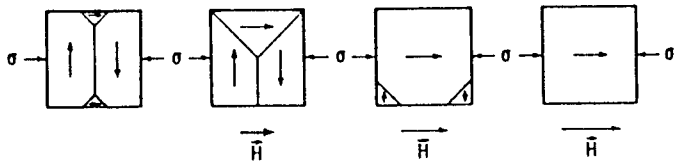

(c)

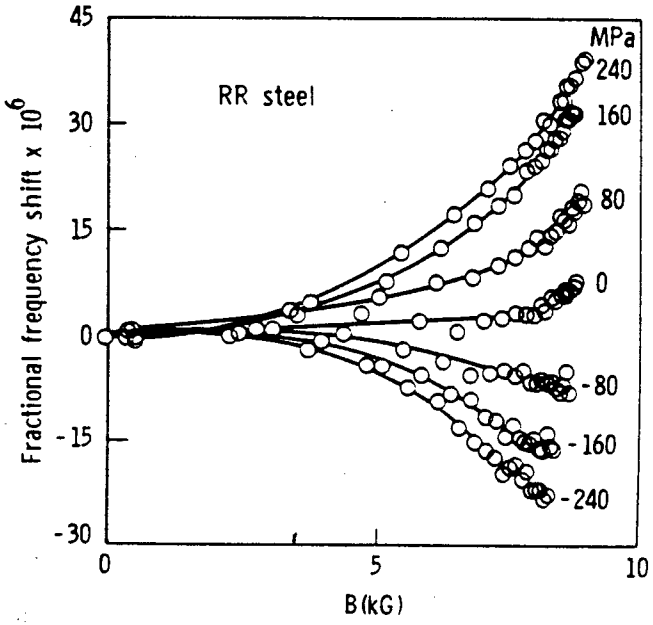
45
30
15
0
-15
-30
0
5
10
B(kG)
Fractional frequency shift x 10^6
RR steel
MPa
240
160
80
0
-80
-160
-240

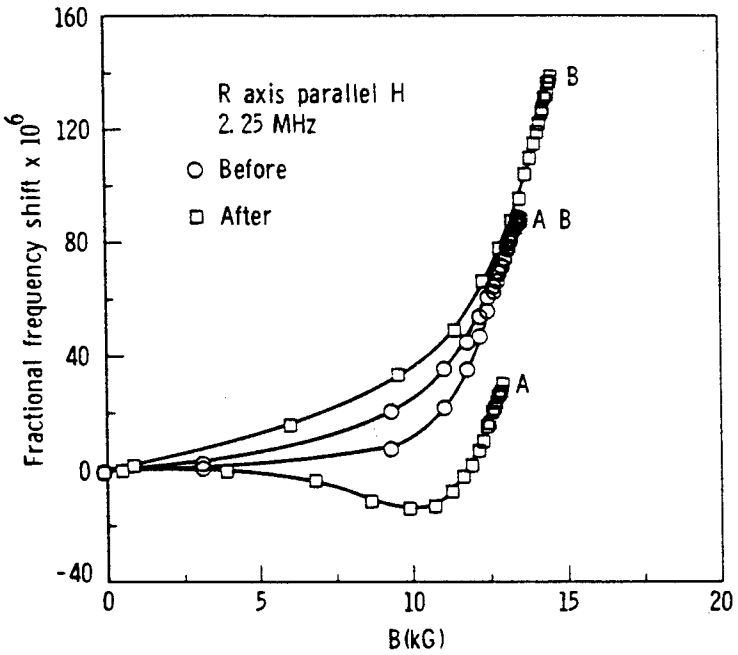
R axis parallel H
2.25 MHz
O Before
□ After
Fractional frequency shift x 10^6
160
120
80
40
0
-40
0
5
10
15
20
B(kG)
A
A B
B

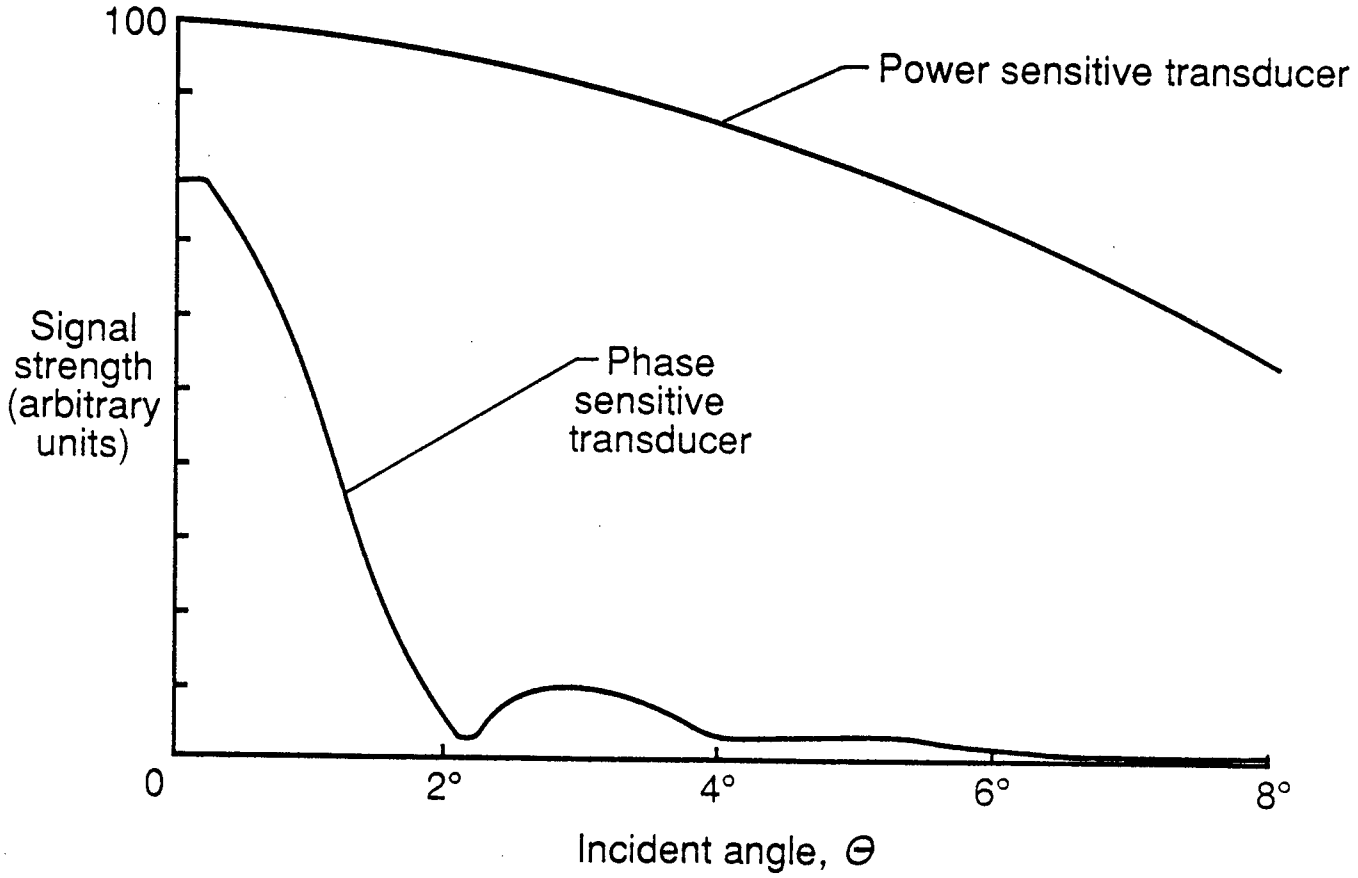
100
Power sensitive transducer
Signal strength (arbitrary units)
Phase sensitive transducer
0
2°
4°
6°
8°
Incident angle, Θ

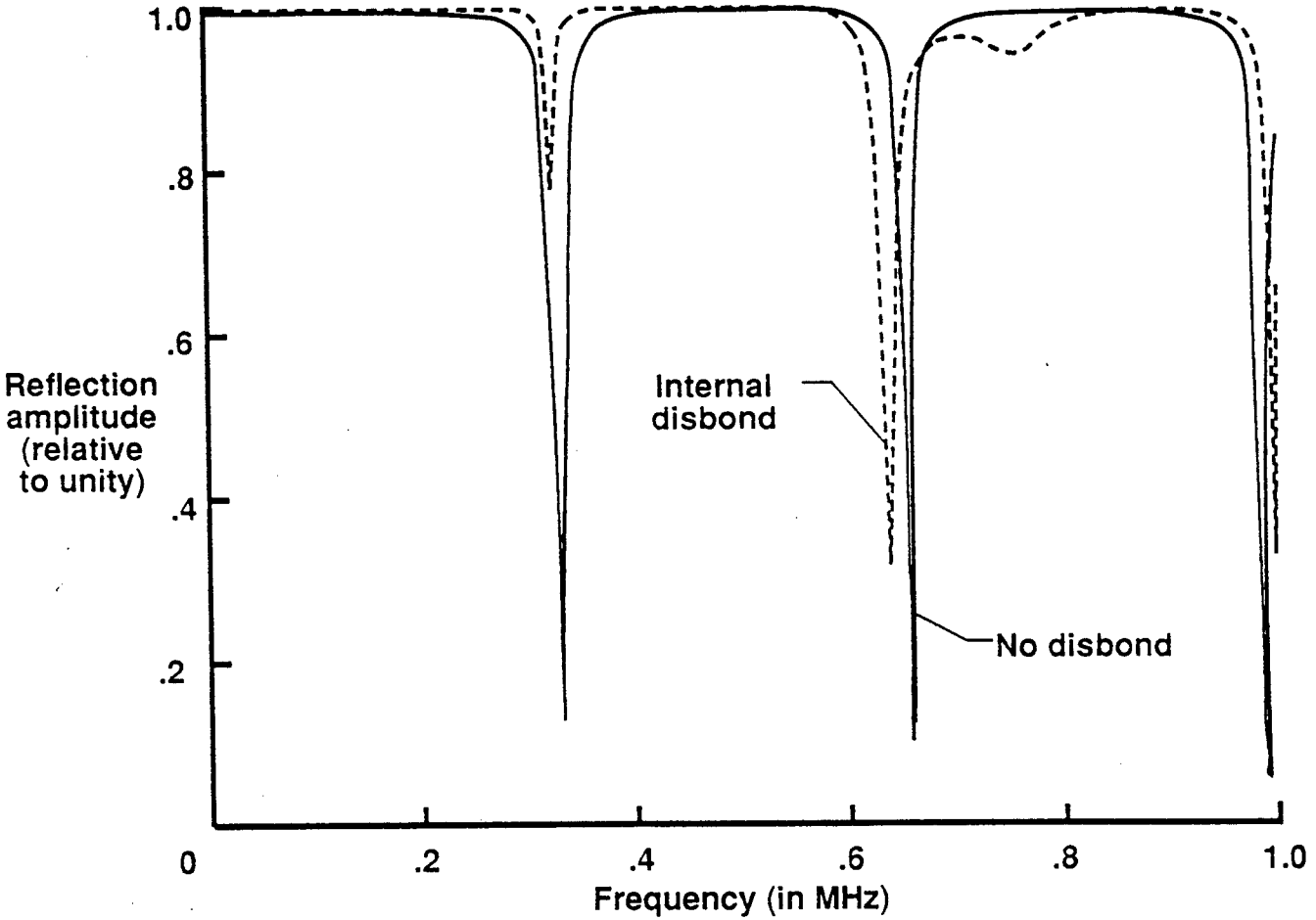
1.0
.8
.6
.4
.2
0
.2
.4
.6
.8
1.0
Reflection amplitude (relative to unity)
Frequency (in MHz)
Internal disbond
No disbond

mRS

J.S. Heyman 1 of 10

QUANTITATIVE NDE APPLIED TO COMPOSITES AND METALS

JOSEPH S. HEYMAN, WILLIAM P. WINFREE, F. RAYMOND PARKER, D. MICHELE HEATH, CHRISTOPHER S. WELCH*

NASA, Langley Research Center, Nondestructive Measurement Science Branch, Hampton, VA 23665

*The College Of William And Mary, Williamsburg, VA 23185

ABSTRACT

This paper reviews recent advances at LaRC in quantitative measurement science applied to characterizing materials in a nondestructive environment. Recent demands on NDE have resulted in new thrusts to achieve measurements that represent material properties rather than indications or anomalies in a background measurement. Good physical models must be developed of the geometry, material properties, and the interaction of the probing energy with the material to interpret the results quantitatively.

In this paper are presented NDE models that were used to develop measurement technologies for characterizing the curing of a polymer system for composite materials. The procedure uses the changes in ultrasonic properties of the material to determine the glass transition temperature, the degree of cure, and the cure rate. A practical application of this technology is a closed feedback system for controlling autoclave processing of composite materials.

An additional example is in the area of thermal NDE. Thermal diffusion models combined with controlled thermal input/measurement have been used to determine the thermal diffusivity of materials. These measurements are remote, require no contact with the material under test and thus have interesting promise for NDE applications.

INTRODUCTION

Today, the field of NDE is in a rapid state of flux. Recent advances in electronics, computers and physical models have opened the door to a more comprehensive professionalism that embraces a multidiscipline of sciences and technologies. In the past, NDE was thought of as an after-the-fact technology, used only when a part was built and ready for "inspection" . Today, in contrast, NDE plays an important role in the research of developing new materials, of developing process controls to evaluate and produce precursors of new materials, of fabrication to produce structures, of final quality assurance, and of recertifying structures for service.

The new emerging science of NDE is married to the word quantitative, along with the acronym QNDE. Significantly, by measuring real physical properties, NDE has advanced from a detection process to one of evaluation. It is critical to understand the underlying physics of the observed effects. For example, in an ultrasonic examination of a composite material, a fall-off might be detected in the measured signal strength during a scan of a given material. The important question is what physical property caused that measurement and will that property affect the performance of the material. The analysis is not trivial and involves a broad understanding of the measurement interaction physics, materials science, and the projected use of the material.

The measured signal drop, perhaps, is caused by an increase in attenuation of the material. Attenuation is caused by absorption (conversion to heat), by scattering (reradiation of the wave), by refraction (coherent redirection of the wave), and by mode conversion (changes in propagation mode). Most of these processes are frequency dependant which makes the analysis rather complex. Absorption, for example, can vary linearly with frequency, as a square power, or as the fourth power, to mention a few of the more likely interactions. In addition, as the acoustic intensity in the wave increases, such as at the focus of a transducer, nonlinear effects begin to play a more important role and lead to harmonic generation and the formation of shock waves both of which effect attenuation. Such nonlinear interactions can significantly alter the requirements for measuring as well as the analysis of the data.

Inaddition, there are critical situations that involve unusual attenuation-like phenomena; these situations are not uncommon and require a high level of expertise to analyse correctly. For example, the fall off in signal strength may have nothing to do with real attenuation. It can be caused by an artifact of the measurement process itself. Most transducers which convert acoustic waves into an electrical signals, are larger than a wavelength. Furthermore, most transducers are phase sensitive. Therefore, if one part of the transducer "sees" a wave of different phase than another part of that transducer, the result will be phase cancellation. This usually results in a measurement error which appears as a signal drop-off. Such phase cancellation occurs in materials of nonplaner geometry, velocity anisotropy, or inhomogenity. Unless one is measuring parallel, homogeneous isotropic solids with normal incidence of perfect plane waves, this can be serious!

That sounds like a bleak situation for ultrasonics NDE. In reality, what that means for ultrasonics, and for most other measurement energies, is that NDE requires an analysis professionalism equal to that in any of the sciences or engineering practices. Clearly, velocity variations in a sample tell a different story than scattering attenuation. If only simple measurements are taken, one cannot differentiate the two phenomena. NDE must not be a study in anomalies, but rather a scientific analysis of material properties. In short, the simple measurements/analysis are not adequate for complex situations.

The exciting future for QNDE, is to be able to identify the mechanisms that cause the measurement and to link those mechanisms to a real property change in a material. That opens the door to communications with the materials scientist, a door that has been partially closed in the past by the inability to link the measurements to physical properties.

In this paper, two areas of QNDE are reviewed that have benefited from recent advances. Those areas are ultrasonic characterization of the curing of composites and thermal NDE applied to composites and to complex geometries, such as the solid rocket motor (SRM). Each of these advances is based on physical models of the interactions; models that identified meaningful measurements that resulted in improved understanding of the phenomena.

COMPOSITES PROCESSING

An important problem facing practical use of composite materials on a broad scale is cost. Costs are driven by the raw material, labor intensive fabrication, and by poor yield. The use of QNDE can reduce costs by permitting automation of process through reliable sensors and through increased yield through process control feedback. A large composite wing

section can cost in the $100,000 range before it is even cured. The part must be placed in an autoclave for curing where it undergoes a heating and pressurization schedule inside a vacuum bag to insure compaction during cure.

The autoclave process first raises the temperature causing a decrease in the viscosity of the resin permitting it to flow easily. Any excess is removed by a bleeder cloth surrounding the part. Further into the cycle, the viscosity begins to increase as the molecular length of the polymer chains increases. It is necessary to increase the pressure in the autoclave during this time to insure compaction of the composite, to reduce the amount of gas volitiles and the size of any porosity present. As the process continues, the viscosity further increases until the polymerization is complete.

Usually, the only monitoring in an autoclave is of time, temperature and pressure. Is that adequate to insure good parts? Yes, if all the starting material is uniform and known, if the part cures at the same rate over its geometry, if the part cures at the same rate for variations in thickness, and if the autoclave environment is uniform. The last factor is easily controlled. Are all the other factors controlled? Is the starting resin of the same chemistry as the sample test run weeks (or years) earlier to determine the schedule? Did the resin sit at room temperature for a period of time changing its initial degree of cure?

Some say proper monitoring is accomplished by placing thermocouples on the part itself. Such monitoring proceedures are risky in that they measure only the environment in which the part sits. It is more quantitative to measure properties of importance, in the part itself, such as viscosity or degree of cure. A sensor is needed to control the autoclave so that pressure is not applied too early in the curing cycle thus forcing out too much resin, or too late, unable to compact the material. Either error could result in an inferior part. There are physical relationships between the degree of cure and ultrasonic parameters of the resin. These are shown in the next section, to be possible inputs for feedback control of autoclaves improving the reliability, yeild, and cost effectiveness of composites.

Relationship Between Polymer Cure And Ultrasonics

The longitudinal velocity is related to the degree of cure using the principle of additive moduli. The principle of additive moduli, which relates the bulk moduli of an organic liquid to a sum of contributions from the different molecular groups, was first found for liquids by Rao[1], then expanded on by Van Krevelin[2] and has been shown to be applicable for solids[3]. The analytical expression for relating the moduli (K) to the contributions of different molecular groups is given by the expression

$$K(t) = \rho \, (\Sigma C_i \, (t) \, R_i \, / \, (\Sigma C_i \, (t) \, V_i \,)^6 \qquad (1),$$

where C_i are the concentrations, R_i is the Rao function and V_i is the molecular volume for each molecular group and the sum is over all molecular groups. From this expression, the velocity as a function of degree of cure can be shown to be[4]

$$V(t) = [\, (\, S_2 + \alpha(t) \, S_3 \,)^6 \, (\, 1 + 4/3 \, A \,) \, -4/3 \, A \, S_2{}^6]^{1/2} \qquad (2),$$

where S_2 and S_3 are sums of Rao functions., A is an experimentally

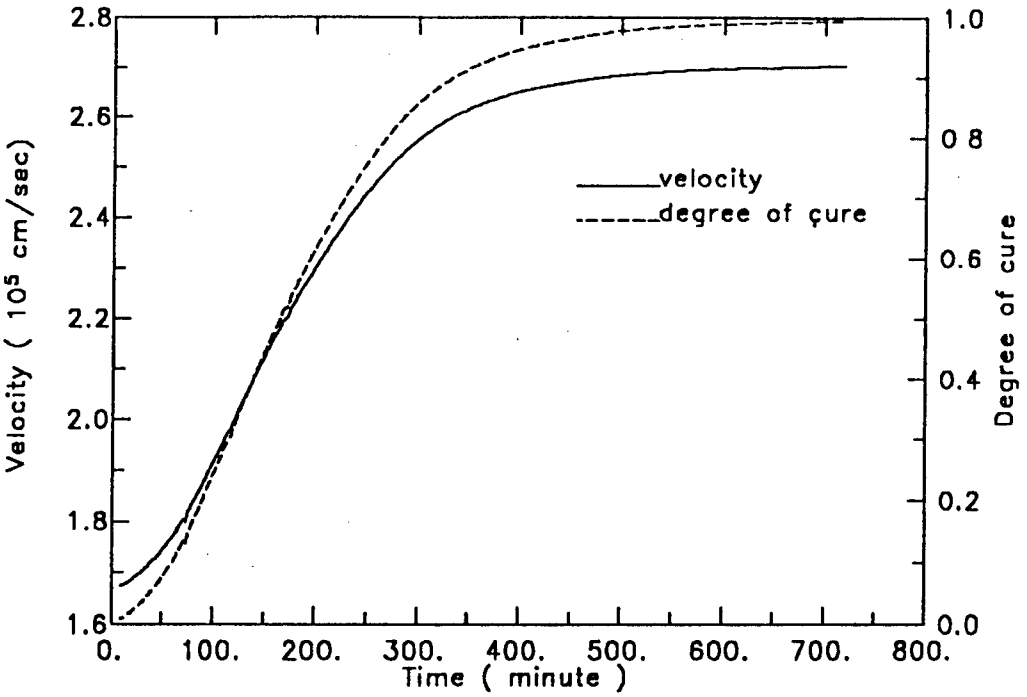

Figure 1. Longitudinal velocity measured during cure two part resin system with the degree of cure calculated from the velocity using equation (2).

determined constant, and $\alpha(t)$ is the degree of cure.

Experimental Results - Ultrasonics

The experimental configuration consists of a parallel plate cell with a 20 Mhz transducer bonded to one of the outside faces. The cell is placed in an oven to control the temperature of the resin during the cure reaction. A test material is prepared by mixing resin and curing agent and then introduced the mixture into the cell. The raw data is obtained from the digitized pulse-echo ultrasonic signals. The data is processed to improve the signal-to-noise and to remove the effects of the transducer/cell from the measurements of the propagation in the resin. The signal processing is based on a physical model of the test cell. The model adjusts the acoustic propagation parameters of the model to determine a best estimate of the velocity, the attenuation, and the frequency dependance of the attenuation. Based on a criteria of least squares error, the processing uses all the data rather than just the leading edges or peak amplitudes, as is usually done in simple time-of-flight measurements. This approach significantly improves the resolution and accuracy of the data. Velocity as a function of cure time found for a typical run and the degree of cure as calculated by equation (2) is shown by figure 1.

The time dependence of the degree of cure depends on the reaction kinetics of the system. Its time dependence can be changed by changing the temperature of the reaction or the concentration of the reactants. One of the reaction rate constants, K, has a functional dependence on the initial epoxide concentration and the temperature given by the expression

$$K = A_2 \, C_i^2 \exp (-E_g/RT) \qquad (3),$$

where A_2 is a constant, C_i is the initial epoxide concentration, E_g is the

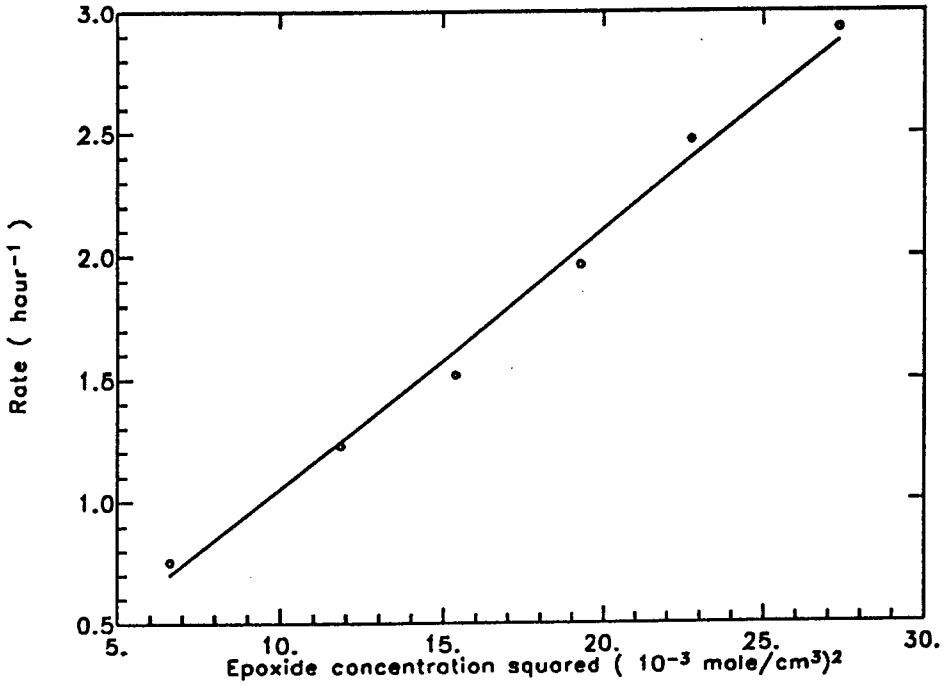

Figure 2. Dependence of the reaction rate on concentration of epoxide for epoxide-amine resin system.

activation energy, R is the universal gas constant and T is the absolute temperature. The functional dependence of K on reactant concentration and temperature can be found from the acoustically measured degree of cure and a comparison made with equation (3).

Different mixtures of the reactants are prepared to test the dependence of K on the concentration. The rates as measured acoustically for these mixtures are shown in figure 2 plotted against the initial epoxide concentration squared. A line has been drawn to facilitate visualizing the

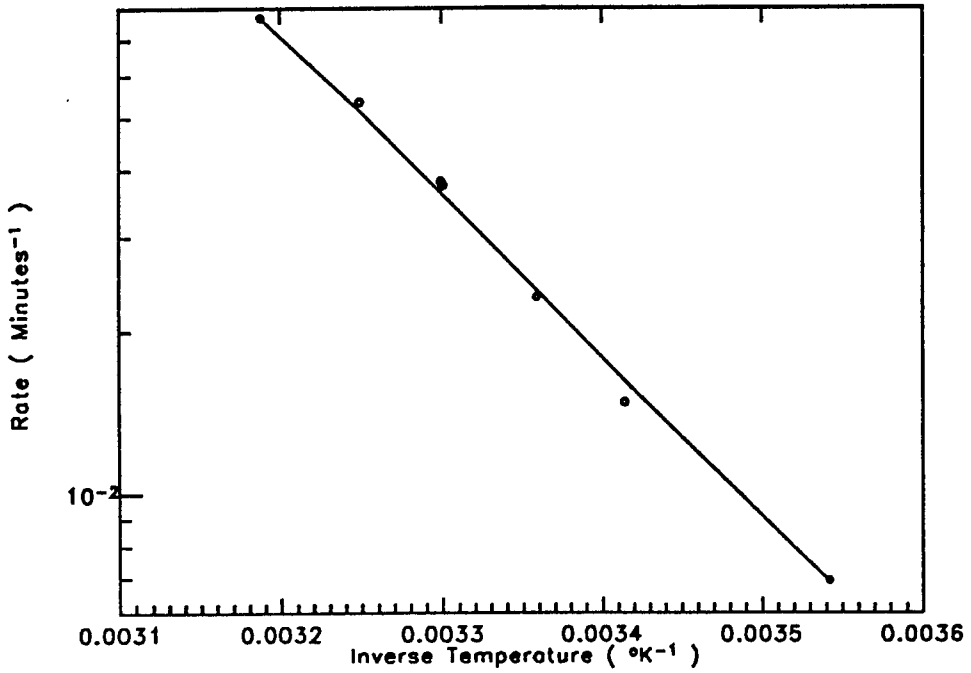

Figure 3. Reaction rate measured as a function of temperature for an epoxide-amine resin system.

linear relationship between the rate and the initial epoxide concentration squared as predicted by equation (3). As can be seen from this figure there is good agreement between the measured values of K and reaction kinetics.

The dependence of the reaction rate on temperature is also given by equation (3). The longitudinal velocity was measured at several different temperatures and, K was calculated using the method described above. For ease of comparison with theory, the log of the rate is plotted against the inverse of the absolute temperature in figure 3. With the data, a linear least squares fit of the data is plotted. As can be seen from figure 4, there is good agreement between the temperature dependence of K and the temperature dependence predicted by reaction kinetics. The slope of the linear least squares fit can also be used to calculate the activation energy of the system. We find an activation energy of 13.9 kcal/mole, which is well within the range expected for cure of aliphatic and aromatic amines/epoxy systems.

PHYSICAL MODELS AND THERMAL NDE IN COMPOSITES

Another technology that has seen rapid and dramatic changes is the field of thermal NDE. Ever since the availability of infrared cameras, it has been easy to use thermal energy to qualify physical situations. One of the early thermal demostrations was an image of an empty theater shortly after a show. Each seat stored thermal information so that one could identify which seats had been occupied during the show. Such simple applications led many researchers to explore this straight-forward technology. The easy experiments were done, and thermal NDE was placed on a shelf for appropriate applications.

However, instead of using thermal information by the seat of the pants as was done in the theater experiment, the current activity is similar to that in X-Ray at the time tomography was discovered. Physical models of heat diffusion are being developed using the heat equation, finite element analysis, and other computational tools. The models are used to invert the data and predict internal structure properties.

Experimental Results - Thermal NDE

In general, the use of thermal energy for quantitative NDE requires extremely tight contol of all the experimental variables. We assume that the sample is at a uniform initial temperature, is then exposed to an initial heating period and then is observed as a function of time during the cooling/diffusion time. The parameters that are involved in the measurement include the energy (assumed optical) focused onto the sample , the sample's absorption coeficient, the sample geometry, diffusivity, and emissivity, and the thermal properties of the medium in which the test is performed.

Simplifing assumptions are usually appropriate for specific examinations. We assume that the input heating profile is a line produced by scanning a laser beam on the sample surface. For thin plate samples [5], such that the temperature profile through the thickness is uniform after heating, one need only solve a one dimensional heat equation of the form

$$T(x,t) = (4\pi kt)^{-1/2} e^{-bt} \int_{-\infty}^{\infty} T(x',0) \exp\left(-\frac{(x-x')^2}{(4kt)}\right) dx' \quad (5)$$

where b is the fractional heat loss rate at the plate surface and k is the diffusivity of the plate. In the general analysis, the measured temperature profile just after the pulse, is used as the initial condition, T(x',0), for the model. Usually, the temperature profile starts as a gaussian, further simplifying the problem so that

$$T(x,t) = T_0 e^{-x^2/a^2} \quad (6)$$

where T_0 is the peak amplitude of the initial heating profile and a is its half width. The analysis shows that if the initial heating profile is of the form of a gaussian, then the time evolution remains a gaussian simply spreading in time such that the half width follows the relationship $c^2 = a^2 + 4kt$. Thus for this case, the square of the half width is used to directly calculate the diffusivity. A comparison of the two diffusivity calculations is given in Table 1.

A specific application of this approach is to determine the fiber orientation of graphite/epoxy composites. Again a heating line is produced on the sample with a scanned laser. The diffusivity is determined as before, but this time as a function of angle with respect to the fibers in

Table 1. Comparison of in-plane diffusivity measurements made in various materials using the two analysis techniques described in the text.

	Stainless Steel	Brass	Aluminum (2024-T6)	Graphite-Epoxy 10[0]
Literature Values	0.042	0.337	0.518	N/A
General Analysis Results				
Mean Diffusivity (cgs)	0.0417	0.350	0.581	0.0326
Standard Deviation	0.0004	0.005	0.011	0.0006
Mean Loss Rate (%/s)	1.04	13.73	19.71	1.39
Standard Deviation	0.08	0.88	0.94	0.07
Chi-Square Range	1.10 -1.55	1.56 - 2.99	8.9 - 16.3	0.59 - 1.07
Gaussian Analysis Results				
Mean Diffusivity (cgs)	0.0413	0.374	0.577	0.0356
Standard Deviation	0.0005	0.004	0.014	0.0004
Mean Loss Rate (%/s)	0.72	10.31	13.91	0.92
Standard Deviation	0.04	0.46	0.55	0.04
Correlation Range	.99967 -.99975	.99865 -.99973	.99790 -.99928	.99912 -.99996

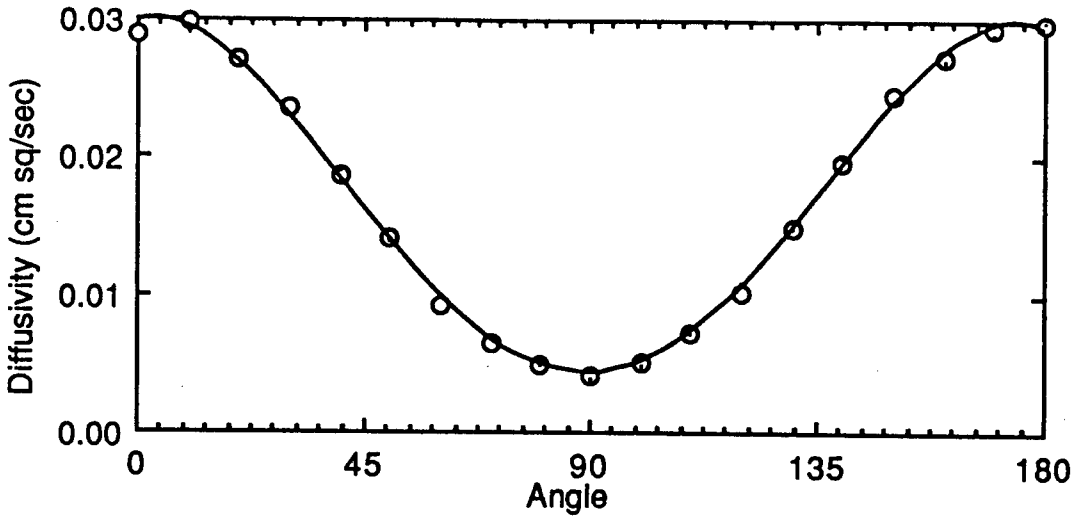

Figure 4. Comparison between measured diffusivity as a function of sample orientation and a least-squares offset cosine curve. The sample is a thin plate of unidirectional graphite-epoxy. The maximum and minumum values of measured diffusivity give the principal values of the two-dimensional diffusivity tensor, while the angle corresponding to the maximum gives the direction of the principal axis, here aligned with the graphite fiber axis.

the composite sample. The diffusivity is much greater along the carbon fibers than in the matrix, resulting in a sinusoidal variation of the measured diffusivity as the heating line is rotated. Figure 4 shows the diffusivity variation as well as its offset providing quantitative vector analysis of the thermal properties of the composite material under examination.

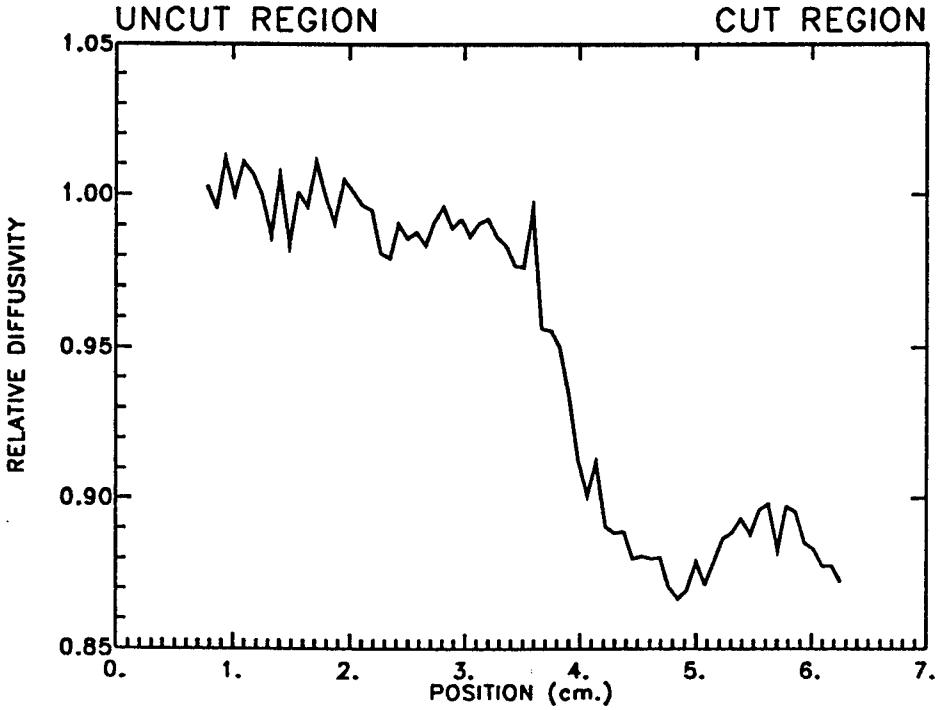

Figure 5. Indication of cut fiber damage in graphite-epoxy sample using diffusivity measurements. In this example, the step change in underlying diffusivity values clearly delineates the region in which fibers were deliberately broken by cutting.scan, clearly revealing the drop in thermal diffusion caused by the internal damage.

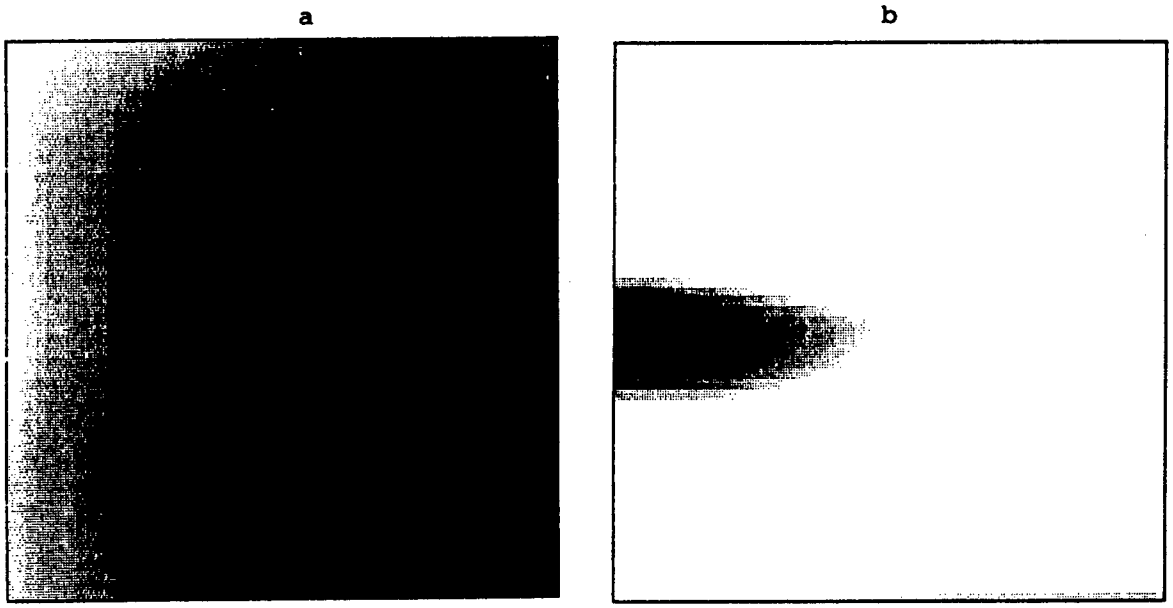

Figure 6. Improvement in contrast obtained by processing thermographic data with the Winfree filter. a. Thermographic data averaged over 100 frames with contrast expansion. b. Same data as a following filtering and application of threshold level.

Another application of thermal NDE, is to determine the internal damage in a composite caused, for example, by impact damage. Since fibers provide most of the tensile strength of these materials, it is important to characterize broken fiber damage. A composite sample was fabricated with internal broken fibers. The fibers were cut with a razor prior to curing so there would be no damage to the matrix. After curing, the sample was scanned with the diffusivity system to see if the broken fibers could be detected. Figure 5 shows the data from that scan, clearly revealing the drop in thermal diffusion caused by the internal damage.

An improved two-dimensional physical model has been developed which permits delaminations in samples of Space Shuttle Solid Rocket Motors (SRM) to be detected in thermograms even in the presence of edge cooling effects and uneven heating [6]. The geometry of the SRM consists of an outer steel skin, followed by a series of insulation layers and then rubber like fuel. By considering heat flow into the insulation and fuel layer behind the steel skin to be that of a distributed sink, a convolution filter was designed which discriminated anomalies in the sink, associated with delaminations, from variations in observed temperature associated with heat flow within the steel skin. The filter design resulted from a physical model analysis of the SRM which underscored the importance of flux imaging. This filter is the central core in in the analysis shown in Figure 6. Figure 6a shows a thermogram of a test sample with the Solid Rocket Motor geometry of 0.5 inches of steel painted on the face and adhesively bonded to 0.1 inch of insulation and several inches of inert propellant. A delamination was formed on the left side of the sample by including a triangular "pull-tab" in the assembly and withdrawing it following the cure cycle. The thermogram was obtained during sample cooling subsequent to applying uniform heating to the steel surface. The temperature distribution in the thermogram is dominated by remnants of uneven heating and uneven cooling caused by sample edge effects. The same data are shown in Figure 6b following processing with the filter. The dark, triangular shape prominant in this figure delineate the edges of the delamination closely. Thus, the primary effect of the filtering operation has been to raise the desired signal above the unwanted noise.

CONCLUSIONS

Project managers want to see a new generation of NDE that will help them make cost effective and safe decisions The present-day technology, as practiced, does not fully achieve that goal. Often, in a readiness review, NDE raises questions, rather than provides answers. There are exciting steps taking place in many labs today in the direction of making NDE more quantitative. A major bridge to be built in the technology, is one that links the physical nondestructive property measurements with the engineering requirements. That bridge will be built by a multidiscipline team that brings together such professions as physicists, materials scientists, chemists, computational scientists and electrical engineers. When that bridge is built, it will provide a path joining the fields of measurement science, NDE, finite element analysis and fracture / failure mechanics. It will result in a safer, more cost effective tomorrow.

REFERENCES

1. R. Rao, J. Chem. Phys. 9, 682 (1941).

2. D. W. Van Krevelen, Properties of Polymers, Correlations with Chemical Structure, (Elsevier, Amsterdam, 1972).

3. B. Hartman and G. F Lee, J. Appl. Phys. 51, 5140 (1980).

4. W. P. Winfree, F.R. Parker, Review Of Progress In Quantitative Nondestructive Evaluation, 5B, ed D. O. Thompson and D. E. Chimenti, 1055, (Plenum, New York, 1986)

5. C. S. Welch, D. M. Heath and W. P. Winfree, J. Appl. Phys. 61, 895 (1987).

6. W. P. Winfree, C. S. Welch, P. H. James, and E. Cramer, 88 Review Of Progress In Quantitative Nondestructive Evaluation, to be published

II. SRM (SOLID ROCKET MOTOR)

83/1-2/2/0

Advanced NDE for Solid Rocket Motors

Joseph S. Heyman

NASA, Langley Research Center
Hampton, Virginia 23665

ABSTRACT

Recent NASA-LaRC advances in NDE for Solid Rocket Motors (SRM) will be discussed. The synthesis of these technologies was initiated through the development of physical models of the SRM for the type of probing energy used to investigate the integrity of the motors. Both ultrasonic and thermal energy models were used to optimize tests of buried SRM delaminations. In each case, the models resulted in experimental techniques that were improvements over standard methodology.

INTRODUCTION

The importance of quantitative NDE to mission assurance is impacting many SRM programs today. It is not enough to "NDE" an item—one must understand critical failure mechanisms in a given design and test for system integrity based on a thorough knowledge of the system in question. The implication of that statement changes the nature of NDE in a significant fashion. In one bold stroke, NDE must take a parallel position to engineering designs such as stress, thermal, fatigue and fracture, etc. As an example, use of finite element analysis has allowed design engineers to "fly" a structure on

a computer without building a single element to assess a particular concept. Of course, promising models require verification and experimental testing. Today, NDE must be raised to a similar professional level.

A first approach to a new design should include design for inspection with the same dedication as shown by the engineers to design for intended stresses. That goal, unfortunately, has not been achieved on a broad scale. One of the reasons NDE has not been elevted to the parallel professions, has been the annecdotal history of our trade. We have all participated in discussions where a statement of NDE is made such as "that part looks OK!" In contrast, one may ask a designed what stress level a part has been designed for, and get a numerical answer. For NDE to be accepted as one of the design sciences, it must become a measurement science.

In this paper, we present two applications for NDE that were developed from models of the propagation of energy in complex structures representing SRM geometries. In each case, a normal approach to the NDE application did not reveal the required information and would have resulted in establishing a standard that did not represent the best information available from an inspection. A more careful analysis of the physical models, dictated technologies that improved the ultimate resolution and evaluation of the observed measurements.

ULTRASONIC EVALUATION OF BURIED SRM BONDLINES

A conventional application of ultrasonics to the SRM involves using broadband pulse-echo to insonify the material. Normal analysis of the returning signals consists of setting a time gate of interest and a signal threshold level established from test parts with defects. Such tests

were made on samples simulating the Shuttle SRM internal bondlines between the fuel, liner, insulation, bond layer and steel case. Case/insulation disbonds were easily detected while disbonds between the liner and the fuel were difficult to detect with certainty. Multiple ringing of the ultrasonic pulse in the low-loss steel case obscured energy coming from the buried bonds.

An ultrasonic numerical model of the SRM structure was developed[1] to evaluate performance of unconventional approaches. The model insonified the structure with a long tone burst[2] plane wave normal to the steel surface. A transmission line impedance was calculated including the effects of each reflecting interface in the structure. The resulting reflected wave consists of the superposition of all reflected waves and was examined as a function of frequency. The values used for the model are shown in Table 1.

Figure 1 shows the calculated spectral response of the SRM viewed from the steel case side as a function of frequency. The two curves represent a numerical evaluation of a good bond and an unbond, between the fuel and the liner. The figure shows small differences between the two bond conditions with the average difference decreasing with frequency. The decrease is caused by the high attenuation of the insulation and liner material preventing ultrasonic energy from penetrating into the

TABLE 1- Ultrasonic values used in the model.

Material	Velocity m/sec	Density kg/m^3	Attenuation nepers/m
Steel	6080	7600	0
Insulation	1810	1218	$1.11 \times 10^{-5} f^{1.225}$
Liner	1500	999	$23.0 f^0$
Fuel	2170	1503	$213. f^0$

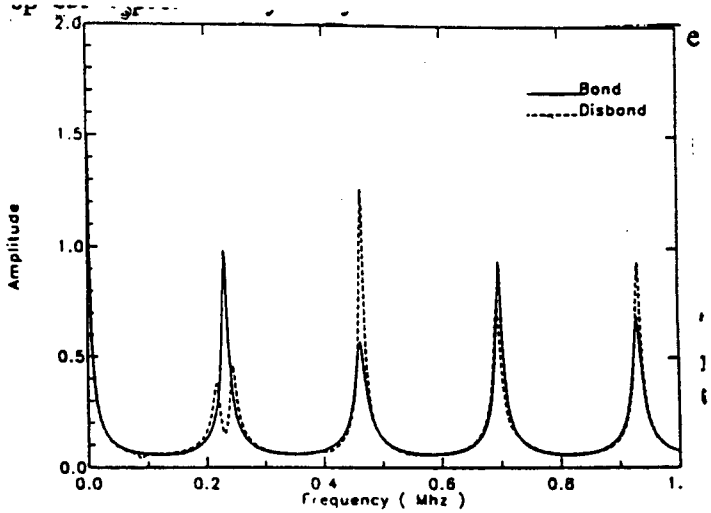

FIGURE 1- Calculated spectral response of the SRM for two conditions representing good bond and lack of bond between the fuel and the liner.

deeper structures. The difference between the two curves depends strongly on frequency, with maximum contrast (difference between the bond and unbond condition) occurring at resonance peaks spaced approximately every 240 kHz.

The difficulty in examining the deeper bondline with pulse-echo is now clear. Pulse-echo uses a narrow pulse which comprises many frequencies. Only those frequencies which lie in the narrow range of a mechanical resonance contribute to the measurement of the disbond. The other frequencies represent background noise through which the weaker bondline signals must be discriminated.

The results of the numerical calculations point to the benefit of using a narrow band of ultrasonic frequencies near the composite resonance of the structure involved.

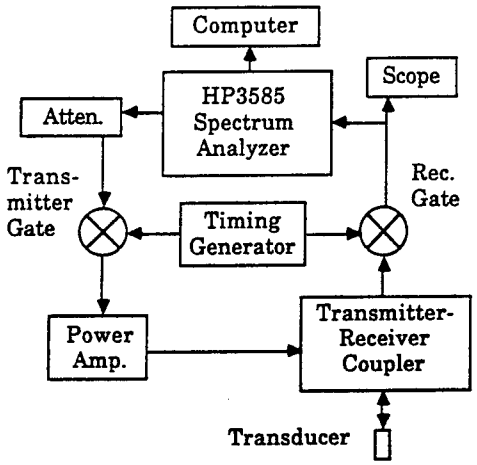

FIGURE 2- Block diagram of the experimental test set-up used to obtain ultrasonic spectral information on the SRM.

The resonance of choice would be the one near 0.2 MHz, where the bonded signal is nearly twice the unbonded signal, or near 0.5 MHz where the opposite is true. To verify the model, we built a sample consisting of a flat steel plate with multiple layers of a rubber material similiar to the insulation/liner followed by either an unbond (an air gap) or a bond (coupling directly to water). The thicknesses were choosen to simulate the SRM itself.

A block diagram of the experimental test is shown in fig. 2. A spectrum analyzer measured the response of the sample. The output from a tracking generator in the spectrum analyzer was gated (40 microseconds) and amplified to drive the insonifying 0.5 MHz, 3.2 cm diameter flat transducer which was coupled to the sample through a 70 microseconds water delay line. The reflected wave was time gated into the spectrum analyzer at a time that eliminated the reflection interface between the steel and the

water delay line. The spectral response of the sample is shown in fig. 3 which is in excellent agreement with the calculated response.

A more realistic sample of the SRM was fabricated by Morton Thiokol using the same materials, processes and thickness as are used in the SRM. The sample was 30.5 cm (12 in.) square with the 3.66 m diameter (12 feet) radius of curvature as found in the motor steel case. A brass wedge shaped shim was cured into the sample at the liner/fuel interface. The wedge extended from the sample and was pulled after curing to create a disbond in the desired location. The shape of the sample is shown in fig. 4.

An image of the sample was made using the spectrum analyzer system scanning the sample with a step size of 0.2 cm with the image area 8 × 12 cm. A similar scan was made using a conventional pulse-echo system gating the signal for the liner/fuel interface using peak detection and various threshold levels. The conventional scan could not resolve the disbond above background variations in the signal. The image obtained with the tone burst

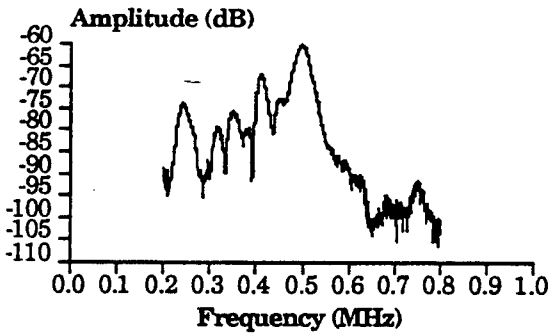

FIGURE 3- Spectral response of the SRM sample showing the computation model resonance peaks. Detection of internal disbonds is optimized using ultrasonic frequencies corresponding to the high contrast indicated in fig. 1.

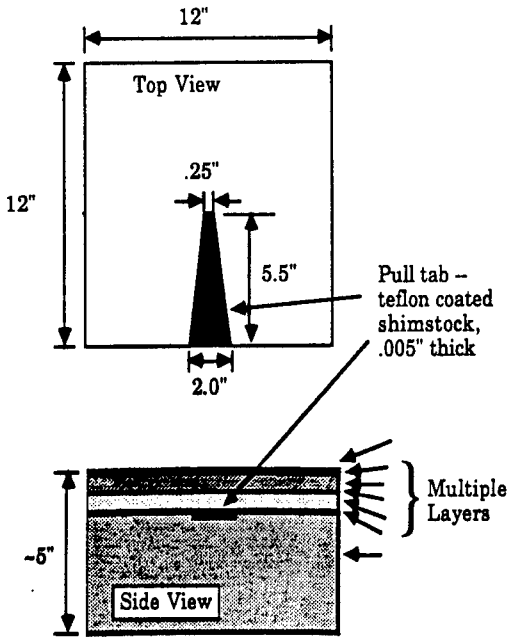

FIGURE 4- SRM samples with built-in disponds to simulate possible manufacturing defects. Disbonds were placed in various bondlines to evaluate their detection.

system of fig. 2 clearly resolved the wedge delamination shown in fig. 5.

The improved signal to noise was made possible by using the physical model information. A practical scan system is currently under development at LaRC to lock an ultrasonic system to the SRM resonance peak and track any changes in that frequency caused by variations in the layered structure. The returning signal strength is also monitored, forming a pair of measurements representing both amplitude and phase information for improved reliability.

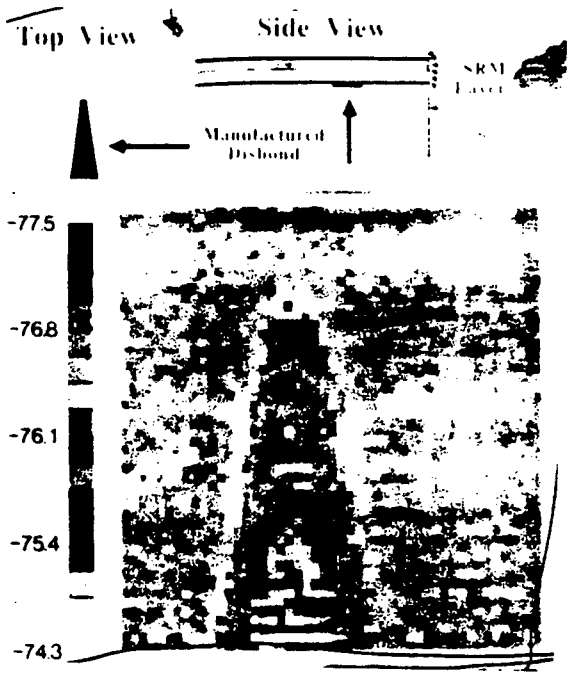

FIGURE 5- Grey scale ultrasonic image of reflection amplitude at the resonance frequency (240 kHz) of the SRM motor. Image shows the wedge disbond between the fuel and the liner.

THERMAL EVALUATION OF BURIED SRM BONDLINES

Although ultrasonics is a logical approach to examine the SRM, it is not the only technology appropriate for the motor. Different, complimentary techniques add significant reliability factors to the inspection. In addition, for thermal energy, there may be significant cost benefits for large area rapid scanning. Traditional thermal NDE con-

sists of surface heating while measuring the temperature radiometrically with an IR camera. A near surface disbond would appear as a transient hot spot.

We have developed OPTITHERMS (OPTIcal THermal InfraRed Measurement System),[3] a thermal NDE system composed of a scanned modulated laser, an IR camera, an image frame grabber, and most important, a thermal model. Similar to ultrasonics, the model is used to interpret the data and to point the way to improved signal-to-noise measurements.

The thermal dynamics are simulated using an equivilent circuit analysis where voltage is temperature difference, resistance is related to diffusion (thermal impedance) and capacitance to heat capacity. The different layers of the motor are represented by a series/parallel circuit of the proper elements with values determined to map the thermal diffusion physics into the equivalent electrical analogues.[4] Figure 6 shows the general model with the

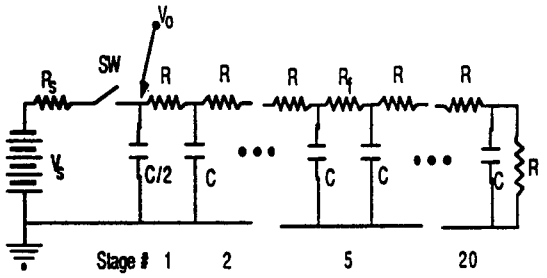

FIGURE 6- Equivalent electrical model of the thermal properties of the SRM in the inhibitor region. The switch/battery with internal resistance R_s represents the thermal source while R_f is a flaw. The rest of the model corresponds to internal elements in the SRM with V_0 expressing the surface temperature. The switch closes at time = 0.

switch/battery representing the input heat source with its source impedance and thermal difference.

The results of the analysis of this straightforward model show that the best signal-to-noise one can achieve is equal to the highest contrast defined as the maximum difference in voltages, V_0, for the case with and without a flaw. The time evoluation of that voltage difference (difference in surface temperature) is shown in fig. 7 for two cases of surface impedance.

The curve labled "source pulsed" represents heating/cooling the inhibitor region of the SRM which is in contact

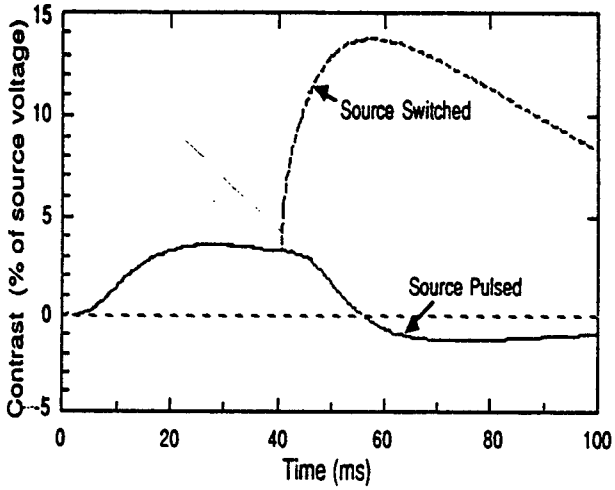

FIGURE 7- Computational results from the model of fig. 6. The results show the effect of the water bath heating and acting as a low surface impedance. Source pulsed corresponds to alternate flow of hot and cold water in the bath while source switched corresponds to removing the hot bath after the soak time. The contrast is the surface temperature difference with and without a flaw.

with a liner and the fuel. The heat is applied with a hot water bath in contact with the sample while the temperature is monitored on the sample under the water bath. The curve labled "source switched" represents opening the switch (SW) thus changing the surface impedance. Such a heating condition is simulated by placing the hot water bath in contact with the sample, and then lifting that bath off the sample at 30 seconds time (40 milliseconds in the electrical model). The increase in contrast for the water bath technique shows that the source imped-

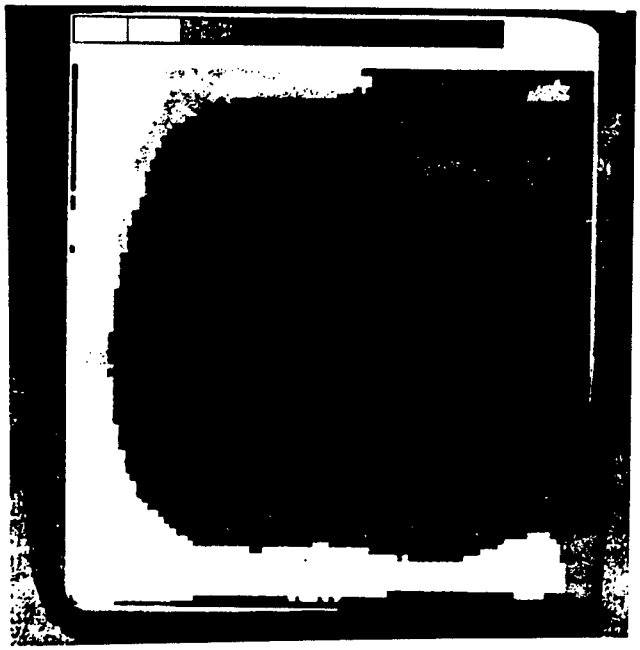

FIGURE 8a- Surface temperature profile of the SRM steel case after uniform surface heating followed by a cooling time period.

ance, related to the water contact with the sample, can play a significant role in signal-to-noise optimization.

A more complex analysis of the thermal system involves the determination of equivalent thermal sources and sinks that effect the flow of thermal energy. This is similar to saying that we do not want to measure voltages since voltage differences may be small. Instead, we wish to measure current flow into or out of the sample. An example of the power of this approach is shown in fig. 8a where the image shows the temperature of the surface

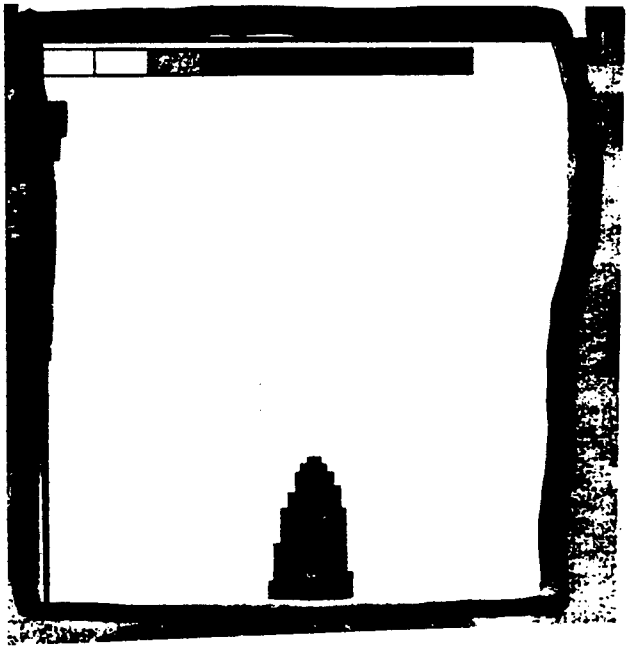

FIGURE 8b- Thermal NDE image showing the wedge disbond. The image is the second spacial derivative of the temperature and represents the flaw as a thermal source.

of the SRM sample. Note that the main visible feature is the effect of heat loss at the edges producing a central peak in temperature with edge cooling dominating the image.

Figure 8b, on the other hand, was obtained from the second spacial derivative of this image to extract thermal sources. The wedge shaped delamination clearly stands out from the background. A delamination appears as a heat source since it can provide more energy to the surface than the surrounding material. By imaging the processed data as a heat source, we are able to differentiate delaminations from other processes in the sample thus improving our ability to interpret the image.

CONCLUSION

The analysis of ultrasonic and thermal physical models of the SRM have resulted in test proceedures with improved buried defect detectability for the SRM bondlines. In each case, the normal NDE test would not have been able to characterize or locate the defect in the tested structure. Many labs are now applying similar physical analysis to raise the professional level of NDE to parallel other engineering and scientific disciplines.

It is important that program management embrace these new thrusts and include NDE considerations at project initiation. "Design for inspection" should be part of any criteria spelled out in contract specifications with the same emphasis as is placed on "'design for stress." The significance of these changes will be improved safety, reliability, adherence to schedule, and cost savings. A side benefit will be the assurance of project managers that what is measured, is quantifiable—or what you see is what you get!

References

1. Madaras, Eric I., Winfree, William P., Smith, B. T. and Heyman, Joseph S., "Detection of Bondline Delaminations in Multilayer Structures wth Lossy Components," *1987 IEEE Ultrasonics Symposium Proceedings*, 1987 (in publication).
2. Cantrell, John H.; Heyman, Joseph S.: "Ultrasonic Spectrum Analysis Using Frequency-Tracked Gated RF Pulses," Acoust. Soc. Am. *67*, 1623–1628 (1980)
3. Heath, D. M., Welch, C. S., Winfree, W. P., Heyman, J. S. and Miller, W. E., "Quantitative Thermal Diffusivity Measurements of Composites," *Review of Progress in Quantitative Nondestructive Evaluation*, Vol 5B, D. O. Thompson and Dale E. Chimenti, eds, 1986, pp 1125–1132.
4. Welch, C. S. "Contrast Enhancement Through Source Impedance Control In Thermal NDE," *Review of Progress in Quantitative Nondestructive Evaluation*, Williamsburg, VA 1987, (in press).

NDE OF SPACE SHUTTLE SOLID ROCKET MOTOR FIELD JOINT

By

Patrick H. Johnston

NASA Langley Research Center
Mail Stop 231
Hampton, Virginia 23665

Presented at the 1987 IEEE Ultrasonics Symposium
Denver, Colorado
October 14-16, 1987

NDE OF SPACE SHUTTLE SOLID ROCKET MOTOR FIELD JOINT

Patrick H. Johnston

NASA Langley Research Center
Hampton, Virginia 23665

ABSTRACT

One of the most critical areas for inspection in the Space Shuttle Solid Rocket Motors is the bond between the steel case and rubber insulation in the region of the field joints. The tang-and-clevis geometry of the field joints is sufficiently complex to prohibit the use of resonance-based techniques. One approach we are investigating is to interrogate the steel-insulation bondline in the tang and clevis regions using surface-travelling waves. A low-frequency contact surface wave transmitting array transducer is under development at our laboratory for this purpose. The array is placed in acoustic contact with the steel and surface waves are launched on the inside surface of the clevis leg which propagate along the steel-insulation interface. As these surface waves propagate along the bonded surface, the magnitude of the ultrasonic energy leaking into the steel is monitored on the outer surface of the case. Our working hypothesis is that the magnitude of energy received at the outer surface of the case is dependent upon the integrity of the case-insulation bond, with less attenuation for propagation along a disbond due to imperfect acoustic coupling between the steel and rubber. Measurements on test specimens indicate a linear relationship between received signal amplitude and the length of good bond between the transmitter and receiver, suggesting the validity of this working hypothesis.

INTRODUCTION

The Solid Rocket Motors (SRM) for the Space Shuttle launch system are constructed of several segments stacked together and joined prior to launch. As shown in Fig. 1, a segment is 12.2 feet in diameter and 27 feet in length. Each segment consists of a cylindrical shell of steel lined with a layer of silica-filled neobutyl rubber insulation (NBR) and filled to a hollow central bore four feet in diameter with solid rocket propellant.

The segments are joined together via interlocking tang-and-clevis joints, called field joints, and sealed with 177 one-inch diameter steel pins spaced at three-inch intervals around the circumference of the joint. Cross-sectional views of the geometry of the field joints in the stacked and unstacked configurations are presented in Fig. 2. Grooves are provided to accommodate rubber O-rings for sealing the joint, and holes for the steel pins are drilled through the outer clevis leg, the tang, and partially through the inner clevis leg.

In order to assure the safety and reliability of the SRM, we are investigating methods to nondestructively evaluate the integrity of the bonded interface between the steel case and the NBR insulation. Researchers at our laboratory have developed resonance-based methods for evaluating the steel-insulation and the insulation-propellant interfaces of the SRM on the cylindrical sides of the motor segments, where the steel is a uniform one-half inch in thickness and the insulation is of relatively uniform thickness [1,2]. The tang and clevis geometry is sufficiently complex to prohibit the use of these resonance-based techniques except over a very small fraction of the area of the steel-insulation bond in the joint region. In order to interrogate a larger portion of the steel-insulation bond, we have pursued an alternative method based on surface waves propagating on the interface between the insulation and the steel case in the region of the joint.

SURFACE WAVE APPROACH

We have focused to date on examination of the clevis in the unstacked configuration, where direct access is provided to the inside surface of the inner clevis leg, allowing us to launch surface waves directly into the steel-insulation interface. Our approach, shown schematically in Fig. 3, is to launch Rayleigh surface waves on the inner clevis leg which couple to the steel-insulation interface. Because of the disparate acoustic properties of the steel and NBR, the interface wave is leaky, coupling to bulk modes in the steel [3] which may be monitored from the outer surface of the steel case. Further, we expect the attenuation of the interface wave to be dependent upon the condition of the bond along its propagation path. A well-bonded interface represents the condition of maximum coupling of the wave to the lossy insulation, leading to maximum attenuation. In a disbonded region the coupling to the insulation would be diminished, reducing the attenuation and leading to an increased signal at the receiver.

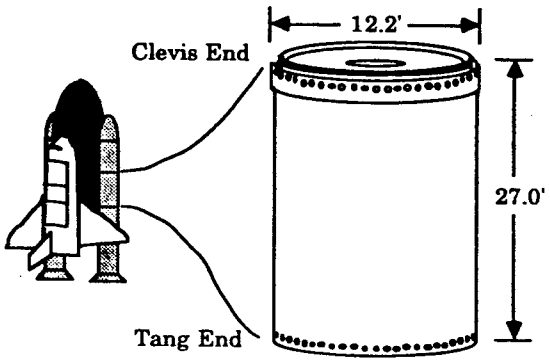

Figure 1. The solid rocket motor (SRM) of the Space Shuttle launch vehicle is made up of several segments, one of which is shown here. Each segment is a cylindrical shell of steel with a lining of silica-filled rubber insulation, filled with solid propellant.

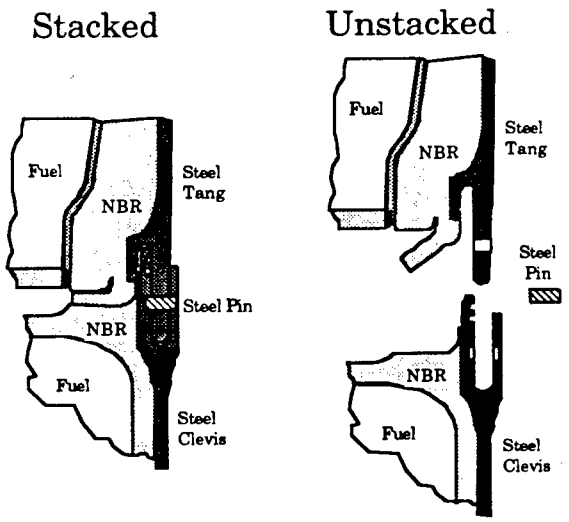

Figure 2. Cross-sectional view of the SRM field joints with segments stacked (left) and unstacked (right). Testing of the bond between the steel case and the neobutyl rubber insulation (NBR) is hampered by the relatively complex geometry of the tang and clevis. Our efforts have focused on inspection of the clevis in the unstacked configuration, where access is allowed to the inside of the inner clevis leg.

SURFACE WAVE ARRAY TRANSMITTER

One conventional method for producing surface waves is the use of an angle-block transducer. This approach sends a longitudinal wave beam incident upon the angle-block-steel interface at the Rayleigh angle. However, the beam from a practical transducer is composed of the superposition of an angular spectrum of plane waves, most of which would couple to surface waves at the interface. Some fraction of the angular spectrum of plane waves are incident at angles shallower than the critical angle, and thus couple to bulk modes in the steel, propagating away from the surface. When applied to the inside leg of the SRM clevis, these waves would be available to scatter from internal structures such as O-ring grooves or flat-bottomed pin holes. Because bulk waves travel at higher speeds than the leaky interface waves, these waves may overtake the interesting leaky interface waves and confuse the received signal.

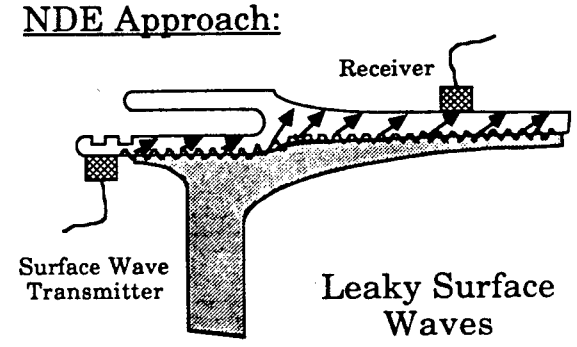

Figure 3. Our measurement approach is based on leaky surface waves propagating along the steel-insulation interface. Rayleigh waves are launched on the inner steel surface of the clevis. These couple into a wave on the steel-insulation interface, which leaks energy into bulk modes in the steel due to the mismatch of acoustic properties of the two materials. The magnitude of the leaky waves should depend upon the condition of the steel-insulation bond along its path.

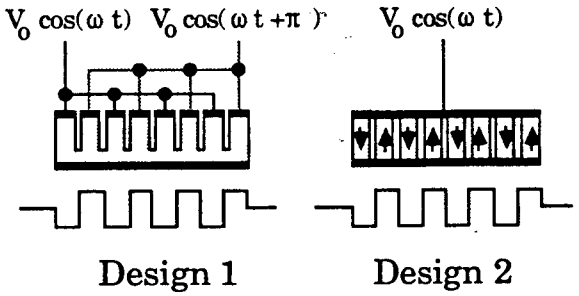

Figure 4. Two designs for a contact surface wave transducer which is intended to maximize the ratio of energy coupled into surface waves to that coupled into bulk waves. Arranging the elements to have spacing equal to one-half the wavelength of Rayleigh waves and driving the elements 180 degrees out of phase with their neighbors, an acoustic field is generated which drives Rayleigh waves in both directions on the face of the steel.

Ideally we would like to maximize the fraction of applied ultrasonic energy initially injected into the surface mode propagating on the steel-insulation interface and to reduce or eliminate any initial bulk modes. We have designed a low-frequency contact surface wave array transducer in an attempt to achieve this goal. Our initial design is designated as Design 1 in Fig. 4. A PZT longitudinal disk transducer was cut into a rectangular shape and saw cuts were made three-fourths of the way through the thickness as shown in the cross-sectional view in the figure. The spacing of the cuts was equal to one half wavelength of a 500 kHz Rayleigh wave on steel. In operation, the common front face of the array is coupled to the steel surface and each element of the transducer is driven with a 500 kHz signal which is 180° out of phase with its neighbors. Thus, when one element expands, its neighbors contract, and vice versa. The resulting acoustic field at the surface of the steel is approximated by the square wave sketched in the figure. Because this spatially-varying field matches the Rayleigh wavelength, it drives a Rayleigh surface wave in both directions along the steel surface.

In addition, because the array resembles a truncated acoustic diffraction grating, bulk modes will also be generated at very specific angles determined by the periodicity of the array and the bulk wave speeds. However, we believe that careful matching of the element spacing with the Rayleigh wavelength will result in maximum coupling of energy into the surface mode and minimal bulk wave generation.

In a variation of this design, designated as Design 2 in Fig. 4, the saw cuts are made completely through the PZT plate, and every other array element is physically inverted so that the polarization direction of the elements alternates across the array. Common front and back electrodes allow a single signal source to drive the array, and the elements automatically vibrate 180° out of phase with their neighbors. When in contact with the steel clevis leg, the same acoustic field is produced on the surface of the steel as in Design 1. Simplified electroding

makes this the superior of the two designs.

SAMPLES

Two clevis samples, provided by Morton-Thiokol, Inc., the makers of the SRM, were used in this work. These are sketched in Fig. 5. The upper panel depicts a bare steel clevis sample. This sample is approximately seven inches long and three inches across, including part of a pin hole on each side. This cross-sectional view of the joint clearly shows one of the recessed flat-bottomed pin holes in the inner clevis leg. Because the bottom of these holes comes within one Rayleigh wavelength of the surface of the steel, we anticipate that they could affect the propagation of interface waves on that surface. With pin holes located every three inches around the circumference of the motor segment, such effects would be important to the interpretation of the results of an inspection of the clevis.

A second sample, eight inches wide and nine inches long, is shown in the lower panel of Fig. 5. This specimen was fabricated with a one-half inch thick layer of NBR insulation bonded to the inner surface of the clevis. Two disbonds were fabricated into the sample by laying thin strips of teflon-coated brass shimstock between the steel and the uncured rubber during

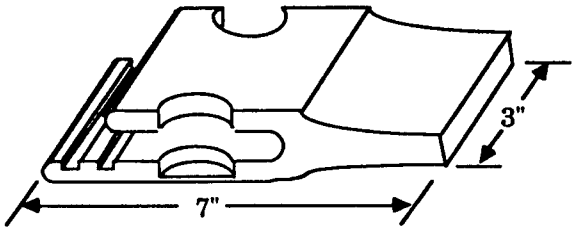

Bare Steel Clevis Sample

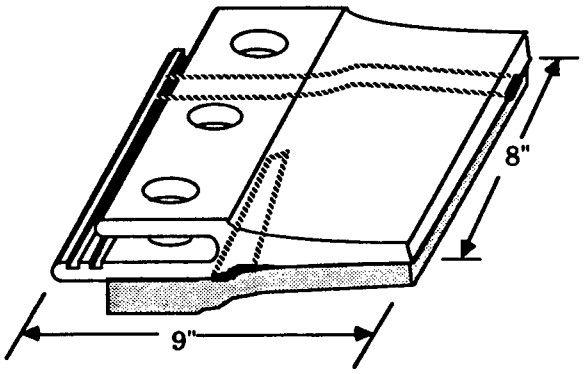

Clevis Sample with NBR and Disbonds

Figure 5. The two clevis samples used in this study. The first sample is a bare steel sample three inches across and seven inches long. The second sample is eight inches across and nine inches long, with NBR insulation bonded to it. Two disbonds were fabricated into this sample, indicated by dashed lines: a one-inch wide disbond running the length of the specimen and a wedge-shaped disbond running across the specimen and varying from two inches at the edge to approximately one-quarter inch at the center of the sample.

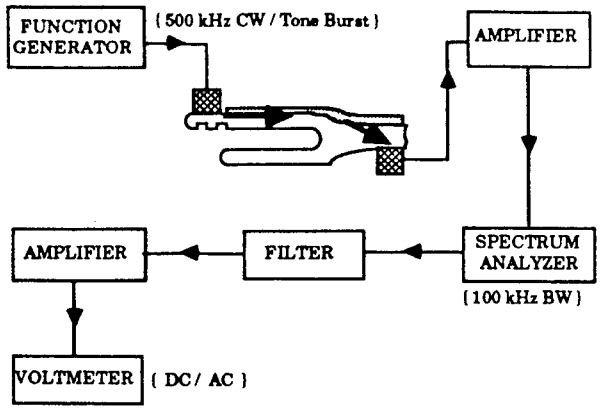

Figure 6. Block diagram of the measurement system employed for this work. A surface wave transmitting transducer is driven with a function generator tuned to 500 kHz. The signals from the receiving transducer are amplified and fed to a spectrum analyzer, tuned to 500 kHz with 100 kHz bandwidth. The vertical output is conditioned and measured with a voltmeter.

sample layup. Following the curing of the rubber, the strips were removed, leaving a disbond in each location. The disbonds are indicated in the figure by dashed lines. One disbond was a one-inch wide strip running the entire length of the specimen directly in line with one of the pin holes. The second disbond was wedge-shaped, approximately two inches wide at the edge of the sample, tapering to one-quarter inch at its tip, approximately four inches across the sample.

MEASUREMENTS

Fig. 6 shows a block diagram of the measurement system employed in this work. A function generator, operating at or near 500 kHz in either continuous or tone burst mode was used to drive either an angle-block transducer or a surface wave array transmitting transducer. A planar 500 kHz longitudinal wave contact transducer was used as receiver. The received signals were amplified and fed to a spectrum analyzer, tuned to the frequency of the transmitted signal with 100 kHz bandwidth. The vertical output of the spectrum analyzer was conditioned using an active filter and an amplifier and measured by a digital voltmeter. For continuous wave transmission, the output of the spectrum analyzer was at DC. For tone burst transmission, the pulse repetition rate and the signal conditioning filter were adjusted to present a 50% duty cycle AC signal to the voltmeter.

The first set of measurements were performed using the bare steel clevis sample. Strips of neoprene rubber, which has similar acoustic properties to NBR, were bonded to the inner clevis surface using double-sided tape to simulate insulation. Surface waves were introduced on the clevis leg, using an array transmitter of Design 1 and tone burst transmission mode, and the acoustic signal was monitored at the opposite end on the outer surface of the sample. The strips of neoprene were then repeatedly removed and replaced as the signal was monitored. The results are plotted in Fig. 7. The signal amplitude is plotted versus the length of rubber bonded to the clevis sample. We note a linear relationship between the signal and the length of bond with a slope of -0.13 V/in, i.e. lower signal for longer bond length. This result is consistent with our assumption that a good steel-insulation bond would attenuate the surface wave.

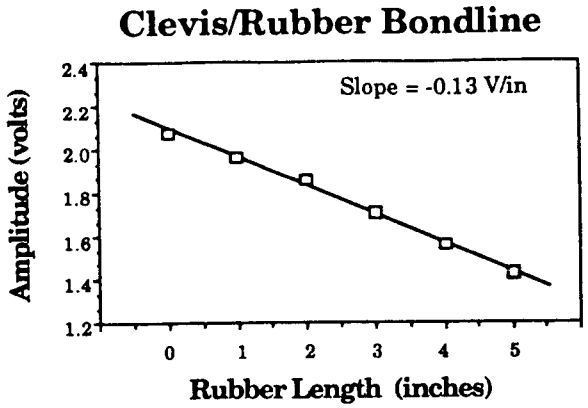

Figure 7. Received signal monitored as strips of neoprene rubber were repeatedly bonded with double-sided tape and removed from the surface of the bare steel clevis sample, yielding a linear decrease in signal with length of rubber bonded to the clevis. These measurements were performed using a Design 1 array transmitter and toneburst mode.

Our second set of measurements was performed on the disbond sample. A transmitter and receiver were positioned in line with each other at opposite ends of the clevis sample, the transmitter on the inner clevis surface and the receiver on the outer surface. The transducers were manually translated by half-centimeter steps across the specimen and measurements of the signal amplitude were obtained at each position. Measurements were made using both an angle-block transducer and a Design 2 contact surface wave array as transmitting transducers.

Fig. 8 summarizes the results of these measurements. The sketch in panel (a) shows the sample from directly above, with the disbonds indicated as shaded regions. The scale of the sketch is matched to the position scales of the data plots below in order to show the relationship of the measurements to the sample.

Panel (b) shows the results of measurements made using continuous wave mode. Data obtained using an angle-block transmitting transducer are plotted as open boxes, while the results for the array are plotted as filled boxes. We note that the angle-block results exhibit a periodic variation with minima centered at the locations of the pin holes and maxima between the holes. We also note a very large peak at the location of the full-length disbond. The presence of this peak is consistent with our proposed model, and with the previous result. There is no conclusive evidence of signal variations due to the wedge disbond.

The results for the array transmitter do not exhibit the periodic variations seen in the angle-block results. Although quite variable, the signals remain relatively constant over to position 16 cm, where a large peak occurs, corresponding to the position of the full-length disbond. As for the angle-block results, there is no firm evidence of effects due to the wedge disbond.

The results plotted in panel (c) of Fig. 8 were obtained using transmitted tonebursts 50 cycles in duration. The open boxes are the data obtained using an angle-block transmitting transducer, and the filled boxes are those obtained using the array. Once again, the angle-block results exhibit a periodic shape with minima corresponding to the positions of the pin holes. A peak is noted at the position of the full-length disbond. While not as large as for CW measurements, it is significantly

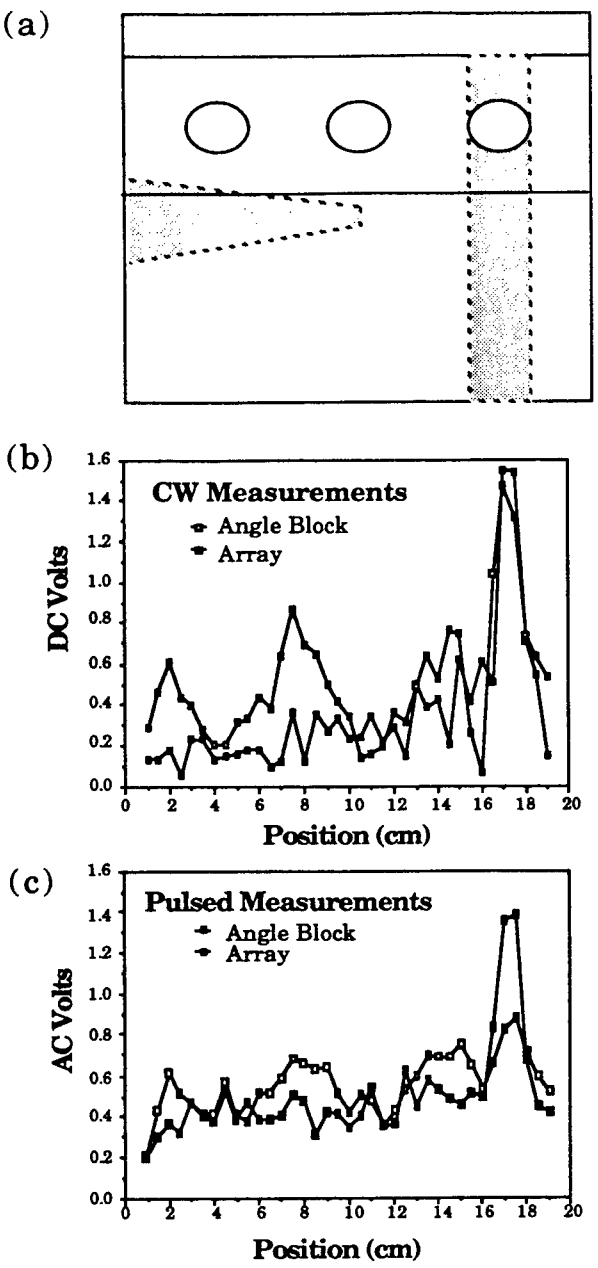

Figure 8. Results obtained from the disbond sample. (a) A sketch of the sample from above, showing the positions of the disbonds as shaded regions. (b) Results of measurements in continuous wave transmit mode. (c) Results obtained using tone burst transmit mode.

above the level of the adjacent minima, which represents the expected normal at this location. There is no indication of the wedge disbond.

The results obtained with the array transmitter do not

exhibit the periodic variation found using the angle-block. The signal varies about a relatively constant value except between positions 16-18 cm, where a large peak occurs, corresponding to the full-length disbond. No evidence is observed of the wedge disbond.

DISCUSSION

Our approach to evaluating the steel-insulation interface on the SRM clevis is based upon the propagation of leaky surface waves along the interface and the interaction of these waves with disbonded regions. In our initial data set, we found that we could launch surface waves on the inside of the clevis leg and receive a signal on the outer surface of the part which varied linearly with the length of bonded rubber. Logical extension of this result to the SRM must be made cautiously, for the following reasons. The presence of a signal in the absence of any bonded rubber shows that the signal could not arise solely from a leaky surface mode resulting from the presence of the rubber. There is a strong possibility that the limited spatial dimension of the specimen led to signals reflected from the edges of the sample that would not be present in an actual motor segment. (This is supported by the fact that the pulsed signals in the larger disbond specimen exhibited less ringing than those in the bare steel sample.) We also recognize that double-sided tape is a weaker, more compliant bond than that formed when NBR is cured against steel. Still, it is encouraging that our measured signal, whatever its source, was simply related to the length of bond.

The results obtained from the disbond sample suggest a number of things. It is encouraging that the full-length disbond was measurable with all four combinations of transmitting transducer and transmit mode, with the peak signal rising to 2 to 8 times the background level. If we take for example the pulsed measurement using the array transmitter, the signal at the full-length disbond rose to 1.4 V compared with a background of about 0.4 V. Assuming a linear relationship between signal magnitude and disbond length, we obtain a sensitivity of 0.125 V/in for this 8-inch disbond. This is surprisingly in agreement with the slope of 0.13 V/in found for the neoprene-clevis measurements, considering the difference in bond type. With this level of sensitivity and the observed level of spatial variation in signal it is not surprising that we do not see the wedge disbond which is only two inches across at maximum.

The spatial fluctuations in our measurements are due in part to errors resulting from manual positioning of the transmitting and receiving transducers using visual markers for placement. A mechanical device is being designed for future measurements to prevent the transmitting and receiving transducers from translating and/or rotating relative to one another, which should substantially reduce the variability. Another possible source of variability is the curvature of the clevis specimens which were cut from an actual motor case and have approximately a six-foot radius of curvature. As a consequence, the flat contact transducers used in this work may have suffered variable coupling to the steel due to bubbles or variable couplant thickness.

Because our array transducers drive surface waves in both the forward and the backward directions, it is possible that the backward wave may reflect from the end of the clevis leg and propagate out into the steel-insulation interface, interfering with the direct forward wave and leading to fluctuations in received signal dependent upon the distance of the array from the end of the clevis leg. Although this phenomenon may be used to advantage by judicious placement of the array to achieve constructive interference between the direct and reflected wave, maximizing the transmitted signal, we are investigating an alternative array design which should launch surface waves only in the forward direction, eliminating the need for such careful placement.

Another significant observation is the presence of periodic spatial variation in the signal derived from an angle-block transmitter which is absent in the data taken with the array transmitter. An explanation consistent with our motivational argument for the array is that the majority of the acoustic energy from the array is coupled into a surface mode which propagates over the pin holes with little effect, while the angle-block transducer launches a larger fraction of energy into bulk modes which interact with the pin holes, reducing the signal reaching the receiving transducer. Although this is an attractive explanation, additional measurements and theoretical analysis will be necessary to ascertain whether this is truly the mechanism underlying these results.

CONCLUSIONS

In this work we investigated the use of surface waves to interrogate the steel-insulation interface on the clevis end of an SRM segment. We observed in test specimens a linear dependence between received signal and bond length. We designed and fabricated a low frequency contact surface wave array transducer to yield maximum coupling of energy into a Rayleigh wave on the steel with minimum coupling to bulk modes. Our measurements suggest that the results obtained using the array transmitter are insensitive to the flat-bottomed pin holes in the inner clevis leg, while the results using an angle-block transmitter show substantial variation apparently due to the pin holes.

We were able to distinguish a disbond condition in which there was no good bond between the transmitting and receiving transducers, but we observed no evidence of a second smaller wedge-shaped disbond located several inches of good bond away from the transmitting transducer. Spatial signal fluctuations due to a number of causes were of sufficient magnitude to mask any effects caused by the disbond. Measures are being considered to correct a number of the known sources of spatial fluctuation for future measurements.

There is still much work to be done to develop these methods for practical application to the SRM. Additional work to be done includes improvement of transducer mounting and positioning, fabrication and measurement of a series of specimens with a variety of disbonds, and development of a more complete understanding of the wave modes being produced in these specimens and their impact on both the transmission and reception of the acoustic signal.

REFERENCES

[1] Madaras, Eric I., William P. Winfree, B.T. Smith, and Joseph S. Heyman, "Detection of Bondline Delaminations in Multilayer Structures with Lossy Components," *Proc. 1987 IEEE Ultrasonics Symposium*, (1987).

[2] Kishoni, Doron, "Removal of Dominant Reverberations from Ultrasonic Time-Records of Layered Material by Digital Predictive Deconvolution," *Proc. 1987 IEEE Ultrasonics Symposium*, (1987).

[3] Phinney, Robert A., "Propagation of Leaking Interface Waves," *Bull. Seism. Soc. Am.* **51**, pp. 527-555, (1961).

THERMOGRAPHIC DETECTION OF DISBONDS

William P. Winfree
MS 231
NASA, Langley Research Center
Hampton, VA 23665

Patricia H. James
Analytical Services & Materials
MS 231
NASA, Langley Research Center
Hampton, VA 23665

ABSTRACT

The presence of disbonds significantly decreases the integrity of many laminated structures used in aerospace applications. A thermographic technique is presented which is able to detect subsurface delamination. The technique uses one of several heat sources (such as hot water, hot air, IR lamps, etc.) to increase the surface temperature of the structure. The subsequent temperature profiles of the surface are detected with an IR camera. A novel spacial filter developed at NASA Langley Research Center eliminates the effects of uneven heating to give clear images of the subsurface delaminations. Defects are detectable in samples as diverse as solid rocket motor samples and laminated wood for wind tunnel blades. Numerical simulations are presented for comparison with experiment results.

INTRODUCTION

With increased cost of payloads there is a need for an increased reliability in delivery systems. The loss of one expensive payload can easily pay for increased cost of inspecting the critical areas of many delivery systems, thereby reducing the average cost of placing a payload in space.

One inspection technique of current interest for inspection of solid rocket motors is thermography.[1] Solid rocket motors can be considered to be laminated structures with an outer layer of steel, backed by a layer of insulation, then with a final thick layer of fuel. Thermography is able to detect disbonds between the steel casing and insulation as well as delaminations between the insulation and fuel by heating the steel layer and observing subsequent temperature profiles with an infrared (IR) imager. For an even application of heat, an elevated temperature profile will appear in the areas of a disbond, as a result of the reduction in heat flow from the surface layer to subsurface layers. Two advantages of the thermographic technique over more conventional ultrasonic techniques are that it can be easily made noncontacting and that large areas can be inspected in a short period of time.

A difficulty of thermographic inspection for disbonds is that it is often difficult to apply heat evenly to a large area. The result often is a temperature profile dominated by the initial heating profile rather than the presence of disbonds. A second difficulty when inspecting a structure such as the solid rocket motor, is the surface layer has a thermal conductivity significantly higher than that of the insulation. For this case the size of the thermal contrast profile resulting from the disbond is much larger than the size of the disbond, and so the image of the disbond does not clearly delineate the region of the disbond.

This paper presents a technique for enhancing the contrast due to a delamination, as well as more clearly delineating the region of the delamination. The technique also reduces the effects of uneven heating. The technique uses a two-dimensional filter convolved with the thermal image. The filter is designed to approximate operating on the temperature images with a Laplacian operator. For prescribed conditions, this operation approximately gives the image of heat flux from the top layer to the subsequent layer. The filtering results in an image which clearly delineates the disbond. Measurements were performed on samples with fabricated defects, and a comparison is presented between the resulting temperature images and the filtered images.

MEASUREMENT SYSTEM

The measurement system consisted of a heating source, which for the cases investigated here were a hot air gun and hot water, and a commercial IR imager. The imager uses a scanned HgCdTe detector cooled by liquid nitrogen and outputs standard video frames. The video images were then input into a image processor, which was capable of digitizing and averaging 30 frames a second. Up to 256 frames were averaged then transferred the averaged signal to a minicomputer for analysis and archival. Average profiles were recorded at time intervals of 15 to 150 seconds after heating until the sample cooled, were the length of the time interval depended on the cooling rate of the samples.

THEORY AND ANALYSIS

A thermogram of structure with a defect has an increase in the temperature over a subsurface disbond. While this temperature increase is a signature of the disbond, an image of the heat flow or flux out the back surface of the first layer gives a much clearer indication of regions where the heat flow has been stopped by a disbond. The heat flow out the back surface of the top layer can be found by considering the equation for heat flow in a thin layer described by the equation

$$\nabla^2 T(x,y,t) - \frac{F(x,y,t)}{wK} = \frac{1}{\kappa}\frac{\partial T(x,y,t)}{\partial t} \quad (1),$$

where $F(x,y,t)$ is the flux into the second material, κ is the thermal diffusivity of the material, w is the thickness of the layer and K is the thermal conductivity of the material. If the diffusivity of the backing material is significantly lower than that of the first layer (which is the case for a solid rocket motor), the flux quickly becomes nearly constant in time, and Equation (1) reduces to

$$\nabla^2 T(x,y,t) - \frac{F(x,y)}{wK} = \frac{1}{\kappa}\frac{\partial T(x,y,t)}{\partial t} \quad (2).$$

The solution to Equation 2 can be divided into two parts, a dynamic part $T_d(x,y,t)$ and a static solution $T_s(x,y)$, such that

$$\nabla^2 T_d(x,y,t) = \frac{1}{\kappa}\frac{\partial T_d(x,y,t)}{\partial t} \quad (3)$$

and

$$\nabla^2 T_s(x,y) = \frac{F(x,y)}{wK} \quad (4).$$

For $T_d(x,y,t)$, it can be shown with Fourier analysis that temperature fluctuations with a characteristic length of L will decay over a time on the order of $L^2/(4\kappa\pi^2)$, leaving a temperature profile dominated by the static contribution to the solution at that characteristic size. Thus, for a delamination of size L, if one waits for a time greater than $L^2/(4\kappa\pi^2)$, the local temperature distribution then is dominated by the flux variations caused by the delamination, and the Laplacian of the local temperature distribution (Eq. 4) gives an image of the flux variation out of the plate. If the delamination region is clearly delineated by the flux pattern, then it is clearly delineated in the Laplacian of the temperature profile.

To approximate the Laplacian of the thermal image, a square array of temperature data centered on a point of interest was fit to the expression

$$T(x,y) = A_1 + A_2 x + A_3 x^2 + A_4 y + A_5 y^2 + A_6 xy \quad (5),$$

by a linear least squares fitting routine. This fit was performed at each point in the image to build up images of the A's. A sum the A_3 and A_5 images times two is approximately equal to the Laplacian.

To reduce the processing time, a square filter was designed which was equivalent to this process. The coefficients of the filter are given by the expression

$$\frac{f(i)+f(j)+4\ S_2 - n\ (1+n)^2}{2\ n\left(S_2^2 - n\ S_4\right)} \quad (6)$$

where n by n is the size of the filter and n is odd, i is the column and j is the row of the filter element. S_2 and S_4 are defined by the expression

$$S_2 = \sum_{i=-m}^{m} i^2 \quad (7)$$

and

$$S_4 = \sum_{i=-m}^{m} i^4 \quad (8),$$

where m is (n-1)/2. The function f(i) is given by the expression

$$f(i) = 2\ n\ (\ i\ (\ n+1\ ) - i^2\ ) \quad (9).$$

For the case where n is equal to 7, the coefficients of the filter are given in Table I. The filter was then convolved with the thermal image to give its Laplacian.

Table I. Elements of 2 Dimensional filter convolved with thermal image to approximately calculate its Laplacian. Each element has been multiplied by 294.

10	5	2	1	2	5	10
5	0	-3	-4	-3	0	5
2	-3	-6	-7	-6	-3	2
1	-4	-7	-8	-7	-4	1
2	-3	-6	-7	-6	-3	2
5	0	-3	-4	-3	0	5
10	5	2	1	2	5	10

RESULTS

To investigate the technique samples were fabricated with known defects. The samples consisted of a sheet of steel .16 cm thick, backed by a rubber layer .63 cm thick, backed by an aluminum layer 2.5 cm thick, all 15.0 cm square. The layers were bonded together with a slow curing two-part epoxy system. To produce a disbond a portion of the rubber was removed to form a hole before assembly.

Measurements were made by heating the steel surface of the samples for approximately 15 seconds with a hot air gun capable of heating the air to a temperature greater than 200 C. The temperature profiles consisting of 256 video frames averaged were recorded at 15 second intervals, for a period for 240 seconds.

A typical thermal image for a sample with two disbonds formed by two 1.2 cm wide by 2.5 cm long slots in the rubber separated by 1.6 cm is shown in Figure 1. From the temperature image it is difficult to discern two separate defects, due to the overlap of the effect from the two disbonds. The results of a 7 by 7 Laplacian filter on the temperature, shown in Figure 2, clearly delineates the regions of disbond and fully resolves the two disbonds. Profiles of the temperature and its Laplacian are shown in Figure 3. The width at half maximum of the Laplacian profiles are approximately the width of the defect indicating that the filtered image gives a good definition of the area of the disbond.

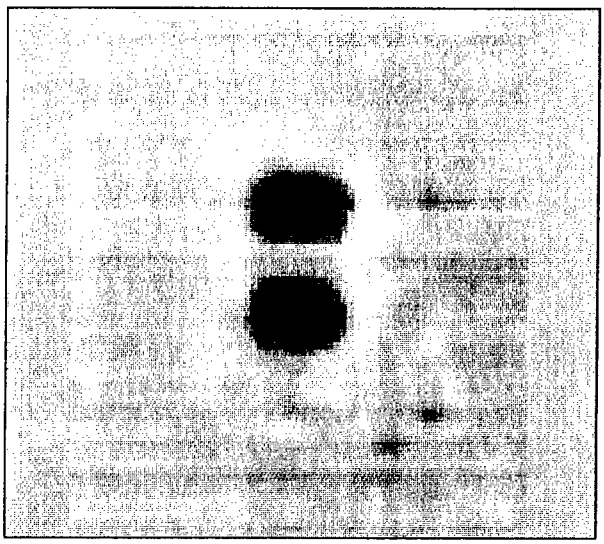

Figure 2. Laplacian of Thermal Image in Figure 1 for Sample with Two Rectangular Delaminations in Center.

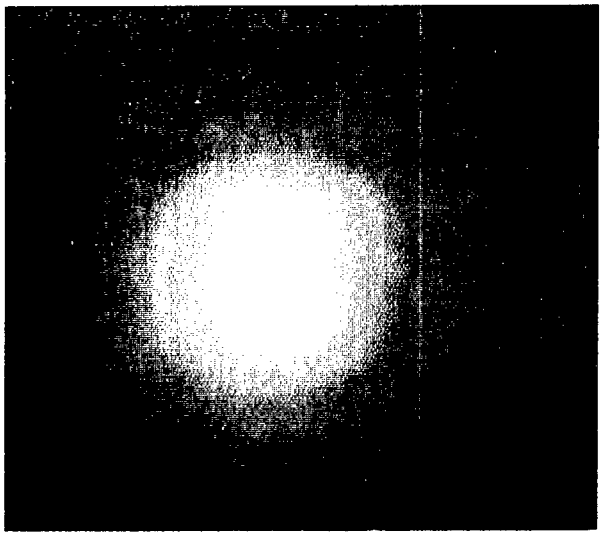

Figure 1. Thermal Image for Two-Disbond Sample.

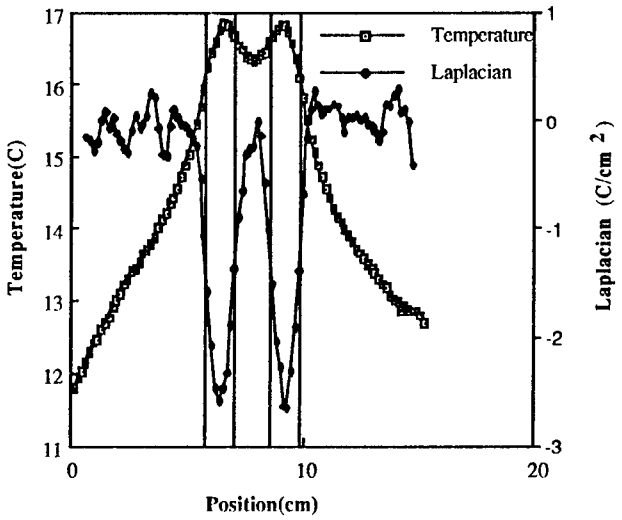

Figure 3. Profiles of Temperature and its Laplacian Across the Center of the Delaminations with Lines Drawn to Show Edges of Delaminations.

A second series of samples were fabricated at Morton Thiokol to simulate the geometry of the shuttle solid rocket motor. These consisted of a steel plate 1.27 cm thick, bonded with an epoxy to 0.13 cm NBR insulation, then backed by 10.1 cm of inert propellent all 30.5 cm square. A liner material was used between the NBR insulation and propellant to insure adhesion. To simulate a defect, a wedge shape pull tab was place between the NBR insulation and inert fuel during sample preparation. After the fuel was cured, the pull tab was removed to leave a wedged shaped disbond between the fuel and the NBR insulation.

The steel side of the sample was immersed in 55° C water for approximately 1 minute, then removed from the water and the temperature profiles consisting of 70 video frames averaged were recorded at 150 second intervals, for a period of 1 hour. A typical temperature image is shown in Figure 4. The uneven heating of the surface of the steel makes it impossible to discern the presence of the defect. The results of a 13 by 13 filter are shown in Figure 5. The wedge shape defect is clearly delineated in this image, indicating the advantage of reducing the temperature image to a flux image.

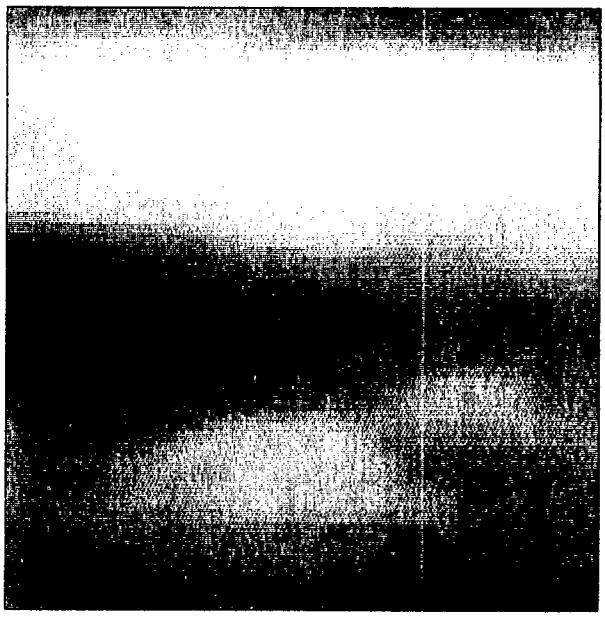

Figure 5. Laplacian of Thermal Image in Figure 4 for SRM Sample. A 13 by 13 Filter was Applied to the Thermal Image.

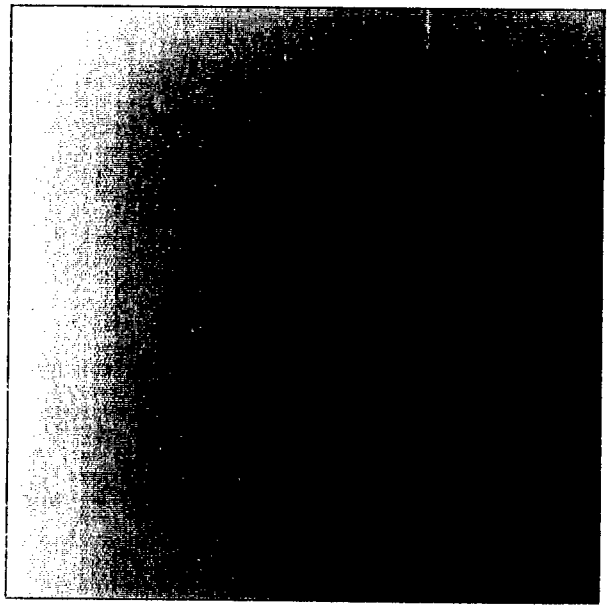

Figure 4. Typical Thermal Image for Shuttle Solid Rocket Motor Sample with Wedge Shaped Disbond.

A third sample which indicates the versatility of the technique is a laminated wood panel, used for fabrication of wind tunnel blade base, suspected to have delaminations between layers. A waterless technique was desired to remove the possibility of moisture damage to the wood. The back of the panel was heated for approximately 5 minutes with a hot air gun. A typical thermal image after 15 minutes is shown in Figure 6. Once again the contrast in the image is largely dominated by uneven heating of the sample. A 21 by 21 filter of this image is shown in Figure 7. This image indicates a circular delamination near the bottom. Its position and size were verified by ultrasonic inspection. These results indicate the technique is applicable for inspection of many different materials.

Figure 6. Thermal Image After 15 Minutes of Heating from a Laminated Wood Panel used for Fabrication of Wind Tunnel Blade Base.

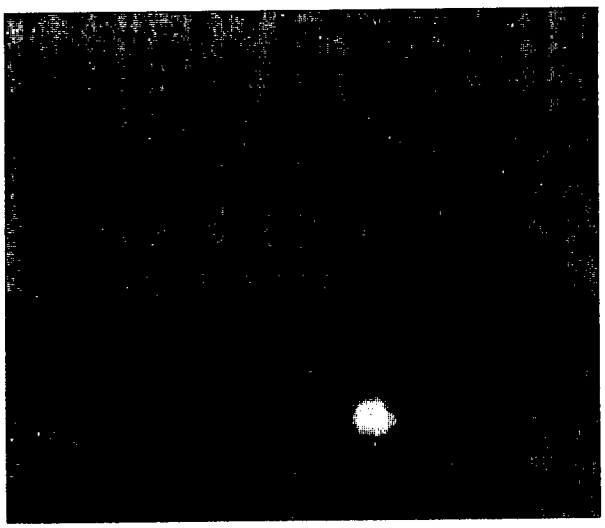

Figure 7. Results of a 21 by 21 Filter on Figure 6. Circular Delamination Near Bottom now Clearly Visible.

TECHNIQUE LIMITS

The limits of the technique for detection of disbonds in solid rocket motors was investigated by computational simulation of the thermographic technique. This has an advantage over experimental measurements, since many sample configurations and flaw sizes can be investigated at a fraction of the cost and time required for sample fabrication and data acquisition. A finite element heat transfer algorithm developed at Lawrence Livermore National Laboratory was used to model the laminated structure.[2] To generate the grid necessary for a finite element solution, an algorithm was developed using a hyperbolic sine transformation equation.[3] The transformation equation is used to refine the grid about the material interface where the temperature gradients will be largest and smoothly increase the spacing as the grid moves away from this boundary.

A two dimensional simulation of a three layered structure was performed, with a defect at the center of one of the interfaces. This model is equivalent to a structure with a long thin disbond. The thermal properties of the layers were chosen to correspond to the thermal properties of the three major layers of the shuttle solid rocket motor (steel, NBR insulation and fuel) and are given in Table II. For the first 60 simulated seconds the front surface boundary condition chosen to simulate application of water at 30°C above ambient (30°C+T) was a flux given by 728 $W/m^2/C^o$, where T is the temperature above ambient of the front surface. To simulate the removal of water and the subsequent air cooling, after 60 simulation seconds the surface boundary condition was chosen to be a flux given by 7.28 $W/m^2/C^o$ at ambient conditions, and the simulation continued for another nine simulation minutes.

Table II. Thermal Properties of Shuttle Solid Rocket Motor Materials.

	K (W/m/°C)	C_p (J/Kg/°C)	ρ (Kg/m^3)
Steel	37.4	460.6	7833
NBR	0.268	1591	1290
Fuel	0.381	1214	1763

A set of simulations were performed to determine the dependence of maximum observed temperature contrast to disbond width. For these simulations the thickness of the steel, NBR insulation and fuel were 1.270 cm, 0.254 cm, and 10.160 cm respectively. A disbond was placed at the NBR and fuel interface. The maximum contrast as a function of disbond width found

from these simulations is shown in Figure 8. The contrast found from the simulations are within the range found in the experiment and are found to be linearly dependent on disbond width. The time after removal of the thermal load for maximum contrast tended to increase as the flaw width increased, varying from 100 seconds to 215 seconds after heating for .508 cm to 5.080 cm respectively. From these simulations and a analysis of the experiment, it is estimated that a long disbond with a width of .5 cm would be detectable for this configuration.

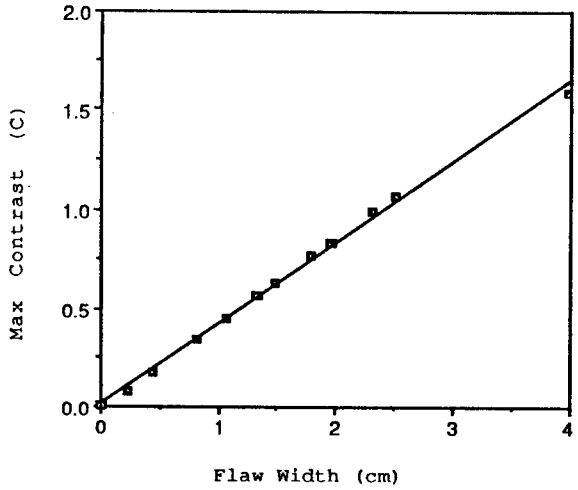

Figure 8. Maximum Contrast is Linearly Dependent on Disbond width.

A second set of simulations were performed to determine the dependence of the maximum contrast to steel thickness. For these simulations, two layers of steel and fuel were used with a 2.54 cm disbond at the interface. The results of this set of simulations is shown in Figure 9. For the range of thicknesses investigated, the maximum contrast is inversely proportional to steel thickness. From these simulations the maximum thickness of steel through which a disbond is detectable is 3.5 cm.

SUMMARY

A technique has been presented for processing thermal images which clearly delineates regions of sub-surface disbonds. The processing is approximately equivalent to taking a Laplacian of the temperature image. The technique is shown to discriminate against thermal contrast due to uneven application of heat. For a conductive layer backed by an insulating layer, when a quasi-static condition for flow is met, the technique gives the heat flux through the back surface of the conductor.

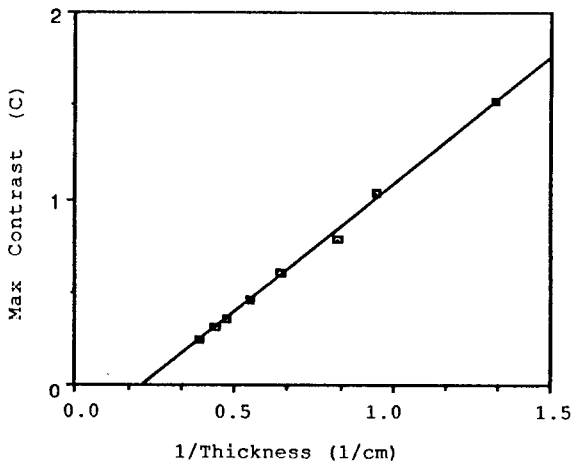

Figure 9. Maximum Contrast is Inversely Proportional to Steel Thickness.

REFERENCES

(1) Quinn, M. T., Hribar, J. R., Ruiz, R. L., Hawkins, G. F., "Thermographic Detection of Buried Debonds", Review of Progress in Quantitative Nondestructive Evaluation, Ed. 7, Vol. B, Plenum Press, New York, NY, 1988, pp.1117-1123.

(2) Shapiro, Arthur, "TOPAZ2D - A Two-Dimensional Finite Element Code for Heat Transfer Analysis, Electrostatics, and Magnetostatics Problems," UCID-20824. Lawrence Livermore National Laboratory, Livermore, California 94550, July, 1986.

(3) James, Patricia H., Welch, Christopher S., Winfree, William P., "A Numerical Grid Generation Scheme for Thermal Simulations in Laminated Structures," Proceedings of the 15th Annual Review of Progress in Quantitative NDE, University of California, San Diego, July 31 to August 5, 1988.

Ultrasonic Study of Adhesive Bond Quality at a Steel/Rubber Interface Using Quadrature Phase Detection Techniques

By

Alphonso C. Smith and Haesuk Yang†

Langley Research Center

Hampton, Virginia 23665-5225

†Analytical Services & Materials, Inc.

Hampton, Virginia 23666

ABSTRACT

The Quadrature Phase Detection technique was used to monitor simultaneously the phase and amplitude of a toneburst signal normally reflected from adhesively-bonded steel/rubber interface. The measured phase was found to show a positive shift for all bonded samples with respect to the disbonded state -- the phase shift being larger for samples with less stronger bonds as manifested by smaller values of applied tensile loads at failure. A model calculation which incorporates the concept of interfacial strength into the usual problem of wave propagation in multi-layered media was used to deduce a bond-quality parameter from an experimentally measured phase shift. This bond-quality parameter was found to be correlated with the tensile strength of the adhesive bonds at failure loads.

I. INTRODUCTION

In recent years the trend has been expanding rapidly to the use of structural adhesives in various aerospace material applications. It has become increasingly important to develop a reliable method for quantitative nondestructive evaluation of the bond strength and the quality of structural interfaces.

Numerous studies noted in Ref. 1 have been conducted in the past that evaluate the effects of various processing parameters on the strength characteristics of adhesive bonds. However, it has become obvious that the measurement of a good bond or disbond is not adequate for predicting bond strength. It was pointed out in Ref. 1 that perfectly uniform bonds with no disbond areas can have variations in strength by as much as 300%; therefore, great value should be placed on the measurement of an intermediate bond quality between disbond and a perfect bond. Because of the expanding use of composite materials, the problem of evaluating the quality of structual adhesive joints and making predictions on the bond strength using various ultrasonic techniques has received a considerable amount of attention by several investigators[2-10]. Nevertheless, there does not exist to date a single method known to be capable of assessing adhesive joint strength.

In the present work attention was focused on an adhesively-bonded steel/rubber interface in order to study the feasibility of future applications to the case/insulation bond in the Space Shuttle.

II. MODEL OF THE INTERFACE

Following the approach of Tattersall[2], it was assumed that the interfacial forces between two media can be represented by a density of weightless springs with the coupling strength K defined as

$$K=\Delta\sigma/\Delta u \qquad (1)$$

where $\Delta\sigma$ is the increase in stress on the adjacent surfaces and Δu the increase in separation between the surfaces. In case of a longitudinal wave normally incident on the boundary, the stress will be transmitted instantaneously through these hypothetical springs. The boundary condition assumes that the stress on either side of the interface is equal to the stress exerted by the springs, i.e.

$$\sigma_1 = \sigma_2 = K\,(u_2 - u_1)_{boundary} \qquad (2)$$

where σ_i's and u_i's are the stress and displacement, respectively, of the ultrasonic wave in each material. It can be shown easily that the boundary condition in Equation 2 leads to an expression for the pressure reflection coefficient

$$R_{12} = \frac{Z_2 - Z_1 - i\omega(Z_1Z_2/K)}{Z_2 + Z_1 + i\omega(Z_1Z_2/K)} \qquad (3)$$

where Z_i is the acoustic impedance of each material and $\omega=2\pi f$ with f the frequency of the ultrasonic wave.

If the thickness of adhesive layer is of the same magnitude as the acoustic wavelength (which was the case in the present investigation for a 0.016 in (0.041cm) thick adhesive layer with f = 5 MHz), one has to consider the problem of wave propagation in a three-layered medium with the boundary condition given by Equation 2 active at the two interfaces as illustrated in Fig. 1. It was found that the failure in adhesive bond under tensile loads occurred invariably at interface 1,2 leaving the adhesive layer intact at the rubber surface. Therefore, for the model chosen it was assumed that there was a rigid contact between layers 2 and 3 at all times, i.e. $K'\rightarrow\infty$. Then the expression for the input impedance (the impedance at interface 1,2) can be found in the literature[11] as

$$Z_{in} = \frac{Z_3 - iZ_2\tan(k_2 t)}{Z_2 - iZ_3\tan(k_2 t)} Z_2 \qquad (4)$$

where $k_2 = 2\pi f/v_2$ and v_2 is the velocity in the adhesive layer. Replacing Z_2 in Equation 3 by Z_{in} of Equation 4 and rearranging in terms of dimensionless quantities, the reflection coefficient can be expressed as

$$R = \frac{P_0 - P_1 - iP_0P_1/Q}{P_0 + P_1 + iP_0P_1/Q} \qquad (5)$$

where $P_0 = [Z_3\text{-}iZ_2\tan(k_2t)]/[Z_2\text{-}iZ_3\tan(k_2t)]$, $P_1 = Z_1/Z_2$, and $Q = K/ 2\pi fZ_2$.

It can be seen that an ideally perfect bond will correspond to $Q=\infty$ while a complete disbond is represented by $Q=0$. By defining the bond-quality parameter as $B = \tanh(\alpha Q)$, where α is a constant to be determined experimentally, Q can be expressed in terms of B as

$$Q = \frac{1}{2\alpha} \ln \frac{1+B}{1-B}. \qquad (6)$$

In Equation 6 one can see that the Q-values in the $\{0, \infty\}$ range can be readily converted to B-values in a finite $\{0, 1\}$ interval.

Finally, one can see from Equations 5 and 6 that, for fixed frequency and adhesive thickness, both the magnitude and phase of the reflection coefficient can now be expressed as a function of the bond-quality parameter. Figure 2 shows the results of this calculation with α =0.5, f=5MHz, and t=0.016in (0.041cm) for the case of steel/adhesive/rubber interface. It is noted that the acoustic impedance of each

layer as well as the velocity in the adhesive, which are necessary for this calculation, were measured using standard ultrasonic methods. They are $Z_1=45x10^5$ g/cm^2-sec, $Z_2=3.0x10^5$ g/cm^2-sec, $Z_3=2.5x10^5$ g/cm^2-sec, and $v_2=2.3x10^5$ cm/sec.

Using Fig. 2 it is possible to deduce the quality of the bond from experimentally determined values of either the phase or the magnitude of the reflection coefficient. However, It should be noted that, as can be seen from Fig. 2, for a given measured value of phase angle the bond-quality parameter can not be determined uniquely -- generally one has to choose between two possible values.

III. EXPERIMENTAL

A. Specimen Preparation

An example of the specimen assembly and configuration is shown schematically in Fig. 3. A 5 MHz longitudinal transducer was spring-mounted inside part B with its front surface 1/2 in (1.27cm) from the interface B/D under examination.

For testing purposes it was important that interface D/C remain securely bonded at all times. Therefore, the top surface of C was roughened by sandblasting with 120 grit at 60 psi (413 kPa) prior to bonding to the rubber. This insured that disbonding under tension loads invariably occurred at the proper interface (B/D). The bonding surfaces of the rubber and steel parts were solvent cleaned with alcohol and methyl ethyl ketone before applying a thin layer of Scotch-Weld structural adhesive EC-2216 from a recommended mixture of accelerator (7 parts) and base (5 parts by weight). The normal curing time for the adhesive was 24 hours at room temperature.

It was also important to control the thickness of the adhesive layer at the interface B/D to a constant value for all specimens. This was accomplished by placing several pieces of small diameter (0.016in, 0.041cm) stainless steel wires

across the interface.

To provide varying adhesive/cohesive strength at the interface, several samples were prepared by adding a few drops of Nonaq Stopcock grease to the adhesive mixture.

B. Quadrature Phase Detection

The phase and amplitude of the ultrasonic echo reflected normally from the steel/adhesive/rubber interface were measured using the quadrature phase detection technique. Shown in Fig. 4 is a block diagram of the data acquisition and measurement system. The system consisted of a MATEC MBS-8000 system which was comprised of the following plug-in modules: Computer Interface (CI-800), Pulse Repetition Rate & Width Generator (RW-815), Gated Amplifier (GA-822), Broadband Receiver (BR-835), Quadrature Phase Detector (QD-855), and Sample & Hold (SH-865). The parameters for all operational functions of the modules as well as data acquisition were controlled by HP-85B computer.

A 5-MHz CW signal from HP-3325A synthesizer was fed into the Gated Amplifier to produce a toneburst with 2-μs pulse width, which was then applied to a transducer/specimen assembly in the pulse-echo operational mode. With a narrow (0.3 μs) Sample & Hold gate placed within the first echo, the outputs of the two phase detectors at quadrature (V_0 and V_{90}) were measured. The phase angle between the signal and the reference, ϕ, and the amplitude of the signal, A, could then be computed since $\phi = \tan^{-1}(V_{90}/ V_0)$ and $A = (V_0^2 + V_{90}^2)^{1/2}$.

It should be noted that it was important in each measurement of the phase angle to use appropriate correction procedures[12] for three major sources of errors: 1) Base line shifts, 2) Deviation from quadrature in the phase detector references, and 3) Amplitude difference between phase detectors. The first can be compensated for by placing the sample and hold gate at a position in time where no signal is present

and subtracting this value from the signal measurement. The effect of the last two deviations is more complicated because the resultant error in angle measurement will be a fuction of the angle itself. However, since this error function repeats itself every π radians, it can be removed by repeating the measurement at a new frequency such that the initial phase angle is increased by $\pi/2$ radians and then averaging the two measurements.

C. Tensile Strength Measurement

While the phase angle and amplitude of the signal were repeatedly (about every 3 seconds) measured, the specimen was subjected to a tensile load in the direction shown by two arrows in Fig. 4. A continuously increasing ramp at a rate of 1 lb/sec (454 g/sec) was provided by MTS-810 Material Testing System until a failure in the adhesive bond occurred. The value of this failure load was used to approximately represent the tensile strength of each adhesive bond.

IV. RESULTS AND DISCUSSION

It was found for almost all cases that both the phase and amplitude of the signal reflected from the interface did not show any appreciable changes from the initial values as a function of increasing tensile load until a failure in the bond started to occur. However, the values of the phase and amplitude measured after complete disbond, ϕ_{db} and A_{db}, were found to be considerably different from those measured initially for bonded state, ϕ_b and A_b, as expected. It is noted here that the quantities ϕ_b-ϕ_{db} and A_b/A_{db} will correspond to the phase and magnitude, respectively, of the reflection coefficient from the bonded steel/adhesive/rubber interface. This is because it was observed that the nature of all bond-failures were found to be

adhesive (rather than cohesive) at the steel/adhesive interface leaving the steel surface free of any adhesive material.

In Table 1 the experimental data of L_F (failure load), ϕ_b-ϕ_{db}, and A_b/A_{db} are listed for six different samples. As was mentioned earlier in Section IIA, samples #3 through #6 were prepared by deliberately adding a few drops of grease to the usual adhesive mixture to provide less bond-strength. As a matter of fact, the measured values of L_F for these greased samples were much lower than the average L_F of about 445 lbs (202 kg) for ungreased sample.

As can be seen from Table I the measured values of A_b/A_{db} were about the same magnitude in the 0.85-0.88 range for all samples without showing any clear sign of correlation with varying bond-strength. Unfortunately, it can also be noticed from Fig. 2 that these values of A_b/A_{db} are almost out of reasonable range thereby making it impossible to deduce the bond-quality parameters from them. However, this shouldn't be too surprising since it is generally accepted that truely accurate measurements of signal amplitudes are practically impossible -- due largely to the effect of phase cancellation.

On the other hand, the measured values of ϕ_b-ϕ_{db} were all positive and well within the expected range. Furthermore, the magnitude of these phase-angle differences were larger for samples with less stronger bonds, revealing a clear distinction between greased and ungreased samples. Using the values of ϕ_b-ϕ_{db}, the bond quality of each sample was deduced from the phase vs bond-quality curve in Fig. 2. It is noted that, as was mentioned in Section II, the ambiguity of having to choose between two possible values of B for a given ϕ_b-ϕ_{db} can be removed by considering the relative strength of each sample given by L_F. These values of B, bond-quality parameter, are listed in the last column of Table I.

In Fig. 5 the values of B are plotted against the tensile strengh represented by the values of L_F for all six samples. Quite surprisingly, we have a reasonably good

linear correlation between B and L_F. A least-squares-fit line through data points can be seen to exptrapolate back close to the origin. It should be noted here that the value of the parameter α in Fig. 2 was chosen such that the least-squares-fit straight line in Fig. 5 could have as small a value of either x or y-intercept as possible. It should also be noted that the distribution of stress is not uniform, but slightly higher on the circumferential edge than at the center of the interface. In fact, the bond-failure was observed in most cases to be initiated from the edge and then propagate across the whole interface almost instantaneously. Therefore, the measured values of L_F may not represent the bond strength in the central region of the interface from which the ultrasonic information is obtained.

V. CONCLUSION

A model calculation is used to deduce a bond-quality parameter from an experimentally measured ultrasonic echo phase shift, using quadrature phase detection methods. The bond-quality parameter was found to show a good linear correlation with the tensile strength of the adhesive bonds at failure loads.

The present investigation shows there still exists a significant number of obstacles that have to be overcome if one hopes to develop a quantitative nondestructive method of assessing the bond strength/quality for a given completed adhesive bond. One of the drawbacks of the present approach in this context is that it is necessary to measure the phase or the amplitude for the reference state of the bond (either prior to bonding or after the disbond) as well as for the completed bond in order to acquire meaningful parameters describing each bond. Nevertheless, it has been shown in this study that the physical model of the adhesive interface outlined in Section II is capable of approximately representing the complex and intriguing nature of interfacial adhesive bond quality evaluation.

REFERENCES

1. Rose, J. L., and P. A. Meyer, "Ultrasonic Procedures for Predicting Adhesive Bond Strength," *Materials Evaluation* , Vol. 31, June 1973, pp 109-114.

2. Tattersall, H. G., "The Ultrasonic Pulse-Echo Technique as Applied to Adhesion Testing," *Journal of Physics D: Applied Physics,* Vol. 6, May 1973, pp 819-832.

3. Alers, G. A., P. L. Flynn, and M. J. Buckley, "Ultrasonic Techniques for Measuring the Strength of Adhesive Bonds, " *Materials Evaluation*, Vol. 35, April 1977, pp 77-84.

4. Kline, R. A., C. P. Hsiao, and M. A. Fidaali, "Nondestructive Evaluation of Adhesively Bonded Joints," *Journal of Engineering Technology*, Vol. 108, July 1986, pp 214-217.

5. Segal, E., G. Thomas, and J. L. Rose, "Hope for Solving the Adhesive Bond Nightmare?," *12th Symposium on Nondestructive Evaluation*, April 1979, San Antonio, Texas; pp 269-281.

6. Chernobelskaya, T., S. Kovnovich, and E. Harnik, "The Testing of Adhesive Bonded Joints by a Very High-Resolution Ultrasonic Probe," *Journal of Physics D: Applied Physics* , Vol 12, May 1979, pp 815-818.

7. Rose, J. L. , and G. H. Thomas, "An Adhesive Bond Strength Prediction Algorithm Based on Ultrasonic Signal Analysis," *International Journal of Adhesion and Adhesives*, Vol. 1, July 1980, pp 29-33.

8. Pilarski, A., and Z. Pawlowski, "Bond Quality Assessment in Layered Materials Using Ultrasonic Methods," *International Journal of Adhesion and Adhesives*, Vol. 1, July 1980, pp 45-49.

9. Williams, R. S., and P. E. Zwicke, "Assessment of Adhesive Properties Using Pattern Recognition Analysis of Ultrasonic NDE Data," *Materials Evaluation,*, Vol. 40, March 1982, pp 312-317.

10. dos Reis, H. L. M., and H. E. Krautz, "Nondestructive Evaluation of Adhesive Bond Strength Using the Stress Wave Factor Technique," *Journal of Acoustic Emission*, Vol.5, October-December 1986, pp 144-147.

11. Brekhovskikh, L. M., *Waves in Layered Media,* 2nd edition (translated by R. T. Beyer), 1980, p 15. Academic Press, New York, NY.

12. Peterson, G., Application Notes #117, MATEC Instruments, Inc., Hopkinton, MA, 1984.

Table 1 Experimental data of the tensile failure load, L_F; difference in phase angles between the bonded and the disbonded states; $\phi_b - \phi_{db}$, and the ratio of the reflection amplitudes for the bonded state to that for the disbonded state; A_b/A_{db}, for six different samples. The values of the bond quality parameter, B, were deduced from Fig. 2 using the data of $\phi_b - \phi_{db}$.

Sample	L_F lb (kg)	$\phi_b - \phi_{db}$ (deg)	A_d/A_{db}	B
#1	423 (192)	0.75	0.87	0.960
#2	465 (211)	0.53	0.88	0.975
#3	335 (152)	2.20	0.86	0.775
#4	280 (127)	3.41	0.88	0.555
#5	271 (123)	3.46	0.86	0.540
#6	215 (97.6)	3.70	0.85	0.460

Table 2 Calculated values of the difference in the phase angle (ϕ_{db}-ϕ_b), and the ratio of reflection amplitudes (A_b/A_{db}) for various values of the bond quality parameter using Equation 5.

B	ϕ_{db}-ϕ_b(deg)	A_b/A_{db}
0.000	0.000	1.000
0.120	1.830	0.991
0.210	2.920	0.975
0.300	3.570	0.956
0.390	3.780	0.937
0.420	3.770	0.930
0.510	3.540	0.915
0.600	3.120	0.902
0.690	2.610	0.893
0.750	2.230	0.888
0.810	1.823	0.884
0.840	1.610	0.882
0.900	1.144	0.879
0.960	0.555	0.877
0.999	0.371	0.877

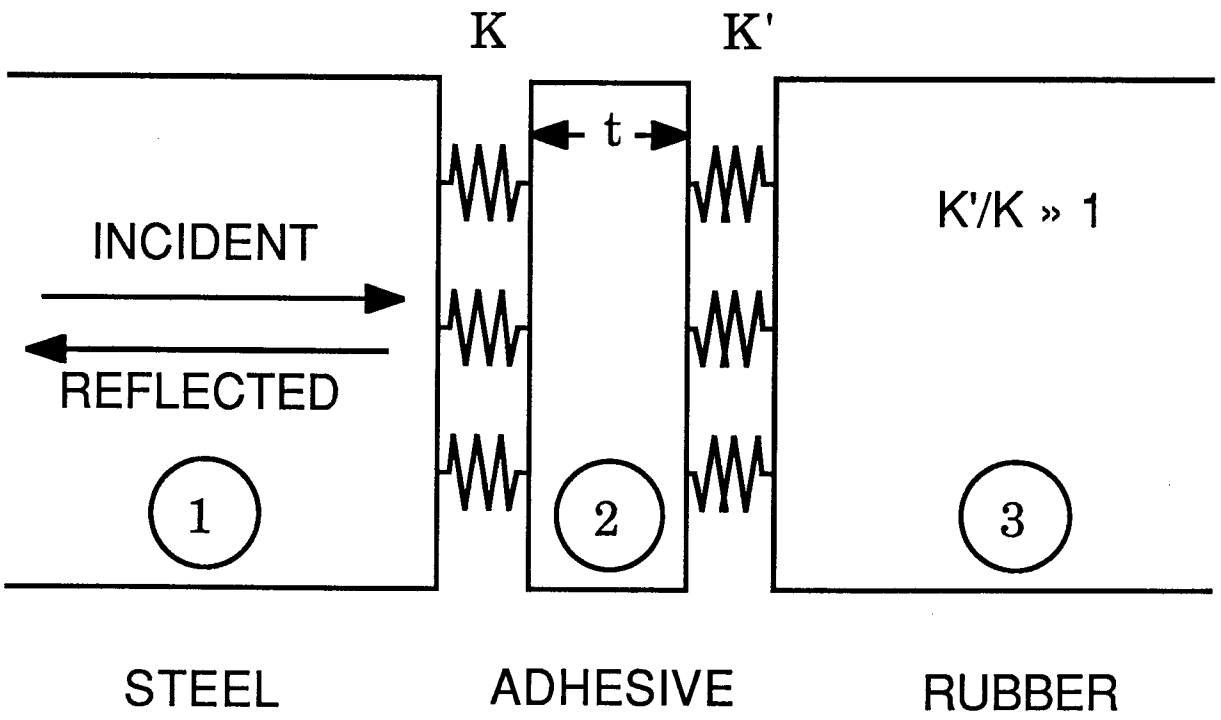

Fig. 1. Model of the adhesively-bonded steel/rubber interface

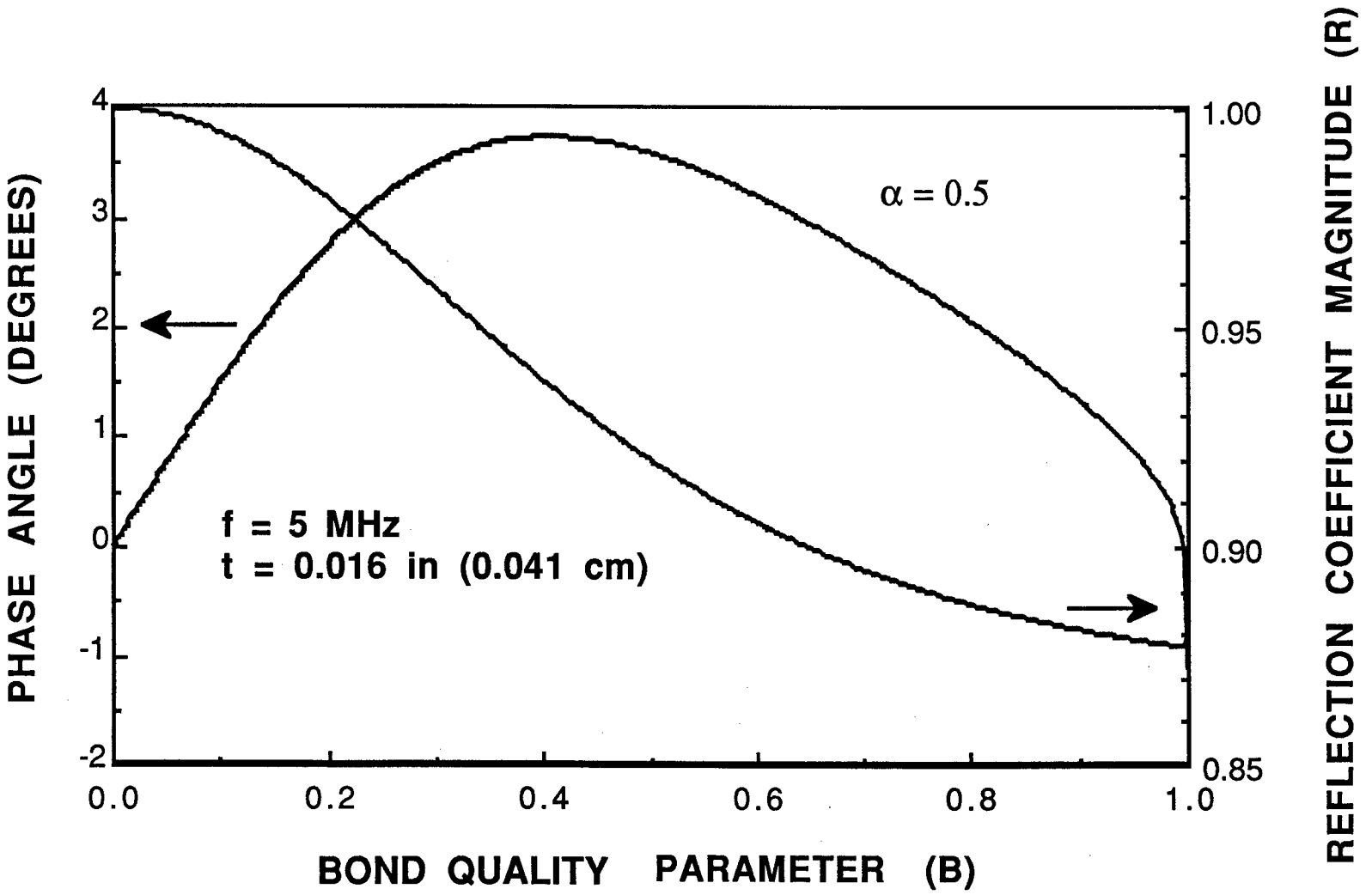

Fig. 2 Plot of the calculated phase and magnitude of the reflection coefficient as a function of bond-quality parameter {defined in Equation (6) for adhesively-bonded steel/rubber interface (Fig. 1).

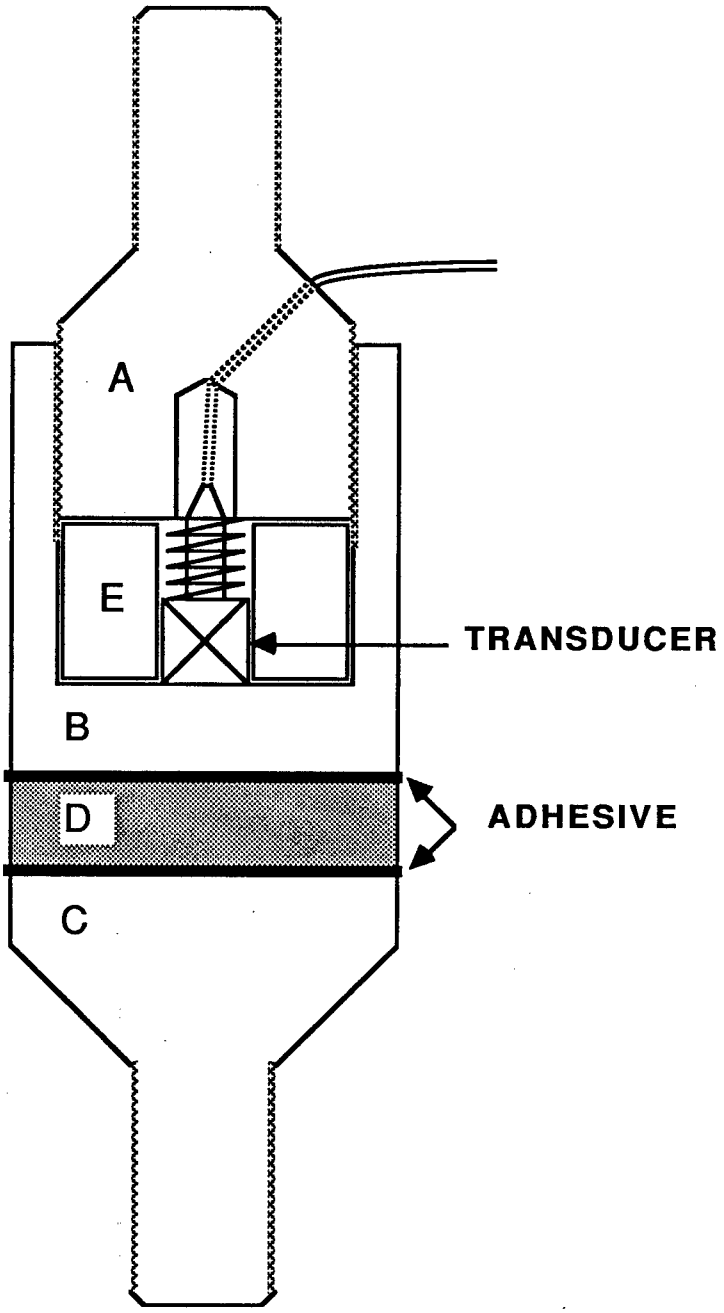

Fig. 3 Schematic diagram of the specimen; A, B, and C: Stainless Steel (15-5), D: Viton rubber, E: Teflon spacer

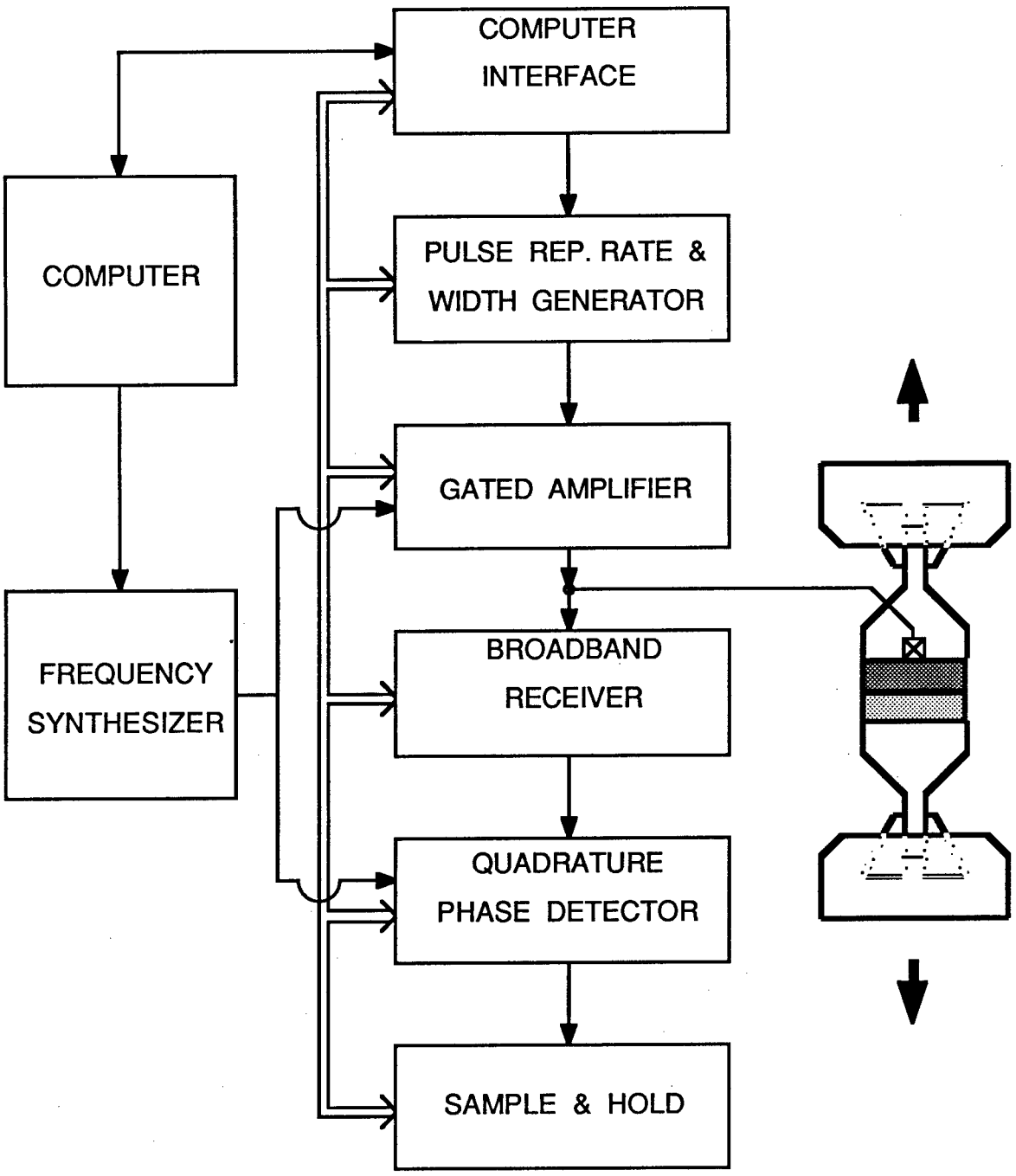

Fig. 4 Block diagram of the system for the measurements of phase and amplitude of reflected signal using quadrature phase detectotion technique. Also shown is a specimen under load for the measurement of its tensile strength.

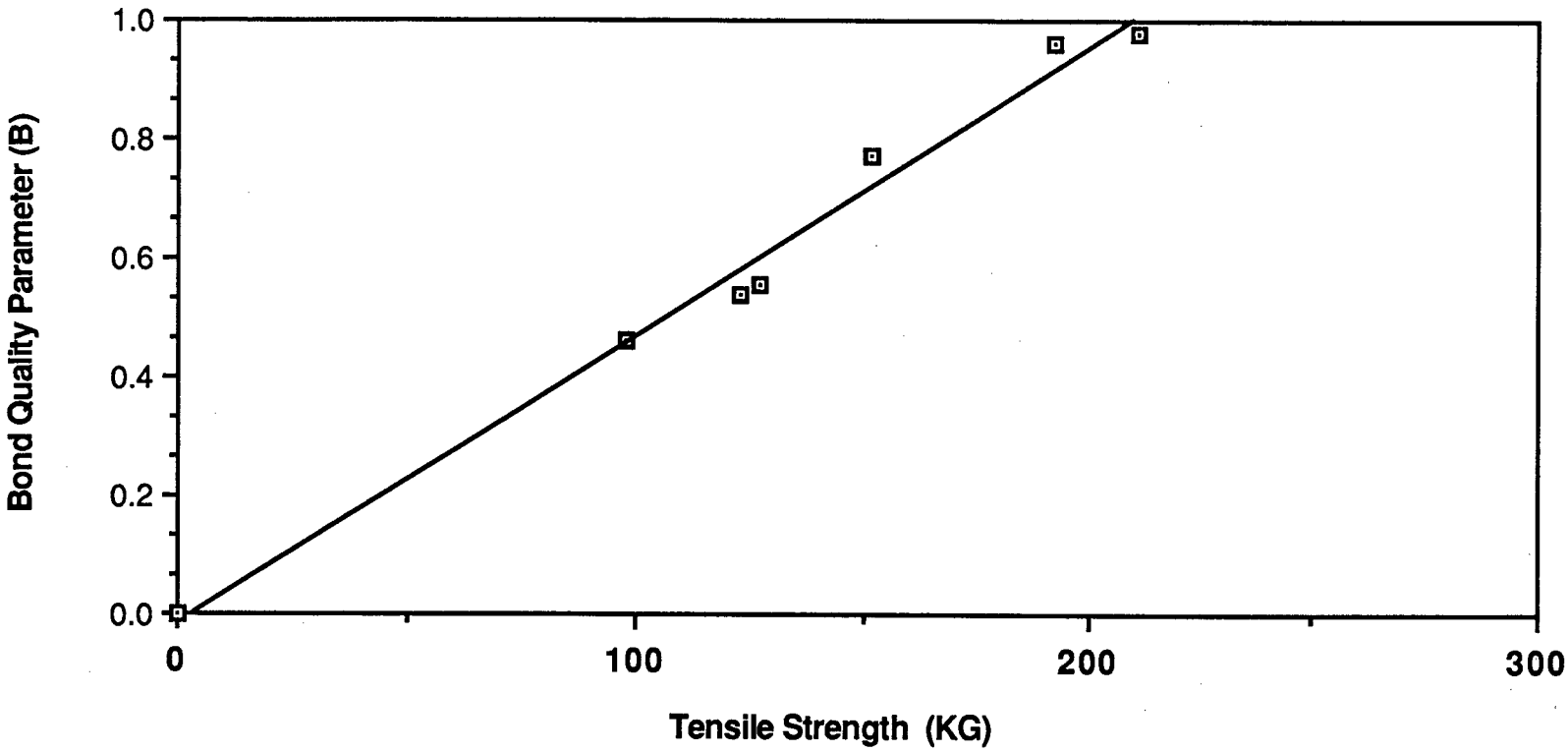

Fig. 5 Plot of the bond-quality parameter deduced from measured phase shift data in Fig. 2 as a function of the measured tensile strength of the bonds. The straight line is a least-square fit through the data points.

III. FIBER OPTICS

FIBER OPTIC SENSOR TECHNOLOGY - AN OPPORTUNITY FOR SMART AEROSPACE STRUCTURES

J. S. Heyman and R. S. Rogowski
NASA Langley Research Center
Hampton, VA 23665-5225
and
R. O. Claus
Virginia Polytechnic Institute and State University
Blacksburg, VA 24061-0249

Abstract

Fiber optic sensors provide the opportunity for fabricating materials with internal sensors which can serve as lifetime health monitors, analogous to a central nervous system. The embedded fiber optic sensors can be interrogated by various techniques to measure internal strain, temperature, pressure, acoustic waves and other parameters indicative of structural integrity. Experiments have been conducted with composite samples with embedded sensors to measure strain using optical time domain reflectometry, modal interference and an optical phase locked loop. Fiber optic sensors have been developed to detect acoustic emission and impact damage and have been demonstrated for cure monitoring. These sensors have the potential for lifetime monitoring of structural properties, providing real time non-destructive evaluation.

Introduction

Advanced aerospace structures will be fabricated in a non-traditional manner and will have integral sensors, actuators and microprocessors for dynamic control of configuration. The most promising candidates for the sensing function are fiber optic devices. Fiber optic sensors have been developed that can measure many physical and chemical properties. In many cases the fiber optic sensor is orders of magnitude more sensitive than conventional devices. The concept of "Smart Structures" integrates fiber optic sensor technology with advanced composite materials. The optical fibers are embedded in a composite material and provide internal sensing capability for monitoring parameters which are important for the performance, safety and reliability of the material and the structure. Several laboratory demonstrations with graphite/epoxy samples containing optical fibers have indicated that "Smart Structures" is a viable concept. This paper will review the progress in the development of materials with embedded sensors and consider future aerospace applications.

Material Processing/Fabrication

The engineering performance of advanced composites is highly dependent on processing conditions which often involve multiple curing stages with different temperatures and pressure regimes. The cost of starting materials and processing is high and for large parts, such as filament wound rocket motors, the expense of a rejected article is prohibitive. Therefore cure process monitoring is a critical requirement to assure the quality of the finished product. Dielectric, acoustic and fiber optic sensors have been investigated for this application.[1-6] We have investigated the use of optical fibers for use in cure process monitoring using several methods including the interferomtric technique shown in Fig. 1. Here two single mode optical fibers are shown embedded in a specimen at different locations. By monitoring the differential optical phase between the the optical signals travelling in the two fibers,the differential temperature, and thus the heat flow may be determined.[7] During cure, pressure and temperature may be simultaneously monitored using multiple wavelengths, multiple modes, or interacting multiple cores in a single fiber.[8-10]

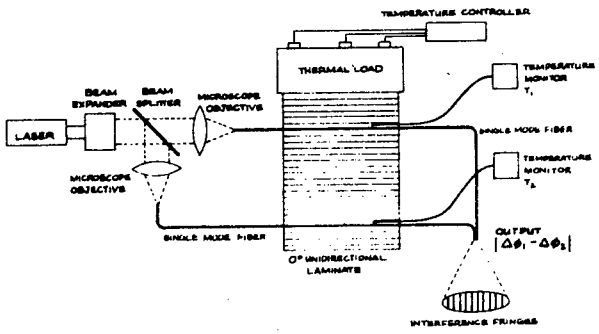

Figure 1. Differential interferometric fiber optic system for the measurement of heat flow in a unidirectional laminate.

In-service Material and Structural Monitoring

The ultimate performance, safety and reliability of future aircraft and spacecraft will depend upon the capability of the crew or the central control system to determine the reaction of the vehicle to its environment and take the proper response. In this area "smart structures" may have their greatest impact on the development of structural components. Embedded or attached optical fiber sensors allow the measurement of distributed strain and vibrational modes for the entire structure.

Strain and vibration measurements have been demonstrated in our laboratories using several different fiber interrogation methods. These include modal domain intereference, optical time domain reflectometry and an optical phase locked loop.

Optical time domain methods were first used to determine external loading in composites by Jackson and Claus[11] and improved time and frequency domain methods have subsequently been used by several investigators.[12-14] We have developed a method which uses in line optical fiber splices as time domain markers for optical time domain reflectometry (OTDR) as shown in Fig. 2. Here, an optical source generates a train of fast risetime optical pulses which propagate in the fiber. Partially reflecting splices, inserted at intervals along the length of the fiber, produce a series of regularly spaced signals and if the fiber is strained the spacing between the signals changes indicating the strain on the fiber between splices.[15] The strain resolution of this OTDR-based system is limited by the risetimes of the optical input pulses and the detection electronics. Currently available systems, for example, allow discrimination of locations spaced as close as 0.1mm.[16]

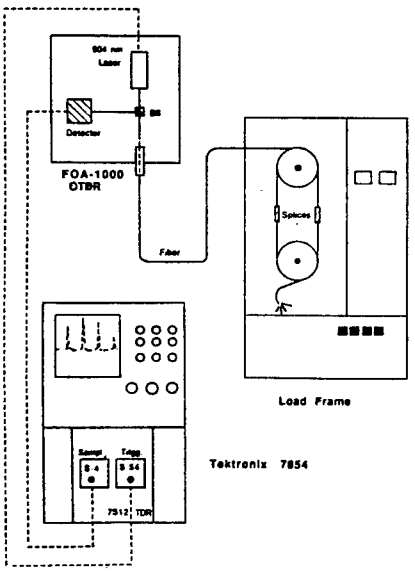

Figure 2. Fiber OTDR strain sensor testing system. Load frame is used to produce known strain in fiber containing multiple reflecting splices.

Distributed structural vibration measurements may be achieved using a modal domain sensing method such as that shown in Fig. 3. The technique is based on the principle that different modes in a waveguide having slightly different propagation times produce intereference patterns. If a waveguide that supports two or three modes is attached to or embedded in a structure, it can sense bends in the structure through the intereference conditions between the modes. We have demonstrated that such methods may be used to evaluate structural vibrations of beams.[17-19] Specifically the mode shape amplitudes of such vibrations may be determined by appropriate processing of the time domain modal interference signals.[20]

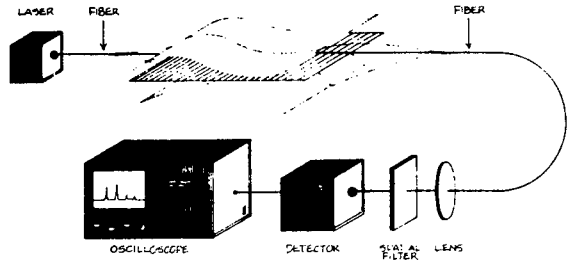

Figure 3. Modal domain optical fiber sensing system. Laser light is coupled to a few-mode fiber and modal to intensity demodulation is accomplished with a spatial filter.

An example of the performance of the sensor is shown in Fig.4 Here a fiber is shown embedded in a graphite/epoxy composite laminate coupon. If the coupon is excited as a cantilever beam, the fundamental and overtone vibrations result with relative amplitudes as shown. The modal interference sensor output signal, transformed, yields the amplitude data indicated in the graph.

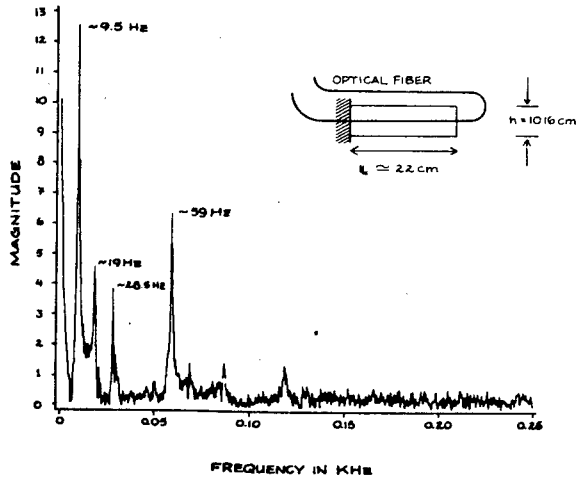

Figure 4. Frequency spectrum of vibration of cantilever beam (inset) obtained with modal domain sensor.

We have also investigated the use of a modulated laser diode system to measure phase modulation in an optical fiber. The system is an optical phase locked loop[21] which is shown schematically in Fig.5. A voltage controlled oscillator is used to directly modulate a GaAlAs laser and to provide a reference signal to a double balanced mixer. The laser radiation passes through a multimode optical fiber, is detected, amplified, and mixed with the reference signal to generate an error voltage. The phases of the two signals are maintained at quadrature by feedback of the DC error voltage from the mixer to the oscillator. The filter removes the radio frequency component coming from the mixer. With this configuration, any change in the phase of the modulation is compensated by a change in the modulation frequency. A change in phase length, ΔL, of the optical fiber will produce a change in frequency, ΔF, according to:

$$\Delta L/L = -\Delta F/F$$

where L is the effective path length (optical plus electronic) and F is the nominal frequency value.

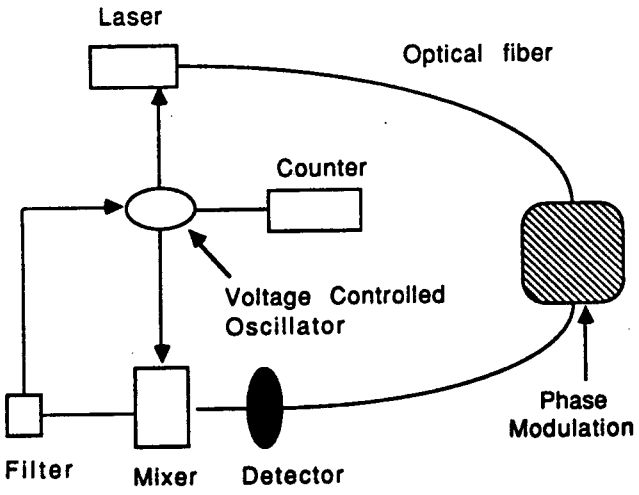

Figure 5. Schematic diagram of optical phase locked loop.

The optical phase locked loop has been applied to the measurement of dynamic strain in a cantilever beam fixed at one end. Both optical fiber and conventional resistance strain gauges were attached to the metal beam, which has a fundamental vibration frequency of 0.6 Hz. Fig. 6 is a plot of the Fourier transform of the signals from the optical fiber and the resistance strain gauge. The major peak in each case, indicated by the cursor , is at 3.8 Hz. In general, the fiber and the strain gauges located at three different positions along the beam produced similar frequency spectra. Because the fiber responds to the average strain along the beam and the strain gauges respond to localized strain, the signals were not always the same. The discrepancies occured when some of the higher order frequency components were not detected by the strain gauge.

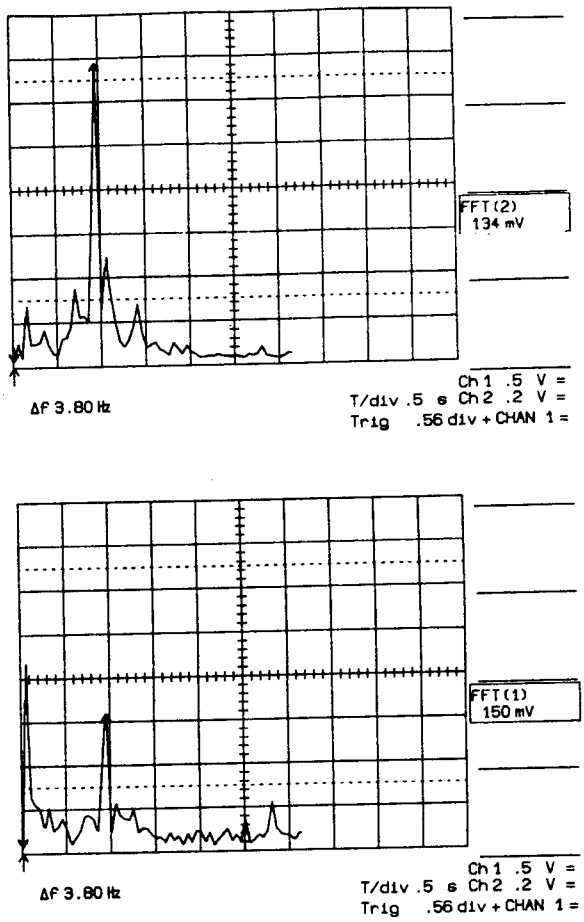

Figure 6. Frequency spectrum of vibration of a cantilever beam obtained with optical phase locked loop. Upper curve is the signal from the strain gauge and lower curve is the signal from the optical fiber.

Non-Destructive Evaluation and Damage Detection

Embedded optical fibers allow not only cure monitoring and in-service lifetime measurements but may also be used to non-destructively evaluate material degradation and damage as the material ages. We have applied the modal domain sensing system described above specifically to the detection of acoustic emission in loaded composite specimens.[21] shows a typical fiber-detected AE event. Note that minimum signal risetime is approximately 0.4 microseconds corresponding to a maximum detected frequency of more than 2.0 MHz, far above the vibration frequency of the specimen containing the fiber sensor. The electronic processing of such signals using conventional acoustic emission analysis procedures is complicated because the impulse response function of the fiber exhibits a much stronger low frequency response than piezoelectric ultrasonic transducers.[22]

Some level of damage detection may also be afforded using embedded optical fiber sensor methods. Initial work in this

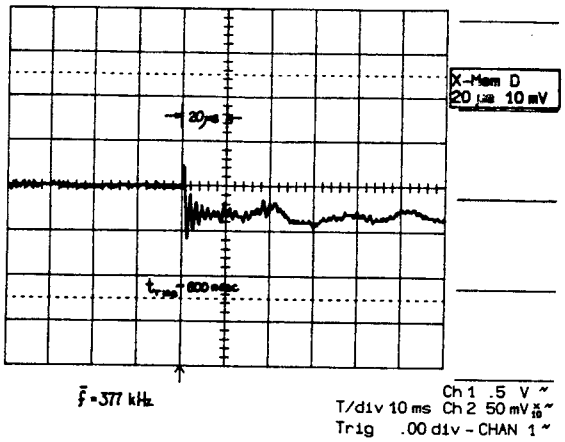

Figure 7. Acoustic emission signal detected using modal optical fiber sensor embedded in a graphite/epoxy laminate coupon.

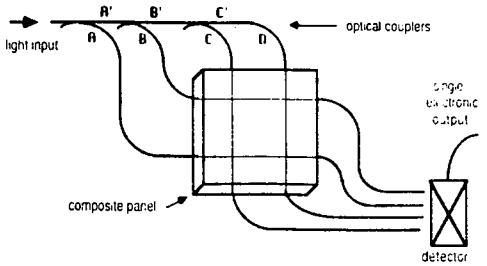

Figure 8. Optical fiber signal processor for multiplexing of multiple sensor signals. This processor has been used in combination with arrays of embedded and attached optical fibers to locate regions of impact damage in composites.

area used the breakage of optical fibers arranged in a two dimensional array to indicate the location of excessive internal strain, such as that produced by impact.[23] The major disadvantage of such techniques is that levels of damage that do not break fibers cannot be detected and once fibers are broken no additional sensing at that site is possible.

We have extended the capability of this type of damage detection system to additionally allow the quantitative determination of two dimensional strain in materials using several methods. First, the two dimensional strain field may be determined using single mode optical fibers embedded in a grid array, with interferometric techniques used to measure strain along the individual fiber lengths, and numerical methods used on the multiple output signals to construct the strain field. This method has been applied to the measurement of quasi-static loads and impact induced residual stresses in simply supported graphite/epoxy composite panels.[24] Alternatively, optical intensity modulation caused by microbending can be used as the sensing mechanism. Loading in a composite specimen causes changes in the microbend characteristics of embedded fibers and thus in the transmitted optical intensity.[25] Similar numerical methods would be required to map two dimensional strain fields from multiple linear measurements obtained using this method. Finally, the real time processing of fiber array signals may be achieved using simple in-line devices such as the gray code optical processor shown in Fig. 8. Here the outputs from an embedded square array of fibers are summed using a network of fiber couplers. The s - parameters of the couplers are designed so that the one output signal from the network is a single valued function of intensity which uniquely specifies the location and quantitative intensity loss, hence local strain in the fiber array. A gray scale coding scheme has been demonstrated for such a system.[26]

Conclusion

We have shown that fiber optic sensor technology can be combined with advanced material and structure concepts to produce a new class of materials with internal sensors for health monitoring - providing the opportunity for "Smart Structures". There are many potential uses of such materials in aircraft and spacecraft, especially where critical structural components have been identified and using the new materials proves cost effective. Space Station will require some type of sensing system to monitor the vibrations of the structure and feedback information to control mechanisms. A fiber optic sensor system for monitoring strain seems ideally suited for this application since the structure is large and flexible and requires a method for dynamic control. We envision that at least some parts of future aircraft will have fiber optic sensors for monitoring strain and impact damage. Commercial aircraft may be able to extend their useful life through proper monitoring of load spectra directly from the fiber optic sensor. In addition, the cost of maintainance may be reduced through "maintainance for cause" based on actual environmental history rather than clock hours. Certainly, military aircraft would benefit from having a damage detection and evaluation capability during engagements. The information would be invaluable to the pilot for deciding on a course of action after suffering damage to the aircraft.

Other exciting uses of this technology may be in monitoring strain in large structures such as buildings,ships, storage tanks, pressure vessles, dams and bridges. The optical fibers with their low attenuation can literally span a bridge for miles and return information regarding structural integrity. The fibers may also find application to geodynamic monitoring as a low cost, large area sensors for strain/vibration associated with earthquake prediction. Fiber sensors have already been applied to monitoring oil pipelines for long distances and represent an emerging and enabling sensor technology.

Future advances in opto-electronics and signal processing will very likely open new avenues for sensing and make this technology an important part of NDE for assuring the safety and reliability of aircraft and spacecraft.

References

[1] D. E. Kranbuehl, S. E. Delos, M. Hoff, P. Haverty, W. Freeman, and R. Hoffman, Proc. SPIE, 45, 1031 (1987).

[2] R. Levy, NASA Workshop on Intelligent Materials (Hampton, VA), February 1987.

[3] M. Gimple and B. A. Auld, "Position and sample feature sensing with capacitive array probes," Review of Progress in Quant. NDE,7A, 1988.

[4] R. Kriz, NASA Workshop on Intelligent Materials (Hampton, VA), February 1988.

[5] R. P. DePaula and E. Udd, Editors, "Fiber-Optic and Laser Sensors IV," Proc. SPIE, vol. 718, 1987.

[6] M. Afromowitz, "Fiber-optic cure sensor for thermoset composites," Proc. SPIE, vol. 986, 1988.

[7] R. O. Claus, "Embedded optical fiber measurements of internal strain in composites," Review of Progress in Quant. NDE, 6A, 1986.

[8] K. D. Bennett, "Optical fiber techniques for remote sensing," MSEE thesis, Virginia Tech, August 1985.

[9] R. O. Claus and K. D. Bennett, "Optical fiber modal domain detection of stress waves," Proc. 1986 IEEE Ultrasonics Symp. (Williamsburg, Va).

[10] G. Meltz and J. R, Dunphy, "Quantitative fiber-optic techniques for the nondestructive evaluation of composites," Proc. Review of Progress in Quantitative NDE, 1982.

[11] R. O. Claus, B. S. Jackson and K. D. Bennett, "Nondestructive evaluation of composite materials by OTDR in embedded optical fibers," Proc. SPIE vol. 566, 1985.

[12] J. S. Schoenwald and P. M. Beckham, "Distributed fiber-optic sensor for passive and active stabilization of large structures," Rev. Prog. Quantitative NDE, 7A, 1987.

[13] B. Zimmermann, "High resolution OTDR and its applications," MSEE thesis, Virginia Tech, 1988.

[14] W. B. Spillman, Jr., P. L. Fuhr, and B. L. Anderson, "Performance of integrated source/detector combinations for smart skins," Proc. SPIE, vol. 986, 1988.

[15] B. D. Zimmermann, K. A. Murphy and R. O. Claus, "Local strain measurements using optical fiber splices and optical time domain reflectometry," Proc. Review of Progress in Quantitative NDE , 7A, 1988.

[16] Opto-Electronics, "Millimeter resolution OTDR system," March 1987.

[17] R. O. Claus and P. A. Ehrenfeuchter, "Optical fiber waveguide methods for advanced materials characterization," Proc. 20th Intl. Symp. Am. Mettal. Soc. (Monterrey, CA), July 1987.

[18] R. O. Claus, "Embedded optical fiber sensors for materials evaluation," NASA Workshop on Intelligent Materials (Hampton, VA), February 1987.

[19] A. Safaai-Jazi and R. O. Claus, "Synthesis of interference patterns in few-mode optical fibers," Proc. SPIE, vol. 986, 1988.

[20] R. S. Rogowski, J. S. Heyman, M. S. Holben, Jr., and P. Sullivan, "A method for monitoring strain in large structures: Optical and radio frequency devices", Rev. Prog. Quant. NDE, vol. 7A, p. 559, 1988.

[21] K. D. Bennett, R. O. Claus and M. J. Pindera, "Internal monitoring of acoustic emission in graphite-epoxy composites using embedded optical fiber sensors," Proc. Review of Progress in Quantitative NDE, vol. 6, 1986.

[22] R. O. Claus and K. D. Bennett, "Smart structures program at Virginia Tech," Proc. SPIE, vol. 986, 1988.

[23] R. Crane and J. Gagorik, ARO/DARPA Workshop on Polymer-Based Composites (Wrightsville Beach, NC), 1982.

[24] R. O. Claus and J. C. Wade, "Distributed strain measurement in a rectangular plate using an array of optical fiber sensors," Rev. Prog. Quant. NDE, vol. 4, 1985.

[25] K. D. Bennett and R. O. Claus, "Microbending losses of optical fibers embedded in composite materials," Opt. Soc. Am. Annual Meeting (Washington, DC), October 1985.

[26] K. D. Bennett, J. C. McKeeman and R. G. May, "Full-field analysis of modal domain sensor signals for structural control," Proc. SPIE, vol. 986, 1988.

Fiber optic strain measurements in filament-wound graphite-epoxy tubes containing embedded fibers

R. S. Rogowski, J. S. Heyman, M. S. Holben, Jr. and C. Egalon
NASA Langley Research Center
Mail Stop 231
Hampton, Virginia 23665-5225

D. W. Dehart, T. Doederlein and J. Koury
Air Force Astronautics Laboratory
Edwards, California 93523-5000

1. INTRODUCTION

Several planned United States Air Force (USAF) and National Aeronautics and Space Administration (NASA) space systems such as Space Based Radar (SBR), Space Based Laser (SBL), and Space Station, pose serious vibration and control issues. Their low system mass combined with their large size, precision pointing/shape control and rapid retargetting requirements, will result in an unprecedented degree of interaction between the system controller and the modes of vibration of the structure. The resulting structural vibrations and/or those caused by foreign objects impacting the space structure could seriously degrade system performance, making it virtually impossible for passive structural systems to perform their missions. Therefore an active vibration control system which will sense these natural and spurious vibrations, evaluate them and dampen them out is required. This active vibration control system must be impervious to the space environment and electromagnetic interference, have very low weight, and in essence become part of the structure itself. The concept of smart structures meets these criteria. Smart structures is defined as the embedment of sensors, actuators, and possibly microprocessors in the material which forms the structure, a concept that is particularly applicable to advanced composites. These sensors, actuators, and microprocessors will work interactively to sense, evaluate, and dampen those vibrations which pose a threat to large flexible space systems (LSS). The sensors will also be capable of sensing any degradation to the structure.

The Air Force Astronautics Laboratory (AFAL) has been working in the area of dynamics and control of LSS for the past five years. Several programs involving both contractual and in-house efforts to develop sensors and actuators for controlling LSS have been initiated. Presently the AFAL is developing a large scale laboratory which will have the capacity of performing large angle retargetting manuevers and vibration analysis on LSS.

Advanced composite materials have been fabricated for the last seven years, consisting mostly of rocket components such as: nozzles, payload shrouds, exit cones, and nose cones. Recently, however, AFAL has been fabricating composite components such as trusses, tubes and flat panels for space applications.

Research on fiber optic sensors at NASA Langley Research Center (NASA LaRC) dates back to 1979. Recently an optical phase locked loop (OPLL) has been developed that can be used to make strain and temperature measurements. Static and dynamic strain measurements have been demonstrated using this device.[1]

To address future space requirements, AFAL and NASA have initiated a program to design, fabricate, and experimentally test composite struts and panels with embedded sensors, actuators, and microprocessors that can be used to control vibration and motion in space structures.

2. FABRICATON OF EXPERIMENTAL STRUT

To demonstrate the feasibility of smart structures a simple composite tube structure with a circular cross-section was fabricated with embedded fiber-optic sensors. A tubular shape was chosen because it is a key structural element in most space truss systems. Optical fibers were chosen as the sensing element because of the demonstrated capability of the OPLL developed at NASA LaRC. To date, a total of three tubes have been fabricated at the AFAL and tested at NASA LaRC. The results obtained with two of these tubes are presented in this paper.

All three tubes were fabricated in a similar manner. The fabrication process used was filament winding. The winding was done on an En-Tec computer filament winding machine. The first two tubes were wound as one single tube on the same steel mandrel and then cut into two. The composite material used was graphite epoxy prepreg roving from Fiberite composed of medium strength G-40 graphite fibers from Union Carbide and 5245 epoxy resin. The single tube prior to cutting was approximately five and one half feet in length, with an inside diameter of one and one half inches. The single tube consisted of one layer of 90 degree fiber; one layer of +/- 45 degree fiber; one layer of optical fiber; and one layer of 90 degree fiber. A schematic diagram of the tube layup is shown in figure1. The fiber optics, made by the Newport Corporation, are F-MSD multimode fiber. The core has a diameter of 49 μm with a combined core and

cladding diameter of 125 μm. The fiber optics were layed in longitudinally with both ends of the fiber coming out of the same end of the tube. They were located every 90 degrees throughout the tube with a total of four sets of fiber optics embedded in the tube. After winding, the single tube was bagged using standard bagging techniques. Special care was given in bagging the optical fibers since they are very delicate and fragile. Prior to autoclaving, the optical fibers were coated with a silicone (RTV) coating. This coating prevents the jacket from melting during the curing process leaving the very brittle bare core and cladding.

The single tube was then placed in a Baron-Blackslee autoclave and cured at 350 degrees F for two hours. Upon cooling, the tube was removed from the mandrel and cut in two, giving special care to the optical fibers. Both tubes were then packaged and delivered to NASA LaRC for strain and vibration testing.

The third filament-wound tube was fabricated in a similar manner, except for the differences in the raw materials and the angle of the composite plies. The composite material used was graphite epoxy prepreg roving from Fiberite composed of medium strength IM-6 graphite fibers from Hercules and 934 epoxy resin.

The first tubes had a fundamental frequency of approximately 33 hertz when cantelivered. The third tube was designed to have a significantly lower fundamental frequency. According to a composite design program, a tube with a length of 68 inches and a ply orientation of 90-(+/-)60-90-90 would have a fundemental frequency of 10 hertz. This is how the third tube was fabricated. The fiber optics were embedded in between the 60 and the second 90 degree layer. In this tube only two sets of fiber optics were embedded at 180 degrees to one another in the composite material. Also, the fiber optics did not come out of the end of the tube as in the first two tubes. The fiber optics came out of the top and bottom of the tube at a distance of four inches from the end of the tube. This change allowed clamping of the tube at the end without crimping the optical fibers.

2. STRAIN AND VIBRATION MEASUREMENTS

The vibration and strain experiments were conducted at NASA Langley Research Center using a modulated diode laser and an optical phase locked loop (OPLL) which is described in reference 1. The optical fibers exiting the tube were fusion spliced to the fibers of the optical system. One end of the graphite-epoxy tube was clamped over a round piece of metal which was also clamped to a fixture to hold the end of the tube in a fixed position. Four resistance strain gauges were attached to the tube for comparison with the fiber optic sensors. The tube was statically stressed by hanging weights on the free end. When the tube is stressed in this manner the strain in the composite and the optical fiber produces a change in the modulation frequency of the OPLL. Strain on the surface of the tube was monitored with the strain gauges.

The results of these experiments are shown in figure 2 and 3, which graphically indicates the correlation between the strain gauge measurements and the changes in modulation frequency. The data indicate good correlation between the strain gauge readings and the fiber optic strain measurements These runs were repeated with excellent reproducibility. Strain measurements were also made while the tube was vibrating. Figure 4 compares the results obained by simultaneously monitoring a strain gauge and the fiber optic signal for the third tube. The time domain and frequency domain data agree very well, showing a vibration frequency of 9.6 Hz, which is very close to the design vibration frequency.

4. SUMMARY

Graphite - epoxy tubes were fabricated with embedded optical fibers to evaluate the feasibility of monitoring stresss with a fiber optic technique. Resistance strain gauges were attached to the tubes to measure strain at four locations along the tube. Both static and dynamic strain measurements were made with excellent agreement between the embedded fiber optic strain sensor and the strain gauges. The results indicate that fiber optic sensors embedded in composites may be useful as the sensing component of smart structures.

Reference:

1. R. S. Rogowski, J. S. Heyman, M. S. Holben, Jr. and P. Sullivan, " A method for monitoring strain in large structures: Optical and radio frequency devices", Rev. Prog. Quant. NDE, vol. 7a, p559(Plenum Press,1988).

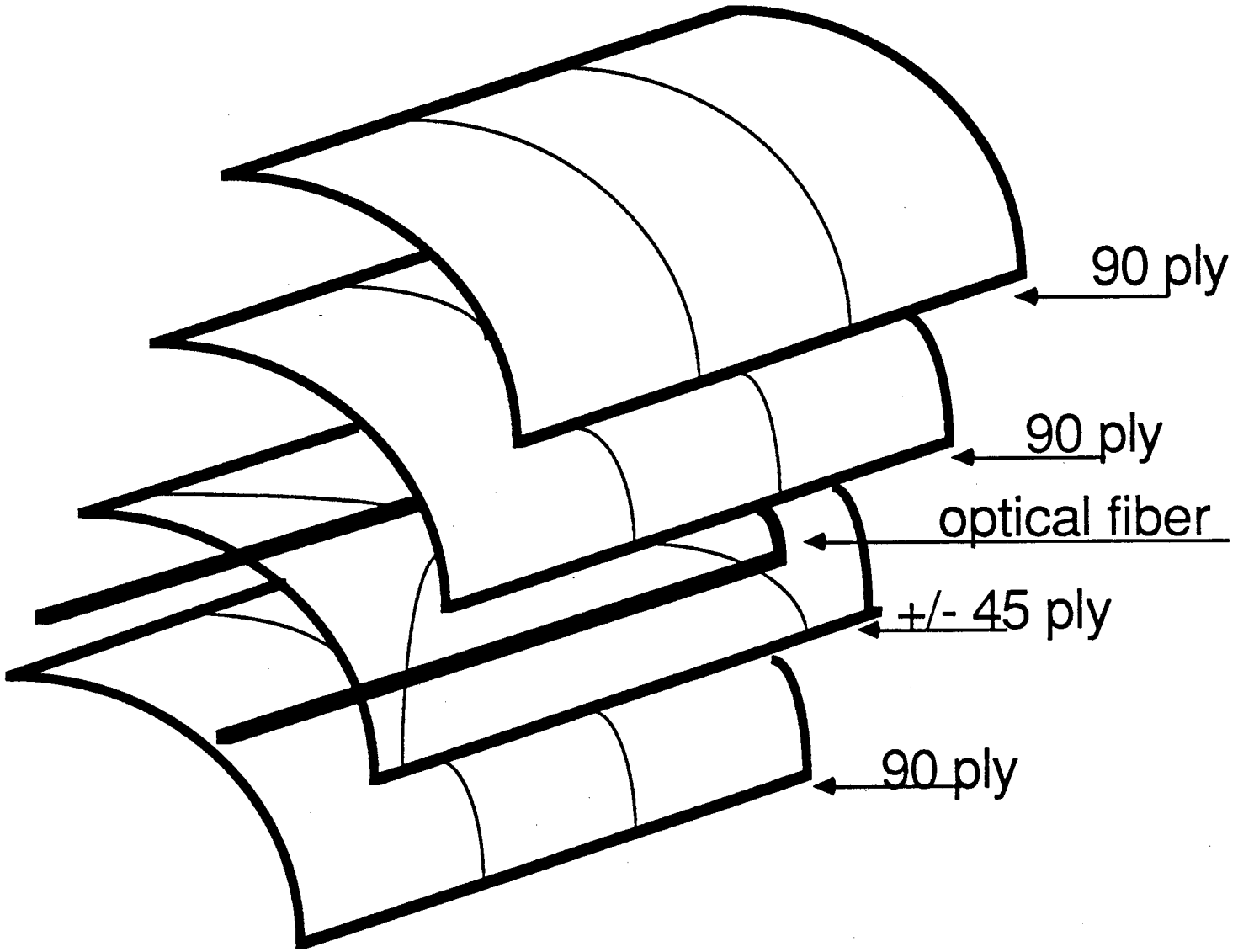

Figure 1. Schematic diagram of layup of first tube fabricated at AFAL.

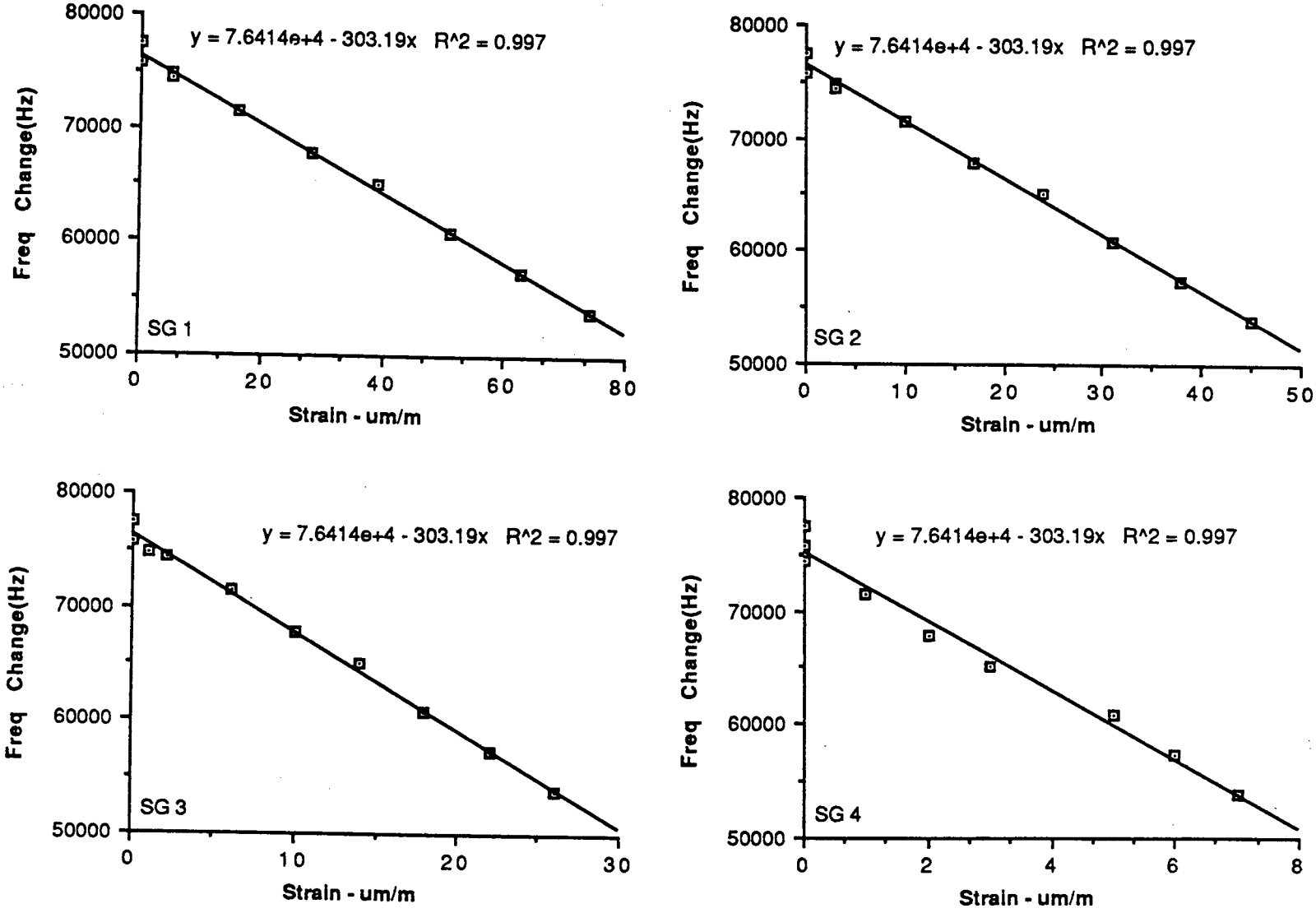

Figure 2. Plots of frequency change of OPLL vs. strain for the first composite tube. Strain gauge number one is closest to the fixed end of the tube. The plot is coded as SG1. Strain gauge 4 (SG4) is at the greatest distance from the fixed end.

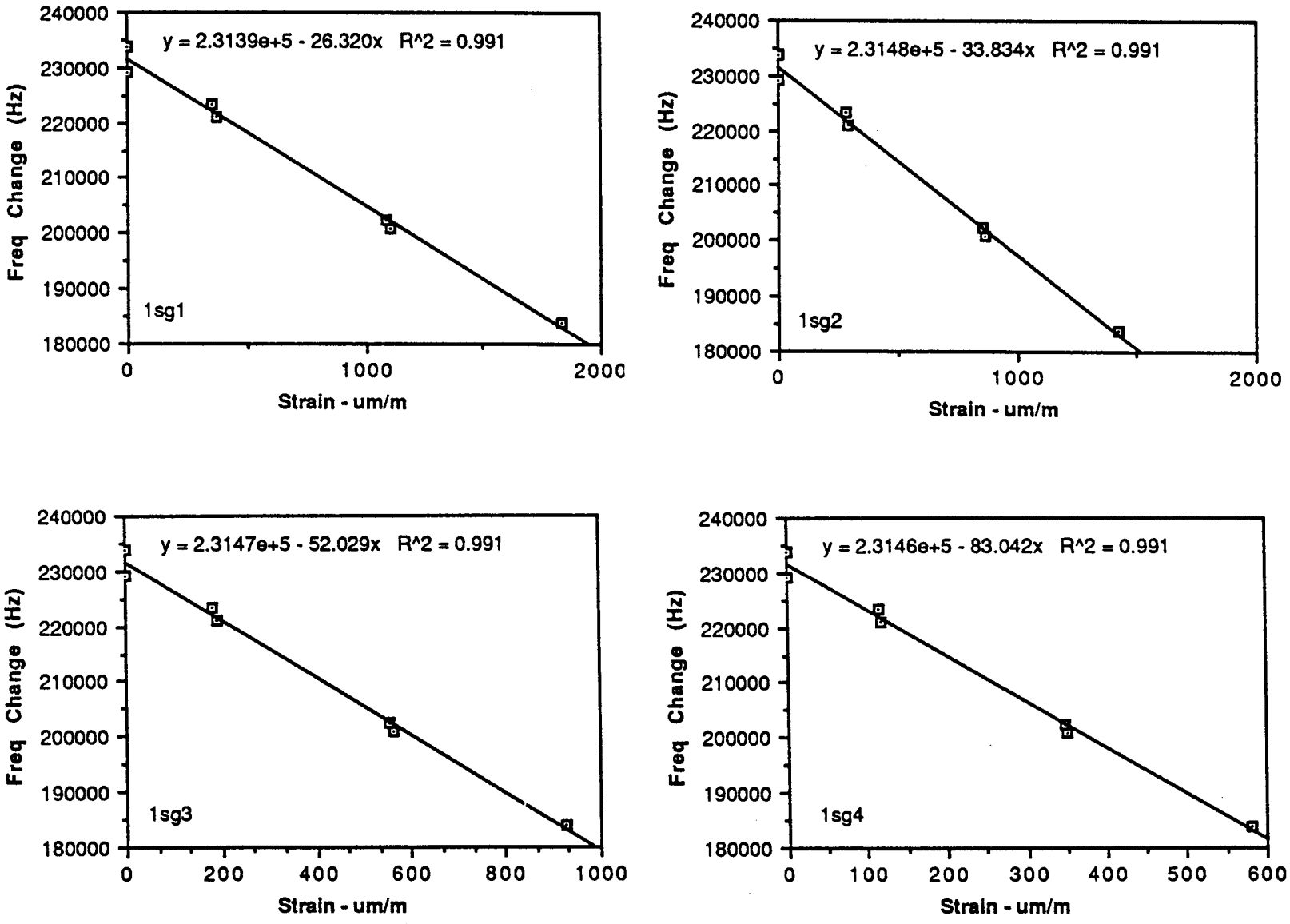

Figure 3. Plots of frequency change of OPLL vs. strain for the third tube. The strain gauges were located as in figure 2. The plots are coded by strain gauge number. (1sg1 is correlation with strain gauge 1)

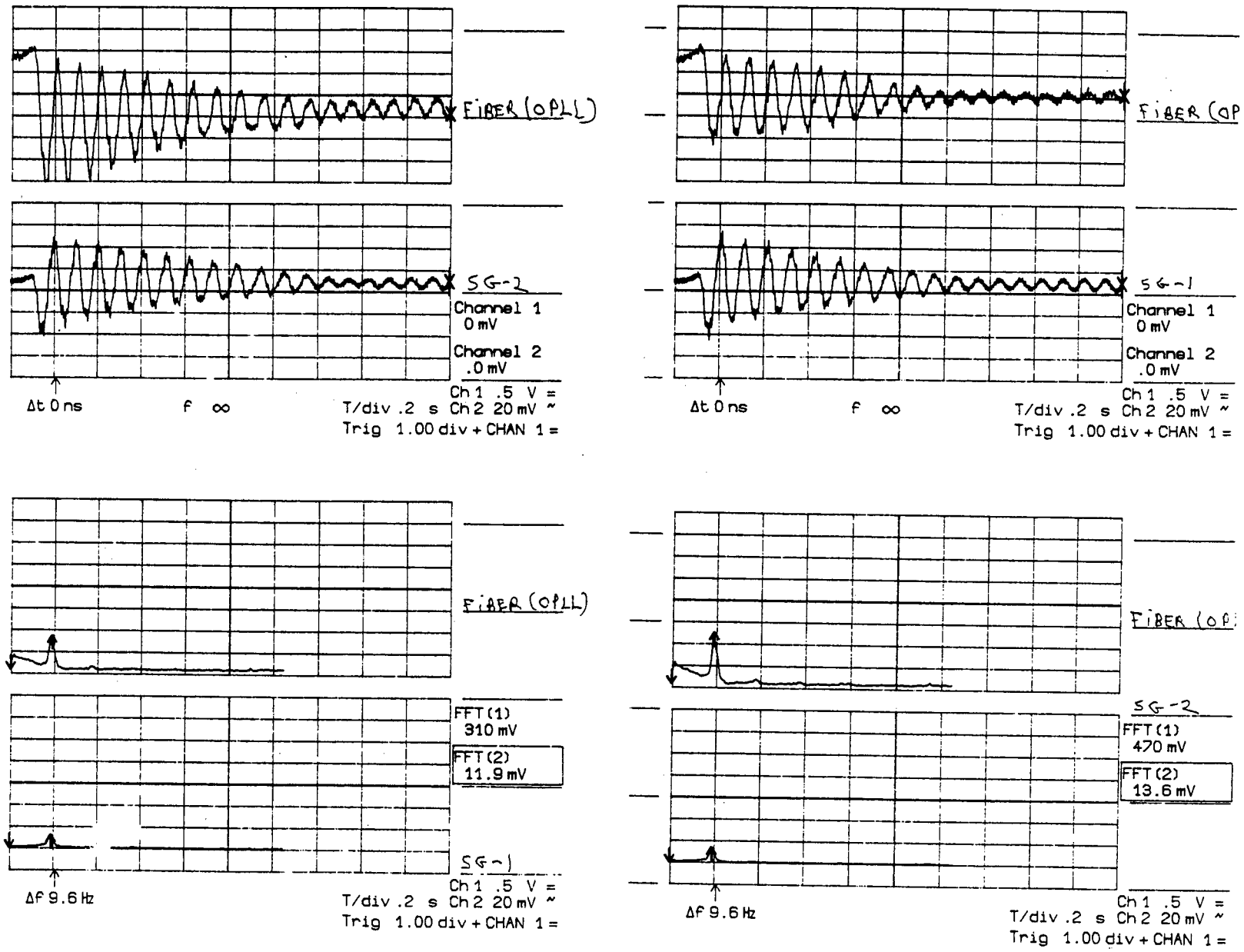

Figure 4. Data obtained for vibrating tube. Signal from the optical fiber is at top of each plot and strain gauge signal is at bottom. (Tube 3).

IV. CHARACTERIZATION OF METAL MATERIALS

NONDESTRUCTIVE EVALUATION OF TEMPER EMBRITTLEMENT IN HY80 STEEL

S. G. Allison, W. T. Yost and J. H. Cantrell
Mail Stop 231, NASA Langley Research Center
Hampton, Virginia 23665-5225

D. F. Hasson
Mechanical Engineering Department, U S Naval Academy
Annapolis, Maryland 21402

INTRODUCTION

The problem of temper embrittlement has accompanied the use of alloy steels for a number of decades and has been thoroughly studied and documented [1,2,3,4]. Temper Embrittlement (used here to include the phenomenon of Stress Relief Embrittlement) is the decrease of impact toughness which occurs in susceptible commercial grade alloy steels when they are heated within or slowly cooled through the embrittling temperature range of approximately 371 to 599 degrees C (700 to 1110 degrees F). It is caused by migration of impurity elements such as sulphur, phosphorus, tin, antimony and arsenic to prior austenite grain boundaries and is primarily encountered during post-fabrication heat treatments such as those used to relieve residual stresses. Studies show that, although these embrittling elements are typically present in bulk weight percentage concentrations of 20 to 200 ppm, grain boundaries of embrittled steel can contain concentrations that are 1 to 2 orders of magnitude greater due to segregation during heat treatment. This is determined by using Auger electron spectroscopy of fracture surfaces of embrittled test samples broken and analyzed in vacuum. Approximately 500 angstroms of material are typically removed from the fracture surfaces by ion milling before the concentration returns to that of the bulk material.

Temper embrittlement does not occur in high purity steels [2]. Unfortunately, manufacturing of high purity alloy steels is prohibitively expensive and is done primarily when research grade material is needed. The alloy examined in this study is commercial grade HY80 (Ni-Cr-Mo-V) casting steel [5] containing various impurity elements which can cause temper embrittlement. Steels such as HY80 [6,7] have been given considerable attention regarding temper embrittlement due to their extensive use and due to continuing trends toward components requiring high yield strength and high impact toughness.

Presently, measurement of temper embrittlement involves destructive mechanical testing [8]. For an existing component this requires cutting a piece from the component, machining samples and breaking them in an impact test machine to measure impact toughness. This is an expensive process which also leaves a hole in the component that must be filled with weld material. A nondestructive test technique is needed to replace the present destructive technique to detect loss of impact toughness by temper

embrittlement in steels. This paper presents the results of preliminary research at NASA Langley Research Center leading to identification of a nondestructive test technique for detecting temper embrittlement in HY80 steel. This technique measures magneto-acoustic emission (MAE) associated with reversible domain wall motion at low magnetic fields. The objective of this project is to develop a laboratory measurement system with accompanying science base that will establish ground work leading to development of a field-usable technique for nondestructively assessing temper embrittlement in large cast components without removal from service.

MATERIAL AND SAMPLES

Commercial grade HY80 casting steel [5] is a quenched and tempered martensite made using the basic electric arc melting process. Water quenching from the austenite range forms martensite with some retained austenite and possibly some pearlite and bainite depending on the cooling rate during quenching. This quenched material is then tempered at 649 to 691 degrees C (1200 to 1275 degrees F) to obtain the desired toughness while producing a yield strength of approximately 80ksi. Significant temper embrittlement usually does not occur until after quenching and tempering. It is primarily brought about by post-fabrication heat treatment for stress relief which, unfortunately, requires heating within the embrittling temperature range.

Test samples used in this study are taken from an argon oxygen decarburizing (AOD) processed material which is poured into a large test block. Metallurgical analysis shows 0.0234 cm grain size and chemical composition weight percentages including 2.88 Ni, 1.40 Cr, 0.52 Mo, 0.009 V, 0.15 C, 0.20 P, 0.008 S, 0.006 Sn, 0.006 As and less than 0.002 Sb. This unembrittled quenched and tempered test block is cut into six slabs. Slab number 6 is left unembrittled and slabs 1 thru 5 are heat treated at 538 degrees C (1000 degrees F) for 1, 5, 24, 50 and 100 hours, respectively, to produce a different amount of embrittlement in each slab. Standard Charpy V-Notch (CVN) impact test samples [8] and NDE research test samples are machined from each of the six slabs following the embrittling heat treatments.

The 6 bar-shaped NDE research test samples are 9.208 +/- 0.005 cm. long by 1.598 +/- 0.003 cm. wide by 1.280 +/- 0.003 cm. thick with faces machined smooth, flat and parallel. The research test samples are forwarded to NASA Langley where surfaces are lapped using 5 micron alumina grit on 0.635 cm (1/4 inch) thick glass.

Impact toughness is measured at -73, -18 and -1 degrees C (-100, 0 and +30 degrees F) test temperatures using a standard pendulum impact energy test machine [8]. In Fig. 1, results of tests conducted at -1 degree C indicate a dramatic loss of impact toughness with heat treatment. Examination of CVN fracture surfaces shows the expected transgranular fracture for the unembrittled material and intergranular fracture for the embrittled material. In contrast to these large changes in the impact toughness, other mechanical properties such as hardness, yield strength and ultimate strength change very little with these embrittling heat treatments.

EXPERIMENTS

In Fig. 2, laboratory 60 Hz, 110 volt power stabilized by a line power regulator and adjustable by a variable transformer (variac) supplies

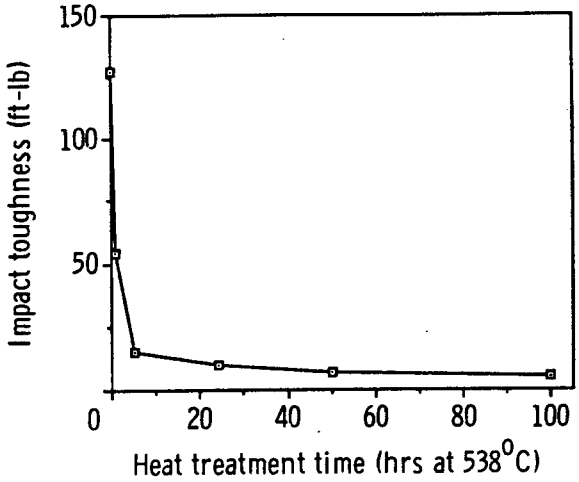

Fig. 1. Impact toughness vs. heat treatment time for CVN samples from slabs heat treated 0, 1, 5, 24, 50 and 100 hours, respectively, at 538 degrees C and broken at -1 degree C.

power through a step-down isolation transformer and switchbox to a pair of water-cooled electromagnets. The step-down isolation transformer decreases variac output to 28 volts maximum and provides isolation from the electrical service. The switchbox is IEEE488 interfaced and turns magnet power on and off by computer command. The electromagnets externally apply a 60 Hz alternating magnetic field to the test sample.

Output of a magnetic induction pickup coil surrounding the test sample is read by an rms voltmeter and is used to duplicate magnetic field intensity in the test material from one sample to the next. An acoustic emission (AE) transducer with a resonant frequency of 175 KHz is acoustically coupled to the sample. The AE transducer is shielded against magnetic field interference [9,10] by two layers of 0.004 inch thick Mu-Metal. The AE signals from the transducer are amplified 60 dB and filtered to pass frequencies from 125 kHz to 1 MHz. AE signals are measured by a Hewlett Packard 3400A rms voltmeter, thereby making it possible to determine the rms power detected by the AE transducer. This information is used in setting up each measurement to assure that the AE transducer is well bonded to the sample. The test apparatus includes foam rubber pads that acoustically isolate the sample from the magnets and also includes conducting straps that ground the sample and magnets to eliminate effects found to influence the MAE measurements.

The amplified AE signal is further amplified 40 dB. A sample/hold and timing generator system establishes a 10 microsecond time window that can be positioned to select voltages at the desired point in time relative to the AE signal pattern. An oscilloscope is used to observe the AE signal forms and the sample/hold marker (the oscilloscope and sample/hold are both triggered synchronous with the ac line). Fig. 3 shows a typical AE envelope pattern seen on the oscilloscope. The AE envelope peaks 120 times per second corresponding to the magnetic field passing through zero 120 times per second. For these tests, the sample/hold is positioned to select voltages at the peak of the AE signal envelope and a lab computer records 20000 voltages within the time window for each sample.

RESULTS AND DISCUSSION

The 20000 AE pulse heights obtained for each test sample are divided

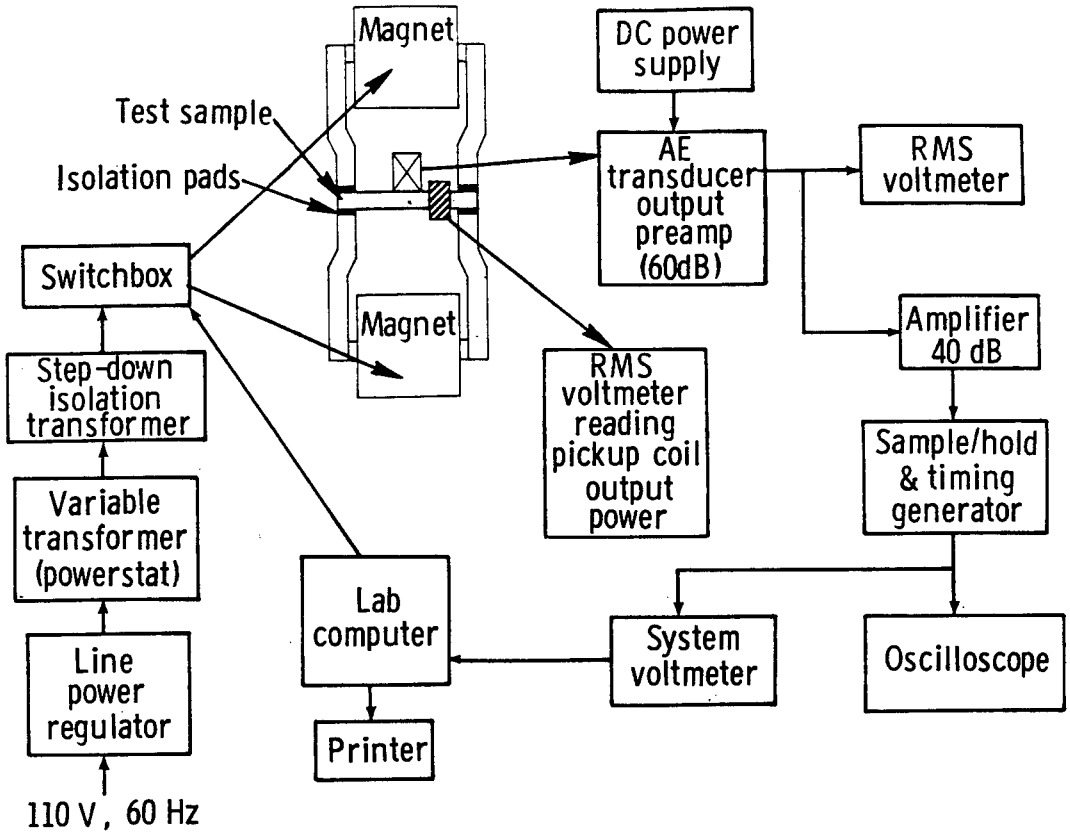

Fig. 2. System for measuring magneto-acoustic emission (MAE). A transducer detects AE generated by alternating magnetic field. A lab computer reads AE signals from a voltmeter-sample/hold arrangement.

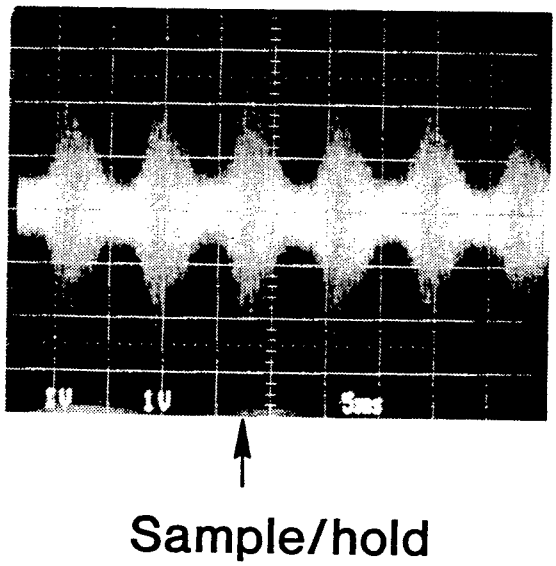

Fig. 3. AE pattern resulting from magnetic field alternating at 60 Hz. A sample/hold system samples voltages at the AE envelope peak.

among 41 equal voltage intervals and the resulting distributions are plotted. In Fig. 4 histograms for HY80 in the unembrittled (not heat treated) and the embrittled (heat treated 1 hour) conditions are shown in the left and right hand graphs, respectively. Data outside the center electronic noise region of the pulse height distribution is fitted by a gaussian distribution function. The center region of the pulse height distribution is not used in the gaussian fit because it is rich in electronic (background) noise not generated by the test sample. This center background noise region is identified by generating a separate histogram without applying power to the electromagnets. The full width at half maximum (FWHM) is obtained from the fitted equation for each sample and is plotted vs impact toughness in Fig. 5 thereby showing differences in pulse height distribution (i.e. histograms for embrittled steel are wider than those for unembrittled steel). These observed difference in pulse height distribution indicate that the embrittled steels produce more of the larger AE events than does the unembrittled steel.

These results led to a preliminary model based on the concept that grain boundaries of embrittled steel are larger obstacles to magnetic domain wall motion than are grain boundaries of unembrittled steel. The phenomenon of embrittled steel producing more of the larger AE events than does unembrittled steel can be explained in terms of the magnetoelastic-type interaction between domain walls (mostly 90 degree domain walls) and grain boundaries. The applied alternating magnetic field causes discontinuous motion of magnetic domain walls [10,11] as they cross over effective potential barriers such as grain boundaries which resist domain wall motion. This results in generation of stress pulses (AE events), particularly when 90 degree domain walls move since this interaction results in sudden 90 degree changes in unit cell elongation direction. The action of magnetic domain walls jumping across larger obstacles produces larger AE events. The enhanced concentration of tramp materials at grain boundaries [12] of embrittled steel is proposed herein as the cause of these grain boundaries being larger obstacles to domain wall motion than are grain boundaries of unembrittled steel.

To add support to the preliminary model, magnetic retentivity

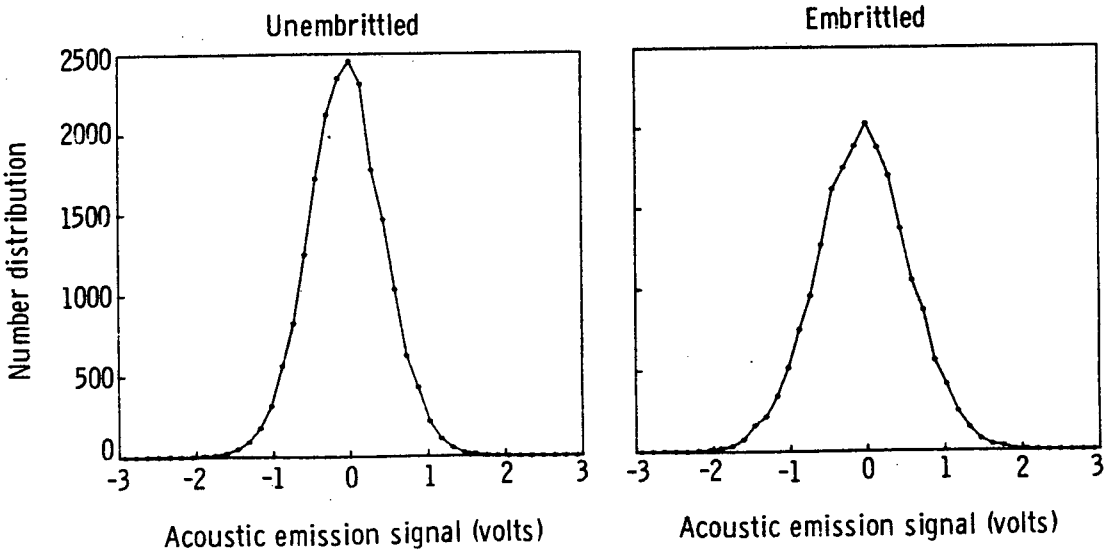

Fig. 4. Histograms of 20,000 AE pulse heights divided among 41 equally spaced voltage intervals. Histograms for embrittled HY80 steel, such as that shown in the right hand graph for HY80 heat treated 1 hour, are wider than histograms for unembrittled HY80 steel.

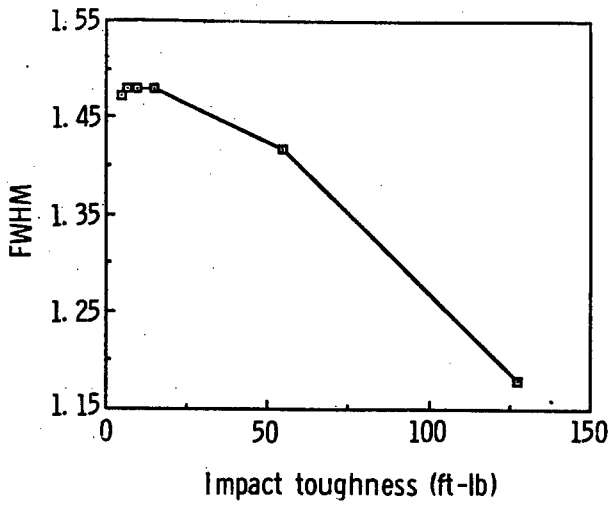

Fig. 5. Plot of full width at half maximum (FWHM) vs. impact toughness showing that histogram shape is influenced by temper embrittlement.

(remanence) is measured after simple modification of the system to allow generation of magnetization curves. For this measurement, a dc power supply provides current to the magnets while an integrating flux meter reading output of a calibrated pickup coil measures magnetic induction in the test sample. Each sample is initially demagnetized using a degaussing procedure. Following demagnetization, incrementally increasing magnet current is applied until the test sample is magnetically saturated. Magnet power is then incrementally decreased to zero and the amount of magnetic field retained after turning the magnet off is measured. Results of the magnetic retentivity measurements are shown in Fig. 6 where remanence, expressed in kilogauss (KG), for each of the six samples is plotted against known impact toughness. These results show that when the externally applied magnetic field is removed, the embrittled samples retain more magnetic field than does the unembrittled sample.

These remanence test results point to the same explanation as did the MAE results and can be explained in terms of the magnetoelastic

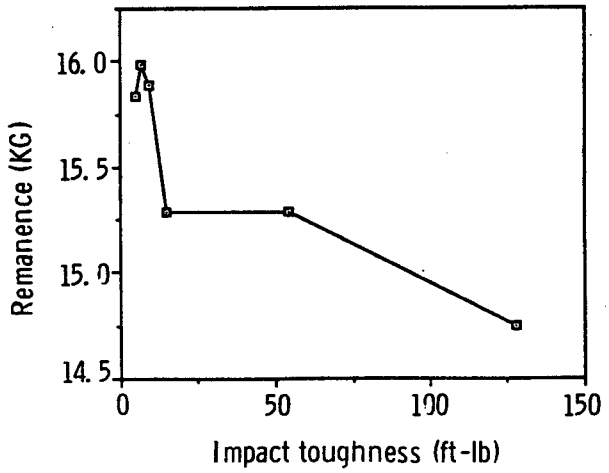

Fig. 6. Plot of remanence vs. impact toughness showing that retentivity is influenced by temper embrittlement.

interaction with grain boundaries. By driving the material to magnetic saturation, magnetic domain walls are forced to cross over grain boundaries. Upon removing the applied field, magnetic domain walls attempt to move back across grain boundaries and, in doing so, hang up more on grain boundaries of embrittled steels than on grain boundaries of unembrittled steel. This further supports the model basis that grain boundaries of embtittled steel are larger obstacles to domain wall motion than are those of unembrittled steel.

For additional differentiation between embrittled and unembrittled specimens, the raw histograms from the MAE tests (Fig. 4) are subtracted from each other and the area enclosed by the number distribution is calculated as follows: Histograms from two separate measurements obtained for the unembrittled steel with the transducer re-bonded for each measurement are subtracted from each other. Results are shown in the left hand graph in Fig. 7. The unembrittled sample histogram is then subtracted from histograms for each of the embrittled steels and the enclosed areas associated with these subtractions are calculated. Result of subtraction for a test sample heat treated one hour is shown in the right hand graph in Fig. 7. In Fig. 8, these enclosed areas are plotted against impact toughness. These measurements show that by duplicating the magnetic power level in samples of identical geometry taken from the same quenched and tempered casting and using the same transducer consistently well bonded, differences in MAE corresponding to temper embrittlement are observed that allow distinction between unembrittled and embrittled HY80 steel.

CONCLUSIONS

This study shows that magnetic and magnetoacoustic properties of HY80 appear to be influenced by temper embrittlement. A preliminary model has been developed based on the concept that the same segregation of tramp materials at grain boundaries that causes temper embtittlement also increases grain boundary resistance to domain wall motion. This increased resistance of grain boundaries to magnetic domain wall motion causes an increase in the number of larger AE events generated by magneto-acoustic emission as observed experimentally. Additional testing is required to broaden the science base for this work and is to include characterizing

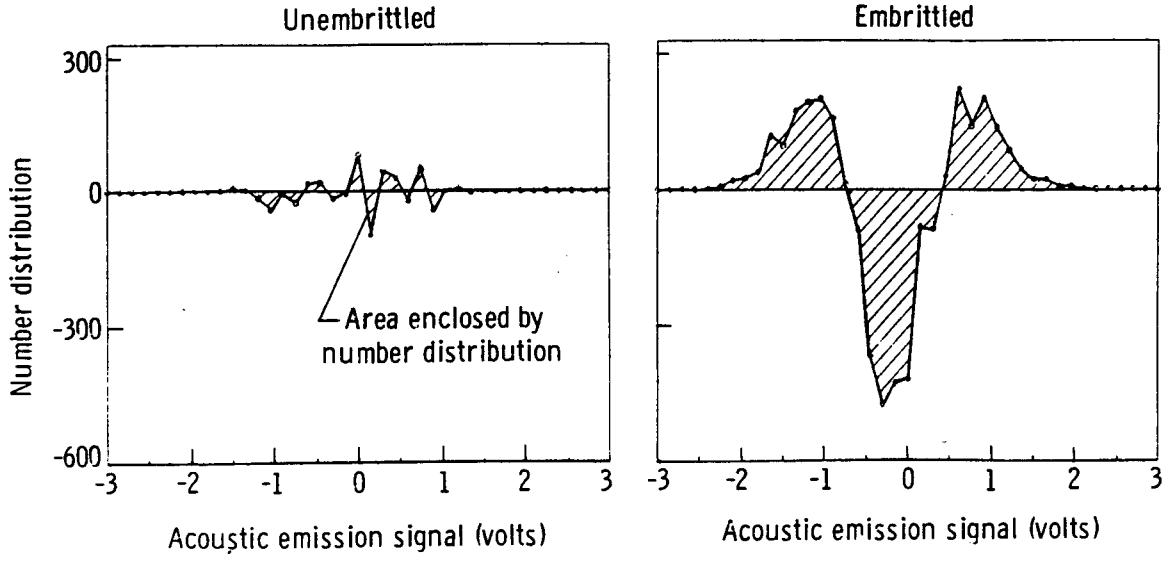

Fig. 7. Results of histogram subtraction. Area enclosed by number distribution is used to compare embrittled samples to unembrittled sample.

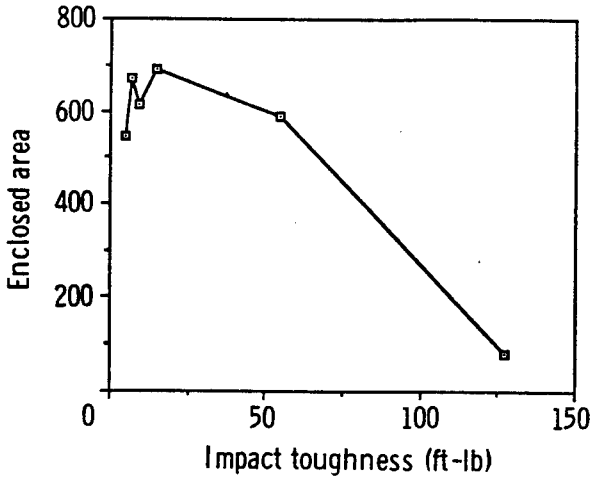

Fig. 8. Enclosed area vs. impact toughness.

stress effects [11] and temperature effects. Also, test samples from an HY80 casting having different metallurgical characteristics such as grain size and impurity concentrations are being obtained for comparison of measurement results.

ACKNOWLEDGEMENTS

This work is being sponsored by the David Taylor Naval Ship Research and Development Center (DTNSRDC) through an interagency agreement. The authors are grateful for helpful discussions with Mr. Robert De Nale of DTNSRDC and for the invaluable assistance of Mr. Dale Stone of NASA Langley.

REFERENCES

1. J. H. Hollomon, Trans., ASM, 36, 473- 540 (1946).

2. D.L. Newhouse, ASTM STP 407 (1967).

3. D.L. Newhouse, ASTM STP 499 (1971).

4. C.L. Briant and S.K. Banerji, "Treatise on Materials Science and Technology", Vol. 25 (Academic Press, 1983).

5. MIL-S-23008C (16 August 1982).

6. D. A. Woodford and R. W. Stepien, Metal. Trans. A, 11A, 1951 (1980).

7. R. Viswanathan and T. P. Sherlock, Metal. Trans., 3, 459 (1972).

8. ASTM-E23-86 (1986).

9. J. D. Jackson, "Classical Electrodynamics", John Wiley & Sons, (1962).

10. B. D. Cullity, "Introduction to Magnetic Materials", Addison-Wesley, Menlo Park (1972).

11. H. Kusanagi, H. Kimura and H. Sasaki, J. Appl. Phys., 50 ,4 (1979).

12. K. E. Szklarz and M. L. Wayman, Scripta Metall., 29, 341-349 (1980).

GENERATION OF ELASTIC WAVES BY

ELECTROMAGNETIC INDUCTION

D. J. Mayton*† and William P. Winfree
MS 231
NASA Langley Research Center,
Hampton, VA 23665

INTRODUCTION

Photoacoustics in solids provides a useful technique for both characterization of material properties and the detection of defects. In photoacoustics, a periodic thermal source is used to generate an elastic wave. Typically the thermal source is a laser or charged particle beam, however other sources are currently being investigated. A need for other sources is required for objects which have reflective surfaces or are too large to fit into a vacuum chamber, such as large metallic structures.

For metallic structures, inductive heating may provide an appropriate thermal source. Inductive heating occurs when a time varying magnetic field is coupled into a conductor. Since the interaction is between the conductor and the magnetic field to approximately the skin depth of the material, no coating is required to absorb the energy. In addition the power is easily modulated and a coil can be tailored to reach areas of the structure inaccessible to other sources.

This paper investigates the generation of elastic waves in a conductor with induction heating. Elastic waves were generated in an aluminum rod and detected with an accelerometer. The technique is shown to be able to detect simulated defects far below the thermal wavelength or the skin depth for the respective excitation frequencies. Section II discusses the technique for generating and detecting the elastic waves. A series of measurements on rods with different depth defects is reported in section III.

MEASUREMENT SYSTEM

Inductive heating results from the resistance of a conductor to eddy currents induced by a time varying magnetic field. To efficiently couple a magnetic field into a conductor, a portion of a toroid core was removed and the remainder wrapped with wire as shown in figure 1. The core was driven with a broad band power amplifier with a 50 ohm output impedance. To increase the efficiency of the system, capacitors were added in parallel and series to the core on the sample, forming a tank

*Analytical Services and Materials, Inc.
† current address Department of Materials Science and Engineering,
102 Maryland Hall, Johns Hopkins University, Baltimore MD 21218

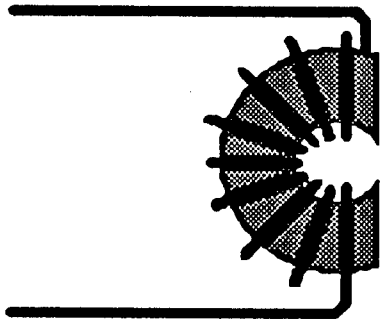

Figure 1. Cross section of typical toroid core used for coupling the magnetic field into the sample.

circuit with an impedance 50±3 ohms at a resonant frequency between 100Khz and 1 Mhz. The tank circuit was then driven at its resonant frequency to give an inductive heating source.

Photoacoustics has demonstrated elastic waves can be generated by periodically cycling a thermal source. For the inductive source described above this was easily obtained by amplitude modulating the drive at a frequency at least 2 decades below the drive frequency. The generated elastic wave was then detected by an accelerometer attached to the sample. The accelerometer signal after charge amplification was input into a lockin detector which was synchronously detecting at the modulation frequency of the drive. To obtain a signal which was above the noise, the modulation frequency was varied until a resonance of the sample, described later, was located.

To simulate the process used in photoacoustics, the core was mounted on a computer controlled scanner arm, so that the thermal source could be scanned over the sample surface. A length of the sample was then scanned with the coil and the in phase and quadrature signals from the accelerometer recorded as a function of position along the rod. The measurement system with a rod mounted is shown in figure 2.

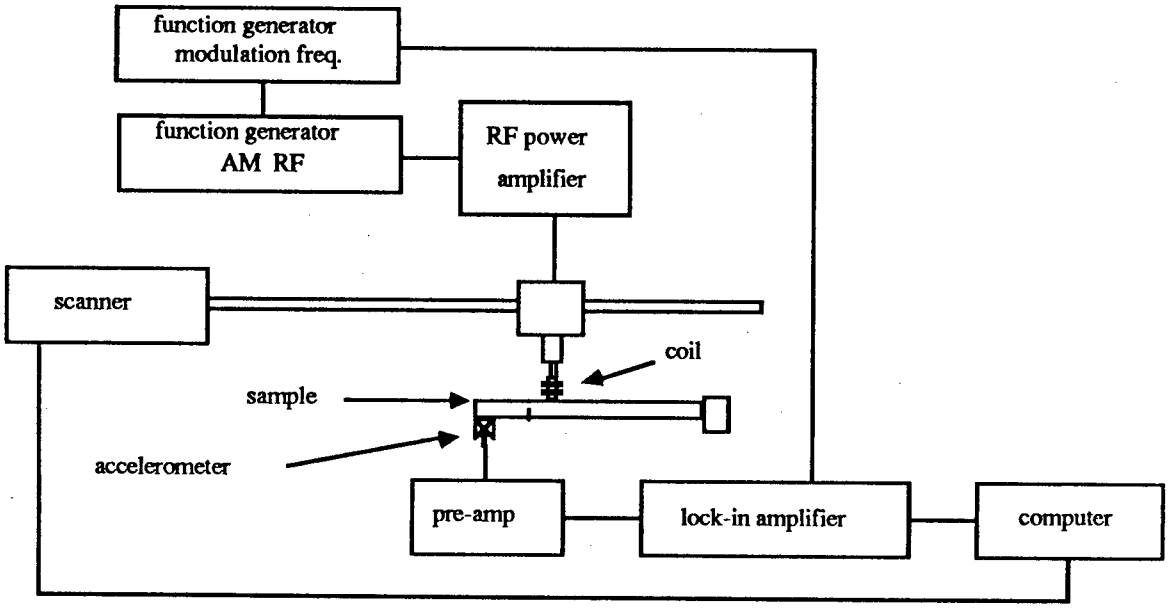

Figure 2. Experimental setup for scanning induction heating source across sample with defect.

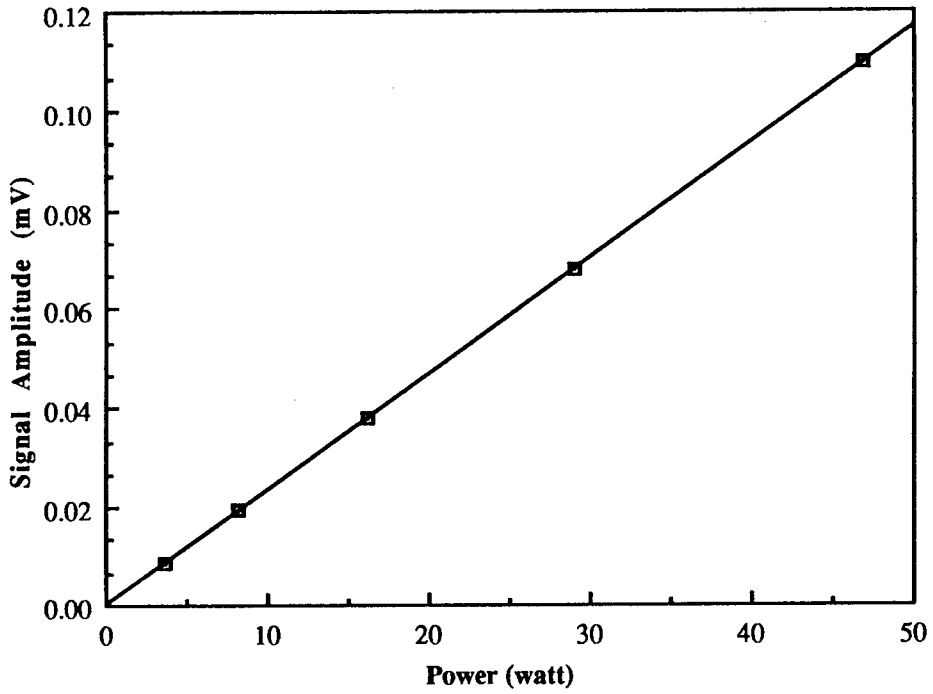

Figure 3. Amplitude of signal received at accelerometer as a function of power to the toroid core.

RESULTS AND DISCUSSION

In photoacoustics, an elastic wave generated by a thermal source has an amplitude which is proportional to the thermal expansion of the solid. Since the thermal expansion is linearly proportional to the power absorbed by the solid, a signal resulting from a thermally generated elastic wave is proportional to the input power rather than the input amplitude. To demonstrate that the elastic wave generated by the induction heating is the result of a thermally induced strain as is the case for photoacoustics, the power applied to the coil was varied and the amplitude of the received signal was measured. The data, shown in figure 3 with a straight line drawn for comparison, indicates the signal is thermally induced, and therefore can be analysed in a manner similar to photoacoustics.

Measurements were then made by scanning the coil over a 1.27 cm square aluminum rod which was 101.6 cm long and mounted at both ends. The accelerometer was secured to the center of the rod by drilling a hole through the rod and screwing the accelerometer to the back. The head of the screw was recessed to allow scanning over the length of the rod. A 0.1 cm wide, 0.9 cm deep band saw cut 17.5 cm from the center of the rod formed a slot which simulated a defect.

A thermally induced strain will exist principally to a depth of one thermal diffusion length into the sample. The thermal diffusion length for the lowest modulation frequency (144 Hz) was found to be much less than the width of the rod (~0.07 cm). Therefore the thermally induced strain is confined to one side of the rod, generating a bending which can excite transverse waves and modes.

If a transverse wave is excited in a slender rod with both ends rigidly bound, the frequencies of the normal modes are given by the roots of the equation

$$1 - \cosh(k l) \cos(k l) = 0 \qquad (1),$$

Table I. Calculated and measured frequencies for first seven modes of 101.6 cm long, 1.27 cm square aluminum rod.

Mode #	Calculated frequency (Hz)	Observed frequency (Hz)
1	64	
2	178	144
3	350	305
4	579	510
5	865	752
6	1208	1187
7	1609	1464

where l is the length of the rod, and k is given by the expression

$$k = \frac{12\,\rho}{Y\,W^2}\,\omega^{1/2} \qquad (2),$$

where Y is the Young's modulus, W is the width of the rod, ρ is the density and ω is the angular frequency. For the long aluminum rod bound at both ends, the frequencies of the first few modes are given in table 1, with corresponding modulation frequencies of resonances found close to these values. For all cases the measured value was found to be lower than expected for a perfect rod. The rod, of course, was far from perfect, with a hole drilled through the center, a mounted accelerometer, and a slot which was 70% of the thickness of the rod deep.

The amplitude of displacement for the normal modes of a slender rod is given by the expression

$$\eta(x) = A[\sinh(k\,x) + \sin(k\,x)] + B[\cosh(k\,x) - \cos(k\,x)] \qquad (3),$$

where

$$A = B\,\frac{\cosh(k\,l) - \cos(k\,l)}{\sinh(k\,l) - \sin(k\,l)} \qquad (4).$$

The displacement of mode 5 as a function of position is shown in figure 4, along with the in phase and quadrature signals measured for the modulation frequencies found to excite a resonance closest to these modes. The calculated displacements correlate with the quadrature signal for all modes and this suggests that for a perfect rod, all the measured signal would be quadrature to the modulation. The correlation between calculated displacements and measured signals, and the correlation between measured and calculated mode frequencies, indicate that the thermally induced strain is exciting transverse waves in the rod.

For transverse waves propagating along a slender rod, a change in the dimension of the rod changes the phase velocity and impedance of the rod. A wave propagating across an interface between a thick segment of the rod to a thinner segment would therefore be partially reflected and partially transmitted. If this thinning exists only for a short segment of the rod compared to the wavelength of the transverse wave, the effect

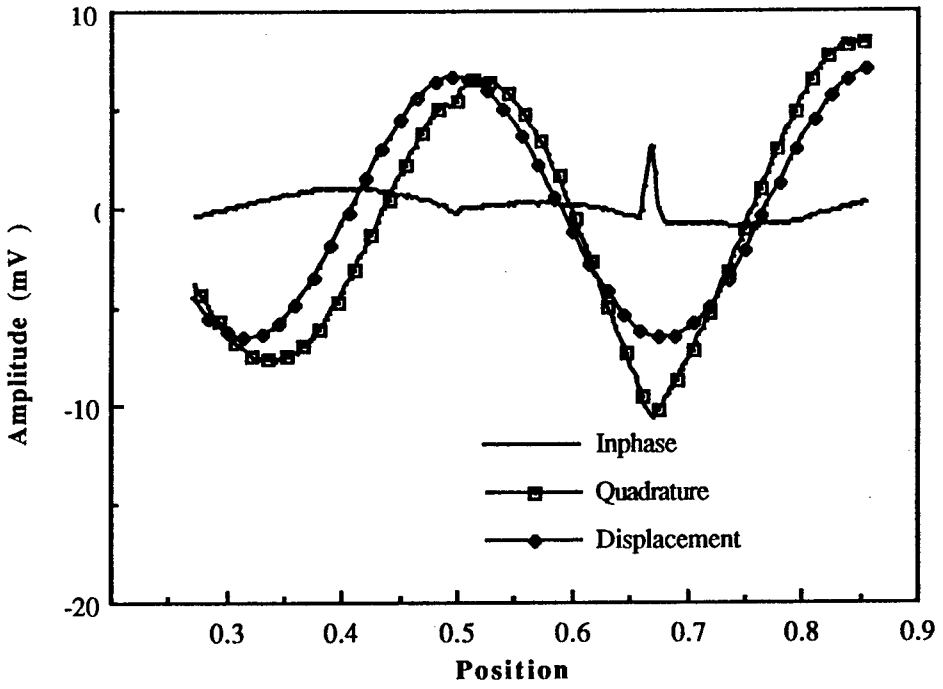

Figure 4. The inphase and quadrature signals for 752 hz mode as a function of position of the toroid normalized to the length of the rod.

is small, and increases as the wavelength decreases. The slot produces a thin segment in the rod. The effect of this thinning of the rod can be seen in both the in phase and quadrature signals, however is more pronounced in the quadrature signal. It is apparent that the transverse waves are being reflected off the defect and that these reflections can be detected a considerable distance from the defect. A second result of thinning a segment of the rod occurs when the elastic wave is generated over the thinner section, and since the width of the rod has decreased, the magnitude of the bending is greater. This results in a localized effect as the core traverses over the defect, and can easily be seen in the data.

The shape of this signal contains information on core size, defect size, and the rod dimension. To identify the contribution from the core size, four different footprint sizes were used to excite the elastic waves and measurements were taken over the segment with the slot. As the size of the footprint increased, the signal level amplitude decreased for the same input power. To compare the different footprint sizes, the phase shift between received signal and source was measured as a function of position with a modulation frequency of 752 Hz. The width of the signal peak increases and the magnitude decreases as the footprint size increases. The width of each peak as a function of footprint size is a quantitative indicator of the core size's effect on the resolution of the system and is shown in table II. The minimum width obtainable for

Table II. Width of localized signal due to defect as a function of size of toroid core footprint.

Footprint Size(cm)	Width of signal(cm)
0.25	0.85
0.50	1.02
1.10	1.87
1.80	3.05

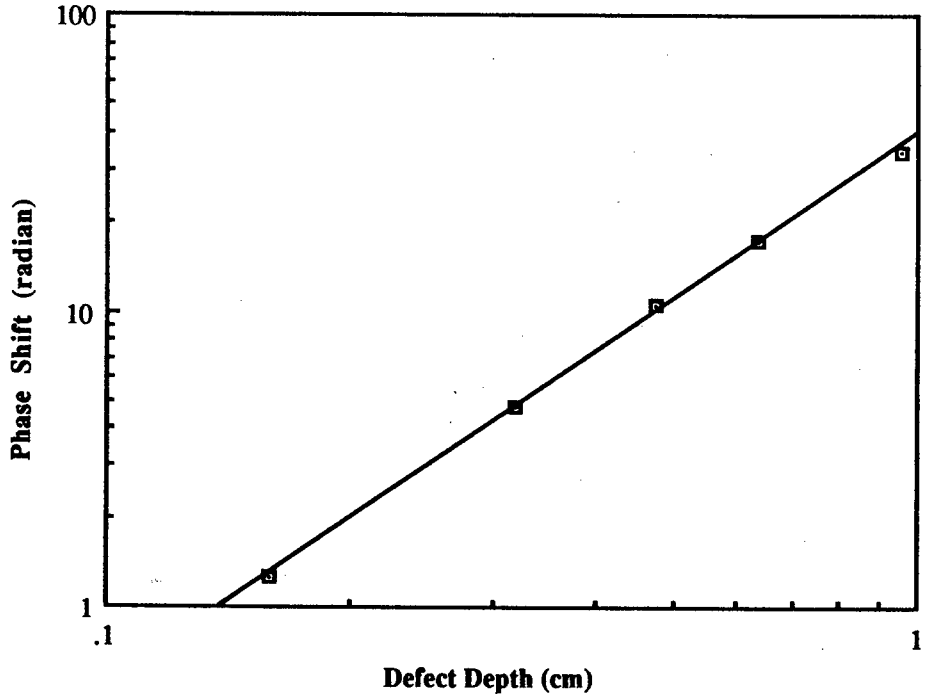

Figure 5. Amplitude of phase shift in the received signal as the core passed over the defect for slots of different depths from the back side of the rod. Plotted with the data is a log fit to the data indicating the phase shift goes as the depth of the slot to approximately 1.9 power.

this system was approximately one half the width of the rod. As can be seen from the table, after reducing the size of the core to about one quarter the size of the rod, further reductions will not significantly increase the resolution of the system.

In order to determine the contribution of defect depth to the signal shape, a series of 9 shorter rods with simulated defects varying in depth and position were tested. These aluminum rods were all 30.5 cm long with 0.1 cm wide band saw cuts. These samples were divided into two sets to examine two different affects of the simulated defect on the observed signal. For one set, each rod had a slot cut at a different location, all the approximately 75% of the thickness of the rod. For the second set, each rod had a slot cut to a different depth at 6.72 cm from the free end of the rod. The samples were mounted in the system with only one end clamped and a accelerometer attached, using phenol salicilate, to the free end. Phase shift relative to the source was then measured as a function of position and the natural log of these results for bars 1-6 are shown in figure 5. The slope of the best fit line is about 1.9 indicating a power relationship of 1.9 between the phase shift and defect depth.

Since the presence of the slot results in a reduction in the effective stiffness of the rod as a whole, it would be expected to reduce the resonant frequency of the rod. This expected trend can be seen in the measurements of the resonant frequency as a function of slot size shown in figure 6. This is true, however, only if the slot occurs in a region of large strain. As the slot moves towards the center of the rod, which is a nodal point in the transverse standing wave, its effect on the resonant frequency decreases, and the resonant frequency approaches that of a rod with no slot. This can be clearly seen from the measurement of

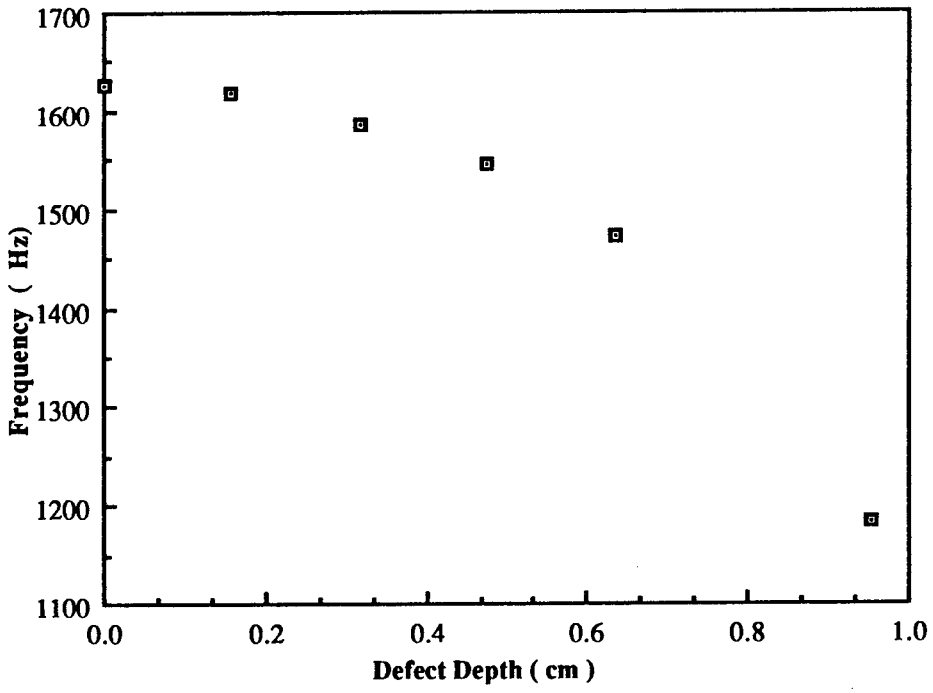

Figure 6. Resonant frequency of rod measured for the series of rods with the slots to different depths.

resonant frequency as a function of position in figure 7. Sufficient modal analysis at several different frequencies could detect the size and position of such a defect, with the excitation at a single point and the measurement at a single point, as has been demonstrated elsewhere.

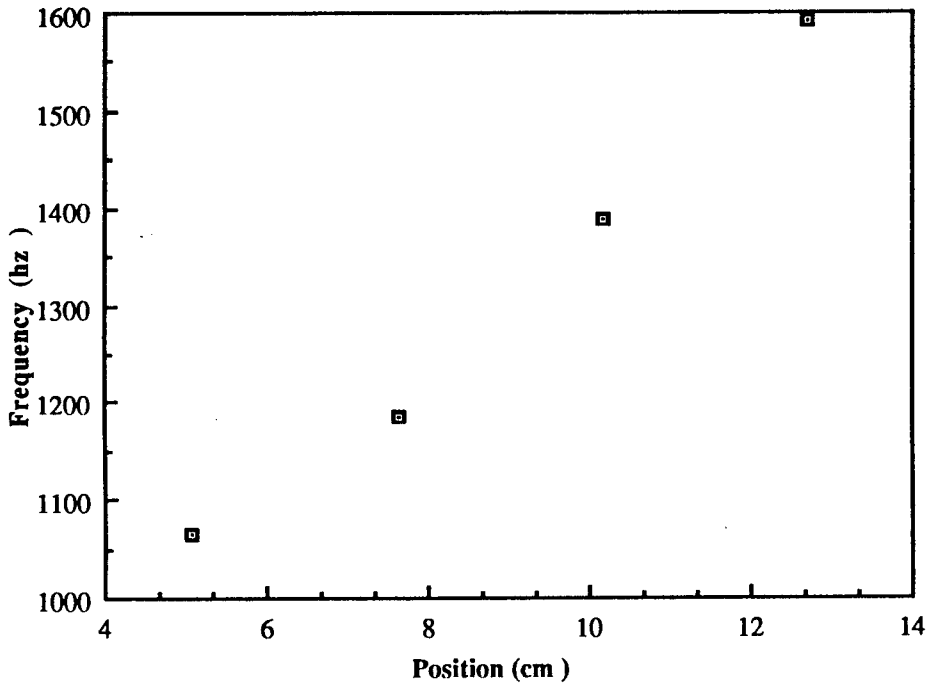

Figure 7. Resonant frequency of rod measured for the series of rods with the slots to different distances from the end of the rod.

SUMMARY

It has been shown that it is possible to generate elastic waves by induction heating in a conductor. For the case of a rod, it is possible to excite transverse waves at different positions along the sample and detect them far from the source. The transverse waves reflect off defects perturbing the normal modes of the rod. Both the depth and position of the defect effect the resonant frequency of the rod. In addition, a defect in the rod changes the magnitude of the bending as well as the phase shift between input signal and response as a thermal source passes over it.

DETECTION OF TEMPER EMBRITTLEMENT IN STEEL

BY MAGNETOACOUSTIC EMSSION TECHNIQUE

M. Namkung, W. T. Yost, J. L. Grainger* and
P. W. Kushnick**
NASA Langley Research Center
Hampton, VA 23665

INTRODUCTION

A bulk ferromagnet possesses two types of domain walls: 180° and non-180° [1]. In the case of iron-like ferromagnets, the latter type of walls are 90° domain walls. As a result of the magnetoelastic interaction, unit cells of a ferromagnet deform slightly in a way that is unique to particular types of domains [2]. Such a spontaneous deformation, called magnetostriction, causes local lattice strains at domain walls with the strain fields being particularly strong for 90° domain walls [3]. The motion of the 90° domain walls is followed by a redistribution of local lattice strain fields. Elastic energy is being released by this process and propagates in the material as acoustic waves. Acoustic emission (AE) generated due to magnetic domain wall motion is thus defined as magnetoacoustic emission (MAE).

Magnetic domain walls and lattice defects "see" each other through the local strains that they create, so the domain wall defect interaction is much stronger for 90° domain walls. In the course of external field-induced motion, 90° walls encounter strong resistance by defects. The presence of these defects, hence, creates effective potential barriers against 90° domain wall motion [4,5]. During this process of domain wall motion, 90° walls are stalled at the defect sites and, with a higher driving force, these walls execute abrupt jumps over the barrier. A sudden AE burst is produced by such discrete 90° wall motions.

During the thermally activated difussional motions at elevated temperatures, impurity atoms of certain alloys are trapped and accumulated at grain boundaries causing significant reductions in the impact strength of the material. For ferromagnets, these impurities further stregthen the potential barriers at the grain boundaries resisting the motion of 90° domain walls and the MAE characteristics of such materials should be related to the degree of temper embrittlement.

---

* AS&M Inc.
107 Research Rd., Hampton, VA 23665

** PRC Kentron Inc.
303 Butler Farm Rd., Hampton, VA 23665

Our initial study of NDE temper embrittlement detection was performed for HY80 steel samples employing a statistical method to analyze the MAE spectra produced by the application of AC magnetic field to the samples [6]. In this study the MAE signal samplitudes were detected in the 10 microsecond time-window poistitioned at the peak of the MAE bursts. These MAE amplitueds were then processed for pulse height distribution analysis. The resultant histrograms were fitted to the Gaussian distribution function and the results showed a good correlation with the impact strength of these samples.

Some questioned arised from the previous results, for example, only one MAE peak was observed in a period corresponding to a half cycle of the hysteresis loop centered at the coercive field point whereas two peaks were expected. The purpose of the present study is to resolve this discrepancy and to provide a deeper insight into the basic characteristics of MAE related to various material properties. For this, improvments were made in MAE instrumentation to provide some added control on the experimental conditions.

EXPERIMENT

A detailed description of the HY80 steel samples, magnetizing units and AE detction system can be found in Ref.1 and will not be repeated here. The experimental setup, however, has been modified to vary the AC external magnetic field frequency and to adjust the functional form of the applied field, H(t), such that the pickup coil output, e(t), can be obtained close to a desired shape. This was possible by using the feedback circuit shown in Fig. 1. Use of the feedback circuit, however, limited MAE generation and was employed only for certain occasions.

Among the six HY80 steel samples, two samples were used mainly for the present experiment. These are untreated (unembtrittled) and heat treated for 50 hours (embrittled) samples.

A waveform digitizer was used to record the MAE signal. Histograms of the MAE signal could be constructed directly by using a multichannel analyzer, or numerically from the data stored in the digitizer.

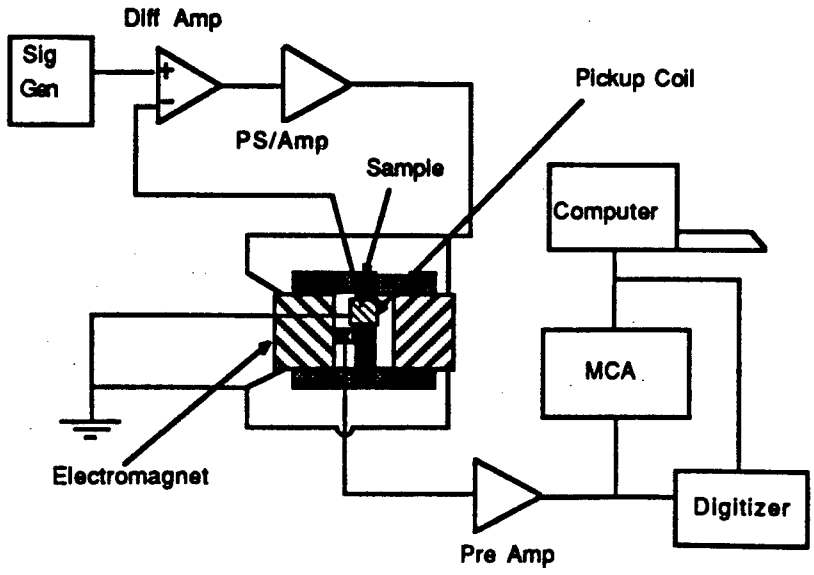

Fig. 1. Block diagram of the MAE setup including magnetizing unit, AE detection circuits and data acquisition system.

RESULTS AND DISCUSSION

Fig. 2 shows the MAE spectrum and waveform of e(t) obtained for an unembrittled HY80 steel sample at the 60 Hz AC field frequency. An approximately sinusoidal form of e(t) was obtained without using the feedback circuit. The waveform of magnetic induction, B(t), should be similar to that of e(t) except it is phase-shifted by 90^{o}. The period of e(t) corresponds to a complete sweep over the hysteresis loop. The major irrverssible domain wall motions occur just before and after B=0. This means that two MAE peaks should be observed in each one half cycle of the hysteresis loop. The MAE spectrum in Fig. 2 shows apparently a single peak which slightly lags in time behind the peak of e(t). The slight phase lag of the MAE peak with respect to that of e(t) is believed to be due to the delayed motion.

Fig. 3 shows the results obtained for the embrittled sample under the same conditions as in Fig. 2. At almost the same peak amplitude of e(t), the MAE peaks in this sample are dictinctively larger than that of the unembrittled sample. Such a difference in MAE peak amplitudes is apparently consistent with the original assumption of enhanced effetive potentail barriers in embrittled samples due to accumulation of impurties at the grain boundaries.

Fig. 4 shows the waveforms of MAE sprectrum and e(t) obtained for the umbrittled sample at .7 Hz of AC field frequency using the feedback circuit. The MAE envelope begins to spread as seen in the figure. It is shown in the next figure that the increase in the AC magnetic field intensity produces the complete two-peak structure of MAE spectrum in a half cycle of hysteresis loop. It is clear that the results in Fig. 3 were obtained by sweeping over a minor hysteresis loop reaching only the lower portion of the irreverssible domain wall motion region.

A clear double-peak structure of MAE bursts is obtained when the AC field intensity is increased at .7 Hz as shown in Fig. 5. The lack of double-peak MAE pattern at 60 Hz can be, now, explained easily. Due to the strong interaction of 90^{o} domain walls with defects, these walls are pinned during their motion. Since they are coupled with relatively

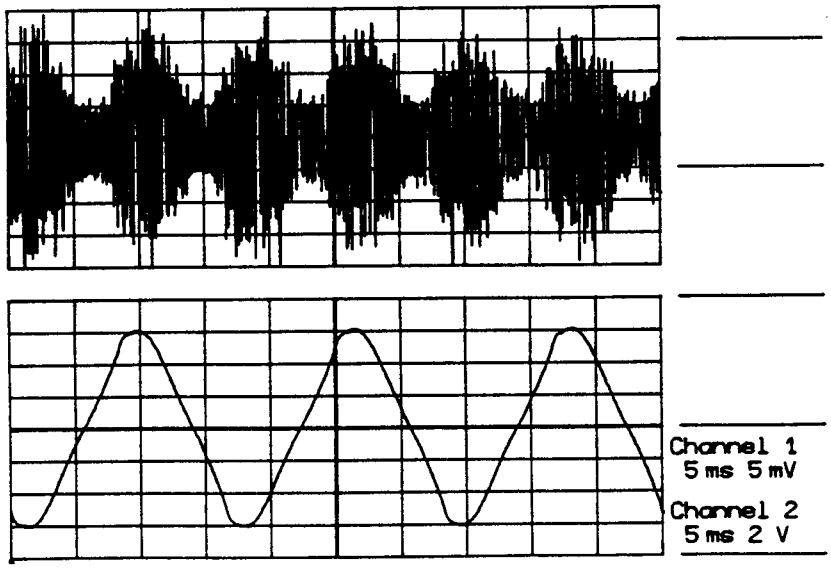

Fig. 2. MAE spectrum obtained for the unembrittled HY80 steel sample at 60 Hz AC magnetic field frequency.

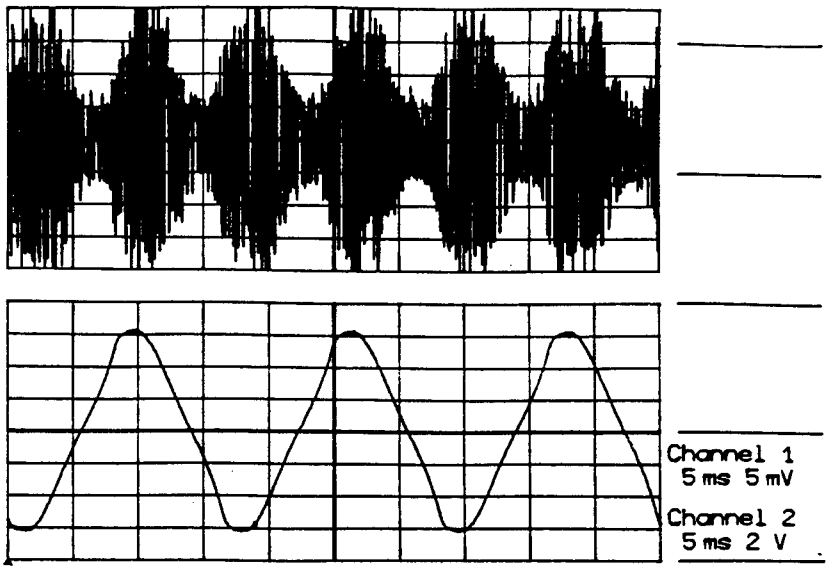

Fig. 3. Results for the embrittled sample obtained at 60 Hz. The peak MAE amplitude in this sample is considerably higher than that of unembrittled sample at the same level of B(t).

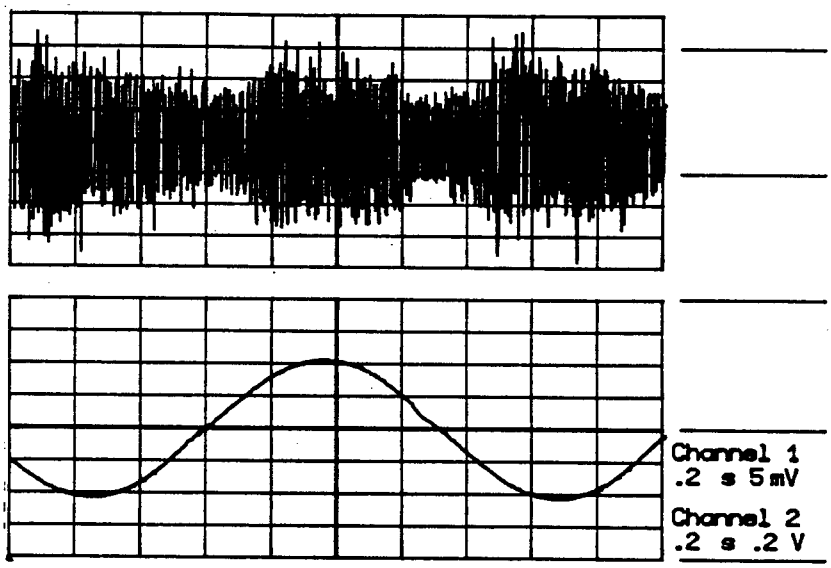

Fig. 4. Results for the unembrittled sample obtained at .7 Hz showing a spread of MAE peaks.

resistance-free 180° walls, 90° walls are bent at defect sites. At a higher frequency, fast moving 180° walls enhance the motion of 90° walls after they are freed from the defects. Hence the 90° walls spend less time in between the two major potential barriers they encounter before and after passing the point where B=0.

The results of the same measurements for the embrittled sample are shown in Fig. 6. The MAE pattern in this figure is seen to be asymmetric and its amplitude is not any higher than that shown in Fig. 5, for the same shape of e(t). There are two possible reason for such asymmetry in the MAE pattern. First, if the sample was not sufficiently demagnetized before the AC field application, the actual hysteresis loop could have been shifted above the horizontal axis of the B-H coordinate. Second, as the sample being embrittled, the intensity AC field may not be sufficient enough to drive certain portion of 90° walls over some unusually strong

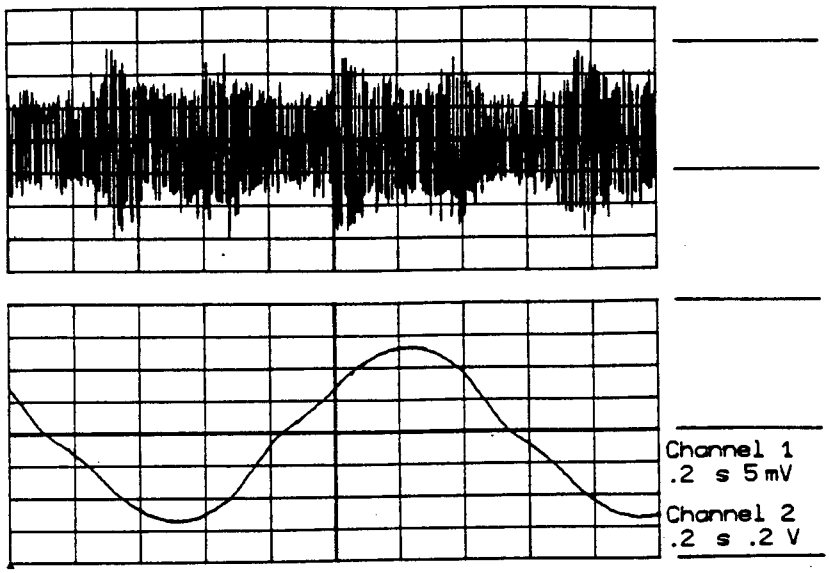

Fig. 5. Results of repeated measurements of Fig. 4 with an increased AC magnetic field intensity showing two peaks of MAE in one half cycle of hysteresis loop.

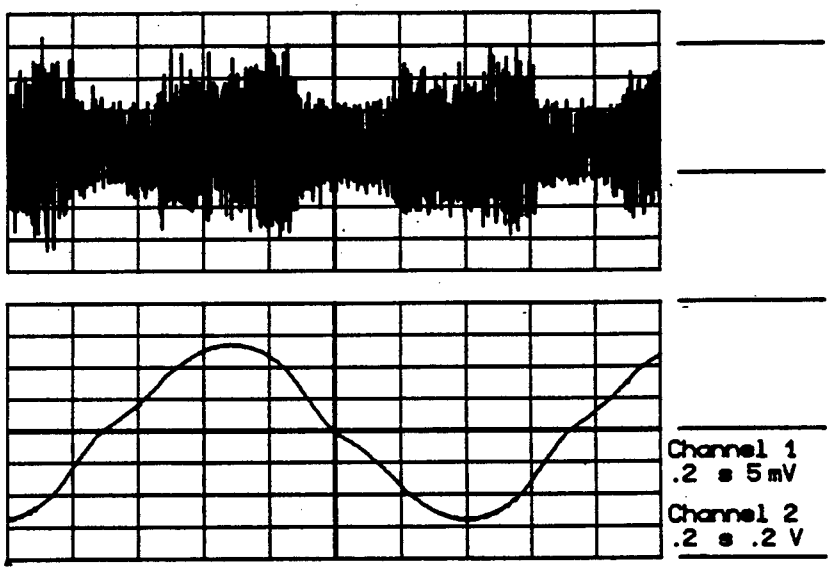

Fig. 6. Results of the same measurements as in Fig. 5 for the embrittled sample showing asymmertic MAE burst in one half cycle of hysteresis loop.

poential barriers. The 90° wall motions under such a condition will certainly contribute to the asymmetry in the overall pattern of MAE spectrm. Even though the first speculation is thought to be unlikely, it cannot be excluded since the measurement procedure did not exactly control the initial phase of AC field to be zero. As the asymmetry in MAE burst has been observed in embrittled sample only, it is more likely that the main effect is due to the severe potentai barriers at the grain boundaries where impurities are trapped and accumulated. This means that a symmetric MAE pattern should be obtained by the application of much stronger AC filed.

The results of pulse height distribution analysis performed by using a multichannel analyzer showed some very interesting characteristics of histograms obtained for unembrittled and embrittled samples. The measurements, however, have not been repeated and the presentation of

result will be deffered until complete reproduciblilty has been confirmed.

SUMMARY AND FURTHER DISCUSSION

The phase lag of MAE peak behind that of induction pickup coil output observed at 60 Hz AC field frequency implies strongly that the 90° wall-defect intercation is mainly responsible for the generation of MAE. The difference in the peak MAE amplitudes in the unembrittled and embrittled samples provides the evidence of strengthened potential barriers resisting 90° domain wall motion at the grain boundaries of embrittled sample. The presence of asymmetric MAE pattern observed only in the embrittled sample also supports the idea of stronger potential barriers as the material becomes embrittled. To provide complete validity of the fact, the recovery of a symmetric MAE pattern in embrittled samples should be confirmed by applying a stronger AC magnetic field.

ACKNOWLEDGEMENT

The authors would like to thank Mr. Robert DeNale of the David Taylor Naval Ship Researcg Center for his support inthis research.

REFERENCES

1. H. Trauble, in Magnetism and Metallurgy, edited by A. E. Berkowitz ans E. Kneller (Academic Press, New Yorkm 1969), Vol. II.
2. C. Kittel, Rev. Mod. Phys. 21, 541 (1949).
3. B. D. Cullity, Introduction to Magnetic Materials (Addison-Wesley, Menlo Park, 1972).
4. A. H. Morrish, The Physical Principles of Magnetism (John Wiley and Sons, New York, 1965).
5. S. Chikazumi, Physics of Magnetism (John Wiley and Sons, New York, 1964).
6. S. G. Allison, W. T. Yost, J. H. Cantrell and D. F. Hasson, in Review of Progress in Quantitative NDE, edited by D. O. Thompson and D. E. Chimeti (Plenum Press, New York, 1987), Vol. 7B, pp 1464-1470.

EFFECTS OF MICROSTRUCTURE OF FERROMAGNETIC ALLOYS ON MAGNETOACOUSTIC EMISSION

M. Namkung, W. T. Yost, D. Utrata*, J. L. Grainger** and P. W. Kushnick***

NASA Langley Research Center
Hampton, VA 23665

ABSTRACT

Acoustic noise pulses are generated by discontinuous motions of magnetic domain walls over lattice defect-created effective potential barriers in ferromagnets. The spectral characteristics of magetoacoustic emission (MAE), therefore, depend on the defect structure. The origin of MAE is mainly due to the interaction between 90° walls and defects as evidenced by the phase lag of the MAE with respect to magnetic induction, B(t), found under certain conditions. Our recent experiments for HY80 steel samples showed an asymmetry of MAE bursts in a period corresponding to a half cycle of the hysteresis loop for embrittled HY80 steel samples and it was not explained satisfactorily. The present study was performed to investigate fully the origin of this asymmetry with an improved scheme of AC magnetic field application. The results show that critical information on the material characteristics can be obtained directly from the shape of MAE spectra and the asymmetry is reduced by increasing the AC field intensity. It is also found that the generation of square wave-like form of dB/dt is desirable to enhance the rate of data collection at low AC field frequency.

I. Introduction

As a result of magnetoelastic interaction, the unit cells of iron-like ferromagnets are slightly tetragonal with the longer edges oriented parallel to the direction of the magnetization vector in a domain which is one of the six easy magnetization axes ($\pm x, \pm y$ and $\pm z$) [1,2]. Such a spontaneous deformation of the lattice causes apparent lattice mismatch at walls separating two neighboring domains magnetized perpendicular to each other [3]. Hence the local lattice strain fields of the 90° walls are stronger and longer-ranged than that of the 180° walls [3,4].

* Association of American Railroads
3140 S. Federal St., Chicago, IL 60616

** AS&M Inc.
107 Research Rd., Hampton, VA 23666

*** PRC Kentron Inc.
303 Butler Farm Rd., Hampton, VA 23665

Local strain fields, due to lattice mismatch, are also created at the defect sites. Magnetic domain walls and lattice defects, therefore, "see" each other through such local strain fields. Thus, lattice defects create effective potential barriers against domain wall movements.

The motion of 90° domain walls is followed by the reorientation of tetragonal axes of the unit cells, e.g., from the x to y-direction. Releasing elastic energy due to change in lattice deformation, such reorientation of tetragonal axes produces acoustic noise. The abrupt motion of 90° domain walls over the defect sites, hence, causes a sudden burst of acoustic noise.

Our initial study concentrated mainly on the amplitude distribution analysis of the pulses detected in a time window positioned at the peak of the MAE burst generated by a 60 Hz AC magnetic field [4]. The results indicated clearly the growing domain wall-defect interaction as the potential barriers of the grain boundaries in the HY80 steel samples became stronger.

In our recent study, the AC field frequency dependence of the MAE spectra was investigated and the histograms were constructed with much higher resolution and statistical accuracy [5]. The results showed, among other peculiar aspects, an asymmetry in MAE bursts, with generally decreased amplitudes in the more embrittled samples when driven with .7 Hz of AC field. This was thought to be caused by the lack of magnetic field intensity needed for the 90° walls to overcome the strong potential barriers in these samples.

The purpose of the present study is to investigate thoroughly the dependence of overall MAE spectral patterns on AC field amplitude at a given frequency.

II. Experiments

The experimental setup, shown in Fig. 1, consists of an AC current source, electromagnets with steel core, acoustic emission (AE) detection system, and data acquisition and analysis systems. A feedback technique was used to obtain a sinusoidal time dependence of magnetic induction. The sample was isolated from the steel core by a thin layer of foam rubber to serve as sound insulation. The AE transducer, which apparently contains a magnetic element, was shielded by three layers of μ metal

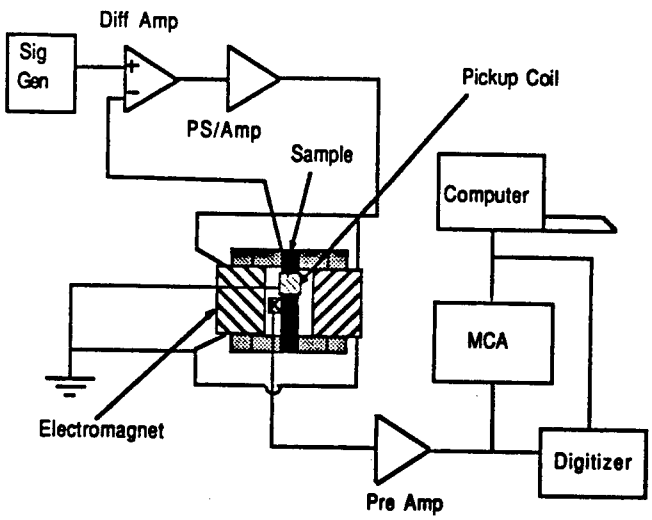

Fig.1. The block diagram of experimental setup.

sheet to prevent interference from stray magnetic fields. Histograms can be constructed directly by using a multichannel analyzer or numerically from the digitized waveform of the MAE spectra.

Two HY80 steel samples were used in the present experiment. The first sample had no heat treatment history and the second sample had been heat treated for 50 hours at 538° C (detailed properties of these samples can be found in Ref. 4). Due to this heat treatment, the second sample is known to be highly embrittled. The dimension of these rectangular bar-shaped samples was 12.5 x 16 mm^2 in cross-section and 95 mm in length.

III. Results and Discussion

Fig.2 shows the MAE spectra obtained for the unembrittled sample at the AC field frqeuency of 60 Hz. The pickup coil output, e(t), in this figure is 90° phase-shifted with respect to the induction curve, B(t), as $e(t) = -d\phi/dt$, where ϕ is the integration of B(r) over the cross-section of the sample. The period of the sinusoidal pickup coil output corresponds to a complete sweep over the hysteresis loop, a full B-H curve, where H is the magnetic field internal to the material.

The portion of a hysterisis loop between remanence (B=Br, H=0) and coercive field (B=0, H=Hc) is where the irreversible domain wall motion is most active. An MAE peak is expected to appear in this portion. After passing H=Hc, domain wall motion proceeds in the direction opposite to the previous magnetization and the same trend in MAE is repeated. This means two MAE peaks should be present in symmetry about the peak of e(t) which corresponds to H=Hc. The figure, however, shows only one peak of MAE and this peak is delayed slightly in time with respect to that of e(t). The AE band between the bursts is contributed mainly by the constant background noise produced in the transducer and amplifier circuit, and some MAE signals generated after the major irreversible domain wall motion.

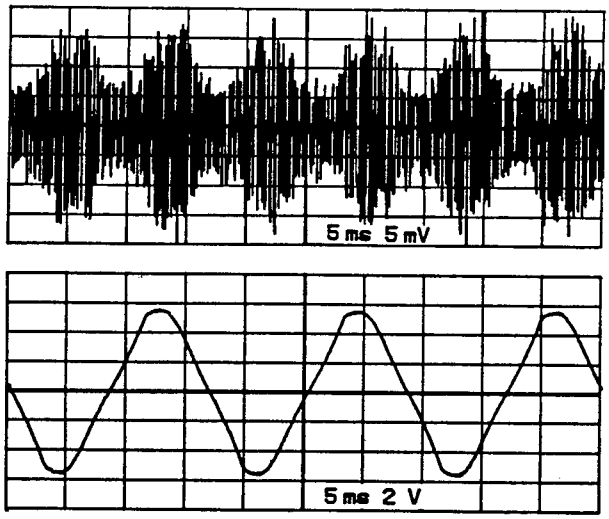

Fig.2. MAE spectrum obtained for the unembrittled sample at AC field frequency of 60 Hz. The upper trace is MAE spectrum and the lower trace is the induction pickup coil output, e(t).

Due to the strong interaction with defects, 90° doamin walls are blocked at defect sites, while 180° walls continue to move without experiencing much resistence. Since these two types of walls are coupled together, 90° walls bend and swell until the magnetic field strength reaches a certain critcal value sufficient to drive them over the barriers. The change in induction at the same time is contributed by relatively freely moving 180° domain walls. Hence the phase lag of MAE peak behind e(t) exists.

Fig 3. shows the MAE spectrum obtained for the embrittled sample at 60 Hz. Here, the MAE peak amplitudes are much larger than that found for the unembrittled sample in Fig. 2. This figure also shows a noticeable phase delay of MAE signal with respect to e(t). Since the grain boundaries of the embrittled sample create higher potential barriers against the 90° wall motion, the observed effects are exactly consistent with the above discussion.

The lack of a double peak-like structure at the MAE burst in these two figures can be explained by a relatively high AC field frequecy of 60 Hz. This is because at this frequency 90° walls are forced to jump over the major potential barriers, those they encounter before and after Hc, at once. This means that the double peak should appear in the MAE burst at a lower AC field frequency.

Fig. 4 show the MAE spectrum obtained for the unembrittled sample at .7 Hz and is much different from that observed in the previous study despite almost the same experimental conditions. Such a disagreement is probably due to the difference in the actual form of H(t) in the material for the two measurements using different AC current sources.

Beyond the limit of the feedback circuit, the pickup coil output was distorted and no longer had a sinusoidal waveform. Fig. 5 shows the results

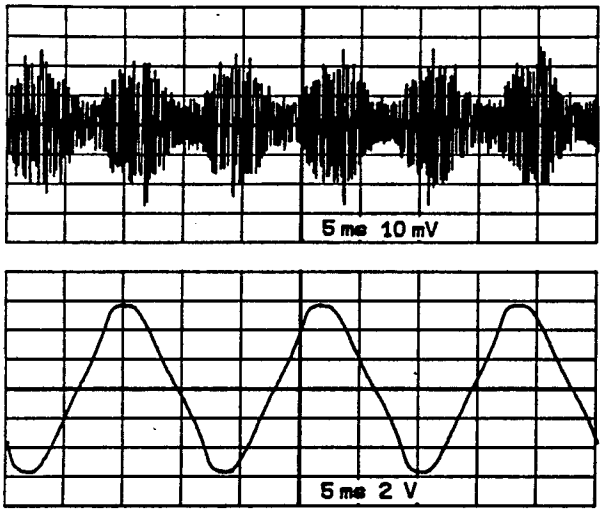

Fig. 3. MAE spectrum obtained for the embrittled sample at 60 Hz.

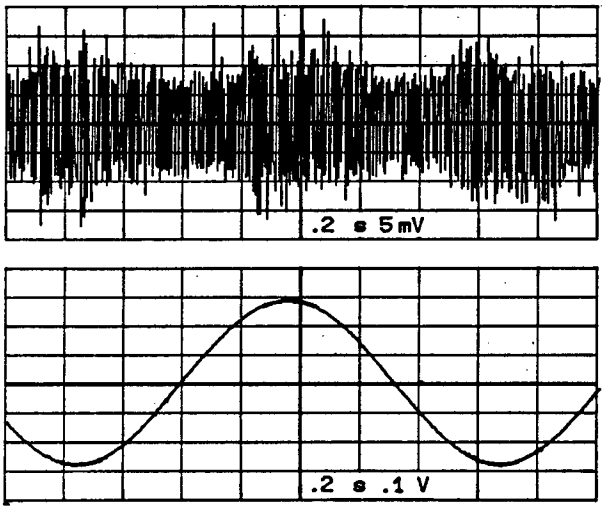

Fig.4 MAE spectrum obtained for the unembrittled sample with at .7 Hz.

obtained at the same frequency but with a higher AC current intensity. It is seen clearly that more MAE activity occurs with a slow increase in induction. This region should correspond to the upward movement of 90° walls towards the top of the major potential barriers during which the 90° walls encounter strong resistance. During the period between the time when e(t) reached its peak and the time when it started changing the sign, some 90° walls moved over the barriers as indicated by somewhat reduced but apparent MAE activity. The maximum field intensity in thi measurement was not strong enough to move all the 90° walls evenly over the barriers during the entire cycle of the hysteresis loop. This means that any initial asymmetry existed in the sample was still retained. With an increased AC current amplitude, the MAE spectrum takes a different shape. The spectrum in Fig. 6 was obtained without using the feedback circuit. The increase in AC field is reflected by

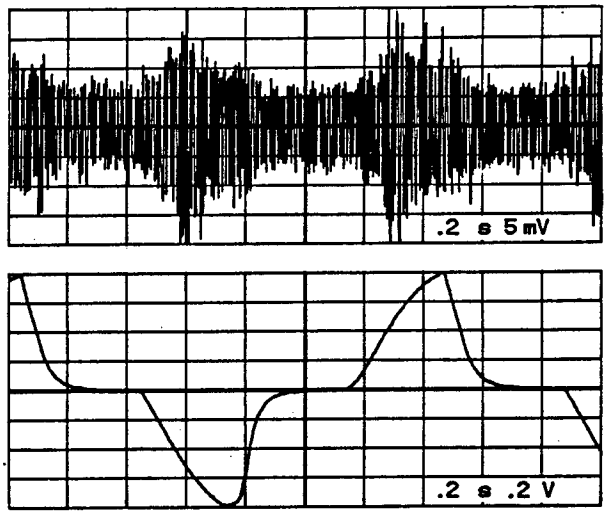

Fig. 5. The results of repeated measurements of Fig. 4 with an increased AC current.

the amplitude of e(t) which is about twice as large as that observed in the previous figure. A rapid change in amplitude of e(t) suddenly slowed down but was kept steady for a while before it began to decrease. This is clear evidence that the domain walls traveled far after passing the major potential barriers, probably to the point where domain rotation began to occur.

In this figure the symmetric double peaks are seen during the one half cycle sweep over the the hysteresis loop. This trend, however, is not repeated for every half cycle sweep. This is because the process involves an ensemble of domains in the ferromagnetic system in which the individual domain walls move along different paths, while they are constantly being annhilated or recreated. In addition, the defect structure interacting with these domain walls is by no means a rigid system. The shape of the potential barriers is expected to keep changing slightly by the interaction. The observed MAE activities are, therefore, the results of statistical fluctuations in the dynamics of the ferromagnetic system.

Comparing the results in Fig. 5 and Fig. 6, one can see clearly that, beyond a certain value, the increase in AC field amplitude does not necessarily increase the MAE envelop peak amplitude. This means that, even at a low frequency, the magnet/power-amplifier system does not have to be excessively powerful. In addtion, these results suggest a desirable method of AC field application which creates a square function-like waveform of $d\phi/dt$. This is because that the rate of collecting useful data for histogram construction can be enhanced by shaping the waveform of $d\phi/dt$ as shown in Fig. 6.

The same measurements were repeated for the embrittled sample. The results showed generally the same trend as described above but with an expected difference. Fig. 7 shows the results obtained for the sample under similar conditions which were applied to the measurements of Fig. 4.

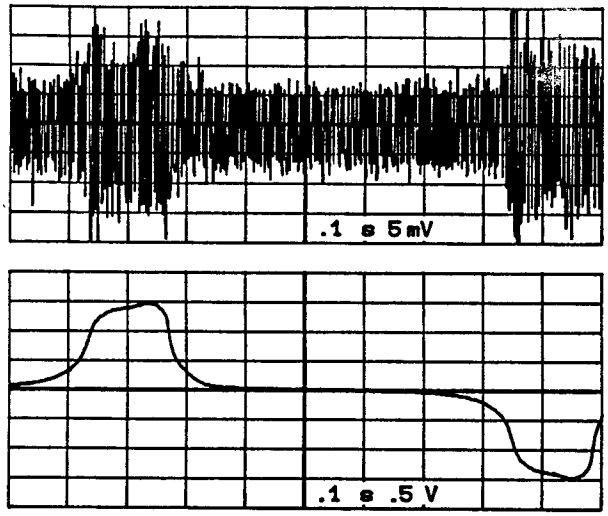

Fig. 6. The results of repeated measurements of Fig. 5 with an increased AC current.

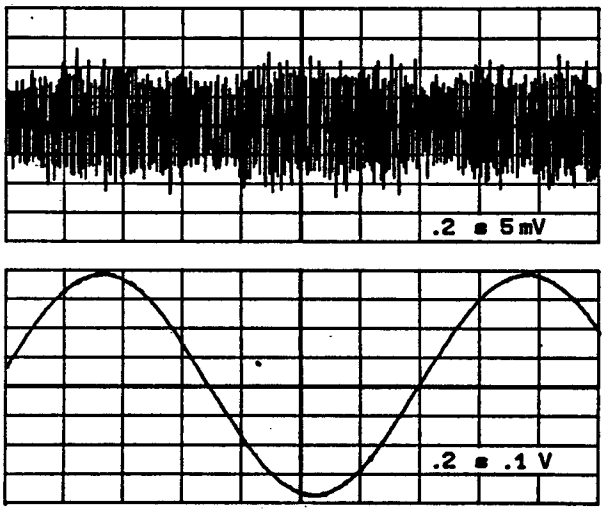

Fig. 7. The low-field MAE spectrum of the embrittled sample at .7 Hz.

Despite the larger amplitude of e(t), the MAE amplitudes in this figure are much lower than that observed in Fig. 4. Such a trend is exactly consistent with what is expected for the production of MAE with a low AC field applied to a highly embrittled sample. This probably is the best example showing the major roles of 180° and 90° walls during their motion, i.e., to increase the total magnetic induction and produce MAE, respectively.

IV. Summary

The dependence of MAE sprectra on externally controlled parameters were investigated in the present study. The results shown in Fig. 2 and Fig. 3 obtained at 60 Hz validate clearly the basic assumption of the interaction between 90° domain walls and defect-created potential barrier that grows by trapping more impurities at the grain boundaries in HY80 steel samples. The low frequency results in the later figures indicate that the desirable waveform of magnetic induction in the material is such that a square wave-like rate of change in magetic flux is produced. In this case useful MAE signals can be detected in well defined time domain intervals.

Acknowledgement

The authors are grateful to Mr. Robert De Nale of the David Taylor Naval Ship Research and Development Center for his support in this research.

References

[1]. D. M. Bozorth, Ferromagnetism (Van Nostrand, New York, 1951).

[2]. B. D. Cullity, Introduction to Magnetic Materials (Addison-Wesley, Menlo Park, 1972).

[3]. H. Trauble, The influence of Crystal Defects on Magnetization Processes in Ferromagnetic Single Crystals: Magnetism and Metallurgy Vol. II, edited by A. E. Berkowwitz and E. Kneller (Academic Press, New York, 1967).

[4]. S. G. Allison, W. T. Yost, J. H. Cantrell and D. F. Hasson, Review of Progress in Quantitative Nondestructive Evaluation 7B, 1463 (1987).

[5]. M. Namkung, W. T. Yost, J. L. Grainger and P. W. Kushnick, Submitted to Review of Progress in Quantitative Nondestructive Evaluation, La Jolla, CA (August, 1988).

EFFECTS OF GRAIN BOUNDARY CHARACTERISTICS OF STEEL ON MAGNETOACOUSTIC EMISSION SPECTRA

M. Namkung*, W. T. Yost*, D. Utrata**, J. L. Grainger*** and P. W. Kushnick****
*NASA Langley Research Center, Hampton, VA 23665
**Association of American Railroads, 3140 S. Federal St., Chicago, IL 60616
***AS&M Inc., 107 Research Dr., Hampton, VA 23666
****PRC Kentron Inc., 303 Butler Farm Rd., Hampton, VA 23666

ABSTRACT

The pulse height distribution of a magnetoacoustic emission (MAE) spectrum is expected to be generally Gaussian due to its random nature. The functional form of distribution depends on the microstructure of a ferromagnet since the domain wall-lattice defect interaction produces MAE. The present study investigated the effects of grain boundary characteristics on the properties of MAE spectra obtained by external AC magnetic field-driven domain wall motions. The results show the enhancement of domain wall-defect interaction as more grain boundary disorder is introduced to HY80 steel samples. This was confirmed by the growth of a non-Gaussian-like distribution in the tail section of histograms with increased population of impurities trapped at the grain boundaries causing embrittlement. It is found that the enhancement of domain wall-defect interaction, which is responsible for generation of high amplitude MAE pulses, also tends to reduce the rate of such MAE events by limiting domain wall motions. Application of a stronger AC magnetic field is expected to remove such a self inhibiting effect of embrittlement in this material.

INTRODUCTION

Strong local lattice strain fields are created at 90° domain walls of an iron-like ferromagnet due to spontaneous magnetostriction [1]. The strain fields at 180° domain walls are much weaker and shorter-ranged than that of 90° domain walls [1,2]. Lattice mismatch at defects also creates strong local strain fields. The domain walls and lattice defects interact with each other through the strain fields they create and the interaction is much stronger for 90° domain walls [2]. Lattice defects, therefore, play effective potential barriers against 90° domain wall motion.

Motion of 90° walls is followed by the rearrangement of lattice strain fields that release elastic energy. A discontinuous motion of 90° domain walls, therefore, produces a sudden burst of MAE signals. Since the abrupt motion of 90° walls is due to pinning and unpinning of these walls at the defect sites, it is natural to assume that the characteristics of large amplitude MAE signals are related to the properties of the grain boundary where lattice mismatch is may be severe.

Our initial study has proven that differentiation between embrittled and unembrittled HY80 steel samples is possible by pulse height analysis applied to the MAE spectra obtained with a 60 Hz AC external magnetic field [3]. The results have shown broader Gaussian-like distributions of histograms in the embrittled samples which is consistent with the assumption of domain wall-defect interaction at the grain boundaries. By varying AC field frequencies and amplitudes, our recent study in the same HY80 steel samples has provided a complete verification of the above assumption [4,5]. The results also have shown that much information on temper embrittlement of these steel samples can be obtained directly from the MAE spectra.

In our earlier study, a distinct non-Gaussian-like structure has been observed in the tail section of histograms obtained for the HY80 samples. The appearance of this tail structure in repeated measurements, however, was not very reproducible, presumably due to a lack of statistical accuracy. The purpose of the present study is to investigate this tail structure with an enhanced statistical accuracy in the histograms.

EXPERIMENTS

The detailed properties and treatment history of the HY80 steel samples have been documented in Ref. 3, and only a brief description will be given here. The casting steel was quenched and tempered to obtain the desired toughness while producing a yield stress of approximately 80 ksi. During the stress relief heat treatment after the above stages, impurity atoms execute thermally activated diffusional motion in the lattice. Trapping of certain types of impurities at the grain boundaries in this process is known to cause embrittlement. Sets of test samples were obtained from the blocks heat treated at 538°C for 1, 5, 24, 50 and 100 hours to produce different amounts of temper embrittlement. A separate Charpy V-notch test has shown a rapid decrease in impact toughness from 127.5 ft-lbs for unembrittled HY80 samples to 54.5, 15.0, 9.5, 6.5 and 5.0 ft-lbs by increasing the hours of heat treatment time as given above.

Fig. 1 shows the block diagram of the MAE instrumentation used for the experiment. The magnetizing unit consists of a function generator that controls the power supply/amplifier. A digitizer was used to record the MAE spectra. Histograms were constructed directly by using a multichannel analyzer. Since the multichannel analyzer accepts positive voltage signals only, an inverting circuit was used to accumulate both positive and negative MAE pulse counts. For the present experiment, the multichannel analyzer was used to process about 100 million events for each histogram.

RESULTS AND DISCUSSION

The upper part of Fig. 2 shows the MAE spectrum obtained at a 60 Hz AC field frequency with the HY80 sample heat treated for 24 hours. The lower part of this figure shows an approximately sinusoidal waveform of the induction pickup coil output. The random noise band between the MAE peaks is due to system background noise.

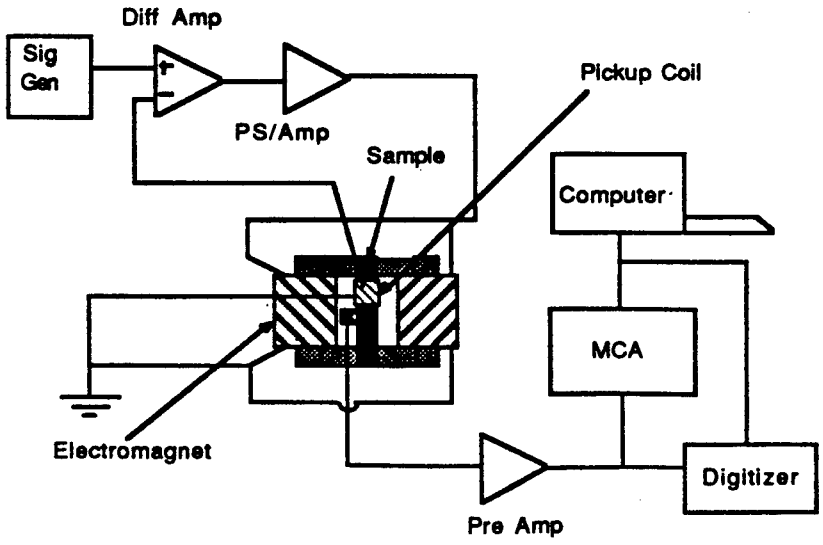

Fig.1. Block diagram of the MAE instrumentation.

The MAE envelope in Fig. 2 is seen to be asymmetric. This is because some 90° domain walls are not able to jump over the potential barriers at the grain boundaries due to strong resistance. An immediate proof of such incomplete 90° domain wall motion over the barriers is given in Fig. 3. The symmetry of the MAE envelope is seen to be recovered by increasing the AC field intensity as reflected by the peak amplitude of the pickup coil output. Whether these MAE peaks shown in Fig. 3 have reached their possible maximum amplitude or not is, however, not clear at the present stage.

Fig. 4 shows the histogram of the system background noise. The horizontal resolution of the histogram is about 2.44 millivolts and the channel 2048 corresponds to zero. The figure shows the range of background noise in the histogram to be approximately ± 250 channels about the center. Except for the region between the two peaks, the histogram shows a smoothly decaying Gaussian-like distribution indicating the random nature of the noise spectrum.

The histogram obtained for the unembrittled HY80 sample is shown in Fig. 5. Since no filtering scheme has been applied, the histogram consists of a mixture of background noise and low amplitude MAE signals in the range identified in Fig. 4. Beyond this range, the histogram maintains Gaussian-like distribution except at both ends. The appearance of such a

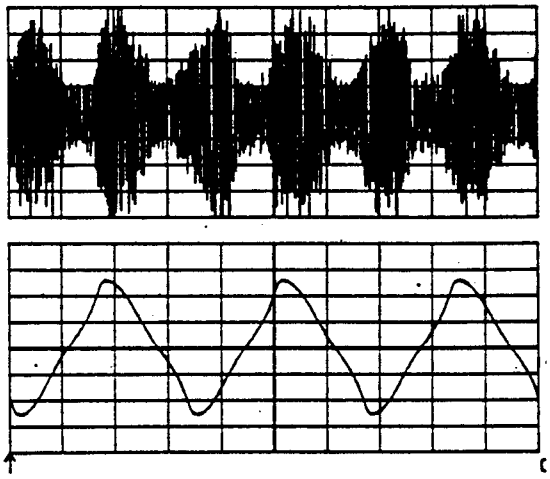

Fig. 2. MAE spectrum obtained at 60 Hz for the HY80 steel sample heat treated for 24 hrs..

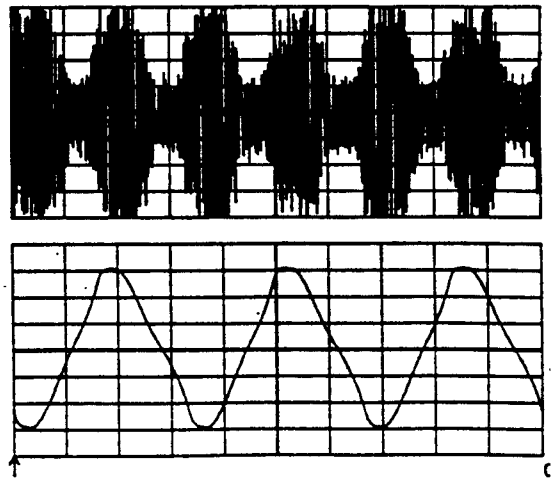

Fig. 3. Results of repeated measurements of Fig. 2 with an increased AC magnetic field amplitude.

discontinuity, of course, indicates the existence of a different contributing mechanism. It is assumed that a mixture of the domain wall-defect interactions inside grains and at grain boundaries contribute to the Gaussian-like distribution. The interactions at the grain boundaries with pronounced lattice mismatch, on the other hand, are assumed to be the sole contributor to the non-Gaussian-like distribution at the tail.

Fig. 6 shows the histogram obtained for the HY80 steel sample which has been heat treated for 5 hours. The increased count rate of low amplitude MAE signals in this sample is seen to remove the smooth transition at the end of background noise region. At the same time, a growth in count rate is seen at the tail sections of the histogram indicating clearly an increased high amplitude MAE activity as the domain wall-defect interaction becomes stronger.

All the histograms obtained for the embrittled HY80 steel samples show such a distinct tail structure which is not found in the histogram of the unembrittled sample. The trend of growing count rate in the tail secton of the histogram, however, is found to level off and decrease somewhat as the samples become more embrittled. Fig. 7 shows the high-amplitude portion of

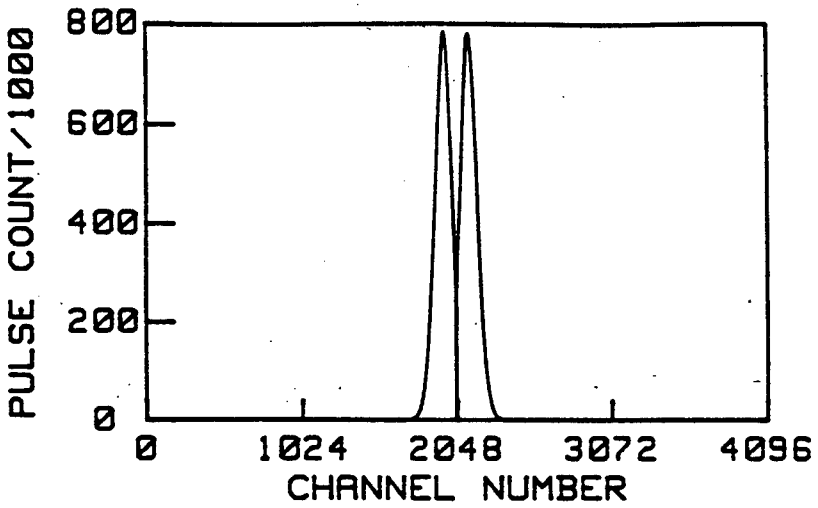

Fig. 4. Histogram representing the pulse height distribution of system background noise.

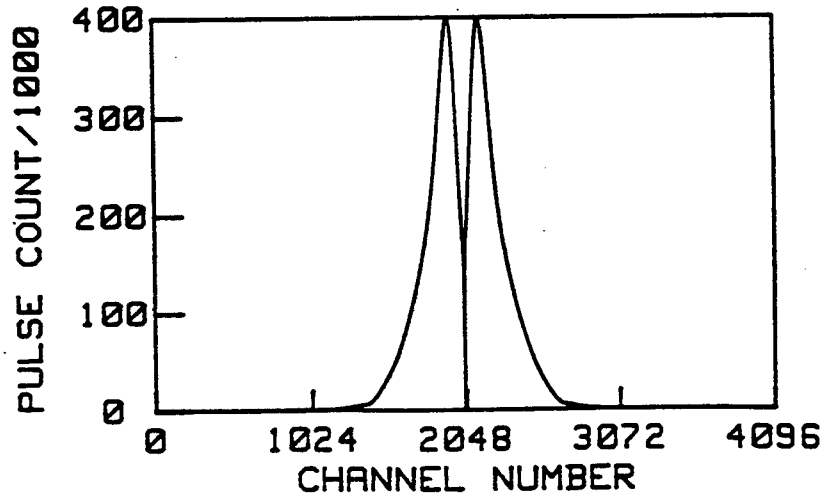

Fig. 5. Histogram obtained for the unembrittled HY80 sample at 60 Hz AC field frequency.

histograms for the first three samples. The curve for the unembrittled sample residing in the lowest position shows an almost straight line for the last 300 channels. Between the two curves of the embrittled samples, the count rate in the same region is shifted upward as the heat treatment time is increased from 1 hour to 5 hour. The same results are shown in Fig. 8. In this figure the curves shifted downward as the heat treatment time is increased to 24, 50 and 100 hours.

The decreased count rate in the tail section found in Fig. 8 is not a surprise. As the grain boundaries become stronger potential barriers against 90° domain wall motions, those 90° walls succesfully jumping over the bounaries will generate high amplitude MAE signals. The presence of enhanced potential barriers, however, allows fewer 90° domain walls to execute such jumps, and consequently, results in decreased MAE activity in the more embrittled samples. A clear evidence of such an effect has been observed from the AC magnetic field amplitude dependence of MAE peaks in unemrittled and embrittled samples [5]. Comparing those curves in the tail section, it appears that the MAE peaks in Fig. 3 have not reached the possible maximum amplitude.

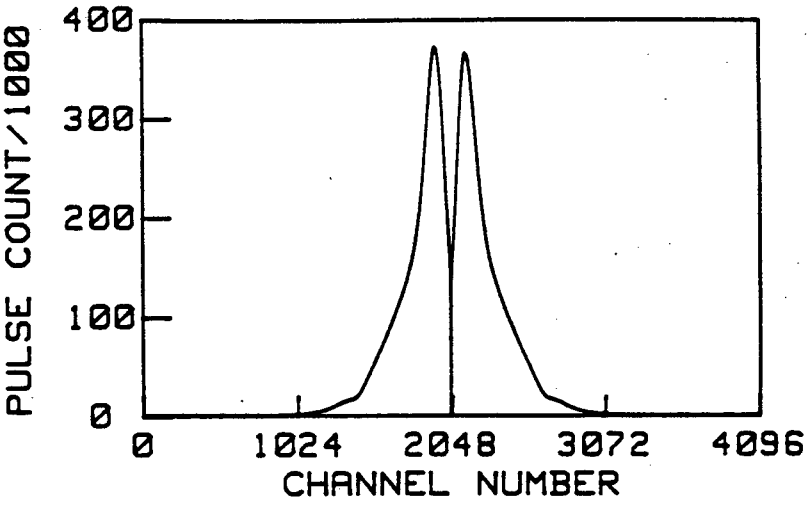

Fig. 6. Histogram obtained for the HY80 sample heat treated for 5 hours.

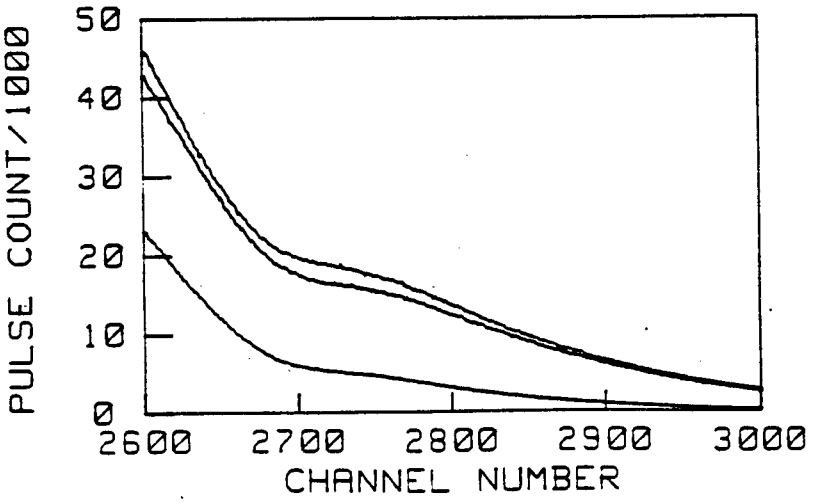

Fig. 7. Non-Gaussian tail structure of histograms. The curve at the bottom is for the unembrittled sample. Upward shift is observed between the two curves at the top as the heat treatment time is increased from 1 to 5 hours.

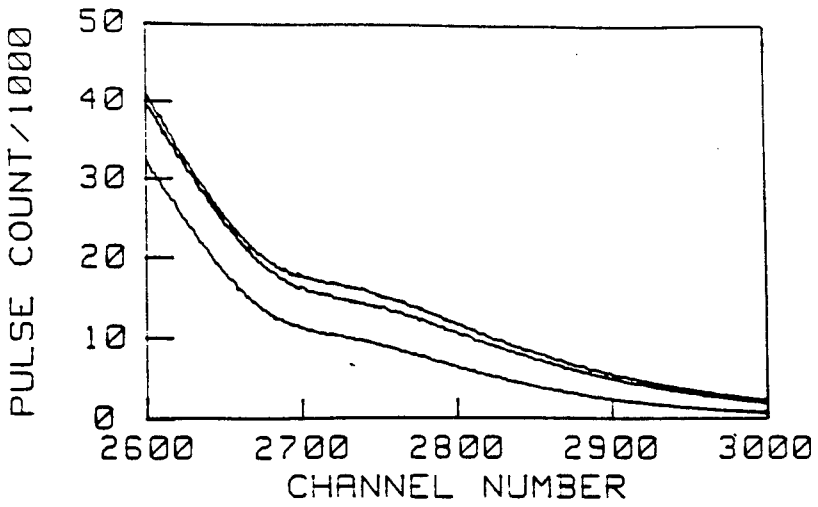

Fig. 8. Tail structure of histograms for the samples heat treated for 24, 50 and 100 hours. The curves shift downward with increased heat treatment time.

SUMMARY

This paper presents the initial results of MAE pulse height analysis of the unembrittled and embrittled HY80 steel samples obtained by using a multichannel analyzer. The enhanced 90° domain wall-defect interaction in the embrittled sample is seen to generate high amplitude MAE signals as evidenced by the presence of the distinct tail structure of the histogram that is not found in the unembrittled sample. Such a trend is seen to level off and reverse slightly in the highly embrittled samples due to the enhanced potential barriers at the grain boundaries that tend to limit 90° domain wall motions. It is, therefore, necessary to repeat these measurement with a stronger AC magnetic field.

ACKNOWLEDGEMENT

The authors are grateful to Mr. Robert DeNale of the David Taylor Research Center for his support in this research and provision of test samples with metallurgical information.

REFERENCES

1. B. D. Cullity, Introduction to Magnetic Materials (Addison-Wesley, Menlo Park, 1972).
2. H. Trauble, in Magnetism and Metallurgy, Vol. II, edited by A. E. Berkowitz and E. Kneller (Academic Press, New York, 1969).
3. S. G. Allison, W. T. Yost, J. H Cantrell and D. F. Hasson, in Review of Progress in Quantitative Nondestructive Evaluation 7B, 1463 (1987).
4. M. Namkung, W. T. Yost, J. L. Grainger and P. W. Kushnick, submitted to Review of Progress in Quantitative Nondestructive Evaluation, La Jolla, CA (August, 1988).
5. M. Namkung, W. T. Yost, D. Utrata, J. L. Grainger and P. W. Kushnick, submitted to IEEE Ultrasonics Symposium, Chicago, IL (October, 1988).

REVIEW OF MAGNETOACOUSTIC RESIDUAL STRESS MEASUREMENT TECHNIQUE FOR IRON-LIKE FERROMAGNETIC ALLOYS

M. Namkung, D. Utrata*, P. Langlois**,
P. W. Kushnick*** and J. L. Grainger****
NASA Langley Research Center
Hampton, VA 23665

INTRODUCTION

The stress dependence of the magnetoacoustic response in ferromagnets is based on two distinct, but not mutually independent, phenomena: stress dependence of domain structure and domain structure dependence of elastic modulus [1,2,3]. A difference in magnetoelastic energy density exists between two neighboring domains unless α, the angle between the uniaxial stress axis and magnetization vector, is the same for both domains. This difference is a net pressure acting on domain walls and, apparently, is non-zero only for 90° domain walls as long as α is different from 45° [4]. Application of uniaxial stress, hence, induces motion of 90° domain walls such that domains in iron-like ferromagnets align parallel (perpendicular) to the uniaxial tensile (compressive) stress axis. Producing local 90° domain wall motions, the same trend is valid for a stress wave propagating in these materials.

Motion of any non-180° domain wall always produces ε_{me}, magnetoelastic strain. When stress-induced, the sign of ε_{me} can be shown to be the same as that of the applied uniaxial stress [2]. The elastic modulus of a nonlinear solid can be expressed as

$$E = \frac{\Delta\sigma}{\Delta\varepsilon_{el} + \Delta\varepsilon_{me}}$$

where $\Delta\varepsilon_{el}$ and $\Delta\varepsilon_{me}$ are direct elastic and magnetoelastic strains, respectivley, produced by the application of $\Delta\sigma$. The elastic moduli of

---

* Association of American Railroads
3140 S. Federal St., Chicago, IL 60616

** UA-CNRS-ENSAM, Paris, France and
Virginia State University, Petersburg, VA 23803

*** PRC Kentron Inc., 303 Butler Farm Rd., Hampton, VA 23666

**** AS&M Inc., 107 Research Dr., Hampton, VA 23666

steel sample under uniaxial tension and compression, respectively. The behavior of the $\Delta f(B)/f$ curves under tension, being shifted downward as the stress amplitude increases, is seen to be consistent with what was predicted. The results in Fig. 2 show exactly the expected trend by showing a decrease in acoustic velocity as the moudulus decreases until domain wall motion expands the total area of 90° walls in the material. The inflection point of the $\Delta f(B)/F$ curve under compression shifted downward as the stress amplitude increases.

The results for the 1045 steel sample, shown in Fig. 3, differ drastically from those for the 1020 steel sample, especially for the effect of tensile stress on the $\Delta f(B)/f$ curves. Such effects of tensile

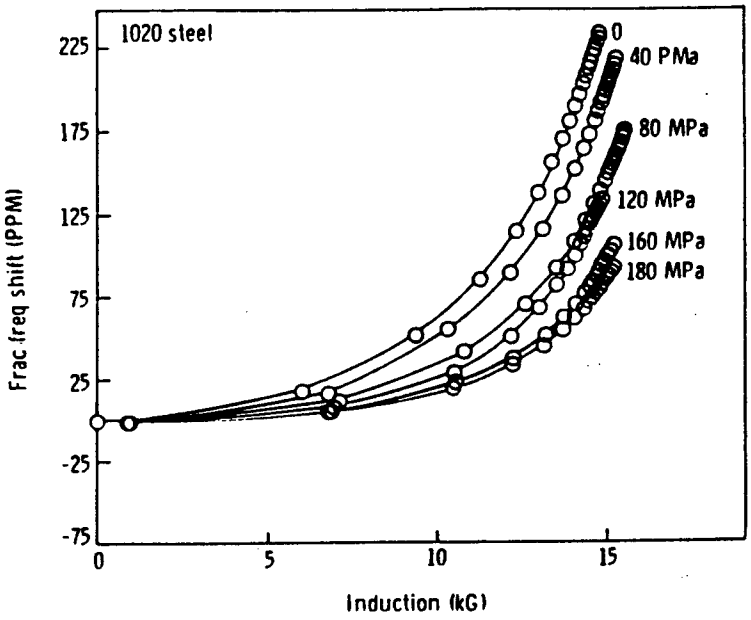

Fig. 1. $\Delta f(B)/f$ curves obtained for the 1020 steel sample under uniaxial tension.

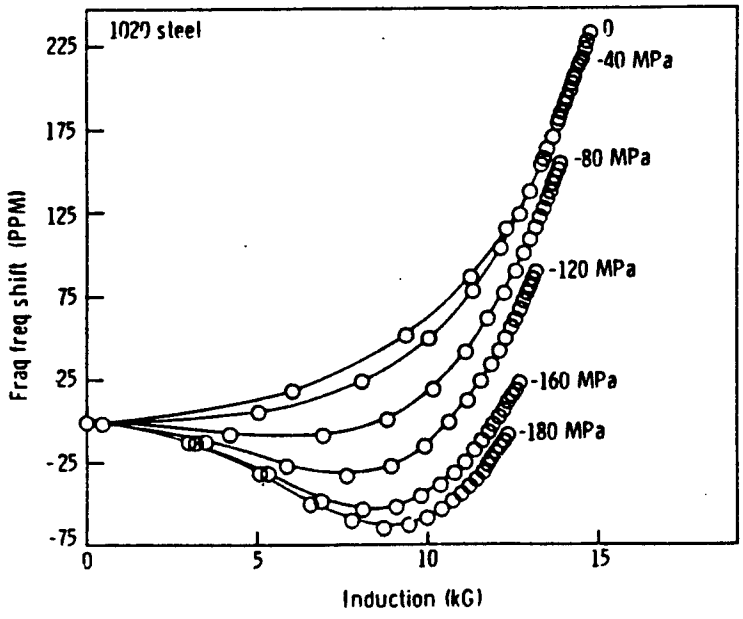

Fig. 2. $\Delta f(B)/f$ curves obtained for the 1020 steel sample under uniaxial compression.

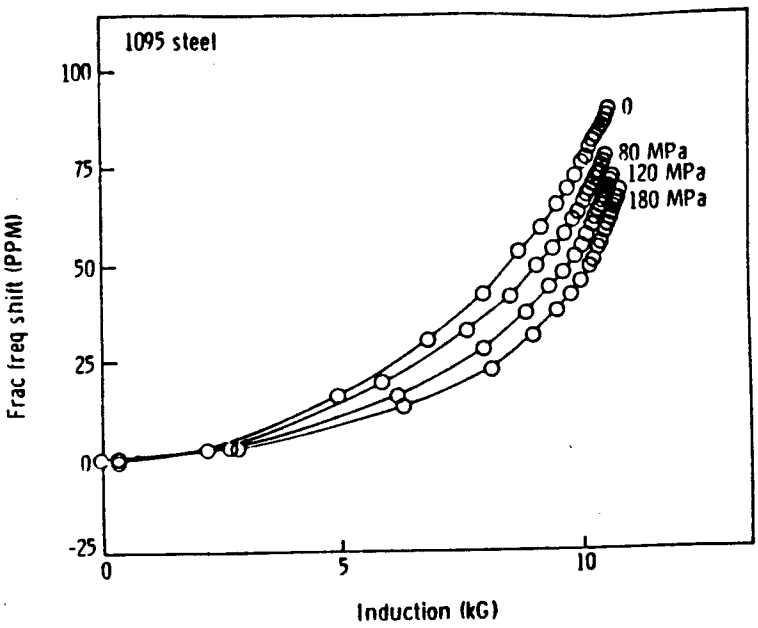

Fig. 4. $\Delta f(B)/f$ curves obtained for the 1095 steel sample under uniaxial tension.

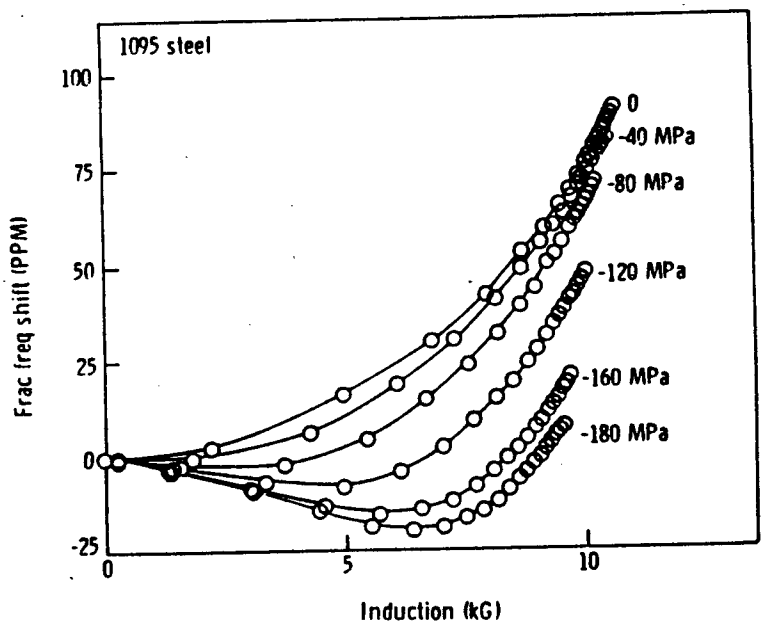

Fig. 5. $\Delta f(B)/f$ curves obtained for the 1095 steel sample under uniaxial compression.

types of railcar wheel steel. The results showed much smaller differences between the tension and compression curves in this case compared to that obtained by applying a magnetic field parallel to the uniaxial stress axis. Further, the initial negative slope of $\Delta f(B)/f$ has never been seen until a significant improvement was made to the acoustic instrumentation [6].

Acoustic shear waves have been proven to be more effective than compressional waves in differentiating the sign of the uniaxial stress with perpendicular magnetization. At least one mode of shear wave propagation, its wave vector perpendicular to both the magnetic field and

uniaxial stress axes, and the polarization vector parallel to the stress axis, provides a negative initial slope under tension.

EXPERIMENTS AND RESULTS FOR PURE IRON

All the analysis made for these results have been based on the magnetic properties of pure iron. Therefore, it is necessary to perform experiments with a pure iron sample. Well annealed pure iron plates shaped as fatigue samples with a thickess of 6 mm were used for the measurement by propagating 2.25 MHz compressional waves perpendicular to the uniaxial stress axis which was also chosen as the magnetization axis.

The next two figures show the results obtained for two pure iron samples. These results show clearly the similar effects of tensile stress seen in the 1045 steel sample above, and railroad wheel and railroad rail steel samples. One can wonder why this happens, while the stress dependences of $\Delta f(B)/f$ are consistent with the magnetic properties of pure iron. A possible answer to this question is that domain wall movements are simply based on the magnetic properties of iron without considering the initrinsic local lattice residual stress state. It is well known that such local lattice stresses exists in ferromagnets absolutely free of metallurgical defects, i.e., vacancies, impurities, dislocations and so on. In addition, some experimental evidence shows that pure iron crystals contain a higher degree of local lattice stresses that some iron base alloys [9]. This means that the argument made for the tesile stress effect of $\Delta f(B)/f$ for 1045 steel may be applied to the case of pure iron.

Variation between the results of Fig. 6 and Fig. 7 is seen to be rather severe considering that these sample were prepared in a manner to achieve metallurgucally identical conditions. Assuming the sensitivity of $\Delta f(B)/f$ to small fluctuations, a study is being made to identify microstructural characteristics, especially, for the presence of texture variations in these samples.

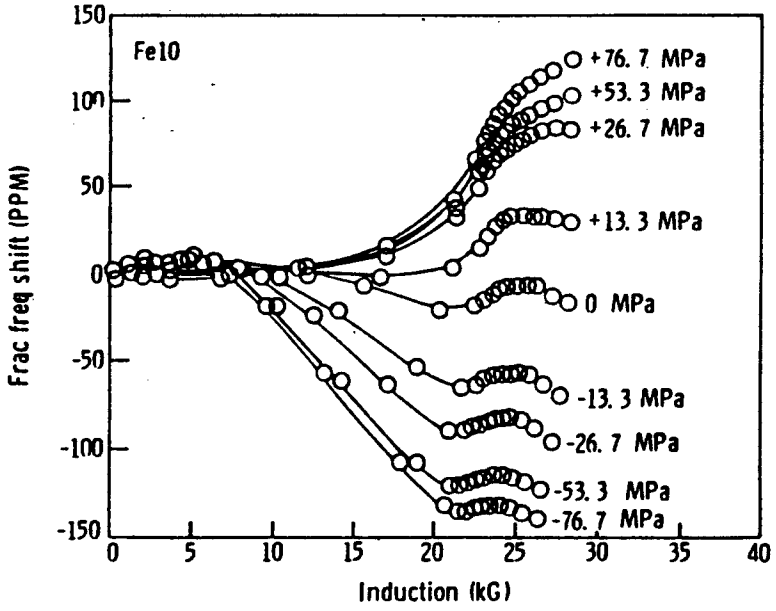

Fig. 6. $\Delta f(B)/f$ curves obatined for a pure iron sample by applying the magnetic field parallel to the stress axis and propagating compressional waves through the field axis.

Fig. 8 shows the $\Delta f(B)/f$ and magnetizaation curves obtained in a pure iron sample under uniaxial compression. During reversible domain wall motion, $\Delta f(B)/f$ shows very little change. No appreciable change in $\Delta f(B)/f$ is seen untill about B=10 kG. Such an increase in induction is apparently contributed mainly by the 180° domain wall motions. Beyond this point, 90° domain walls abruptly jump over the pinning sites to expand the total area. These 90° domain walls travel as far as they can and domian rotaion process begins afterward. The minimum of $\Delta f(B)/f$ under uniaxial compression occurs during the transition between domain wall motion and rotation regions.

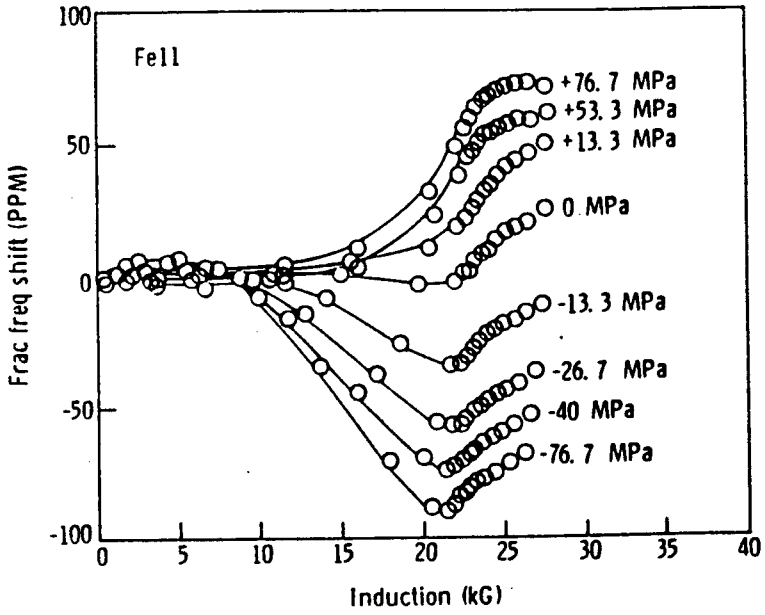

Fig. 7. $\Delta f(B)/f$ curves obtained for another pure iron sample prepared under identical conditions.

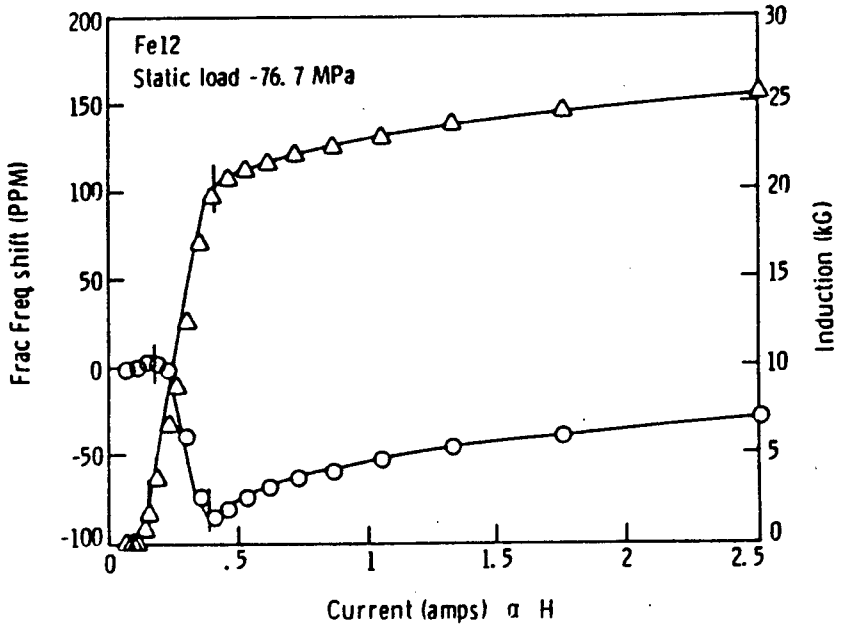

Fig. 8. $\Delta f(B)/f$ and magnetiztion curves obtained for a pure iron sample.

SUMMARY AND FURTHER DISCUSSION

The present and previous experimental results on the subject indicate clearly that the magnetoacoustic response of ferromagnets involves various microstructural mechanisms. Nevertheless, the general effects of uniaxial stress on $\Delta f(B)/f$ are (1) the presence of an inital negative slope of $\Delta f(B)/f$ when net magnetization is induced parallel to the compressive stress axis, and (2) separation of the tension curve from the compression curve by the unstressed curve for a certain range of carbon content in steel.

As shown in Fig. 8, the portion of $\Delta f(B)/f$ carrying stress information coressponds to the domain wall motion region. All the theoretical analysis of magnetoacoustic interaction has been made for domain rotation and pure para process (well beyond technical saturation), and has never been made for the region of domain wall motion. The difficulty that limits the practical application of the technqiue, however, is induction of uniform magnetization of known magnitude in a region where the stress information needs to be otained. Hence, future devlopment should involve some extensive computational work on the magnetic field distribution in ferromagnetic objects as well as an effort to gain a deeper insight into the related physical processes.

ACKNOWLEDGEMENT

The present research project is sponsored jointly by National Aeronautics and Space Adminstration (NASA), The Association of American Railroads (AAR), and the Federal Railroad Adminstration (FRA). One of us (PL) was supported separately by NASA under the Grant #NAG1-416.

REFERENCES

1. D. M. Bozorth, Ferromagnetism (Van Nostrands, New York, 1951).
2. B. D. Cullity, Introduction to Magnetic Materials (Addison-Wesley, Menlo Park, 1972).
3. S. Chikazumi, Physics of Magnetism (John Wiley and Sons, New York, 1964).
4. W. F. Brown, Jr., Phys. Rev. 75, 147 (1949).
5. S. G. Allison, J. S. Heyman, K. Smith and K. Salama, in Proc. IEEE 1984 Ultrasoincs Symposium, edited by B. R. McAvoy (IEEE Publishing Service, New York, 1984), Vol. 2, pp 997-1002.
6. M. Namkung, D. Utrata, W. T. Yost, P. W. Kushnick and J. L. Grainger, in Proc. IEEE 1987 Ultrasoincs Symposium, edited by B. R. McAvoy (IEEE Publishing Service, New York, 1987), Vol. 2, pp 1061-1065.
7. M. Namkung, D. Utrata, S. G. Allison and J. S. Heyman, in Review of Progress in Quantitative NDE, edited by D. O. Thompson and D. E. Chimenti (Plenum Press, New York, 1986), Vol. 5B, pp 1481-1487.
8. M. Namkung and D. Utrata, in Review of Progress in Quantitative NDE, edited by D. O. Thompson and D. E. Chimenti (Plenum Press, New York, 1987), Vol. 6B, pp 1585-1592.
9. W. J. Kossler, M. Namkung, B. Hitti, Y. Li, J. Kempton, C. E. Stronach, L. R. Goode, Jr., W. F. Lankford, B. D, Patterson, W. Kundig and R. I. Grynszpan, Phys. Rev. B. 32, 293 (1985).

Requirements For Science In NDE

Joseph S. Heyman
NASA - Langley Research Center, MS 231
Hampton, VA 23665

Abstract

Nondestructive Evaluation (NDE) is the technology of measurement, analysis, and prediction of the state of material systems, for safety, reliability and mission assurance. It is an old technology yet still in its infancy. The opportunities for research and application are great and the shortfall in technology demands attention. In this paper, we shall review aspects of aerospace NDE and discuss recent advances in ultrasonics for aerospace applications.

Keywords: Nondestructive Evaluation; Ultrasonics; Physical Models; Aerospace; Bolt Tension; Nonlinear Acoustics

Introduction

The modern laboratory has taken a quantum leap in the past decade reflecting the changes that have occurred in electronics and measurement science. The usual scene of the scientist gently adjusting a precision measurement device has been replaced by that of a glowing computer display with the scientist tapping away on a keyboard attached to a strange anatomically incorrect mouse running over the

desktop!

Instrumentation and technology has advanced with entire waveforms digitized and stored for analysis or processed for time or frequency domain information.

Although conventional NDE has been quite successful, it is generally based on complex, correlative relationships based on four main factors - quantitative measurement science, physical models for computational analysis, realistic interfacing with engineering decisions, and direct access to management priorities. The first two of these factors deal with technical issues of measurement and its interpretation while the last two deal with the decision process. All four components are necessary to achieve reliable standards, life prediction capability, extended safe economic life, and enhanced reliability with smart systems.

Most of the standard NDE acceptance or rejection criteria are still based on physical measurements that have not changed in 30 years. For example, the information in today's standard "C"- scan is still based on the simple assumption that acoustic waves interact with the sample and reveal "important" properties.

Such assumptions have been effective for finding delaminations, porosity, and inclusions for simple geometries of uniform materials. However, for complex samples, simple interpretations may be flawed. Perhaps the greatest need in NDE today, as decades ago, is the integration of materials science and measurement science resulting in an improved interpretation of data.

The decision factors deal with the integration of NDE with engineering and management priorities and are a most

difficult challenge. It is critical that the cost savings from NDE be made visible, including the complex areas of safety and reliability. NDE must improve its communication skills and change its image from the red ink side of the ledger.

This paper shall address recent advances in aerospace ultrasonics NDE. Examples are presented of acoustic propagation models that have led to the development of new measurement technologies advancing our ability to assure that materials and structures will perform as designed.

The Need For Science

An important focus in modern ultrasonic NDE is the development of meaningful physical models of critical measurements which are necessary to fully interpret data. Models require a clear statement of the underlying simplifying assumptions and the relevant interactions between the acoustic wave and the media. The most useful models can generally be inverted to either verify the model, result in corrections, or a different interpretation of the data is necessary, often resulting in a different perspective.

The new emerging science of NDE is married to the word quantitative, along with the acronym QNDE. Significantly, by measuring real physical properties, NDE has advanced from a detection process to one of evaluation. It is critical to understand the underlying physics of the observed effects. For example, in an ultrasonic scan of a material, the measured signal strength may decrease. What change in physical property caused that measurement and will that property affect the performance of the material.

The measured signal decrease, perhaps, is caused by an increase in attenuation caused by absorption (conversion to heat), by scattering (reradiation of the wave), by refraction (coherent redirection of the wave), or by mode conversion (changes in propagation mode). Most of these processes are frequency dependent which makes the analysis more complex. Absorption, for example, can vary linearly with frequency, as a square power, or as the fourth power. In addition, as the acoustic intensity increases, such as at the focus of a transducer, nonlinear effects may play a more important role and lead to harmonic generation and the formation of shock waves both of which effect attenuation. Such nonlinear interactions can significantly alter the requirements for both measurement as well as analysis of the data.

In addition, there are critical situations that involve unusual attenuation-like phenomena, caused by an artifact of the measurement process itself. Most transducers are larger than a wavelength and are phase sensitive. Therefore, if one part of the transducer "sees" a wave of different phase than another part of that transducer, the result will be phase cancellation which results in a measurement error of signal reduction. Such phase cancellation occurs in materials of nonplaner geometry, with velocity anisotropy, or with inhomogenity. Erroneous measurements can occur, unless one is measuring parallel, homogeneous, isotropic solids with normal incidence of perfect plane waves.

If only simple measurements are taken, one cannot differentiate the two phenomena. NDE must not be a study of anomalies, but rather a scientific analysis of material

properties. The simple measurements/analysis are not adequate for complex situations. The multidiscipline nature of NDE demands expertise in science and engineering that bridge the traditional technologies. An example follows that illustrates this point.

Fastener Stress

The ultrasonic bolt monitor is an excellent application of acoustics to an engineering problem. The scientific foundation of the concept matured over the past 20 years[1-3] and resulted in many experimental concepts, some developed by this author[4-6], based on the nonlinear theory of sound propagation in stressed media.

The basic problem is to insure that critical fasteners achieve proper preload needed to perform their design function. Torque is the common bolt preload procedure but is related to preload through friction which cannot be accurately controlled. Friction varies with lubricant, surface finish, geometry, and material. Therefore, torqued fasteners are only loaded to a limiting accuracy which at best is on the order of $\pm$ 20%. Often, the accuracy is no better than a factor of 2!

Physical models show that a fastener under stress elongates and experiences a change in sonic velocity. Therefore, if a sound wave travels along the axis of a fastener, it experiences an increase in round-trip-time or total phase shift. The amount of change depends on the bolt's third order elastic constants and the applied stress.

The analysis is covered in the references and leads to a

relationship :($\Delta t/t$) = (Δl / l - Δv / v), where t is time, v is velocity and l the length of the bolt.

Figure 1 shows ultrasonic bolt monitor data obtained from the fasteners of the Space Shuttle's landing wheels. A variety of lubricants were used in this test to demonstrate the effect of small changes in friction. The x's are data obtained with torque measurements, while the o's are the ultrasonic data. Note that even in the presence of frictional variations, the ultrasonic bolt monitor can correctly achieve the desired preload, in contrast to the significant errors produced by torque.

The Future of NDE

The example above is typical in all fields of NDE. Yet new sensors, instrumentation, and analysis are leading to fundamental scientific advances in our understanding needed to link physical measurements to engineering property values. How is strength measured today? Samples are broken. How is fatigue toughness determined? Samples are fatigued. That is not nondestructive evaluation. Our current understanding of physical measurements and materials science is incomplete yet the future of NDE science is bright and is heading toward that understanding.

Cooperation between the technologies of materials science and measurement physics are part of the next generation of QNDE. The priorities of management must also play a role in elevating this technology to one of significant economy.

Figure Caption

Figure 1). Comparison of ultrasonic bolt monitor with conventional torque for achieving critical fastener preload. Ultrasonic data is presented as a ratio related to the velocity change. A variety of lubricants were used to simulate frictional variations, a common problem facing torque measurements.

References

1) Hughes, D. S. and Kelly, J. L., "Second Order Elastic Deformation Of Solids," Phys. Rev. 92, pp 1145 - 1149 (1953).

2) Thurston, R. N., and Brugger, K., " Third Order Elastic Constants And The Velocity Of Small Amplitude Elastic Waves In Homogeneously Stressed Media," Phys. Rev. 133, p A1604-A1610, (1964).

3) Cantrell, J. H., " Anharmonic Properties Of Solids From Measurements Of The Stress Acoustic Constant," J. of Testing and Evaluation, 10, pp 223-229 (1982).

4) Heyman, Joseph S., "A CW Ultrasonic Bolt-strain Monitor," Experimental Mechanics, 17, pp 183-187, (1977).

5) Heyman, Joseph S., " Pseudo Continuous Wave Instrument," United States Patent 4,117,731 (1978).

6) Heyman, Joseph S., and Chern, E. J., " Ultrasonic Measurement of Axial Stress," Journal Of Testing And Evaluation, 10, pp202-211, (1982).

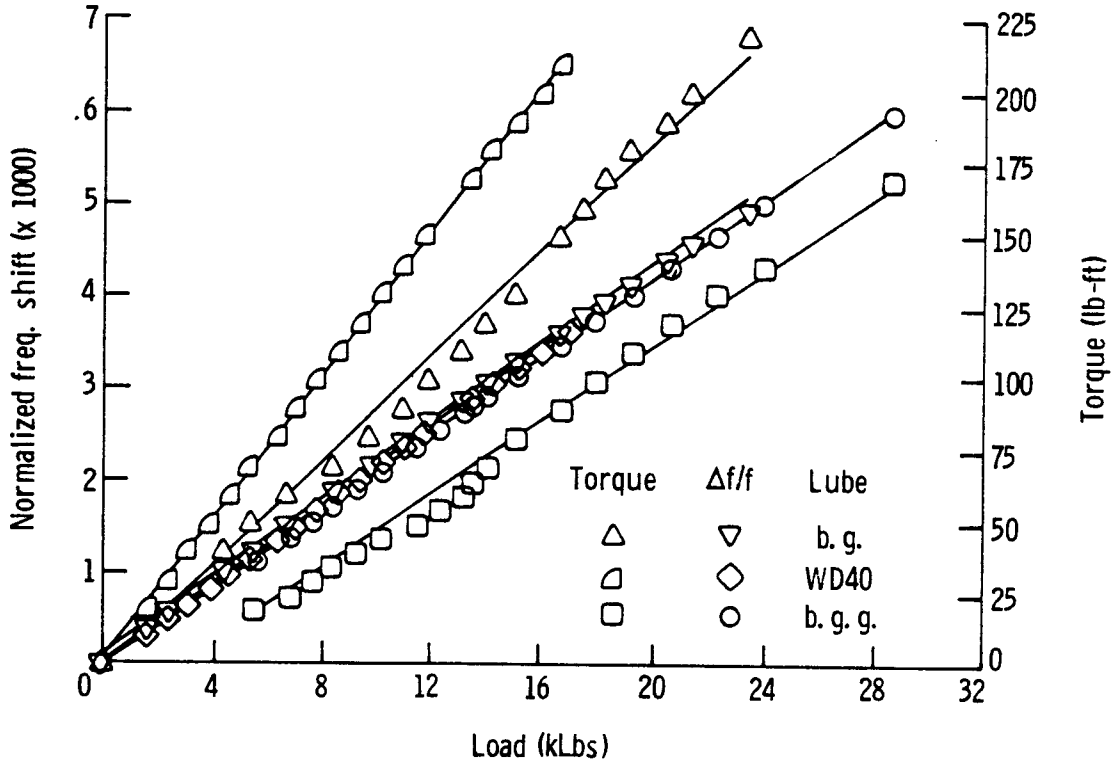
Normalized freq. shift (x 1000)
7
.6
5
4
3
2
1
0
4
8
12
16
20
24
28
32
Load (kLbs)
225
200
175
150
125
100
75
50
25
0
Torque (lb-ft)
Torque
Δf/f
Lube
b. g.
WD40
b. g. g.

ULTRASONIC PULSED PHASE LOCKED LOOP INTERFEROMETER FOR BOLT LOAD MEASUREMENTS

S. G. Allison and C. G. Clendenin
NASA Langley Research Center
Hampton, Va. 23665-5225

ABSTRACT

Obtaining the proper bolt preload in critical situations is essential for reliable assemblies. Conventional means of tensioning bolts using torque or other friction-related methods usually offer only 20% accuracy at best which is not acceptable for most critical assemblies. The Pulsed Phase Locked Loop Bolt Monitor (P2L2) uses ultrasonic waves to measure bolt preload with accuracies ranging from 1% to 3% depending on the specific bolt. This is accomplished by measuring load-induced acoustic phase shifts in the bolt which are independent of friction. Examples of critical applications including space shuttle landing gear wheels and NASA wind tunnel fan blades are discussed. In addition to bolt load measurements, the system has been used for stress measurements on other components and for material characterization studies. However, this paper will focus on use of the P2L2 for bolt load measurements only. Key words: Bolt preload, ultrasonics, phase measurement.

INTRODUCTION

The conventional approach of tightening bolts using torque to control preload has proven to be unacceptable when bolt preload accuracy of better than about 20% is required. In such critical bolting situations, numerous solutions have been offered. For example, bolts have been instrumented with strain gauges placed in a hole drilled down the bolt center line or mounted to the bolt's outside surface. Although this approach can offer acceptable accuracy, it is costly and requires modification of not only the bolt but sometimes the components being assembled. Another solution has been to measure bolt elongation using a micrometer. This approach can give acceptable accuracy if bolt end surfaces allow repeatable length measurements and if both ends of the bolt are accessible for insertion of the micrometer. In some cases where the bolt end is uneven, a metal ball is inserted to provide a point to measure from with the micrometer.

In recent years, ultrasonics has been used to solve some of these problems. The P2L2 was developed at NASA Langley Research Center in 1980 (1,2,3) and is an ultrasonic phase measurement technique. Other ultrasonic techniques such as time of flight are in use but are not addressed herein. This paper describes the P2L2, its applications and its load recertification capabilities. Additional uses of the P2L2 include load measurements in plates (4,5) and studies of nonlinear elastic material constants (6,7) which are beyond the scope of this paper.

P2L2 BOLT MONITOR

Figure 1 describes the P2L2 in block diagram form. It uses a voltage-controlled oscillator (VCO) and gate to send out an electronic pulse consisting of a few cycles of RF energy to drive an ultrasonic transducer. This produces an acoustic tone burst or sound wave pulse that travels down the length of the bolt and bounces off of the far end. The returning echo produces an electronic signal that is received back into the P2L2, is amplified and goes to a phase detector. The phase detector compares the phase of the received signal to that of the signal that went out and generates a voltage proportional to the difference in phase. An adjustable sample/hold selects a point on the ultrasonic echo and locks to that phase point. When locked, the P2L2 forces the ultrasonic phase to be constant by changing the instrument's output

frequency. Therefore, as the bolt is tightened, an exact frequency shift proportional to the change in bolt load results. This frequency change is due to load-induced changes in acoustic pathlength and sound velocity. Additional details regarding the P2L2 are available elsewhere (1,2,3).

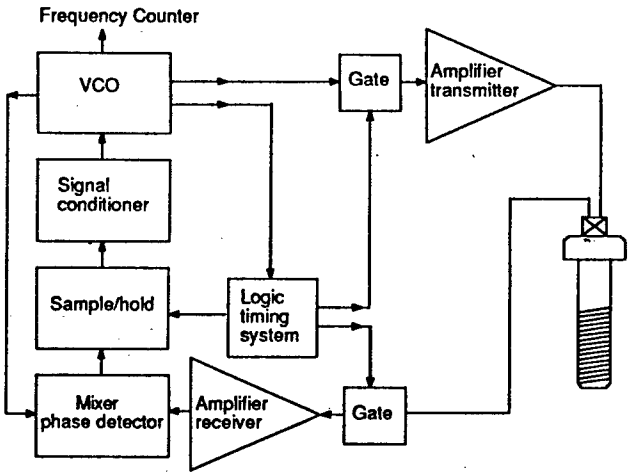

Figure 1 Block diagram, Pulsed Phase Locked Loop Bolt Monitor.

To use the bolt monitor, a calibration is first performed on the bolt to be tightened or on one like it. Figure 2 shows a typical calibration system in which the bolt is placed in a load cell duplicating the actual field joint thickness where the bolt is to be installed. The ultrasonic transducer is bonded to the bolt and the P2L2 output frequency as well as the load cell output voltage are read by a computer as the bolt is tightened. Figure 3 shows a typical bolt calibration (in this case, for a shuttle wheel rim tie bolt) in which the slope of the load vs. normalized frequency shift curve is determined and is used as the calibration factor. Bolt load is then determined in the actual field joint by measuring the frequency shift and applying the calibration factor.

Figure 4 illustrates that the P2L2 system measures bolt load independently of friction. A shuttle wheel bolt was tightened in a load cell using several different lubricants (WD40, wheel bearing grease and wheel bearing grease with graphite), each resulting in a different amount of friction. Torque and ultrasonic data were recorded while tensioning the bolt. Figure 4 shows that the relationship between load and torque varies with

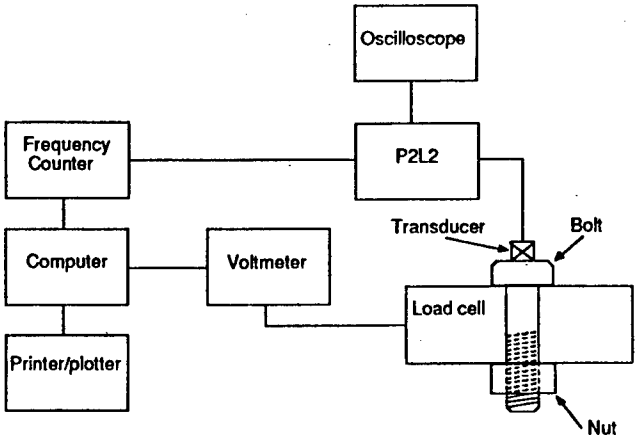

Figure 2 Calibration measurement system.

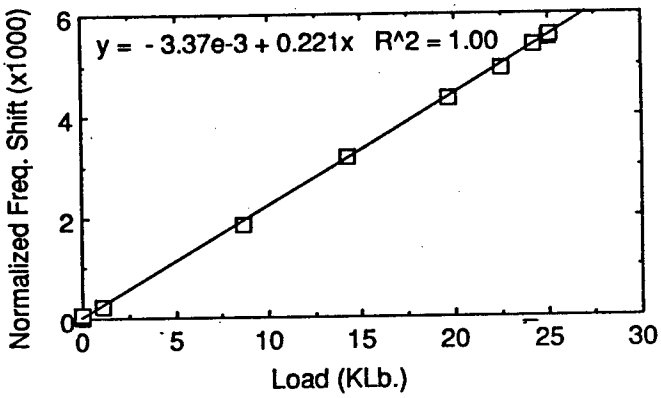

Figure 3 Bolt ultrasonic calibration (shuttle wheel).

different lubricants as evidenced by differences in the slope of the load vs. torque curves whereas the relationship between load and ultrasonic frequency shift does not vary.

APPLICATIONS

The P2L2 has seen wide use for critical bolting applications including spacecraft hardware, helicopter main rotor assemblies, railroad car bearing caps, mine safety roof bolts, space shuttle main landing gear wheels and wind tunnel fan blades. Two of the more recent projects (the space shuttle wheels and the Magnetic Suspension Tunnel fan blades) are addressed herein.

Space Shuttle Wheel Rim Tie Bolts

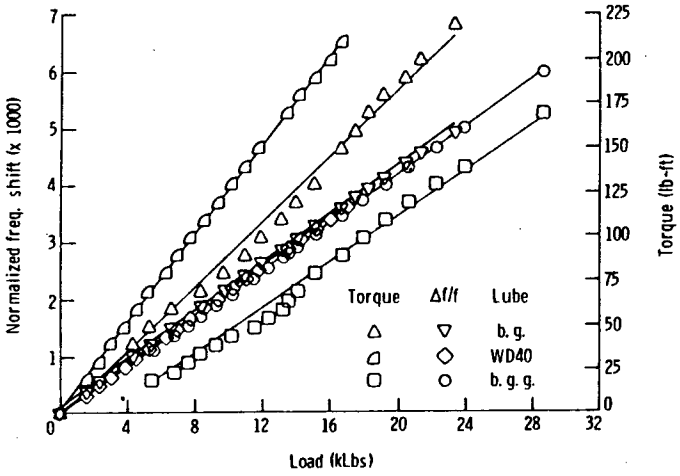

Figure 4 Influence of friction variations on torque-load relationship.

The shuttle main landing gear wheels use a two-piece rim that bolts together using 18 tie bolts. Accurate preloading of these bolts is important because it extends the usable life of the assembly by reducing fatigue. Design specifications call for 41000 pounds of preload in each bolt to give optimum fatigue life of the assembly. Bolt overtensioning results in wheel rim fatigue and bolt undertensioning causes bolt bending fatigue. Calculations show that increasing bolt load accuracy from 20% to 5% results in a 70% increase in usable life of the wheel assembly. Current wheel buildup procedures use torque to control bolt load which gives only about 20% accuracy. Use of ultrasonics to improve control of shuttle wheel tie bolt preload is in progress and is discussed below.

These wheel tie bolts are 5/8 inch diameter, 3-1/4 inch long high strength MP35-N cap screws with a flat-bottomed hole in the head. A holder clips into the tie bolt head and presses a 1/4 inch diameter 2.25 MHz compressional wave transducer against the bolt using a spring. Light machine oil ultrasonically couples the transducer to the bolt. An oscilloscope displays the ultrasonic echoes, the phase signal and the sample/hold marker and is used to verify sufficient echo amplitude as well as to verify good phase signal and to select a sample/hold position. Calibration is performed by placing a tie bolt in a load cell, locking the P2L2 and measuring load and frequency as the bolt is tightened. From this data, the slope of the load vs. normalized frequency shift curve is determined as previously shown in figure 3 and is the calibration factor for determining load from the ultrasonic readings in the field.

To demonstrate use of this system for shuttle wheel tie bolts, load was applied to a tie bolt in a hydraulic load cell. This device measured actual load while the P2L2 system predicted the load ultrasonically. In five loading tests, the P2L2 predicted the load with 0.6% to 1.4% accuracy (see bar graph in figure 5). Another demonstration was performed in which tie bolt load was measured ultrasonically in a non-flight wheel referred to as an "instrumented" wheel (see photograph in figure 5). One bolt in this wheel had strain gauges bonded to it so that actual load could be measured (strain gauging of these tie bolts is acceptable for testing of shuttle wheels but is impractical on flight hardware due to wheel rim modification requirements and expense associated with instrumenting of bolts). When this bolt was tightened, the P2L2 load prediction agreed within 0.5% with the strain gauge load prediction (see bar graph in figure 5).

The P2L2 also demonstrated compatibility with wheel buildup and pointed out the inaccuracy of the current torque approach. Ultrasonics was used to monitor bolt load achieved using torque during buildup of two non-flight qualification test wheels. The 18 bolts in each of these wheels were tightened according to the current wheel buildup procedure which uses a criss-cross bolt tightening pattern in three torque steps, i.e. 75 ft.-lb., 145 ft.-lb. and 184 ft.-lb. measured with a pre-set torque wrench. Ultrasonically measured bolt loads for one of the qualification test wheels are plotted in figure 6 and show that the target load of 41,000 pounds per bolt was missed by as much as 20% using torque. These tests also demonstrated that use of ultrasonics does not significantly slow down the wheel buildup process (wheel buildup was done in 70 minutes for one wheel and 60 minutes for the other which is well within the allowable time).

In another test, ultrasonics controlled bolt load (rather than monitoring it) in an instrumented wheel. The computer displayed the load as each of the 18 bolts was tightened and also gave an audible indication when the target load was achieved. Results of this demonstration are seen in figure 7 and show that much better control of bolt load is achieved using ultrasonics than is achieved using torque. Also note that torque information need not

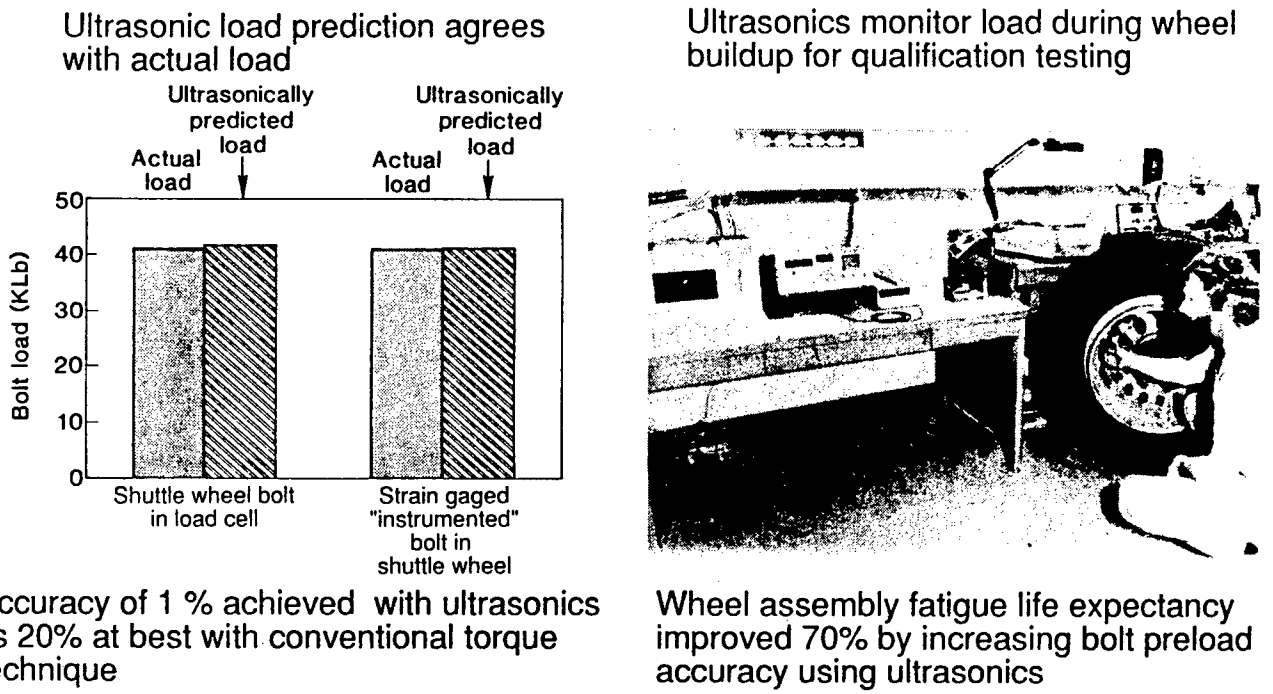

Figure 5 Ultrasonics for space shuttle landing gear wheel rim tie bolts.

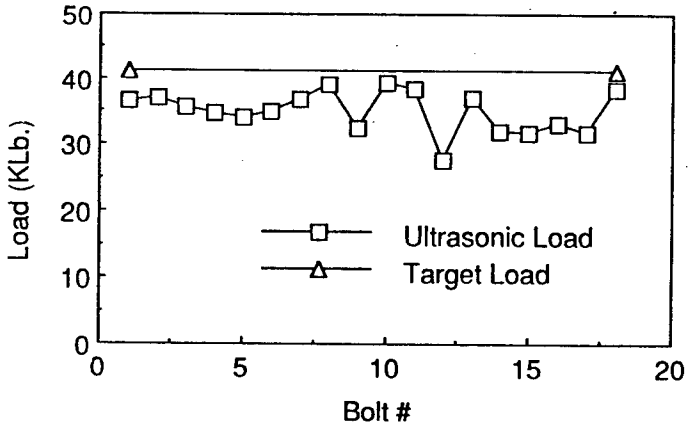

Figure 6 Ultrasonics show inaccuracy of torque control for shuttle wheel bolt preloading.

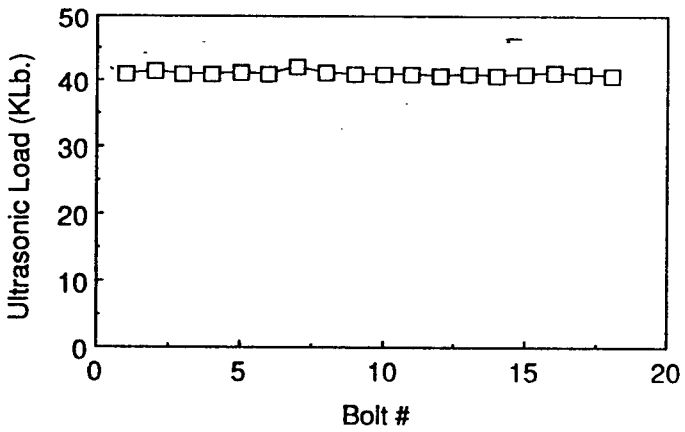

Figure 7 Ultrasonics control shuttle wheel bolt preload accurately.

be lost just because ultrasonics is used to control bolt load. Torque can still be recorded for future reference as additional information.

Magnetic Suspension Tunnel Fan Blade Bolts

Figure 8 shows bolt installation using ultrasonics for a replacement fan hub/blade assembly recently built for the Magnetic Suspension Tunnel at NASA Langley. Ultrasonic tensioning of fan blade bolts to 8300 pounds is specified on design drawings for these critical fasteners since 5% accuracy is required. Each fan blade attaches to the hub using a 1/2-20 UNF hex head cadmium plated grade 8 steel bolt. For this work, a 5 MHz, 0.25 inch diameter compressional wave transducer in a permanent magnet housing was used. Magnetic clamping of the transducer to the bolt allowed the transducer to remain undisturbed during calibration and blade installation so as to give acceptable accuracy. To

Ultrasonic calibration in load cell

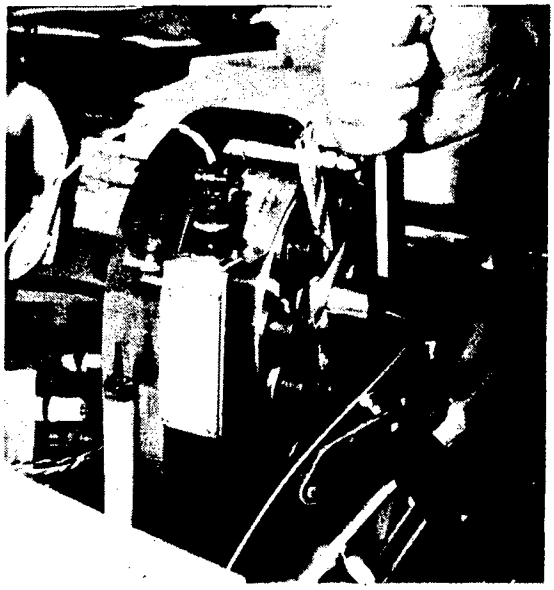

Ultrasonic shift vs load is determined

Critical blade installation in fan hub

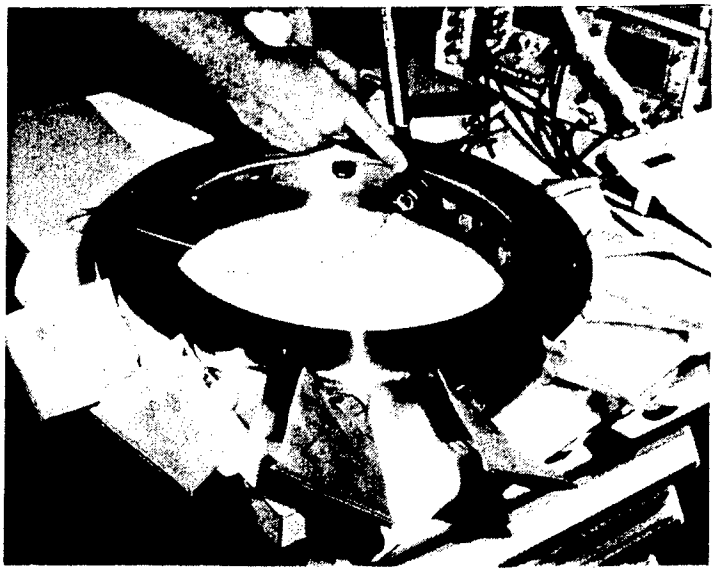

Preload accuracy improved from 20% at best to closer than 5% by using ultrasonics instead of torque

Figure 8 Ultrasonics improve accuracy of fan blade/hub assembly bolt tension for Magnetic Suspension Tunnel.

better facilitate the ultrasonic measurement, the head and threaded end of each of these bolts were machined smooth, flat and parallel since project personnel indicated this would not degrade the bolts.

A nonmagnetic deep-well 3/4 inch socket was used for the bolt tensioning during calibration to prevent transducer movement. Calibrations were performed on each bolt (see left hand photograph in figure 8) immediately before bolting the accompanying blade into the hub. In achieving the desired bolt load during blade installation (see right hand photograph in figure 8), the computer provided real-time display of ultrasonic load and also gave an audible beep when the desired load was achieved to help the operator determine when to stop tightening.

During installation of these blades, a bolt load decrease of a few hundred pounds was observed as soon as the tightening torque was removed. This was accredited to a torsional spring-back effect and was compensated for by overtightening the bolt by a few hundred pounds before removal of torque so that the spring-back loosening upon removal of torque left the proper preload. Also, a relaxation of about 30 pounds was determined to occur within the first minute after tightening as observed using the load cell. Therefore, in determining final bolt load in the hub/blade assembly, 30 pounds was subtracted from the load reading seen immediately after torque was removed. Figure 9 shows final ultrasonic loads in these blade bolts.

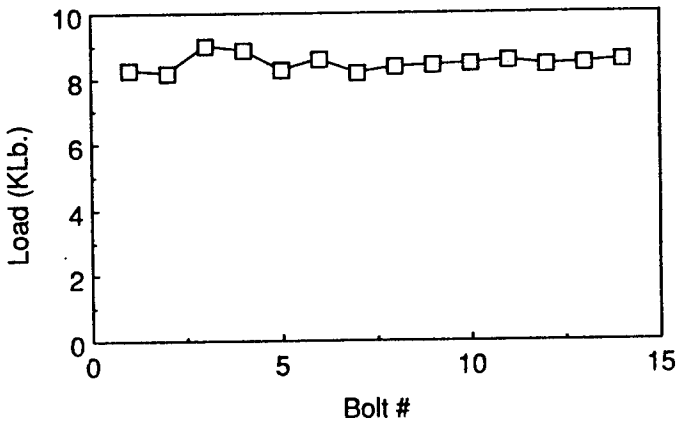

Figure 9 Magnetic Suspension Tunnel fan blade bolt loads.

Load Recertification

The P2L2 has primarily been used to measure load changes while tightening bolts as described thus far in this paper. To remeasure bolt load after installation, a thermal calibration factor compensates for bolt temperature changes and a standard reference block allows correction for acoustic phase errors due to measurement equipment configuration changes such as use of a different transducer, cable or couplant. Details regarding this are documented in a recently submitted NASA Langley patent application and are not presented here.

SUMMARY & CONCLUSION

Ultrasonic techniques provide an excellent means to measure bolt preload. Conventional techniques which rely on torque are very inaccurate because they measure friction which can vary greatly. The P2L2 measures bolt preload with accuracies ranging from better than 1% for prepared (good geometry) bolts to about 3% for poor geometry bolts. It eliminates the need for costly alternatives such as strain gauged bolts and is being packaged in a portable microprocessor-based unit for ease and convenience of use. Reliability of this system to make accurate bolt preload measurements has been demonstrated through a number of critical applications within both the government and the private sector. In addition to measurement of bolt preload addressed herein, additional uses of the pulsed phase locked loop system such as characterization of material properties and measurement of stress in wind tunnel nozzle plates and other structures are discussed elsewhere.

REFERENCES

(1) Heyman, J. S., "Pulsed Phase Locked Loop Strain Monitor", NASA Patent Disclosure. LAR-12772-1, 1980.

(2) Heyman, J. S. and Chern, E. J. "Ultrasonic Measurement of Axial Stress", Journal of Testing and Evaluation. Vol. 10, No. 5, Sept. 1982, pp. 202-211.

(3) Allison, S. G. and Heyman, J. S., "Nondestructive Ultrasonic Measurement of Bolt Preload Using the Pulsed Phase Locked Loop Interferometer", The Second Symposium on Welding, Bonding and Fastening. NASA Langley Research Center, Hampton, Va., October 23-25, 1984.

(4) Heyman, J. S. and Issler, W. "Ultrasonic Mapping of Internal Stresses", Proceedings, 1982 IEEE Ultrasonic Symposium. Oct. 27-29, 1982.

(5) Allison, S. G., Heyman, J. S. and Salama, K. "Ultrasonic Measurement of Residual Deformation Stress in Thin Metal Plates Using Surface Acoustic Waves", Proceedings, 1983 IEEE Ultrasonic Symposium. Atlanta, Ga., Oct. 31-Nov. 2, 1983.

(6) Heyman, J. S. and Chern, E. J. "Characterization of Heat Treatment in Aluminum Based on Ultrasonic Determination of the Second and Third Order Elastic Constants", Proceedings, 1981 IEEE Ultrasonic Symposium. Chicago, Il., 1981.

(7) Allison, S. G., Heyman, J. S. and Salama, K. "Influence of Carbon Content on Higher-Order Ultrasonic Properties in Steels", Proceedings, 1983 IEEE Ultrasonic Symposium. Atlanta, Ga., Oct. 31-Nov. 2, 1983.

THE USE OF ULTRASONIC HARMONIC GENERATION TO DETERMINE CRACK OPENING CONDITIONS IN COMPACT TENSION SPECIMENS

William T. Yost, Min Namkung, and S.G.Allison

NASA-Langley Research Center
Mail Stop 231
Hampton, VA 23665-5225

INTRODUCTION

In 1971, Elber reported the discovery of a crack closure phenomenon that occurs with fatigue. He noted that closure of the crack planes near the crack tip can occur while the applied stress is still tensile [1]. The existence of a closure stress opens the way of defining an effective stress intensity factor, K_{eff}, given by

$$K_{eff} = (\sigma - \sigma_{closure}) (\pi a)^{1/2}$$

where σ is the applied tensile stress, $\sigma_{closure}$ is the crack closure stress, and a is the crack half length. The stress intensity factor is useful in correlating fatigue crack propagation data, especially after overloads [2]. The precision of K_{eff} depends upon how well one can determine $\sigma_{closure}$. However it is difficult to experimentally determine $\sigma_{closure}$, since conventional crack opening determination is imprecise. The purpose of this paper is to present an ultrasonic technique that shows promise as a means to accurately determine when the crack is open.

SOME OF THE PRESENT TECHNIQUES TO MEASURE CRACK OPENING LOAD

The compact tension specimen is shown schematically in Fig. 1. It is loaded using clevis grips placed in a load frame. An extensometer is placed across the mouth of the specimen. Tension is applied cyclically between a maximum and a minimum value. As this is done, the crack initiates at the notch, and propagates into the specimen. The crack growth rate depends upon the parameters established for the loading cycle, the material properties of the specimen, and environmental factors as well as test sample geometry.

As a cycle of specimen loading begins, the applied load is measured with a load cell. The displacement across the mouth is measured with the extensometer. One can, in theory, plot the load vs. displacement, and determine the crack opening load by determining the point where the load vs displacement takes on a constant slope for the higher value loads. However, such a plot is not very sensitive to crack opening vs load, so other data analysis techniques are preferred. We will briefly present two of these, which are currently in use. (The authors are indebted to Dr. J. Newman and E. Phillips of NASA-Langley Research Center for their helpful discussions about these techniques). In both of the techniques presented here, one first loads the specimen to maximum and then decreases the load. During the part of the cycle where the load is decreased from maximum, one determines a straight line fit from the values measured while unloading from maximum. We call this the "upper data".

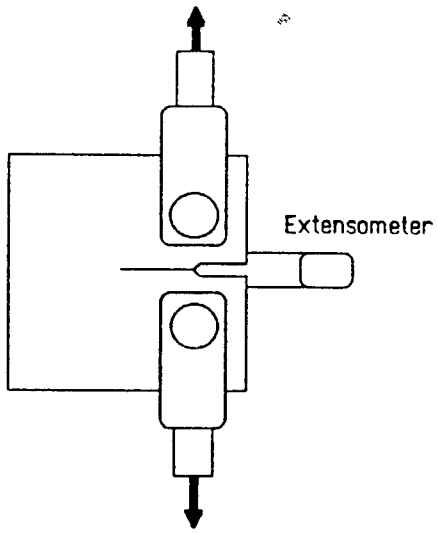

Fig. 1 Compact Tension Specimen

The "Load-Reduced Displacement" method for data analysis is shown in Fig. 2. One defines "reduced displacement as the difference between the straight line fit of the upper data and the measured displacement. This is shown in Fig. 2a. Next, one plots the load vs the reduced displacement, which is shown in Fig. 2b. The crack opening load is determined as the point where the curve goes vertical, as marked with the arrow.

The "Load-Slope Change" method for data analysis is shown in Fig. 3. In this method, one determines a series of slopes during the unloading portion of the cycle, as shown in Fig. 3a. By plotting Load vs. slope increase (the difference between the reference slope measured at the top, and the slopes along the rest of the curve) as in Fig. 3b , one can determine the crack opening load by marking the load where the slope increase first deviates from zero. This is marked with an arrow.

We illustrate the "Load-Slope Change" method with measurements that we took on a compact tension specimen used in this study. The specimen is machined from Al 2219-T851 material. The maximum and minimum loads are 4000 lbs and 400 lbs. Fig. 4 is a plot of the Load vs Slope Increase data. One can observe that the data clearly exhibit the effects of noise in the measurement system. It is difficult to precisely determine where the load-slope increase plot is tangent to the vertical axis. The problem of noise causes substantial uncertainty in the determination of the crack opening load.

USING HARMONIC GENERATION TO DETERMINE CRACK OPENING

The use of ultrasonic harmonic generation to measure lattice anharmonicity is well documented in the literature [3,4,5]. Also, Hikata and Elbaum have studied the effects of dislocation motion on harmonic generation [6,7]. Buck et. al. [8] have used harmonic generation by surface waves to look at fatigue states in aluminum. Richardson [9] has described the generation of harmonics at the interface of unbonded surfaces. While all effects mentioned above apply to this problem, we use the fact that as a crack in a compact tension specimen is opened, harmonics are generated at the (unbonded) surfaces of the crack interface.

The equipment diagram sketch is shown in Fig. 5. A 5 Mhz tone burst is generated by the function generator (a Hewlett-Packard #3314A), is power-boosted by an amplifier (an ENI A-150), and is converted into an acoustic wave by the 5 MHz undamped transducer (a lithium niobate compressional transducer). After the wave traverses the sample, it is received by the 10 MHz transducer (a lithium niobate 10 MHz undamped compressional transducer), where the ultrasonic wave is converted into an electrical signal. The output signal is amplified and detected by a receiver (ICOM IC-R71A). A 40 dB attenuator is placed in the path when receiving the fundamental signal. The receiver is tuned to the appropriate frequency, and its detected output is measured with an oscilloscope (Tektronix 2445), which is triggered from the function generator and delayed to compensate for the traversal time of the ultrasonic signal through the sample.

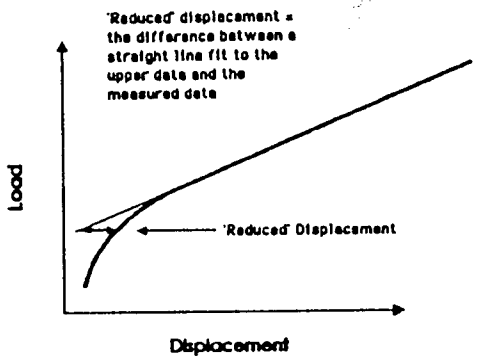

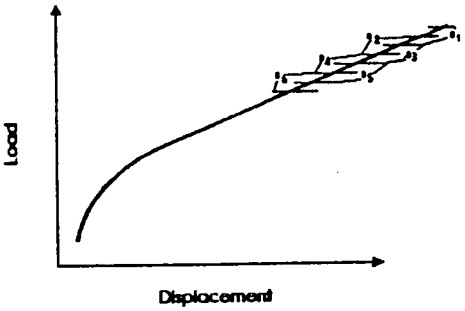

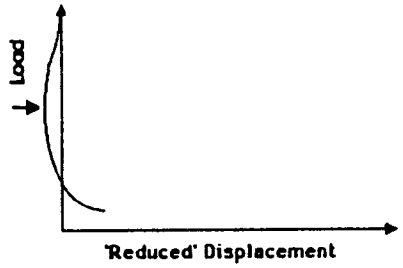

Fig 2. Load-Reduced Displacement Method to Determine Crack Opening Load

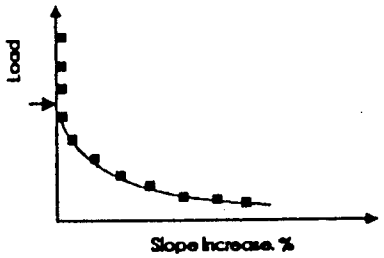

Fig. 3. Load-Slope Change Method to Determine Crack Opening Load

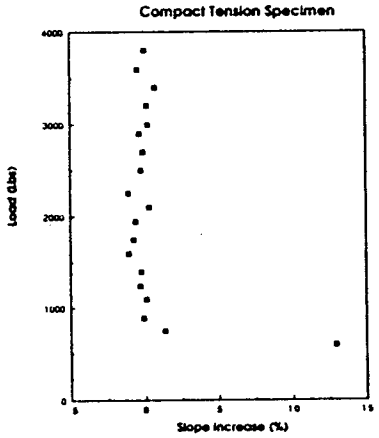

Fig.4 Load Vs. Slope Increase

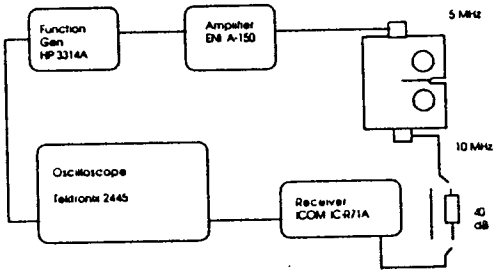

Fig. 5 Equipment Diagram

Using the above arrangement, we measured both fundamental and the harmonic output from the 10 MHz transducer in a specimen of AL 2219-T851 (1 in thick by 7.5 in. length x 7.19 in. high) that had been previously cracked. The measurement sets were taken as follows: (1) near one end of the sample in a region away from the crack to determine the response of the measurement system and the material; (2) over the cracked region to determine the characteristics of ultrasound propagation across the crack; and (3) over the cracked region during the loading cycle to determine any difference in harmonic generation content during the loading cycle. Before the measurements under load were taken, we cyclically loaded the specimen from 400 to 4000 lbs in tension, until the crack propagated an additional 0.275 in. to a total crack length of 2.9 in. The transducers (5 MHz and 10 MHz) were mounted in aluminum housings, and placed on the compact tension specimen and axially aligned, as shown in Fig. 6. For (2) and (3) the axial line of the transducer pair approximately intersected the crack tip.

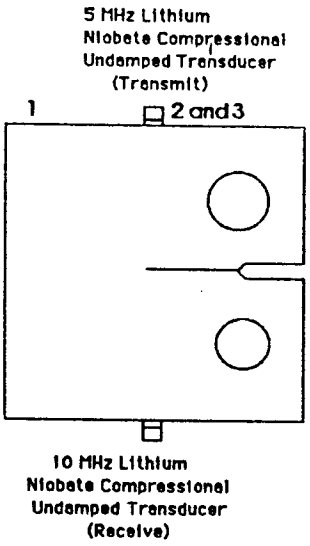

Fig. 6 Transducer Placements

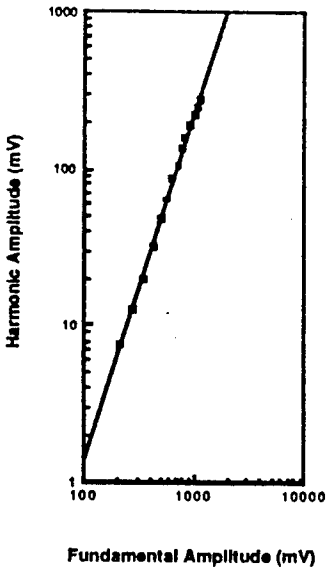

Fig. 7 Harmonic Amplitude Vs Fundamental Amplitude

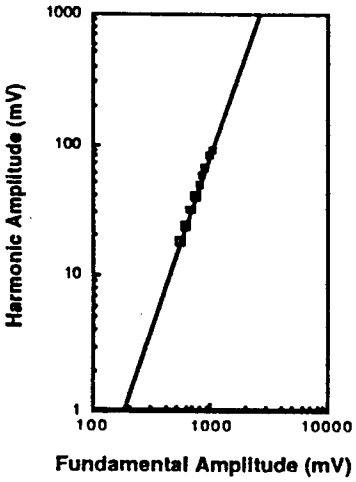

Fig. 8 Harmonic Amplitude Vs Fundamental Amplitude

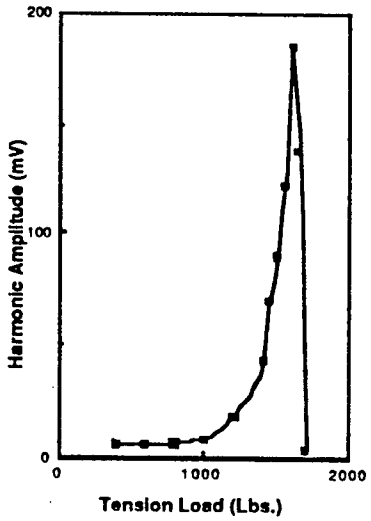

Fig. 9 Harmonic Amplitude Vs Load

Fig. 7 is a log plot of harmonic amplitude vs fundamental amplitude where the wave is propagated through material far from the crack. Fig. 8 is a log plot of harmonic amplitude vs fundamental amplitude when the ultrasonic wave is propagated across the crack without any load applied. In comparison of the two graphs, we notice that the slopes are slightly different, and that the harmonic output is diminished in the case of propagation through the crack. The increase in slope for the propagation through the crack can be explained by the fact that some additional harmonic generation could occur at the crack (most probably around the asperities).

The specimen was placed under load. The harmonic output from the receive transducer was measured and plotted as a function of load. The received fundamental amplitude was held constant during the measurements. The results are shown in Fig. 9. We notice that the maximum harmonic output occurs at a load of 1550 lbs, and abruptly drops to its premaximum level at a load of 1600 lbs. This value is in agreement with theoretical calculations using finite element analysis.

CONCLUSIONS

It appears that ultrasonic harmonic generation can be a useful tool in the monitoring of crack opening dynamics in compact tension specimens. The value obtained in this case was in agreement with the value predicted by theory. Moreover, this technique seems to be immune to the noise problems that plague other techniques.

ACKNOWLEDGEMENT

The authors are indebted to Mr. Jerry Clendenin for his help in some of the technical aspects of these measurements.

REFERENCES

1. Elber,W. ASTM-STP 486, 1971, P 230
2. Weertman,J. "Fatigue Crack Propagation Theories" from the book, Fatigue and Microstructure, American Society for Metals, Metals Park, OH 44073, 1979
3. Breazeale, M.A., and Ford, Joseph, J. Appl. Phys. 36 3486 (1965)
4. Gauster, W.B., and Breazeale, M.A. Phys Rev 168 655 (1968)
5. Yost, W.T., Cantrell Jr, John H. and Breazeale, M.A. , J. Appl. Phys. 52 126 (1981)
6. Hikata, A., Chick, B., and Elbaum, C. Appl. Phys. Letters 3 195 (1963)
7. Hikata, A. , and Elbaum, C., Phys. Rev. 144 469 (1966)
8. Buck, O., Morris, W. L., and Richardson, J. M., Appl. Phys. Letters 33 371 (1978)
9. Richardson, J. M., Int. J. Eng. Sci. 17 83 (1979)

V. CHARACTERIZATION OF SUPERCONDUCTING MATERIALS

Ultrasonic Attenuation Measurements on $LuBa_2Cu_3O_7$ and $HoBa_2Cu_3O_7$

Keun J. Sun[†]

NASA-Langley Research Center

Hampton, VA 23665

Moises Levy[††] and Bimal K. Sarma[††]

Department of Physics

University of Wisconsin-Milwaukee

Milwaukee, WI 53201

H. C. Ku[*], H. D. Yang[*], R. N. Shelton[*], R. W. McCallum[*], and P. Klavins[*]

Ames Laboratory — USDOE and Department of Physics

Iowa State University

Ames, IA 50011

(July, 1987)

[Abstract]

$HoBa_2Cu_3O_7$ and $LuBa_2Cu_3O_7$ show very different ultrasonic attenuation behavior at temperatures below 220 K. Both samples do not exhibit the sharp change in attenuation due to electron-phonon interaction mechanism as described in the BCS theory.

[Text]

I. Introduction

The recent discovery of superconductors with high superconducting phase transition temperatures has induced broad interests in investigating these materials. It has been speculated that the particular crystal structure of these samples plays an important role in causing the relatively large values of their transition temperatures. Consequently, whether the electron-phonon interaction mechanism as described in the BCS theory is still responsible for the superconducting behavior of these samples is an interesting subject. And, this has stimulated various types of measurements to characterize the physical quantities of the superconducting properties of these samples such as energy gaps, specific heat, and critical fields. Of particular interest is the determination of the existence of an energy gap and its quantitative measurement.

Ultrasonic attenuation and velocity measurements are useful techniques for detecting crystal structure changes, phase transitions, dislocations and internal friction in solids. Ultrasonic attenuation in the superconducting state of a conventional superconductor exhibits a characteristic behavior as a result of electron-phonon interaction, and can be employed to find the value of the temperature dependent energy gap,[1] the superconducting transition temperature, critical magnetic fields, the electron mean free path and the first and the second Ginzburg Landau parameters.

II. Experiments and Results

The temperature dependent ultrasonic attenuation coeifficent was measured on sintered samples of $LuBa_2Cu_3O_7$ and $HoBa_2Cu_3O_7$ in this study, and has also been measured on sintered $YBa_2Cu_3O_7$.[2] A 10 MHz $LiNbO_3$

longitudinal wave transducer of 0.32 cm diameter was epoxy bonded to each of the samples. The dimensions of $LuBa_2Cu_3O_7$ are 0.35 cm in thickness and 0.95 cm in diameter, and those for $HoBa_2Cu_3O_7$ are 0.27 cm in thickness and 1.01 cm in diameter. The ratios of mass density of these powder samples to that of a primitive cell are 67% and 57% for $LuBa_2Cu_3O_7$ and $HoBa_2Cu_3O_7$ respectively. A pulse echo technique was employed to obtain the attenuation and velocity data. It was found that the room temperature sound velocities at 10 MHz are 2.98×10^3 m/sec and 3.05×10^3 s/sec for $LuBa_2Cu_3O_7$ and $HoBa_2Cu_3O_7$ respectively with $\pm$ 3% experimental errors.

Relatively, the variation scale of attenuation as a function of temperature for $HoBa_2Cu_3O_7$ is much smaller than that for $LuBa_2Cu_3O_7$. For the former there were three echoes which could be observed and measured in the whole temperature range that was investigated. There were only two echoes at room temperature and one echo at liquid nitrogen temperature[3] for the latter $LuBa_2Cu_3O_7$. The experimental results shown in the figures are the data of relative change of attenuation as a function of temperature at 10 MHz obtained by measuring the amplitude change of the first echo of each sample between 50 K and 280 K. The rate of temperature ramping is slow enough to obtain reproducible data. Room temperature thickness of the sample was used to determine the value of attenuation in units of dB/cm.

Qualitatively, above 220 K, Figures 1 and 2, the temperature dependent attenuation of both samples displayed the same features: The attenuation coefficient had a steep decrease when the samples were cooled down from room temperature to 250K, and relatively small changes from 250 K to 220 K. The attenuation of polycrystalline $YBa_2Cu_3O_7$ exhibited almost the same behavior in this temperature range. As it can be seen in Figures 1 and 2, below 220K the attenuation goes in the opposite direction for the two samples. The attenuation curve of $LuBa_2Cu_3O_7$ undergoes a relatively large slope change

around 130 K and shows a much slower increasing trend as the sample temperature was lowered further. Around 81 K where the sample enters the superconducting state, the attenuation does not show observable variations. The attenuation of $HoBa_2Cu_3O_7$ decreases with temperature below 220 K. A relatively fast decrease in attenuation appears at 84 K and below. Resistivity measurements showed the superconducting transition occurred between 96 and 82 K, and the mid point of the resistivity change was located at 85 K. Figure 3 displays the attenuation of $HoBa_2Cu_3O_7$ sample between 77 K and 100 K. Although there are fluctuations at temperatures between 97 K and 91 K, the decrease of attenuation below 84 K is quite obvious. A similar decrease has been observed in the attenuation data of $YBa_2Cu_3O_7$ at temperatures close to its T_c.[2]

Thermal expansion measurements have not been performed on these samples. However, the large velocity changes in certain temperature ranges may be attributed to other effects; and, therefore, sample thickness variations caused by thermal effects will be initially neglected.

Figure 4 displays the normalized velocity as a function of temperature for both samples. The fast increase in velocity from room temperature to around 250 K is the common feature of the two curves. There are about a 5 percent and a 2 percent velocity increase in this temperature range for $LuBa_2Cu_3O_7$ and $HoBaCu_3O_7$ respectively.

IV. Discussion

The ultrasonic attenuation of $YBa_2Cu_3O_7$[2] and $HoBa_2Cu_3O_7$ qualitatively exhibit similar temperature dependent behavior as shown in Figure 2. However, except for the part at temperatures above 200 K, $LuBa_2Cu_3O_7$ has a

quite different attenuation curve. If the crystal structure of $LuBa_2Cu_3O_7$ is a little different from those of the other rare-earth-Ba-Cu-O samples as stated in reference (3), then the attenuation measurements may therefore confirm this difference.

The time for sound wave propagating in the samples has been measured for the $YBa_2Cu_3O_7$, $HoBa_2Cu_3O_7$ and $LuBa_2Cu_3O_7$. Although the thermal expansion measurements on these samples have not been done, it seems that the velocity change of these samples at temperatures above 250 K is too large to be solely attributed to thermal thickness variations. In addition to the drastic decrease in attenuation when the sample temperature was lowered from 290 K, the sound velocities of the three samples became 2 to 10 percent faster than they are at room temperature. If the sample temperature was lowered further and reached liquid nitrogen temperatures, the velocities would generally keep increasing but at a more moderate rate. A detailed analysis of the sound velocity and the frequency distribution of the sound wave may give useful information about phase transitions in these samples.

Although the attenuation shows a decrease at temperatures below 84 K for the $HoBa_2Cu_3O_7$ sample, it does not change as sharply as for conventional superconductors, such as vanadium, niobium, etc. And, $LuBa_2Cu_3O_7$ does not exhibit an attenuation change around its superconducting transition temperature at all. Therefore, mechanisms other than electron-phonon interaction may be necessary to interpret this attenuation behavior.

The causes of the drastic variations of attenuation above 200 K remain unknown. It may be a precursor to the full-volume superconducting transition of the sample at lower temperatures.[4] Attenuation measurements at higher frequencies with and without an applied magnetic field may provide information which would be helpful in interpreting these experimental results.

Figure Captions

Figure 1 Relative change of attenuation as a function of temperature of $LuBa_2Cu_3O_7$ between 50 K and 280 K.

Figure 2 Relative change of attenuation as function of temperature of $HoBa_2Cu_3O_7$ between 77 K and 280 K.

Figure 3 Relative attenuation change as a function of temperature of $HoBa_2Cu_3O_7$ between 77 K and 100 K.

Figure 4 Normalized sound velocity of $LuBa_2Cu_3O_7$ and $HoBa_2Cu_3O_7$ as a function of temperature.

References

†This work was done when the author held a National ~~Science~~ Research Council (NASA - Langley) Research Associateship.

††Research supported by Air Force Office of Scientific Research under grant No. AFOSR 84-0350

*Ames Laboratory is operated for the U.S. Department of Energy by Iowa State University under contract no. W-7405-Eng-82.

1. J. Bardeen, L. N. Cooper, and J. R. Schrieffer, Phys. Rev. Vol. 108, No. 5, 1175 (1957).

2. K. J. Sun, M. Levy, B. K. Sarma, P. H. Hor, R. L. Meng, Y. Q. Wang and C. W. Chu (to be published).

3. P. H. Hor, R. L. Meng, Y. Q. Wang, L. Gao, Z. J. Huang, J. Bechtold, K. Forster and C. W. Chu, Phys. Rev. Lett. 48, 1891 (1987).

4. J. T. Chen, L. E. Wenger, C. J. McEwan, and E. M. Logothetis, Phys. Rev. Lett. 58, 1972 (1987).

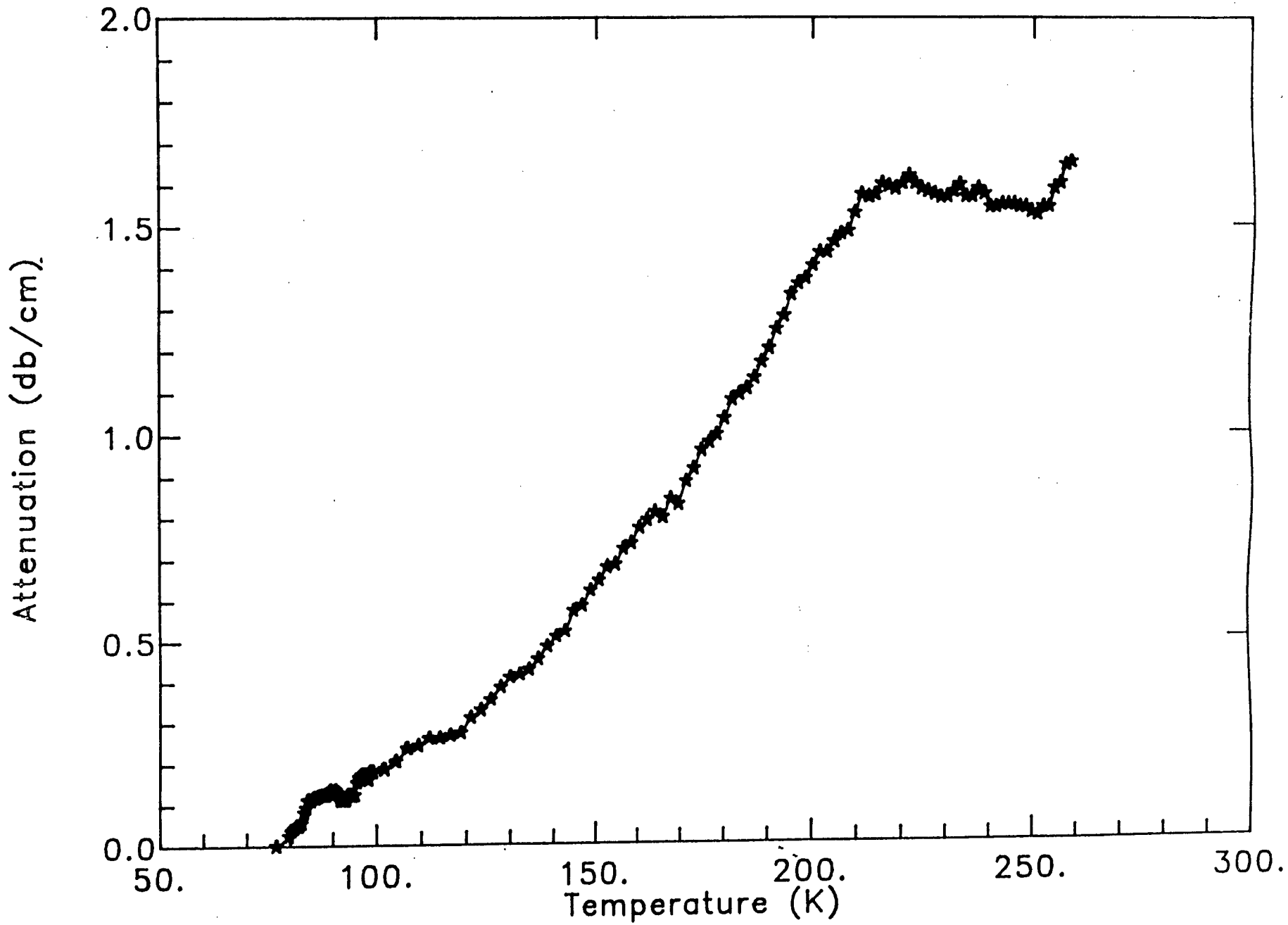
2.0
1.5
1.0
0.5
0.0
Attenuation (db/cm)
50.
100.
150.
200.
250.
300.
Temperature (K)

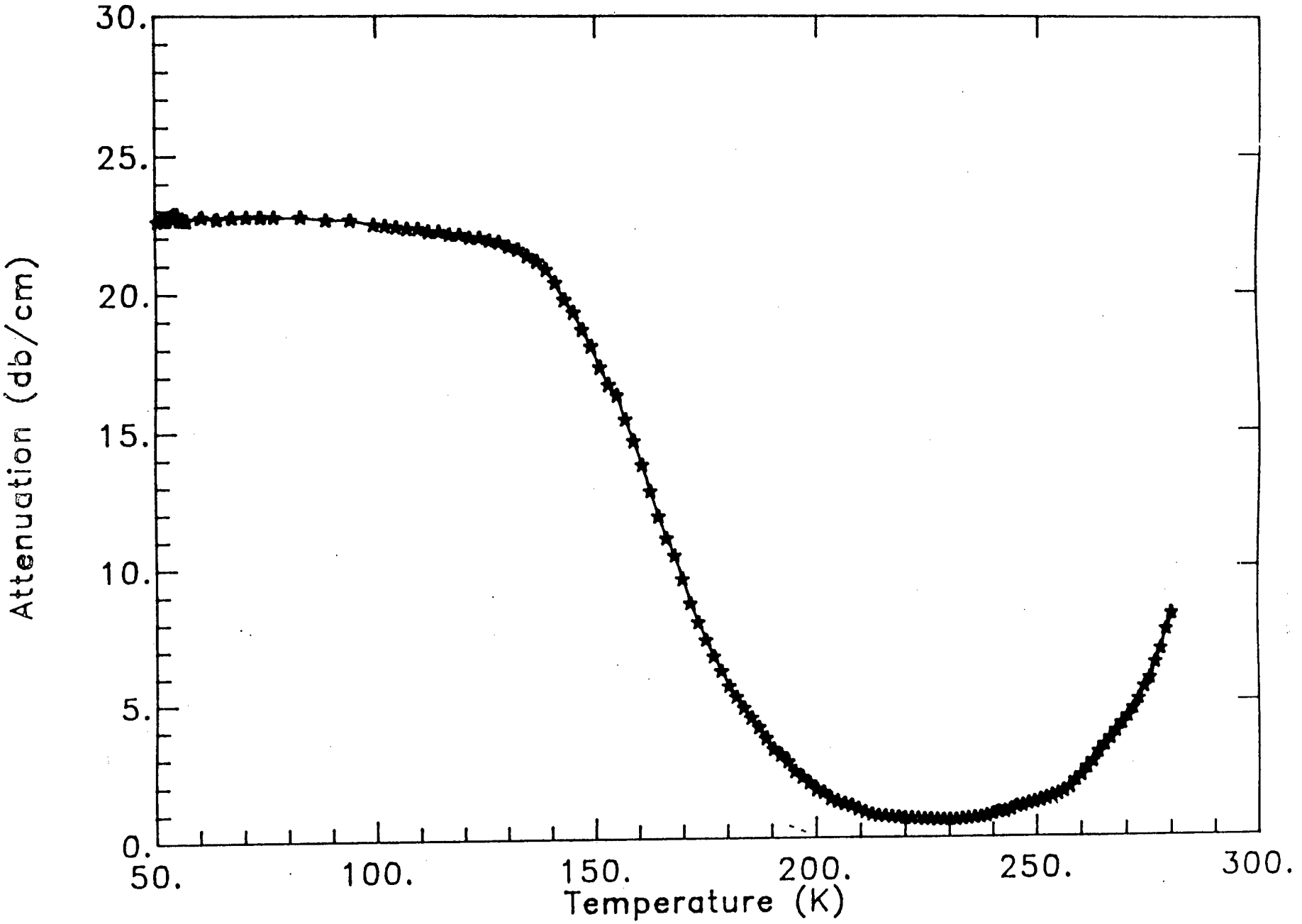
30.
25.
20.
15.
10.
5.
0.
Attenuation (db/cm)
50.
100.
150.
200.
250.
300.
Temperature (K)

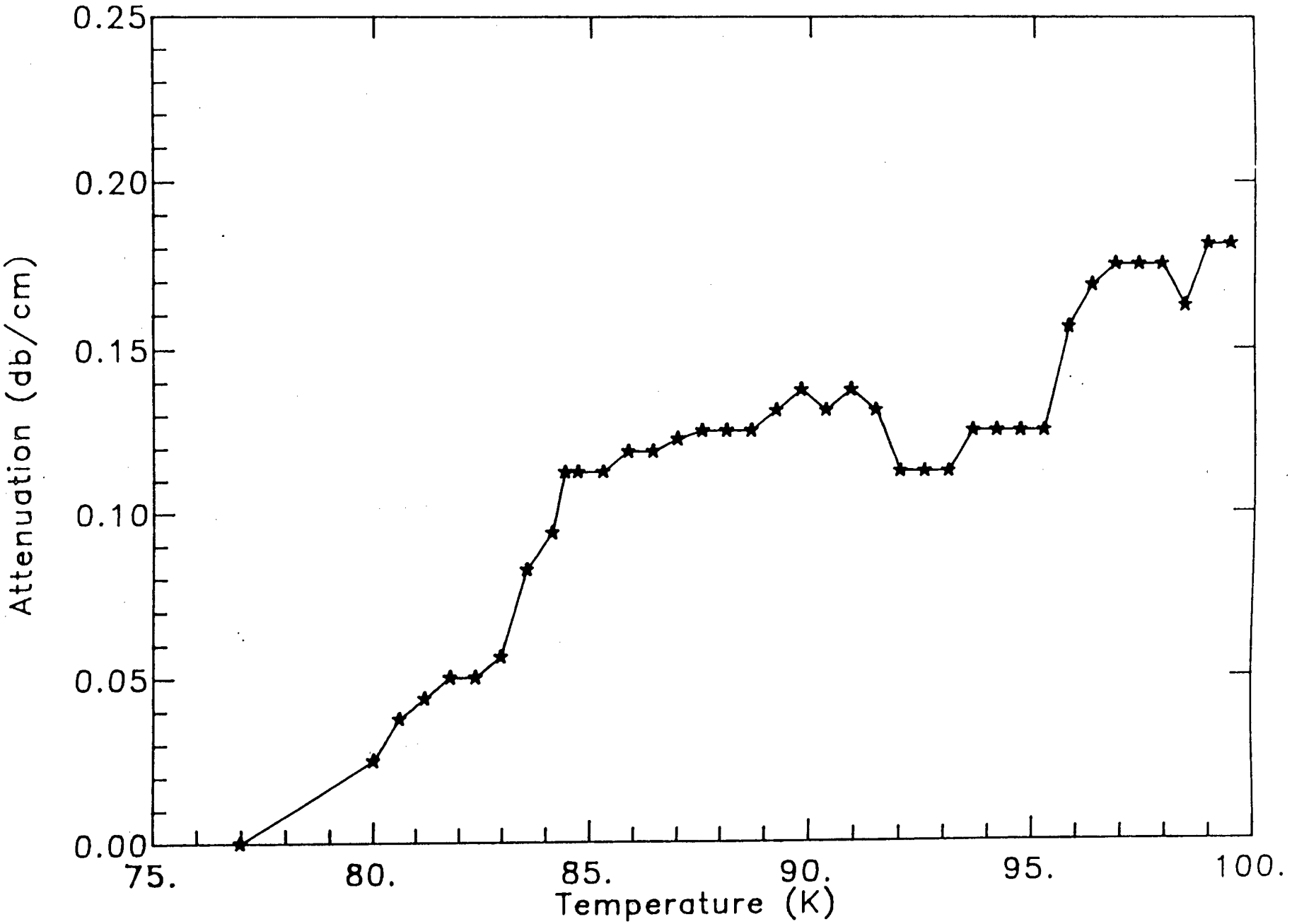
0.25
0.20
0.15
0.10
0.05
0.00
Attenuation (db/cm)
75.
80.
85.
90.
95.
100.
Temperature (K)

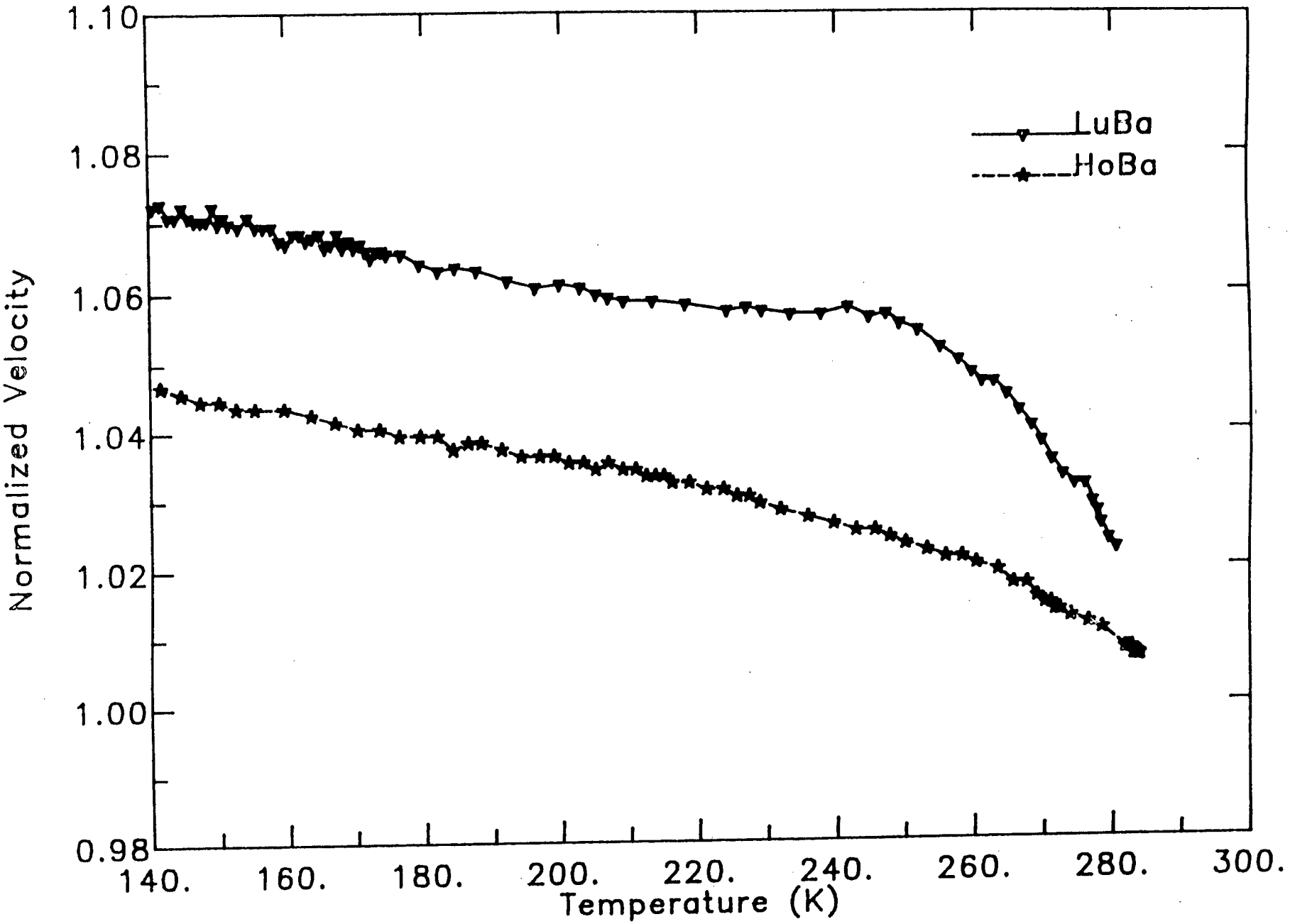
1.10
1.08
1.06
1.04
1.02
1.00
0.98
Normalized Velocity
140.
160.
180.
200.
220.
240.
260.
280.
300.
Temperature (K)
LuBa
HoBa

Ultrasonic-attenuation measurements in single-phased $YBa_2Cu_3O_7$

M-F. Xu, H-P. Baum, A. Schenstrom, Bimal K. Sarma, and Moises Levy
Physics Department, University of Wisconsin–Milwaukee, Milwaukee, Wisconsin 53201

K. J. Sun
NASA-Langley Research Center, Hampton, Virginia 23665

L. E. Toth,* S. A. Wolf, and D. U. Gubser
Naval Research Laboratory, Washington, D.C. 20375-5000
(Received 31 August 1987)

Ultrasonic attenuation at 15 MHz has been measured between 300 K and liquid-helium temperatures on a single-phased $Y_1Ba_2Cu_3O_7$ sample with a 91-K superconducting transition temperature. The attenuation data show similarities to the behavior of heavy-fermion superconductors, with a local maximum just below T_c and a nearly quadratic dependence of the attenuation at lower temperatures. At higher temperatures there is evidence for a relaxation maximum at 252 K, with an effective relaxation time of 1.1×10^{-8} s.

Since the recent discovery of high-temperature superconductors (HTS), many questions have arisen concerning the nature of the interaction leading to superconductivity in these new materials, and many theories have been presented in an effort to answer them.[1-5] We have measured ultrasonic attenuation on a HTS polycrystalline sample, and have observed features reminiscent of the results obtained for heavy-fermion superconductors. These observations may provide a clue for revealing the nature of the interaction which produces superconductivity in the HTS perovskite system.

Our results of ultrasonic attenuation α as a function of temperature T do not exhibit a sharp drop at the transition temperature, as expected in a simple and well-behaved classical Bardeen-Cooper-Schrieffer (BCS) system, with a well-defined isotropic energy gap. However, the curve of $\alpha(T)$ presents a striking resemblance to a heavy-fermion system, having a local maximum slightly below T_c, and following a near-quadratic dependence down to liquid-helium temperatures.

The sample we studied comes from a batch prepared by mixing, grinding, pressing, and sintering powders to obtain 1–2 g pellets of $Y_1Ba_2Cu_3O_7$. The processing procedure and its relationship to crystal structure and transition temperature (T_c) have been reported earlier.[6] The sample used in this study is single phased and has a mass density of approximately 78% of the single-crystal density. These samples have also been investigated by x-ray diffraction and neutron scattering,[7] and by ultraviolet resonant photoelectron emission,[8] to assess their vibrational density of states, their atomic structure, and their valence band and electronic structure.

The sample, 0.295 cm thick, was first polished to a 3 μm finish, to plane two opposite faces parallel. An X-cut, 15-MHz fundamental frequency, quartz piezoelectric transducer was then bonded to one face with Epon Resin 815 epoxy. A MATEC Pulse Modulator and Receiver model 6600 in conjunction with a MATEC rf Plug-in model 760 was used to send longitudinal waves at the transducer's fundamental frequency through the sample and pick up the reflected signal. The temperature of the sample was swept between 300 and 7 K. Either a four-point probe resistance measurement, or a susceptibility assessment, both verified not to perturb the ultrasonic data, was concurrently monitored to position the superconducting transition. Although the sample was a pressed and sintered powder instead of a nonporous material, it was still possible to obtain one echo which could be measured.

The temperature dependence of the attenuation coefficient in the single-phased sample of $YBa_2Cu_3O_7$ is shown in Fig. 1. This sample has a density of 4.97 g/cm^3, which is 0.78 times the single-crystal perovskite structure density. The temperature range covered is from 7 up to 289 K. The resistance of the sample measured in the same temperature range on a different experimental run is also displayed in the figure. There is a smooth maximum

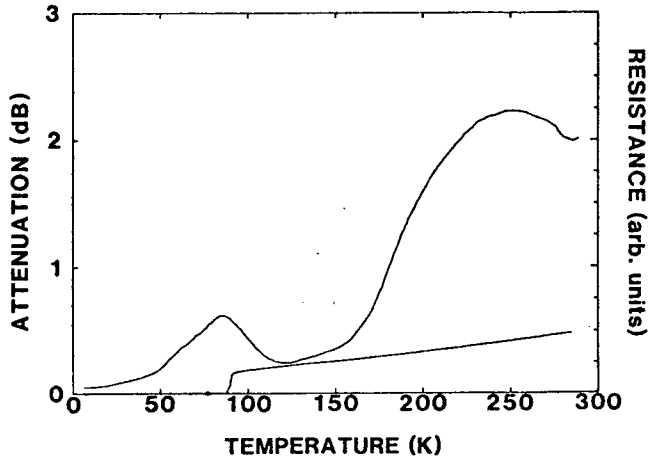

FIG. 1. The attenuation of 15 MHz longitudinal waves in a single-phased sample of $Y_1Ba_2Cu_3O_7$ in the temperature range from 7 to 289 K. The lower curve represents values for resistance measurements.

in the attenuation at around 252 K. There are no shoulders or subsidiary maxima in this temperature range as reported on another sample of $YBa_2Cu_3O_7$.[9] We believe that this is evidence of the fact that the present sample is single phased (SP) and is not plagued by the other phase transitions that multiphased (MP) samples experience. We suggest that these maxima are produced by a relaxation mechanism where the attenuation is given by $\alpha \simeq \omega^2\tau^*/(1+\omega^2\tau^{*2})$ where ω is the angular frequency and τ^* is an effective relaxation time[10] which at the maximum is 1.1×10^{-8} s.

The most surprising data are obtained near the superconducting transition temperature, where the attenuation goes through a maximum and monotonically decreases. Figure 2 shows data obtained during a different experimental run which covered the temperature range between 7 and 120 K. The resistance of the sample was measured simultaneously. It goes to zero at 88 K with the midpoint of the transition located at 91 K. In this figure it is evident that the maximum in attenuation lies about 7 K below the midpoint of the superconducting transition. These data are similar to ultrasonic attenuation measurement obtained in the heavy-fermion superconductors, particularly UPt_3,[11-14] where a maximum in attenuation is observed at $T_m/T_c \simeq 0.96$, which is similar to the value obtained for the present sample, $T_m/T_c \simeq 0.92$. In order to determine the extent of the similarity, the data obtained in Fig. 2 were plotted on a log-log plot in Fig. 3. The slopes of the straight line portions yield T^n temperature dependences, where $n_1 = 2.1$ above 42 K and $n_2 = 1.6$ below 42 K. Again, this power dependence is very similar to that obtained for UPt_3 where values varying from $n=1$ to $n=3$ have been obtained.[11-14] Therefore, heavy-fermion models could be proposed for explaining the properties of the HTS, such as the Anderson-Brinkman-Morel (ABM) excitation spectrum with an anisotropic superconducting energy gap that vanishes at points on the Fermi surface, and which gives a T^2 dependence for the attenuation in the superconducting state.[15]

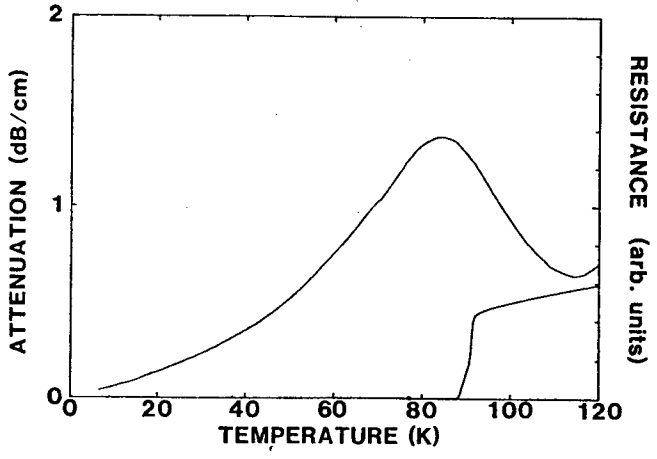

FIG. 2. Attenuation coefficient obtained during a different experimental run from the one displayed in Fig. 1 on the same sample of $Y_1Ba_2Cu_3O_7$. The temperature range covered was 7 to 120 K. The lower curve represents values for simultaneous resistance measurements.

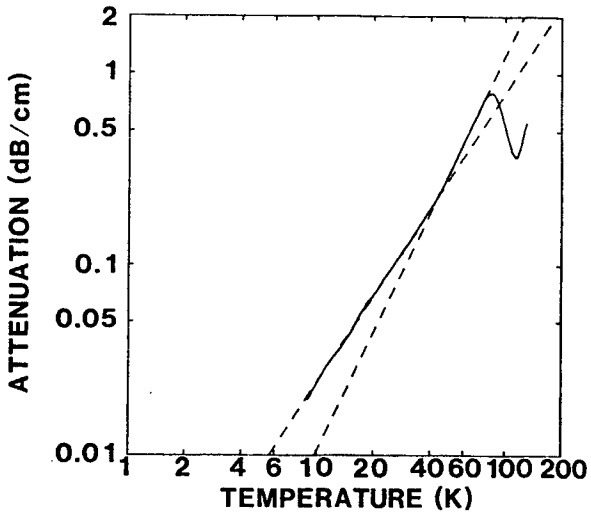

FIG. 3. Log-log plot of data in Fig. 2. The dashed lines yield T^n dependences in the superconducting state, where above 42 K $n_1 = 2.1$ and below 42 K $n_2 = 1.6$.

The sample is a pressed sintered pellet. Consequently there exists the possibility that the observed effects could be due to some sort of interference of echoes which follow different paths in the material. In order to minimize this possibility, the transducer was detached from the sample, the sample ends were repolished, and a new bond was made. Attenuation data could be obtained at the lower temperatures on the first, second, and third echoes. The data on the first echo looked the same as that which are shown in Fig. 2. The data on the second and third echoes also looked qualitatively similar to the data in Fig. 2, and for the second echo, the attenuation was about twice as large as for the first echo. Therefore, we are reasonably certain that the curves we are displaying represent attenuation in the sample and not some sort of interference phenomenon.

The total attenuation change in the superconducting state from the maximum near T_c to the lowest temperature is $\Delta\alpha \simeq 1.5$ dB/cm. This is the amount of attenuation that we could assume is being contributed by the electrons in the normal state. At this frequency this is several orders of magnitude larger than that which would be expected for a conventional superconductor. For instance, for vanadium with a resistivity ratio of 20,[16] one would expect $\Delta\alpha \simeq 1.5\times10^{-3}$ dB/cm. The attenuation is proportional to the electron mean free path and the Fermi velocity, and is inversely proportional to the density and to the cube of the sound velocity. These samples have a resistivity ratio of 3, and if we assume that the electron mean free path of the Y compound is comparable to that of V at room temperature, then the difference of resistivity ratios makes the attenuation 6.7 times smaller. The Fermi velocity of V, 1.8×10^7 cm/s is probably twice as large as that of the Y compounds. However, the sound velocity is 1.7 times larger for V. This contributes an increase of 4.9, and the difference in density contributes another increase of 1.2. Taking these factors into account, one would expect an attenuation coefficient of 6.6×10^{-4} dB/cm. Thus the observed change in attenuation is about three orders of mag-

nitude larger than what would be expected for a normal superconductor.

One of the sources of measurable attenuation in a metal at low temperatures is electron-phonon interaction. When the electron mean free path l is smaller than the sound wavelength, the attenuation is proportional to l, since the energy imparted to the electrons during a collision is returned to the lattice out of phase with the sound wave by an amount that is proportional to l. In the superconducting state, the sound waves only interact with excited quasiparticles whose population in a BCS superconductor decays exponentially with temperature. In the present sample the attenuation does not decay exponentially but almost quadratically. This relationship would still be consistent with a superconductor that has an anisotropic energy gap such as that postulated for the heavy-fermion superconductors. And, in fact, there are estimates for the effective mass of the electrons in $YBa_2Cu_3O_7$ of about $100m_e$.[17] The maximum in attenuation that we observe slightly below the superconducting transition is consistent with observations made on the heavy-fermion superconductors UPt_3 and URu_2Si_2.[18] In these superconductors, the observed contribution of electron-phonon interaction to the attenuation is about what is observed in regular BCS superconductors whose effective electron masses are close to unity. Thus it does not appear that the value of the effective mass contributes a large factor to the attenuation. However, the attenuation change observed in our sample of $YBa_2Cu_3O_7$ is about three orders of magnitude larger than that which would be expected in a BCS superconductor. The possibility exists that the one and two dimensional CuO conducting planes,[19] in conjunction with the large effective electron masses, may account for this anomalous attenuation change. It should be noted though, that a two-dimensional electron gas would only contribute some geometrical factors to the electron-phonon interaction integrals, and could not account for this effect.[20] It may be possible that the one-dimensional nature of the CuO networks may contribute some fluctuations near the phase transition, which could account for this anomalous attenuation. Another model that may account for this large effect could be the mean-field resonating valence bond (RVB) model[5] wherein boson holes Bose condense to make a superconductor. Although at present no predictions have been formulated for the interaction of such a system with sound waves, it seems reasonable to presume that such an interaction would involve all the bosons present as opposed to just the fermions at the Fermi surface. The ratio of these two quantities may yield the factor of 1000 which appears to be missing in the interaction.

It is obvious that attempts should be made to measure the attenuation in single crystals of $YBa_2Cu_3O_7$, and at higher frequencies. These measurements might yield information which will be necessary for interpreting the present measurement and understanding the mechanisms which produce superconductivity in these systems. After submitting this paper we received a copy of the unpublished work of Bhattacharya *et al.*[21] Their attenuation measurements are qualitatively similar to those reported in this paper.

The authors would like to acknowledge stimulating and enlightening discussions with Professor Richard Sorbello. The Naval Research Lab wishes to acknowledge the following offices for their support: Office of Naval Research, U.S. Defense Advanced Research Projects Agency, Strategic Defense Initiative Organization/Innovative Sciences and Technology and Defense Nuclear Agency. Research at the University of Wisconsin–Milwaukee was supported by Air Force Office of Scientific Research under Grant No. AFOSR 84-0350.

*On leave from the National Science Foundation, Washington D.C.

[1]V. Kresin, Phys. Rev. B **35**, 8716 (1987).

[2]J. Ashkenazi, C. G. Kuper, and R. Tyk, Solid State Commun. **63**, 1145 (1987).

[3]P. W. Anderson and E. Abrahams, Nature **327**, 363 (1987).

[4]J. Yu, S. Massida, A. J. Freeman, and D. D. Koeling, Phys. Lett. A **122**, 203 (1987).

[5]P. W. Anderson, G. Baskaran, Z. Zou, and T. Hsu, Phys. Rev. Lett. **58**, 2790 (1987).

[6]L. E. Toth, E. F. Skelton, S. A. Wolf, S. B. Qadri, M. S. Osofsky, B. A. Bender, S. H. Lawrence, and D. U. Gubser (unpublished).

[7]J. J. Rhyne, D. A. Neumann, J. A. Gotaas, F. Beech, L. Toth, S. Lawrence, S. A. Wolf, M. Osofsky, and D. U. Gubser (unpublished).

[8]R. L. Kurtz, R. L. Stockbauer, D. Mueller, A. Shih, L. E. Toth, M. Osofsky, and S. A. Wolf, Phys. Rev. B **35**, 8818 (1987).

[9]K. J. Sun, M. Levy, B. K. Sarma, P. H. Hor, R. L. Meng, Y. Q. Wang, and C. W. Chu (unpublished).

[10]K. J. Sun, R. S. Sorbello, M. Levy, M. B. Maple, and M. S. Torikachvili, in *Proceedings of the IEEE 1986 Ultrasonics Symposium* edited by B. R. McAvoy (IEEE, New York, 1986), p. 1123.

[11]D. J. Bishop, C. M. Varma, B. Batlogg, E. Bucher, Z. Fisk, and J. L. Smith, Phys. Rev. Lett. **53**, 1009 (1984).

[12]V. Muller, D. Maurer, E. W. Scheidt, Ch. Roth, K. Luders, E. Bucher, and H. E. Bommel, Solid State Commun. **57**, 319 (1986).

[13]B. S. Shivaram, Y. H. Jeong, T. F. Rosenbaum, and D. G. Hinks, Phys. Rev. Lett. **56**, 1078 (1986).

[14]Y. J. Qian, M-F. Xu, A. Schenstrom, H-P. Baum, J. B. Ketterson, D. Hinks, M. Levy, and B. K. Sarma, Solid State Commun **63**, 599 (1987).

[15]J. P. Rodriguez, Phys. Rev. Lett. **55**, 250 (1985).

[16]J. A. Waynert, H. Salvo, Jr., and M Levy, Phys. Rev. B **10**, 1859 (1974).

[17]V. Z. Kresin and S. A. Wolf, in *Novel Mechanisms,* edited by S. A. Wolf and V. Z. Kresin (Plenum, New York, 1987), p. 287.

[18]M. Levy, A. Schenstrom, K. J. Sun, and B. K. Sarma, in *Novel Mechanisms,* edited by S. A. Wolf and V. Z. Kresin (Plenum, New York, 1987), p. 243.

[19]F. Herman, R. V. Kasowski, and W. Y. Hsu, Phys. Rev. B **37**, 2309 (1988).

[20]R. Sorbello (private communication).

[21]S. Bhattacharya, M. J. Higgins, D. C. Johnston, A. J. Jacobson, J. P. Stokes, J. T. Lewandowski, and D. P. Goshorn (unpublished); and S. Bhattacharya (private communication).

RELAXATION BEHAVIOR OF ULTRASONIC ATTENUATION IN $YBa_2Cu_3O_7$

K. J. Sun*
Physics Department
College of William and Mary
Williamsburg, VA 23185

W. P. Winfree
NASA-Langley Research Center
Hampton, Virginia 23665

M. F. Xu+, Bimal. K. Sarma+ and M. Levy+
Physics Department
University of Wisconsin-Milwaukee
Milwaukee, Wisconsin 53201

R. Caton# and R. Selim#
Christopher Newport College
Newport News, Virginia 23665

Abstract

At temperatures near T_c, experimental results of temperature dependent ultrasonic attenuation measurements on $YBa_2Cu_3O_7$ exhibit anomalies at three frequencies. These attenuation maxima may result from a relaxation process associated with the superconducting transition.

Introduction

Since the high temperature superconductors were discovered, ultrasonic velocity measurements[1] on $YBa_2Cu_3O_7$ have been reported at frequencies in the mega hertz range. It was observed that there occurred a slope change on the velocity vs. temperature curve at a temperature near T_c. In addition, temperature dependent ultrasonic attenuation[2] of single phase $YBa_2Cu_3O_7$ at 15 MHz has also been measured and shows an anomalous maximum located at a temperature close to T_c (90K). Several explanations were proposed for the source of this anomaly[2]: the maximum can be the result of a Debye relaxation process, where the temperature dependent relaxation time may be associated with a two-energy level system, which may be due to defect tunneling, or plasmons, or excitons, or may be caused by the structural phase transitions; It may also be associated with the superconducting transition in a way similar to what happens for the ultrasonic attenuation behavior of some of the heavy fermion superconductors, such as URu_2Si_2 and UPt_3[3]. In order to discriminate between different theoretical models, more experiments are demanded for providing additional information.

Frequency dependent attenuation measurement is an useful probe to identify whether an anomalous sound energy loss is caused by an absorption of phonons associated with a phase transition or results from a relaxation process, which in turn could identify the possible mechanisms that produce the dissipation. It is believed that frequency, at which the sound waves can be employed to obtain the mechanical and superconducting properties of the high T_c superconductors prepared by the current metallurgical methods for powder samples, would be approximately below 30 MHz.

Manuscript received August 22, 1988.

For our sample, pulsed 10 MHz signals which are good for attenuation as well as velocity measurements can be obtained in the temperature range from room temperature to liquid helium temperatures. However, at higher frequencies which are obtained from overtones of the same transducer with a 10 MHz fundamental frequency, clean and measurable signals are only obtainable at temperatures below 150K.

Experiment and Results

A 10 MHz $LiNbO_3$ longitudinal wave transducer was epoxy bonded on the surface of a pellet powder $YBa_2Cu_3O_7$ sample with a 1.23 cm. diameter and 4.35 cm. in thickness. By using the pulse echo technique, a clean three-echo pattern was obtained at 10 MHz over the whole temperature range. Both the temperature dependence of attenuation and propagation time of the sound wave in the sample (using the echo overlapping method) could be measured. For the 27 MHz and 32 MHz signals, because their attenuation was much larger (approximately proportional to the square of frequency), a single echo would be tuned for each frequency;

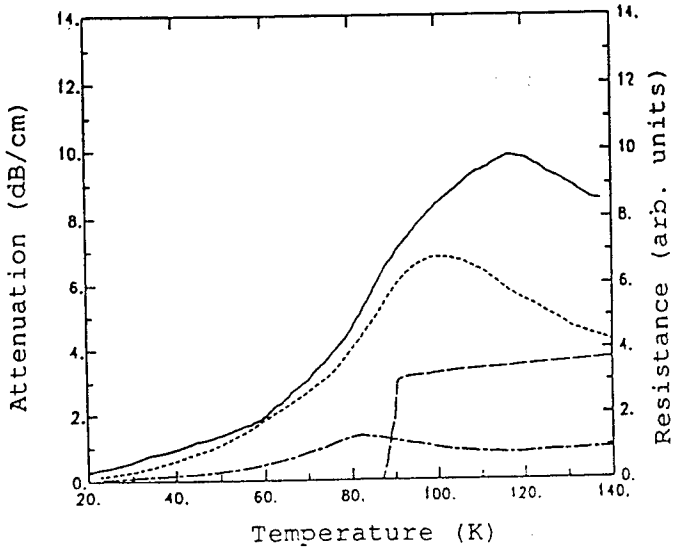

Figure 1. Temperature dependent ultrasonic attenuation and resistance curves of $YBa_2Cu_3O_7$ (Curves from top to bottom belong to 32 MHz, 27 MHz, resistance, and 10 MHz respectively).

In order to monitor the occurrence of the superconducting transition, electrical resistance as a function of temperature of the sample was also measured simultaneously.

Figure 1 displays the temperature dependence of the ultrasonic attenuation coefficient at three frequencies 10, 27, and 32 MHz, and of the electrical resistance, of the $YBa_2Cu_3O_7$ sample. Several features can be observed: (1) An attenuation anomaly at a temperature near T_c for each frequency. This same behavior has been reported when ultrasonic attenuation was measured at 15 MHz by using a quartz transducer on a different sample[2]. (2) The attenuation maximum has approximately a quadratic frequency dependence (as shown in figure 2). (3) The temperature at which the maximum occurs increases as the frequency of the sound wave increases.

The shift of temperature with frequency of the attenuation anomaly illustrates the possible occurrence of a relaxation process, for which the attenuation can be qualitatively described by $\omega^2\tau/(1+\omega^2\tau^2)$, where ω is the angular frequency of the sound waves and τ is the temperature dependent relaxation time. By examining the variation of relaxation time with temperature, a possible mechanism which induces the relaxation process can then be figured out.

To find the relaxation time τ, experimental data of the attenuation at any temperature were normalized to the maximum attenuation of the respective frequency, and then the following equation was used.

$$\alpha(T)/\alpha_{max} = 2\,\omega\tau(T)/(1+\omega^2\tau^2(T)) \quad (1)$$

where α is the attenuation and α_{max} is the maximum of attenuation.

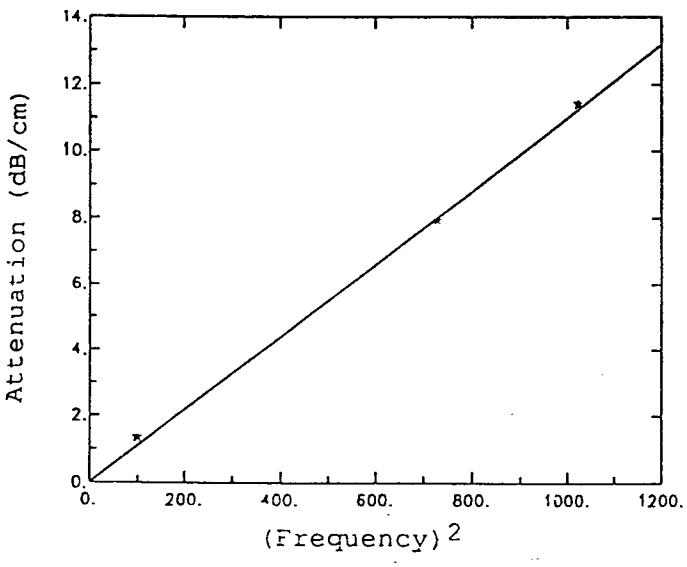

Figure 2. The maximum of ultrasonic attenuation at temperature close to T_c as a function of square of sound frequency.

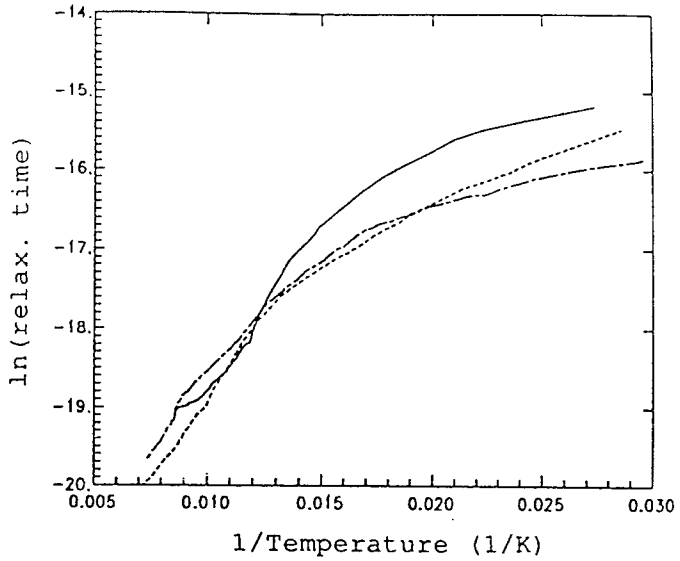

Figure 3. Natural logarithm of relaxation time as a function of inverse of temperature of $YBa_2Cu_3O_7$.

By doing so, the natural logarithm of the obtained $\tau(T)$ is plotted with respect to the inverse of temperature in Figure 3. Although these three curves do not fall on top of each other, especially at low temperatures (below 70K), we believe that an appropriate background attenuation subtraction would improve the agreement among the three curves.

To extract information from these relaxation time curves, proper curve fitting technique was conducted. It was found that the data of relaxation time at high temperatures are proportional to exp(450/T) while that at low temperatures yields $\tau \sim \exp(50/T)$. The expression

$$1/\tau(T) = 1.3\times10^7/(\exp(50/T)-1)+9.95\times10^9/(\exp(450/T)-1) \quad (2)$$

gives a reasonable fit to the data in Figure 3. A relaxation time expressed by the above forms can mean that there exist relaxation processes with activation energies of 38mev (450K) and 4.3mev (50K). The former value is roughly equal to the value of the Debye temperature obtained by specific heat measurements on $YBa_2Cu_3O_7$. This amount of energy is certainly much less than the electron pair coupling energy needed for high superconducting transition temperatures.

The sound velocity in this $YBa_2Cu_3O_7$ sample has also measured as a function of temperature at 10 MHz. In general, the sound velocity increases with temperature decreasing from 270K to 77K. However, in the neighborhood of the superconducting transition, the velocity decreases from its increasing trend and exhibits a small dip on the velocity vs. temperature curve. In addition, a faster increase in velocity below T_c was also observed.

Discussion

A recent report by P. M. Horn et al.[4] about the temperature variations of the lattice constants of $YBa_2Cu_3O_7$ indicated that an orthorhombic distortion occurs at temperatures between 60K and 140K and showed that a maximum difference between lattice constants b and a appeared around the superconducting transition. This distortion does not result in changes of the volume of the unit cell and the area of an unit basal plane. It may be possible that the softening of the sound velocity which occurs around T_c reflects this structural instability. It has been found[5] that softening due to the change of shear modulus at T_c is predominant over that of the bulk modulus. This further illustrates that the distortion is shear in nature. In fact, the results of temperature dependent velocity measurements of $YBa_2Cu_3O_7$ in constant external magnetic fields up to 8 tesla[7] showed that this softening shifted to lower temperatures with increasing field, which may evidence that this softening around T_c is an intrinsic property of $YBa_2Cu_3O_7$ and is closely related to the superconducting transition.

It is possible that this distortion also enhances the energy loss of sound at temperatures around T_c. The difference between the temperature variation rates of the lattice constants a and b, may produce anisotropic grain boundary expansion or constriction with respect to the propagation direction of sound wave. These grain boundary motions (dc motions) together with their vibrations (ac motion) induced by the travelling sound waves result in a relaxation attenuation.

However, a relaxation process can also be attributed to a perturbed tunneling effect when the sound wave deforms the lattice potential. It was reported[7] that the activation energy for the migration of oxygen is inferred to have a mean value close to 1.3ev. Therefore, if the activation is associated with a tunneling mechanism, it may be related to the motion of the copper electrons in a multi-well potential set by the surrounding oxygens in the Cu-O plane.

A similar effect is the acoustoelectric effect[8], which arises from the simultaneous bunching of electrons and holes found in semiconductors caused by the passing of sound waves. The return of these carriers to their instantaneous equilibrium state in a multi-well potential shows a relaxation time, which exponentially depends on the inverse of temperature and has a similar mathematical expression to that of the equation (2) The attenuation coefficient of this effect is also proportional to the square of frequency of the sound wave. The fact that the electric current carriers of $YBa_2Cu_3O_7$ are hole-like in the ab plane and electron-like along the c axis (or ac plane) could provide an environment for this type of relaxation process to happen. Although the above effects could account for the magnitude of activation energy that we obtained, measurements on the metal doped $YBa_2Cu_3O_7$ samples are necessary to select between these different mechanisms.

In order to examine how the attenuation background changes with temperature, the relaxation attenuation at the three frequencies can be calculated by using the right hand side of equation (1) times ω^2, with τ as expressed in terms of 1/T in equation (2), and using the slope of the straight line (1.11×10^{-2} dB-μsec^2/cm) shown in the figure 2. If these calculated curves are subtracted from the experimental attenuation data with appropriate adjustment of the zero in attenuation, it is found that an attenuation peak survives in the vicinity of T_c for all the three frequencies. The magnitudes of these remaining peaks are between 10 and 15 percent of the heights of the original peaks, and their temperature positions are much closer to T_c and not frequency dependent. Determining whether the remaining peak is associated with the superconducting transition or is just due to experimental uncertainties will require attenuation measurements of longitudinal and shear waves with magnetic fields applied on the sample.

In summary, temperature dependent ultrasonic attenuation data of $YBa_2Cu_3O_7$ at various frequencies exhibit anomalies at temperatures close to T_c. These attenuation maxima are found to be the result of a relaxation mechanism added on top of an unusual attenuation background. It is proposed that the grain boundary motions induced by the structural distortion and the propagation of sound wave enhances the energy dissipation around T_c. Whether this structural distortion is the consequence of the onset of a superconducting state remains undetermined. It is also possible that either a tunneling effect or the acoustoelectric effect will contribute to sound energy dissipation. Furthermore, the temperature dependence of ultrasonic velocity shows a softening around T_c which may be an intrinsic property of high temperature superconductors.

---

*Present address: NASA-Langley Research Center, MS 231, Hampton, VA 23665. This work was done while the author held a National Research Council-(NASA-Langley) Research Associateship.

+Research was supported by the Office of Naval Research under grant No. ONR N00014-88-K-0046.

#This work was supported by NASA Grant No. NAG-1-796.

References

[1] D. J. Bishop, A. P. Ramirez, P. L. Gammel, B. Batlogg, E. A. Rietman, R. J. Cava, and A. J. Millis, "Bulk-modulus Anomalies at the Superconducting Transition of Single-phase $YBa_2Cu_3O_7$", Phys. Rev. B36 pp. 2408-2410, August 1987.

[2] M-F. Xu, H-P Baum, A. Schenstrom, B. K. Sarma, M. Levy, K. J. Sun, L. E Loth, S. A. Wolf and D. U. Gubser, "Ultrasonic-attenuation Measurements in Single-phased $YBa_2Cu_3O_7$", Phys. Rev. B37 pp. 3675-3677, March 1988.

[3] M. Levy, A. Schenstrom, K. J. Sun, and B. K. Sarma, Novel Superconductivity, ed. by S. A. Wolf and V. Z. Kresin, Plenum Press New York, 1987, pp. 243-251.

[4] P. M. Horn, D. T. Keane, G. A. Held, J. L. Jordan-Sweet, D. L. Kaiser, and F. Holtzberg, "Orthorhombic Distortion at the Superconducting Transition in $YBa_2Cu_3O_7$: Evidence for Anisotropic Pairing", Phys. Rev. Lett. Vol. 59, pp. 2772-2275, December 1987.

[5] S. Bhattacharya, M. J. Higgins, D. C. Johnston, A. J. Jacobson, J. P. Stokes, D. P. Goshorn, and J. T. Lewandowski, "Elastic Anomalies and Phase Transition in High-T_c Superconductors", Phys. Rev. Lett., vol. 60, pp. 1181-1184, March 1988.

[6] D. J. Bishop et al. presented in the 1988 APS march meeting (New Orleans, LA.) the experimental results of the ultrasonic velocity as a function of temperature at constant external magnetic fields, which showed that the softening at T_c became broader in temperature, more pronounced in magnitude and shifted to lower temperature at 8 tesla.

[7] B. S. Berry, "Defect-Related Anelastic Behavior of Superconducting Oxides", Bulletin of Ame. Phys. Soc., vol. 33 pp. 512 March 1988.

[8] W. P. Mason, Physical Acoustics and The Properties of Solids, D. Van Nostrand Company, Inc. 1958

Frequency-dependent ultrasonic attenuation of $YBa_2Cu_3O_7$

K. J. Sun and W. P. Winfree
NASA Langley Research Center, Hampton, Virginia 23665

M. F. Xu, Bimal K. Sarma, and M. Levy
Physics Department, University of Wisconsin-Milwaukee, Milwaukee, Wisconsin 53201

R. Caton and R. Selim
Christopher Newport College, Newport News, Virginia 23665
(Received 9 June 1988; revised manuscript received 15 September 1988)

At temperatures near T_c, experimental measurements of temperature-dependent ultrasonic attenuation at three frequencies exhibit maxima, and velocity measurements display softening of the lattice. These attenuation maxima result from a relaxation process which occurs around the superconducting transition, and the softening of velocity around T_c may evidence a structural instability of $YBa_2Cu_3O_7$ at these temperatures.

Recently, ultrasonic velocity measurements[1] on high-temperature superconductors of $YBa_2Cu_3O_7$ have been reported at frequencies in the megahertz range (≤ 10 MHz). It was observed that there occurred a slope change on the velocity versus temperature curve at a temperature near T_c. In addition, temperature-dependent ultrasonic attenuation[2] of single-phase $YBa_2Cu_3O_7$ at 15 MHz has also been measured and shows an anomalous maximum located at a temperature close to T_c (90 K). Several explanations were proposed for the source of this anomaly.[2] The maximum can be the result of a Debye-relaxation process, where the temperature-dependent relaxation time may be associated with a two-energy-level system, which may be due to defect tunneling, plasmons, or excitons, or may be caused by structural phase transitions. It may also be associated with the superconducting transition in a way similar to what happens for the ultrasonic attenuation behavior of some of the heavy fermion superconductors, such as URu_2Si_2 and UPt_3.[3] While the mechanism of superconductivity for producing the high-temperature superconductors is not quite understood, it is important to determine if these variations of the acoustic properties that occur around T_c are a direct consequence of the onset of superconductivity, because they may provide useful information for discriminating between different theoretical models. Frequency-dependent attenuation measurements are a useful probe to identify whether an anomalous sound energy loss is caused by an absorption of photons associated with a phase transition or results from a relaxation process, which in turn could identify the possible mechanisms that produce the dissipation.

Based on current preparation methods for powder samples, it is believed that ultrasonic measurements, which can be employed to obtain the mechanical and superconducting properties of the high-T_c samples without involving Rayleigh scattering, would be at sound frequencies below 30 MHz. For our sample, pulsed 10-MHz signals which are good for attenuation as well as velocity measurements can be obtained in the temperature range from room temperature to liquid-helium temperatures. However, at higher frequencies which are obtained from overtones of the same transducer with a 10-MHz fundamental frequency, clean and measurable signals are only obtainable at temperatures below 150 K.

The samples were prepared from carbonate and oxide powders by calcining and sintering at high temperatures. The starting purities were as follows: $BaCO_3$, 99.999%; Y_2O_3, 99.999%; and CuO, 99.999%. The proper ratios of starting powders were mixed thoroughly in a mechanical mixer-grinder and pressed into 0.5-in.-diam pellet with a force of ~ 5 tons. The samples were then heated in air to $\sim 950\,^{\circ}C$ over a period of several hours and left at that temperature for ~ 24 h. The resulting pellet was crushed and ground in alcohol in the grinder-mixer to reduce the particle size and produce a more homogeneous sample. The powder was repelletized and given a second air treatment identical to the first. After further grinding and pelletizing, the samples were given a final treatment in flowing oxygen (~ 0.2 ℓ/min through a 1-in.-diam quartz tube) with a dessicant in line to trap out water vapor. The heating schedule was as follows: Heat to $950\,^{\circ}C$ in a few hours; stay at $950\,^{\circ}C$ for 24 h, cool to $650\,^{\circ}C$ in a few hours, remain at $650\,^{\circ}C$ for 16 h to allow the completion of the tetragonal-to-orthorhombic transition; cool to $400\,^{\circ}C$ in a few hours; remain at $400\,^{\circ}C$ for 8 h to allow maximal oxygen take-up; and finally cool to room temperature in a few hours. The resulting samples were black, tough, with a mass density about 75% of that of a single crystal, and produced strong levitation of a magnet at 77 K.

A 10-MHz $LiNbO_3$ longitudinal wave transducer was epoxy bonded on the surface of a pellet of a $YBa_2Cu_3O_7$ sample with a 1.23-cm diameter and 4.35 mm in thickness. By using the pulse-echo technique, a clean three-echo pattern was obtained at 10 MHz over the whole temperature range. Therefore, both the temperature dependence of attenuation and propagation time of the sound wave in the sample (using the echo overlapping method) could be measured. For the 27-MHz and 32-MHz sig-

nals, because their attenuation was much larger (approximately proportional to the square of frequency), only a single echo would be tuned for each frequency. In order to monitor occurrence of the superconducting transition, electrical resistance as a function of temperature of the sample was also measured simultaneously.

Figure 1 displays the temperature dependence of the ultrasonic attenuation coefficient at three frequencies, 10, 27, and 32 MHz, and of the electrical resistance, of the $YBa_2Cu_3O_7$ sample. Several features can be observed.

(1) There is an attenuation anomaly at a temperature near T_c for each frequency. This same behavior has been reported when ultrasonic attenuation was measured at 15 MHz by using a quartz transducer on a different sample.[2]

(2) The attenuation maximum has approximately a quadratic frequency dependence (see the inset in Fig. 1).

(3) The temperature at which the maximum occurs increases as the frequency of the sound wave increases.

Among these features, the temperature shift of the attenuation anomaly with frequency may be the most significant one. It illustrates the occurrence of a relaxation process, for which the attenuation can be qualitatively described by $\omega^2\tau/(1+\omega^2\tau^2)$, where ω is the angular frequency of the sound wave and τ is the temperature-dependent relaxation time. A possible source which induces the relaxation process can then be figured out by examining how the relaxation time varies with temperature.

To find the relaxation time τ, experimental data of the attenuation at any temperature were normalized to the maximum attenuation at the respective frequency, and then the following equation was used:

$$\alpha(T)\alpha_{\max}=2\omega\tau(T)/[1+\omega^2\tau^2(T)]\,, \qquad (1)$$

where α is the attenuation and $\alpha_{\max}$ is the maximum of attenuation. In Fig. 2, the natural logarithm of $\tau(T)$ is plotted with respect to temperature. A straight-line fit of the high-temperature data yields $\tau\sim\exp(450/T)$ while the low-temperature data yields $\tau\sim\exp(50/T)$. Although these three curves do not fall on top of each other, especially at low temperatures (below 70 K), we believe that an appropriate background attenuation subtraction would improve the agreement among the three curves. However, a relaxation time expressed by the above forms can mean that there exist relaxation processes with activation energies of 38 meV (450 K) and 4.3 meV (50 K). The former value is roughly equal to the value of the Debye temperature obtained by specific-heat measurements on $YBa_2Cu_3O_7$. This amount of energy appears to be less than the electron pairing energy needed for producing a high superconducting transition temperature; however it may be sufficient when both phonon and nonphonon mechanisms are produced,[2,4] especially when the multigap or anisotropic energy-gap models are considered.[5]

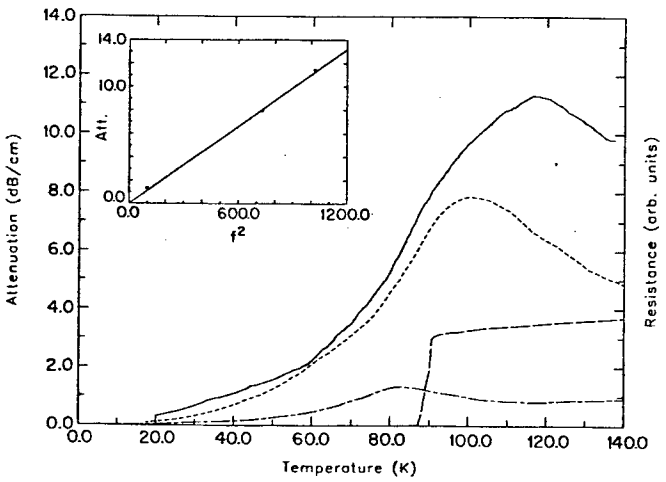

FIG. 1. Temperature-dependent ultrasonic attenuation and resistance curves of $YBa_2Cu_3O_7$ (curves from top to bottom belong to 32 MHz, 27 MHz, resistance, and 10 MHz, respectively). The inset shows the quadratic dependence of attenuation maximum on frequency.

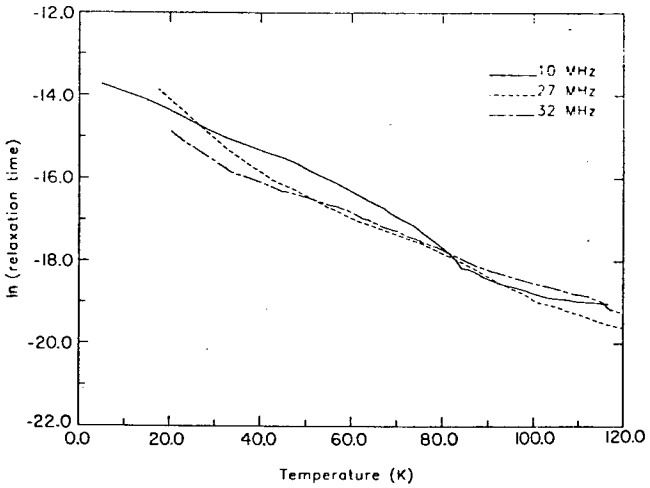

FIG. 2. Temperature-dependent relaxation time of $YBa_2Cu_3O_7$.

Temperature dependence of sound velocity in this $YBa_2Cu_3O_7$ sample at 10 MHz was calculated by using the room-temperature thickness of the sample divided by the propagation time measured with echo-overlapping method. Since the thermal expansion coefficient of $YBa_2Cu_3O_7$ is relatively small [the total change is within 20 ppm (Ref. 6) from room temperature to below 10 K] as compared with the measured variation of velocity, the thickness corrections were not taken into account in this treatment. In general, the sound velocity increases with decreasing temperature from 270 to 77 K. However, at temperatures close to T_c, the velocity decreases, deviating from its increasing trend, and exhibits a small dip on the velocity-versus-temperature curve. Also, the velocity increases faster in the superconducting state than it does in the normal state.

A recent report by Horn *et al.*[7] about the temperature variations of the lattice constants of $YBa_2Cu_3O_7$ indicated that an orthorhombic distortion occurs at temperatures between 60 and 140 K and showed that a maximum difference between b and a appeared around the superconducting transition. This distortion does not result in changes of the volume of the unit cell and the area of a unit basal plane. It may be possible that the softening of the sound velocity which occurs at T_c reflects this structural instability. It has been found[8] that softening due to the change of shear modulus at T_c is predominant

over that of the bulk modulus. This further illustrates that the distortion is shear in nature. In fact, the results of temperature-dependent velocity measurements of $YBa_2Cu_3O_7$ in constant external magnetic fields up to 8 T (Ref. 9) showed that this softening shifted to lower temperatures with increasing field, which may be evidence that this softening around T_c is an intrinsic property of $YBa_2Cu_3O_7$ and is closely related to the superconducting transition.

It is possible that this distortion also enhances the energy loss of sound at temperatures around T_c. The difference between the temperature variation rates of the lattice constants a and b may produce anisotropic grain-boundary expansion or constriction with respect to the propagation direction of the sound wave. These grain-boundary motions together with their vibrations induced by the traveling sound waves result in a relaxation attenuation. Usually, for a relaxation process, the α_{max} varies with ω. The quadratic dependence of α_{max} on ω in our data may also be interpreted to be caused by this broad-temperature-range structural distortion. Some of the $A15$ structure superconductors have the similar frequency-dependent attenuation behavior resulting from their structural transformations at low temperatures.[10]

However, the possibility that an attenuation anomaly results directly from the intrinsic properties of $YBa_2Cu_3O_7$ cannot be totally excluded. As has been mentioned, a relaxation process can also be attributed to a perturbed tunneling effect when the sound wave deforms the lattice potential. It was reported[11] that the activation energy for the migration of oxygen is inferred to have a mean value close to 1.3 eV. Therefore, if the activation energy of 38 meV which we obtained is associated with a tunneling mechanism, it may be related to the motion of the copper electrons in a multiwell potential set by the surrounding oxygens in the Cu-O plane. A similar effect is the acoustoelectric effect,[12] which arises from the simultaneous bunching of electrons and holes in semiconductors caused by the passing of sound waves. The return of these carriers to their instantaneous equilibrium state in a multiwell potential shows a relaxation time, which exponentially depends on the inverse of temperature and has a similar mathematical expression to

$$1/\tau(T) = 1.3\times10^7/[\exp(50/T)-1] + 9.95\times10^9/[\exp(450/T)-1], \quad (2)$$

which gives a reasonable fit to the data in Fig. 2. The attenuation coefficient of this effect is proportional to the square of the frequency of the sound wave. The fact that the electric current carriers of $YBa_2Cu_3O_7$ are holelike in the ab plane and electronlike along the c axis (or ac plane) could provide an environment for this type of relaxation process to happen. Although the above effects could account for the magnitude of activation energy that we obtained, measurements on the metal-doped $YBa_2Cu_3O_7$ samples are necessary to select between these different mechanisms.

In order to examine how the attenuation background changes with temperature, the relaxation attenuation at the three frequencies can be calculated by using the right-hand side of Eq. (1) times ω^2, with τ as expressed in terms of $1/T$ in Eq. (2), and using the slope of the straight line (1.11×10^{-2} dBμsec^2/cm) shown in the inset of Fig. 1. If these resulting curves are subtracted from the experimental attenuation data with appropriate adjustment of the zero in attenuation, it is found that an attenuation peak survives in the vicinity of T_c for all three frequencies. Figure 3 shows the result of this subtraction for the data of 15 MHz. The magnitudes of these remaining peaks are between 10% and 20% of the heights of the original peaks, and their temperature positions are much closer to T_c and not frequency dependent. Determining whether the remaining peak is associated with the superconducting transition or is just due to experimental uncertainties (which is about 5% in our measurements) will require attenuation measurements of longitudinal and shear waves with magnetic fields applied on the sample.

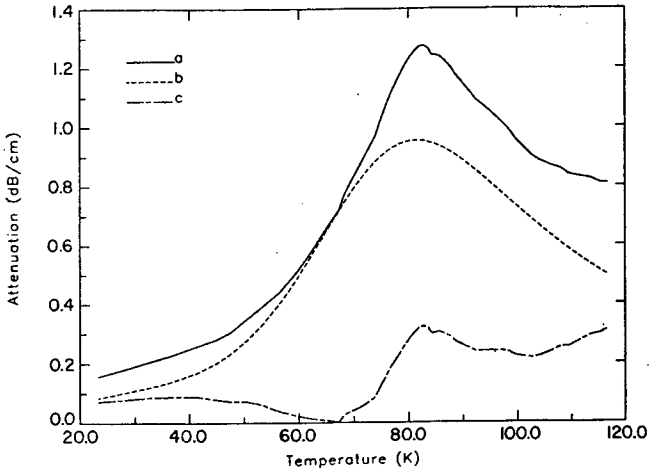

FIG. 3. An attenuation peak remains at temperature close to T_c (curve c) when the calculated relaxation attenuation (curve b) is subtracted from the experimental results (curve a). Experimental error is within 5% in our measurements.

In summary, temperature-dependent ultrasonic attenuation data of $YBa_2Cu_3O_7$ at various frequencies exhibits anomalies at temperatures close to T_c. These attenuation maxima are found to be the result of a relaxation mechanism added on top of an unusual attenuation background. It is proposed that the grain-boundary motions induced by the structural distortion and the propagation of the sound wave enhances the energy dissipation around T_c. Whether this structural distortion is the consequence of the onset of a superconducting state remains undetermined. It is also possible that either a tunneling effect or the acoustoelectric effect will contribute to sound energy dissipation. Furthermore, the temperature dependence of ultrasonic velocity shows a softening at T_c which may be an intrinsic property of high-temperature superconductors.

The work at University of Wisconsin–Milwaukee was supported by the Office of Naval Research under Grant No. ONR N00014-88-K-0046, and the work at Christopher Newport College was supported by NASA Grant No. NAG-1-796. One of us (K.J.S.) acknowledges support from the National Research Council (NASA Langley Research Center).

[1]D. J. Bishop, A. P. Ramirez, P. L. Gammel, B. Batlogg, E. A. Rietman, R. J. Cava, and A. J. Millis, Phys. Rev. B 36, 2408 (1987).

[2]M.-F. Xu, H-P Baum, A. Schenstrom, B. K. Sarma, M. Levy, K. J. Sun, L. E. Toth, S. A. Wolf, and D. U. Gubser, Phys. Rev. B 37, 3675 (1988).

[3]M. Levy, A. Schenstrom, K. J. Sun, and B. K. Sarma, in *Novel Superconductivity,* edited by S. A. Wolf and V. Z. Kresin (Plenum, New York, 1987), p. 243.

[4]V. Z. Kresin, in Ref. 3, p. 309.

[5]V. Z. Kresin, Solid State Commun. 63, 725 (1987).

[6]E. Salomons, H. Hemmes, J. J. Scholtz, N. Koeman, R. Brounwer, A. Driessen, D. G. De Groot, and R. Griessen, Physica B **145**, 253 (1987); V. Bayot, C. Dewitte, J.-P. Erauw, X. Gonze, M. Lambricht, and J.-P. Mhichenaud, Solid State Commun. **64**, 327 (1987).

[7]P. M. Horn, D. T. Keane, G. A. Held, J. L. Jordan-Sweet, D. L. Kaiser, and F. Holtzberg, Phys. Rev. Lett. 59, 2772 (1987).

[8]S. Bhattacharya, M. J. Higgins, D. C. Johnston, A. J. Jacobson, J. P. Stokes, D. P. Goshorn, and J. T. Lewandowski, Phys. Rev. Lett. 60, 1181 (1988).

[9]D. J. Bishop *et al.* [Bull. Am. Phys. 33, 606 (1988)] performed an experiment on the ultrasonic velocity as a function of temperature at constant external magnetic fields, which showed that the softening at T_c became broader in temperature, more pronounced in magnitude, and shifted to lower temperatures at 8 T.

[10]L. R. Testardi, in *Physical Acoustics, Vol. 10,* edited by W. P. Mason and R. N. Thurston (Academic, New York, 1973), p. 193.

[11]B. S. Berry, Bull. Am. Phys. Soc. 33, 512 (1988).

[12]W. P. Mason, *Physical Acoustics and the Properties of Solids* (Van Nostrand, Princeton, New Jersey, 1958).

VI. CHARACTERIZATION OF POLYMER COMPOSITES

TEMPERATURE DEPENDENCE OF THE ULTRASONIC PROPERTIES OF AS4/LEXAN AND XAS/LEXAN COMPOSITE*

B.T. Smith
Department of Physics
Christopher Newport College
Newport News, VA 23606

INTRODUCTION

The integration of composites into critical components of aerospace structures requires that their integrity can be nondestructively evaluated. Conventional ultrasonic techniques are sufficient for gross flaw detection but nondestructively measuring matrix consolidation, fiber matrix adhesion and fiber breakage calls for the development of new techniques. Presented here is an approach which will aid in the understanding of the interaction of ultrasonic waves with composite materials.

The interaction of ultrasonic energy with composite material is complicated by the inherent anisotropy of the structure. The matrix is a viscoelastic material with appreciable acoustic absorption which also supports low acoustic velocity. The fiber which is crystalline provides little acoustic absorption, has a high ultrasonic wave speed and will have negligible temperature dependence for interaction with ultrasonic waves. The properties of the material at the matrix-fiber interface are unknown. Taking advantage of the different temperature dependence of the constituent parts the contribution of the matrix and the graphite fiber to the propagation and total scattering of the ultrasonic wave can be evaluated. Thus a comparison of the pure matrix and the composite samples over a wide temperature range will allow separation of contributions of the matrix and the fiber to interaction with an ultrasonic wave.

The temperature dependence of the ultrasonic properties of polymeric materials has been previously investigated by Hartmann and Jarzynski [1], who determined the temperature dependent values of the ultrasonic wave speed and elastic constants. Sutherland and Lingle [2] also examined polymeric materials and determined the master equation as well as the temperature dependent ultrasonic velocity. Smith and Winfree [3] have reported the temperature dependent acoustic properties of polysulfone and polysulfone/graphite fiber composite. In that study [3] the approximate contribution of the fiber and matrix to the total attenuation was determined. In continuation of that earlier work the

*Work Supported by NASA Grant NAG-1-431

temperature dependence of the velocity and attenuation for both the matrix and composite materials is presented here. This introduction is followed by a description of the experimental technique, a section on data reduction and a concluding section on the results.

EXPERIMENTAL TECHNIQUE

The experiment was performed in an insulated bath of 70% solution ethylene glycol with mechanical refrigerant cooling to vary the temperature from -40C to 20C. A broadband immersion transducer with a center frequency of 5 MHz was used in a pulse echo mode with pulse excitation. The front surface and subsequent round trip echoes where digitized at 100 megasamples/sec, signal averaged 100 times, and stored for later analysis. An air dam behind the specimens provided total reflection at the back surface. A chromel-alumel thermocouple with an electronic zero point reference was used to record the sample temperature. The system was cooled to -40C and allowed to warm to room temperature over the course of tens of hours assuring thermal equilibrium of the sample and liquid. The digitized waveforms where recorded for every half degree variation. The samples included a 100% lexan, 8 and 16 ply uniaxial XAS/lexan specimens with differing fiber volume fractions (V_f= 0.58, 0.61, 0.36, and 0.35), and a 16 ply uniaxial AS4/lexan sample with a fiber volume fraction of 0.55. All of the specimens had undergone the same processing history. The resin content and corresponding fiber volume fraction were determined by measuring pre- and post-processing parameters and are accurate to a few percent.

DATA REDUCTION

A representative ultrasonic waveform is shown in figure 1. The front surface echo is evident as well as the first and second round trips through the sample. To solve for the ultrasonic velocity, attenuation, and reflection coefficient, the front surface reflection at each temperature is convolved with a plane wave model of the round trip waveforms. This is a variation of the technique suggested by Papadakis [4]. The model used is shown here:

$$\frac{(1-R^2)e^{-2d(K_1+K_2\omega)-2i\omega d/c}}{R} + \frac{R(1-R^2)e^{-4d(K_1+K_2\omega)-4i\omega d/c}}{R}$$

where R is the reflection coefficient, c is the wave speed, ω is the radial frequency and K_1 and K_2 give the frequency dependence of the attenuation, which is assumed to be a constant plus a frequency dependent term. This model calculation is compared to the data using a Levenburg-Marquardt non-linear fitting routine [5] for the variables R, c, K_1 and K_2.

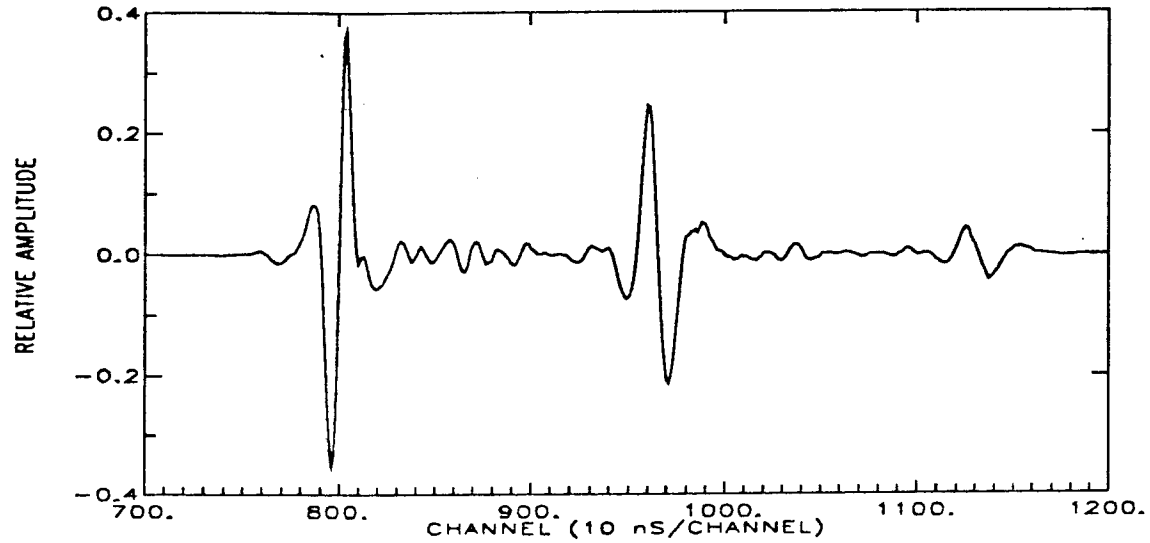

Fig. 1. Acoustic response of the AS4/lexan (V_f = 0.55) sample at -4C.

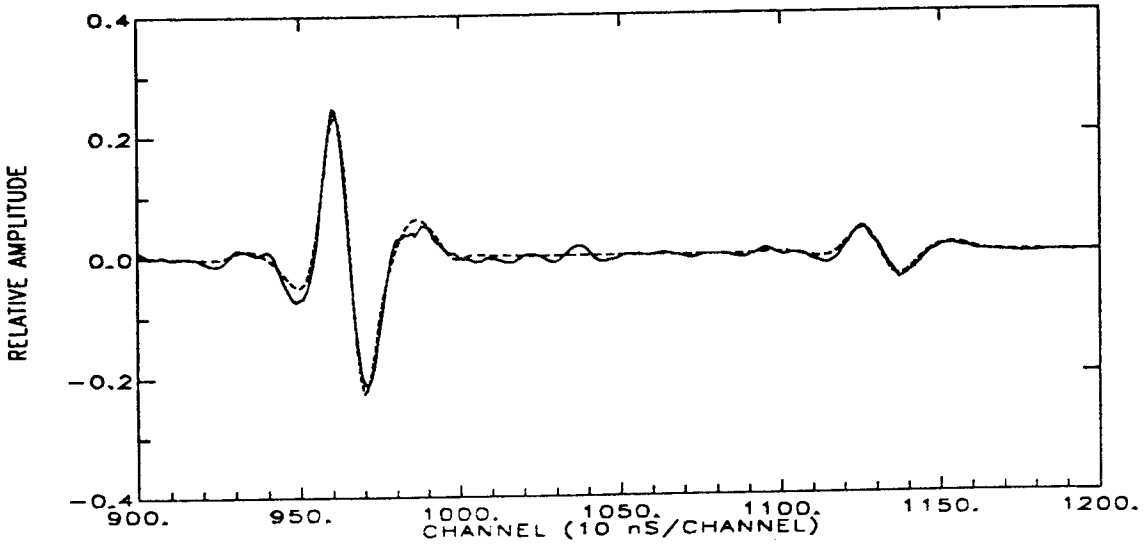

Fig. 2. Experimental data (-) and fit (---) for the AS4/lexan sample -4C.

RESULTS

An example of the first and second round trip response and the fit to the data is shown in figure 2. The fit is quite good and the same procedure is applied to all the data.

The attenuation for the AS4/lexan and the 100% lexan sample is shown in figure 3. The total attenuation is calculated by adding the K_1 and 5 MHz times the K_2 value ($K_1 + 5*K_2$) at each temperature. Although the transducer used is broadband the choice of 5 MHz locates the approximate centroid of the energy distribution in the ultrasonic wave. The absorption attenuation of the 100% lexan is above that of the composite. The composite is a stiffer structure and losses are due to absorption and scattering of the ultrasonic wave. The relative temperature response of the composite is the same viscoelastic response of the pure matrix and a linear function could be used to fit the lexan data to the composite data.

The attenuation data for representative experiments on XAS/lexan is shown in figure 4 along with the 100% lexan data. The data represents different composite panels that were measured in a different series of experiments. The top attenuation curve is for an 8 ply sample with V_f=0.58 and the other is a 16 ply sample with V_f=0.61. For this case the attenuation is both greater than and less than that of the pure matrix material. This is also the case for the other composite samples when the experiments are repeated at different locations on the sample. The attenuation data can be linearly fit with the 100% lexan attenuation data and the magnitude differences are most likely due to local scatterers in the material. These scatterers are visible as small

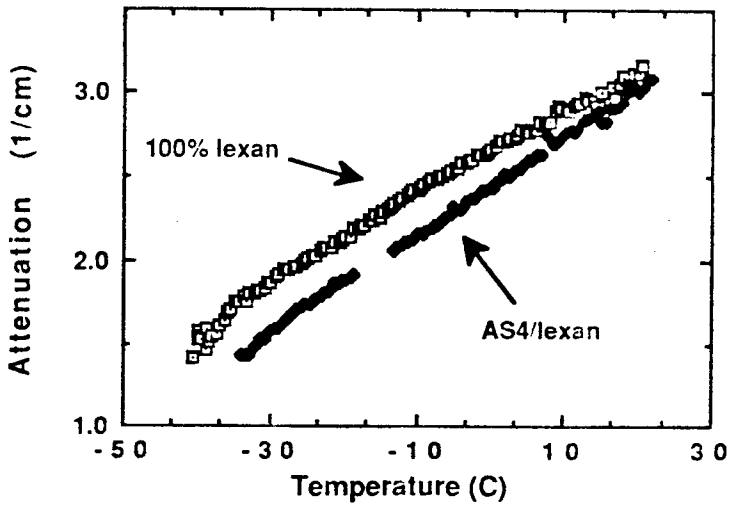

Fig. 3. Attenuation as a function of temperature for AS4/lexan and 100% lexan.

amplitude returns between the surface echoes shown in fig. 1. The data is not corrected for this internal backscatter and only the surface reflections are used in the calculation

The velocity variation with temperature is shown in figure 5. The result is typical of viscoelastic materials where the stiffness increase at lower temperature supports higher wave speeds. The increase with fiber content is representative of the contribution of the fiber

to the increased stiffness of the samples. The progression with fiber content is regular for the XAS fiber samples. For the subset of fiber volumes the difference in the specimen velocity values is the likely result of the variance in the fiber volume fraction which is greater than the accuracy of the known values. The reproducibility of the velocity data on an individual samples is excellent and is independent of the relative attenuation value at the measurement location. Other experimental results for the same samples measured at later times at different locations on the sample are shown on fig. 5 and the data points overlap well.

The results for the AS4/lexan velocity calculations seem out of place on this graph. In fact since the AS4 and XAS fibers have similar properties the AS4/lexan data should lie between the two sets of XAS/lexan data due to its measured value of fiber volume fraction. The offset of the AS4/lexan is greater than the uncertainty in the fiber volume fraction values and is due to a difference in the physical makeup of the AS4/lexan specimen as compared to the XAS/lexan specimen. This difference was noted by other researchers examining the same composite systems. Concurrently with the work reported here the interlaminar fracture toughness of samples identical to the ones studied here was being performed [6]. The properties of the fiber are nearly identical but work by Hinkley [6] revealed that a proprietary surface coating applied to the XAS fiber lead to a probable reaction with the matrix during processing of the samples. He found evidence of a higher porosity for the XAS as compared to the AS4. A post-processing examination of the material at the fiber matrix interface revealed that the molecular weight of the matrix had degraded from initial values. Also, the interlaminar fracture toughness of the XAS/lexan was 40% below that of the AS4/lexan. Therefore, the XAS/lexan velocity data maybe lower than that of the AS4/lexan because of the

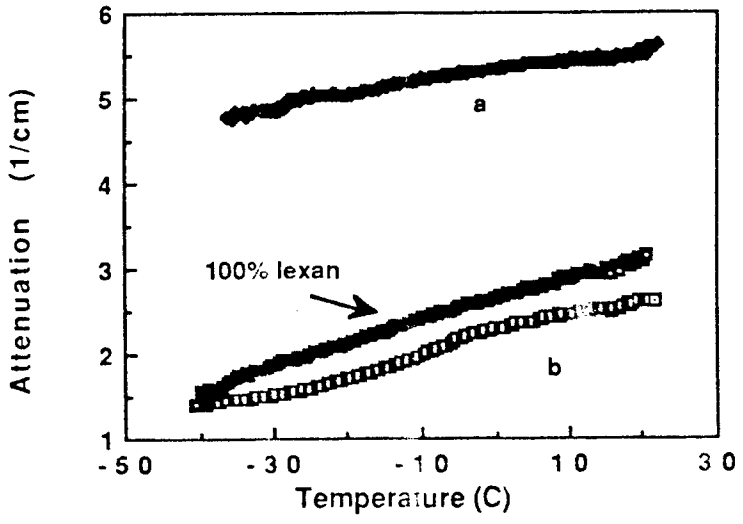

Fig. 4. Attenuation as a function of temperature for XAS/lexan (a) 8-ply: V_f=0.58, (b) 16-ply: V_f=0.61, and 100% lexan.

presence of porosity. The effect of porosity on decreasing the ultrasonic wave velocity has been noted by Reynolds and Wilkinson [7]. The other possibility is that the local variation in molecular weight near the fiber-matrix interface changes the elastic constants sufficiently to dramatically alter the transverse velocity.

CONCLUSION

We have presented here a technique for the measurement of the ultrasonic properties of composite and matrix materials as a function of temperature. This method illustrates the first step towards separating the contributions of the constituent parts to interaction with an ultrasonic wave.

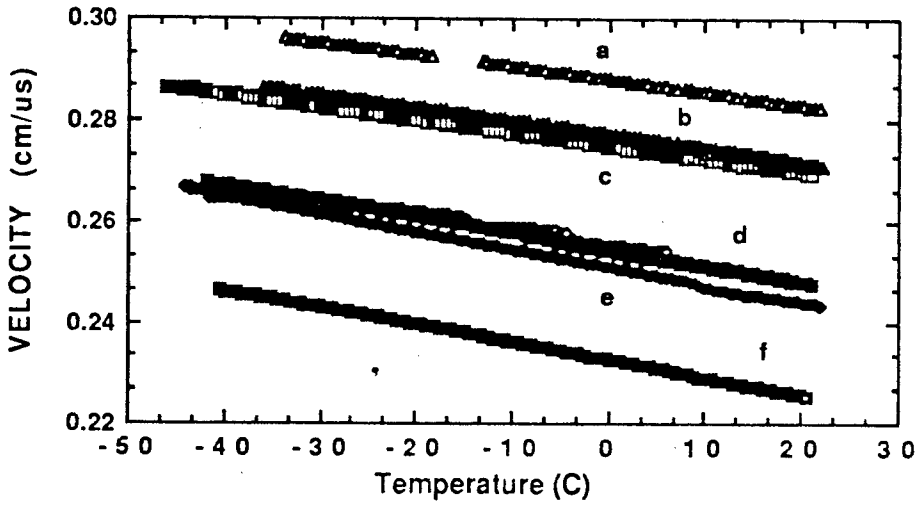

Fig. 5. Velocity as a function of temperature for: (a)AS4/lexan (0.55), (b) XAS/lexan (0.58), (c)XAS/lexan (0.61), (d) XAS/lexan (0.35), (e) XAS/lexan (0.36), and (f) 100% lexan.

REFERENCES

1. B. Hartmann and J. Jarzynski, J. Acoust. Soc., Am, 56, 1469, (1974).
2. H. Sutherland and R. Lingle, J. Appl. Phys., 43, 4022, (1972).
3. B.T. Smith and W.P. Winfree, Proceedings of the 1984 IEEE Ultrasonics Symposium, Nov. 14-16, Dallas, Texas, (1984).
4. E.P. Papadakis, K.A. Fowler, and L.C. Lynnworth, Jour. Accus. Soc. Am., 53, 1336, (1973).
5. W.H. Press, B.P. Flannery, S.A. Teukolsky, and W.T. Vetterling, Numerical Recipes (Cambridge University Press, 1986).
6. J.A. Hinkley, N.J. Johnston, and T.K. O'Brien, NASA TM 100532, Febuary 1988.
7. W.N. Reynolds and S.J. Wilkinson, Ultrasonics, 16, 159, (1978).

DETECTION OF BONDLINE DELAMINATIONS IN MULTILAYER STRUCTURES WITH LOSSY COMPONENTS†

ERIC I. MADARAS, WILLIAM P. WINFREE,
B.T. SMITH*, and JOSEPH H. HEYMAN

NASA Langley Research Center, Hampton, Va. 23665
*Physics Department, Christopher Newport College,
Newport News, Va. 23606

ABSTRACT

The detection of bondline delaminations in multilayer structures using ultrasonic reflection techniques is a generic problem in adhesively bonded composite structures such as the Space Shuttle's Solid Rocket Motors (SRM). Standard pulse echo ultrasonic techniques do not perform well for a composite resonator composed of a resonant layer combined with attenuating layers. Excessive ringing in the resonant layer tends to mask internal echoes emanating from the attenuating layers. The SRM is made up of a resonant steel layer backed by layers of adhesive, rubber, liner, and fuel, which are ultrasonically attenuating. The structure's response is modeled as a lossy ultrasonic transmission line. The model predicts that the acoustic response of the system is sensitive to delaminations at the interior bondlines in a few narrow frequency bands. These predictions are verified by measurements on a fabricated system. Successful imaging of internal delaminations is sensitive to proper selection of the interrogating frequency. Images of fabricated bondline delaminations are presented based on these studies

I. Introduction

NASA has set a goal of testing the Space Shuttle system for safety and reliability as completely as possible. The Rogers Commission Report indicated that detection of delaminations at the bondlines is an important component of quality assurance for the solid rocket motors (SRM). The SRM is made up of a thick steel layer backed by several layers of adhesives, rubber, liners, and fuel, which are ultrasonically attenuating. Standard pulse echo ultrasonic techniques are insufficient to perform the testing reliably on motors from the preferred steel side to avoid the sensitive fuel. The ultrasonic inspection of this structure is compromised by the excessive "ringing" of the steel when acoustically pulsed. This is a generic problem when a high acoustic "Q" layer is bonded to lossy, low acoustic "Q" layers. The echoes from the steel layer last for a significant amount of time, overlapping and interfering with the weaker echoes from the rubber, liner and fuel. These weaker echoes are only a few percent or less in amplitude of the larger steel interface echoes. Our approach is to model the SRM structure as a lossy ultrasonic transmission line. The model calculations provide the starting point to determine which are the best ultrasonic parameters to measure for detecting delaminations at the bondlines. From this treatment one can then try to devise testing techniques that will be robust when applied to actual hardware.

†This work was supported in part by NASA grant NAG-1-431

Testing on actual hardware is difficult and inconvenient because of size and weight considerations (twelve foot diameter motor segments weigh about 250 thousand pounds when loaded) and the expense of relocating equipment and personnel at the production facility. For this reason, Morton Thiokol manufactured laboratory size samples that were more manageable. These samples were built to closely approximate the actual construction of an SRM system and incorporated defects to allow us to test various methods.

II. Theory

To model the SRM sample, a normal incident acoustic wave was assumed to be propagating from a semi-infinite media to a layered system. The reflection of the front of the layer system is given by the expression

$$R = (Z_{1\_N} - Z_0) \; / \; (Z_{1\_N} + Z_0) \qquad (1),$$

where Z_0 is the acoustic impedance of the semi-infinite media and Z_{1_N} is the acoustic impedance of the entire set of layers from 1 to N. The acoustic impedance of the layered system can be found from the expression [1,2]

$$Z_{i\_N} = (Z_i + Z_{i+1\_N} \tanh(\theta_i d_i)) \; / \; (Z_{i+1\_N} + Z_i \tanh(\theta_i d_i)) \qquad (2),$$

where Z_{i+1_N} is the acoustic impedance of the set of layers from layers i+1 to N, Z_i, d_i are the the acoustic impedance and thickness of the i^{th} layer, and θ_i is given by the expression

$$\theta_i = \alpha_i + i\omega/c_i \qquad (3),$$

where c_i and α_i are the acoustic velocity and attenuation of the i^{th} layer. Equation (2) is used initially to solve for the impedance of the

N-1 layer and then successively applied until i is equal to 1. The result is substituted into equation (1) to find the reflection from the layered system.

To isolate the effect of layers 2 to N, the experimental procedure typically does not gate in the echo from the front face of the first layer. To simulate this in the model the reflection coefficient for the semi-infinite media backed by a semi-infinite first layer is subtracted from the results giving,

$$R = (Z_{1\_N} - Z_0) / (Z_{1\_N} + Z_0) - (Z_1 - Z_0) / (Z_1 + Z_0) \qquad (4).$$

Equation (4) can then used to calculate the spectral response of different layer configurations.

Typical acoustical responses for a steel, insulation, liner, inert fuel system with and without a disbond between the liner and fuel are shown in figure 1. The acoustic properties used to calculate the spectra are given in table 1. As can be seen from the figure, the most significant difference between the two spectra occurs at the peaks which correspond to the acoustic resonance of the steel layer. The figure also indicates the sign as well as the magnitude of the amplitude difference between the two spectra which depends on which steel resonance is chosen for investigation.

A similar effect is seen when varying the insulation thickness and finding the peak amplitude, which is shown in figure 2 for both the bonded and disbonded sample. The figure indicates that for most insulation thicknesses, there exist a difference in the amplitude of this peak. However, the contrast between the disbonded and bonded condition goes from positive to negative for some insulation thickness. Therefore, discrimination of disbonded from bonded regions requires an accurate knowledge of the thickness of the different layers. The samples fabricated for our investigation have insulation thicknesses of 0.0025 m and 0.0127 m. For the thinner insulation the contrast is negative, however for the thicker insulation the contrast is positive at the first steel resonance. The figure also indicates for some thicknesses, no difference exists in the peak amplitude between the bonded and disbonded case. Then the additional use of frequency information may be required to help resolve the disbond.

Table 1
Acoustic Material Properties of SRM Components

Material	Velocity m/sec	Density kg/m^3	Attenuation nepers/m
Steel	6080	7600	0
Insulation	1810	1218	$1.11 \times 10^{-5} f^{1.225}$
Liner	1500	999	$23.0\ f^0$
Fuel	2170	1503	$213.\ f^0$

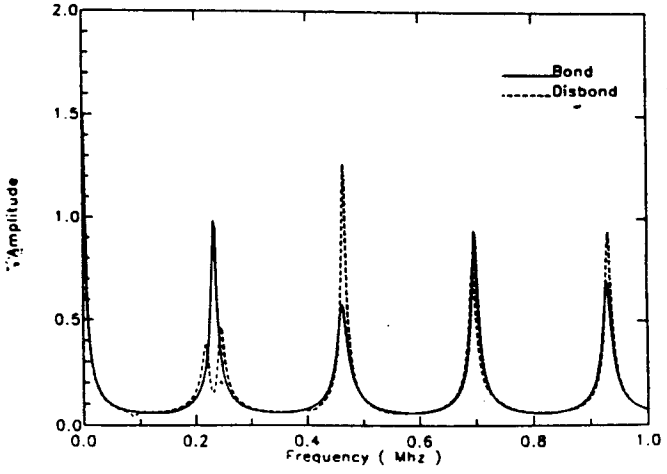

Figure 1. Calculated spectral response of a layered SRM system comparing a normal bonded sample with 0.127 m of steel, 0.0025 m of insulation, .0025 m of liner and 0.1016 m of inert fuel vs. a disbond condition between the liner and fuel.

III. Samples

The samples used in this work were manufactured by Morton Thiokol, the manufacturer of the SRM systems for NASA. The samples were made to represent the SRM system's cross section as close as reasonably possible (see Fig. 3). To emulate a disbonded condition, thin brass wedge shaped shims were cured into the samples at various bondlines. The thin strips of metal extended beyond the sample's edge so that they could be withdrawn after cure to produce an obvious disbond. The

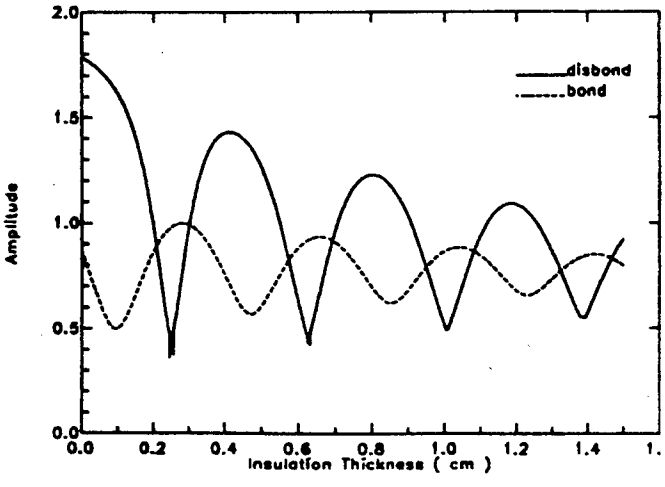

Figure 2. Calculated contrast levels at the first steel resonance of layered SRM system with varying thicknesses of insulation comparing a normal bonded sample with 0.127 m of steel, insulation, .0025 m of liner and 0.1016 m of inert fuel vs. a disbond condition between the liner and fuel.

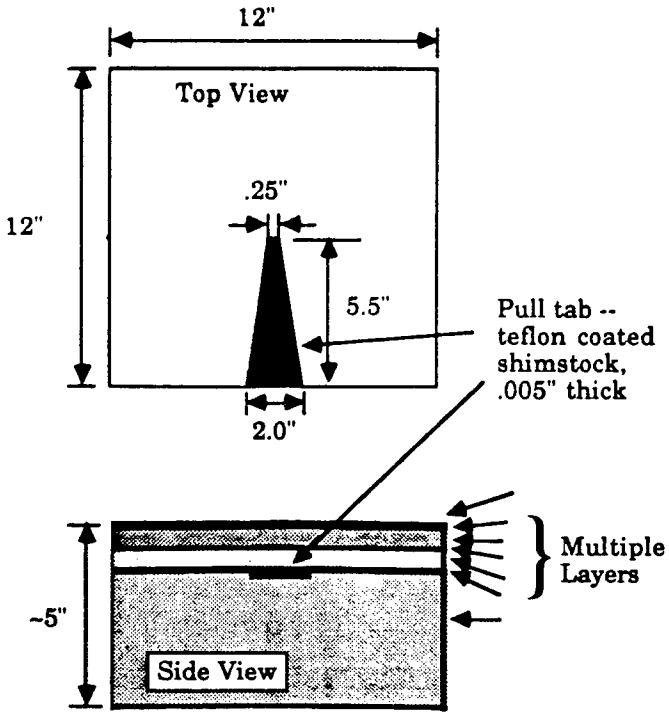

Fig. 3. Sample cross section of the SRM system.

samples were 12 inches by 12 inches square and had different thicknesses of the insulation materials that would go into manufacturing the motors (.0025 m and .0137 m) Fig. 3 shows an example of one of the samples. For safety, the fuel layer was rendered inert by replacing the oxidizer component with sodium chloride. The cross-sectional shape of the delaminations were identical in each sample.

Exposure to water would damage the liner and fuel on these samples. In order to use water as a couplant, we mounted plastic sides from a water tank to the top surface (steel side) of the SRM samples and attached the sides with a caulking compound (RTV). In this manner, the steel side of the sample became a water tight tank which we could scan using water as the couplant on the steel side and not compromise the fuel and insulation layers with moisture absorption. Since the samples had a small amount of curvature, a simple device was made that maintained the transducer perpendicular to the surface of the sample.

IV. Equipment

Using the results of the model calculations it is clear that the physical parameters of the ultrasonic wave interaction with the bondlines can be measured by many techniques. The methods though different rely on the same physics. Three techniques are illustrated here.

Figure 4 shows an outline of the electronic apparatus. The system shown in 4a used a spectrum analyzer to capture the spectral response of the sample to the ultrasonic signal. The spectrum analyzer's tracking generator output was attenuated and fed through a set of transmitter gates to the transmitter. The transmitter gate width was set for approximately a 40 microsecond long tone burst. This length of the tone burst was long enough to generate standing waves in the outer layers of the SRM sample. The ultrasound was coupled into the sample through a water delay line of approximately 70 microseconds long. A flat 500 KHz, 1.125" diameter broadband transducer was used for insonifying the sample. The echoes were then fed into a set of receiver gates to select the desired portion of the RF signals for input into the spectrum analyzer. The receiver gates sampled the RF signal from the tone burst's echo several microseconds after the sample's front surface echo had past but the interior echoes remained. The acoustic "Q" of the system is then being detected. The spectrum analyzer output was recorded on a microcomputer that also controlled a position scanner that allowed us to produce an image of the SRM sample's spectral response.

Figure 4b. shows a simple system that is based on a similar principle. A ten cycle tone burst at a frequency of 500 KHz (the second harmonic of the steel) was used. This tone burst was transmitted using a 500 KHz, 1.125" diameter planar transducer. The reflected signal was gated into the receiver just after the front wall echo had past and the gated signal was detected. The gated detector was also replaced with a waveform digitizer. Signal processing in the frequency and time domains was then applied to extract the physical parameter of interest. the results are similar and are not included in this work.

Figure 4c. demonstrates still a third system that we developed. This system is designed to track an ultrasonic resonance of the sample and measure both the amplitude and phase of the signal [3]. This is desirable if the thickness of the steel or deeper layers should change causing a phase shift in the signal. A slow sinusoidal signal is applied to the control port of a VCO causing the oscillator to FM the output. The echo of the transmitted tone burst is detected after the front wall echo has passed and the resulting signal is measured. The amplitude of the signal varies because of the frequency modulation and this variation is used to generate an error signal that is fed back into the VCO to keep the frequency at the peak of the resonance. In this manner, it could track both the amplitude and frequency of a resonant peak should a thickness change occur and cause the resonance to be different than anticipated.

V. Results

The spectral response of the sample which was convolved with the system's response showed several resonant structures and is shown in figure 5. The spectral response of these SRM samples should have resonances near 250, 500, and 750 KHz which are expected to arise from the 0.0127 m of steel. The general resonant structures that were related to

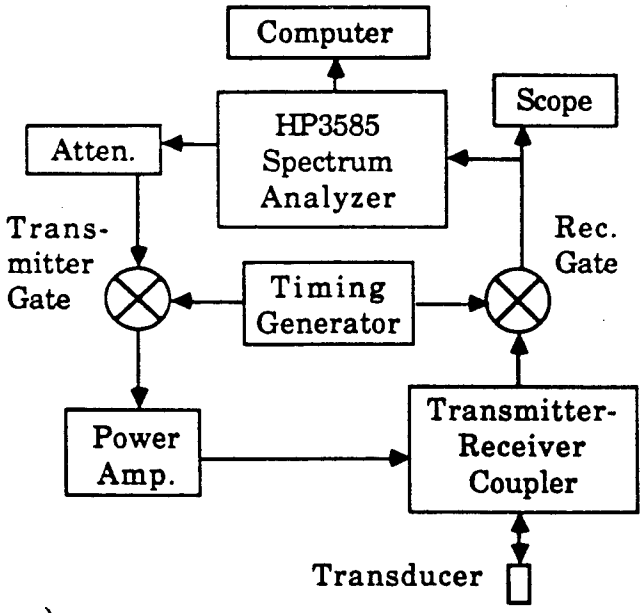

a)

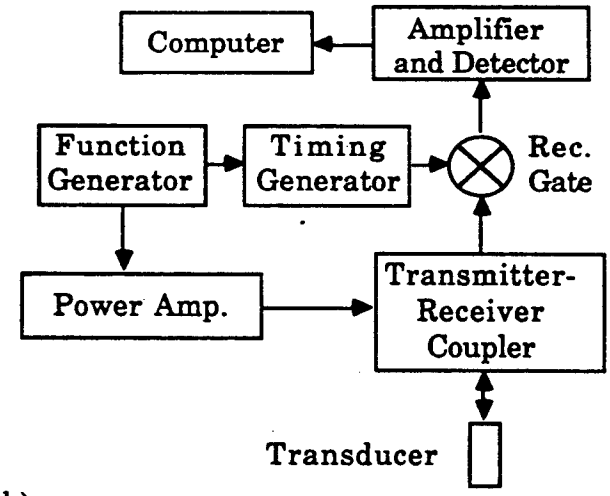

b)

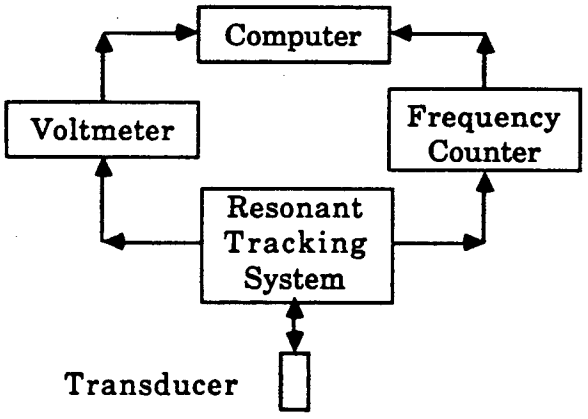

c)

Fig. 4. three different systems used to view the samples with disbond regions.

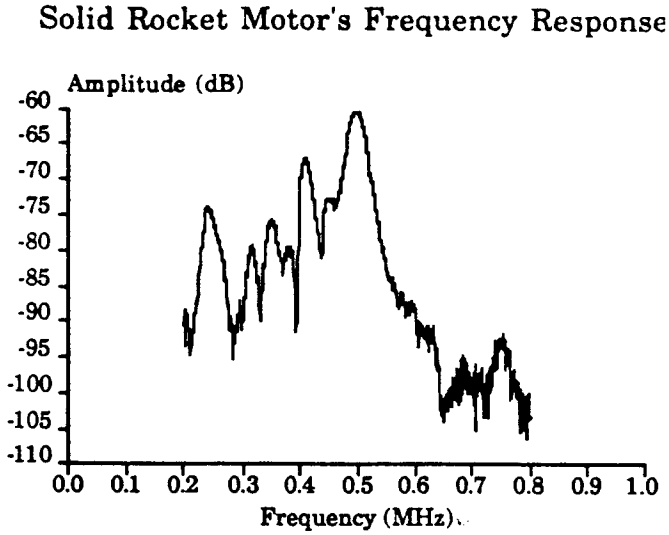

Fig. 5. The frequency response of the system to the SRM samples.

the theoretical predictions were evident. A few others resonances which were not of interest were evident and were possibly generated by side lobe effects or other modes. The 490 KHz resonance dominates because it is near the center frequency of the transducer. The rubber insulation will have less effects on the resonances at the higher frequencies because the attenuation of the rubber is frequency dependent. The rubber will also limit the penetration of the ultrasound and its ability to detail defects deeper into the material. Therefore, the lower frequencies are the most attractive for purposes of deeper interrogation.

Figure 6a. shows an image based on peak detecting a standard pulse echo system. The step size is 0.2 cm and the image size is 8 X 12 cm. The sample has 0.0025 m. of insulation behind the steel and the delamination is at the liner to fuel interface. The delamination is not resolved using this standard technique. These echoes are difficult to resolve in part because the ultrasonic energy is being transmitted over a wide band of frequencies, whereas the sample has a stronger response at the resonance frequencies. In contrast, figure 6b, shows the results of the tone burst system shown in figure 4b. This figure represents the same scan area as figure 6a. The delamination is now resolved by transmitting energy at a sensitive resonance. This image has the inverse contrast as predicted by theory. This is undoubtedly due to difficulties in laying up the samples. In particular, materials like the liner and fuel are viscous liquids when they are applied. In small samples, it can be difficult to maintain their thicknesses. Also, the cured liner material is fairly soft, and it would be easy to disturb its shape when the insert that creates the disbond is cured into the system

Figures 7a and 7b show the results of images based

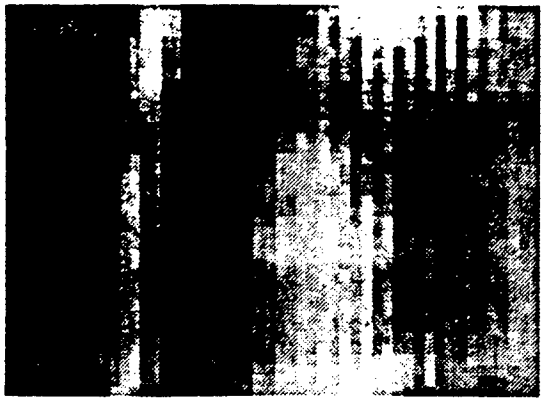

a)

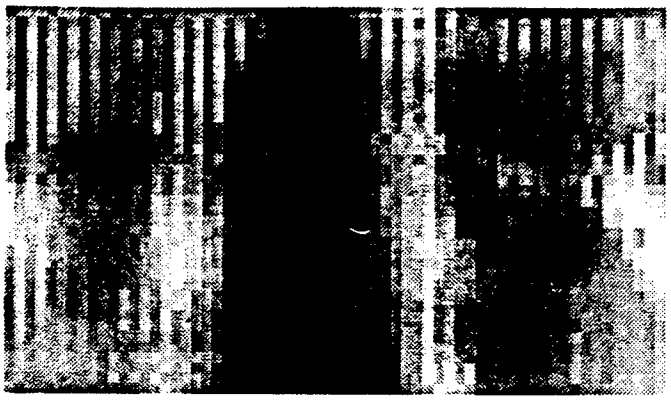

b)

Figure 6 Ultrasonic images of manufactured disbonds with 0.0025 m of insulation behind the steel. (a) Represents a standard peak detection system. (b) Represents a tone burst at the second steel harmonic resonance detected system.

on the first steel harmonic (~240 KHz) and the second steel harmonic (~490 KHz) using the technique based on the spectrum analyzer. The scans were from a 50 by 50 pixel scan with a 0.25 cm step size per pixel. This sample had 0.0137 m of insulation behind the steel with a disbond between the liner and fuel. The spectra were smoothed and the peak signal intensity near the desired frequency was selected. The image based on the first harmonic displayed the shape of the delamination reliably, with about a 2-3 dB increase in intensity at the disbond region. The contrast of the image is lost in the image based on the second harmonic and does not show the disbond region with as much reliably as the 240 KHz image. The second harmonic image is in a frequency range where the contrast is predicted to be poorer.

Figure 8 shows the results of imaging a sample, which has 0.0025 m of insulation behind the steel, with the system that would track the resonant frequency as well as the amplitude at the resonant peak. In this case, a frequency shift of the

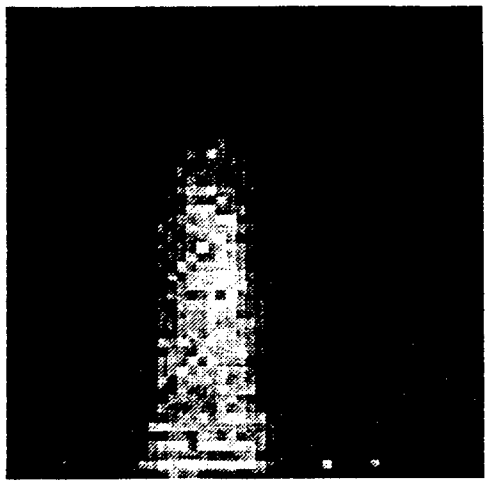

(a)

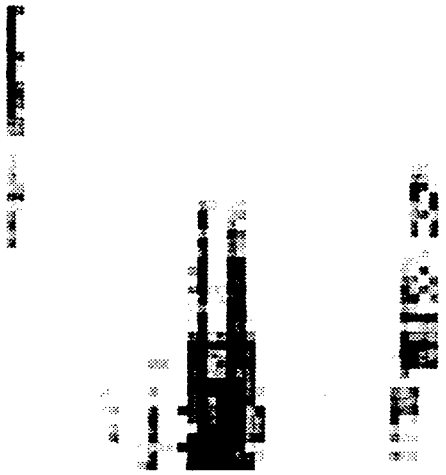

(b)

Figure 7. Ultrasonic images of manufactured disbonds with 0.0127 m of insulation behind the steel using system depicted in figure 4(a). (a) Represents the first steel harmonic resonance peak. (b) Represents the second steel harmonic resonance peak.

resonance is evident in figure 8b. This results in a very high contrast image in the frequency scan, and a lower contrast in the amplitude image. As was indicated in the theory section, the amplitude contrast may be small at the peak for some material thicknesses, and the addition of the frequency information could greatly help in the interpretation.

Each of the frequency selective techniques we tried showed the delamination regions. They each have their respective advantages and disadvantages. In the system shown in figure 4a, the use of the whole spectrum is very time consuming. It is helpful in demonstrating the model, but it

(a)

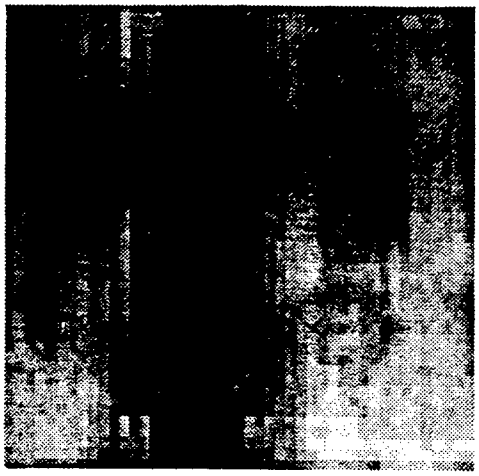

(b)

Figure 8. Ultrasonic images of manufactured disbonds with 0.0025 m of insulation behind the steel using system depicted in figure 4(c). (a) Represents the phase of the second steel harmonic resonance peak. (b) Represents the amplitude of the second steel harmonic resonance peak.

would not be practical in a production setting. The system depicted in figure 4b, is simple and quick, but the possibility of small shifts in frequency due to thickness changes in either the steel or deeper layers could cause false indications if one is not careful, especially with the added effects of the transducer response. The third system shown in figure 4c, is a compromise between the first two systems. In this system, care must be used in setting the frequency modulation level in case there are nearby resonances. It would be easy to jump to a different peak if the FM modulation is set high enough, and this could result in an image that would lose its significance.

VI. Conclusion

For systems such as the Solid Rocket Motor, large regions of the case are constructed of uniform layers of steel, insulation, liners and fuel. The curvature of the motor is large so that the layers can be approximated as nearly planar layers. For low frequencies, the wavelength of sound is long enough so that phase cancellation effects due to the curvature are not detrimental to ultrasonic testing. Under these conditions, the treatment of this layered system as an ultrasonic transmission line appears to be valid.

The ultrasonic model indicates that the best contrast can be obtained near resonances of the system. Our measurements show that this is true. Often the application of materials such as liners and adhesives are applied unevenly. Because of these possible variations in thickness, acoustic amplitude and phase will be important in helping to interpret measurements. Indications are that successful testing of some areas of the SRM should be attainable.

VII. Acknowledgments

The authors would like to acknowledge the assistance of Dale Stone and Mark Froggart in the construction of the "Pseudo Continuous Wave" instrument used in this experiment.

VIII. References

1. O'Donnell, M., Busse, L. J., and Miller, J. G., "Piezoelectric Transducers", Methods of Experimental Physics: Ultrasonics, Ed. Peter. D. Edmonds, vol. 19, pp 29-66, Academic Press, Inc. N. Y. (1981).
2. Brekhovskikh, L. M., Waves in Layered Media, Trans. by R. T. Beyer, Academic Press, Inc., N. Y. (1980).
3. Heyman, J. S., "Pseudo Continuous Wave Instrument", United States Patent 4,117,731, (1978).

AN INVESTIGATION OF THE RELATIONSHIP BETWEEN CONTRAST AND AZIMUTHAL ANGLE FOR IMAGING POROSITY IN GRAPHITE/EPOXY COMPOSITES WITH ULTRASONIC POLAR BACKSCATTER

S.M. Handley*, J.G. Miller*, and E.I. Madaras**

*Department of Physics, Washington University, St. Louis MO 63130
**NASA Langley Research Center, Hampton, VA 23665

ABSTRACT: The effect of uniformly distributed porosity is to increase the value of integrated backscatter. The objective of this study was to investigate the relationship between contrast and azimuthal angle, with the working hypothesis that the contrast between porous and pore-free regions should decrease as the azimuthal angle of insonification nears perpendicularity to any fiber orientation. Porosity was simulated by the introduction of spherical hollow-carbon inclusions, uniformly distributed, in a localized region of a 16-ply uniaxial graphite/epoxy composite. Two-dimensional integrated backscatter images were acquired for azimuthal angles (measured relative to the fiber axis) of 0°, 45°, 65°, 70°, 75°, 80°, 85°, 90°. For each azimuthal angle 169 sites in a pore-free region and 169 sites in the "porous" region (containing 2% volume fraction of "porosity") were averaged to obtain a spatially averaged integrated backscatter value for each region. We define the contrast of the image as the difference between the spatially averaged integrated backscatter value of the "porous" and pore-free regions for a specific azimuthal angle ϕ. As the azimuthal angle of insonification was varied from 0° to 90° the contrast decreased monotonically from a value of 9.1 dB to a value of 0.8 dB. These results provide an approach for determining the upper limits of detectability of porosity in composites of increasingly complex fiber orientations by indicating the contrast that is available for a known concentration of porosity at the optimum azimuthal angle for interrogation of a specific ply lay-up.

I. INTRODUCTION

The use of ultrasonic polar backscatter techniques for the detection and characterization of porosity in graphite/epoxy laminates has been explored in a number of laboratories over the past few years.[1-12] We have previously reported that the anisotropy of ultrasonic polar backscatter may provide a useful index for characterizing porosity.[6] For the case of a pore-free region in a uniaxial composite, integrated backscatter is maximum for insonification perpendicular to the fiber axis ($\phi = 90°$) and minimum for insonification having an azimuthal angle parallel to the fiber axis ($\phi = 0°$). Previous work by this Laboratory[4] has demonstrated that the effect of uniformly distributed porosity is to increase the overall value of integrated backscatter. Similar results were obtained from the graphite/epoxy specimens studied in the present work, as illustrated in Figure 1. As an approach to generalizing these results for the study of porosity in composites with more complex fiber orientations, we hypothesized that the optimum contrast for imaging regions of porosity should be obtained by selecting an azimuthal angle that is maximally removed from perpendicularity to any fiber orientation. The objective of this study was to investigate the relationship between contrast and azimuthal angle, with the working hypothesis that the contrast between porous and pore-free regions should decrease as the azimuthal angle of insonification nears perpendicularity to any fiber orientation.

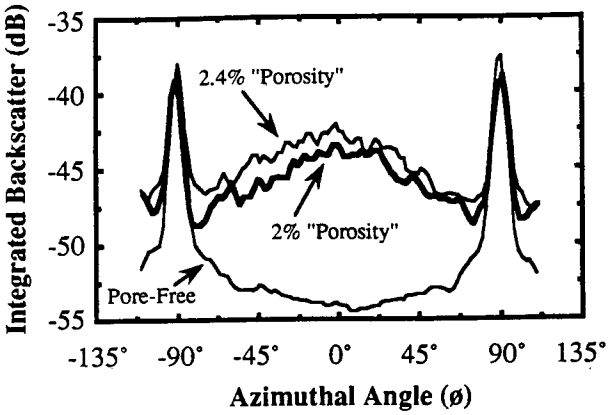

Figure 1: Integrated backscatter plotted as a function of azimuthal angle, ϕ, for a pore-free and two "porous" regions of a uniaxial graphite/epoxy composite. For nonperpendicular insonification, uniformly distributed porosity increases the overall value of the integrated backscatter.

II. EXPERIMENTAL METHODS

A. SAMPLE PREPARATION

Porosity was simulated by the introduction of spherical hollow-carbon inclusions between the 12th and 13th layers of a 16-ply uniaxial graphite-fiber/epoxy-matrix composite. The inclusions were drawn from a distribution having diameters ranging from 5 to 150 microns. The bleeder cloth impressions were removed by surface grinding the top and bottom surfaces of the samples, as suggested by Bar-Cohen.[13] The final thickness of the samples was approximately 2 mm. The present study focused on a sample containing 2% by volume fraction of "porosity". For a more complete description of the sample preparation see Reference [12].

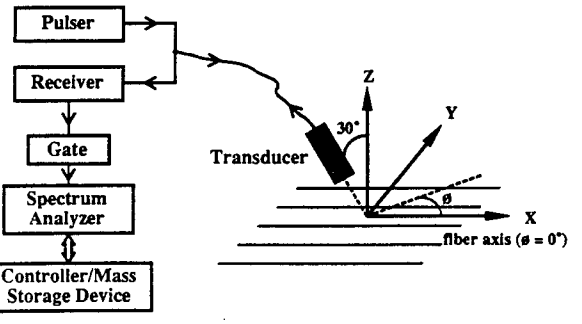

Figure 2: Block diagram of the polar backscatter data acquisition system.

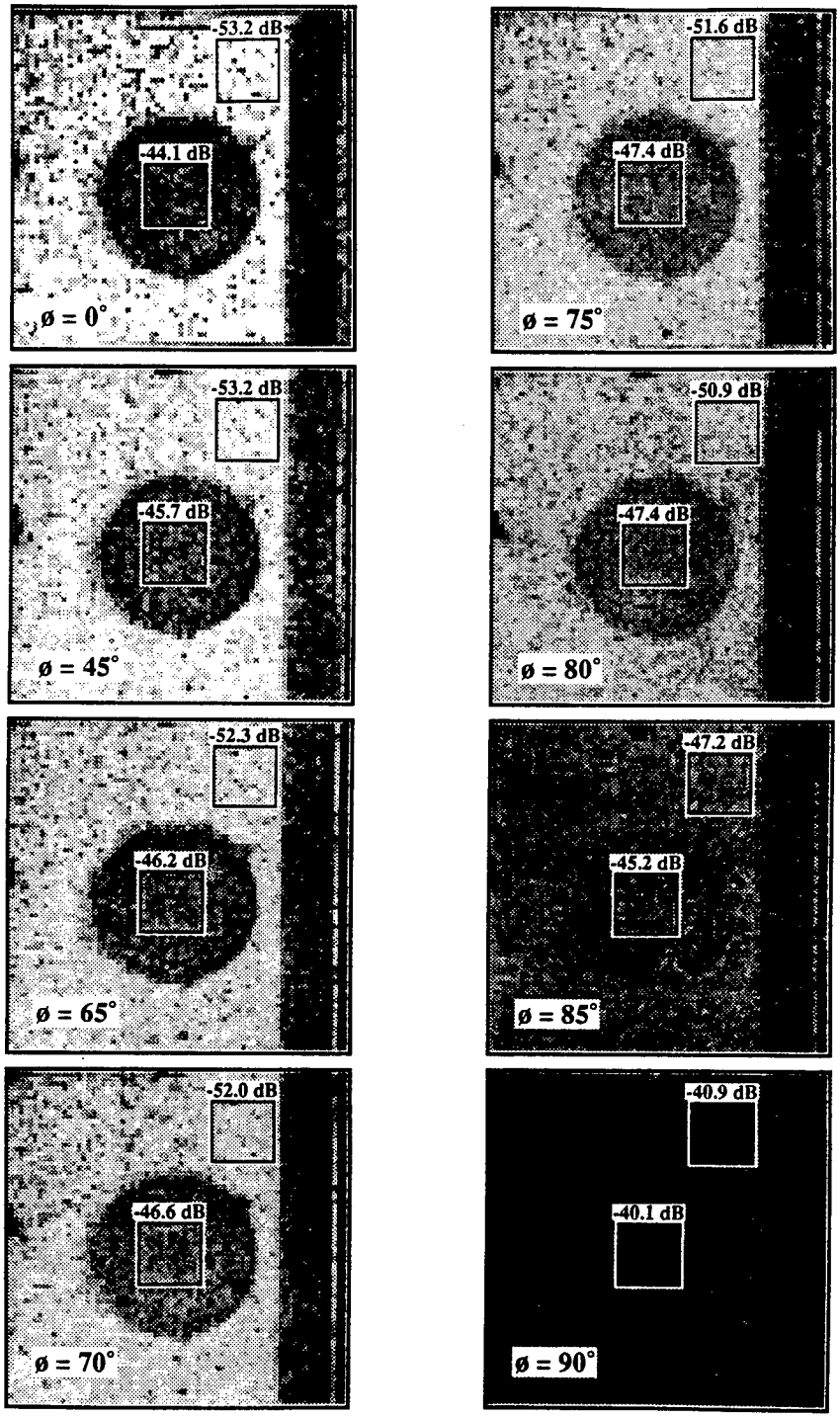

Figure 3: Quantitative two-dimensional mappings (integrated backscatter) for specific azimuthal angles.

B. MEASUREMENT METHODS

The polar backscatter technique, introduced by Bar-Cohen and Crane[1] and employed in several investigations reported from this[2, 4-6, 12] and other[3, 7, 9] laboratories, eliminates the strong but relatively uninteresting specular surface reflections from the backscattered signal. Thus the received backscattered signals are due to the variations in average material properties within the insonified volume of the specimen.

Ultrasonic polar backscatter measurements were performed using a broadband 10 MHz center-frequency, 0.5 inch diameter, 4 inch focal length transducer employed in a pulse-echo mode. The sample was scanned by translating the specimen over a 70 by 70 grid pattern in 1.5 mm steps. The transducer was oriented at a polar angle of 30° and a specific azimuthal angle, ϕ, ranging from 0° to 90°, as depicted in Figure 2.

At each acquisition point on the grid pattern, data were collected over the frequency range from 6 to 12 MHz by gating a 9 μsec segment of the backscattered signal into an analog spectrum analyzer. Using a generalized substitution method[14-16] the frequency spectrum was normalized to be independent of the electromechanical efficiency of the transducer and the properties of the system electronics. The normalized frequency spectrum was integrated (frequency averaged) to reduce the degrading influence of phase cancellation[16-20] and other interference effects which can compromise the results of the backscatter measurement. Integrated backscatter, which represents an average energy received over the useful bandwidth, is the ultrasonic parameter plotted in the two-dimensional images presented below.

III. RESULTS

Quantitative two-dimensional mappings were obtained for azimuthal angles ϕ of 0°, 45°, 65°, 70°, 75°, 80°, 85°, and 90°, where $\phi = 0°$ corresponds to the fiber direction. Figure 3 displays, in grayscale format, the integrated backscatter images obtained from these measurements. The 2 inch circular region, best seen for the $\phi = 0°$ case, is the region of localized "porosity". The 1 inch wide vertical strip at the right of the images corresponds to a region where the depth of the surface grinding, to remove the bleeder cloth impression, was limited so that a faint impression of the bleeder cloth remained. The effects that bleeder cloth impressions can have on polar backscatter measurements were reported by our Laboratory[12] at the Review of Progress in Quantitative Nondestructive Evaluation meeting in August of 1988.

As the azimuthal angle of insonification is increased from 0° (parallel) toward 90° (perpendicular), distinguishing the "porous" region from the background (pore-free region) becomes increasingly difficult. For the case of perpendicular insonification the "porous" region is almost completely masked.

For each azimuthal angle ϕ, spatially averaged integrated backscatter values were obtained by averaging values for 169 sites in the "porous" region (containing 2% by volume fraction of "porosity") and for 169 sites in a pore-free region. We define the contrast of the image as the difference between the spatially averaged integrated backscatter value of the "porous" and pore-free regions for a specific azimuthal angle ϕ, i.e.,

$$Contrast(\phi) \equiv Spatially\ Averaged\ Integrated\ Backscatter_{porous}(\phi) - Spatially\ Averaged\ Integrated\ Backscatter_{pore\text{-}free}(\phi) .$$

The relative contrast is defined as

$$Percent\ Relative\ Contrast(\phi) \equiv \frac{Contrast(\phi)}{Contrast(0°)} \times 100 .$$

In Figure 4 we plot the contrast for each of the azimuthal angles at which two-dimensional images were obtained. A relatively large contrast (9.1 dB) is observed for $\phi = 0°$. As the azimuthal angle of insonification increases toward $\phi = 90°$, the contrast decreases monotonically toward a value of 0.8 dB for $\phi = 90°$. In Figure 5 the corresponding percent relative contrast is displayed as a function of azimuthal angle. As the azimuthal angle of insonification approaches $\phi = 90°$, the contrast decreases to approximately 10% of the value obtained for $\phi = 0°$, the optimum value. The decrease in relative contrast with increasing azimuthal angle of insonification can make it very difficult to distinguish the "porous" region from the pore-free region.

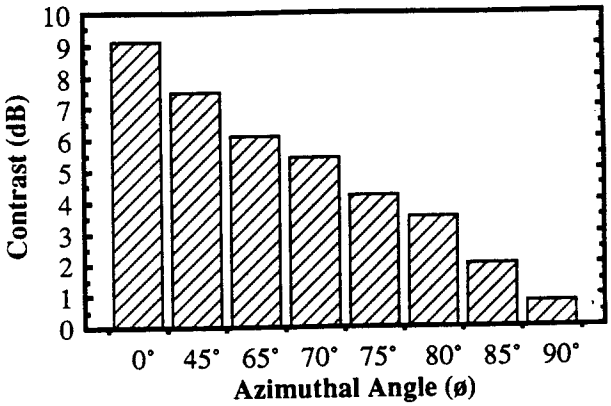

Figure 4: Contrast for several choices of azimuthal angle, ϕ. The contrast decreases monotonically from a value of 9.1 dB for $\phi = 0°$ to a value of 0.8 dB for $\phi = 90°$.

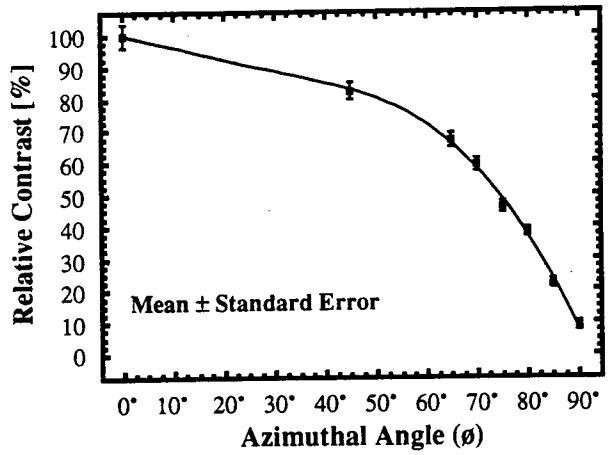

Figure 5: Percent relative contrast plotted as a function of azimuthal angle, ϕ. For the case where $\phi = 90°$ the contrast is down to approximately 10% of the optimum value.

IV. DISCUSSION

Practical applications employing the polar backscatter technique to produce quantitative images for the detection and characterization of regions of porosity need to take into account the azimuthal angle dependence of the contrast. The reduction of contrast as the direction of insonification becomes closer to perpendicular substantially degrades detection and characterization of zones of porosity. The optimum contrast for imaging regions of uniformly distributed porosity, which increases the overall value of integrated backscatter, should be obtained by selecting an azimuthal angle that is maximally removed from perpendicular to any fiber orientation. Thus the optimum azimuthal angle with respect to fiber orientation would change from 0° for uniaxial to 45° for biaxial. Similarly, the optimum angle would be 22.5° from any fiber axis for a [±45,0,90] quasi-isotropic lay-up.

These results provide an approach for determining the upper limits of detectability of porosity in composites of increasingly complex fiber orientations by indicating the contrast that is available for a known concentration of porosity at the optimum azimuthal angle for interrogation of a specific ply lay-up.

---- Supported in part by NASA grant NSG 1601 ----

References

1. Y. Bar-Cohen and R.L. Crane, "Acoustic-Backscattering Imaging of Subcritical Flaws in Composites," *Materials Evaluation*, vol. 40, pp. 970-975, 1982.
2. Lewis J. Thomas III, Eric I. Madaras, and J.G. Miller, "Two-Dimensional Imaging of Selected Ply Orientations in Quasi-Isotropic Composite Laminates Using Polar Backscattering," *Proc. IEEE Ultrasonics Symposium*, vol. 82 CH 1823-4, pp. 965-970, (1982).
3. D.E. Yuhas, C.L. Vorres, and Ronald A. Roberts, "Variations in Ultrasonic Backscatter Attributed to Porosity," *Review of Progress in Quantitative NDE*, vol. 5, pp. 1275-1284, Plenum Press, New York, 1985.
4. Earl D. Blodgett, Lewis J. Thomas III, and J.G. Miller, "Effects of Porosity on Polar Backscatter From Fiber Reinforced Composites," *Review of Progress in Quantitative Nondestructive Evaluation*, vol. 5B, pp. 1267-1274, (1986).
5. Earl D. Blodgett, S.M. Freeman, and J.G. Miller, "Correlation of Ultrasonic Polar Backscatter With the Deply Technique for Assessment of Impact Damage in Composite Laminates," *Review of Progress in Quantitative Nondestructive Evaluation*, vol. 5B, pp. 1227-1238, (1986).
6. S.M. Handley, M.S. Hughes, J.G. Miller, and E.I. Madaras, "Characterization of Porosity in Graphite Epoxy Composite Laminates With Polar Backscatter and Frequency Dependent Attenuation," *IEEE Ultrasonics Symposium*, vol. 87CH2492-7, pp. 827-830, (1987).
7. Ronald A. Roberts, "Porosity Characterization in Fiber-Reinforced Composites by Use of Ultrasonic Backscatter," *Review of Progress in Quantitative NDE*, vol. 6B, pp. 1419-1156, Plenum Press, New York, 1987.
8. J. Qu and J.D. Achenbach, "Analytical Treatment of Polar Backscattering From Porous Composites," *Review of Progress in Quantitative NDE*, vol. 6B, pp. 1137-1146, Plenum Press, New York, 1987.
9. Ronald A. Roberts, "Characterization of Porosity in Continuous Fiber-Reinforced Composites with Ultrasonic Backscatter," *Review of Progress in Quantitative NDE*, vol. 7B, pp. 1053-1062, Plenum Press, New York, 1988.
10. J. Qu and J.D. Achenbach, "Backscatter From Porosity in Cross-Ply Composites," *Review of Progress in Quantitative Nondestructive Evaluation*, vol. 7B, pp. 1029-1036, 1988.
11. T. Ohyoshi and J.D. Achenbach, "Effect of Bottom-Surface Reflections on Backscatter From Porosity in a Composite Layer," *Review of Progress in Quantitative Nondestructive Evaluation*, vol. 7B, pp. 1045-1052, 1988.
12. S.M. Handley, J.G. Miller, and E.I. Madaras, "Effects of Bleeder Cloth Impressions on the Use of Polar Backscatter to Detect Porosity," in *Review of Progress in Quantitative Nondestructive Evaluation*, vol. 8B, Plenum Press, New York, 1989. In Press
13. Yoseph Bar-Cohen, *Nondestructive Characterization of Defects in Multilayered Media Using Ultrasonic Backscattering*, McDonnell-Douglas Corp., 1987. Douglas Paper 7781. Unpublished.
14. M. O'Donnell, J.W. Mimbs, and J.G. Miller, "The Relationship Between Collagen and Ultrasonic Backscatter in Myocardial Tissue," *J. Acoust. Soc. Am.*, vol. 69, pp. 580-588, (1981).
15. M. O'Donnell and J.G. Miller, "Quantitative Broadband Ultrasonic Backscatter: An Approach to Non-Destructive Evaluation in Acoustically Inhomogeneous Materials," *J. Appl. Phys.*, vol. 52, pp. 1056-1065, (1981).
16. J.G. Miller, J.E. Perez, Jack G. Mottley, Eric I. Madaras, Patrick H. Johnston, Earl D. Blodgett, Lewis J. Thomas III, and B.E. Sobel, "Myocardial Tissue Characterization: An Approach Based on Quantitative Backscatter and Attenuation," *Proc. IEEE Ultrasonics Symposium*, vol. 83 CH 1947-1, pp. 782-793, (1983).
17. J.S. Heyman, "Phase Insensitive Acoustoelectric Transducers," *J. Acoust. Soc. Am.*, vol. 64, pp. 243-249, 1978.
18. L.J. Busse and J.G. Miller, "Detection of Spatially Nonuniform Ultrasonic Radiation with Phase Sensitive (Piezoelectric) and Phase Insensitive (Acoustoelectric) Receivers," *J. Acoust. Soc. Am.*, vol. 70, pp. 1377-1386, (1981).
19. L.J. Busse and J.G. Miller, "A Comparison of Finite Aperture Phase Sensitive and Phase Insensitive Detection in the Near Field of Inhomogeneous Material," *Proc. IEEE Ultrasonics Symposium*, vol. 81 CH 1689-9, pp. 617-626, (1981).
20. L.J. Busse and J.G. Miller, "Response Characteristics of a Finite Aperture, Phase Insensitive Ultrasonic Receiver Based Upon the Acoustoelectric Effect," *J. Acoust. Soc. Am.*, vol. 70, pp. 1370-1376, (1981).

EFFECTS OF BLEEDER CLOTH IMPRESSIONS ON THE USE OF POLAR BACKSCATTER TO DETECT POROSITY

S.M. Handley*, J.G. Miller*, and E.I. Madaras**

*Dept. of Physics, Washington University, St. Louis, MO 63130

**NASA Langley Research Center, Hampton, VA 23665

INTRODUCTION

The potential of ultrasonic polar backscatter measurements for detecting and characterizing porosity in composite laminates has been investigated in a number of laboratories[1-11]. The objective of this study was to evaluate the influence of the nature of the composite's surface on such measurements. The deleterious effects of bleeder cloth impressions, previously noted by Bar-Cohen[12], led to the hypothesis that the periodic surface features due to bleeder cloth impressions remaining after the cure process contribute significantly to the received backscattered signal, possibly masking the anisotropy of backscatter which is used to estimate porosity.

One measure of the anisotropy of polar backscatter is the integrated backscatter difference, defined as the difference in decibels between the maximum and minimum integrated backscatter as a function of azimuthal angle in a pore-free region. Figure 1 displays a typical polar backscatter anisotropy plot for a pore-free region of a uniaxial graphite/epoxy laminate. For ultrasound insonifying a planar composite laminate at a polar angle θ of 30°, backscatter is seen to be the strongest for insonification perpendicular to the fiber axes ($\phi = \pm 90°$). As illustrated in Figure 2 the anisotropy of polar backscatter can provide a useful index for quantitatively estimating the volume fraction of porosity. Results from measurements on two regions of the same specimen are displayed to contrast the difference between "porous" and pore-free regions. Except for azimuthal angles $\phi \simeq \pm 90°$, strength of the received backscattered signal is significantly larger in the "porous" region than in the pore-free region, thus decreasing the anisotropy of polar backscatter. We therefore made use of the integrated backscatter difference to investigate the detrimental effects of the presence of bleeder cloth impressions on the capability of ultrasonic polar backscatter imaging to detect and characterize porosity. The integrated backscatter difference was computed as the difference between measured values of integrated backscatter at the angles determined previously from the pore-free measurement, i.e., 90° and 0° for the case shown in Figure 2. (In previous work[6] we illustrated the advantages of averaging over a modest range of azimuthal angles to minimize background variations not attributable to porosity.)

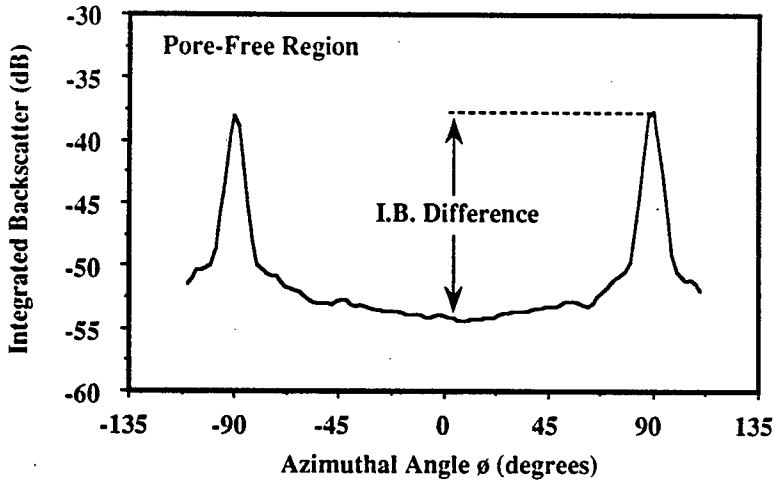

Figure 1: One measure of the anisotropy of polar backscatter is the integrated backscatter difference, defined as the difference in decibels between the maximum and minimum integrated backscatter as a function of azimuthal angle in a pore-free region. Data were obtained from a pore-free region of a uniaxial graphite/epoxy composite.

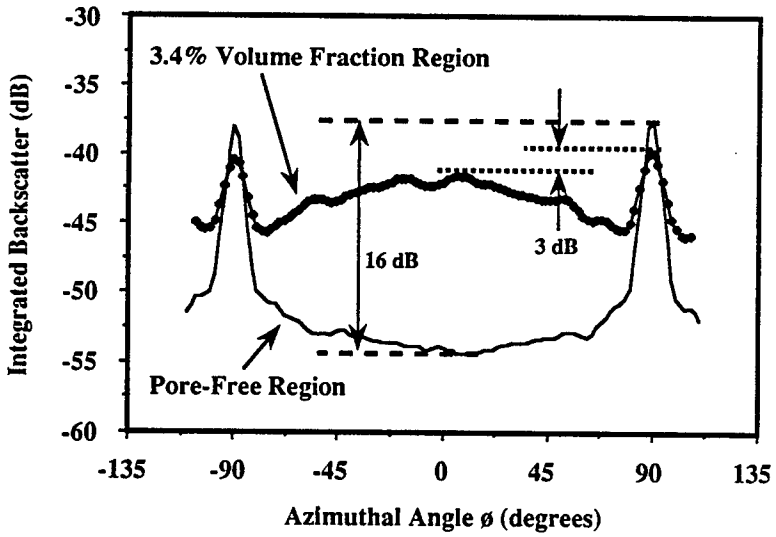

Figure 2: Results from two anisotropy scans: one in a pore-free region, the other in a "porous" region.

EXPERIMENTAL METHODS

Sample Preparation

All the composites used in this study were fabricated at NASA Langley Research Center using #5208-T300 prepreg tape and a standard #234 TFP porous teflon coated fiberglass bleeder cloth. The effects of porosity were simulated by introducing hollow-carbon beads, having a distribution of diameters ranging from 5 to 150 microns, into a 16 ply uniaxial graphite-fiber/epoxy-matrix composite approximately 2 mm. thick. Measured amounts of hollow-carbon spherical inclusions were introduced between the 12th and 13th layers during the lay-up of a 12 by 16 inch laminate. The beads were dusted onto circular regions 2 inches in diameter at sites on a square grid with centers 4 inches apart. The sample was autoclaved and cured in an oven using a standard cure protocol. The 12 by 16 inch sample was cut into smaller samples (approximately 3.75" by 3.75") so that each contained a single zone of "porosity". In the present study we focused on samples of 2% and 3.4% volume fraction of "porosity".

Measurement Methods

Backscatter measurements were performed using a 10 MHz center frequency, 0.5 inch diameter, 4 inch focal length transducer employed in a pulse-echo mode. The transducer was oriented at a polar angle of 30° and at various azimuthal angles as described below. The polar backscatter technique, introduced by Bar-Cohen and Crane[1] and employed in several investigations reported from this[2,4-5] and other laboratories[3,7,9], eliminates the strong surface reflections from the backscattered signal. Thus the specularly reflected signal is directed away from the transducer, which then receives only signals backscattered from variations in average material properties within the insonified volume of the specimen.

Data were collected over the frequency range 6 to 12 MHz in 0.04 MHz steps using the system shown in Figure 3. Backscatter was measured quantitatively using a generalized substitution technique[13-15]. The power spectrum of the backscattered signal was obtained by gating a 9 μsec segment into an analog spectrum analyzer. This power spectrum was then normalized to the power spectrum obtained in a second (calibration) measurement in which the specimen was replaced by a nearly perfect (flat stainless steel) ultrasonic reflector, insonified at normal incidence. The result of this normalization, the backscatter transfer function, is independent of the electromechanical efficiency of the transducer and the properties of the system electronics. The backscatter transfer function is a relative measure of the backscattering efficiency as a function of frequency. The frequency average of the backscatter transfer function, termed the integrated backscatter, provides a useful index of backscatter efficiency over a finite bandwidth[15,16]. Frequency averaging over a broad bandwidth reduces the degrading influence of phase cancellation[15,17-20] and other interference effects which can compromise the results of backscatter measurements. The useful bandwidth chosen for all of the results presented in Section III of this manuscript was over a range from 6 to 12 MHz.

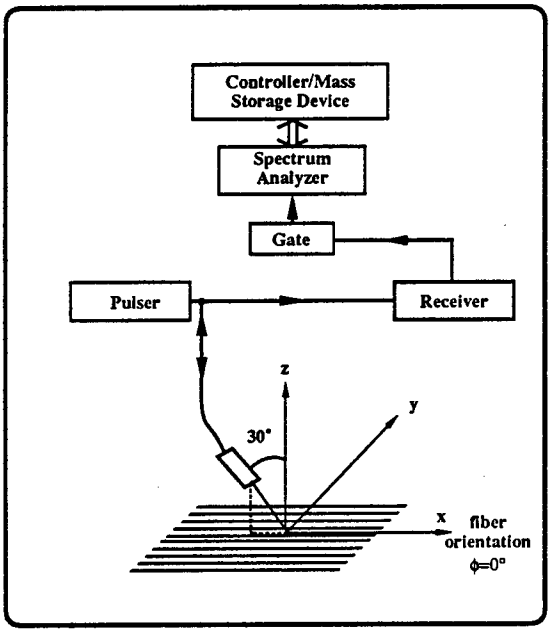

Figure 3: Block diagram of the polar backscatter data acquisition system.

RESULTS

Anisotropy of Polar Backscatter

Results of measurements performed with the bleeder cloth impressions intact were compared with the corresponding results obtained after their complete removal by surface grinding. Figure 4 displays the integrated backscatter difference in a graphite/epoxy laminate for measurements taken in a "porous" and pore-free region. With bleeder cloth impressions removed, the integrated backscatter difference was 16 dB for a pore-free region and 3 dB for a region containing approximately 3.4% volume fraction of "porosity". In contrast, for measurements made on the

same sample prior to the complete removal of the bleeder cloth impression, the integrated backscatter difference was 5.5 dB for a pore-free region and 5.6 dB for the region containing approximately 3.4% "porosity". Thus the measurements carried out after the bleeder cloth impressions were completely removed displayed a large difference (12 dB) between the "porous" and pore-free regions. In contrast, measurements carried out with the bleeder cloth impressions intact yielded virtually identical results in the "porous" and pore-free regions. These results indicate that the presence of bleeder cloth impressions remaining after the cure process can contribute significantly to the received backscatter signal, masking the anisotropy of polar backscatter.

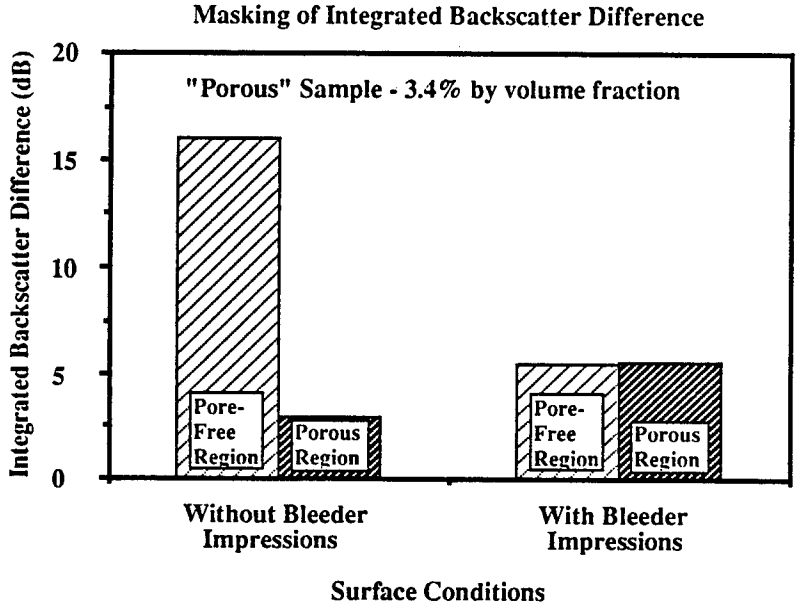

Figure 4: Influence of surface conditions on the integrated backscatter difference for measurements taken in a "porous" (3.4% by volume fraction) and a pore-free graphite/epoxy laminate.

Systematic Reduction of Bleeder Cloth Effects

In order to delineate the relative contributions of undesirable scattering from bleeder cloth impressions on the top and bottom surfaces, three sets of anisotropy scans were performed on the same region of a pore-free uniaxial graphite/epoxy composite. Prior to Scan 1, one side of the sample had been surface ground to remove the bleeder cloth impression and the other side had the bleeder cloth impression left intact. Insonification was from the side with the bleeder cloth impression. Scan 2 was performed with the composite in the same state as for Scan 1 except that the sample was flipped over and insonified from the side from which we had completely removed the bleeder cloth impression. Prior to Scan 3, we surface ground the second side and then repeated the measurement.

Scans were carried out at a polar angle of 30° and azimuthal angles varying from -110° to +110° in 2° increments. Each sample was scanned on a 4 by 4 grid in 2.5 mm steps and the acquired frequency spectra were averaged to reduce the effects of spatial variations. Integrated polar backscatter is plotted as a function of azimuthal angle for each of the scans in Figure 5. As illustrated previously (see Figure 1) the polar backscatter signal is expected to be the largest for azimuthal angles where the insonifying beam is perpendicular to the fiber axes ($\phi = \pm 90°$) and smallest for angles of insonification approximately parallel to the fiber axis ($\phi = 0°$). Although the results from Scan 1 of Figure 5 display the expected maxima for $\phi = \pm 90°$, there is an unexpected peak at $\phi = 0°$ and a substantial backscattered signal for azimuthal angles between -90° and +90°. The relative contributions of these unexpected results are significantly diminished in Scan 2 (bleeder cloth impression on opposite side) relative to those in Scan 1 (bleeder cloth impression on insonified side). It is interesting to note that the unexpected peak at $\phi = 0°$ is still evident in

Scan 2. Inspection of the data trace from Scan 3 for which the bleeder cloth impression had been removed from both sides reveals the expected results for a uniaxial composite laminate. That is, for angles of insonification perpendicular to the fiber orientation the polar backscatter displays peaks that are significantly stronger than signals received for nonperpendicular angles, and the minimum occurs for insonification parallel to the fibers.

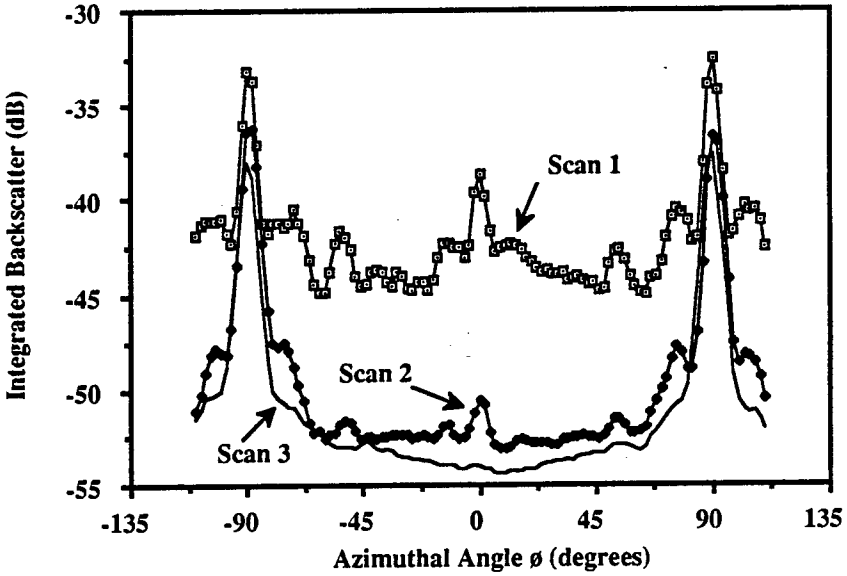

Figure 5: Anisotropy scans displaying results for 3 surface conditions. In Scans 1 and 2, one side of the composite had been surface ground. The side with the bleeder cloth impression intact was insonified in Scan 1. The side with the bleeder cloth impression removed was insonified in Scan 2. For Scan 3, both sides had been surface ground.

Quantitative Imaging

Practical applications of the methods of polar backscatter to characterize porosity require the generation of two dimensional images to map suspected regions of porosity. Figure 6 displays the results obtained from a quantitative mapping of a composite containing a localized region of "porosity", 2% by volume fraction. A raster scan was performed over a square grid using a step size of 1.5 mm. The azimuthal angle of insonification was fixed parallel to the fiber orientation ($\phi = 0°$). The value (in dB) shown for each region is the mean of 169 sites. The circular region in the center of the scan in Figure 6 corresponds to the region of "porosity". The region exhibits an average value of integrated backscatter 44.1 dB below that from a stainless steel (reference) plate. In contrast, typical integrated backscatter values in the pore-free regions average 53.2 dB below that from a stainless steel plate. As an illustration of the potentially confounding role of bleeder cloth impressions, a 1 inch wide vertical strip at the right of the image corresponds to a region where the depth of the grinding to remove the bleeder cloth impression was limited so that a faint impression remained. Even this relatively faint impression on the insonified surface was sufficient to produce a value of integrated backscatter of -42.5 dB relative to that of a stainless steel plate. This value is 1.6 dB larger than that (-44.1 dB) characteristic of the zone of "porosity".

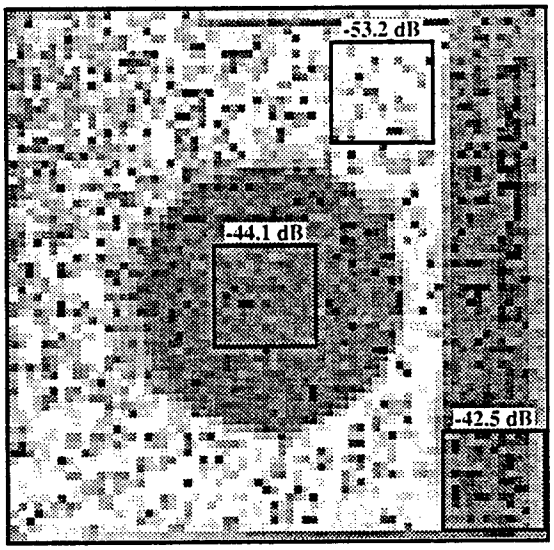

Figure 6: A quantitative mapping ($\phi = 0°$) of a composite containing a localized region of "porosity", 2% by volume fraction.

DISCUSSION

Considerable progress has been reported in recent experimental and theoretical investigations of the potential role of polar backscatter in detecting and characterizing porosity[7-10]. Nevertheless, practical implementation of this approach will be feasible only after the confounding effects of surface conditions can be reliably eliminated from the measured signals. The results of this investigation indicate that the presence of the bleeder cloth impressions substantially influences the degree of anisotropy. Furthermore, for relatively thin samples in which selective time gating is not feasible, not only the state of the insonified surface but also the state of the back surface influences the received signal. Some additional effects pertinent to the study of relatively thin laminates have been investigated by other authors[11]. Although removing these impressions by surface grinding provided a satisfactory approach for this laboratory investigation, an easily reversible surface treatment to minimize scattering from bleeder cloth impressions and similar surface features will be required in practical applications.

---- Supported in part by NASA grant NSG 1601 ----

References

1. Y. Bar-Cohen and R.L. Crane, "Acoustic-Backscattering Imaging of Subcritical Flaws in Composites," *Materials Evaluation*, vol. 40, pp. 970-975, 1982.
2. Lewis J. Thomas III, Eric I. Madaras, and J.G. Miller, "Two-Dimensional Imaging of Selected Ply Orientations in Quasi-Isotropic Composite Laminates Using Polar Backscattering," *Proc. IEEE Ultrasonics Symposium*, vol. 82 CH 1823-4, pp. 965-970, (1982).
3. D.E. Yuhas, C.L. Vorres, and Ronald A. Roberts, "Variations in Ultrasonic Backscatter Attributed to Porosity," *Review of Progress in Quantitative NDE*, vol. 5, pp. 1275-1284, Plenum Press, New York, 1985.
4. Earl D. Blodgett, Lewis J. Thomas III, and J.G. Miller, "Effects of Porosity on Polar Backscatter From Fiber Reinforced Composites," *Review of Progress in Quantitative Nondestructive Evaluation*, vol. 5B, pp. 1267-1274, (1986).

5. Earl D. Blodgett, S.M. Freeman, and J.G. Miller, "Correlation of Ultrasonic Polar Backscatter With the Deply Technique for Assessment of Impact Damage in Composite Laminates," *Review of Progress in Quantitative Nondestructive Evaluation*, vol. 5B, pp. 1227-1238, (1986).

6. S.M. Handley, M.S. Hughes, J.G. Miller, and E.I. Madaras, "Characterization of Porosity in Graphite Epoxy Composite Laminates With Polar Backscatter and Frequency Dependent Attenuation," *IEEE Ultrasonics Symposium*, vol. 87CH2492-7, pp. 827-830, (1987).

7. Ronald A. Roberts, "Porosity Characterization in Fiber-Reinforced Composites by Use of Ultrasonic Backscatter," *Review of Progress in Quantitative NDE*, vol. 6B, pp. 1419-1156, Plenum Press, New York, 1987.

8. J. Qu and J.D. Achenbach, "Analytical Treatment of Polar Backscattering From Porous Composites," *Review of Progress in Quantitative NDE*, vol. 6B, pp. 1137-1146, Plenum Press, New York, 1987.

9. Ronald A. Roberts, "Characterization of Porosity in Continuous Fiber-Reinforced Composites with Ultrasonic Backscatter," *Review of Progress in Quantitative NDE*, vol. 7B, pp. 1053-1062, Plenum Press, New York, 1988.

10. J. Qu and J.D. Achenbach, "Backscatter From Porosity in Cross-Ply Composites," *Review of Progress in Quantitative Nondestructive Evaluation*, vol. 7B, pp. 1029-1036, 1988.

11. T. Ohyoshi and J.D. Achenbach, "Effect of Bottom-Surface Reflections on Backscatter From Porosity in a Composite Layer," *Review of Progress in Quantitative Nondestructive Evaluation*, vol. 7B, pp. 1045-1052, 1988.

12. Yoseph Bar-Cohen, *Nondestructive Characterization of Defects in Multilayered Media Using Ultrasonic Backscattering*, McDonnell-Douglas Corp., 1987. Douglas Paper 7781. Unpublished.

13. M. O'Donnell, J.W. Mimbs, and J.G. Miller, "The Relationship Between Collagen and Ultrasonic Backscatter in Myocardial Tissue," *J. Acoust. Soc. Am.*, vol. 69, pp. 580-588, (1981).

14. M. O'Donnell and J.G. Miller, "Quantitative Broadband Ultrasonic Backscatter: An Approach to Non-Destructive Evaluation in Acoustically Inhomogeneous Materials," *J. Appl. Phys.*, vol. 52, pp. 1056-1065, (1981).

15. J.G. Miller, J.E. Perez, Jack G. Mottley, Eric I. Madaras, Patrick H. Johnston, Earl D. Blodgett, Lewis J. Thomas III, and B.E. Sobel, "Myocardial Tissue Characterization: An Approach Based on Quantitative Backscatter and Attenuation," *Proc. IEEE Ultrasonics Symposium*, vol. 83 CH 1947-1, pp. 782-793, (1983).

16. M. O'Donnell, D. Bauwens, J.W. Mimbs, and J.G. Miller, "Broadband Integrated Backscatter: An Approach to Spatially Localized Tissue Characterization In Vivo," *Proc. IEEE Ultrasonics Symposium*, vol. 79 CH 1482-9, pp. 175-178, (1979).

17. J.S. Heyman, "Phase Insensitive Acoustoelectric Transducers," *J. Acoust. Soc. Am.*, vol. 64, pp. 243-249, 1978.

18. L.J. Busse and J.G. Miller, "Detection of Spatially Nonuniform Ultrasonic Radiation with Phase Sensitive (Piezoelectric) and Phase Insensitive (Acoustoelectric) Receivers," *J. Acoust. Soc. Am.*, vol. 70, pp. 1377-1386, (1981).

19. L.J. Busse and J.G. Miller, "A Comparison of Finite Aperture Phase Sensitive and Phase Insensitive Detection in the Near Field of Inhomogeneous Material," *Proc. IEEE Ultrasonics Symposium*, vol. 81 CH 1689-9, pp. 617-626, (1981).

20. L.J. Busse and J.G. Miller, "Response Characteristics of a Finite Aperture, Phase Insensitive Ultrasonic Receiver Based Upon the Acoustoelectric Effect," *J. Acoust. Soc. Am.*, vol. 70, pp. 1370-1376, (1981).

CHARACTERIZATION OF POROSITY IN GRAPHITE/EPOXY COMPOSITE LAMINATES WITH POLAR BACKSCATTER AND FREQUENCY DEPENDENT ATTENUATION

S.M. Handley*, M.S. Hughes*, J.G. Miller*, and E.I. Madaras**

Physics Dept., Washington University*, St. Louis MO 63130 and
NASA Langley Research Center**, Hampton VA 23665

ABSTRACT: Five uniaxial graphite/epoxy composites with 1% to 8% volume fraction of solid glass inclusions to model "porosity" were investigated using two complementary techniques. For the polar backscatter method, samples were insonified at a polar angle of 30° and an azimuthal angle centered at 0° with respect to the fiber orientation. For each specimen data were acquired at 121 sites by translating the sample over an 11 by 11 grid in 2 mm steps. At each site the azimuthal angle was varied in 5° steps from -10° to 10° and the resulting spectra were averaged in order to remove background variations not attributable to porosity. Integrated polar backscatter was obtained by averaging over the useful bandwidth and correlated with the volume fraction of "porosity" (R = 0.96). For the frequency dependent attenuation method, data were acquired at 441 sites on a 21 by 21 grid in 1 mm steps. Signal loss relative to a water-only path was obtained as a function of frequency using log spectral subtraction. The normalized data were analyzed by performing a two-parameter polynomial fit about the center of the useful bandwidth. The rate of increase with frequency of excess attenuation exhibited a good correlation with the volume fraction of "porosity" (R = 0.98).

I. INTRODUCTION

The goal of this research was to evaluate two complementary ultrasonic techniques for characterizing porosity in fiber-reinforced composite laminates. Five uniaxial graphite-fiber/epoxy-matrix composites having a range of 1% to 8% volume fraction of solid glass inclusions to model porosity were investigated. In one technique, signal loss was measured in transmission mode and the slope of attenuation, obtained from the first order coefficient of a two parameter polynomial fit about the center frequency of the useful bandwidth, was used as the ultrasonic parameter to characterize the "porosity". The results of these transmission mode measurements displayed a good correlation between the volume fraction of "porosity" and the slope of attenuation. Integrated polar backscatter was used as a second ultrasonic parameter for the characterization of the "porosity" in these samples. A single transducer insonified the samples and measured the resulting backscatter at a polar angle of 30° with respect to the normal of the sample surface with the azimuthal angles centered at 0° with respect to the fiber orientation (i.e., along the fibers). Integrated polar backscatter also displayed a good correlation with the volume fraction of "porosity".

II. EXPERIMENTAL METHODS

A. SAMPLE PREPARATION

The effects of porosity were simulated by introducing solid glass beads, having a distribution of diameters ranging from 75 to 150 microns, into a 16 ply uniaxial graphite-fiber/epoxy-matrix composite. The composite was fabricated at NASA Langley Research Center using 5208-T300 prepreg tape. Measured amounts of glass beads were introduced between the 12th and 13th layers during the lay-up of a 12 by 16 inch laminate. The beads were dusted onto circular regions 2 inches in diameter at sites on a square grid with centers 4 inches apart. The sample was autoclaved and cured in an oven using a standard cure protocol. The 12 by 16 inch sample was cut into smaller samples (approximately 3.75" by 3.75") so that each contained a single zone of "porosity" with a volume fraction of 1%, 2%, 4%, 6%, or 8%. The bleeder cloth impressions were removed by polishing the top and bottom surfaces of the samples, as suggested by Bar-Cohen.[1]

B. MEASUREMENT METHODS

1. Transmission Mode Measurements

The signal loss was measured in transmission mode with a specimen placed in the overlapping focal zones of a matched pair of 25 MHz center frequency, 0.25 inch diameter, 1 inch focal length transducers. Each sample was scanned on a 21 by 21 grid in 1 mm steps and the acquired frequency spectra were averaged to reduce the effects of spatial variations of "porosity" within each porous region.

The measurement system used for data acquisition is illustrated schematically in Figure 1. The transmitting and receiving transducers were oriented so that the insonifying beam was perpendicular to the surfaces of the sample and were aligned by viewing the received signal on a spectrum analyzer. A Metrotek MP215 wideband pulser was used to drive the transmitting transducer. The output of a MR106 wideband receiver was routed to a stepless gate and the 0.4 μsec gated signal was subsequently used as the input to the spectrum analyzer. A DEC PDP 11/73 computer was used to control

0090-5607/87/0000-0827 $1.00 © 1987 IEEE

the motor driven apparatus on a C-scan tank (in which the samples were placed for data acquisition) as well as to acquire the data from the spectrum analyzer for storage and subsequent analysis.

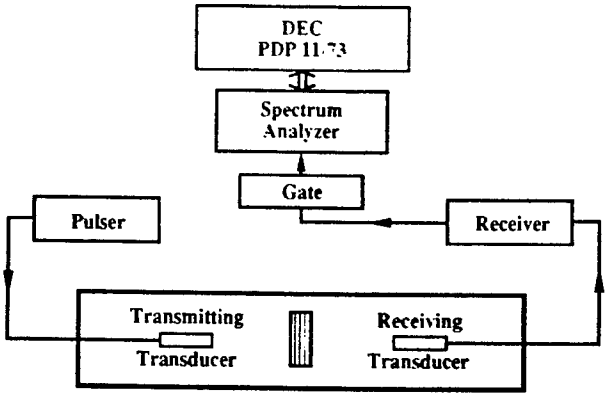

Figure 1: Block diagram of the transmission mode data acquisition system.

The signal loss through the composite laminate was obtained by normalizing the averaged acquired frequency spectrum with a calibration spectrum obtained from a water-only-path trace,

$$\text{Signal Loss} = \log[\text{calibration spectrum}] - \log[\text{sample spectrum}]. \quad (1)$$

This method of log spectral subtraction removes systematic effects arising from the electromechanical response of the transducers and front-end electronics from the sample's spectrum. The normalized data were analyzed by performing a two-parameter polynomial fit about the center frequency $\bar{f}$ of the useful bandwidth,

$$\text{Signal loss} \approx K_0 + K_1 \times (f - \bar{f}) \ , \quad (2)$$

where K_0 is an estimate of the average signal loss over the useful bandwidth and K_1 is the rate of change of the signal loss with respect to frequency. This procedure is illustrated in Figure 2, where the signal loss of a typical spectrum is plotted as a function of frequency along with the appropriate two parameter polynomial fit. The useable bandwidth of this system was 4 to 12 MHz.

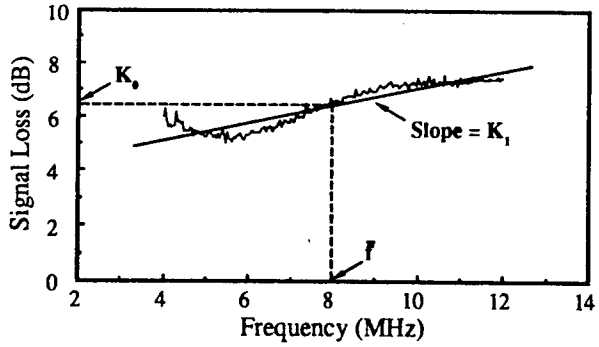

Figure 2: A typical signal loss spectrum and the corresponding two-parameter polynomial fit represented by Eq.(2).

2. Polar Backscatter Measurements

Backscatter measurements are performed with a single transducer that emits a short burst of ultrasonic energy and subsequently receives the ultrasonic signal backscattered from the specimen. In practice, the ultrasonic signal received at perpendicular incidence in the usual pulse-echo mode from a sample immersed in a coupling medium such as water is frequently dominated by the relatively uninteresting specular reflections from the front and back surfaces. In order to reveal more subtle variations in internal material properties it is useful to eliminate surface reflections. To achieve this goal the transducer was oriented at a polar angle different from zero degrees, i.e., at non-perpendicular incidence. This so-called polar backscatter approach, originally introduced by Bar-Cohen and Crane[2] and employed in several investigations reported from our laboratory,[3,4,5] eliminates the strong surface reflections from the backscattered signal. Thus the specularly reflected signal is directed away from the transducer, which then receives only signals backscattered from inhomogeneities within the volume of the specimen.

Because the composites contain systematically-oriented fibers, the strength of the backscattered signal is dependent on the azimuthal orientation of the insonifying beam when a non-zero polar angle is used. This sensitivity to specific fiber orientations may be understood in a qualitative way on the basis of the following considerations (see Figure 3). Ultrasonic backscatter from cylindrical shaped fibers is largest for azimuthal angles ϕ for which the direction of insonification is perpendicular to the longitudinal axis of the fibers. Thus, for ultrasound insonifying a planar composite laminate at a non-zero polar angle θ, backscatter arising primarily from the individual fibers can be minimized by orienting the transducer such that the insonification is approximately parallel to the fiber axis. Polar backscatter was measured using a 10 MHz center frequency, 0.5 inch diameter, 4 inch focal length transducer. Each sample was scanned by translating the specimen over an 11 by 11 grid in 2 mm steps. Backscatter measurements were performed by insonifying the samples at a polar angle of 30° with respect to the normal of the sample surface, with the azimuthal angles centered at 0° with respect to the fiber orientation. At each site the azimuthal angle (ϕ) was varied in 5° steps from -10° to +10° and the resulting backscatter spectra averaged over site and azimuthal angle in order to minimize background variations not attributable to porosity.

Data were collected over the frequency range 4 to 12 MHz in 0.25 MHz steps using the system shown in Figure 3. Backscatter was measured quantitatively using a generalized substitution technique. The power spectrum of the backscattered signal was obtained using an analog spectrum analyzer This power spectrum was then normalized to the power spectrum obtained in a second (calibration) measurement in which the specimen was replaced by a nearly perfect (flat stainless

steel) ultrasonic reflector. The result of this normalization, the backscatter transfer function, is independent of the electromechanical efficiency of the transducer and the properties of the system electronics. The backscatter transfer function is a relative measure of the backscattering efficiency at a specified frequency.[6,7] The frequency average of the backscatter transfer function, termed the integrated backscatter, provides a useful index of backscatter efficiency over a finite bandwidth.[8] Frequency averaging over a broad bandwidth reduces the degrading influence of phase cancellation and other interference effects which can compromise the results of backscatter measurements. The integrated backscatter over the range 4 to 12 MHz is used as the basis for the quantitative backscatter correlation plots presented in the Section III of this manuscript.

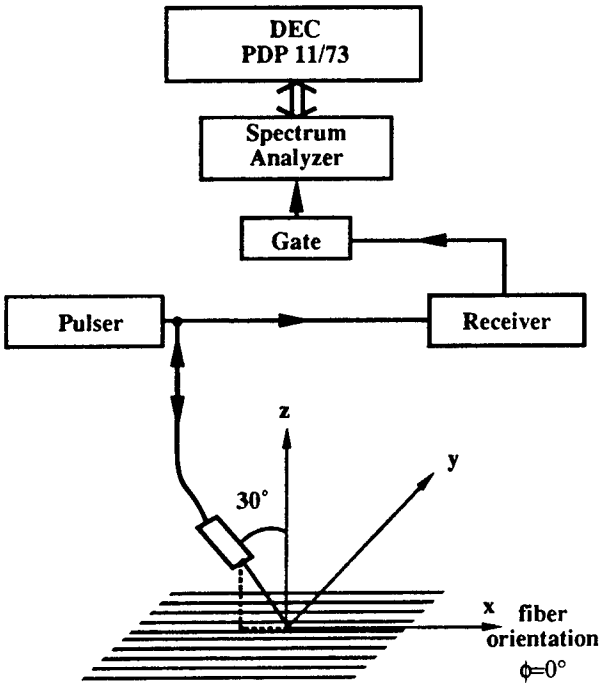

Figure 3: Block diagram of the polar backscatter mode data acquisition system.

III. RESULTS

A. TRANSMISSION MODE MEASUREMENTS

Figure 4 displays the signal loss spectra and corresponding two-parameter polynomial fit for the samples with the minimum and maximum values of volume fraction of "porosity", 1% and 8%. The slope of the fit for the 8% sample is significantly larger than that for the 1% sample. It is this change in slope as a function of volume fraction that is used as the ultrasonic parameter to characterize the "porosity".

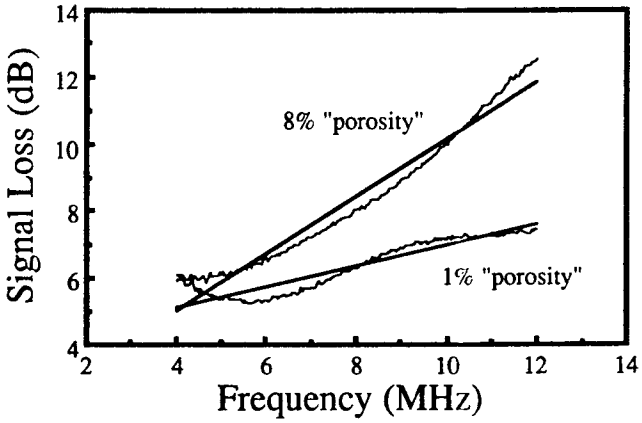

Figure 4: Spectra and corresponding two-parameter polynomial fits for 1% and 8% "porosity" samples plotted as functions of frequency.

The results of the transmission mode measurements for each of the five samples are displayed on a scatter plot in Figure 5. The vertical axis represents K_1, the first order coefficient of the two parameter polynomial fit (or the rate of increase of attenuation with respect to frequency), and the horizontal axis the volume fraction of "porosity". A clear trend exists between the slope of attenuation and the volume fraction of "porosity" as indicated in the figure. A linear least-squares fit performed on the data from this scatter plot yields a correlation coefficient of R = 0.98.

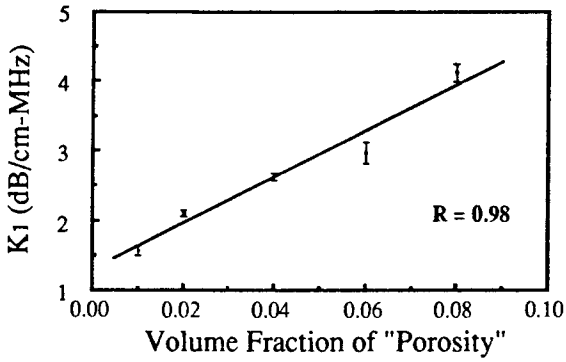

Figure 5: Correlation plot between the slope of attenuation and volume fraction of "porosity".

B. POLAR BACKSCATTER MODE MEASUREMENTS

The results of the reflection mode measurements for each of the five samples investigated in the present study are displayed on a scatter plot in Figure 6. The vertical axis represents the integrated polar backscatter and the horizontal axis represents the volume fraction of "porosity". A correlation coefficient of R = 0.96 was obtained by performing a linear least-squares fit to the data.

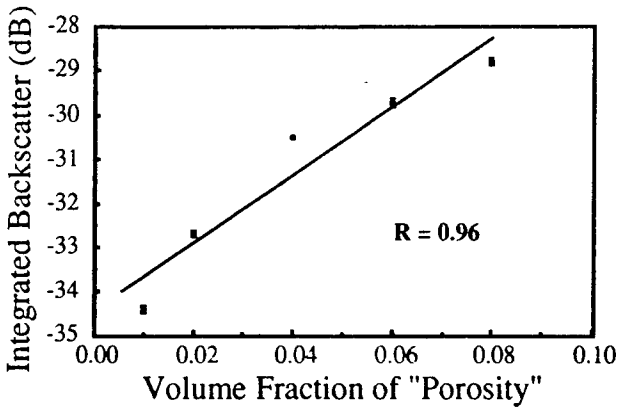

Figure 6: Correlation plot between the integrated polar backscatter and volume fraction of "porosity".

In summary, both the rate of increase with frequency of attenuation and integrated polar backscatter exhibited a good correlation (R > 0.9) with the volume fraction of "porosity". Attenuation based techniques are most readily applied under circumstances in which access to both sides of the specimen is feasible, whereas backscatter techniques lend themselves to measurements limited to single surface access. Results of these investigations suggest the potential value of these techniques for the nondestructive characterization of porosity in graphite/epoxy composites.

ACKNOWLEDGEMENTS

Portions of this work were supported by NASA grant NSG 1601 and NGT 26010800.

References

1. Yoseph Bar-Cohen, *Nondestructive Characterization of Defects in Multilayered Media Using Ultrasonic Backscattering*, McDonnell-Douglas Corp., 1987. Douglas Paper 7781. Unpublished.
2. Y. Bar-Cohen and R.L. Crane, "Acoustic-Backscattering Imaging of Subcritical Flaws in Composites," *Materials Evaluation*, vol. 40, pp. 970-975, 1982.
3. Lewis J. Thomas III, Eric I. Madaras, and J.G. Miller, "Two-Dimensional Imaging of Selected Ply Orientations in Quasi-Isotropic Composite Laminates Using Polar Backscattering," *Proc. 1982 IEEE Ultrasonics Symposium*, pp. 965-970, 1982. (IEEE Cat. No. 82 CH 1823-4).
4. Earl D. Blodgett, Lewis J. Thomas III, and J.G. Miller, "Effects of Porosity on Polar Backscatter From Fiber Reinforced Composites," *Review of Progress in Quantitative Nondestructive Evaluation*, vol. 5B, pp. 1267-1274, 1986.
5. Earl D. Blodgett, S.M. Freeman, and J.G. Miller, "Correlation of Ultrasonic Polar Backscatter With the Deply Technique for Assessment of Impact Damage in Composite Laminates," *Review of Progress in Quantitative Nondestructive Evaluation*, vol. 5B, pp. 1227-1238, 1986.
6. M. O'Donnell and J.G. Miller, "Quantitative Broadband Ultrasonic Backscatter: An Approach to Non-Destructive Evaluation in Acoustically Inhomogeneous Materials," *J. Appl. Phys.*, vol. 52, pp. 1056-1065, 1981.
7. J.G. Miller, J.E. Perez, Jack G. Mottley, Eric I. Madaras, Patrick H. Johnston, Earl D. Blodgett, Lewis J. Thomas III, and B.E. Sobel, "Myocardial Tissue Characterization: An Approach Based on Quantitative Backscatter and Attenuation," *Proc. 1983 IEEE Ultrasonics Symposium*, pp. 782-793, 1983. (IEEE Cat. No. 83 CH 1947-1).
8. M. O'Donnell, D. Bauwens, J.W. Mimbs, and J.G. Miller, "Broadband Integrated Backscatter: An Approach to Spatially Localized Tissue Characterization In Vivo," *Proc. 1979 IEEE Ultrasonics Symposium*, pp. 175-178, 1979. (IEEE Cat. No. 79 CH 1482-9).

Tensile Stress Acoustic Constants of Unidirectional Graphite/Epoxy Composites

W. H. PROSSER
NASA Langley Research Center
M. S. 231
Hampton, VA 23665-5225
(804) 865-3036

ABSTRACT

Previously, the stress acoustic constants (SAC's) of unidirectional graphite/epoxy composites were measured to determine the nonlinear moduli of this material. These measurements were made under compressive loading in order to obtain the sufficient number of values needed to calculate these moduli. However, because their strength in tension along fiber directions can be several times greater, most composites are used under tensile loading. Thus, it is important to characterize the nonlinear properties of these materials in tension as well.

The SAC's which are defined as the slope of the normalized change in ultrasonic "natural" velocity as a function of stress were measured in a unidirectional laminate of T300/5208 graphite/epoxy. Tensile load was applied along the fiber axis with the ultrasonic waves propagating perpendicular to the fiber direction. Changes in velocity were measured using a pulsed phase locked loop ultrasonic interferometer with the nominal frequency of the ultrasonic waves being 2.25 MHz.

INTRODUCTION

The stress acoustic constant (SAC) as defined by Heyman [1] and Cantrell [2] provides a measure of a mixture of second and third order elastic coefficients. This parameter thus provides information about the nonlinear elasticity of a material which is useful in understanding interatomic bonding forces in crystalline solids. The SAC also is needed in ultrasonic evaluation of applied and residual stresses in a material. Additionally, investigations have established a possible relationship between the SAC and ultimate strength in aluminum [3] and carbon steel [1].

Previous measurement of SAC's in composites were made under compressive stress [4]. Compression was used so that measurements could be made with the stress direction other than along the fiber direction without premature failure of the sample. These measurements were necessary to actually calculate the third order elastic moduli.

However, since composites are most often used under tensile loading because of their high tensile strength along fiber directions, it is important to evaluate their properties under this mode of loading. In this research, the SAC's for longitudinal and shear waves propagating perpendicular to the fiber direction were measured while tensile stress was applied in the direction of the fibers.

THEORY

The "natural" ultrasonic velocity (W) was defined by Thurston and Brugger [5] as the velocity referred to the unstressed or natural state. It is given by

$$W = \frac{L_0}{t} , \tag{1}$$

where L_0 is the specimen length in the unstressed state and t is the time of flight of the ultrasonic wave. Since L_0 is a constant, the normalized change in "natural" velocity with respect to stress is given by

$$\frac{\Delta W}{W} = - \frac{\Delta t}{t} . \tag{2}$$

The stress acoustic constant (H) is then given by

$$H = \frac{\frac{\Delta W}{W}}{\Delta \sigma} , \tag{3}$$

where σ is the applied stress.

Measurements of this quantity were made using a pulsed phase locked loop (P2L2) ultrasonic interferometer developed by Heyman [6]. The basis of this instrument, shown schematically in Figure 1, is a voltage controlled oscillator (VCO). A portion of the signal from the VCO is gated into a tone burst to excite the ultrasonic transducer. The received echo signal from the transducer is phase compared with the signal from the VCO at a preselected phase point using an electronic sample and hold device. The sampled voltage is then used to drive the VCO to a condition of quadrature. This causes the acoustic phase shift (θ), given by

$$\theta = 2\pi f t , \tag{4}$$

where f is the frequency, to be maintained as a constant. It can then be shown that

$$\frac{\Delta \theta}{\theta} = 0 = \frac{\Delta f}{f} + \frac{\Delta t}{t} \tag{5}$$

and thus,

$$\frac{\Delta f}{f} = -\frac{\Delta t}{t} = \frac{\Delta W}{W} . \tag{6}$$

Therefore, by monitoring the normalized change of frequency of the P2L2,the normalized change in "natural" velocity is determined which is used to calculated the SAC.

EXPERIMENT

A tensile specimen was cut from a 50 ply unidirectional laminate of graphite/epoxy with nominal dimensions of 28 cm. along the fiber direction (x_3), 0.66 cm. in the laminae stacking direction (x_1), and 2.5 cm. in the remaining orthogonal direction (x_2). The original laminate had been previously C-scanned for defects and none were found to be present. The cross sectional area used for stress calculations was that measured at the center of the specimen where the transducer was attached and had a value of 1.677 +/- 0.004 cm^2. Load was ramped in tension along the fiber direction to a maximum stress value of approximately 330 MPa at a rate of approximately 400 MPa/min.

The acoustic measurements were made using commercial damped 2.25 MHz transducers. A frequency counter monitored the frequency of the P2L2 which was recorded by a computer which also read voltage values from the load cell. The frequency and load voltage were measured at one second intervals during the load ramp. Following the ramp to maximum stress and return to zero, the stress and normalized frequency shifts were plotted and stored. Since the curves exhibited nonlinear (quadratic) behavior, they were fitted using a quadratic least squares routine. A block diagram of the apparatus used is shown in Figure 2.

Since variations in natural velocity are sensitive to temperature changes as well as stress, the sample was insulated during the test in an attempt to maintain a constant temperature. Following any disturbance of the sample and transducer, approximately thirty minutes was allowed to settle the temperature to equilibrium. Also, to determine the effects of bond thickness variations which sometimes can be significant in these measurements, each SAC measurement was repeated at least nine times with the transducer removed and rebonded every third measurement.

The shear wave SAC measurements were completed with transverse mode acoustic waves propagating along the x_1 direction. The direction of polarization was either along the fiber direction in which case the measurement was designated H_{313} or along the x_2 direction and designated H_{312}. The data from the measurement of H_{313} is displayed in Figure 3. The measured points for all nine measurements are shown with the quadratic least squares fit displayed as the solid line. The quadratic fit parameters are shown in Table 1 along with the value measured under compressive loading. The values for the compressive SAC's for comparison are the negative of those presented in [4]. This is to account for the fact that in both tests the stress was taken to be positive. The data from this measurement was the most reproducible which is to be expected as it is the one in which the largest frequency change occurs.

Measurements of H_{312} are shown in Figure 4 with the fitted parameters again displayed in Table 1. The data for this measurement were not as reproducible as shown by the scatter in the graph. The majority of the measurements were within good agreement. However, three of the measurements which were taken in sequence following rebonding of the transducer did not exactly follow the trend. This may indicate that there was a bond irregularity such as dust contamination in these three measurements.

Longitudinal SAC measurements were made with the waves propagating

along the laminate stacking direction (x_1) with the polarization in the same direction. These measurements were designated H_{311} and the data is presented in Figure 5. The fit parameters are shown in Table 1. These measurements showed the worst reproducibility due to the small frequency shifts exhibited. Again bonding variations contributed to the scatter in the data.

DISCUSSION

Although the tensile SAC values of unidirectional graphite/epoxy do not agree with those made under compression to within experimental uncertainty, in each case the values were of the correct sign and agree to within an order of magnitude. There are a number of possible causes to explain the discrepancy between the tensile and compressive SAC values. It may be due to sample to sample variation in material properties as the specimen for each test were cut from different laminates. The difference in specimen geometry needed in an attempt to obtain pure tensile or compressive loading and the difference in the method of applying the load may also account for some of the discrepancy. It may also be due to differences in the material behavior under compressive and tensile loading. Further experimentation with a large number of specimen cut from the same and different laminates is needed to separate out these effects.

Another difference in the tensile measurements is the much higher stress levels applied during the test. Because of the greater tensile strength, these tests were carried out to higher loads without damaging the specimen. Higher order elastic nonlinearities were manifested at these higher stresses by the nonlinearity of the measured curves. This caused the need for using a quadratic fit to determine the SAC values but should not contribute to the discrepancy between compressive and tensile values.

CONCLUSIONS

This study provides the first measurements of tensile SAC's in unidirectional graphite/epoxy composite materials thus yielding further information on the mechanical behavior of fiber reinforced composite materials. These measurements may be useful in developing nondestructive techniques to monitor applied and residual stresses in composites. They may also be helpful in nondestructively determining other important engineering properties such as ultimate strength and fiber-matrix interfacial properties.

REFERENCES

1. Heyman, J. S., Allison, S. G., and Salama, K. IEEE Ultrasonics Symposium, 991-994 (1983).
2. Cantrell, J. H., Jr. J. of Testing and Evaluation, 10:223-229 (1982).
3. Heyman, J. S., and Chern, E. J. IEEE Ultrasonics Symposium, 936-939 (1981).
4. Prosser, W. H. NASA Contractor Report 4100 (1987).

5. Thurston, R. N., and Brugger, K. Physical Review, 133:A1604-A1610 (1966).
6. Heyman, J. S. NASA Patent Disclosure LAR 12772-1, (1980).

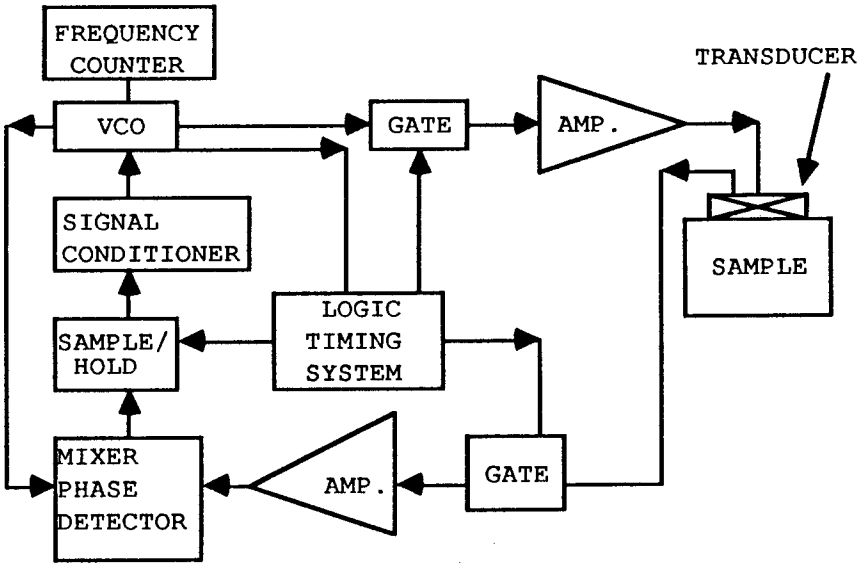

Fig. 1. Block diagram of the pulsed phase locked loop ultrasonic interferometer.

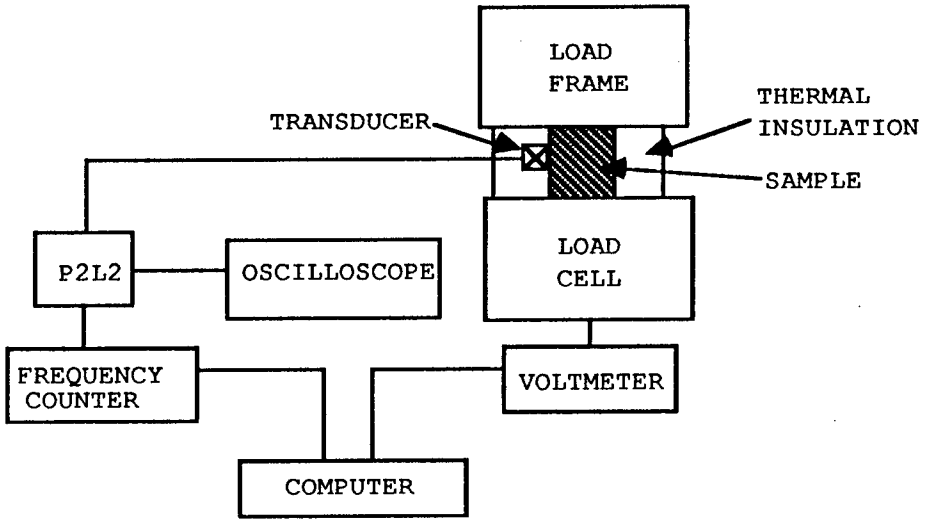

Fig. 2. Block diagram of stress acoustic constant measurement apparatus.

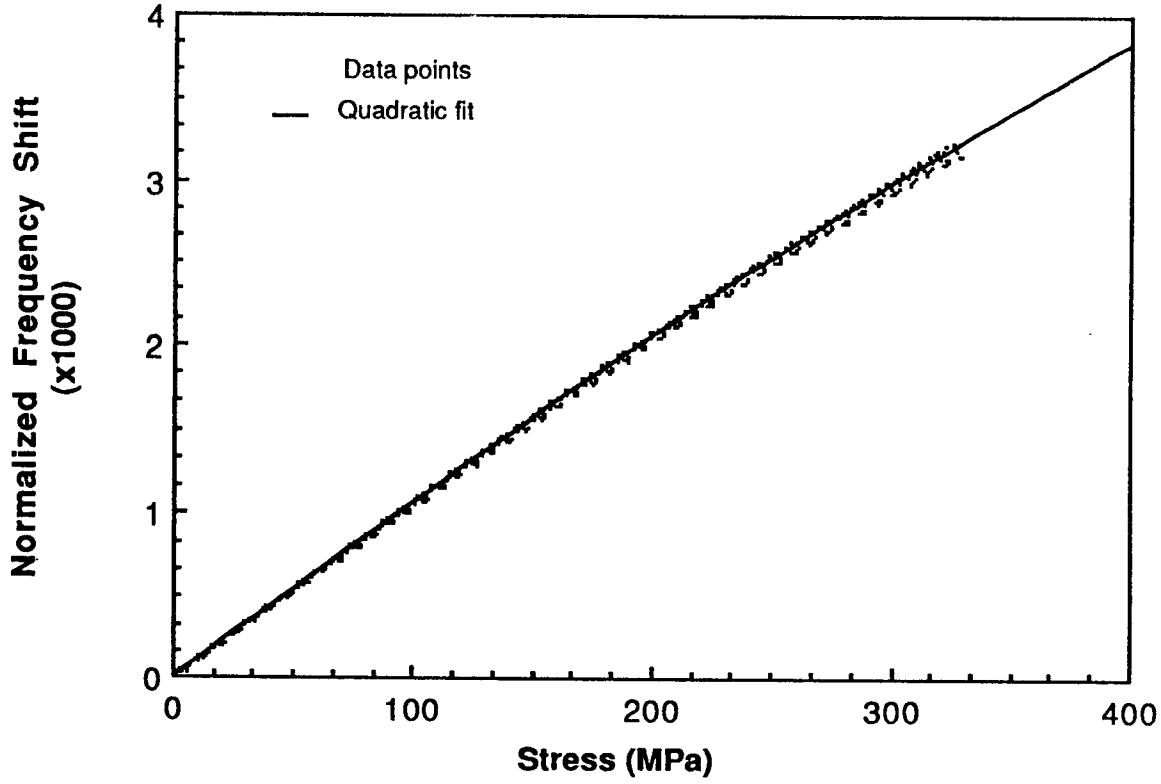

Fig. 3 H_{313} SAC measurement

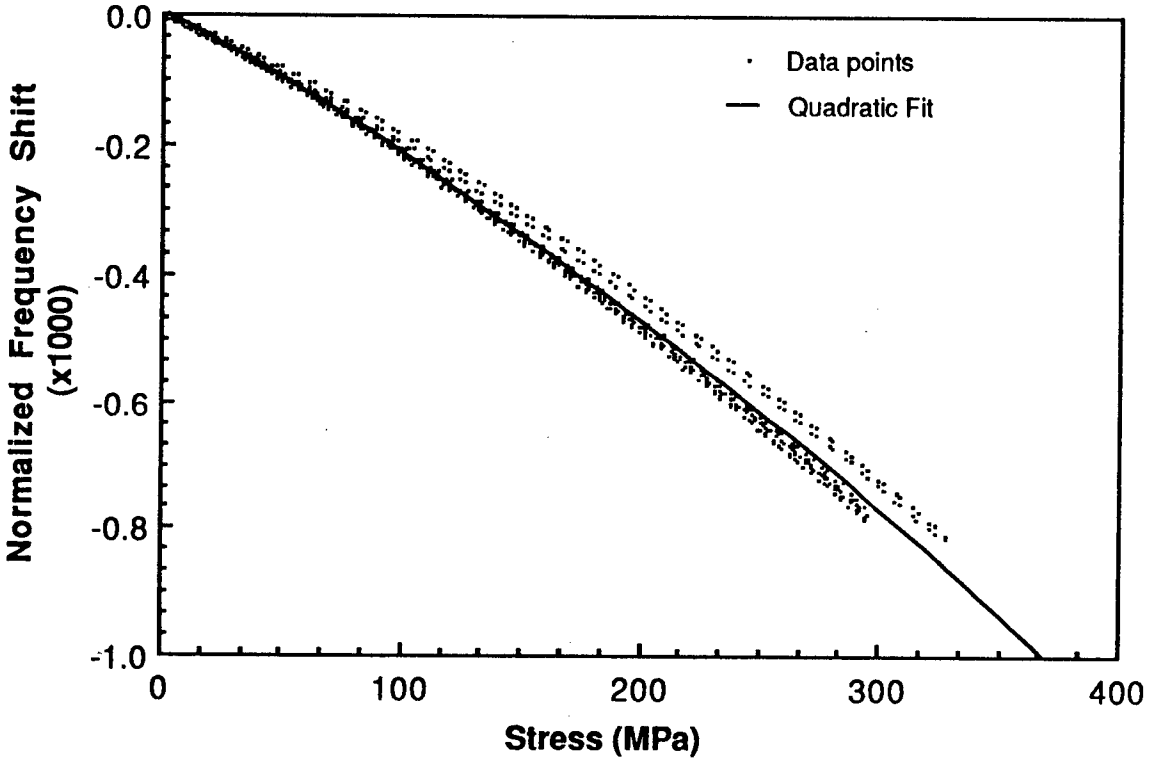

Fig. 4 H_{312} SAC measurements

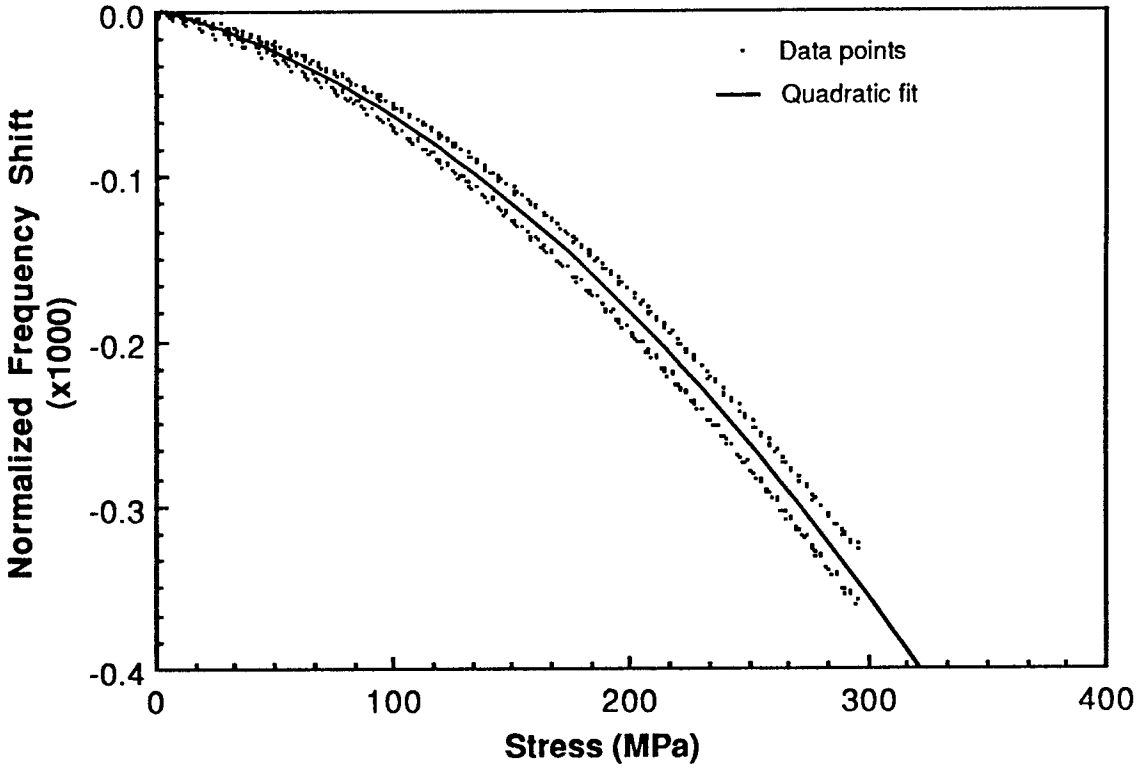

Fig. 5 H_{311} SAC measurements

Table 1

	Quadratic Coef. (Pa^{-2})	Y-intercept	Tensile SAC (Linear Coef.) ($\times 10^{-12}$ Pa^{-1})	Compressive SAC [4] ($\times 10^{-12}$ Pa^{-1})
H_{313}	-3.5×10^{-21}	-2.5×10^{-6}	10.99 +/- 0.01	9.2 +/- 0.3
H_{312}	-2.1×10^{-21}	4.6×10^{-6}	-2.0 +/- 0.1	-2.8 +/- 0.1
H_{311}	-2.7×10^{-21}	1.7×10^{-6}	-0.39 +/- 0.07	-1.23 +/- 0.01

SURFACE GENERATION AND DETECTION OF COUPLED FIBER-MATRIX MODE ACOUSTIC WAVE PROPAGATION IN FIBER-REINFORCED COMPOSITES

W. T. Yost and John H. Cantrell

NASA-Langley Research Center

Hampton, Va. 23665

INTRODUCTION

A problem of great practical importance to the aero-space industry is the NDE of composite structures. Specifically, it would be advantageous to locate damage sites and to quantitatively investigate the extent of damage at these sites through various NDE techniques. A particular technique would be more useful if the appropriate measurements could be completed from one side of the material in question. For ultrasonics methods this means the launching and receiving of a wave from the same surface. It would also be useful if the technique possessed relatively simple circuitry requirements for the measurements.

This presentation deals with a technique to transmit and receive bulk ultrasonic waves launched from the surface of a composite sheet by means of transducers mounted on variable angle blocks. The wave propagation vector is along the direction of the fibers. A straightforward approach to measure velocity and attenuation of this wave is presented. Moreover, preliminary data suggests that such a wave is sensitive to impact damage.

Launching and Receiving of Bulk Waves

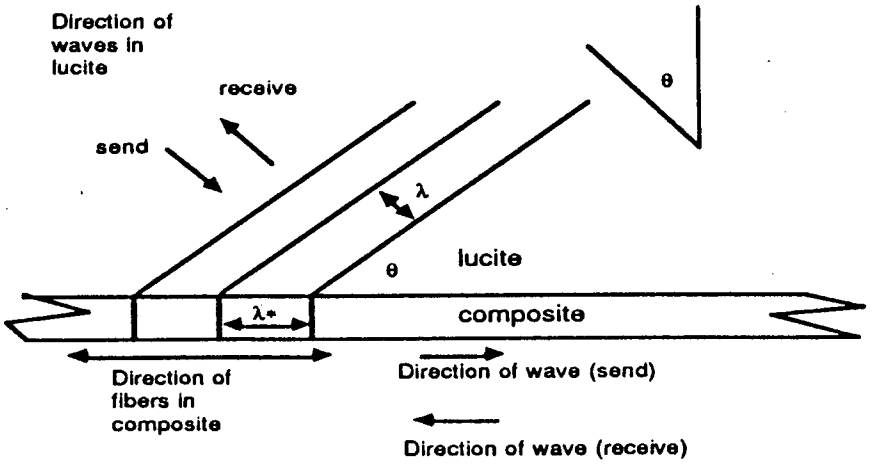

Fig. 1 Launching And Receiving The Wave

Figure 1 shows schematically the launching and receiving of bulk ultrasonic compressional waves. A block of lucite is placed on the surface of the composite. Consider a compressional wave in lucite whose longitudinal velocity is v_{lucite} and whose propagation vector is at an angle θ to the normal of the surface . Assume that a wave propagating in the direction of the fibers of the composite has a velocity of v*. If Snell's Law is satisfied ($\sin \theta = v_{lucite}/v^*$), then as the wave in the lucite impinges on the interface between the lucite and the composite, the bulk wave in the composite is generated. Neglecting any time delay to traverse the sample thickness (i.e. a consequence of the long wavelength approximation) this wave is launched in the composite material with wave fronts perpendicular to the surface.

Similarly, as the bulk wave, propagating in the direction of the fibers in the composite, arrives at the receiving lucite-composite interface, a compressional wave will be generated in the lucite at the interface. The angle between its propagation vector and the normal to the interface is also given by Snell's Law.

EXPERIMENTAL DETAILS

Samples

All samples used in this study were prepared from an 8-ply unidirectional composite sheet made from T-300 fibers in 5208 epoxy. Most of the measurements presented here were taken on a long section of the sheet of dimensions 122.9cm. by 9.5cm. The top surface used for the measurements was a smooth surface, whereas the bottom surface had a woven texture inpression. Neglecting effects of this texture on the thickness measurement, the thickness of the sample material is 3.00 ± .03 mm.

Equipment Arrangement

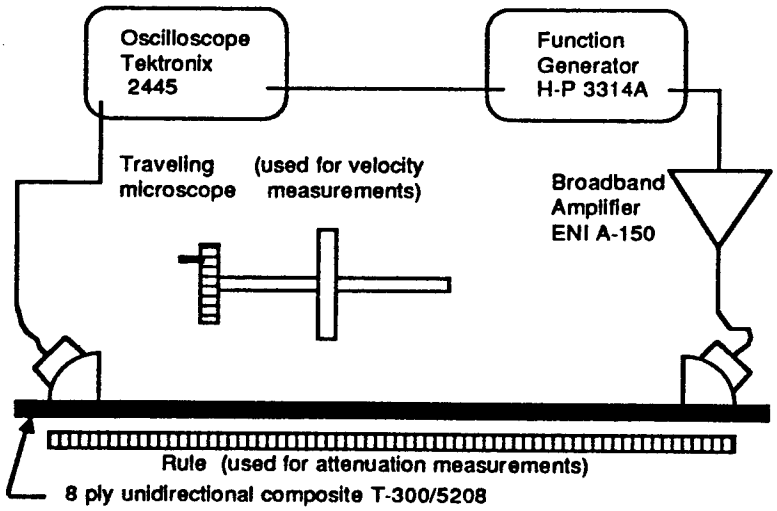

Fig.2 Equipment Arrangement for Velocity and Attenuation Measurements

Figure 2 shows the basic layout for the velocity and attenuation measurements. A Hewlett-Packard model 3314A function generator was used to form the tone-burst, which was amplified by a ENI model A-150 broadband amplifier. The amplified signal was sent to a broadband 1 MHz. transducer

(1/2 in. by 1/2 in. cross section) bonded to a variable angle block with light machine oil and mechanically fastened to it. Both the transducer and the variable angle block were manufactured by Harisonics Laboratories. A transducer-variable angle block (T-VAB) system, identical to the system used to launch the wave, is used as a receiver. The angles in both blocks were adjusted for maximum amplitude of the received signal. The value of the angle is approximately 18^{o} to the vertical. The output from the receive T-VAB was connected to a Tektronix 2445 oscilloscope to measure the amplitudes and the timing. Synchronization was obtained from the function generator. During a series of measurements the voltage amplitude from the function generator was fixed.

Measurement Details

Direct Method

A direct method was employed to measure velocity and attenuation. Measurements were taken by noting the changes in time (T_2-T_1) and in received signal amplitudes (A_2/A_1) ,as the distance between the send and receive T-VAB's were varied (d_2-d_1). The velocity and attenuation of the acoustic wave were calculated using the following:

$$v= (d_2-d_1)/(t_2-t_1)$$

$$\alpha= (20\cdot \log(A_2/A_1))/(d_2-d_1)$$

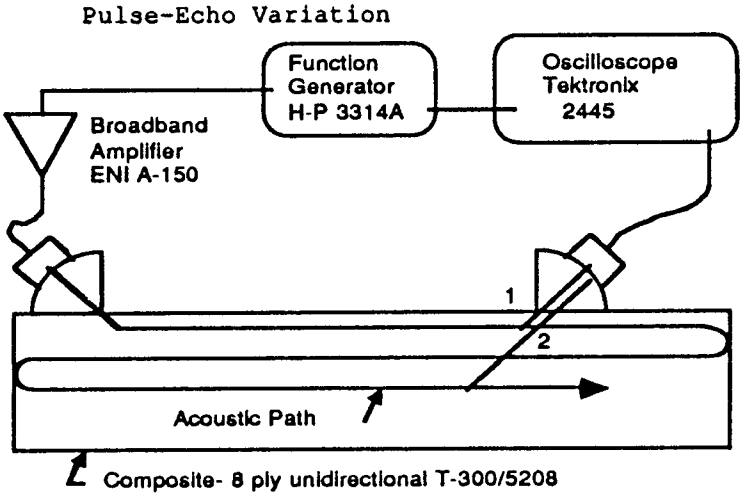

Fig.3 Equipment Arrangement for Pulse-Echo Velocity Measurements

A variation of the pulse-echo method was also used to measure the velocity, as shown in figure 3. In this case, the receive T-VAB system picks up the signals; from the first pass (1) of the wave along the fibers, and its echo (2), following its reflection from first one end and then the other end of the sample. In this case the distance traveled by the acoustic tone burst between the receptions is twice the sample length. The time difference (T_2-T_1) was determined. The distance (d_2-d_1) was set to twice the length of the sample. Again the calculations were made, using the above velocity formula.

Distances, Amplitudes, and Time Intervals

The distance measurements for the velocity determination using the direct method were made with a Gaertner model M1180-303 traveling microscope. The measurements were taken at 1 cm intervals for a total path change of 7 cm. The uncertainty in these length measurements due to the traveling microscope is 0.001mm.

The distance measurements for the attenuation determination and the modified pulse-echo method were made with a millimeter scale inscribed on a stainless steel rule. This was also used to measure the length of the sample.The uncertainty in these length measurements is estimated to be 0.2mm.

The amplitude and time measurements were made with the cursor system on a Tektronix model 2445 oscilloscope . The uncertainty of the time measurements is estimated to be 0.8% and the amplitude uncertainty is estimated to be 2%

Bonds and Alignment

In all cases the bond between the T-VAB receive assembly and the sample was made with a light machine oil. For the velocity measurements the transmit T-VAB was bonded to the sample surface with machine oil. However, the T-VAB transmit assembly used a different bonding material for attenuation measurements. Ethyl alcohol was used because of the rapid evaporation of the excess whenever the transmit T-VAB was moved. Within the accuracy of the measurement system the bonds gave reproduceable results. The region between the T-VABs was kept clean and dry. Alignment of the transducers was assured by placing the appropriate side of the T-VABs against a straight edge aligned in the direction of the fibers.

RESULTS

The results of the measurements are summarized in Table 1.

Table 1 Measured Values of Velocity and Attenuation at 1 MHz.

Velocity at 1 MHz.

Variable Pathlength Technique	**$9.30 \pm .03 \times 10^5$ cm/sec**
Pulse-Echo Technique	**$9.28 \pm .074 \times 10^5$ cm/sec**

Attenuation at 1 MHz.

Variable Pathlength Technique	**$0.098 \pm .003$ dB/cm**

Velocity

Using the direct method as outlined above, a typical velocity data set was taken by moving the send T-VAB unit in increments of 1.000 cm over a 7 cm interval, as outlined above, and measuring the corresponding increments of time. A mean value and a standard deviation were calculated for each set. The deviation given in the table represents the standard deviation of the actual data. The systematic uncertainty is estimated to be less than $\pm 0.07 \times 10^5$ cm/sec where the major source is the timing measurement uncertainty.

The modified pulse-echo method was also used to determine the velocity, as outlined above. The time between echoes and the sample length were measured. The velocity was calculated. Its value is given in Table 1. The systematic uncertainty is estimated to be less than $\pm 0.07 \times 10^5$ cm/sec, which is the value listed in Table 1.

Attenuation

The attenuation was measured using the direct method as outlined above. The distance between the send T-VAB and the receive T-VAB was changed in 5 cm increments over a distance of 45 cm. The region between the transducers was kept clean and dry. At each location the amplitude of the received signal was measured and recorded. The attenuation was calculated . Its value is listed in Table 1. The uncertainty listed by the value is the standard deviation of the measurements. The systematic uncertainty is estimated to be ±0.017 dB/cm. Because of the unusual geometry and the high attenuation of acoustic signals perpendicular to the fiber direction, no diffraction correction was attempted.

DISCUSSION

The results presented here indicate that a 1 MHz acoustic wave of low attenuation can easily be launched and received when its propagation constant is parallel to the fiber direction of an 8-ply unidirectional T-300/5208 carbon fiber composite. These results were obtained by using variable angle blocks with damped transducers to launch and receive the waves. We believe this wave to be that of a coupled fiber-matrix mode, with an effective modulus calculated from the method of mixtures. Preliminary calculations indicate that the velocity obtained from such an assumption is consistent with the experimental results, and will be the subject of a follow-up report.

Efforts were made to ascertain if the wave were possibly associated with other sources - for example a plate mode or a surface wave. A stainless steel plate of thickness 0.95 cm and length 14.3cm was bonded to the smooth side of the specimen with a light machine oil. The velocity of the measured wave was unchanged. This strongly indicates that the wave is not a plate or surface wave, and reinforces the coupled fiber-matrix bulk wave hypothesis.

CONCLUSIONS

By using transducers mounted on variable angle blocks, it is possible to launch and receive a bulk compressional wave in an 8-ply unidirectional composite. The wave launched and received in this manner has a velocity of 9.3×10^5 cm/sec. The attenuation of the wave has a value of 0.098 dB/cm at room temperature.

The equipment demands required for these measurements are simple and the set-ups are straightforward. It is important to note that the precision of the technique is sufficient to detect variation within a sample, especially in the attenuation measurements.

We do not believe that this wave is associated with a plate mode, nor is it likely to be a surface wave, since bonding the sample to the stainless steel plate did not affect the velocity. Preliminary calculations indicate that the wave is a coupled fiber-matrix mode with the method of mixtures giving the appropriate modulus. Additional research to check this is underway.

Preliminary results also indicate that parameters associated with this wave might be sensitive to accumulated damage in composites. Moreover, the wave can be launched and received from the same side of the composite with the transducers set at the appropriate angle. We think that further exploration of this technique is highly worthwhile, since this has a potential for NDE in composite materials and structures made from composites.

DETECTION OF FIBER DAMAGE IN A GRAPHITE EPOXY COMPOSITE USING CURRENT INJECTION AND MAGNETIC FIELD MAPPING

Travis N. Blalock and William T. Yost

NASA-Langley Research Center
Mail Stop 231
Hampton, VA 23665

INTRODUCTION

Graphite-epoxy composites are a class of composite materials finding increased use in many of today's more demanding aerospace applications. As with any material used in such applications, there is a great need for quantitative non-destructive evaluation to insure safe operation of the host vehicle. Conventional NDE techniques (techniques developed for homogeneous metals) are inadequate in that their results are difficult to interpret when applied to inhomogeneous composite materials. The work described here has been developed specifically for examination of fiber states in composite materials.

The technique to be described here involves injecting electric current along the graphite fibers of a composite and measuring the resulting magnetic fields. In areas of fiber damage, there will be disruptions in current paths, detectable as perturbations in the measured magnetic field.

MEASUREMENT DESCRIPTION

Referring to figure 1, we define a coordinate frame such that the sample lies in the x-y plane with bulk electric current along the x direction. The y component of the magnetic field is measured directly above the surface of the material. The distance between the surface of the material and the magnetic field detector is z. The current is a 30 Khz oscillating current and is coupled to the fibers by clamping copper electrodes onto the edges of the sample. A conducting gel is also employed to insure good coupling between the fibers and the electrodes.

The y component of the magnetic field was measured with a magnetic audio tape head. The tape head contains an air gap toroid and offers an

excellent compromise between directional discrimination, sensitivity, and spatial resolution. The detector output signal was input to the detection circuit, shown in fig. 2.

The detection circuitry includes a high gain preamplifier, a second order bandpass filter, a synchronous detector, and a lowpass filter, in that order. The output of the detection circuit is a dc level directly proportional to the strength of the magnetic field seen across the tape head air gap. The gain of the total detection system is approximately 350 volts/gauss.

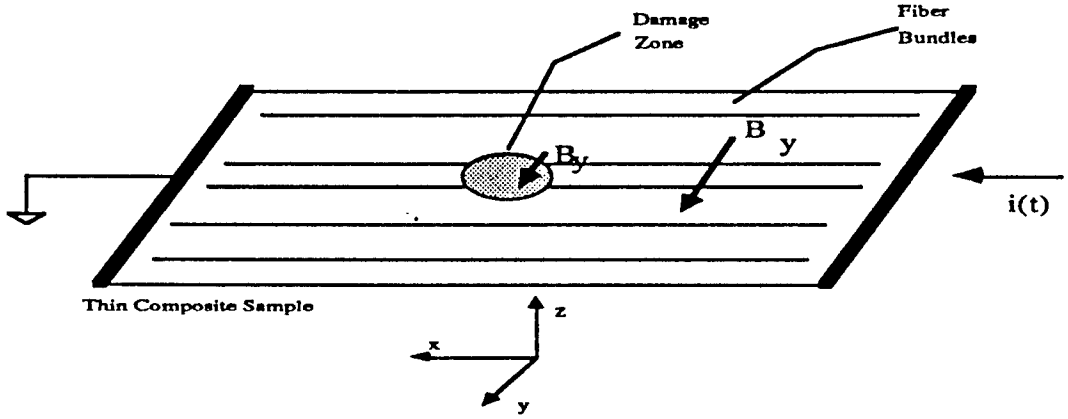

Figure 1: Simple model of measurement approach. Detection of anomalies in By leads to detection of fiber damage sites.

Two thin plates of dimensions 35 cm X 10 cm X 1.0 mm were chosen. The first was an 8 ply unidirectional T 300/5208 composite. The other was an 8 ply 0,±45,90 T-300/5208 composite. A 1/16" hole was drilled in the center of each plate to simulate a region of broken fibers.

The measurements were taken in the form of an x-y scan across the surface of the material. A block diagram of the scanning system is shown in figure 3. The 30 Khz source signal originates at the HP 3314 function generator and is amplified by an ENI 240L power amplifier. The output current of the 240L is injected into the sample at each end. An audio tape head is scanned across the surface of the material under computer control. The detected signal is input to the detection circuit via a shielded cable to minimize noise. A sync signal is also input to the detection circuit so the detected signal can be synchronously demodulated for further noise reduction. The output DC level is then digitized by the system voltmeter and recorded by the VAX for each x-y point within the scan.

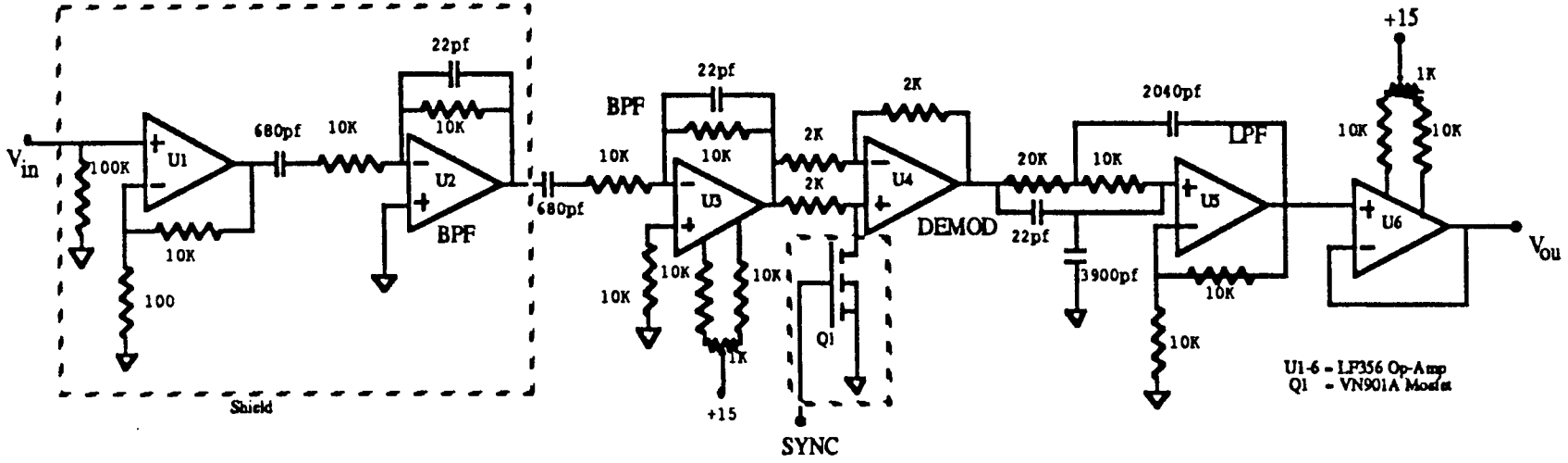

Figure 2: Detection Circuitry

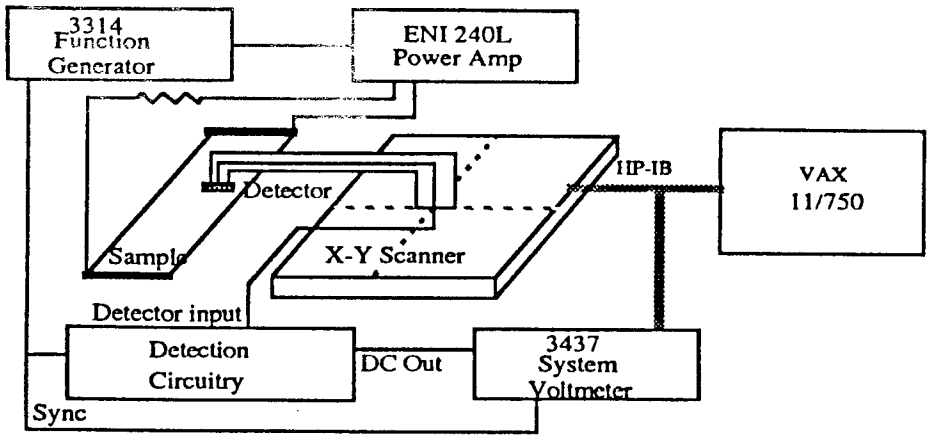

Figure 3: Experimental Setup

Figures 4 and 5 are magnetic field scans of the two samples described above. Both of the scans are 2 cm wide. The 1/16 inch hole is in the center of each image. The hole appears as a horizontal stripe in figure 4 due to the extremely low conductivity in the y direction in the unidirectional composite. The multi direction layup of the sample in figure 5, coupled with a relatively high conductivity between layers, results in a bulk conductivity in the y direction approximately 1/9 that of the conductivity in the x direction. This high conductivity in the y direction results in a current pattern that 'bleeds' around the flaw in figure 5 in a relatively short distance.

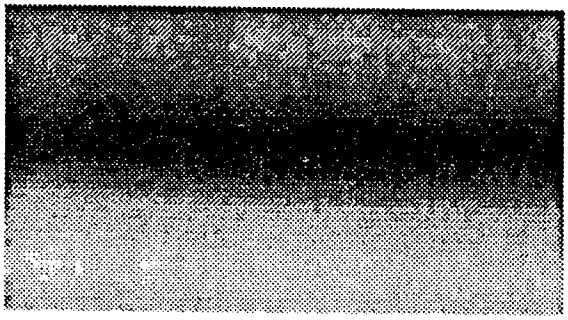

Figure 4: Magnetic image due to injected current in a uni-directional composite with a 1/16 inch hole.

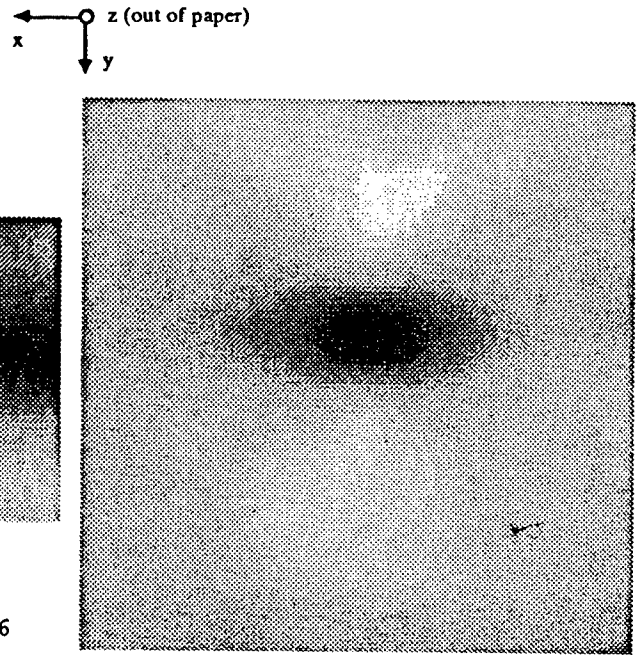

Figure 5: Magnetic image of a 0 ±45 90 composite with 1/16 inch hole.

MODELING

In order to formulate a model for this measurement, the following considerations must be taken into account. First, the two dimensional nature of the composite ply conductivity must be accounted for. For

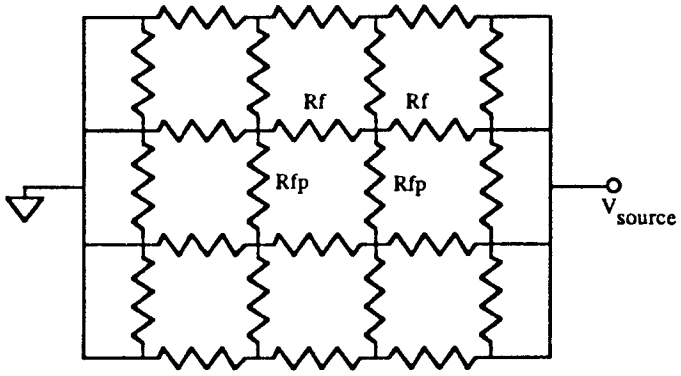

Figure 6: Two dimensional resistive model of composite conductivity

simplicity, the ply-to-ply interactions will not be directly modeled here. Also, the model must be quantitatively related to the material in question.

A model which satisfies these basic criteria is the simple two dimensional resistive network seen in figure 6. The network in figure 6 was extended to a size of 40 x 40 nodes in the actual model. The conductivity of the fibers is modeled with Rf and the conductivity perpendicular to the direction of the fibers is represented by Rfp. The hole in the material is modeled with resistances five orders of magnitude higher than Rf and Rfp. The model being presented here was the 0 ±45 ±90 sample discussed above. The inspected area is 2 cm X 2 cm. For the purposes of this model, this sample was represented as an infinitely thin sheet having conductivity components in the bulk current direction (x) and perpendicular to the bulk current direction (y). Applying the boundary conditions shown in figure 6, a nodal analysis is performed and all of the currents in the bulk current direction (x) are solved for. After calculating the individual current elements at each node, the magnetic field component B_y was calculated by application of the Biot-Savart law in the following manner:

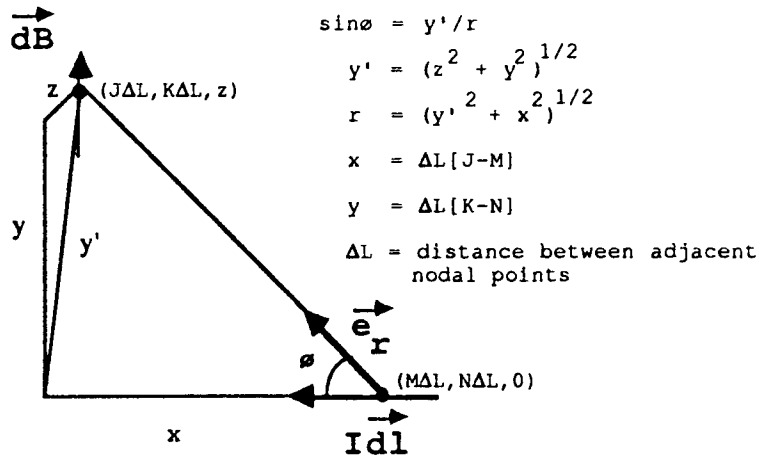

Figure 7: Application of Biot-Savart Law

The general differential form of the Biot-Savart law is shown below.

$$\vec{dB} = \frac{u_0}{4\pi} \frac{\vec{Idl} \times \vec{e_r}}{r^2}$$

Substitution from figure 7 results in the following expression for the magnetic field at a discrete point due to a single current element:

$$\Delta B_y = \frac{u_0 I \Delta L \, y'/r}{4\pi r^2}$$

Rewriting in terms of z,y,x

$$\Delta B_y = \frac{u_0 I \Delta L (z^2 + y^2)^{1/2}}{4\pi([z^2 + y^2] + x^2)^{3/2}}$$

Summing the contributions from all of the discrete current elements results in the total field at a point (J,K,z). Introducing two summing indices, n (to cover the sums in the x direction), and m (to cover the sums in the y direction, we have

$$B_y(J,K) = \sum_{n=1}^{N} \sum_{m=1}^{M} \Delta B_y$$

RESULTS

The calculated field component By is presented in an image format in figure 9. For purposes of comparison, figure 5 is presented again here as figure 8. As one can see, the model has all of the key features of the actual measurement image. These features include the current 'bleeding' resulting in an apparent elongation of the hole, and the lobes above and below the hole where the current density has increased due to the fault in the center of the sample. The model seems to give good agreement to the actual measured fields of the composites tested.

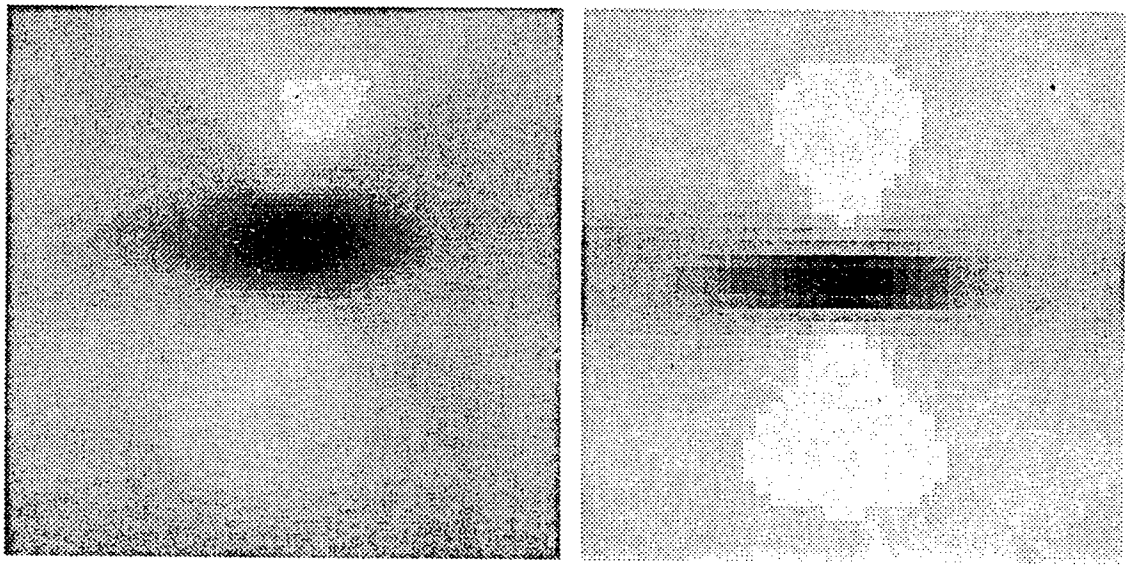

Figure 8: Magnetic image due to injected current in a 0 ±45 90 composite with a 1/16 inch hole.

Figure 9: Model of measurement presented in figure 5.

CONCLUSIONS

Current injection and magnetic field mapping has been demonstrated as a means for detecting disruptions in current paths (i.e. fiber damage) in graphite epoxy composites. Also, a simple resistive model has been demonstrated as a means for modeling two dimensional conductivity patterns in graphite composites. Future work will emphasize detection of real world fiber damage and theoretical modeling of the conductivity parameters of graphite composites.

DISCUSSION

Mr. R. C. Chivers (Cornell): What was the relationship between the detector size and the size of the hole?

Mr. Blalock: The sensitive area of the detector was one-tenth the size of the hole.

Mr. Chivers: Thank you.

REMOVAL OF DOMINANT REVERBERATIONS FROM ULTRASONIC TIME–RECORDS OF LAYERED MATERIAL BY DIGITAL PREDICTIVE DECONVOLUTION

Doron Kishoni[1]
Department of Physics
The College of William and Mary
Williamsburg, VA 23185

ABSTRACT

The interest in non–destructive evaluation of the space shuttle Solid Rocket Motor (SRM) calls for inspection of the integrity of the structure, mostly from the external side only. Difficulties however are encountered as the acoustic impedances combination of the various layers are such that the external steel layer generates strong multiple reflections that virtually mask everything that happens below. A method is presented to separate the steel reflection component from the deeper layers. Based on the fact that the reverberations are a predicted event, directly correlated to the first reflection, while variations deep in the material are pseudo–random, the predictive deconvolution estimates the next signal value based on previous signal values, over the prediction distance. The optimized operator is used to remove the predicted reverberations so that the residue that represents events such as defects in the deeper layers can be extracted and investigated.

I. Introduction

An important class of problems in NDE is the ultrasonic investigation of a layered system where the acoustic impedances combination are such that the first layer acts as an Energy trap for the incoming ultrasonic waves. Multiple reflections from this layer dominate the received signal for a long time period, and identification of reflections from deeper layers that arrive within that time period is virtually impossible. Such is the case of NASA's Solid Rocket Motor (SRM) that has an external steel layer over a rubber–like insulator and solid fuel. One approach for reducing the reverberations from the first layer is by trying to redesign the transducer to match its impedance to that layer [1]. However, when the immediate layer next to the transducer is an intermediate coupling material such as water, in water tank or when squirters are being used, removal of reverberation in the steel layer is not achieved. Even with a contact method, pre–knowledge of the inspected material is needed, and hardware requirements are constraining. Post–processing is more flexible. The following method is based on the property that the various multiple reverberations are related to previous ones, while defects and other discrete acoustic events inside the material can be regarded as pseudo–random in the sense that anomalies of the material/structure are not predicted from the preceding portion of the time–record signal.

[1]Mailing address: NASA - Langley Research Center, Mail Stop 231, Hampton, VA 23665

II. Theory

Consider an interface between two layers, one with an acoustic impedance of z_1, on top of the other with an impedance of z_2. An elastic wave propagating from layer 1 towards layer 2, normal to the surface of the interface, will partially be reflected at the interface, and partially be transmitted through it into the second material. Expressing amplitudes of the particle displacement for harmonic waves as a_i for the incoming wave, a_t for the transmitted wave and a_r the reflected wave, the ratio between them can be obtained by solving the wave equation, using the boundary conditions for continuity of displacement and stress:

$$A_i + A_r = A_t$$
$$A_i - A_r = (z_2/z_1)A_t$$

yielding the displacement reflection coefficient c and the transmission coefficient t [2]:

$$\therefore \begin{cases} \dfrac{A_r}{A_i} = \dfrac{z_1 - z_2}{z_1 + z_2} \equiv c & [-1, 1] \\ \dfrac{A_t}{A_i} = \dfrac{2z_1}{z_1 + z_2} \equiv t & [0, 2] \end{cases} \tag{1}$$

where $t = 1 + c$. The same relations hold for the magnitude of the particle velocity or the particle acceleration as well, while magnitude of the stress follows the relations:

$$\begin{cases} c_{Stress} = -c \\ t_{Stress} = \dfrac{z_2}{z_1} t \end{cases} \tag{2}$$

and the average power density follows the relations:

$$\therefore \begin{cases} \dfrac{\langle P_r \rangle}{\langle P_i \rangle} = \dfrac{(z_1 - z_2)^2}{(z_1 + z_2)^2} & [0, 1] \\ \dfrac{\langle P_t \rangle}{\langle P_i \rangle} = \dfrac{4z_1 z_2}{(z_1 + z_2)^2} & [0, 1] \end{cases} \tag{3}$$

For waves propagating the other direction, from layer 2 towards layer 1, the reflection and transmission coefficients, c' and t', can be expressed in terms of the opposite direction coefficients as:

$$\begin{aligned} c' &= -c \\ tt' - cc' &= 1; \quad tt' = 1 - c^2 \\ t' &= 1 - c \end{aligned} \tag{4}$$

Consider now a multilayered system, where the first layer, with a thickness corresponding to a one-way travel-time of $n/2$ units of time, has a relative acoustic impedance such that strong multiple reflections occur when a wave arrives from a transducer, attached to the surface or located at a distance in a water tank for example [Fig. 1] (the normal waves are offset for clarity here and in the rest of the figures). The consecutive multiple reflections can be expressed by their z-transform representation [3,4] as:

$$\text{I: } c_1; \quad \text{II: } t_1 c_2 t_1 z^n; \quad \text{III: } \ldots \tag{5}$$

These reverberations comprise the initial ringing effect, which can be expressed be their summation:

$$c(z) = c_1 + \left[\left(1 - c_1^2\right) c_2\right] z^n \frac{1}{1 + c_1 c_2 z^n} \tag{6}$$

The transmitted waves propagate in media 2 until they are partially reflected by a discontinuity at depth $m/2$ units of time, with a reflection coefficient ε'_t. On the return way, a second ringing event should be considered. The z-transform representation of this sequence can be shown to have the same form as the initial ringing sequence (Eqn. 6) [Fig. 2]. The total

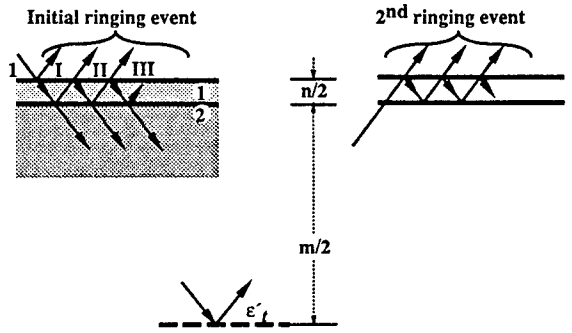

Fig. 1. Initial & second ringing events.

effect on the signal is the convolution $c*\varepsilon'*c$, which can be rearranged to the form $c^**\varepsilon'$ where c^* is $c*c$. For a physical material, absolute value of the reflection coefficient is not greater than 1, thus, c as well as c^* can be assumed to have a minimum-delay nature. In general, the various acoustic discontinuity inside the material, beyond the ringing layer, can be expressed by the reflection coefficient series ε_t. If b_t is the response of the transducer to a delta-function, then, the general response from the first layer is $r_t = b_t * c^*_t$, and the total response of the complete system is $x_t = r_t * \varepsilon_t = b_t * c^*_t * \varepsilon_t$ [Fig. 3].

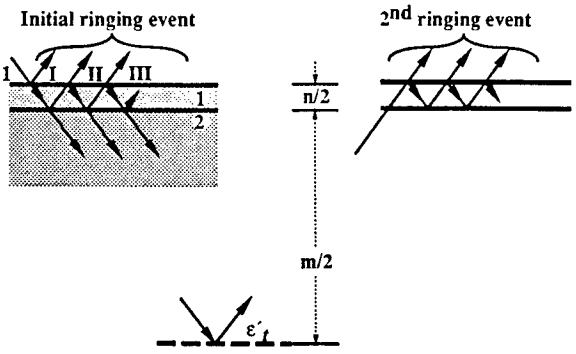

Fig. 2. Reverberation & reflection from an internal layer.

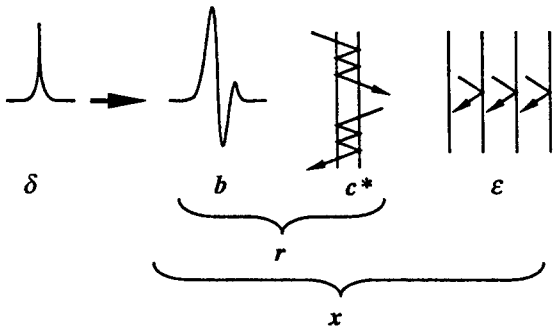

Fig. 3. Schematic representation of the components of the wave.

We can assume that the reflection coefficient series ε_t is uncorrelated and random in the sense that each reflection component is not predictable from previous reflections. On the other hand, r_t is predictable, when b_t and c_t are minimum delay. The autocorrelation ϕ of x_t, written using the expectation operator $E\{x_t x_{t+\tau}\}$, can be expressed as:

$$\phi_\tau = E\left\{x_t x_{t+\tau}\right\} = E\left\{r_t r_{t+\tau}\right\} * E\left\{\varepsilon_t \varepsilon_{t+\tau}\right\} \tag{7}$$

but for ε_t uncorrelated and random, $E\{\varepsilon_t \varepsilon_{t+\tau}\} = E\{\varepsilon_t^2\} = P\delta_{\tau_0}$, P is the power of ε_t. Therefore, the autocorrelation of x_t is proportional to the autocorrelation of r_t. Thus, prediction of the reverberation component c^*_t can be obtained and removed from x_t, to yield the residue $b_t * \varepsilon_t$. Enhancement of resolution can then be performed by pulse shaping if desired [5], reducing the effect of b. The prediction operator a will predict a desired signal at a delay of n units of time as a reverberation component of a previous event imbedded in the raw data x. The degree of success can be measured by the error:

$$Err = \sum_{t=0}^{\infty} \left(b_{t+n} - \sum_{s=0}^{m} a_s b_{t-s}\right)^2 \tag{9}$$

Minimizing the deviation from the actual signal as function of the coefficients of a will yield the next set of equations:

$$\sum_{s=0}^{m} a_s r_{j-s} = r_{j+n} \qquad j = 0, 1, 2, \ldots, m \tag{10}$$

a - Prediction operator (unknown)
n - Prediction distance (from autocorrelation, searchable for minimum error)
m - Length of prediction operator
r - Autocorrelation function (obtained from raw data x)

The prediction operator coefficients can be found by solving this set of linear equations. These coefficients are then used to construct the operator f,

$$f(z) = 1 - \sum_{s=0}^{m} a_s z^{n+s} \tag{11}$$

which will remove the reverberations from the raw data x, and give the processed signal g, using the convolution

$$g = x * f \tag{12}$$

III. Applications

We applied the method to a set of data that was generated to simulate a case of multiple reflections that are much stronger than another reflective event deeper in the material [Fig. 4a]. Inspection of the autocorrelation function of the signal, Fig. 4b, shows an indication of the location of the buried reflection. However, it is still difficult to analyze the trace. Processing the wave using the described method, with a prediction distance set to the estimated location of the first reverberation. yields the results shown in Fig. 4c, which are much more successful. The multiple reflections are diminished while the new events stays. Now the internal structure is very clear.

In order to see the effect of the value of the prediction distance, it was changed up to 20% with respect to the actual location of the reverberation signal. Fig. 4d shows results for a prediction distance value larger by 20% than the actual. The reverberation were reduced significantly, although not as much as before. Further inspection of the processed wave shows that the both reflection events were modified to two–spiked signals, related to the overestimation of the distance. This however can be corrected by pulse shaping technique as described in [5]. Fig. 4e shows that a prediction distance value smaller by 20% than the actual does not effect the results, a desired property. In both cases, choosing prediction value can be eliminated altogether by enabling the program to search for minimum value of the least squares error.

Next, we applied the method to an actual measured data from a layer that caused several multiple reflections as shown in Fig. 5a. In the processed data, shown in Fig. 5b, the reverberations are reduced by almost 90%, while the first reflection is not changed.

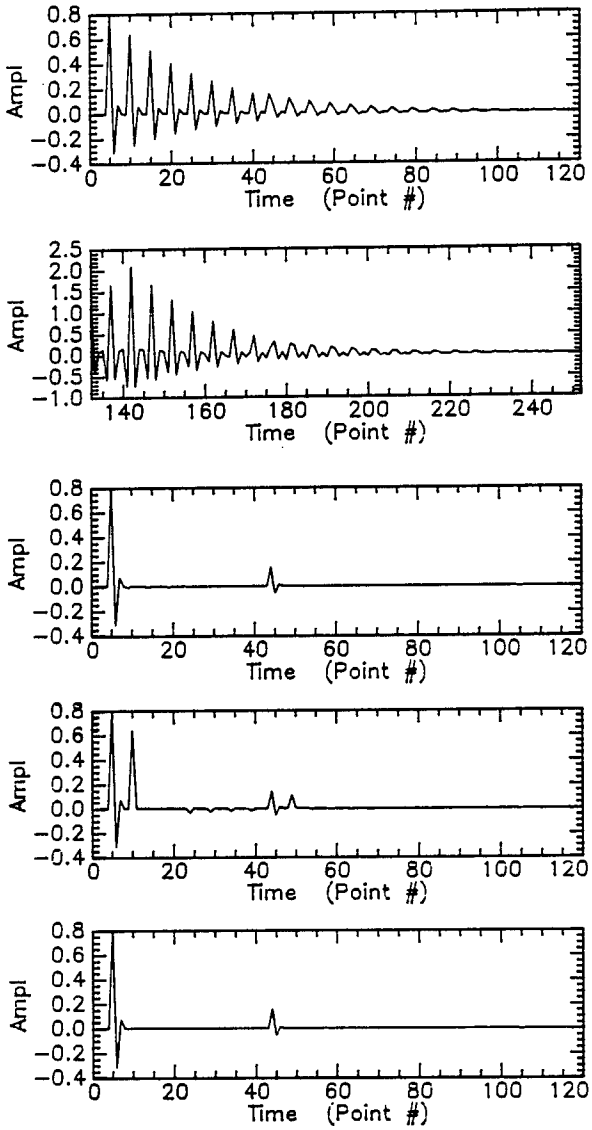

Fig. 4. (a) - Unprocessed signal with multiple reflection, synthetic. (b) - Autocorrelation function of (a). (c) - Processed data; prediction distance set to the estimated location of the first reverberation. (d) - Processed data; prediction distance is 20% larger than actual. (e) - Processed data; prediction distance is 20% smaller than actual.

Fig. 6 shows a two layered sample that generates strong multiple reflections, together with the expected acoustic rays. The measured raw data is shown in Fig. 7a, where a relatively small–amplitude internal reflection appears in the middle of the trace. After processing, seen in Fig. 7b, the amplitude of the multiple reflections due to the first layer is reduced significantly, to a much smaller value than the new reflective events, which clearly can be identified. Note that the DC offset which exist in the early part of the raw signal close to the saturated electric

excitation of the transducer shows some influence in the processed wave, yet extraction of the reflective events is possible.

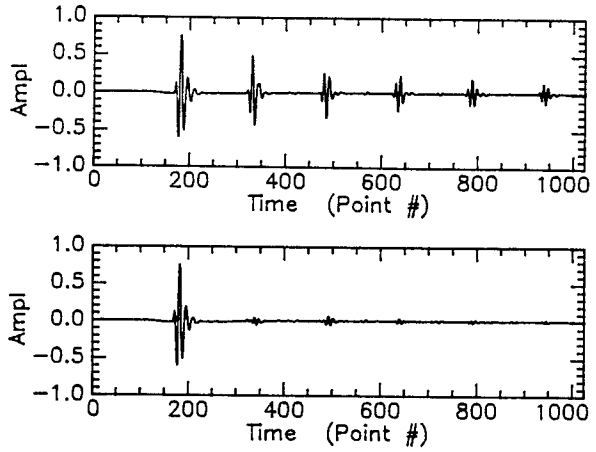

Fig. 5. (a) - Unprocessed signal with multiple reflection; measured data. (b) - Processed signal.

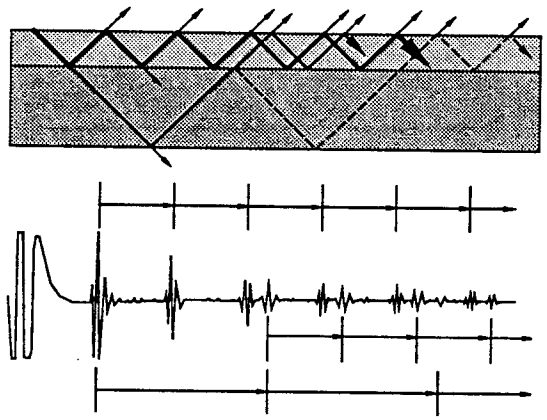

Fig. 6. (a) Layered sample, and the expected acoustic rays generated. (b) The expected trace signal and the corresponding travel times through the thickness of the layers.

Investigating the sensitivity of the method to modifying the length of the operator from a 64–coefficient operator, for example, to a 128–coefficient one shows virtually no change in the processed signal.

IV. Discussion and conclusions

The described method is able to effectively remove the dominating reverberations, with minimal assumptions about the investigated structure and its dimensions. The processed signal is not critically sensitive to the few entered parameters, and the reported examples shows stable results. These properties are highly desired when analyzing laboratory and field data, where

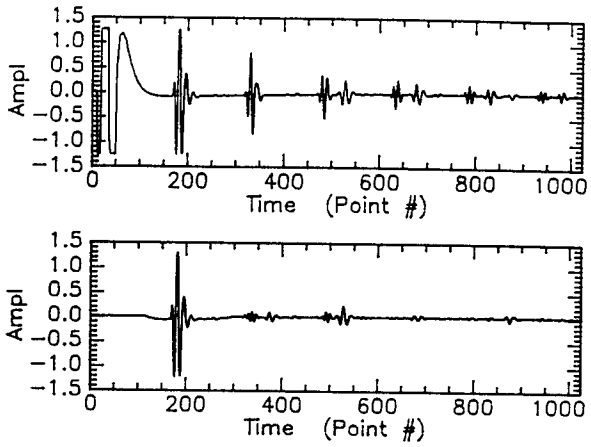

Fig. 7 (a) - Measured raw data; reverberations much stronger than the buried reflection event. (b) - Processed signal.

such a method may be utilized, benefiting the most in cases of a complex structure, and when overlapping of waves is unavoidable. In such cases, the conventional approach of identifying single reflections can not be successfully used, while the described procedure improves the signal and enhances our capabilities to identify defects in the material.

Acknowledgment

This work is supported by NASA Grant # NAS1–17303

References

[1] C. S. Desilets, J. D. Fraser and G. S. Kino, "The Design of Efficient Broad–Band Piezoelectric Transducers," *IEEE Trans. on Sonics Ultrason.*, vol. SU-25, pp. 115–125, May 1978.

[2] J. Miklowitz, *The Theory of Elastic Waves and Waveguides*, New York: North–Holland Publ., 1978.

[3] A. V. Oppenheim and R. W. Schafer, *Digital Signal Processing*, New Jersy: Prentice–Hall, 1975.

[4] E. A. Robinson and M. T. Silvia, *Digital Foundations of Time Series Analysis*, CA: Holden–Day, 1981.

[5] D. Kishoni, "Application of Digital Pulse Shaping by Least Squares Method to Ultrasonic Signals in Composites," *Review of Progress in Quantitative NDE* (June 23–28, 1985), edited by D. O. Thompson and D. E. Chimenti, Vol. 5A, pp. 781–787, New York: Plenum Press, 1986.

ULTRASONIC CORRELATOR VERSUS SIGNAL AVERAGER AS A SIGNAL TO NOISE ENHANCEMENT INSTRUMENT

Doron Kishoni
Senior Research Scientist
Department of Physics, The College of William and Mary
NASA Langley Research Center
Mail Stop 231, Hampton, VA 23662

Benjamin E. Pietsch
Electronics Engineer
Industrial Quality Inc.
19634 Club House Rd., Suite 320
Gaithersburg, MD 20879

ABSTRACT

Ultrasonic inspection of thick and attenuating materials is hampered by the reduced amplitudes of the propagated waves to a degree that the noise is too high to enable meaningful interpretation of the data. In order to overcome the low Signal to Noise (S/N) ratio, a correlation technique has been developed. In this method, a continuous pseudo-random pattern generated digitally is transmitted and detected by piezoelectric transducers. A correlation is performed in the instrument between the received signal and a variable delayed image of the transmitted one. The result is shown to be proportional to the impulse response of the investigated material, analogous to a signal received from a pulsed system, with an improved S/N ratio. The degree of S/N enhancement depends on the sweep rate. This paper describes the correlator, and compares it to the method of enhancing S/N ratio by averaging the signals. The similarities and differences between the two are highlighted and the potential advantage of the correlator system is explained.

INTRODUCTION

Ultrasonic inspection of materials involves generation of elastic waves using a transducer. These waves are transmitted through the media, detected by a receiver and analyzed. In order to retain meaningful interpretation of the data, a sufficient Signal to Noise (S/N) ratio must be obtained. This poses a problem whenever thick and attenuating material is involved. Using high-gain amplifiers to amplify the highly attenuated waves introduces more noise to the system, and events of interest in the signals are often too small to detect. One method of enhancing the S/N ratio is by averaging several of the received signals, using a digitizer that has this capability. The source impulse signals are repeated several times, and the detected signals are digitized and averaged. The temporal resolution of the events in the received signal depends on the impulse width. The pulse maximum repetition rate is limited by the depth of the investigated area. The pulse source should not be repeated until ultrasonic waves of the previous pulse have significantly dissipated. Another limitation is that the pulse amplitude cannot exceed the breakdown voltage of the transducer. These limit the maximum input energy and determine the limit of the signal to noise enhancement by averaging. The following discussion which describes a correlator, is based on a different principle, and can overcome some of the limitations of the averaged pulse system.

THE CORRELATOR

Principle:

A block diagram of the correlator is shown in Figure 1. A pseudo-random digital pattern is repeatedly generated and used to drive a transmitting transducer after proper amplification. The ultrasonic waves which propagate through the inspected material are detected by a receiver transducer. A correlation is performed between the received signal and a reference signal generated by the second pattern generator which is identical in shape to the drive signal, but delayed by a linearly varying amount, governed by the sweep rate. The use of a digitally delayed reference has the advantage of greater accuracy and stability than complicated analog delay lines [ref. 1 for example].

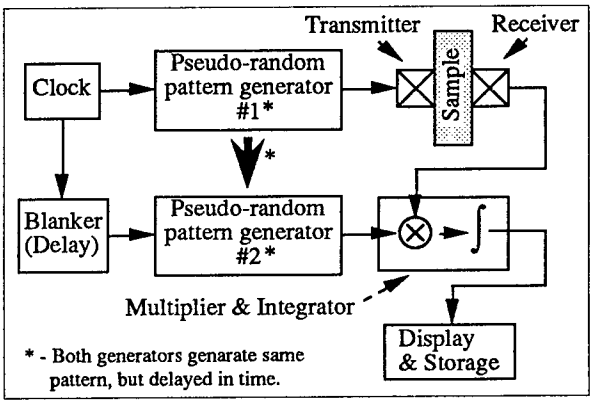

Figure 1. Correlator, schematics.

Theory:

An output $y(t)$ from a linear system can be expressed as the convolution of the system impulse response $h(t)$ with the input $x(t)$ (Figure 2):

$$y(t) = h(t) * x(t) = \int_{-\infty}^{\infty} h(\upsilon)\, x(t-\upsilon)\, d\upsilon \qquad (1)$$

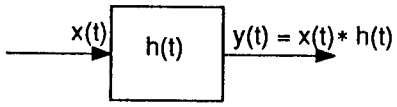

Figure 2. The output as a convolution of the input and the impulse response.

The cross correlation R_{xy} of $x(t)$ and $y(t)$ can be written as:

$$R_{xy}(\tau) = \lim_{T\to\infty} \frac{1}{T} \int_{-T}^{T} x(t)\, y(t+\tau)\, dt \qquad (2)$$

and auto-correlation $R_{xx}(\tau\text{-}\upsilon)$ of $x(t)$ as:

$$R_{xx}(\tau\text{-}\upsilon) = \lim_{T\to\infty} \frac{1}{T} \int_{-T}^{T} x(t)\, x[t+(\tau\text{-}\upsilon)]\, dt \qquad (3)$$

Substituting (1) and (3) into (2) we get:

$$R_{xy}(\tau) = \int_{-\infty}^{\infty} h(\upsilon)\, R_{xx}(\tau\text{-}\upsilon)\, d\upsilon \qquad (4)$$

therefore, the cross-correlation of the input and the output is the convolution of the impulse response with the auto-correlation of the input signal:

$$R_{xy} = h * R_{xx} \qquad (5)$$

R_{xx} for white noise is the delta-function, (up to a factor k), therefore,

$$R_{xy}(\tau) = k\, h(\tau) \qquad (6)$$

so that if white noise is injected to the material, the correlation of the input with the detected output $y(t)$ is the impulse response $h(t)$ of the system (Figure 3).

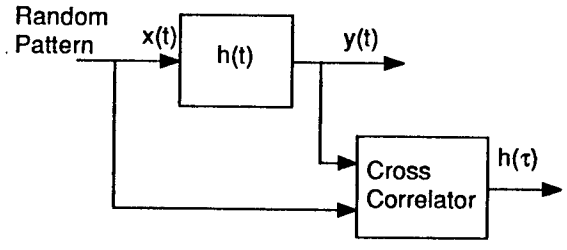

Figure 3. Correlation of random sequenced input with the output yields the impulse response.

In a single-channeled configuration, as applied in the current correlator system, τ is slowly varied according to the sweep rate (*S.R.*), thus, the resultant correlation represents the impulse response transformed to a frequency which is reduced by the inverse of the sweep rate.

The Signal to Noise Ratio Enhancement (*SNRE*) of a system can be defined as:

$$SNRE = \frac{SNR_{output}}{SNR_{input}} \qquad (7)$$

where *SNR* is the Signal to Noise Ratio. This can be expressed in terms of bandwidth B of the appropriate signals [2-4], where the $SNRE_{power}$ is given by:

$$SNRE_{power} \approx \frac{B_{input}}{B_{output}} \qquad (8)$$

while the $SNRE_{voltage}$ is given by:

$$SNRE_{voltage} \approx \sqrt{\frac{B_{input}}{B_{output}}} \qquad (8a)$$

Both definitions are equivalent in terms of decibels, since the factor is 20 for voltage as opposed to a factor of 10 for power. As the single-channeled correlation transforms the bandwidth to a frequency reduced by the inverse of the sweep rate *S.R.*, the last equation can be written as:

$$SNRE_{voltage} \approx \sqrt{\frac{1}{S.R.}} \qquad (9)$$

which is fixed for any particular sweep rate. A typical value used for sweep rate is 0.1 μsec/sec. The sweep rate is inversely proportional to the acquisition time T_{aq}.

As a comparison, the averaging process for a pulse-system improves the signal to noise ratio by:

$$SNRE_{voltage} \approx \sqrt{n} \qquad (10)$$

where n is number of averages. Again, the acquisition time is linearly proportional to n, thus,

$$SNRE_{voltage} \approx \sqrt{T_{aq}} \qquad (11)$$

Power efficiency comparison:

In a pulse-system with repetition rate of f pulses per second, the total power P into the material can be approximated as:

$$P_p = V_p^2\, t_p\, f_p \qquad (12)$$

where V is the peak voltage of the pulse, and t is its effective duration. (The index p denotes the pulse-system). Typical values are -300 volts and ~100 nsec duration respectively.

The repetition rate f is limited by the acoustic response in the material. The repetition rate must be low enough to avoid wrap-around of the reflections (Figure 4). The maximum obtained information τ is then not more than the time between the pulses,

$1/f$. The total energy input throughout n averages, w_p, per unit of obtained information, τ_p, can be expressed as:

$$\frac{w_p}{\tau_p} = P_p \frac{T_p}{\tau_p} \geq V_p^2 t_p f_p n \qquad (13)$$

where T_p is the total acquisition time (of n averages), and P_p is the input power during this time.

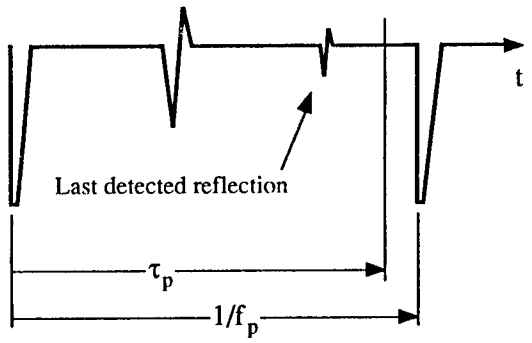

Figure 4. One repetition in a pulse-system that has a repetition rate of f pulses per second, and some possible echoes.

For the correlator system, the input power P is:

$$P_c = \frac{1}{2} V_c^2 \qquad (14)$$

where V is the voltage of the amplified digital random signal, which is on half of the time, on average. (The index c denotes the pulse-system). The acquisition time T is directly related to the duration of the obtained information τ through the sweep rate $S.R.$:

$$\frac{T_c}{\tau_c} = \frac{1}{k\,[S.R.]} \qquad (15)$$

where k is the number of parallel channels that perform the correlation in the correlator. The total energy input, w, per unit of obtained information, τ, would be:

$$\frac{w_c}{\tau_c} = \frac{1}{2} V_c^2 \frac{1}{k\,[S.R.]} \qquad (16)$$

For comparison purposes, if we limit the input power in the correlator system so that both systems input equivalent amounts of power, the ratio of the voltages would have to be:

$$\frac{V_c}{V_p} = \sqrt{2\, t_p f_p} \qquad (17)$$

In such a case, the ratio between the quantities 'total input energy -w, per unit of obtained information -τ' of the two systems would be:

$$\frac{w_p/\tau_p}{w_c/\tau_c} \geq \frac{n}{\left(\frac{1}{k\,[S.R.]}\right)} \qquad (18)$$

which is similar to the ratio between the *SNRE*'s (in term of power) of the systems for a single channel correlator.

EXPERIMENTS

An 11.5 cm thick wood was used as an example of thick highly attenuating material. Two 2.25 MHz half inch transducer were used in a pulse-echo configuration. A single pulse, with the pulse-system configured for maximum safe voltage into the transmitter, resulted in a signal to noise in the received signal which was less than 1, as can be seen in Figure 5.

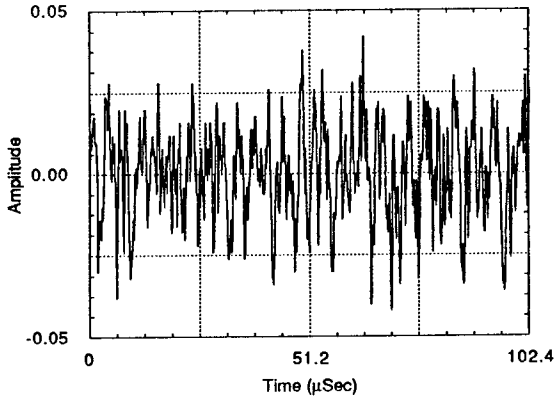

Figure 5. Wood, Single trace obtained with the pulse-system.

Therefore, averaging was required with the pulse-system to be able to detect the signal. A signal obtained after 4096 averages is shown in Figure 6. The excitation is seen on the left side (at relative time 0), and the first arrival through the wood occurs around 57 μsec. Significant noise still exists even in the 4096 averages case, as evident in the time interval 0 to ~57 μsec, before arrival of the first acoustic response of the wood.

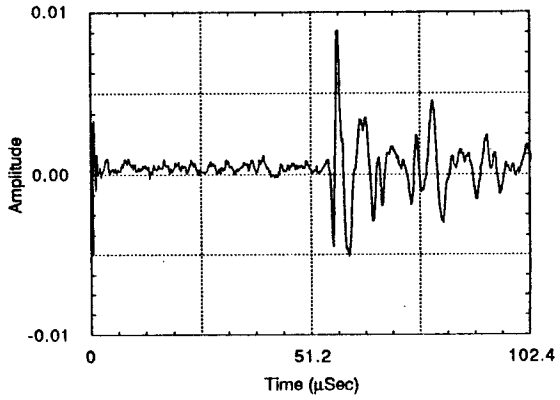

Figure 6. Wood, using the pulse-system, with 4096 averages.

The received signal from a single channel correlator for a sweep rate of 0.1 μsec/sec is shown in Figure 7. The acquisition time was approximately equal to the time required for 4096 averages (hardware dependent of course), although it could be skipped until the expected first acoustic response, thus reduced significantly. The first arrival could be identified again, at ~57 μsec, with a lower noise before first arrival than the noise in the 4096 averages case. (To decrease the noise to the same level, the averaging system required close to 32000 averages). Furthermore, this noise is above the detection frequency of the transducer, thus, further low-pass filtering is possible without deleting actual information.

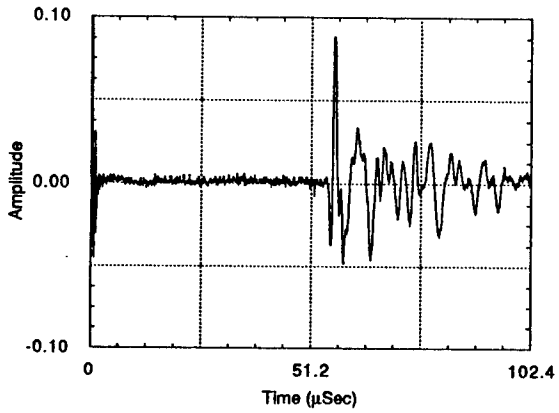

Figure 7. Wood, output from the correlator.

Figure 8 shows the measured signal to noise figures as function of the number of averages in the pulse-system (on a log scale). The noise-level measurements were taken at a region before the expected first arrival, while the signal-level measurements were taken at the region of the first arrival of the acoustic response.

Superimposed on the graph of Figure 8 is the S/N measured from the results of the correlator. The vertical data line on the right represents a single-channel correlator. Increasing values of the input power increased the S/N values as expected. The horizontal coordinate of this data corresponds to an equivalent acquisition time as with the pulse system. A 1024 multiple channel correlator would shorten this time by this factor, thus, shifting this data line to the left, as shown in the left side of the figure.

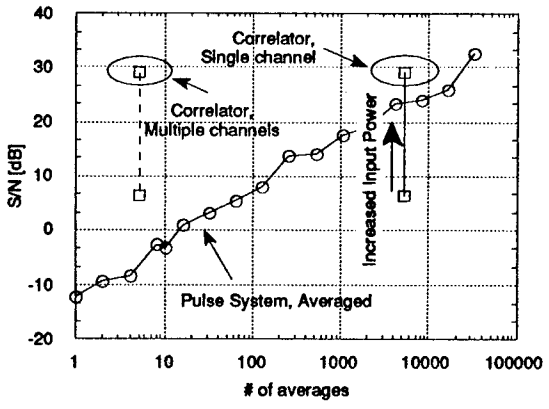

Figure 8. Wood, S/N curve.

A second set of tests were performed measuring ~10 cm thick Teflon. S/N results are shown in Figure 9. Since the attenuation of the material is less than that of the wood sample, the overall S/N figures were better. Yet, the relative behavior of the two systems remain the same. The effect of increasing the number of the channels from a single channel to 1024 channels in a multi-channel correlator is extrapolated in this figure.

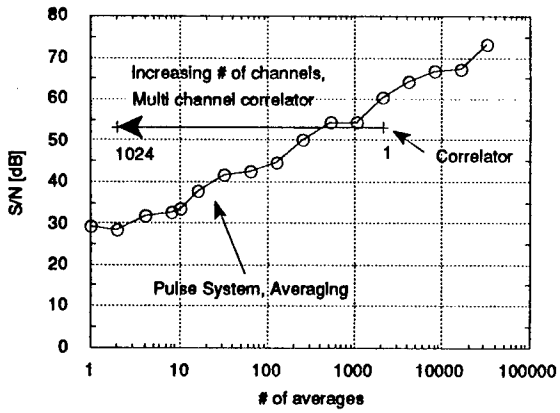

Figure 9. Teflon, S/N curve.

DISCUSSION

Both the correlator system and the averaging pulse-system can enhance the signal to noise ratio, improving it linearly with square root of the acquisition time. The correlator, through its sweep rate *S.R.*, and the averager through the number of averages *n*. The ratio of total input energy per unit of obtained information also have equivalent forms for the two systems.

There are however some important differences between them. While the voltage into the transducer in the pulse-system is limited by the breakdown voltage of the transducer, the correlator system is based on a continuous excitation of the transducer, where the limiting parameter is mainly the maximum power that can be dissipated. The total power can be much higher than in the pulse-system, thus, obtaining stronger signals.

Another major difference is the way the systems collect and enhance the data: A conventional pulse echo averaging system prescribes a fixed minimal time window, according to the thickness of the sample that control the maximum repetition rate. The S/N improves as acquisition time increases (as square root of it). The correlator system, on the other hand, gives prescribed S/N enhancement, according to the chosen sweep rate while the obtained time window increases with the acquisition time. The condition on the correlator corresponding to the maximum repetition rate is the length of the unique pattern in the pseudo-random signal. It should be the inverse of the repetition rate, a condition which is easily obtained.

Furthermore, if the investigated material calls for inspection at a localized suspected region, the correlator system can be configured to skip the early time trace, and start the process of the correlation only at the requested window of time, thus reducing the acquisition time significantly, at any prescribed S/N value. This could not be applied in a conventional pulse echo system, where the minimal time window is fixed.

SUMMARY

The system of choice depends on the relevant problem: The averaging pulse-system is appropriate when the required Signal to Noise Enhancement (*SNRE*) is low and when the full thickness of the material has to be inspected. In this case, fast measurement is possible, where the S/N improves as the averaging continues until adequate signal shows on the screen. The correlator system has the advantage when high *SNRE* is required, particularly when a specific region has to be inspected. The sweep rate will be chosen according to the required *SNRE* and the delay would be set up, and the enhanced trace would almost immediately be obtained. A multi-channel correlator would increase this advantage even more.

REFERENCES

[1] Furgason, E. S., Newhouse, V. L., Bilgutay, N. M. and Cooper, G. R. "Application Of Random Signal Correlation Techniques To Ultrasonic Flaw Detection," Ultrasonics, 13, 1975, pp. 11-17.

[2] Ziemer, R. E. and Tranter, W. H., Principle Of Communication - System Modulation And Noise, Houghton Mifflin Co., Boston, 1976.

[3] Lee, B. B. and Furgason, E. S., "An Evaluation Of Ultrasound NDE Correlation Flaw Detection Systems," IEEE Trans. Sonic Ultrason., vol. SU-29 (6), 1982, pp. 359-369.

[4] Lindgren, E., A., "The Use Of Ultrasonic Correlation Methods For The Investigation Of Phase Transitions In Polytetrafluoroethylene And The Precipitation Hardening Process In 2024 Aluminum Alloy," M.S. Thesis, JHU-CNDE-UCC-1, Johns Hopkins University, 1988.

[5] Kishoni, D., Rosen, M., Berger, H. and Cheng, Y. T., "Signal To Noise Enhancement By An Ultrasonic Cross-Correlator System," IEEE Ultrasonics Symposium, Chicago, Illinois, 1988.

VII. THERMAL NDE

From: REVIEW OF PROGRESS IN QUANTITATIVE
NONDESTRUCTIVE EVALUATION, Vol. 7A
Edited by Donald O. Thompson and Dale E. Chimenti
(Plenum Publishing Corporation, 1988)

CONTRAST ENHANCEMENT THROUGH SOURCE IMPEDANCE CONTROL IN THERMAL NDE

Christopher S. Welch

Department of Physics
College of William and Mary
Williamsburg, VA 23185

INTRODUCTION

Recent non-destructive evaluation (NDE) methods for locating buried delaminations in insulating materials covered with thermal conductors have been reported [1] which utilize uniform application of heat over large areas of the conductor and the subsequent appearance in thermal images of contrast which correlates in position with the delaminations. In some instances, the temperature contrast has been reported to be present immediately on termination of heating, while in other cases, the contrast has appeared subsequent to termination of heating. Even when present following heating, temperature contrast sometimes undergoes a secondary increase following heating termination. The principal objective of this paper is to show that the secondary increase in contrast depends on the change of thermal impedance at the surface associated with the heating protocol as well as on the temperature associated with the heating. As a secondary objective, the qualitative and intuitive concept of temperature contrast will be quantitatively defined so that an equation may be derived describing the genesis and propagation of temperature contrast due to a flaw.

Temperature contrast has historically been associated with flaw detection in thermal NDE because of the immediate qualitative correlation in space between temperature variations and known flaws. Examples of this use are thermograms, as in [2], and phase vs position plots from thermal wave experiments, as in [3]. Thus temperature contrast is a *de facto* variable of interest in NDE. Temperature contrast can further be considered necessary to thermal NDE, for flaws which produce no temperature contrast under a given protocol cannot be detected.

While temperature contrast is often the variable of primary interest, experimental and theoretical work generally uses temperature as the primary variable, obtaining contrast by taking differences of temperatures subsequent to experimental procedures or theoretical solutions. Contrasts obtained this way are often found to be much smaller in magnitude than the temperatures used to calculate them. Furthermore, it is difficult, except by direct comparative tests, to relate observed contrast to quantitative flaw characteristics. If the comparisons are numerical in character, using computer models of heat transfer, they are made more difficult by having to describe the small differences associated with contrast as differences in the much larger values of temperature increase. These considerations make it difficult to predict with confidence the detection limits of flaws. They also make it hard to decide which experimental parameters to vary in order to improve results in any particular setting.

These difficulties provide motivation for the development and analysis of an equation which explicitly describes the generation and evolution of temperature contrast. With such an equation, one may expect contrast to be separated from heat propagation prior to solution, the contrast-generating terms being directly calculated from interactions between the thermal field and the flaw. In a contrast equation, contrast should be of the same magnitude as the largest term in the equation, so numerical difficulties are reduced. The explicit thermal properties of a flaw which produces contrast will appear in a contrast equation, allowing some insight to be developed about the nature of detectable (and undetectable) flaws. In summary, a contrast equation is expected to promote understanding and reduce numerical difficulties.

CONTRAST EQUATION

To obtain an equation for thermal contrast in a simple case, consider the heat equation in an isotropic, inhomogeneous medium

$$K\nabla^2 T - C\frac{\partial T}{\partial t} + \nabla K \cdot \nabla T = 0 . \qquad (1)$$

In this equation, C, the volumetric heat capacity, and K, the thermal conductivity, represent the intrinsic material properties which directly affect evolution of temperature (T). In operator notation, this equation may be represented as $L(T) = 0$, where L denotes the linear operator of equation 1. Source terms are omitted with the understanding that they will be included in boundary conditions

$$-K\nabla T \cdot \hat{n} = h(T - T_S) . \qquad (2)$$

Here, T_S is the temperature of the local environment and h is a heat transfer coefficient. To obtain an equation for thermal contrast, two cases are considered, one in which flaws are present, denoted with primed quantities, and one in which they are absent, denoted with unprimed quantities. In operator notation, the equation for the flawed case may be written $L'(T') = 0$. Contrast, the variable of interest, is defined as $D = T' - T$. In order to relate properties of the flawed material to those of the unflawed material, two normalized damage amplitudes, ϕ and ψ are introduced by the equations $K' = K(1 - \phi)$ and $C' = C(1 - \psi)$. These damage amplitudes are such that they are zero in undamaged regions and unity where the damage is of such an extent that the entire associated property is eliminated by the damage. If the undamaged equation is subtracted from the damaged equation and T' eliminated from the difference, the result can be written as

$$L'(D) = \phi[L(T)] + (\phi - \psi)C\frac{\partial T}{\partial t} + K\nabla\phi \cdot \nabla T . \qquad (3)$$

The first term on the right is identically zero, and the second two may be interpreted conveniently by introducing the thermal flux vector, $\mathbf{f} = -K\nabla T$. With this substitution and application of equation (1) to the second term on the right hand side, Eq. (3) becomes

$$L'(D) = (\psi - \phi)\nabla \cdot \mathbf{f} - \mathbf{f} \cdot \nabla\phi . \qquad (4)$$

In this form, the equation for contrast is inhomogeneous, and its driving terms are calculated as products of terms involving the thermal flux of the undamaged case and terms involving damage amplitudes. The driving terms can be rearranged to separate the effect of reduction of conductivity from that of reduction of heat capacity, giving

$$L'(D) = \psi \nabla \cdot \mathbf{f} - \nabla \cdot (\phi \mathbf{f}) \ . \qquad (5)$$

These driving terms may be calculated for a number of damage cases using a single solution for the undamaged case and the explicit description of various cases of damage in terms of damage amplitudes. If the damaged area is restricted to a small part of the object under study, and in particular if it is buried, the operator on the left hand side becomes identical to that for the undamaged case outside of the damage zone itself. Outside the damage zone the contrast signal propagates in exactly the same manner as does the temperature signal in the undamaged case.

The boundary condition, in terms of D and T, is

$$-K'\nabla D \cdot \hat{n} + K\psi \nabla T \cdot \hat{n} = hD \qquad (6)$$

at the surface. This is an inhomogeneous boundary condition in D, the driving term corresponding to the heat which did not flow through the flawed part of the boundary because of its conductivity anomaly. The environmental temperature is no longer an explicit part of the boundary condition. In the important case of buried damage, for which the surface of the sample is identical in the unflawed and flawed cases, this condition reduces to

$$-K\nabla D \cdot \hat{n} = hD, \qquad (7)$$

a mixed, homogeneous boundary condition. In this case, the effect of the boundary condition on the propagation of contrast is described using an impedance at the boundary. If the flux of contrast is defined in analogy to that of heat, boundary impedance is 1/h.

These results are schematically represented in figure 1. In this figure, corresponding to a buried flaw, heat is injected into the sample, where it interacts with the flaw to generate contrast. The contrast then propagates back through the material to a viewing surface, where it is observable with an infrared imager or other means. In this form, the processes of heat injection, heat propagation to the flaw, contrast generation through an interaction between the flaw and the heat flux in the unflawed case, contrast propagation to the viewing surface, and surface expression of contrast are separated for individual consideration.

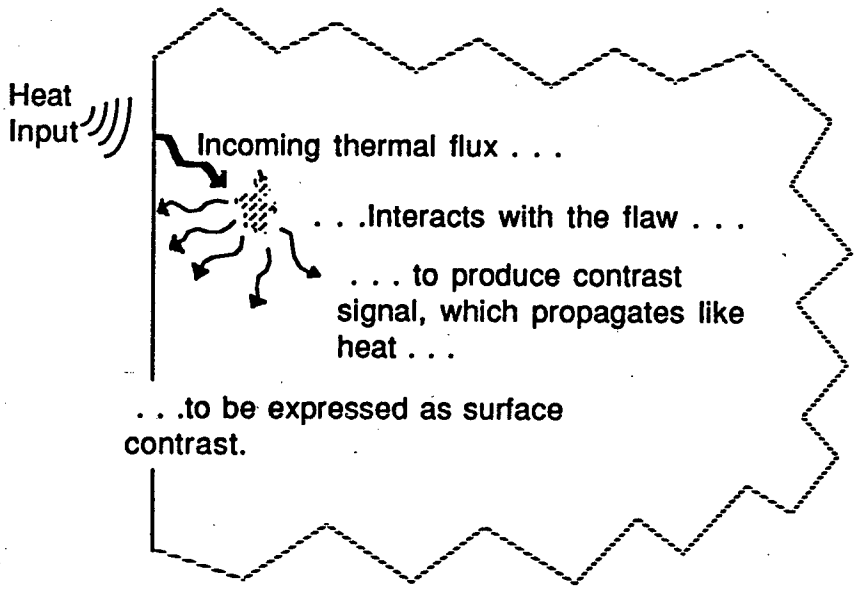

Fig. 1. Schematic representation of the generation, propagation and observation of temperature contrast caused by a flaw.

BOUNDARY IMPEDANCE

If the flaw is buried, the propagation of contrast through the unflawed material between the flaw and the viewing surface is described by the same operator as used in the heat equation. Thus, contrast may be decomposed into sinusoidal components like thermal waves, each having a fixed frequency, ω. Each of these waves is critically damped, with a 1/e attenuation length equal to its reciprocal radian wavenumber. This length scale is related to the intrinsic thermal properties and frequency by

$$L = \sqrt{\frac{2K}{\omega C}} \quad . \tag{8}$$

The dependence on the inverse square root of frequency is the reason that high frequency thermal waves, while allowing high resolution, do not penetrate as deeply into materials as those of lower frequency. Further, if impedance is defined, in analogy with electromagnetism, as the ratio of the contrast to the flux of contrast, the impedance of the thermal wave is

$$Z = \frac{1}{\sqrt{\omega CK}} \quad . \tag{9}$$

This also depends on the inverse square root of frequency, so that for a given material, the impedance of a thermal wave is directly proportional to its length. Thus, the long, deeply penetrating waves also have the largest impedance. When the contrast wave reaches the surface, it encounters the surface impedance which acts on its amplitude much as a termination resistor acts at the end of a transmission line. For a given frequency component, if R is the ratio of the surface impedance to the wave component impedance, the amplitude will be multiplied by a factor 1/(1+R), and so reduced. If R = 1, the amplitude is reduced by a factor of 2. This amplitude reduction limits the depth to which thermal NDE techniques will detect flaws beyond the limit imposed by the exponentially decaying nature of the thermal wave. If signal-to-noise or other considerations limit the permitted impedance ratio to a value of R, the associated depth of penetration is given by

$$L = \frac{\sqrt{2}\,RK}{h} \quad . \tag{10}$$

One result of this formula is that, for a given material, the depth of penetration is inversely proportional to the heat transfer coefficient at the observing surface. Thus, if the depth of penetration is impedance limited, it can be increased by decreasing the heat transfer coefficient.

Equation 10 can be used to calculate a surface impedance limited penetration depth for a given thermal situation. The numbers obtained are highly specific, however, because actual values of h are highly situation dependent, and allowed values of R are also strongly equipment dependent. Values for unity R correspond to an impedance-matched condition and may be used as a scale value, the corresponding amplitude of the surface thermal wave being reduced from the adiabatic case by a factor of 2. In our [4] laboratory setup, with air cooling over a one foot square vertical surface, a value for h of 15.48 Watts/(m^2-deg C.) was empirically determined. Using this value and evaluating equation 10 with conductivities corresponding to the steel and insulation used in the second example below, values of the penetration depth obtained are 3.2 m. for the steel and 2.2 cm. for the insulation.

NUMERICAL EXAMPLES

The inverse relation of the penetration depth limit for thermal and

contrast waves leads to a difficulty in the case for which conductive heat transfer is used on the surface which is also the viewing surface. If the heat transfer coefficient is increased in an effort to transfer more heat into the sample, the penetration depth limit due to surface impedance will be decreased at the same time. One way to increase penetration is to modulate the impedance as well as the surface temperature in performing a one-sided thermal test. If impedance is modulated, a secondary increase in observed contrast, sometimes called a blooming of the image, occurs.

A numerical experiment was performed to test the hypothesis that the secondary increase in observed contrast is related to the modulation of surface impedance during the test. The test was performed using a numerical simulation package (SPICE) as an electrical analogy to the one-dimensional thermal problem. The electrical circuit is shown in figure 2. In this figure, the elements to the left of the node marked V_0 simulate the heat source, while those to the right of that node simulate the material under test. The time evolution of voltage at V_0 corresponds to the temperature at the observed face of the sample. The termination resistor, R_t, is an artificial requirement of SPICE with no particular thermal analog. It is placed after a sufficient number of stages, in the case shown, 20, that it has no effect on the transient voltage at V_0 during the time of interest for the test. In the analogy, a single electrical stage of series resistance and parallel capacitance corresponds to a small slice of the sample, of thickness 1. The electrical resistance (R) corresponds to the thermal resistance of the small slice, and electrical capacitance (C) corresponds to the heat capacity of the slice. With this correspondence, the RC electrical time constant corresponds to the thermal $1^2/k$ time constant, where k is thermal diffusivity. In this analogy, a flaw may be simulated by changing the resistance of the stage corresponding to the location of the flaw from R to a higher value R_f. Tandem runs of the model with and without the flaw were done to obtain temperature which would be observed at the face, and these temperature records were subtracted to obtain contrast. Contrast was obtained in two cases for the source input. In both cases, the source voltage was applied as a square pulse for the same duration. In the non-modulated case, the source voltage was simply set to zero at the end of the pulse. In the modulated case, the source impedance was made infinite following the pulse by opening the switch. The results of this preliminary experiment are shown in figure 3. For the parameters used in the test, which correspond to common electrical circuit parameters, the secondary maximum in contrast clearly occurred when the source was switched, modulating the impedance, rather than when it was simply pulsed.

A second example shows that the contrast enhancement persists in a setting more closely related to NDE. In this case, a thermal model

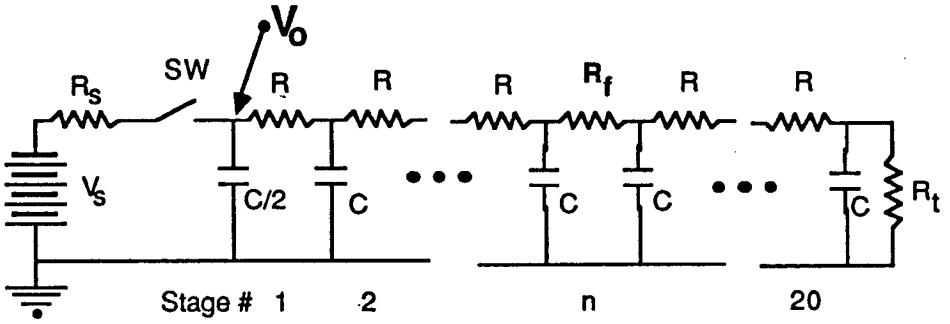

Fig. 2. Electrical circuit analogy to a one-dimensional heat propagation situation using a source connected by conductive transfer.

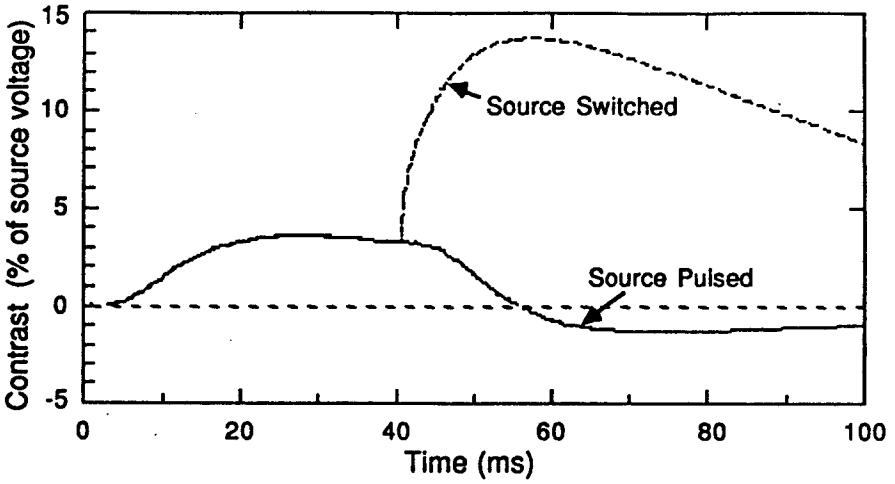

Fig. 3. Calculated voltage in the simulated circuit at the point corresponding to the front surface of a heated sample, where temperature is observed. The two curves correspond to the cases where the source voltage is pulsed with and without opening the switch following the pulse.

(TOPAZ) was used directly in its two-dimensional configuration. Contrast was defined as the difference between the temperature directly over the flaw and that far away, in an unflawed area. This definition, while less mathematically convenient than the previous definition, eliminates the need for tandem runs of the model and corresponds more closely with NDE practice. The situation modeled was a strip delamination behind 0.5 inches of steel and between the steel and an insulating material. The heating protocol modeled was contact with water raised 50 degrees above ambient temperature for 1 minute followed by cooling through contact with air at ambient temperature. This protocol, easily implemented in NDE practice, automatically provides impedance modulation. Results comparable to figure 3 are shown in figure 4a, with the front-face temperature profile at the time of maximum contrast shown in figure 4b. Although not as great as in the SPICE model, the secondary increase in contrast immediately following heating is evident. Thus, the secondary increase in contrast is seen to persist through the transition from a one-dimensional model to a two-dimensional model, from electrically common time scales to

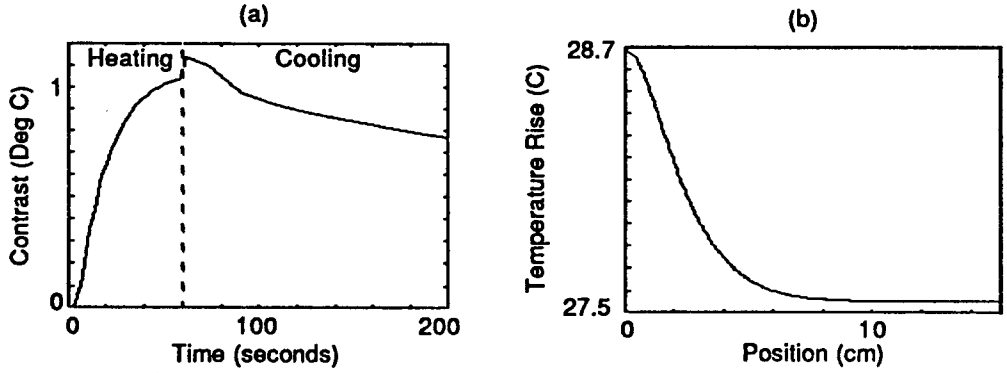

Fig. 4. a. Calculated front surface contrast from a two-dimensional profile in a thermal model having a buried delamination between 0.5 inches of steel and thick insulation. Heating is at 50 degrees C for 1 minute. Heat transfer coefficient is 728 W/(m^2-deg C) during heating and 1 percent of that value during cooling.
b. Temperature profile at the time of maximum contrast. Only one half of symmetrical profile is shown.

thermally relevant time scales, and from a mathematically convenient definition of contrast to one more closely aligned with NDE practice.

CONCLUSION

By introducing a mathematical description of temperature contrast and developing the appropriate theory to describe a simple case, thermal impedance of the observing surface has been shown to be an important characteristic in thermal non-destructive examination. Using numerical models, the secondary increase in thermal contrast found in some thermal imaging data is shown to be associated with modulation of the surface thermal impedance concurrently with application of the driving temperature variation. Thus, modulation of surface impedance has been identified as an important factor in the success of some thermal flaw detection techniques.

As an additional result, the frequency-independent nature of the surface thermal impedance has been shown to reduce the surface expression of thermal waves with sufficiently long wavelengths by substantial amounts. By considering that the wavelength of a thermal wave is associated with its exponential decay depth, a formula has been obtained to describe the penetration depth attainable for observing temperature contrast with a given surface heat transfer coefficient.

ACKNOWLEDGMENT

This work was supported by NASA Langley Research Center.

REFERENCES

1. E. M. Crisman and H. I. Ringermacher, Personal communications

2. E. W. Kutzscher and K. H. Zimmerman, Appl. Optics 7, 1715-1720 (1968)

3. G. Busse, Infrared Physics 20, 419-422 (1980)

4. W. P. Winfree, Personal communication

A NUMERICAL GRID GENERATION SCHEME FOR THERMAL SIMULATIONS IN LAMINATED STRUCTURES

Patricia.H. James*, Christopher S. Welch°,
and William P. Winfree
MS 231
NASA, Langley Research Center
Hampton, VA 23665

INTRODUCTION

Significant efforts are being made to improve the safety of the solid rocket motor (SRM) for the shuttle. The SRM is a laminated structure consisting of four layers of materials: a steel casing, bonded to NBR insulation, the liner, and the propellant. One of the candidate inspection techniques is a thermal technique which analyzes the response of the SRM to an external heat source for detection of disbonds at the interfaces between the steel, NBR and fuel. Computational simulations of experimental measurements can provide limits of the effectiveness of the technique and easily assume a variety of different defect geometries to determine their detectability without the expense of making many different samples. Simulations can also provide useful information for the experimenter including the heating protocol that will provide the greatest contrast and the typical flaw size that can be detected.

The first step in a computational simulation is to discretize the field of interest. This is accomplished through a mapping from a uniform computational domain (ξ, η coordinates) to a nonuniform, boundary conforming physical domain (x,y coordinates) that represents the physical geometry. A proper mapping is fundamental to an accurate computational simulation; the discrete representation of the physical geometry should reflect a knowledge of the physics of the experiment coupled with an understanding of the mathematics of the simulation. This discrete representation of the physical geometry should accurately define the boundaries of the field of interest. The grid must also be refined enough to properly solve the governing equations in regions of large gradients while minimizing the total number of grid points in order to diminish the CPU time required to solve the model. Once a properly constructed grid has been defined with associated boundary and initial conditions, an accurate numerical solution to the partial differential equation (PDE) at these discrete locations can be obtained.

For numerical simulations to be credible, the erroneous results that can be incurred simply through an unacceptable mapping must be understood and corrected. Only then can a finite representation of the differential equations be correctly solved. For example, the

*Analytical Services & Materials °College of William & Mary

seemingly reasonable grid shown below (Fig. 1.) was used to model a thermally loaded "SRM" sample. The sample was modeled as a two-layered laminate with a 1.2 cm thick layer of steel having a thermal conductivity of 36 W/(m°C), a density of 7750 Kg/cubic m, and a heat capacity of 460 J/(Kg°C), bonded to a 8.8 cm thick layer of NBR insulation having a thermal conductivity of 0.242 W/(m°C), a density of 1208 Kg/cubic m, and a heat capacity of 1923 J/(Kg°C). The flaw width was 1/18th the width of the entire sample. The simulation convected heat into the steel face for 200 seconds (h = 7.28 W/(m*m°C)). The grid consisted of 12x37 grid points, taking advantage of the symmetry along the x-axis by reflecting the solution and therefore halving the number of grid points needed. By slightly altering the location of only two grid lines in the insulation, the temperature contrast time histories (defined as the difference between the temperature of a node directly over the flaw and the temperature of a node at the far edge of the sample as a function of time) for nodes on the front face changed dramatically. This discrepancy is larger than the experimentally measured temperature contrast over a delamination 1/12th the width of the SRM samples when heated for 1 minute with 55°C water (approximately 0.5°C).

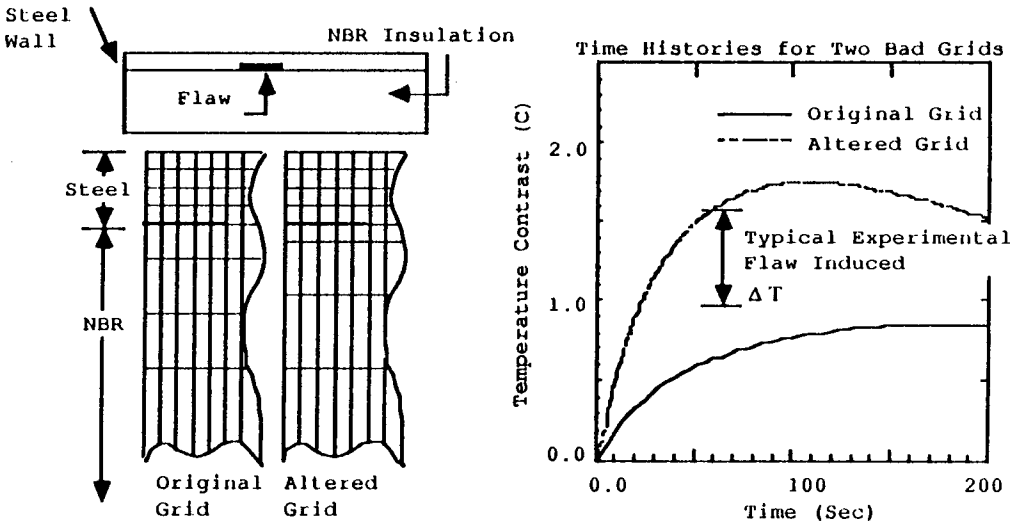

Fig. 1. Simple grid structure inadequate for thermal analyses

Much research has been done in the development of numerical grid generation schemes for computational fluid dynamics [1], [2], [3]. Many of the principles developed in this field can be applied to numerically modeling NDE problems. The necessity of a "good" mapping between the physical and computational domains is very pronounced in the case of laminated structures, in which large material property discontinuities exist between layers. For solutions to the heat equation as a thermal load is applied to the model, clustering of grid points at the material interface is required in order to resolve the details of the heat flux in this region.

GENERAL MESH GENERATION TECHNIQUES

The object of a grid generation algorithm is to transform a uniform mesh in the computational domain to a nonuniform, boundary-conforming grid in the physical domain. Research has shown that the mapping from the computational space into the physical space must be one-to-one and no grid lines should cross [4]. Additionally, the grid

points need to be clustered in regions of large gradients. Mesh generation codes should implement equations that avoid skewness and large cell aspect ratios if feasible; large cell aspect ratios degrade the convergence rate to steady state. Finally, it is very important to retain a smooth variation of the distance between grid lines in order to provide continuous transformation derivatives (metrics) between the physical domain and the computational domain [5].

There are many different methods of grid generation, and each method is useful for specific cases. For simple boundary shapes, such as typical test samples, algebraic generation methods are usually the most efficient. Therefore, an algebraic grid transformation method was chosen for modeling the laminated geometries, and its implementation is explained in the next section. It has been shown that when the variation in spacing in the interior of the model should be large, the interpolating functions best suited for algebraic grid generation methods are the hyperbolic tangent and the hyperbolic sine [6]. For this application, an equation involving the hyperbolic sine was used.

THE TRANSFORMATION EQUATION

Typically, large spatial temperature gradients will occur at the material boundaries of the SRM, and small grid spacing is required in these regions as compared to the spacing necessary in the insulating layer. The laminated structure of the SRM, and the rectangular geometry of the samples, simplifies the mapping conceptually and computationally. A transformation equation capable of refining the mesh about some interior point xc is shown below. Tau is the "stretching" parameter that varies from zero (to produce a uniform grid) to large values (which yield the most refinement near $x=x_c$), ξ is the coordinate in the computational domain that varies from zero to one in divisions equal to the total number of grid elements, and x is the location of the grid points in the physical domain which varies from zero to L, the length of the sample. This transformation has been shown to yield good results for fluid applications [7].

$$x = x_c \left\{ 1 + \frac{\sinh\left[\tau\ (\xi - B)\right]}{\sinh\ (\tau B)} \right\} \qquad \text{Where} \qquad B = \frac{1}{2\tau} \ln \left[\frac{1 + (e^{\tau} - 1)(x_c / L)}{1 + (e^{-\tau} - 1)(x_c / L)} \right] \qquad (1)$$

COMPARISON TO ANALYTIC SOLUTION

To evaluate the effectiveness of the transformation equation and to illustrate the importance of a properly constructed grid, a case with a known analytic solution was modeled [8]. The physical model is shown below (Fig. 2.). Two bodies with different thermal properties and initial temperatures are brought into contact at some initial time t=0, with the simplifying assumption of zero contact resistance between the two layers. The structure is laminated as is the SRM, but it does not include the fundamental problem of the flaw between the laminae, nor the multiple layers of the SRM design. The material properties of the SRM samples (steel and NBR insulation) were used for the two layers. Initial conditions were set to 50°C in the steel and 0°C in the NBR, and the front face of the model was observed as it cooled. To properly resolve the temperature gradient at the interface, the grid points surrounding this region must be closely spaced. Very little change in temperature, however, will occur near the rear of the NBR. To minimize computation time while still maintaining sufficient accuracy, a grid with largely varying spacing is preferable having small spacing near the material boundary which gradually becomes larger in the insulation.

Simulations with different magnitudes of clustering the same number of grid points illustrate the importance of a sufficiently refined grid. For a uniform grid with 31 grid points distributed in a total width of 10 cm, the maximum error on the front face of the model was just over 3°C at 106 seconds. As the clustering parameter was increased to 11 for the same number of grid points, the maximum error was reduced to only 0.12°C at 7 seconds. In both cases the cluster location was at the material interface. The exact solution is compared to solutions using these two magnitudes of clustering in Fig. 2.

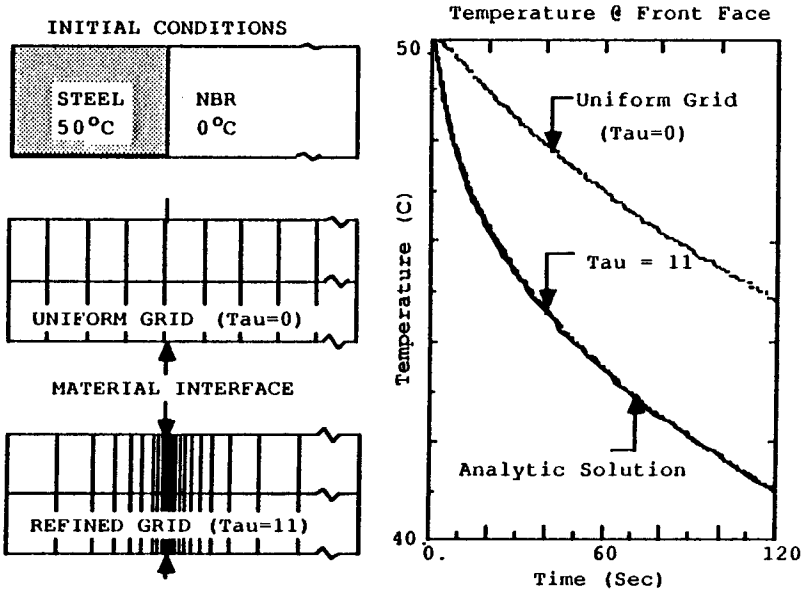

Fig. 2. A properly generated grid exhibits predictive behavior

In terms of maximum percent error, the effect of increasing the clustering for this model is shown in Fig. 3. The method is shown to exhibit a predictable behavior when changing the clustering parameter; as τ is increased at the material interface, the simulation more exactly represents the correct solution until a minimum in error is reached, whereupon further increasing τ only increases the magnitude of the total error due to the increase in roundoff error. As expected, the CPU time is increased as a more exact solution to the governing equation is found. The effect of increasing τ on CPU time is also shown in Fig. 3. However, the 24:1 reduction in error more than compensates for the 1:3.5 increase in CPU time.

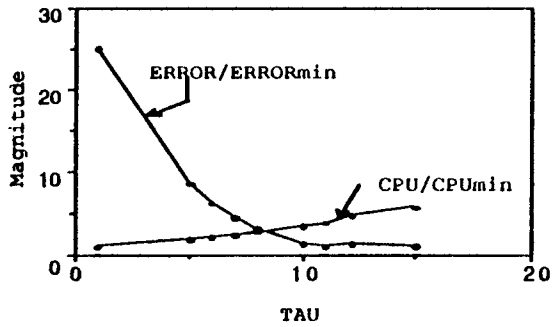

Fig. 3. Large reduction in error ratio / Small increase in CPU Ratio

The specific amount of clustering needed depends largely on the boundary and initial conditions and the material properties of the laminate. For the problem referred to in the introduction, where minor changes in the grid structure produced unacceptably large changes in the solution to the heat equation, a grid was generated using equation (1) with a clustering parameter of $\tau=7$ (Fig. 4). Perhaps the most important requirement for generating a "good" grid is that of a smooth derivative in the distance between grid lines. The derivative of the spacing between grid lines for the original grids are compared below with the grid produced from the transformation equation in Fig. 5. Note the smoothness in the derivative for the grid generated using the transformation equation, while the spatial derivatives for the original and slightly altered grids are not smooth.

The related relative temperature time histories are also shown below (Fig. 6.). Note that the slightly altered grid produces a temperature history relatively close to the "Good" grid solution. This phemomena is probably due to the minimum in spacing at the material interface for the altered grid, which does not occur in the case for the original grid (as shown in Fig. 5.).

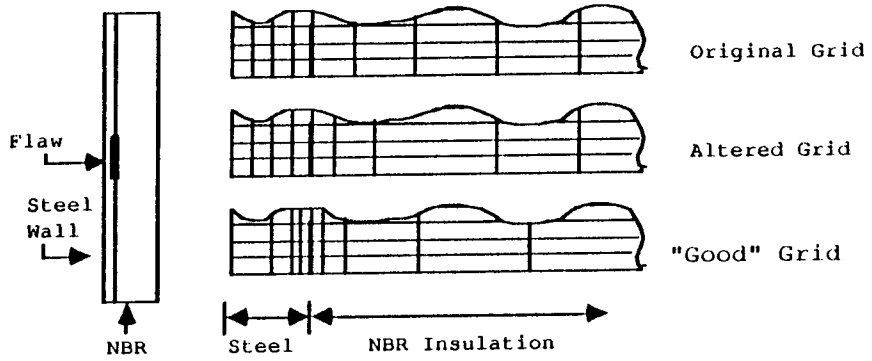

Fig. 4. Comparison of grid structures

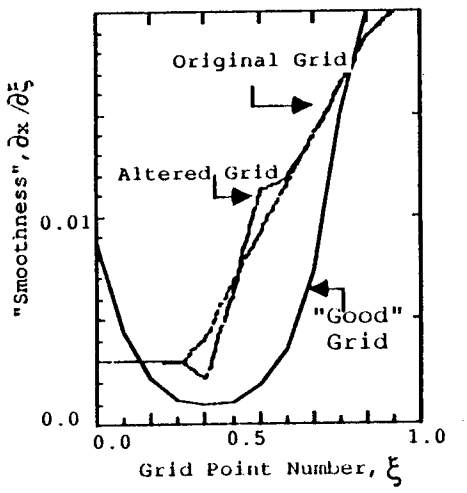

Fig. 5. Transformation equation yields smooth spatial derivative

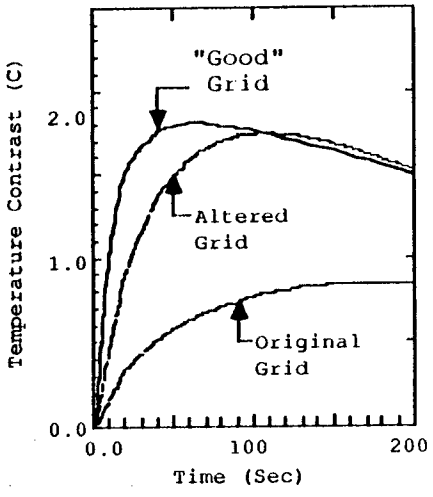

Fig. 6. Comparison of time histories for three grids

ERROR ANALYSIS

Large changes in spacing across the grid can introduce significant truncation error. Thompson, et al.[9] showed that as grid points are added, the truncation error is reduced by the square of the number of additional grid points for the same transformation equation. The truncation error Thompson derived is

$$T.E. = -\frac{1}{2} x_{\xi\xi} f_{\xi\xi} - \frac{1}{6} x_{\xi}^{2} f_{\xi\xi\xi} \tag{2}$$

Where x, the spatial coordinate in the physical domain, is a function of ξ ($0 \le \xi \le 1$), the coordinate in the computational domain. The general transformation function, f, is also a function of ξ. The last term of the series occurs even for uniform spacing, and the first term is dependent on the rate of change of spacing. For a particular transformation function, doubling the spacing from one grid point to the next can introduce large truncation errors. To examine the errors associated with the spatial derivatives of the grids for thermal NDE applications, consider the discrete form of the heat equation

$$\frac{1}{\alpha}\frac{\partial T}{\partial \tau} = \frac{\left(\frac{\partial T}{\partial x}\right)_{j+1/2} - \left(\frac{\partial T}{\partial x}\right)_{j-1/2}}{x_{j+1/2} - x_{j-1/2}} \tag{3}$$

If the spacing from an arbitrary element, j, to the two successive elements changes in the following manner (see Fig. 7.)

$$(\Delta x)_{j+1} = \beta(\Delta x)_j \quad \text{AND} \quad (\Delta x)_{j+2} = \gamma(\Delta x)_j \tag{4}$$

then it is easily shown that the relative error incurred through large changes in spacing is

$$\text{ERROR} \propto C_1 \Delta T_{j+1} + C_2 \Delta T_{j+2} + C_3 \Delta T_j \tag{5}$$

Where $C_1 = 2\left(1 - \frac{1}{\beta(\beta+1)} - \frac{1}{\beta(\beta+\gamma)}\right)$, $C_2 = \frac{2}{\gamma(\gamma+\beta)} - 1$ And $C_3 = \frac{2}{\beta+1} - 1$

(Note that if $\beta = \gamma = 1$, then ERROR = 0) Consider the elements surrounding the material interface. The error will be dominated by the C1 term, since the temperature gradient is largest across the interface. The error parameters for the grids illustrated in Fig. 4. are tabulated below for the elements just before and after the material boundary.

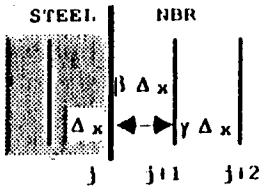

Type of Grid	C1	C2	C3
Original Grid (β=1.38; γ=2.62)	1.04	-0.81	-0.16
Altered Grid (β=0.83; γ=3.33)	0.10	-0.86	0.09
"Good" Grid (β=0.95; γ=1.39)	0.02	-0.39	0.03

Fig 7. Relative error comparison

Comparison of the critical parameter, C1, illustrates the magnitude of the effect of changes in grid spacing; the relative error due to nonuniform spacing at one spatial location is approximately 52 times greater in the original grid than in the computationally generated "Good" grid!

COMPARISON TO EXPERIMENTAL DATA

Having developed a properly generated grid, the method can now be applied to real problems involving flaws between laminates such as those that would exist for the SRM samples. How the simulation compares to experimental data depends on many different factors. A simple physical model (Fig. 8.) was chosen to compare the simulation with the experiment in order to reduce the factors that could possibly introduce discrepancies. A key feature of the geometry includes the laminated structure of the SRM, where the first layer is a conductor (steel), and the second layer is an insulator (plexiglas). To simulate a flaw, a half inch wide section of the plexiglas was excised from the back of the sample.

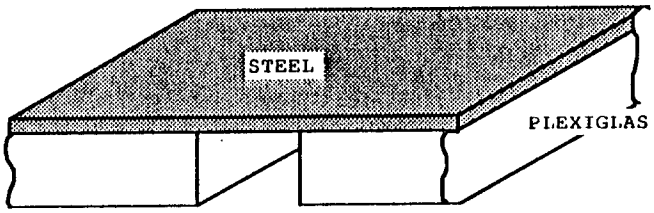

Fig. 8. Geometry of experimental sample

The sample was heated from the steel side for 15 seconds with a heat gun, and temperature data on the steel face was collected by an infrared camera as the sample cooled. Two of these profiles are shown below. The high amplitude curve was the first data set taken after heating, and the lower curve was acquired 40 seconds later.

The application of a thermal load by the heat gun was modeled as a flux input boundary condition and applied for 15 seconds, then removed to observe the model as it cooled. Two temperature profiles across the front face for the corresponding times are shown below.

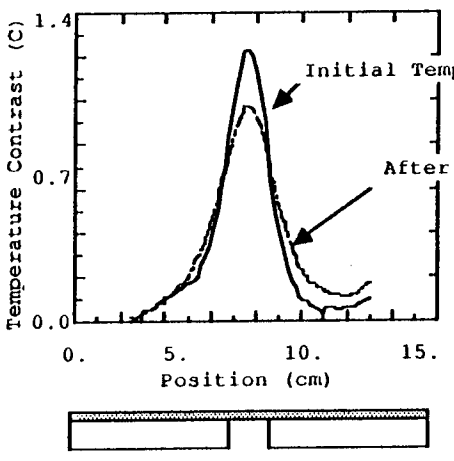

Fig. 9. Experimental data

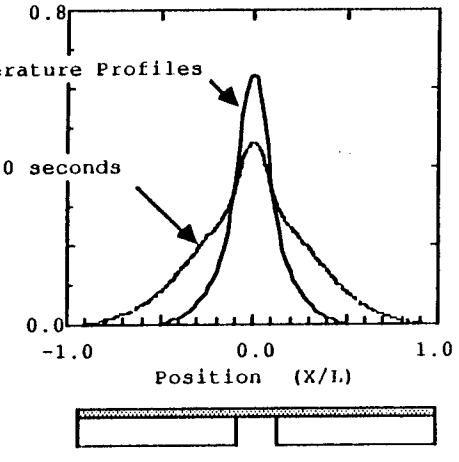

Fig. 10. Computational data

The comparison of the experimental data with the computational results is reasonable. The simulation clearly delineates the presence of a disbond between the laminatae. Since the passage of heat to the second material is inhibited directly over the flaw, the disbond is observed as a temperature increase at the front face of the sample. The grid was highly clustered around the region of the largest temperature gradient as was discussed previously. The change in amplitude during the 40 seconds between data sets for the experimental case is approximately 0.3°C, and approximately 0.2°C for the simulation. The fact that the exact magnitudes of the two figures differ slightly can be attributed to many different facts, not least of which is the uncertainty of the exact magnitude of the flux input from the heat gun. An additional discrepancy between the data sets is that the experimental data does not spread out as much as the computational data. This is probably due to uneven heating of the sample during the experiment.

CONCLUSIONS

A method for numerically generating a grid for laminated structures with simple geometries has been presented. The rationale for using such a method has been discussed, including the importance of the requirement for a grid generation technique which gives a smooth distribution of grid points across the solution domain. The error involved for a nonuniform grid with an irregular distribution is shown to be prohibitive.

Comparing the method for a model where an exact solution is known has provided a measure of absolute error encountered by altering the distribution of a fixed number of grid points. For laminated materials where the material properties vary greatly between layers, significant error has been shown to exist for grids where the temperature gradients have not been properly resolved. Furthermore, comparisons of experimental and numerical results show reasonable agreement and predictive power of the computational method.

REFERENCES

1. Joe F. Thompson, Z.U.A. Warsi, and C.W. Mastin, "Boundary-Fitted Coordinate Systems for Numerical Solutions of Partial Differential Equations - A Review:", Journal of Computational Physics, 47,1, (1982).
2. Peter R. Eiseman, and Robert Smith, "Mesh Generation Using Algebraic Techniques", Ed. Robert E. Smith, NASA CP-2166, (1980).
3. R.L. Sorenson, "A Computer Program to Generate Two-Dimensional Grids About Airfoils and Other Shapes by the Use of Poisson's Equations", NASA Ames Research Center, NASA TM 81198, (1980).
4. Dale A. Anderson, John C. Tannehill, and Richard H. Pletcher, Computational Fluid Mechanics and Heat Transfer, (Hemisphere Publishing Corporation, McGraw-Hill Book Company, New York, 1984), p. 521.
5. Anderson, Tannehill, and Pletcher, p. 521.
6. Joe F. Thompson, Z.U.A. Warsi, and C.W. Mastin, Numerical Grid Generation - Foundations and Applications, (North-Holland Press, New York, 1985), p.306.
7. Anderson, Tannehill, and Pletcher, pp.250-251
8. H.S. Carslaw and J.C. Jaeger, Conduction of Heat in Solids, (Oxford University Press, London, 1959), pp. 319-324.
9. Thompson, Warsi, and Mastin, Numerical Grid Generation Foundations and Applications, (North-Holland Press, New York, 1985), pp. 171-184.

THERMOGRAPHIC DETECTION OF

DELAMINATIONS IN LAMINATED STRUCTURES

William P. Winfree, Christopher S. Welch[†],
P. H. James[*] and Elliott Cramer[**]
MS 231
NASA Langley Research Center,
Hampton, VA 23665

INTRODUCTION

The detection of disbonds in a laminated structure is the focus of many nondestructive techniques. One of the promising techniques is thermography, where heat is applied to a structure, and the subsequent temperature profiles are detected with an infrared (IR) imager. If there is an even application of heat, an elevated temperature profile will appear, as a result of the reduction in heat flow from the surface layer to subsurface layers. Two advantages of the thermographic technique over more conventional ultrasonic techniques are that it can be easily made noncontacting and that large areas can be inspected in a short period of time.

A problem of thermographic inspection for disbonds is that it is often difficult to apply heat evenly to a large area. The result often is a temperature profile dominated by the initial heating profile rather than the presence of disbonds. A second problem occurs when the surface layer has a thermal conductivity significantly higher than that of the next layer in the structure. For this case the width of the thermal contrast profile resulting from the disbond is much larger than the width of the disbond, and so the image of the disbond does not clearly delineate the region of the disbond.

This paper presents a technique for enhancing the contrast due to a delamination, as well as more clearly delineating the region of the delamination. The technique also reduces the effects of uneven heating. The technique uses a two-dimensional filter convolved with the thermal image. The filter is designed to approximate operating on the temperature images with a Laplacian operator. For prescribed conditions, this operation approximately gives the image of heat flux from the top layer to the subsequent layer. The filtering results in an image which clearly delineates the disbond. Measurements were performed on samples with fabricated defects, and a comparison is presented between the resulting temperature images and the filtered images.

[†]College of William and Mary
[*]Analytical Services and Materials, Inc.
[**]Indiana University of Pa

EXPERIMENTAL TECHNIQUE

To investigate the technique samples were fabricated with known defects. The samples consisted of a sheet of steel .16 cm thick, backed by a rubber layer .63 cm thick, backed by an aluminum layer 2.5 cm thick, all 15.0 cm square. The layers were bonded together with a slow curing two-part epoxy system. To produce a disbond a portion of the rubber was removed to form a hole before assembly.

Measurements were made by heating the steel surface of the samples for approximately 15 seconds with a hot air gun which produces temperatures greater than 200 C. The subsequent temperature images were detected with an IR imager which outputs standard video frames. The imager uses a scanned HgCdTe detector cooled by liquid nitrogen. The video images were input into an image processor, which was capable of digitizing and averaging 30 frames a second. The image processor averaged 256 frames and then transferred the averaged signal to a minicomputer for analysis and archival. Averaged temperature profiles were recorded every 15 seconds after heating, for a period for 240 seconds.

THEORY AND ANALYSIS

A thin plate bonded to a backing material with heat flow is described by the equation

$$\nabla^2 T(x,y,t) - \frac{F(x,y,t)}{wK} = \frac{1}{\kappa}\frac{\partial T(x,y,t)}{\partial t} \qquad (1),$$

where $F(x,y,t)$ is the flux into the second material, κ is the thermal diffusivity of the plate, w is the thickness of the plate and K is the thermal conductivity of the plate. If the diffusivity of the backing material is significantly lower than that of the plate, the flux quickly becomes nearly constant in time, and equation (1) reduces to

$$\nabla^2 T(x,y,t) - \frac{F(x,y)}{wK} = \frac{1}{\kappa}\frac{\partial T(x,y,t)}{\partial t} \qquad (2).$$

The solution to equation 2 can be divided into two parts, a dynamic part $T_d(x,y,t)$ and a static solution $T_s(x,y)$, such that

$$\nabla^2 T_d(x,y,t) = \frac{1}{\kappa}\frac{\partial T_d(x,y,t)}{\partial t} \qquad (4)$$

and

$$\nabla^2 T_s(x,y) = \frac{F(x,y)}{wK} \qquad (5).$$

For $T_d(x,y,t)$, it can be shown with Fourier analysis that temperature fluctuations with a characteristic length of L will decay over a time on the order of $L^2/(4\kappa\pi^2)$, leaving a temperature profile dominated be the static contribution to the solution at that characteristic size. Thus, for a delamination of size L, if one waits for a time greater than $L^2/(4\kappa\pi^2)$, the local temperature distribution then is dominated by the flux variations caused by the delamination, and the Laplacian of the local temperature distribution (Eq. 5) gives an image of the flux variation out of the plate. If the delamination region is clearly delineated by the flux pattern, then it is clearly delineated in the Laplacian of the temperature profile.

To approximate the Laplacian of the thermal image, a 7 by 7 array of temperature data centered on a point of interest was fit to the expression

$$T(x,y) = A_1 + A_2x + A_3x^2 + A_4y + A_5y^2 + A_6xy \qquad (6),$$

Table 1. Elements of 2 Dimensional filter convolved with thermal image to approximately calculate its Laplacian. Each element has been multiplied by 294.

10	5	2	1	2	5	10
5	0	-3	-4	-3	0	5
2	-3	-6	-7	-6	-3	2
1	-4	-7	-8	-7	-4	1
2	-3	-6	-7	-6	-3	2
5	0	-3	-4	-3	0	5
10	5	2	1	2	5	10

by a linear least squares fitting routine. This fit was performed at each point in the image to build up images of the A's. A sum the A_3 and A_5 images times two is approximately equal to the Laplacian.

To reduce the processing time, a 7 by 7 square filter was designed which was equivalent to this process. The coefficients of the filter are given in table 1. The filter was then convolved with the thermal image to give its Laplacian.

RESULTS

A typical thermal image for a sample with a 1.2 cm diameter circular disbond in the center 75 seconds after application of heat is shown in figure 1. From the image it is possible to see first that the heat was not applied evenly. There is a large variation in the temperature from corner to corner, greater than the small variation in temperature at the center of the image, attributed to a disbond. The Laplacian of this temperature image is shown in figure 2. In the image of the Laplacian the presence of the disbond is clearly seen and is the largest contrast in the image. Profiles of the image through the delamination are shown in figure 3. The second derivative profile delineates the region of the disbond much more clearly than the temperature profile. As can be seen

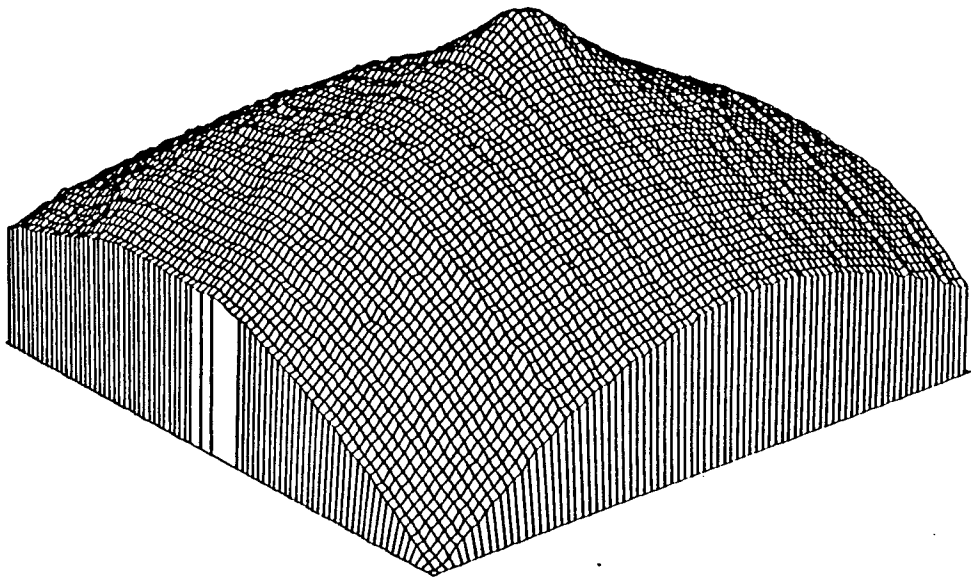

Figure 1. Typical thermal image for first sample described in the text 75 seconds after application of heat

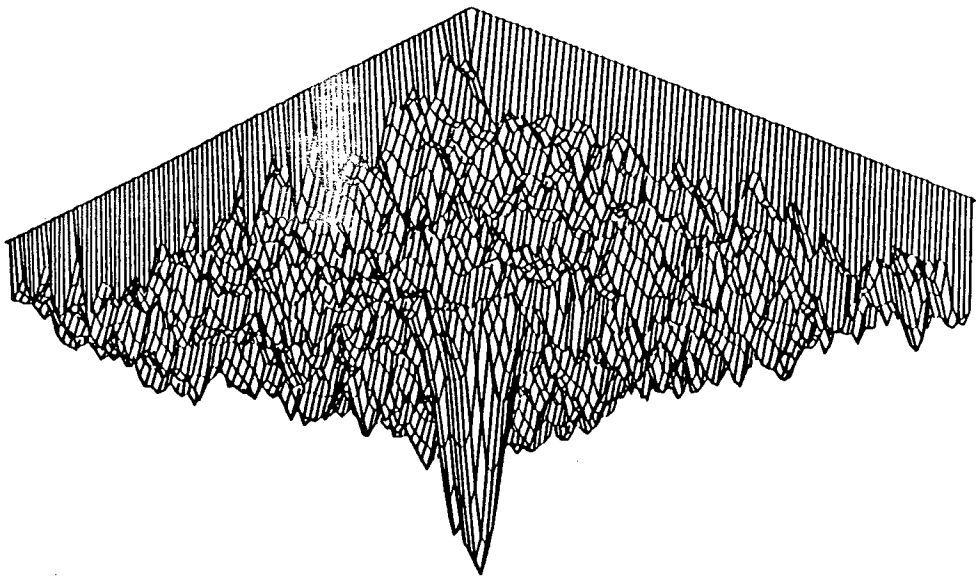

Figure 2. Laplacian of thermal image in figure 1 for sample with single circular delamination in the center.

from figure 3, the width at half maximum of the second derivative profile is approximately equal to the diameter of the disbond.

The thermal image taken 75 seconds after heating of a second sample with two disbonds formed by two 1.2 cm wide by 2.5 cm long slots in the rubber separated by 1.6 cm is shown in figure 4. Once again the Laplacian of the temperature, shown in figure 5, clearly delineates the regions of disbond and fully resolves the two disbonds. Profiles of the temperature and its Laplacian are shown in figure 6. The width at half maximum of the Laplacian profiles are again approximately the width of the defect.

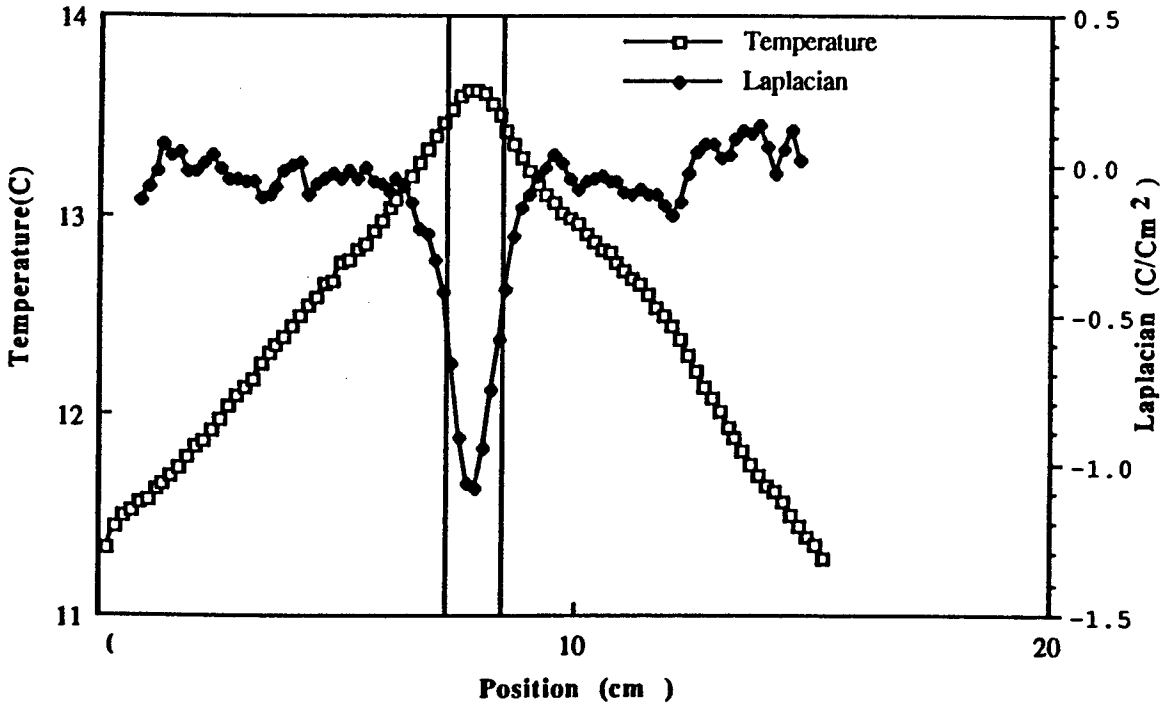

Figure 3. Profiles of temperature and its Laplacian across the center of the delamination with lines drawn to show edges of delamination.

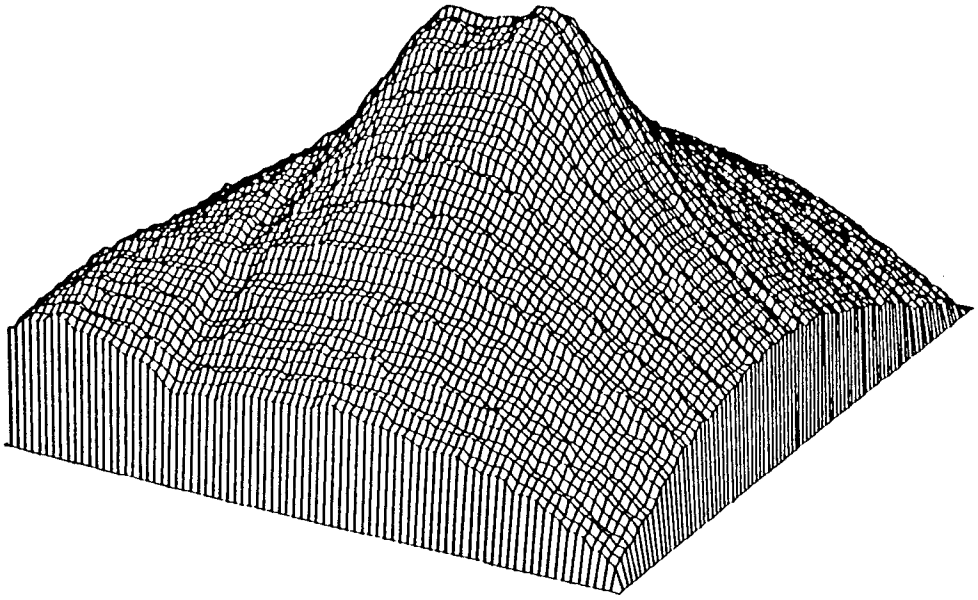

Figure 4. Typical thermal image for second sample described in the text 75 seconds after application of heat

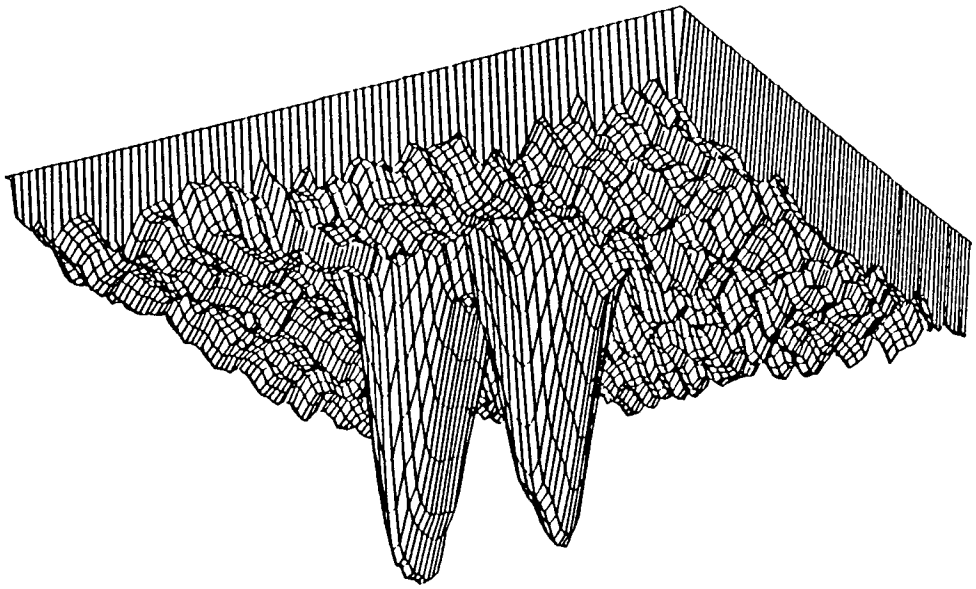

Figure 5. Laplacian of thermal image in figure 4 for sample with two rectangular delaminations in the center.

SUMMARY

A technique has been presented for processing thermal images which clearly delineates regions of sub-surface disbonds. The processing is approximately equivalent to taking a Laplacian of the temperature image. The technique is shown to discriminate against thermal contrast due to uneven application of heat. For a conductive layer backed by an insulating layer, when a quasi-static condition for flow is met, the technique gives the heat flux through the back surface of the conductor.

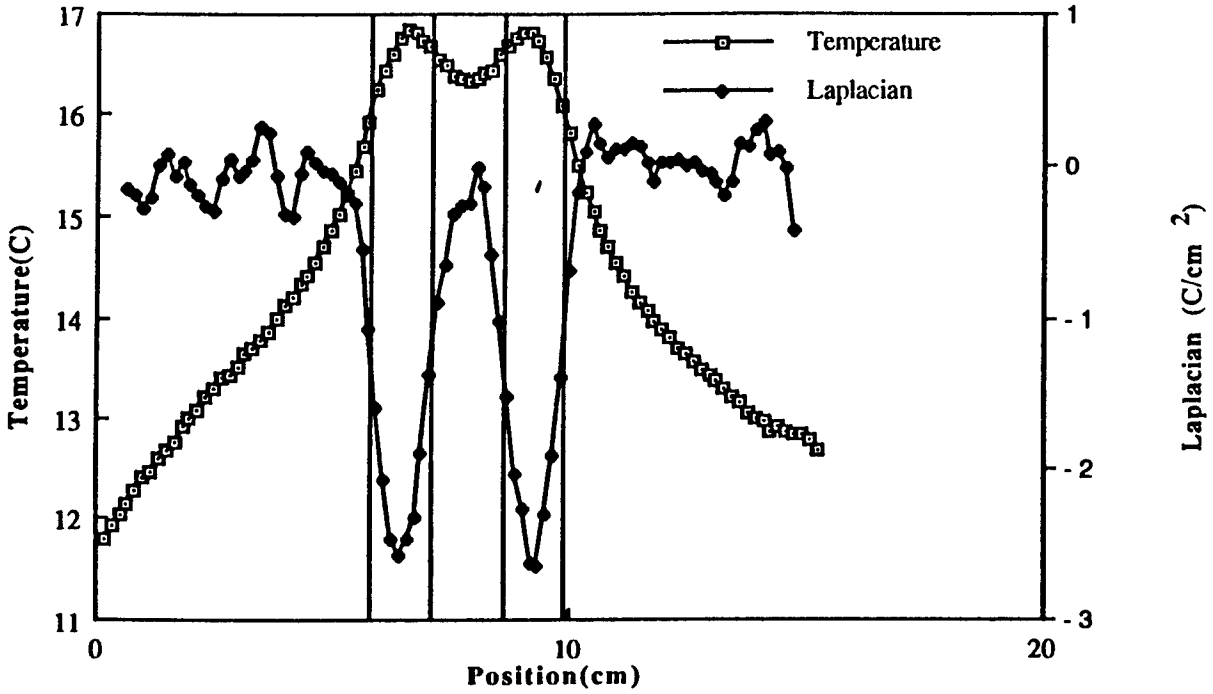

Figure 6. Profiles of temperature and its Laplacian across the center of the delaminations with lines drawn to show edges of delaminations.

THERMAL DIFFUSIVITY MEASUREMENTS IN CARBON-CARBON COMPOSITES

D. Michele Heath and William P. Winfree
NASA
Langley Research Center
Hampton, VA 23665

INTRODUCTION

In recent years, carbon-carbon composite materials have come into widespread use in aerospace industries. These materials are particularly attractive for high temperature applications due to their thermal and mechanical behavior. Few quantitative measurements, however, have been made to characterize these materials. One problem encountered with carbon-carbon composites is porosity. Materials engineers have determined that degree of porosity is correlated to inter-laminar sheer strength in carbon-carbon composites. Since repetition of the carbon-carbon processing cycle reduces porosity, a technique for assessing porosity between processing cycles that is non-contacting and does not contaminate the material would be of value. A material property which is related to density and therefore to porosity, is thermal diffusivity. Thermal diffusivity is easily measured non-contactingly and remotely with infrared techniques and is therefore an attractive candidate measurement for assessing porosity between processing cycles of carbon-carbon composites.

In this work, a non-contacting measurement technique for measuring thermal diffusivity which utilizes a Nd-YAG laser as a thermal wave source and an IR camera detector is described. Thermal diffusivity is extracted from the phase delay between the thermal wave source and a spatially offset detection region. Results are given for three orthogonal directions to indicate the variation of diffusivity with structural anisotropy of the material. Diffusivity measurements taken in a linear pattern over the sample surface are presented to illustrate the effect of local variations in the fiber direction due to fiber weave in the composite lay-up. In addition, results are given for diffusivity measurements of a series of samples which have undergone varying numbers of repetitions of the processing cycle, producing a range of porosity levels. A strong correlation of diffusivity in the through ply direction with the bulk density, and therefore with the level of porosity of the composite material was shown.

EXPERIMENT

By measuring the temperature of carbon-carbon samples as a function of time, at the source of heating and comparing this function to a similar measurement made simultaneously over a region spatially offset

from the source, the phase delay, and thus the thermal diffusivity of the samples were found. Two experimental configurations were used to determine the diffusivity in directions in the plane of the sample face and perpendicular to the sample face, i.e. through the sample thickness. Figure 1 is a schematic diagram of the experimental configuration used for determining diffusivity in the plane of the sample. A Nd-YAG laser

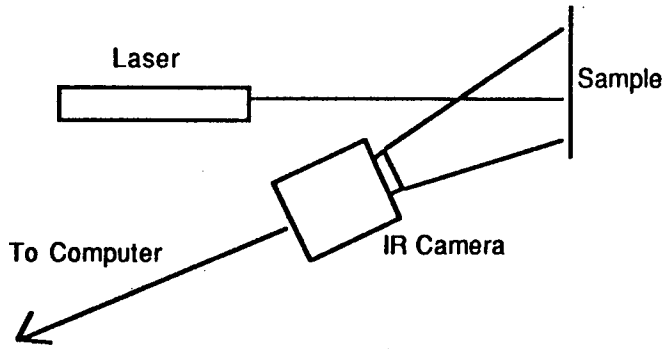

Figure 1: Experimental Schematic for In-Plane Measurements

operating at 1.06 μm was used as a thermal point source. The source was pulsed at 1 Hz. for in plane measurements. The detector was a video format infrared camera, sensitive to 8-12 μm radiation. The temperature images obtained were digitized and stored on disk for the analysis processing described below. For in plane measurements, the detector was positioned on the front face side of the sample, i.e. on the same side that heating occured. A spatial profile of the point source is shown in figure 2, obtained by taking a cross section of one image frame. Vertical cross sections of the temperature images correspond to heat flow in the cross fiber direction, while horizontal cross sections correspond to flow in the fiber direction. Monitoring the temperature at a point 2 cm from the source yields the curve shown in figure 3.

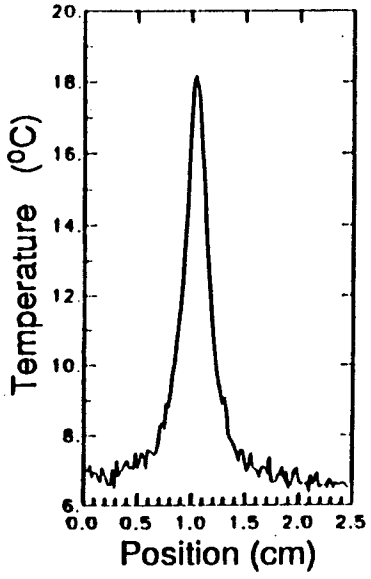

Figure 2: Temperature Distribution of Point Source

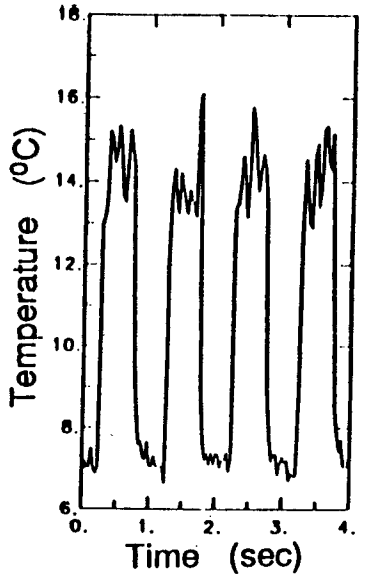

Figure 3: Temporal Temperature Response

When considering flow in the through ply direction, the experimental configuration shown in figure 4 was used. In this configuration, the camera was positioned on the side of the sample opposite to the side that heating occured. A beam splitter was used to direct a portion of the laser beam to the back side of the sample to be used as a timing reference. Due to the low diffusivity in the through ply direction, a lower frequency heating pulse, .08 Hz, was used. In all other aspects,

the experimental technique for the through ply measurement was identical to that for the in plane measurements.

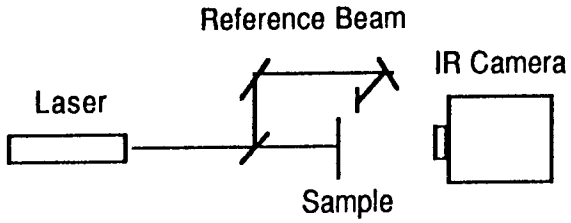

Figure 4: Experimental Schematic for Through-Ply Measurements

THEORY

Frequency domain analysis using the phase delay between a thermal stimulus and response is a common approach to measuring thermal diffusivity in solids. For this variation, a harmonically varying thermal point source is used and the phase lag, measured as a function of distance from the source, is used to calculate the diffusivity of the material. Carslaw and Jaeger show in [1] that for a two dimensional case with periodic heat source, the temperature profile is given by a modified Bessel function. When the distance from the source, x, is sufficiently large, the phase of this thermal wave is approximately linear. The phase versus x curve, then, will approach a linear function for x greater than some critical value x_c. The slope of this line is proportional to the thermal diffusivity of the material by the following equation:

$$k = \frac{\pi F}{m^2} \qquad (1)$$

where k=thermal diffusivity
F= source frequency
m= slope of phase versus position curve.

The phase of the thermal wave at a given point is found by numerically calculating the Fourier transform of the temporal history of temperature at that point. The inverse tangent of the imaginary divided by the real components of the Fourier transform gives the phase of the thermal wave at the given point. Repeating this calculation for each point on the scan line and referencing this phase to that of the phase at the source position, results in the phase versus x curve. Figure 5 depicts a phase versus x curve for one sample, measuring x in the plane of the sample face, parallel to the fiber direction. It can be seen that the phase approaches 0 at x=1.1 cm, corresponding to the location of the source, and increases with distance from the source. For values of x greater than approximately 1.15 cm, the phase function is roughly linear, until distance from the source becomes so great that the signal is lost to noise. A segment of the curve in the linear region, along with its best linear fit, is given in figure 6. It is shown that the linear approximation is reasonable for the segment of the curve where x is between 0.02 and 0.25 cm from the source, for this sample and at the given frequency of 1 Hz. Using the slope of the linear fit then, the diffusivity is calculated from equation 1.

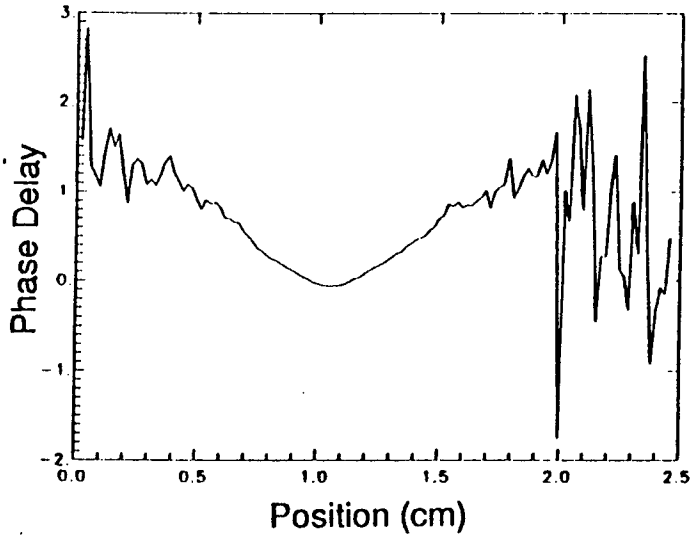

Figure 5: Phase Versus Position

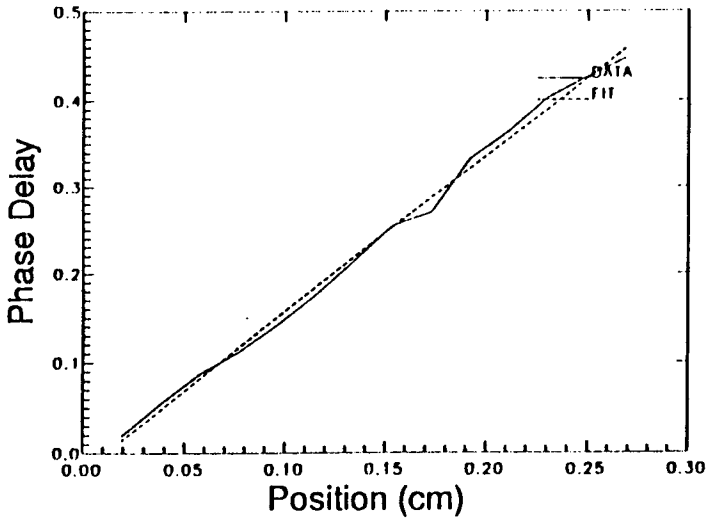

Figure 6: Linear Segment of Phase Distribution

RESULTS

The technique described above was used to determine the diffusivity of carbon-carbon coupons which were fabricated to give a range of porosity levels. The coupons were fabricated in a two dimensional orthogonal weave configuration, with a 0^0-90^0 ply lay-up. Figure 7 depicts the fiber weave-layup configuration used. A series of 7 samples were measured, each of which had undergone a different number of densification cycles during processing. During these densification cycles, the samples are emersed in a phenolic resin and then pyrolized. The resin penetrates the pores and upon pyrolisis, is reduced to carbon residue, which fills the pores. By varying the number of densification cycles, samples were produced with a range of porosity levels. The level of porosity was reflected in the measured bulk density of the sample, which increased when densification was repeated. The 7 samples used, spanned a range of densities from 1.435 to 1.645 gm/cm^3.

Measurements were made on the coupons in the through ply, or z direction. These results are shown in figure 8 which plots diffusivity against density, with the discrete points representing measured data and

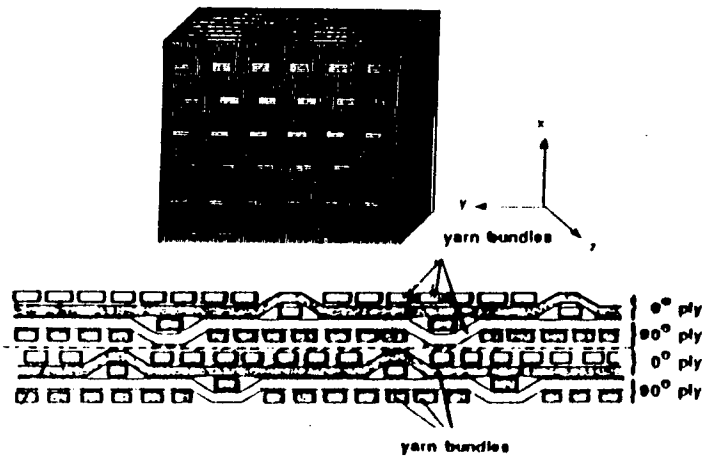

Figure 7: Composite Lay-up

the line representing the best linear fit to these points. A definite upward trend is seen as density increases, with a functional dependence of diffusivity with density that is roughly linear.

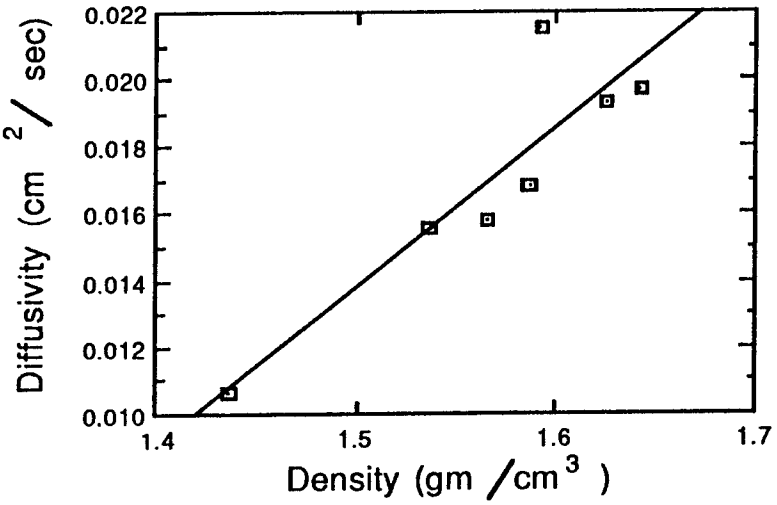

Figure 8: Diffusivity Versus Density
Through-Ply Direction

Measurements were also made in the plane of the sample face, both parallel and perpendicular to the fibers. These results are shown in figures 9 and 10 respectively. As the figures indicate, no consistent trend is seen over the range of densities measured. The values measured for the cross fiber direction, however, were consistently lower than the values found in the fiber direction, as expected.

To further illustrate the fiber orientation effect, a linear source was used which extended over the fiber weave on the sample surface, so that in some areas the measurement represented diffusivity parallel to the fibers, and in other areas represented diffusivity perpendicular to the fibers. The results of these measurements for one sample are shown in figure 11. Diffusivity is plotted here as a function of position across the sample. The positions between 0.15 to 0.4 cm, and 1.15 to 1.4 cm correspond to cross woven fiber bundles, so that measurements here represent diffusivity in the cross fiber direction. Again, the expected increase in diffusivity in the direction of the fibers is seen. A change of approximately 40 percent is shown for this sample.

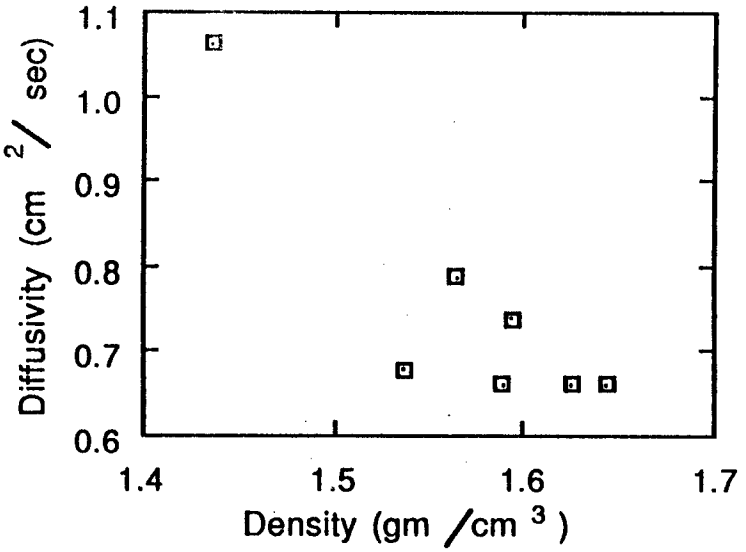

Figure 9: Diffusivity Versus Density
In Fiber Direction

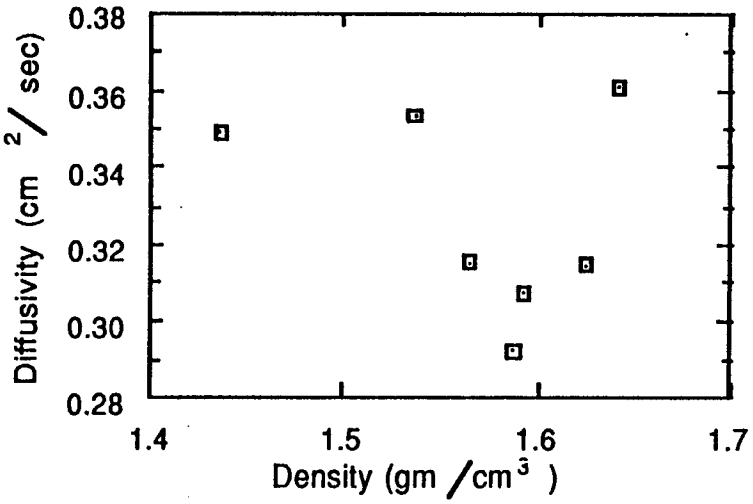

Figure 10: Diffusivity Versus Density
Cross- fiber direction

DISCUSSION

The measurement results presented indicate that standard thermal measurement techniques are applicable to characterizing carbon-carbon composites. The thermal diffusivity values obtained in each of the three orthogonal directions fell within the range of values quoted in the literature. Since the fibers are the prime thermal carriers, the fiber direction is expected to have the highest diffusivity, with the cross-fiber and through-ply directions following. This relationship was observed in these results. Further, the thermal wave phase detection technique, when used in the through-ply configuration, was shown to be sensitive to the level of density changes normally encountered in carbon-carbon processing. Through-ply measurements are expected to be more strongly affected by density changes due to the greater contribution of the matrix properties in this direction. Since the diffusivity in the in-plane directions are highly affected by the fibers, which are not changed by repeated densification of the composite, this may explain the absence of any correlation between diffusivity and density for the in-plane results. In the through-ply direction, a strong correlation was observed, with a roughly linear functional dependence. Care must be

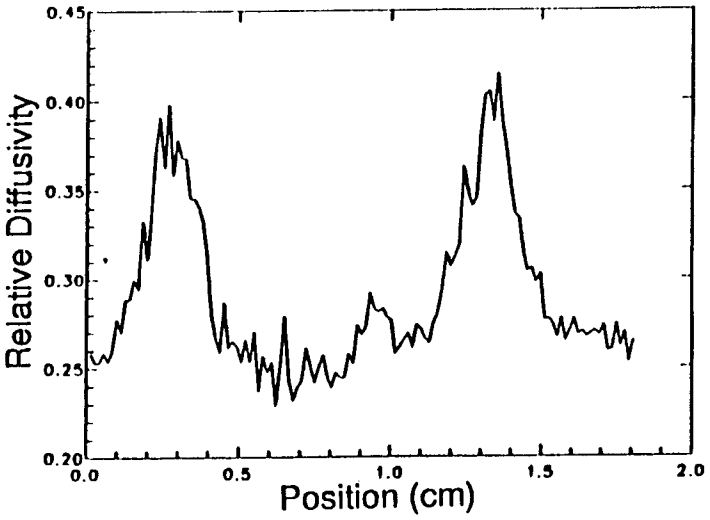

Figure 11: Diffusivity Versus Position

taken when measuring carbon-carbon materials, to account for fiber orientation, since this effect was shown to be larger than the effect of the small density changes of interest. In the through-ply direction, however, this effect is minimized, and the technique can be used to monitor carbon-carbon materials between processing cycles.

REFERENCES

1. H. S. Carslaw and J. C. Jaeger, Conduction of Heat in Solids, 2nd Edition, (Clarendon, Oxford 1959).

Reprinted from PROCEEDINGS OF THE ICIASF RECORD — INTERNATIONAL CONGRESS ON INSTRUMENTATION IN AEROSPACE SIMULATION FACILITIES, Williamsburg, Va., June 22-25, 1987

REMOTE NONCONTACTING MEASUREMENTS OF HEAT TRANSFER COEFFICIENTS FOR DETECTION OF BOUNDARY LAYER TRANSITION IN WIND TUNNEL TESTS

D. Michele Heath, William P. Winfree, Debra L. Carraway, Joseph S. Heyman

NASA Langley Research Center
Hampton, Virginia

Abstract

The existence of turbulent boundary-layer flow conditions over natural laminar flow (NLF) airfoil surfaces is of prime concern in aerospace industries. The resulting increase in drag boosts fuel consumption and costs. In NLF airfoil design it is particularly desirable to detect and locate the position of laminar to turbulent boundary-layer transition on airfoil models. Current techniques require surface modification or complex implementation. A remote, noncontacting infrared measurement technique for measuring heat transfer has been applied to the detection of boundary-layer transition in wind tunnel settings. The measurement system consists of three prime elements: a laser heating source, an infrared camera for data aquisition, and a video recorder for data storage. A laser beam is scanned over an airfoil, heating its surface to a few degrees above ambient. An infrared camera then measures the temperature of the airfoil over a two dimensional field, and these temperatures are stored as a function of time on a video recorder. The resulting temperature pictures are digitized and an iterative approximation algorithm is used to extract the heat transfer coefficient. The resulting values are normalized to the natural convection condition.

The technique has been applied to the detection of boundary-layer transition in low speed wind tunnel tests and compared to well established hot film measurements, which were made simultaneously, to confirm the flow conditions. Heat transfer coefficients were determined using a linear scanning pattern, to indicate the position of natural and of artificially induced transition on an airfoil, at various wind speeds. The technique is shown to be sensitive to transition at low Mach numbers, where previous infrared techniques, using kinetic heating, were found to be insensitive.

Advantages of the technique include noninvasive scanning, ease of use and cost reduction. No complex and costly machining or implementation of contacting sensors during model fabrication is required. No surface preparation is required for the model, barring the case of highly reflective surface finishes. In the reflective case, as for highly polished metal surfaces, a thin film of insulating plastic may be required. The technique also has the potential for viewing flow characteristics over a large field.

Introduction

Many approaches have been used for detecting boundary-layer transition in flow fields. Since flow conditions are characterized by fluid velocity and pressure variations, these variables, and associated parameters such as density, index of refraction and temperature, can be used for flow diagnostics. Convective heat transfer is one such parameter that can be used to detect boundary layer transition. Since turbulent flow evinces an increase in skin friction, heat transfer rates are greater in turbulent flow than in laminar flow. Transition, then, can be indicated by an increase in measured heat transfer.

Extensive work has previously been done measuring each of these parameters, by a variety of techniques. Traditional measurement techniques have relied on invasive probes or complex implementation. The least invasive approach has been radiative, either optical or infrared. Optical techniques (deflection, velocimetry or interferometry) are difficult to implement and sensitive to vibrations and three dimensional flow effects.

Infrared measurement techniques have offered some advantages for heat transfer studies. IR cameras are commercially available which measure the intensity of IR radiation and convert this intensity to temperature by the well known black body radiation relationship. These cameras scan two dimensional fields at video frame rates and detect temperature differences of .2 degrees C. The results are temperature distributions of the model surface which can be recorded and digitized for quantitative analysis of heat transfer rates. The use of IR cameras for flow diagnostics has been demonstrated for the case of kinetic heating [1]. In that work, frictional heat transfer from the fluid to the model skin was monitored by infrared radiation measurements. Good results were achieved for detecting transition at high Mach numbers, but at low Mach numbers the kinetic heating was not large enough to achieve good sensitivity to the transition effect. The work presented here uses an active heating technique, i.e. the model surface is heated radiatively by an external source, and the temperature decay is monitored when heating has ceased. These measurements show good results for detecting transition and boundary layer separation at low Mach numbers. The technique has the advantage of being non-invasive and scannable; no internal probing which can disrupt the flow conditions is required. No model surface preparation or costly machining is necessary. The exception is in the case of a highly reflective or conductive model surface, as for polished metallic models. In these cases a thin film of insulating plastic may be required.

Experiment

An experiment was performed to verify this technique in a .30 x .43 meter, low speed, atmospheric wind tunnel. The model was a well characterized .30 meter chord, .30 meter span natural laminar flow airfoil, constructed with a thin layer of fiberglass epoxy over a high density polyurethane foam core. The foam core had a thermal conductivity of .00013 (cal/sec. $cm.^2$)(cm./ ^0C), and so acted as a highly effective thermal insulator. Two IR transparent windows were installed in the side of a wind tunnel test section, to allow an external source and detector to inject heat and monitor the model surface

temperature.

Measurements were made with OPTITHIRMS (OPTical THermal InfrRed Measurement System), developed at the NASA Langley Research Center for nondestructive evaluation and materials characterization [2],[3]. A schematic diagram of the measurement system is shown in figure 1. The heat source is an 8 Watt, 10.6 micron, CO_2 laser. A voltage controlled deflecting mirror directs the beam. An 8 - 12 micron IR camera with a liquid nitrogen cooled HgCdTe detector measures the temperature distribution of the model surface. These temperatures are relative to ambient.

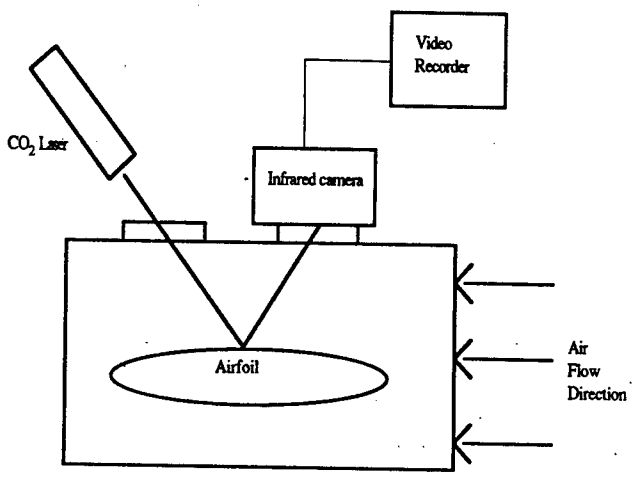

Fig. 1: Experimental Configuration

The camera scans an 18° by 14° field at video frame rates and outputs the temperature image in standard video format. An image processor then digitizes the image, either directly or from a video recording, and transfers the data to a computer for analysis.

For the present work the laser beam was scanned over the model surface in a linear pattern, running parallel to the flow. The laser line source was 15 cm in length, traversing the entire camera field of view. This heating pattern was chosen to reduce the dimensionality of net heat flow, for ease of analysis

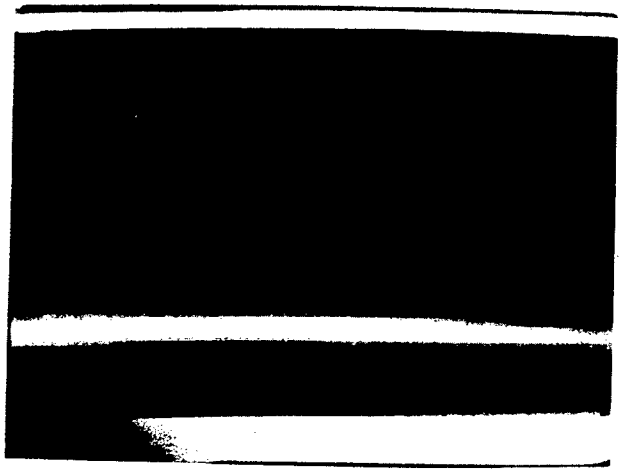

Fig. 2 : Thermal Image

and reduction of computation time. The source was pulsed and allowed to cool cyclically, until the temperature fluctuations reached a periodic equilibrium. This protocol allowed the use

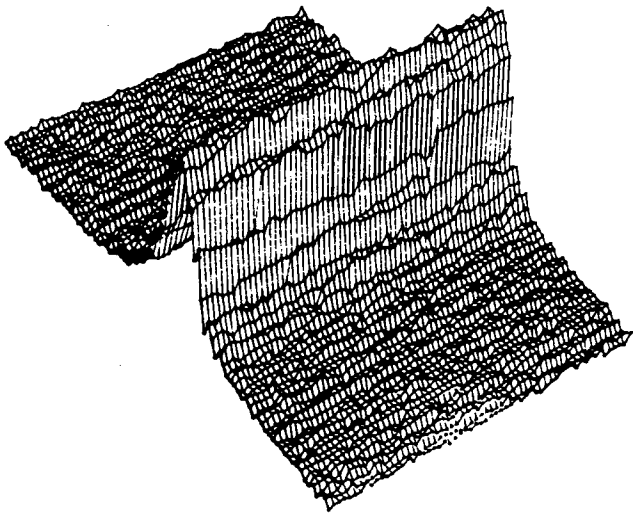

Fig. 3 : Three Dimensional Representation of Thermal Image

of Fourier transform analysis techniques. Measurements were made with laser pulse lengths ranging from .5 to 3. seconds, resulting in peak temperatures of 5. to 20. degrees C. above ambient. The temperature evolution was then recorded on video tape to allow transport to an off site computer for analysis. Metallic tape markers, 1 mil thick were attached to the model surface to provide a reference coordinate system. Figure 2. is a picture of the raw temperature data, and Figure 3. is a three dimensional representation of the temperature distribution.

Measurements were made with this configuration at wind velocities ranging from 0 to 180 mph and at a 5° angle of attack, so that the resulting shift in transition position would be observed. Separate measurements were made with a hot film sensor technique, reported in-[4], to verify the flow conditions. The measurements were repeated with a thin line of grit attached to the model surface, to induce a well defined transition point.

Theory

The three mechanisms by which heat transfer occurs are radiation, conduction, and convection. The magnitude of the heat loss due to radiation is related to the difference in the fourth powers of the temperatures of the body and the surrounding fluid by a proportionality constant incorporating the Steffan-Boltzmann constant and the thermal emissivity of the surface. This effect is generally considered negligible in the absence of high temperatures and will not be considered here.

The relative contributions of conduction through the solid airfoil, and convection to the surrounding fluid, to the overall heat transfer of a system, depend upon physical properties of the interfacing media and the flow characteristics of the fluid. Both mechanisms are proportional to the temperature difference. To accurately reduce the temperatures measured with the system described above, to heat transfer coefficients, a mathematical model is required to separate the convection and conduction contributions. This can be achieved by solving the equation of conduction for the body while applying a boundary condition representing convection loss to the fluid at the interface.

The equation of conduction is well understood for many geometries and boundary conditions. It is stated in one

dimension in equation 1.

$$\frac{\partial^2 v(x,t)}{\partial x^2} = \frac{1}{k}\frac{\partial v(x,t)}{\partial x} \qquad (1)$$

where

v(x,t) = temperature above ambient
x = spatial coordinate
t = temporal coordinate
k = thermal diffusivity

Fourier's integral theorem states that a time dependent function, such as v(x,t), can be represented by the expression:

$$v(x,t) = \frac{1}{\sqrt{2\pi}}\int_{-\infty}^{\infty} e^{i\omega t}\,\bar{v}(x,\omega)\,d\omega \qquad (2)$$

where

ω = angular frequency
$\bar{v}(x,\omega)$ = Fourier transform of v(x,t).

Substituting this expression into equation 1 gives the simpler form:

$$\int_{-\infty}^{\infty}\left(\frac{\partial^2 \bar{v}}{\partial x^2} - \frac{i\omega}{k}\bar{v}\right) d\omega = 0 \qquad (3)$$

The general solution to equation 3 is well known, and is given by:

$$\bar{v}(x,\omega) = A\,e^{-(1+i)\sqrt{\frac{\omega}{2k}}\,x} + B\,e^{(1+i)\sqrt{\frac{\omega}{2k}}\,x} \qquad (4)$$

The appropriate boundary conditions can now be applied to evaluate the constants A and B.

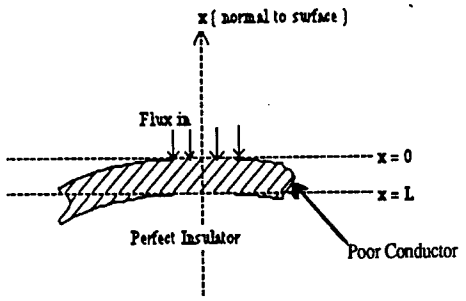

Fig. 4 : Boundary Conditions

As described above, the airfoil used for this work was constructed of a thin layer of poorly conducting material over a highly insulating substrate. These conditions are depicted in figure 4. To find the particular solution to equation 1 for this case, the following boundary conditions were chosen:

$$-K\frac{\partial \bar{v}}{\partial x} + H\bar{v} = \bar{F}\,\varepsilon \qquad \text{at } x = 0 \qquad \text{(i)}$$

$$\frac{\partial \bar{v}}{\partial x} = 0 \qquad \text{at } x = l \qquad \text{(ii)}$$

where

K = thermal conductivity
H = heat transfer coefficient
$\bar{F}$ = Fourier transform of input heating pulse
T = heating pulse length
ε = airfoil emissivity

The condition at the fluid-airfoil interface, x=0, is described by (i). This condition is derived from Fourier's Law and states that the heat flux into the layer, the first term, is equal to the heat flux absorbed from the laser pulse, the last term, minus the heat flux into the fluid, the second term. The insulating substrate is assumed to be perfect for this analysis; therefore, condition (ii) states that there is no heat flux across the back surface of the layer, at x=l. It should be noted that this condition minimizes the effect of heat conduction perpendicular to the line source. Coupled with the reduction in flow dimensionality achieved by the linear heating pattern, the low diffusivity of the airfoil material insures that the one dimensional formalization is a good approximation to the experimental conditions. The majority of the heat flow then, is perpendicular to the model surface, and the prime loss mechanism is convection.

Condition (i) contains a term representing the heat flux input by the laser. Assuming a square wave laser pulse which begins at t=0, and ending at t=τ, The Fourier transform of the heating flux is given by:

$$\bar{F} = \frac{1}{\sqrt{2\pi}}\int_0^{\tau} F\,e^{-i\omega t}\,dt = \frac{1-e^{-i\omega\tau}}{i\omega} \qquad (5)$$

where F is the flux input of the laser when turned on continuously. Using equation 5 in condition (i), and substituting (i) and (ii) into (4), gives two simultaneous equations which can be solved for A and B. Using the resulting expressions for A and B in (4), and substituting (4) into (2), the temporal dependence of the airfoil surface temperature can be calculated, and is given by :

$$v(0,t) = \frac{1}{\sqrt{2\pi}}\int_{-\infty}^{\infty} F\varepsilon\,\frac{i\omega l - e^{-i\omega\tau}}{i\omega}\,\frac{\left(1+e^{-2(1+i)\sqrt{\frac{\omega}{2k}}}\right)}{\left(1-e^{-2(1+i)\sqrt{\frac{\omega}{2k}}}\right)K(1+i)\sqrt{\frac{\omega}{2k}} + \left(1+e^{-2(1+i)\sqrt{\frac{\omega}{2k}}}\right)H}\,d\omega \qquad (6)$$

Equation 6 relates the measured temperatures to the relative heat transfer coefficient, H. The method used to reduce the time dependence of temperature to H is discussed in the next section.

Analysis

This particular experiment is constrained to measurements on an airfoil whose exact material characteristics are uncertain. As a result, exact knowledge of the thickness of the layer of fiberglass-epoxy and its thermal properties, is not available, and determining absolute heat transfer coefficients is not possible. By doing the analysis in two parts, first on the data from the airfoil with no forced flow, to determine the contribution due to conduction in the airfoil and due to natural convection, then on the data from the airfoil in forced flow, it is possible to determine the ratio of the total heat transfer coefficient, to the no-flow contribution.

To characterize the airfoil with no flow, the time

dependence of the surface temperature decay after a laser heating pulse is approximated with equation (6). The form of equation (6) does not lead to independent determinations of L,K,k,H,F and ε. Combinations of these airfoil characteristics are therefore used as parameters to describe the data. The parameters used are

$$P_1 = \frac{\bar{F}\varepsilon}{H} \qquad (7a)$$

$$P_2 = \frac{K}{H\sqrt{2k}} \qquad (7b)$$

$$P_3 = \frac{L}{\sqrt{2k}} \qquad (7c).$$

Substituting (7a-c) into equation (6) reduces it to(8).

$$v(0,t) = \frac{1}{\sqrt{2\pi}} \int_{-\infty}^{\infty} P_1 e^{i\omega t} \frac{1 - e^{-i\omega\tau}}{i\omega} \frac{\left(1 - e^{-2(1+i)\sqrt{\omega P_3}}\right)}{\left(1 - e^{-2(1+i)\sqrt{\omega P_3}}\right) P_2 \sqrt{\omega}\left(1+i\right) + \left(1 + e^{-2(1+i)\sqrt{\omega P_3}}\right)} d\omega \qquad (8)$$

A nonlinear least squares approximation routine is used to vary P_1, P_2 and P_3 to obtain a minimum in the chi-square deviation between the data and equation (8) at each point of interest.

In the presence of forced air, the only parameter describing the thermal response of the airfoil that is not constant is the heat transfer coefficient. It is present in two of the parameters used to characterize the thermal response of the sample. By defining a fourth parameter, Q, which is the ratio of the total heat transfer coefficient in the forced flow case to the no-flow contribution, equation (6) becomes:

$$v(0,t) = \frac{1}{\sqrt{2\pi}} \int_{-\infty}^{\infty} \frac{P_1}{Q} e^{i\omega t} \frac{1 - e^{-i\omega\tau}}{i\omega} \frac{\left(1 + e^{-2(1+i)\sqrt{\omega P_3}}\right)}{\left(1 - e^{-2(1+i)\sqrt{\omega P_3}}\right) \frac{P_2\sqrt{\omega}}{Q}\left(1+i\right) + \left(1 + e^{-2(1+i)\sqrt{\omega P_3}}\right)} d\omega \qquad (9)$$

where P_1, P_2 and P_3 are the parameters calculated in the no-flow case. A nonlinear least squares estimation routine is again used, varying Q, to obtain a minimum in the chi-square deviation between the data and equation (9) at each point of interest, while holding P_1, P_2 and P_3 constant at the values found for no flow. The values obtained from this routine are reported in the next section.

Results

In figures 5 and 6, the calculated heat transfer values are presented. The curves in figure 5 represent heat transfer as a function of position, at the range of wind velocities indicated. Similarly, figure 6 depicts heat transfer as a function of position. In this case transition was artificially induced at 4.8 cm., with the grit attachment described above. The upper curve in figure 6 represents the case of high wind velocity. It was verified by hot film sensor measurements that turbulent conditions existed directly behind the artificial trip but not before it, for this velocity. The two lower curves were obtained at the same low wind velocity, but with different input heat fluxes. The wind velocity in this case was not sufficiently high to induce transition at the artificial trip, as verified by the hot film sensors.

RELATIVE HEAT LOSS VERSUS POSITION

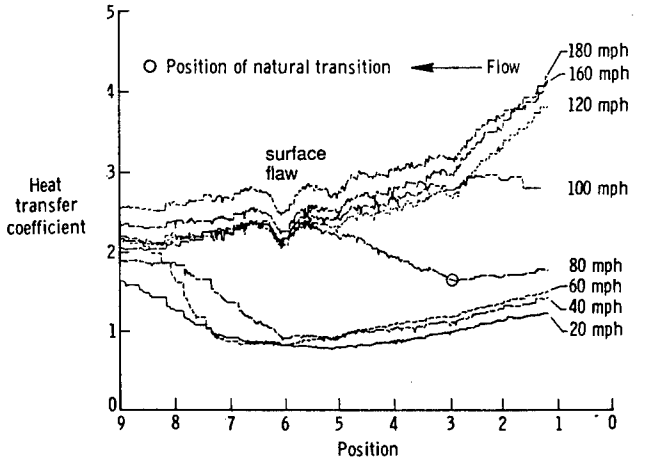

Fig. 5 : h vs. Position, Natural Transition

RELATIVE HEAT LOSS VERSUS POSITION

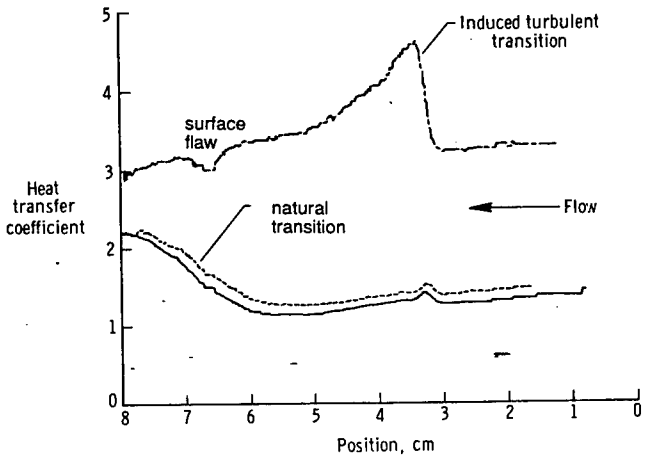

Fig. 6 : h vs. Position, Induced Transition

Discussion

To aid in the interpretation of the data presented in figures 5 and 6, tests were performed using a liquid crystal film, sensitive to shear stress, to give a visual indication of flow characteristics. The liquid crystal flow visualization technique is reported in [5]. Figure 7 is a photograph of the liquid crystal response to 80 mph air flow. The scale at the top of the photograph measures percent of chord, with zero corresponding to the airfoil's leading edge. Natural transition is shown to occur, at this velocity, at 53 percent of chord, and boundary-layer separation is indicated at 70 percent of chord. Additional testing with flow visualization, over the range of velocities and conditions mentioned earlier, indicated that the transition location moves upstream with increasing velocity and that separation, somewhat changing in shape spanwise, occurs between 70 and 80 percent of chord.

The upstream motion of natural transition was detected using the infrared technique described herein. In figure 5, at low wind velocities, the boundary layer is shown to be fully laminar, indicated by a long gradual decline in the heat transfer coefficient, until the position of natural transition is reached,

which is indicated by a rise in the heat transfer coefficient. At 80 mph, this position is approximately 3.1 cm, which corresponds to the liquid crystal flow visualization. The consistent dip in heat transfer coefficient at 6 cm., in the high velocity curves, was found to correspond to an airfoil surface flaw, which is indicated by the circle in figure 7. The 80 mph curve, drawn to scale, is superimposed on figure 7 to indicate the positions at which the measurements in figure 5 were taken.

Figure 6 presents the results of placing a thin line of grit on the airfoil at 3.2 cm. to induce transition. The top curve clearly indicates the change in heat transfer coefficient between fully laminar and fully turbulent flow at 3.2 cm. for this velocity. The bottom curves, obtained at the same low velocity, such that transition was not induced even with the grit, show the effect of using two different input heat pulse lengths, resulting in peak temperature increases of 12^0 C for the upper of the two curves and 16^0 C for the lower curve. Very little offset is observed between the two lower curves, indicating that the heat transfer measurement technique is relatively independent of temperature difference.

Figures 5 and 6 also show the change in heat transfer coefficient with increasing velocity, by an upward shift in the baseline laminar level, as the velocity is increased.

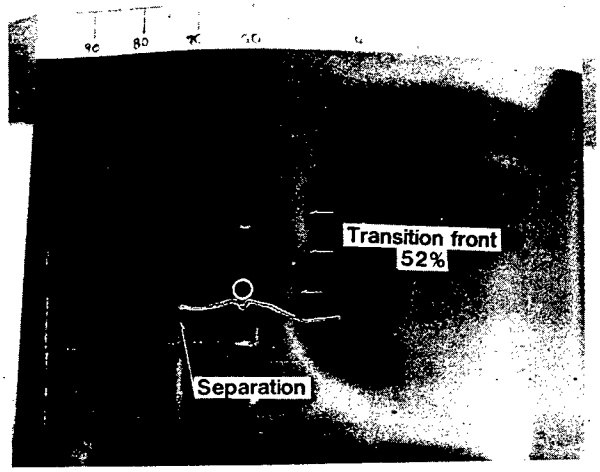

Fig. 7 : Liquid Crystal Verification

Conclusions

An infrared technique for measuring relative heat transfer coefficients, with active heating, is presented. The values obtained are shown to be roughly constant for given flow conditions, independent of the temperature difference between the airfoil and the surrounding fluid. In addition, the incorporation of the material emissivity into one of the fit parameters renders the technique insensitive to local variations in the emissivity of the airfoil surface. The technique is shown to be applicable to detecting the position of boundary layer transition at Mach numbers less than .3. A more quantitative comparison of the technique with standard heat transfer measurements will require the use of a model specifically designed for the purpose, whose thermal properties and thicknesses are known. This will allow a direct comparison of the measured values to theoretical predictions. The use of a one dimensional analysis restricts the generality of the technique to situations with low conduction in the airfoil. The use of low diffusivity airfoil coatings, or the extension of the mathematical model to higher dimensionality will extend the technique's generality.

Acknowledgments

The authors wish to thank G. S. Manuel, NASA Langley Research Center, Hampton, for his flow visualization images.

References

1. Bouchardy, A.; Durand, G.: Processing of Infrared Thermal Images for Aerodynamic Research, Proceedings of SPIE Applications of Digital Image Processing Conference, Vol. 397, Geneva, Switzerland, April 19-22, 1983

2. Welch, Christopher S.; Heath, D. Michele; Winfree, William P.: Remote Measurement of In-Plane Diffusivity Components in Plates, Journal of Applied Physics, Feb.1,1987, vol. 61, number 3.

3. Heyman, Joseph S.; Heath, D. Michele; Welch, Christopher S.; Winfree, William P.; Miller, William E.: NASA Patent Disclosure LAR-13508, Aug. 19, 1985.

4. Bobbitt, P. J.; Waggoner, E. G.; Harvey, W. D.;and Dagenhart, Jr.: A faster "Transition" to Laminar Flow, SAE Technical Paper 851855, presented at the Aerospace Technology Conference and Exposition, Long beach, California, October 14-17, 1985.

5. Holmes, B. J.; Croom, C. C.; Gall, P. D.; Manuel, G. S.; and Carraway, D. L.: Advanced Transition Measurement Methods for Flight Applications, AIAA Technical Paper 86-9786, presented at the SFTE 3rd Flight Testing Conference, Las Vegas, Nevada, April 2-4, 1986.

Corrections

1. Equation 1 should read:

$$\frac{\partial^2 v(x,t)}{\partial x^2} = \frac{1}{k}\frac{\partial v(x,t)}{\partial t} \qquad (1)$$

2. Equation 2 should read:

$$v(x,\omega) = \frac{1}{\sqrt{2\pi}}\int_{-\infty}^{\infty} e^{\iota\omega t} v(x,t)\, dt \qquad (2)$$

3. Equation 5 should read:

$$\bar{F} = \frac{1}{\sqrt{2\pi}}\int_{0}^{\tau} F e^{-\iota\omega t} dt = \frac{F}{\sqrt{2\pi}}\frac{1-e^{-\iota\omega\tau}}{\iota\omega} \qquad (5)$$

4. Equation 6 should read:

$$v(0,t) = \frac{1}{2\pi}\int_{-\infty}^{\infty} F\varepsilon e^{\iota\omega t}\frac{1-e^{-\iota\omega\tau}}{\iota\omega}\frac{\left(1+e^{-2(1+\iota)\sqrt{\frac{\omega}{2k}}L}\right)}{\left(1-e^{-2(1+\iota)\sqrt{\frac{\omega}{2k}}L}\right)K(1+\iota)\sqrt{\frac{\omega}{2k}} + \left(1+e^{-2(1+\iota)\sqrt{\frac{\omega}{2k}}L}\right)H} d\omega \qquad (6)$$

5. Equation 8 should read:

$$v(0,t) = \frac{1}{2\pi}\int_{-\infty}^{\infty} P_1 e^{\iota\omega t}\frac{1-e^{-\iota\omega\tau}}{\iota\omega}\frac{\left(1-e^{-2(1+\iota)\sqrt{\omega P_3}}\right)}{\left(1-e^{-2(1+\iota)\sqrt{\omega P_3}}\right)P_2\sqrt{\omega}(1+\iota) + \left(1+e^{-2(1+\iota)\sqrt{\omega P_3}}\right)} d\omega \qquad (8)$$

6. Equation 9 should read:

$$v(0,t) = \frac{1}{2\pi}\int_{-\infty}^{\infty} \frac{P_1}{Q} e^{\iota\omega t}\frac{1-e^{-\iota\omega\tau}}{\iota\omega}\frac{\left(1+e^{-2(1+\iota)\sqrt{\omega P_3}}\right)}{\left(1-e^{-2(1+\iota)\sqrt{\omega P_3}}\right)\frac{P_2\sqrt{\omega}}{Q}(1+\iota) + \left(1+e^{-2(1+\iota)\sqrt{\omega P_3}}\right)} d\omega \qquad (9)$$

VIII. SENSOR DEVELOPMENT

USING A LARGE APERTURE, PHASE INSENSITIVE ARRAY TRANSDUCER TO IMPROVE ULTRASONIC DETECTION OF DISBONDS AT A ROUGH INTERFACE

Eric Madaras
NASA Langley Research Center
M/S 231
Hampton, VA. 23665

INTRODUCTION

The determination of whether two surfaces are bonded or unbonded is commonly evaluated using conventional ultrasonic transducers which are phase sensitive and are, therefore, very sensitive to surface irregularities. More often than not, interfaces are not flat, but irregular and uneven. Thus, another technique is required to test those interfaces.

This is the condition for some of the bondlines that need to be assessed in NASA's solid rocket motors (SRM), an example of which is illustrated in figure 1. In figure 1a, each SRM motor segment has a layer at both ends called an inhibitor. It is important that this layer be bonded to the fuel for even burning at the segment ends. A close up of the inhibitor layer is seen in figure 1b. The material that bonds the inhibitor to the fuel is called the liner. The liner is thick (~0.1 - 1.0 cm.) and it is uneven at the fuel interface. The thickness of the liner can change rapidly over a few millimeters of lateral distance.

The source of the problem for ultrasonics is shown in figure 2.

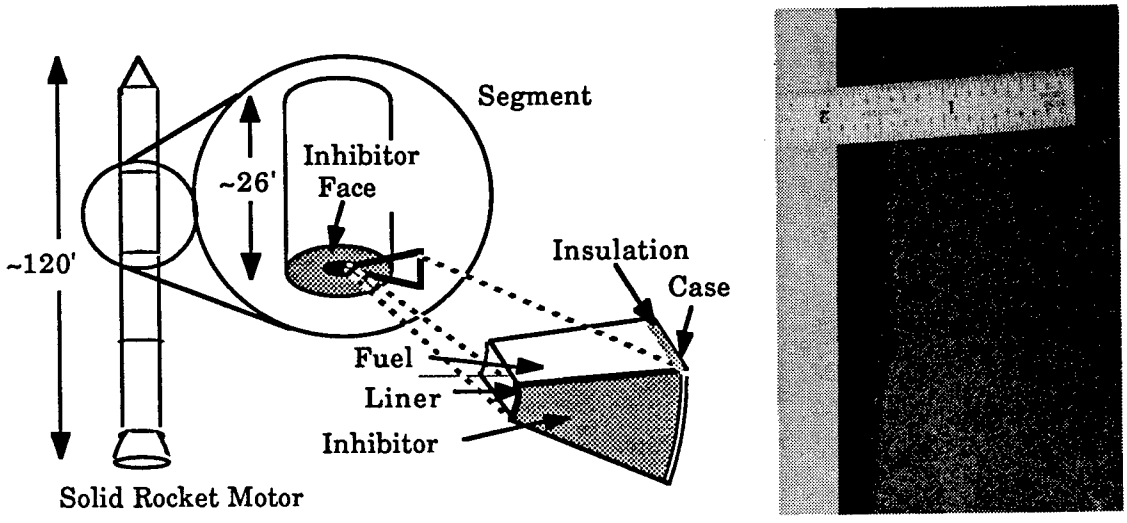

a) b)

Figure 1a) A simplified drawing of the location of the inhibitor. 1b) A close up of the inhibitor-liner-fuel bond line roughness.

This figure, shows a comparison between a conventional pulse echo system's response to a planar interface and a rough interface. For the planar case, the wave fronts are not distorted and the reflection coefficient from a disbond would be quite evident. Since standard piezoelectric transducers are sensitive to the wave front geometry, a rough interface will produce signal artifacts due to phase cancellation.[1-7] Also, some of the energy is reflected away from the transducer's face. Furthermore, some of the ultrasonic wave is mode converted at the interface which also leads to signal loss.

Our objective is to develop a method that is insensitive to some of these loss mechanisms, and to more accurately estimate the coefficient of reflection. Our approach is to demonstrate a method that addresses two of the aforementioned problems, the phase cancellation problem and the beam steering problem.

One possible solution to the problem of the phase sensitive nature of conventional transducers is to consider using lower frequencies, since phase cancellation problems are reduced at longer wavelengths. Unfortunately, the time resolution of the signals will suffer at lower frequencies, and for thin layers, the echoes will overlap causing disruption of conventional techniques. Another solution to the problem is to consider using a phase insensitive transducer[1-4,6,8-12]. There are several methods to attain a phase insensitive transducer response. Semiconductor, piezoelectric material such as CdS will have a response that is phase insensitive in nature[1-4,6,8,9]. This approach is often very awkward to implement and the transducer's sensitivity is lower than the sensitivity for conventional piezoelectric transducers. Another method to approximate a phase insensitive transducer is to use an array of piezoelectric elements each of which are small compared to the wavelength, and are therefore relatively phase insensitive by virtue of their small size[1,9-16]. Each of these elements would be processed independently, and then summed in a phase insensitive manner.

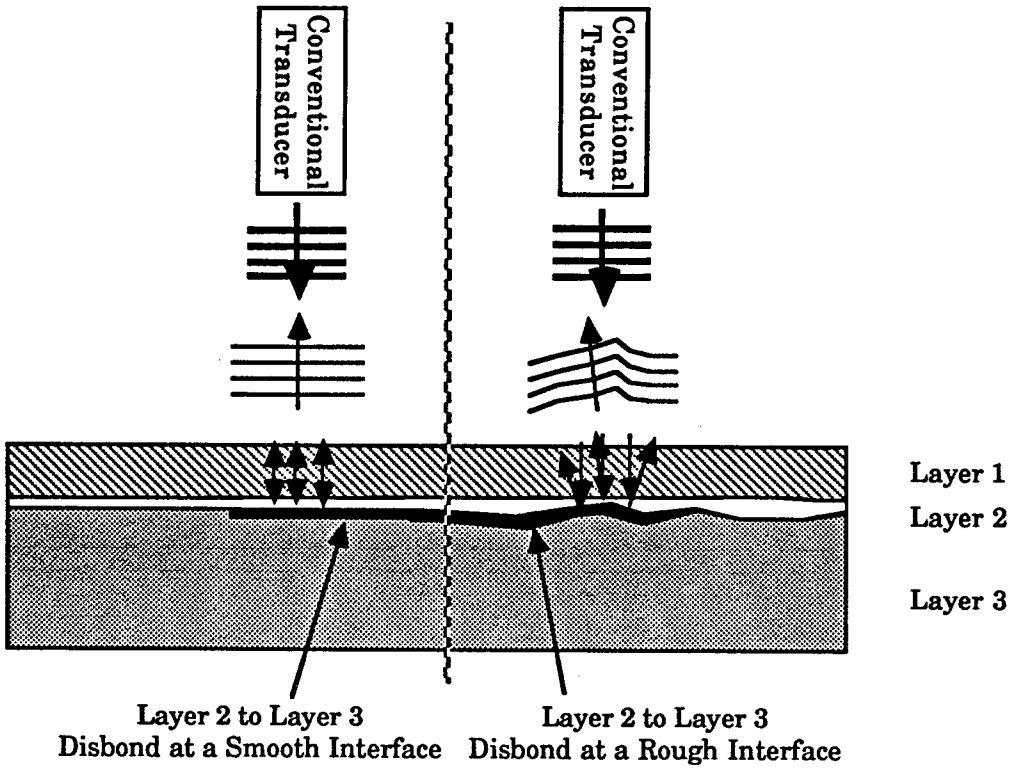

Figure 2. A comparison of the ultrasonic reflection from a smooth surface and a rough surface.

A possible simple solution to the reflection artifact from a rough interface is to use a receiving transducer that is large in area.[7,9,10,11,15] By subtending a large angle on the received signal, one tries to ensure that the energy is still incident on the transducer face and is not lost.

Figure 3 illustrates, the proposed idea. This array would be used as the pulser in a conventional pulse echo system. The reflected signals would be distorted and scattered away from its original direction, but the array would be less sensitive to the phase cancellation artifacts, and its large size should capture most of the reflected wave.

In order to investigate this as a possible solution we emulated a large area array which treated the received signal in a phase insensitive manner. These results were then compared with a conventional pulse echo measurement system.

MEASUREMENTS

We measured two types of samples. One type was cut from sections of the inhibitor-liner-fuel system that is used in NASA's solid rocket motor system and which has a rough interface. We also measured a sample that was specially fabricated with a smooth inhibitor-liner-fuel interface. The measurements were performed in a water tank and the samples were measured in a C-scan format. The step sizes of the C-scans were 0.5 cm in both the x and y directions. Well bonded and unbonded regions were measured.

To emulate a phase insensitive array as if it was a pulse echo system, we used a standard transducer as a transmitter and a small point-like piezoelectric transducer as a receiver in a pitch-catch mode on one side of the sample. The transmitter and receiver were set at opposing angles of about 15° from normal. This was physically the

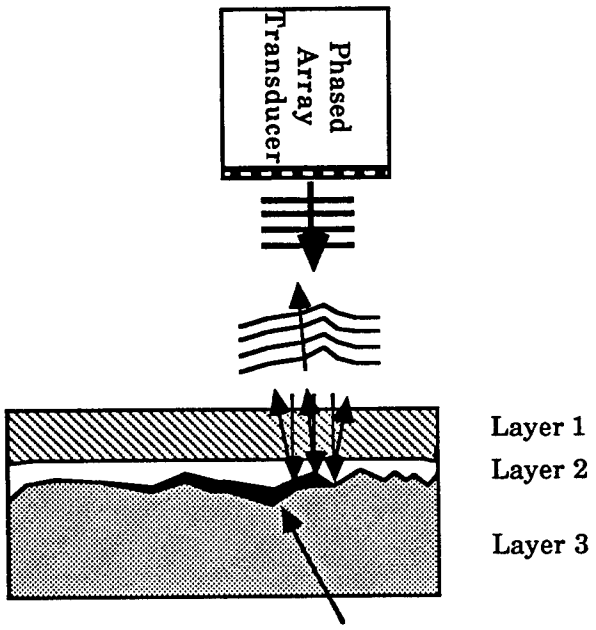

Figure 3. The concept of a phase insensitive array for detecting disbonds at a rough interface.

shallowest angle obtainable for the size of the transducers and their distance from the target being tested. This one point-like receiver was translated to each of 49 locations of a seven by seven point square array. The receiving array positions were spaced by 0.5 cm in each dimension to cover an effective aperture of approximately 3 cm by 3 cm. The measurement system is briefly outlined in fig. 4. We used a 2.54 cm. diameter, 1 MHz transducer with a 10 cm. focus for the transmitter. The receiver was a 0.08 cm. diameter, 1 MHz planar transducer. The transmitter was driven by a square wave pulser which was tuned to provide a relatively broadband pulse measured at the receiver. The received signal was amplified and the signal that emanated from the liner to propellant bondline was gated out, rectified and detected for the peak height. The data was combined to yield a single phase insensitive image representing the result of a simulated two-dimensional array receiver whose output was the sum of the peak energies of its array elements.

Scans from similar regions of the samples were made using a conventional pulse echo system for comparison. The same transducer which was used for the transmitter of the array scans was used for the pulse echo transducer.

In the C-scan images that were generated for both the array system and the conventional system, a threshold level was selected to produce image contrast which reflected the maximum sensitivity to the defect, yet maintain high specificity for the bonded regions. Sensitivity to an unbond defect was defined as the percent of the unbond region that was correctly identified as unbond, and specificity to the bonded regions was defined as the percent of the bonded area that was correctly identified as bonded.

RESULTS

To illustrate how well the system functioned on smooth interfaces, we measured a sample that was constructed of inhibitor-liner-fuel

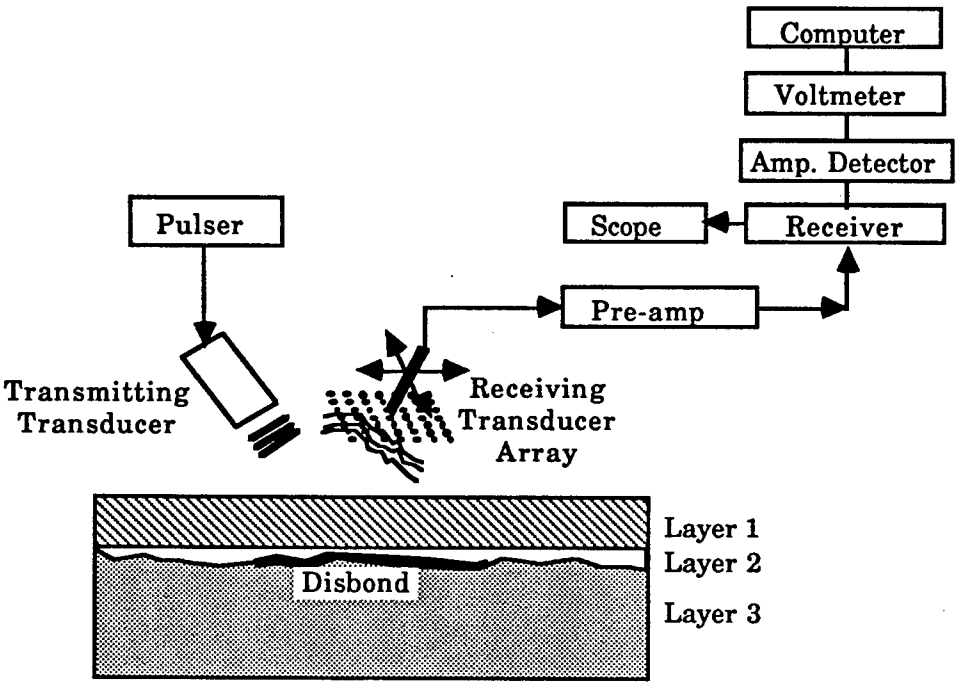

Figure 4. A flow chart of the equipment used to emulate the phase insensitive array.

materials, and with a smooth interfaces. A 0.076 cm. thick brass, wedge shaped shim was built into the sample at the liner-fuel interface. This shim was removed to leave an obvious unbond. Figure 5 shows a drawing of this sample. The inhibitor was 2.54 cm. thick, the liner was 0.127 cm. thick, and the fuel layer was several inches thick. The sample was approximately 20 cm. by 20 cm. across the face.

Figure 6a. shows the image produced by measuring this flat sample using the pulse echo system. This figure shows three groups of signal level. There is the unbonded signal level shown as white which highlights the wedged shaped disbond at the liner to fuel interface, the bonded signal level shown as grey and a third level shown as black which borders the disbond. Although this dark halo highlights the defect in this case, it is an artifact that is not correct. It is actually a phase cancellation artifact that occurs at the edge of the disbond and results from the geometry of the thickness of the wedge.

For comparison, figure 6b. shows the image produced by measuring this same sample with the phase insensitive array system that we generated. Again the wedged shaped defect is clearly illustrated by the white area and the bonded signal level shown as grey. There is no evidence of the halo effect seen in 6a. This illustrates that the phase insensitive array system does handle phase cancellation properly.

An example that illustrates the improvement that was achieved by using the phase insensitive array is shown in figures 7-8. To create an obvious disbond at the rough liner to fuel interface, we excised the fuel completely from the liner over an area 7.6 cm. by 7.6 cm. We further removed a small portion of the liner (2.5 cm by 2.5 cm.) from the sample at one edge. This should create an image that would be distinctive. Figure 7 shows a schematic of the sample. The inhibitor was approximately 1.6 cm thick. The liner varied from about 0.1 cm. to about 0.4 cm. in the regions interrogated. We set our electronic gate to detect only the liner to fuel disbond. This measurement should generate an image that corresponded to the white areas illustrated in figure 7. There was also a defect created to the right side of the image which would help the viewer with the orientation of the image.

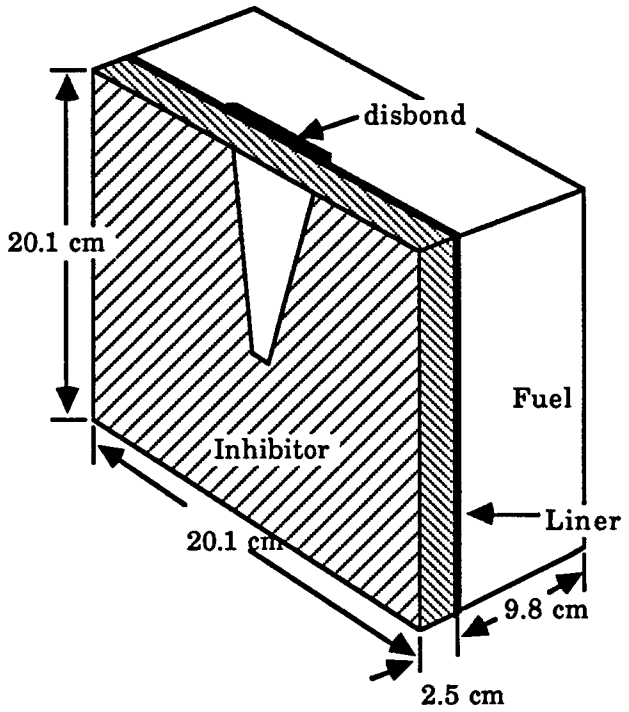

Figure 5. A diagram of the smooth inhibitor-liner-fuel sample.

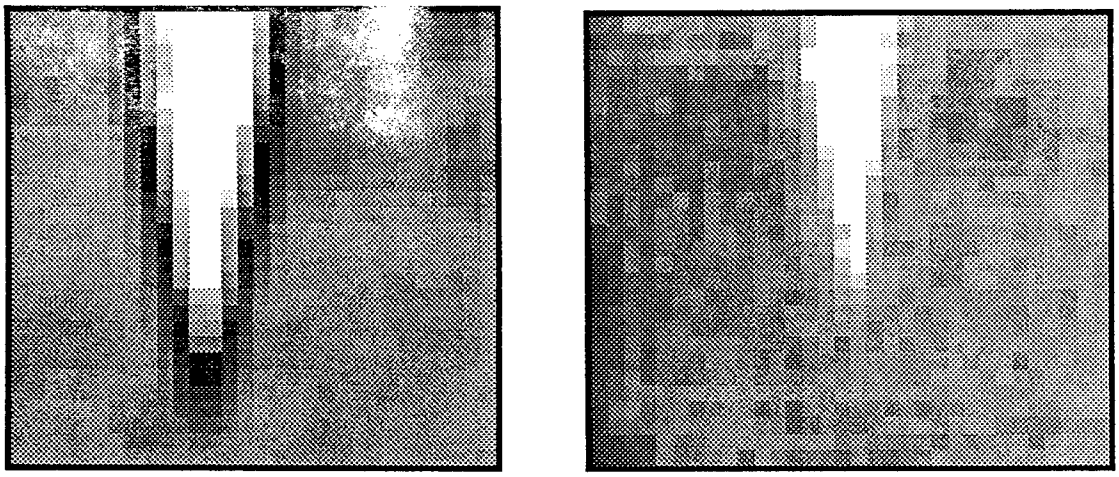

a) b)

Figure 6. a) The C-scan image of the smooth sample using a standard pulse echo system. b) The C-scan image of the smooth sample using a phase insensitive array system.

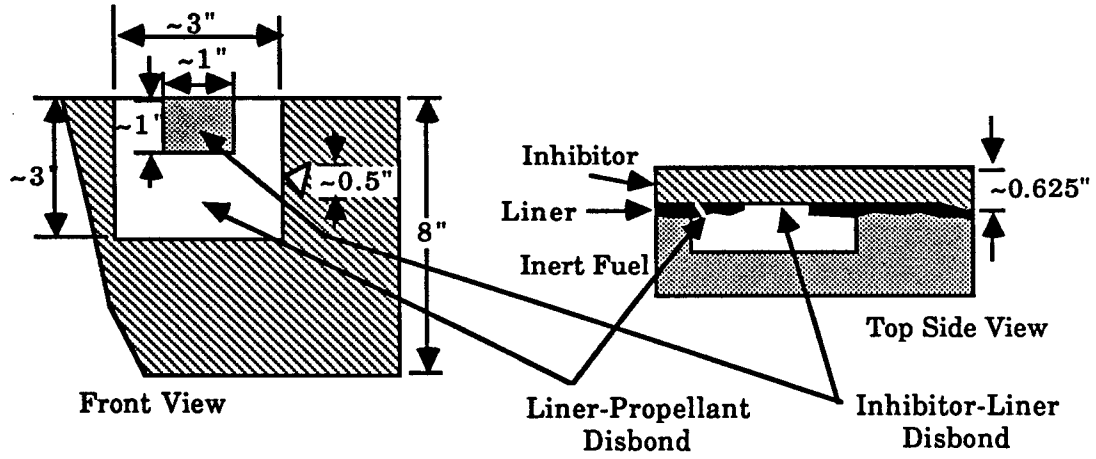

Figure 7. Drawing of the inhibitor-liner-fuel section showing the disbond region.

Figure 8a shows the C-scan image made using a standard phase sensitive system. The thick outline indicates the area of the disbond region. The area within the outlined region appears very spotted. We selected the white level as the optimum level to give the highest sensitivity to the detection of the defect, yet also to have a high specificity and not to select obviously bonded regions as unbonded. This resulted in about a 42% sensitivity for a disbond using a conventional system.

In figure 8b, the C-scan image was made using the phase insensitive array system. The outline indicates the areas of the disbond regions. In this case, the area within the outlined regions appear more uniformly highlighted. As before, we selected the white level as the optimum level to give the highest sensitivity to the detection of the defect, yet also to have a high specificity to the bonded regions. This resulted in a 79% sensitivity for the phase insensitive array system when applied to this sample.

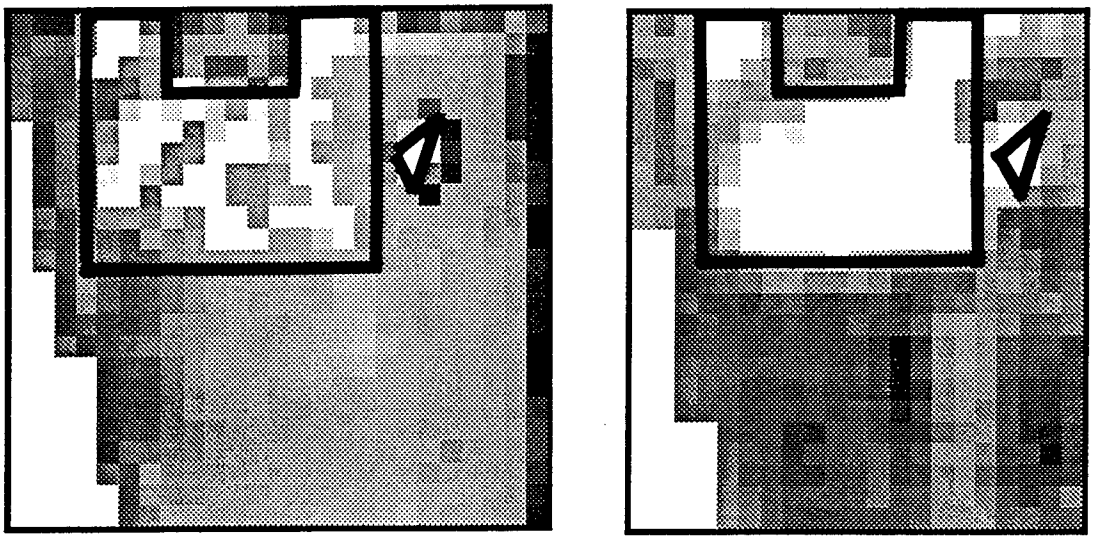

a) b)

Figure 8. a) The C-scan image of the rough interface sample using a standard pulse echo system. b) The C-scan image of the rough interface sample using a phase insensitive array system.

DISCUSSION

Nondestructive detection of the inhibitor to liner to fuel bondlines at the ends of the solid rocket motor segments is a critical problem to the Space Shuttle's safety. Standard pulse echo techniques lack high sensitivity to the bondline integrity in the presence of surface roughness because of several artifacts. Two artifacts that we addressed in this work are phase cancellation at a phase sensitive transducer, and signal loss because of signal reflection away from the receiver.

Significant improvements in the detection of disbonds at the interface of layers with rough surfaces was achieved with a large aperture phase insensitive array technique as compared with a standard pulse echo system. In the samples tested, the system improved the C-scan image degradations of phase cancellation and resulted in an improvement from 42% to 79% in the rough interface sample that we tested. This factor of 2 improvement was also observed in other samples of inhibitor-liner-fuel that we measured.

If one further adjusts the threshold levels to increase the sensitivity to the disbond, in a standard pulse echo system, regions remote to the disbond area start to become highlighted as defective when they are not, so that overall accuracy is degraded. In contrast, when using the phase insensitive array system, if the threshold level is modified the areas near the disbond are highlighted and although this would lead to a misjudgement of the size of the disbond, it would still detect the approximate location correctly.

We feel that a prototype instrument that used an array rather than the manipulation of a single element as was done for this study would probably improve further the phase insensitive array system's response and remove some the the noise that is prevalent with the single receiver technique. Operating in a pulse echo mode and being perpendicular to the sample rather than a pitch catch mode and having the transmit and receive transducers at a shallow angle should also lead to improvements in performance. With this in mind, we are currently aiding in the

design and manufacture of a complete phase insensitive array system for application to the shuttle.

ACKNOWLEDGEMENTS

The author would like to acknowledge the assistance of Rick Millis in scanning and processing this data. He would also like to acknowledge the helpful conversations and comments from Drs. Pat Johnston, Barry Smith and Joe Heyman.

REFERENCES

1. L. J. Busse and J. G. Miller, Proc. 1981 IEEE Ultrasonics Symposium, pp. 617-626, (1981). (IEEE Cat. No. 81 CH 1689-9)
2. L. J. Busse and J. G. Miller, J. Acoust. Soc. Am., vol. 70, pp. 1377-1386, (1981).
3. L. J. Busse, J. G. Miller, D. E. Yuhas, J. W. Mimbs, A. N. Weiss and B. E. Sobel, Ultrasound in Medicine, vol. 3, pp. 1519-1535, (1977).
4. J. G. Miller, Joseph S., Heyman, D. E. Yuhas, and Alan N. Weiss, Ultrasound in Medicine, vol. 1, pp. 447-453, (1975).
5. Steven M. Jones, Fred L. Ketsen, Paul L. Carson, and Elliott J. Bayly, IEEE-EMBS Conference-Frontiers of Engineering in Health Care, pp. 73-76, (1979). (IEEE Cat. No. 79 CH 1407)
6. L. J. Busse and J. G. Miller, J. Acoust. Soc. Am., vol. 70, pp. 1370-1377, (1981).
7. C. R. Meyer, T. L. Chenevert, and P. L. Carson, J. Acoust. Soc. Am., vol. 72, pp. 820-823, (1982).
8. J. S. Heyman, J. Acoust. Soc. Am., vol. 64, pp.243-249, (1978).
9. J. R. Klepper, G. H. Brandenburger, L. J. Busse, and J. G. Miller, Proc. 1977 IEEE Ultrasonics Symposium, pp. 182-188, 1977. (IEEE Cat. No. 77 CH 11264-1SU)
10. Thomas A. Shoup, G. H. Brandenburger, and J. G. Miller, Proc. 1980 IEEE Ultrasonics Symposium, pp. 973-978, (1980). (IEEE Cat. No. 80 CH 1602-2)
11. M. O'Donnell, Ultrasonic Imaging, vol. 4, pp. 321-335, (1982).
12. Patrick H. Johnston and James G. Miller, IEEE Transactions on Ultrasonics, Ferroelectrics and Frequency Control, vol. UFFC-33, no. 6, pp 713-721, (1986.
13. R. M. Schmitt, C. R. Meyer, P. H. Bland, T.L. Chenevert, and P. L. Carson, Proc. 1982 IEEE Ultrasonics Symposium, pp. 663-667, 1982. (IEEE Cat. No. 82 CH 1823-4)
14. D. W. Fitting, R. M. Schmitt, P. Grounds, G. Hansell and P. L. Carson, Proc. 1984 IEEE Ultrasonics Symposium, pp. 794-797, 1984. (IEEE Cat. No. 84 CH 2112-1)
15. D. W. Fitting, P. L. Carson, J. Giesey, P. Grounds, and J. Moskwa, Proc. 1985 IEEE Ultrasonics Symposium, pp. 836-840, 1985. (IEEE Cat. No. 85 CH 2209-5)
16. J. J. Giesey, D. W. Fitting and P. L. Carson, Proc. 1986 IEEE Ultrasonics Symposium, pp. 663-667, 1986. (IEEE Cat. No. 86 CH 2375-4)

MODELING THE PULSE-ECHO RESPONSE OF A TWO-DIMENSIONAL PHASE-INSENSITIVE ARRAY FOR NDE OF LAYERED MEDIA

Patrick H. Johnston and Eric I. Madaras

NASA Langley Research Center
Hampton, Virginia 23665

ABSTRACT

Ultrasonic inspection of interfaces in multilayered media is a common problem in the field of NDE. Inspection of layered media with one or more rough or uneven interfaces presents a number of potential difficulties, such as non-normal reflection and phase-cancellation. One approach to these problems is the use of a large-aperture phase-insensitive two-dimensional array of small-diameter piezoelectric receivers. We are investigating the use of a pulse-echo phase-insensitive array as an approach for the NDE of uneven bondlines in the Space Shuttle Solid Rocket Motor. Experimental results with a scanned-element pseudo-array indicate that the sensitivity of detecting total disbonds at a rough interface between two rubber-like materials can be improved by more than a factor of two by using phase-insensitive detection. We are using computer simulations to evaluate the pulse-echo characteristics of various arrangements of pulse-echo arrays with coplanar interspersed transmitting and receiving elements. This approach allows flexibility for exploring various array configurations and allows independent selection of materials for optimizing transmit and receive characteristics.

INTRODUCTION

The interrogation of interfaces between solids in a layered structure is a common problem in practical NDE. When one or more of the surfaces are rough or uneven, the ultrasonic wavefronts can become distorted which can result in the phenomenon of phase-cancellation at a phase-sensitive receiver. Figure 1 shows a number of physical situations in which phase-distortions are produced which may result in phase-cancellation.

The problem of phase-cancellation can be approached by several means. Receivers which are power-sensitive may be used, such as the acousto-electric transducer [1,2]. Another approach is based on sampling the field with small-aperture piezoelectric elements laid out in a two-dimensional array. This approach has been shown to reduce or eliminate phase-cancellation in transmission [3-6] and backscatter measurements [7,8]. In this work we are applying this approach to address a specific NDE opportunity in the Space Shuttle Solid Rocket Motor (SRM).

PROBLEM

The physical situation we are addressing is similar to that depicted in panel (b) of Fig. 1.

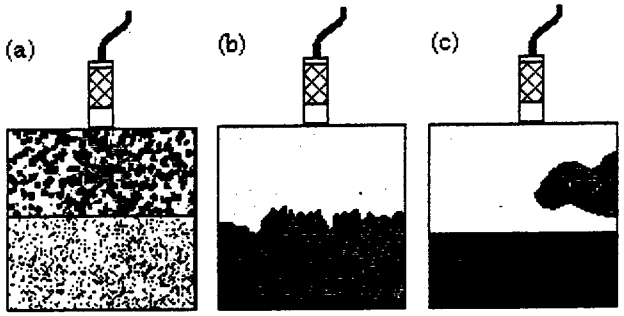

Figure 1. Some physical situations in which the propagation of ultrasound through a layered medium can result in waveform distortions resulting in phase-cancellation: (a) inhomogeneous media; (b) rough or uneven boundary between media; (c) existence of an edge or boundary within a layer.

The solid fuel at the ends of the SRM segments is overlaid and bonded to a rubber insulating material called an inhibitor. As is shown in Figure 2, there is a thick adhesive material between the inhibitor and fuel which produces a rough interface. This material (called the liner) can vary between 0.1 cm and 1.0 cm in thickness. It is imperative that these materials are bonded for safe space flight, so a reliable NDE method is required. Conventional ultrasonics has produced a rather poor result when applied to the inhibitor as a consequence of phase-cancellation.

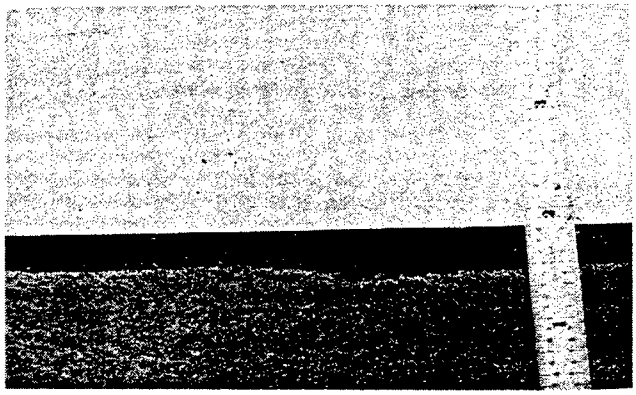

Figure 2. A photograph showing the cross-section of the inhibitor-liner-fuel system used in the SRM. The rough liner-to-fuel interface is visible.

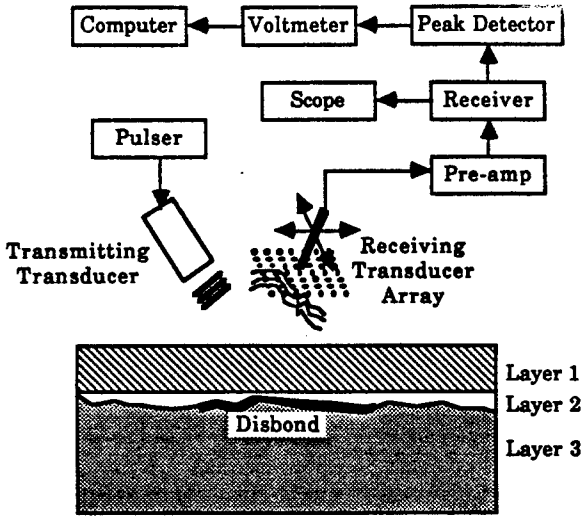

Figure 3. Block diagram of the equipment used in the phase-insensitive pseudo-array system.

In order to assess the benefits of a phase-insensitive array in this application, we performed an experiment to compare a conventional pulse echo system with a phase-insensitive pseudo-array system [9]. Both techniques were applied to a sample having a thick inhibitor layer, a variable-thickness layer of liner, and fuel. In one region, the fuel behind the liner was removed to create an obvious unbond. The pulse echo experiment was performed in a water bath using a 1 MHz, 1.125 inch diameter transducer focused at 3 inches. For the array system, we emulated an array by using a single 1 MHz, 0.080 inch diameter transducer as a receiver and the pulse-echo transducer as the transmitter. The single element receiver was translated to each location of a seven by seven element array in 0.25 inch steps for each site that was insonified by the transmitter. The transducers were set to equal and opposite angles at the most shallow angle possible with respect to the normal to the surface. Figure 3 shows a block diagram of the system. The same electronic equipment was used in both the array system and the pulse echo system, except for the addition of a preamplifier to boost the signal of the small receiving transducer. The data were detected and stored in a computer which also controlled the scanner. After the sample was scanned, the data from the small transducer were summed to produce a phase insensitive image.

Typical results that were seen with these two systems are shown in Figure 4. The thick outline indicates the known area of the disbond region. In both images, the white threshold level shown in the images was selected as the optimum level to give the highest sensitivity to the detection of the defect, yet also to have a high specificity and not to select obviously bonded regions as unbonded. In panel (a), a C-scan image made using a standard phase-sensitive system is displayed. The area within the outlined region appears very spotted. Using a conventional system resulted in about a 42% sensitivity for a disbond. Panel (b) shows the results from the phase-insensitive array system. In this case, the area within the outlined regions appear more uniformly highlighted. The phase-insensitive array system resulted in a 79% sensitivity when applied to this sample. Thus, in these types of samples, we are seeing about a two-fold increase in sensitivity with phase-insensitive detection.

Based on these preliminary results, we are currently aiding in the design of a custom commercial phase insensitive array product to be applied to the SRM system. This design effort is the basis of this report.

APPROACH

The approach taken to this design is based on coplanar transmitting and receiving two-dimensional arrays. This approach may be implemented with a single array of elements for transmit and receive or with two separate sets of elements for transmit and receive. Beam forming with a transmitting array typically requires spacing of the elements at near half-wavelength. Phase-insensitive detection may be performed with a more sparsely-sampled array [3,6]. The combination of two arrays with these and other different requirements necessitates some compromises.

To illustrate the approach, in Figure 5 we show two examples of arrays we have considered. In panel (a) is Array 1, with separate transmit and receive elements. The nine transmit elements are circular disks 4.2 λ in diameter and are spaced by 4.2 λ on a square 3x3 grid. The 16 receiving ele-

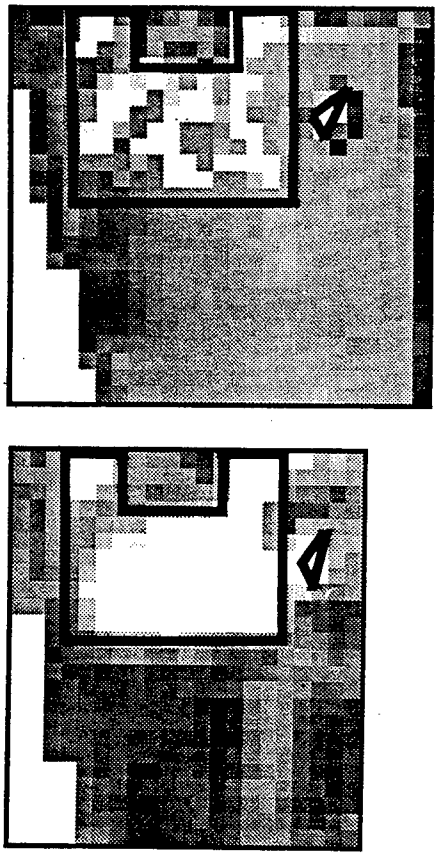

Figure 4. a) A C-scan image of the rough interface sample using a standard pulse-echo system. b) A C-scan image of the rough interface sample using a phase-insensitive pseudo-array system.

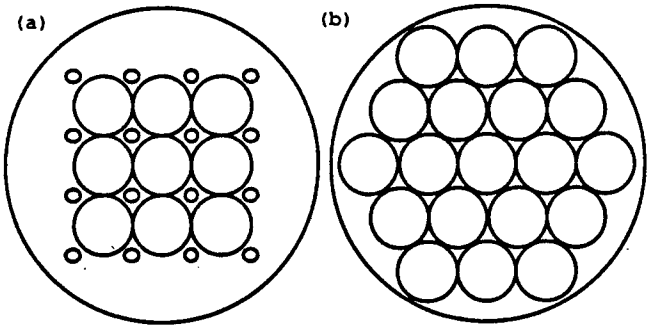

Figure 5. Two examples of pulse-echo phase-insensitive arrays: (a) Array 1, with transmitting array (larger elements) and receiving array interspersed on square grid; (b) Array 2, with transmit/receive array laid out on a hexagonal grid.

ments are 1.0 λ in diameter spaced by 4.2 λ on a square 4x4 grid interspersed with the transmitting array. The use of separate elements for transmit and receive arrays allows the independent selection of materials for optimized transmit and receive characteristics.

Array 2 in panel (b) is laid out in a hexagonal grid and uses the same elements for both transmit and receive. Each circular element is 4.2 λ in diameter and the center-to-center spacing is 4.2 λ. The hexagonal arrangement produces a more circular symmetry and has a larger fill factor. This arrangement provides a larger transmitting area for improved power transmission, but the fill factor precludes interspersed receive elements. The use of the relatively large elements for receive increases the overall susceptibility to phase-cancellation.

MODEL

We model the field generated by a transmitting array as the sum of the fields of the individual elements

$$p(x,y,z) = \sum_n \frac{\exp(ikz)}{z} D_n(x,y,z) \quad , \tag{1}$$

$$D_n(x,y,z) = \exp\left(ik\rho_n^2/2z\right) \frac{2J_1(ka\rho_n/z)}{(ka\rho_n/z)} \quad , \tag{2}$$

$$\rho_n^2 = (x-x_n)^2 + (y-y_n)^2 \quad . \tag{3}$$

Here (x_n,y_n) is the location of the n^{th} transmitting element on the array plane, a is the radius of the transmitting element, and (x,y,z) is the field point. We have used the far-field paraxial approximation for the individual elements, which is valid for distances z greater than a^2/λ.

For the physical situation in which we are presently interested, that of layered media with approximately parallel interfaces, we may say that the field presented back at the array after reflection from an interface at distance L is equivalent to the field generated by the array at distance 2L in that same medium. Thus, we evaluate the effectiveness of the receiving array in sampling the reflected field by examining the receive array geometry with respect to the transmitted field at range 2L.

We also evaluated the effective point-spread function for the array, i.e. the image that would be formed by scanning over a point target at distance L. Assuming that the point target acts as a point source of strength proportional to the transmitted field incident upon it, the point spread function (PSF) is given by the product of the phase-sensitive transmit directivity and the phase-insensitive directivity of the receiving array:

$$PSF(x,y;z) = \left|D_{PS}(x,y;z)\right|^2 \left|D_{PI}(x,y;z)\right|^2 \quad , \tag{4}$$

$$\left|D_{PS}(x,y;z)\right|^2 = \left|\sum_n D_n(x,y;z)\right|^2 \quad , \tag{5}$$

$$\left|D_{PI}(x,y;z)\right|^2 = \sum_n \left|D_n(x,y;z)\right|^2 \quad . \tag{6}$$

DESIGN CONSIDERATIONS

Many factors come into play when attempting to optimize the parameters for a two-dimensional array. For our particular application, some parameters were fixed within some limited ranges. The axial range was fixed to the thickness of the inhibitor and liner, approximately one inch, although a delay line could be employed if necessary. The relatively high ultrasonic attenuation exhibited by the rubber inhibitor material necessitated the use of low ultrasonic frequencies. Also, there was a need to limit the lateral dimensions of the array within an upper limit set by existing scanning apparatus in use on the SRM. Other factors were thus required to be set based on these values, as considered below.

With the range fixed, the attenuation of the material forces a trade-off between lower ultrasonic frequency, to improve signal-to-noise ratio, and beam width, which varies inversely with frequency. Broader beam width degrades lateral resolution and necessitates larger receiver array aperture. In our case, the fixed maximum array size would thus limit the lower frequency which could be employed to achieve a given desired signal-to-noise ratio.

Expected beam deflection caused by non-parallel interfaces also comes into play. For a fixed range R, a surface angled at angle θ results in a deflection of a reflected beam by angle 2θ with respect to the line of its original path. The received beam therefore is shifted on the receiving array by a distance $d = R \tan(2\theta)$. In a case where the interrogated interface can be expected to be parallel to the front surface to within an angle θ_{max}, then the receiving aperture must have a width A greater than or equal to the maximum beam width plus twice the maximum deflection due to the non-parallel interface, i.e., $A > (\text{max beamwidth}) + 2R \tan(2\theta_{max})$. Thus, with a fixed maximum receiver aperture, the minimum allowable frequency must be adjusted to accommodate the expected shifts in the reflected beam.

The maximum frequency of the array is limited by the element spacing. The beamwidth decreases as the ultrasonic frequency increases, so for a given array element spacing, the maximum frequency is limited by the requirement that the main beam intersects several receiving elements. However, it

has been shown that interpolation can be used for expanding the sampled beam for interpretation [6].

SAMPLING OF THE BEAM

Figure 6 presents the magnitude of the ultrasonic field produced at a distance of 134 λ by the transmitting arrays in Fig. 5. This represents the field presented to the receiving array after reflection for a flat surface 67 λ from the array. Superposed on the grayscale plot of the field is a sketch of the receiving array, indicating how the field would be sampled in a pulse-echo situation. Panel (a) shows the result for Array 1. We note the sampling appears to be too sparse over the beam, and the total aperture does not allow for any shift in the beam due to an angled interface. The field of Array 2 is shown in panel (b). Here, although there is sufficient aperture to allow for some shifting of the beam, the elements are so large relative to the beam size that most of the energy falls on a single element. By these criteria, then, both of these arrays are somewhat deficient in sampling their respective reflected fields.

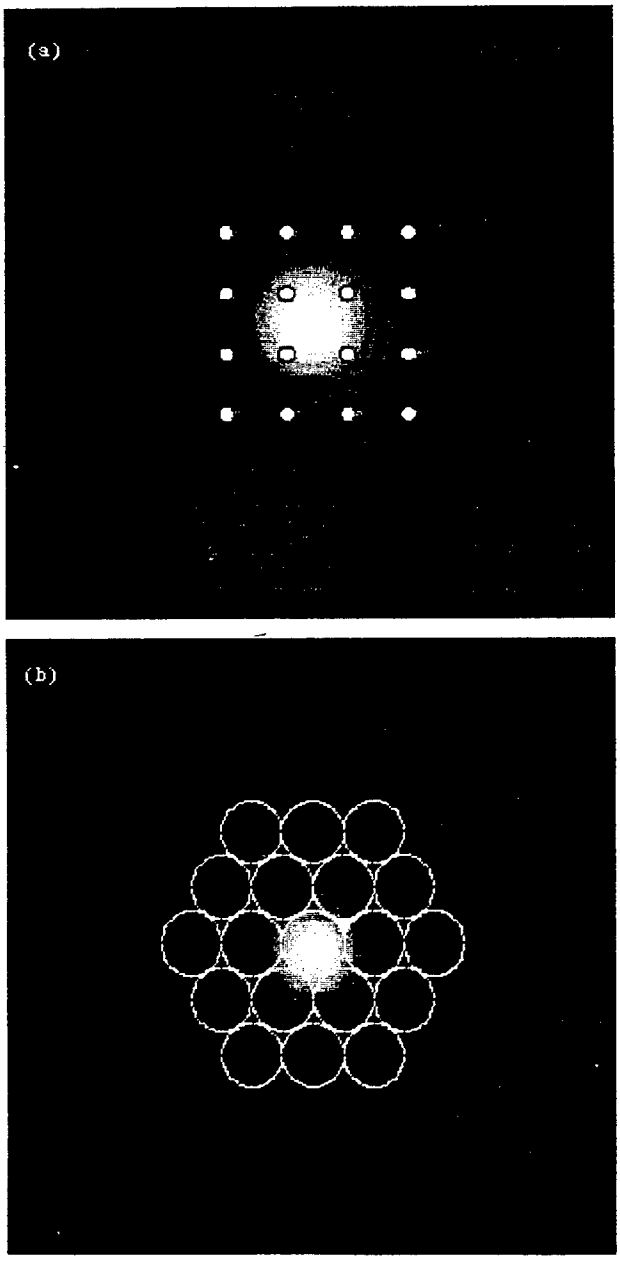

Figure 6. The magnitude of the pressure field presented to the receiving arrays in Fig. 5. (a) The field of Array 1 with its receive array superposed. (b) The field of Array 2 with its receive array superposed.

POINT SPREAD FUNCTION

Figure 7 presents the point spread functions for the example arrays in Fig. 5. The upper two panels show the directivities of the transmitting arrays at a range of 67 λ in front of the arrays. The main beams are fairly well formed and we note the presence of low-level sidelobe structures which reflect the symmetries of the respective sources, four-fold for Array 1 and six-fold for Array 2. The middle two panels show the phase-insensitive directivities of the receiving arrays at that same distance. These are expected to be dominated by the directivity of an individual array element, which is consistent with these results, with the smaller elements of Array 1 exhibiting the broader response than those of Array 2. The bottom panels show the results of multiplying the phase-sensitive transmitting directivities by the phase-insensitive receiving directivities. These figures show that the lateral resolution of a pulse-echo array device constructed based on these designs is dominated by the directivity of the transmit array. Both arrays exhibit reasonable point spread functions.

CONCLUSION

Phase-cancellation caused by reflection from a rough interface has been shown to be problematical in the NDE of the inhibitor of the SRM. Laboratory experiments have shown that phase-insensitive detection improves the detection of disbonds in the inhibitor. The considerations described in this paper are being developed to aid in the design of a practical two-dimensional phase-insensitive pulse-echo array for possible application on the SRM inhibitor. We have shown two examples to illustrate the difficulties involved in such design.

ACKNOWLEDGEMENTS

The authors would like to acknowledge the assistance of Rick Millis in scanning and processing the experimental data.

REFERENCES

[1] J. S. Heyman, J. Acoust. Soc. Am., vol. 64, pp.243-249, (1978).
[2] L. J. Busse and J. G. Miller, J. Acoust. Soc. Am., vol. 70, pp. 1370-1377, (1981).
[3] Thomas A. Shoup, G. H. Brandenburger, and J. G. Miller, Proc. 1980 IEEE Ultrasonics Symposium, pp. 973-978, (1980). (IEEE Cat. No. 80 CH 1602-2)
[4] J. J. Giesey, D. W. Fitting and P. L. Carson, Proc. 1986 IEEE Ultrasonics Symposium, pp. 663-667, 1986. (IEEE Cat. No. 86 CH 2375-4)
[5] D. W. Fitting, P. L. Carson, J. J. Giesey and P. M. Grounds, IEEE Transactions on

Ultrasonics, Ferroelectrics and Frequency Control, vol. UFFC-34, no. 3, pp 346-356, (1987).

[6] Patrick H. Johnston, 1987 Acoustical Imaging, (Chicago, Ill, June, 1987). In press.

[7] M. O'Donnell, Ultrasonic Imaging, vol. 4, pp. 321-335, (1982).

[8] Patrick H. Johnston and James G. Miller, IEEE Transactions on Ultrasonics, Ferroelectrics and Frequency Control, vol. UFFC-33, no. 6, pp 713-721, (1986).

[9] Eric I. Madaras, 1988 Review of Quantitative NDE, (La Jolla, CA, Jul 31- Aug 5, 1988). In press.

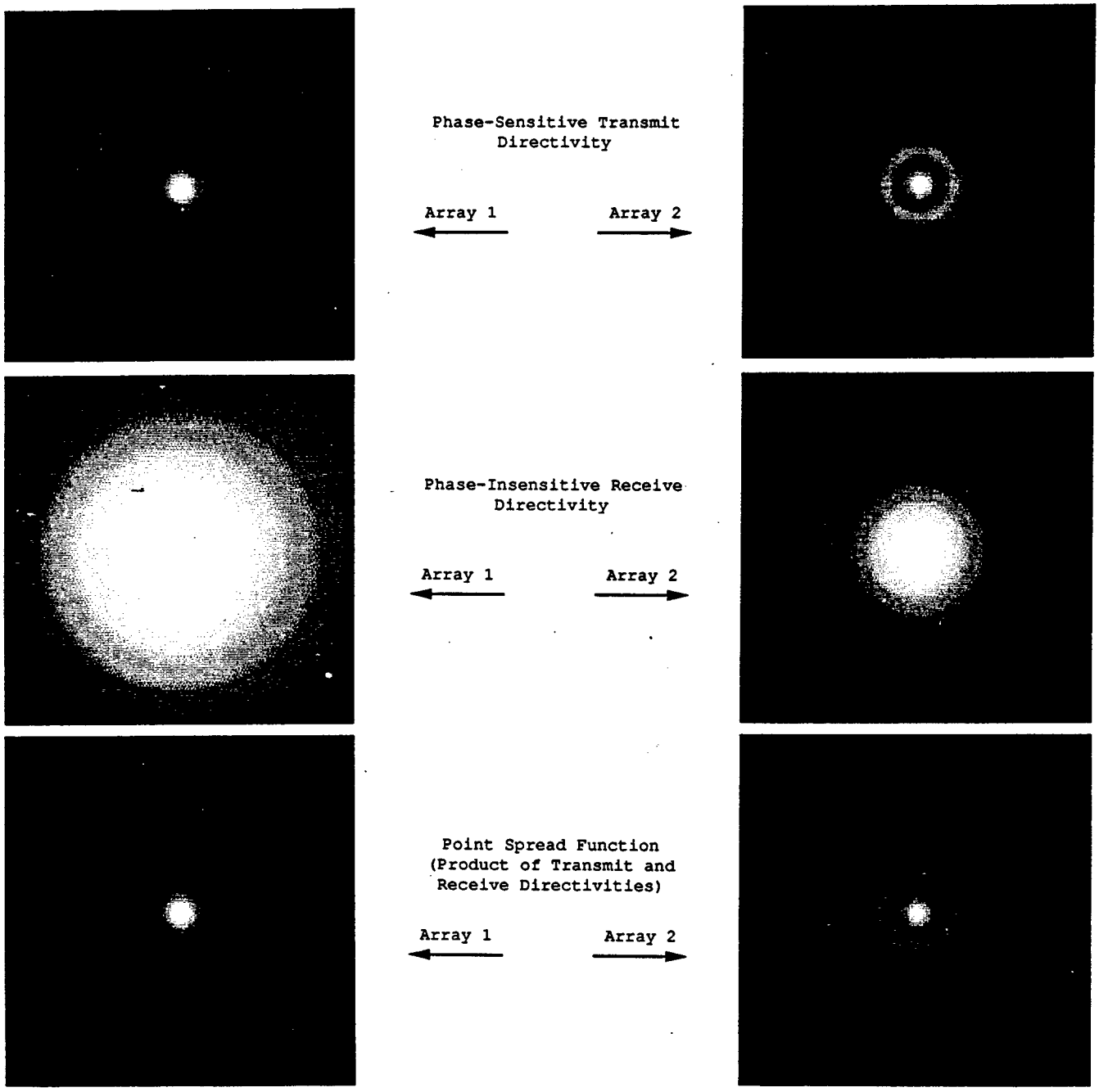

Figure 7. The development of the point spread functions for the arrays in Fig. 5. (top) The phase-sensitive directivities of Array 1 and Array 2 at range 134 λ. (middle) The phase-insensitive directivities of Array 1 and Array 2 at range 134 λ. (bottom) The point spread functions of Array 1 and Array 2 derived by multiplying the phase-sensitive responses by the phase-insensitive responses.

Determination of the Absolute Sensitivity of Damped MHz Range Ultrasonic Transducers.

Pamela D. Hanna*, William T. Yost, and John H. Cantrell

NASA-Langley Research Center, Hampton, Va. 23665-5225

I. Introduction

A broadband capacitive electrostatic acoustic transducer (ESAT) has been developed for ultrasonic measurements in liquid environments[1]. We have used this device to calibrate the particle displacement amplitudes of a Panametrics 500 KHz Damped Transducer and to determine its absolute sensitivity as a function of frequency.

II. The ESAT

The mechanical features of the ESAT are covered in detail[1,2] elsewhere. For completeness, we briefly describe the mechanical, electrical, and acoustical features here.

A. Mechanical features

The functional components of the ESAT are shown in Figure 1. A

metallic membrane is stretched across a brass housing and is held in place with a retainer ring. A central (1/2 inch diameter) electrode, suspended approximately 10μM below the membrane, is mounted on a flat of plate glass for electrical isolation and mechanical stability. The spacing between the membrane and the central electrode is pneumatically controlled by changing the air pressure within the ESAT, using a sealed, external bellows. The pressure is monitored with a pressure sensor, with a sensitivity of 10^{-4} psig.

B. Electrical features

As an ultrasonic incident wave impinges on the membrane, it causes a variation of the gap spacing at the frequency of the ultrasonic wave. When the central electrode is DC biased with a voltage V_b, a

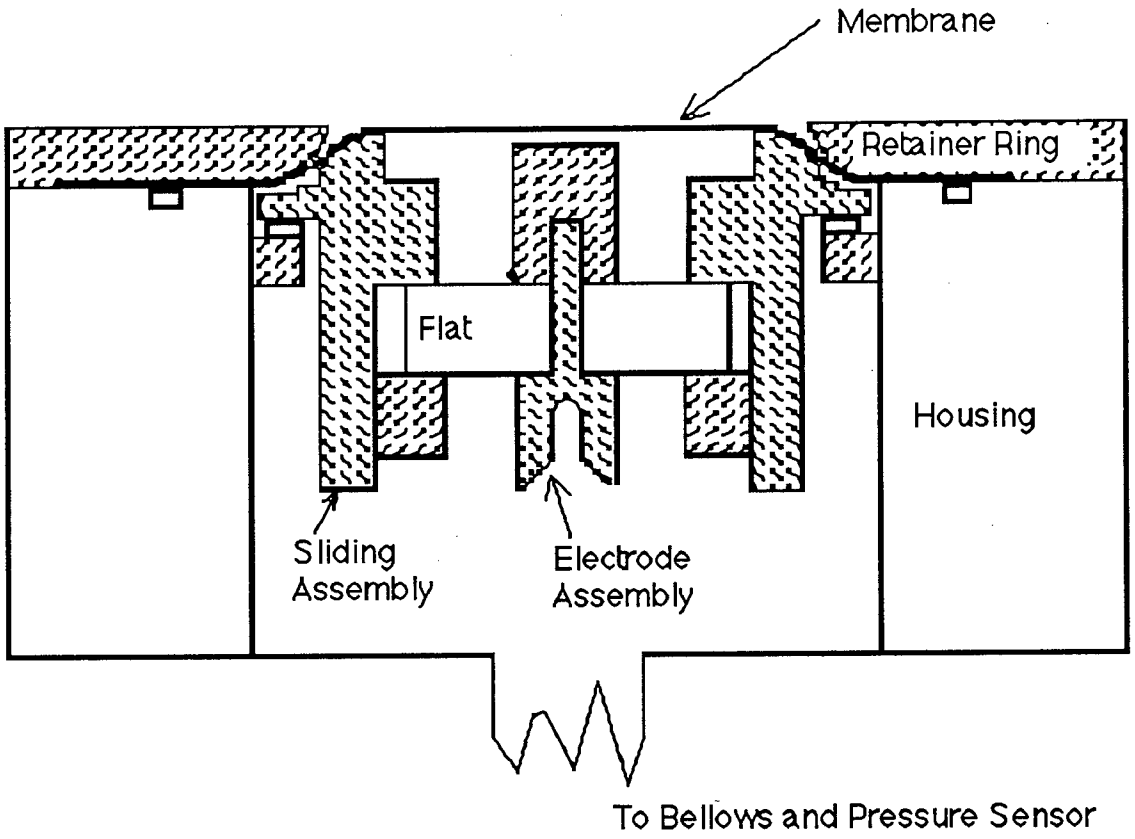

Figure 1. Mechanical Diagram of the ESAT

displacement of the membrane develops an AC signal at the same frequency of the ultrasonic wave. Consider the membrane displacement to be represented by

$$\eta = \eta_o \sin\omega t \quad , \qquad (1)$$

where η = membrane displacement and η_o is the amplitude. The ESAT is essentially a parallel plate capacitor whose plate area is A, and whose

plate seperation distance is s_o. The gap spacing can be represented by

$$s = s_o + \eta_o \sin \omega t \quad , \tag{2}$$

where s_o is the quiescent gap spacing. The DC bias voltage is obtained from a battery connected in series with a 1 megohm resistor between the membrane and the central electrode. We assume, therefore, that the charge separation is essentially constant. Under these conditions, an AC voltage of amplitude v is developed by the membrane displacement.

$$v = V_b(\frac{\eta_o}{S_o}) \sin \omega t \quad , \tag{3}$$

which is in agreement with previous work[1]. By measuring v, V_b, and s_o, we can determine η_o.

C. Acoustical features; the membrane

A compressional ultrasonic wave is launched from the piezoelectric transducer, which is axially aligned with the ESAT. As the wave impinges upon the membrane, a portion is transmitted through the membrane, Yost and Cantrell have shown[2] that the membrane displacement amplitude, η_o, can be written as

$$\eta_o = \frac{2\,\xi_o}{\sqrt{1 + (\frac{\sigma\omega}{\rho c})^2}} \quad , \tag{4}$$

where

ξ_o = particle displacement amplitude of the impinging wave,

σ = areal density of the membrane,

ρ = density of the liquid, and

c = compressional wave velocity of the liquid.

Therefore, absolute measurement of η_o makes it possible to determine ξ_o, the particle displacement amplitude of the ultrasonic wave.

III. Experimental Setup

The experimental setup of the ESAT is shown in Figure 2. Adjustments were made to assure that the transducer, membrane and central electrode were axially aligned, parallel, and level. The gap capacitance was set so that the membrane was flat while the ESAT was in operation. A pressure bias was added to compensate for the electrical attraction between the central electrode and membrane. Throughout the measurement, the gauge pressure was held constant to assure proper gap spacing.

The function generator was set for a long tone burst (greater than 20 cycles) at the desired frequency and its output was amplified by a linear amplifier and applied to the piezoelectric transducer. The transducer-generated acoustic wave traversed the water and impinged on the membrane whose vibration caused an output voltage that was

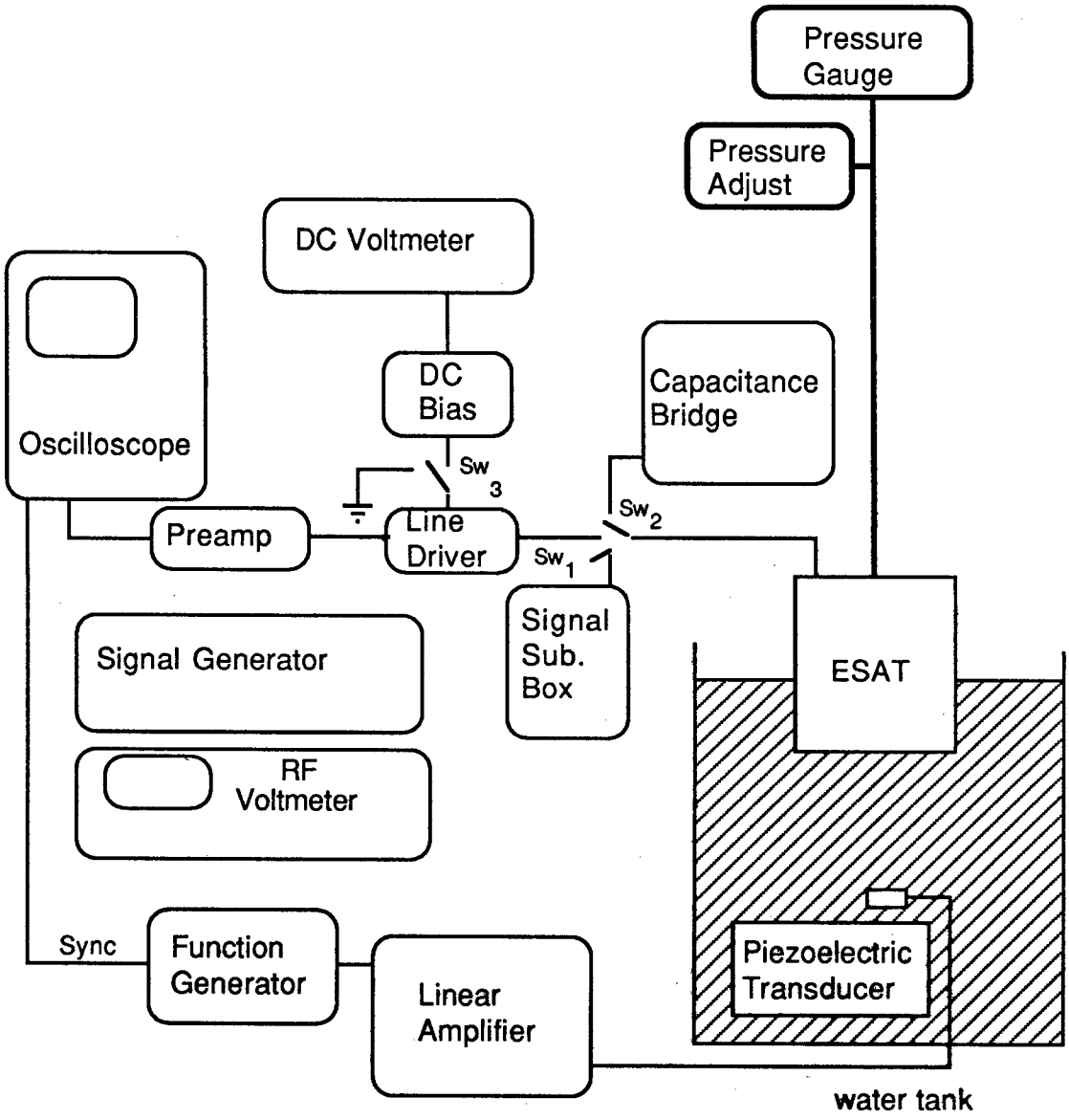

Figure 2. Experimental Setup

amplified by the line driver-preamp and displayed on the oscilloscope.

To measure this voltage the ESAT was disconnected and the Signal Substitution Box, which had the same electrical characteristics as the ESAT, was connected to the line driver-preamp-oscilloscope system. A signal generator was set at the same frequency as the acoustic wave and its voltage was adjusted until the amplitude displayed on the oscilloscope was the same as the amplitude displayed from the ESAT. An RF voltmeter was used to measure the voltage to the substitutional circuit. This substitutional voltage then has the same amplitude as the voltage amplitude generated by the ESAT.

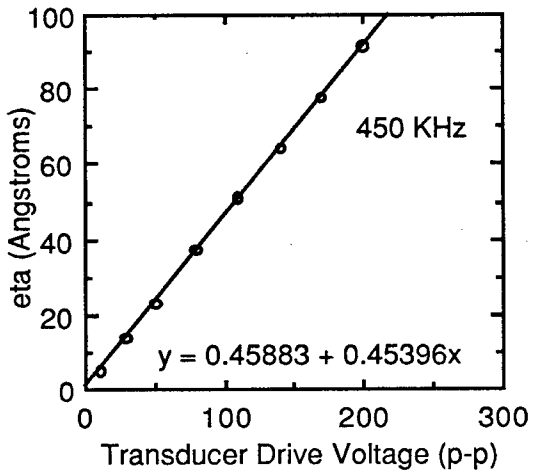

Figure 3. A Plot of Membrane Displacement Amplitude vs. Voltage Applied to the Transducer

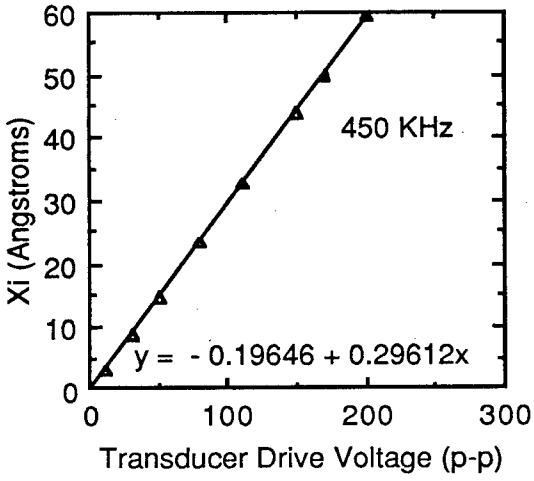

Figure 4. A Plot of Particle Displacement Amplitude vs. Voltage Applied to the Transducer

VI. Data and Results

While holding the frequency constant, a series of measurements of membrane displacement amplitudes were made as the drive voltage to the transducer was varied. This process was repeated for 13 different frequencies, chosen to span the range of maximum transducer sensitivity. A typical plot of one series is shown in Figure 3. The tone burst frequency for this plot is 450 KHz.

From the membrane displacement data, the particle displacement amplitude data was determined, using the results of Eq. (4), and the fact that the areal density for the membrane was $9.82 \pm 0.16 \times 10^{-3}$ gm/cm^2. A typical plot of the particle displacement amplitude vs. transducer drive voltage is shown in Figure 4. As in the earlier plot, the drive frequency was 450 KHz.

The sensitivity at a frequency is the slope of a least squares line fit to the data, and is determined from the series of measurements at each frequency. The sensitivity for each of the measured frequencies is plotted against frequency as shown in Figure 5. From this plot, we find that the transducer's center frequency is 426 KHz and the bandwidth (3dB points) is 346 KHz. The maximum sensitivity is $3.10 \pm 0.07 \times 10^{-1}$ angstroms/volt (peak to peak) applied to the transducer.

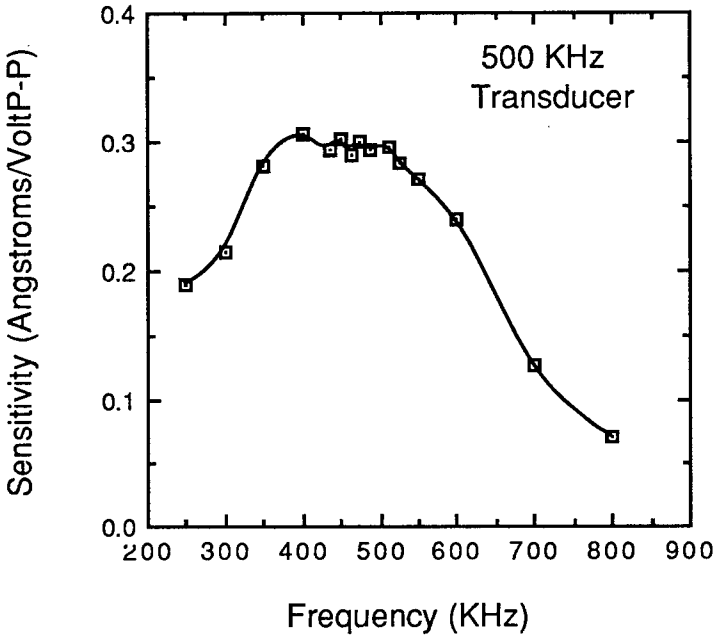

Figure 5. A Plot of Transducer Sensitivity vs Frequency for a Damped 500KHz Transducer

VII. Conclusions

The ESAT is capable of measuring the absolute displacement amplitudes of ultrasonic waves in water by considering the electrical characteristics of the ESAT and the acoustic characteristics of its membrane. The transducer used for this study (A Panametrics 500 KHz transducer) has a maximum sensitivity of $3.10 \pm 0.07 \times 10^{-1}$ angstroms/Vp-p and a bandwidth of 346KHz (at the 3dB points).

With the ESAT it is possible to make absolute measurements of particle displacement amplitudes to an accuracy of better than 4%.

From these measurements, other quantities, such as energy density and pressure amplitudes can be determined.

REFERENCES

1. J. H. Cantrell, J. S. Heyman, W. T. Yost, M. A. Torbett, and M. A. Breazeale, Rev. Sci. Instrum. 50 31(1979)
2. W. T. Yost and J. H. Cantrell, in Proceedings of the IEEE Ultrasonic Symposium, 87CH 2492.7 edited by B. R. McAvoy (Denver, Colorado 1987) pp 693-696 (1987)
3. HAVAR is the commercial name of a high tensile strength alloy manufactured by Hamilton Tech, Inc., Lancaster, PA 17604

*Analytical Services and Materials, 107 Research Drive, Hampton, Va. 23665.

EFFECTS OF DIFFRACTION ON THE MEMBRANE RESPONSE OF THE SUBMERSIBLE ELECTROSTATIC ACOUSTIC TRANSDUCER.

Pamela D. Hanna* and William T. Yost, NASA-Langley Research Center, Hampton, Va. 23665-5225, *AnalyticalServices and Materials, 107 Research Drive, Hampton, Va. 23665.

Much interest has been expressed recently regarding an absolute calibration technique for megahertz-range ultrasonic transducers. We have developed a technique for absolutely calibrating the displacement amplitudes of megahertz waves in liquids by using a liquid-immersible electrostatic acoustic transducer. We examine the effects of diffraction on the liquid-membrane coupling and absolute transducer calibration by comparing near-field (Fresnel diffraction) and far-field (Fraunhoffer diffraction)measurements. Results are obtained from the measurements of absolute wave displacements in the angstrom and sub-angstrom range in water. The diffraction-corrected absolute sensitivity of a low-frequency (500KHz) damped transducer is also presented.

I. Introduction

A broadband capacitive electrostatic transducer (ESAT) has been developed for ultrasonic measurements in liquid environments[1]. We have used this device to calibrate the displacement amplitudes of megahertz-range piezoelectric ultrasonic transducers and determined the absolute sensitivity of damped ultrasonic transducers as a function of frequency. In this paper, we examine diffraction corrections to data obtained from the near field to the far field to show their effects on the absolute sensitivity of a transducer.

II. The ESAT

The mechanical features of the ESAT are covered in detail[1,2] elsewhere. We briefly descirbe the mechanical, electrical, and acoustical features here.

A. Mechanical features

The functional components of the (ESAT) are shown in Fig. 1. A metallic membrane is stretched across a brass housing and is held in place with a retainer ring. A central (1/2 inch) electrode, suspended approximately 10μM below the membrane, is mounted on a flat of plate glass for electrical isolation and mechanical stability. The spacing between the membrane and the central electrode is pneumatically controlled by changing the air pressure within the ESAT. This is done by adjusting a sealed, external bellows. The pressure is monitored with a pressure sensor, with a sensitivity of 10^{-4} psig.

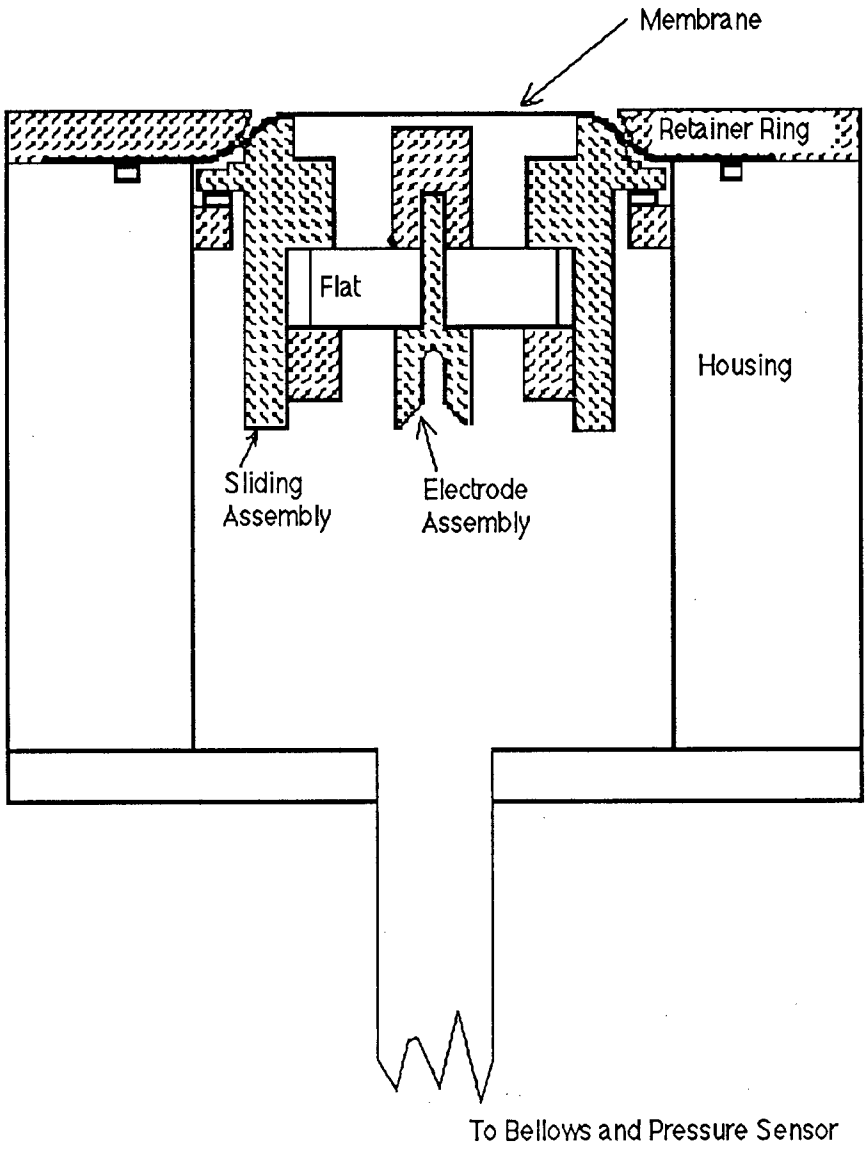

Fig. 1 Mechanical Diagram of the ESAT

B. Electrical features

An ultrasonic incident wave impinges on the membrane which causes a variation of the gap spacing at the frequency of the ultrasonic wave. When the central electrode is DC biased with a voltage V_b, a displacement of the membrane develops an AC signal at the same frequency as the ultrasonic wave. Consider the membrane displacement to be represented by

$$\eta = \eta_o \sin\omega t \qquad (1)$$

where η = membrane displacement. The ESAT is essentially a parallel plate capacitor whose plate area is A, and whose plate seperation distance is S_o. The gap spacing can be represented by

$$S = So + \eta_o \sin\omega t \qquad (2)$$

where S_o = quiescent gap spacing. The DC bias voltage is obtained from a battery connected in series with a 1 megohm resistor between the membrane and the central electrode. We assume, therefore, that the charge separation is essentially constant. Under these conditions, an AC voltage of amplitude v is developed by the membrane displacement.

$$v = V_b(\frac{\eta_o}{S_o})\sin\omega t \qquad (3)$$

By measuring v, V_b, and S_o, we can determine η_o.

C. Acoustical features; the membrane

A compressional ultrasonic wave is launched from the piezoelectric transducer, which is axially aligned with the ESAT. As the wave impinges upon the membrane, a portion is transmitted through the membrane, Yost and Cantrell have shown[2] that the membrane displacement amplitude, η_o, can be written as

$$\eta_o = \frac{2\,\xi_o}{\sqrt{1 + (\frac{\sigma\omega}{\rho c})^2}} \qquad (4)$$

where

ξ_0 = particle displacement amplitude of the impinging wave,

σ = areal density of the membrane,

ρ = density of the liquid, and

c = compressional wave velocity of the liquid.

Therefore, absolute measurement of η_0 makes it possible to determine ξ_0, the particle displacement amplitude of the ultrasonic wave.

III. Experimental procedure

Fig. 2 is a diagram of the equipment arrangement. Mechanical alignments were made so that the piezoelectric transducer and the ESAT were axially aligned. Furthermore, the ESAT was set level with the liquid surface. We set the gap capacitance of the ESAT to its value when there was no pressure differential across the membrane. Using the pneumatic control we added a pressure bias to exactly compensate for the attraction between the central electrode and membrane due to the bias voltage. These two actions assure that the membrane is flat and that the gap spacing is accurately known. Throughout the measurements the gauge pressure was held constant to assure proper gap spacing.

The procedure for a measurement was as follows: The function generator developed a tone burst at the desired frequency which was amplified by a linear amplifier and applied across the piezoelectric transducer (a Panametrics 500KHz 1/2" diameter damped transducer).

The generated acoustic wave transversed the water and impinged on the membrane of the ESAT causing a (high impedance) AC voltage output that was amplified through a line driver and preamp and displayed on the oscilloscope. A substitutional technique was employed to determine the ESAT output. After marking the peak to peak display on the oscilloscope screen, the ESAT was disconnected from the measurement system, and a Signal Substitution Box, which had the same electrical characteristics as the ESAT, was connected to the line driver and preamp. A signal generator set at the same frequency as the acoustic wave was used to develop a substitute voltage, which was adjusted until the peak to peak display of the oscilloscope was equal to the similar display of the ESAT voltage. This voltage from the signal generator has the same amplitude as the

voltage generated by the ESAT. The signal generator voltage was then measured with an RF voltmeter.

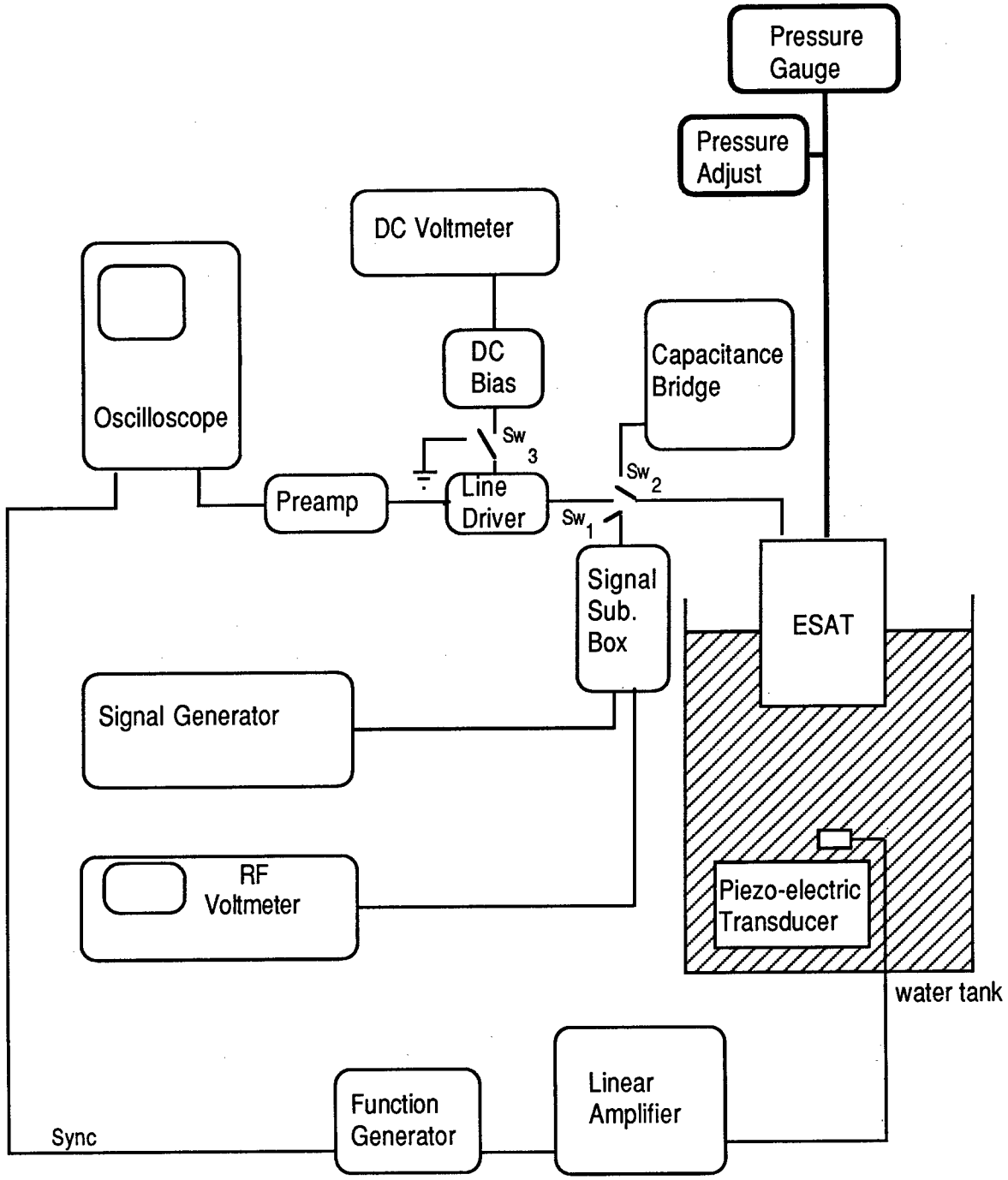

Fig. 2 Equipment Arrangement

VI. Data and Results

To cover near field to far field conditons three different distances of propagation were used. At each distance the transducer was driven at five different frequencies. At each distance and frequency, the sensitivity of the transducer was determined from a plot of particle displacement amplitude vs peak to peak drive voltage applied to the piezoelectric transducer. A typical plot of this is shown in Fig. 3. Using the least squares fit to the data, the sensitivity of the transducer,

$$\frac{\text{particle displacement amplitude (Angstroms)}}{\text{volt (peak to peak)}}$$

was determined. The results are shown in Table 1, in the column labeled as "uncorrected".

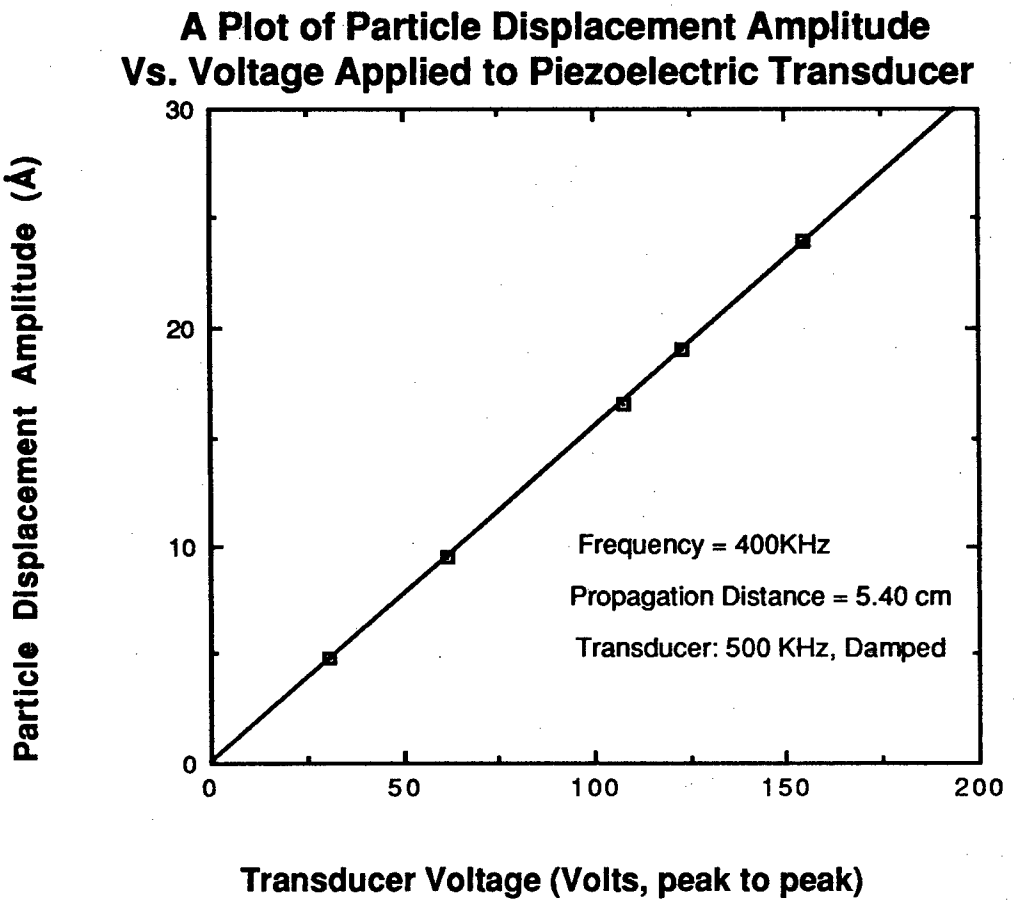

Figure 3 A Plot of Particle Displacement Vs. Applied Voltage.

We applied three well-known diffraction corrections to our data[3,4,5], in an attempt to find which of the three best covered near field-to-far field conditions. These are listed in Table 1. We notice that corrections from Benson and Kiyohara gave essentially the same result and those from Khimunin, while those from Papadakis gave results which were consistently lower.

We then calculated the spread in the diffraction corrected sensitivities at each frequency. The spread defined as

$$\frac{\text{largest sensitivity - smallest sensitivity}}{\text{mean}} = \text{spread},$$

was calculated for each frequency and an average spread was calculated. The results are:

Correction Applied	Average Spread
A (Benson & Kiyohara)	0.060
B (Papadakis)	0.047
C (Khimunin)	0.054

From this, we notice that diffraction corrections from Papadakis gives the best near field-to-far field consistency.

Table 1 Sensitivity

Frequency (KHz)	Uncorrected	Sensitivity (Angstroms/Voltp-p) withDiffraction Correction A	withDiffraction Correction B	withDiffraction Correction C
400				
z=5.40cm	.155	.2801	.2672	.2811
z=3.75cm	.184	.2649	.2573	.2629
z=0.75cm	.223	.2661	.2576	.2610
450				
z=5.40cm	.162	.2694	.2584	.2704
z=3.75cm	.195	.2677	.2643	.2677
z=0.75cm	.225	.2696	.2613	.2652
500				
z=5.40cm	.162	.2521	.2423	.2529
z=3.75cm	.178	.2375	.2299	.2364
z=0.75cm	.203	.2396	.2324	.2385
550				
z=5.40cm	.139	.2047	.1981	.2048
z=3.75cm	.161	.2121	.2054	.2107
z=0.75cm	.178	.2078	.2022	.2066
600				
z=5.40cm	.129	.1824	.1773	.1825
z=3.75cm	.141	.1851	.1786	.1835
z=0.75cm	.172	.2011	.1934	.1975

Diff. Corr. A Benson & Kiyohara
Diff. Corr. B Papadakis
Diff. Corr. C Khimunin

VII. Conclusions

We have made absolute sensitivity measurements on a 500 KHz damped 1/2" ultrasonic transducer. Using three different applicable diffraction corrections, we have examined the effects as one goes from a near field to a far field measurement with the ESAT. We find that all of the corrections show a reasonable degree of consistency, with corrections by Benson & Kiyohara giving nearly identical results as corrections by Khimunin. Corrections by Papadakis gave results that were consistently lower. However, when we examine the spread, we finds that the corrections by Papadakis were slightly better for this transducer working in this frequency range. This was interesting in that these corrections involved only the Seki parameter[3,4,5]. (The corrections developed by Khimunin were more complex) The corrections by Benson and Kiyrohara resulted in spreads that were slightly higher than the other two.

We have shown that absolute amplitude sensitivities, measured with the ESAT, can be corrected for diffraction. These correction work reasonably well in near-field to far-field measurements.

REFERENCES

[1]J. H. Cantrell, J. S. Heyman, W. T. Yost, M. A. Torbett, and M. A. Breazeale, Rev. Sci. Instrum. 50 31(1979)

[2]W. T. Yost and J. H. Cantrell, in Proceedings of the IEEE Ultrasonic Symposium, 87CH 2492.7 edited by B. R. McAvoy (Denver, Colorado 1987) pp 693-696 (1987)

[3]G. C. Benson and O. Kiyohara, J. Acoust. Soc. Am. 55 184 (1974)

[4]E. P. Papadakis, J. Acoust. Soc. Am. 40 863 (1966)

[5]A. S. Khimunin, Acustica 27 173 (1972)

IX. GENERAL

Anisotropy of the ultrasonic backscatter of myocardial tissue: II. Measurements *in vivo*

E. I. Madaras,[a] J. Perez, B. E. Sobel, J. G. Mottley,[b] and J. G. Miller
Department of Physics and Cardiovascular Division, Washington University, St. Louis, Missouri 63130

(Received 22 January 1987; accepted for publication 29 October 1987)

The purpose of this investigation was to determine the angular dependence of the backscatter from canine myocardial tissue *in vivo* and to compare it with the variation of backscatter over the cardiac cycle that has been recognized and reported previously. The backscatter was measured from regions of left ventricular wall in canine hearts in which the fibers of the muscle lay parallel to the surface of the heart and were oriented predominantly in a circumferential fashion. Because of technical considerations, the angle of insonification was varied systematically through two cycles in which the angle relative to the muscle fiber axes ranged from 60°–120°. Backscatter was maximum at angles of interrogation perpendicular to the myocardial fibers and minimum at those most acute (60°) relative to the orientation of the fibers. The previously observed variation of integrated backscatter over the heart cycle was evident at each angle of interrogation. At end systole, the average maximum-to-minimum angular variation of integrated backscatter as 5.0 ± 0.4 dB. At end diastole, the average maximum-to-minimum angular variation was 3.2 ± 0.4 dB. Thus, even though angular dependence of the backscatter from tissues with directionally oriented structures is substantial, the anisotropy does not account for cardiac-cycle-dependent variation of backscatter. Accordingly, the angular dependence should be incorporated in approaches to quantitative tissue characterization with ultrasound.

PACS numbers: 43.80.Cs, 43.35.Yb, 43.20.Fn

INTRODUCTION

Angular dependence, or anisotropy, is a characteristic of ultrasonic properties *in vitro* of several types of tissue with organized components such as directionally oriented fibers. It has been correlated with the orientations of fibers within tissue samples such as skeletal muscle[1–4] of diverse types and with histopathologic features.[5] Reports from our laboratory[6–8] have characterized anisotropic attenuation and backscatter of canine myocardium *in vitro* and correlated both the previously delineated[9,10] fiber orientation within the left ventricle. As the angle of insonification relative to the fiber axes was varied from parallel to perpendicular, the slope of the attenuation coefficient as a function of frequency varied by more than 100% and the backscatter changed by approximately 6 dB. Shore *et al.* demonstrated more than twofold increases in attenuation when propagation was parallel as opposed to perpendicular to the fibers of *post rigor* bovine skeletal muscle.[11] The presence of angular variations of this magnitude may result in significant distortion of ultrasonic images. Brandenburger *et al.*[12,13] have shown that systematic variations with angle can compromise attenuation tomography based on filtered backprojection.

The ultrasonic backscatter from myocardium studied *in vivo* varies during the cardiac cycle.[7,14–17] Cyclic variation of backscatter may provide useful criteria for characterizing local contractile performance.[18,19] Measurements of cyclic variation reported previously have been obtained with the ultrasonic beam oriented perpendicular to the predominant fiber direction in order to minimize the possible effects of anisotropic attenuation and backscatter. Extensions of this approach to the clinical setting will require quantification of the effects of anisotropy in intact tissue and appropriate incorporation of its influence in analytical procedures. The magnitude of anisotropic effects in myocardium undergoing contraction or relaxation is difficult to ascertain by study of tissue *in vitro*. Accordingly, this study was performed to characterize the anisotropy of backscatter from canine myocardium *in vivo* and to relate the anisotropic behavior to the previously demonstrated cyclic variation of backscatter. The approach we used was modeled after a nondestructive testing technique referred to as polar backscatter,[20–24] in which the interrogating transducer is maintained at a fixed angle (in these experiments, 30°) from the surface normal, and the azimuthal angle is then varied systematically. A water-filled cylinder served as an acoustic delay line so that the interrogated tissue volume was at the transducer's focus. The end of the cylinder was coupled directly to the epicardial surface of canine hearts during open-chest measurements of dogs. Time-gating circuitry permitted characterization of the backscatter from the middle segment of the myocardial thickness where the fibers were predominantly oriented circumferentially. Backscatter was measured over a range of angles by rotating the transducer about the perpendicular axis. This allowed interrogation of the midmyocardial fibers at angles ranging between 60° and 90° relative to the fiber

[a] Permanent address: NASA Langley Research Center, Hampton, VA 23665.
[b] Permanent address: Department of Electrical Engineering, University of Rochester, Rochester, NY 14627.

 0001-4966/88/020762-08$00.80

axes. Although the range of angles available for interrogation was limited, our previous measurements *in vitro*[6,7] indicated that it should not preclude recognition of the anisotropy of myocardial backscatter.

Integrated backscatter was measured throughout the cardiac cycle with previously described techniques[25] to assess the presence and magnitude of anisotropy during the cyclic variation of backscatter. As a control, each region of myocardium from which the backscatter was measured as a function of angle was characterized also with a second transducer held perpendicular to the surface of the tissue. For both the angle-dependent measurement and the normal incidence control measurement, the depth of the electronic gate was varied synchronously with wall thickening in order to keep the measurement volume within the tissue layer of interest, in contrast to previous procedures for measurement of cyclic variation in which the gate depth was held constant relative to the epicardium.[7,14–16,18,19] In addition, each measurement of backscatter was corrected for attenuation based on the appropriate depth and on an average attenuation coefficient derived from previous measurements performed *in vitro*.[6,26] The correction assumed that any cyclic variation of the attenuation coefficient over the cardiac cycle was negligible.[27] The results obtained after correction for attenuation were similar to values of the cyclic variation of backscatter reported previously.[7,14–19]

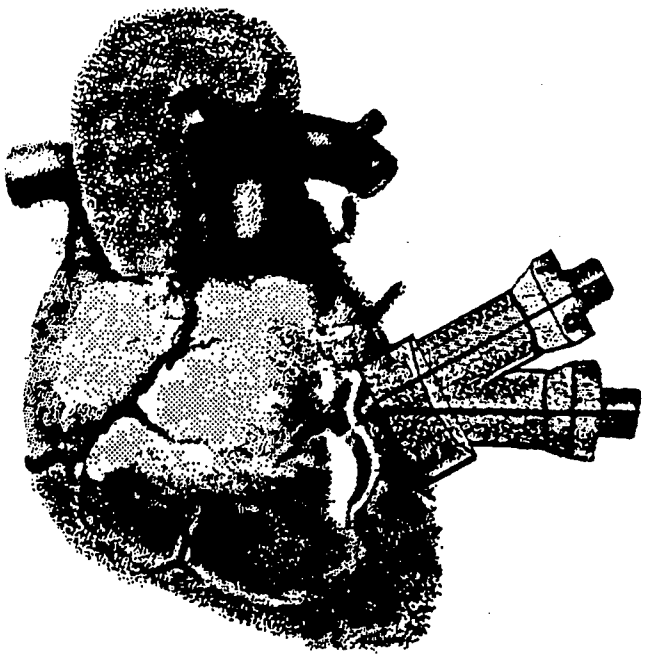

FIG. 1. Drawing of the transducer holder used in these experiments. The water-filled holder served as an acoustic delay line and held the two transducers, one at normal incidence and the second at a fixed polar angle (θ) of 30° from the first.

I. EXPERIMENTAL METHODS

A. Animal preparation

Eleven large mongrel dogs were studied. Each animal was anesthetized with sodium pentobarbital (25 mg/kg IV) and ventilated with oxygen with the use of a Harvard respirator. A right thoracotomy was performed and complete atrioventricular node blockade was induced by the local injection of 1–3 ml of formalin. Electrodes were attached to the right ventricle, and the right ventricle was paced at a fixed rate of 80 beats/min. The right thoracotomy was closed, and a left thoracotomy was performed at the fifth intercostal space. The fifth and sixth ribs were excised to provide access to the left ventricle for ultrasonic measurements, and the heart was suspended in a pericardial cradle. A fluid-filled catheter inserted through the apex was connected to a pressure transducer for monitoring left ventricular pressure. The electrocardiogram was monitored throughout the experiment.

B. Ultrasonic measurement system

Two transducers were employed simultaneously (Fig. 1) in a specially fabricated holder. One was perpendicular to the base of the holder and the other at a fixed polar angle of 30° from perpendicular. A block diagram indicating the manner in which each of the transducers was operated is presented in Fig. 2. A Honeywell/Biosound Ultra-Imager System was used to operate the perpendicular transducer in standard M-mode imaging format. Monitoring of the M-mode display enabled the operator to maintain the perpendicular transducer orientation. The criteria for determining perpendicularity were that the transducer appeared by visual inspection to be perpendicular to the surface of the heart, that the M-mode image showed sharp delineation of the epicardial surface, that wall thickening during systole and thinning during diastole were appropriately synchronized with respect to the electrocardiogram, and that observed wall thinning reflected an appropriate minimum value.

Both transducers were broadband (5-MHz nominal center frequency), 1.2 cm in diameter, and were focused at 5 cm. The base of the holder was sealed with a flexible latex layer and its body was filled with water, which provided an acoustic delay line. When applied to the epicardial surface of the heart, the holder positioned the transducers so that the focal zones of the transducers overlapped within the midmyocardial region in diastole. In systole, the epicardial surface of the heart pushed upward, compressing the latex tip toward the transducers, shortening the ultrasonic water

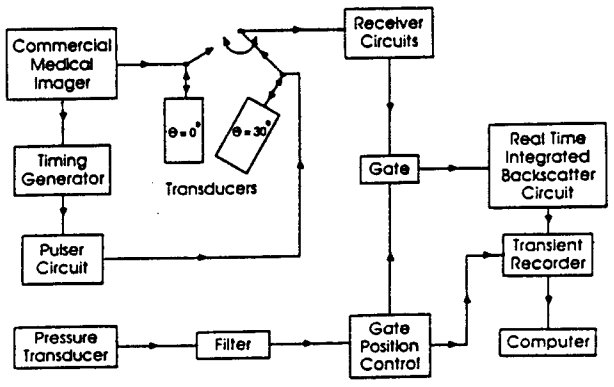

FIG. 2. Block diagram of the data acquisition system.

path by a few millimeters. The focal zones were cyclically deeper in the myocardium in systole and shallower in diastole. However, they remained within the middle segment of the myocardial wall throughout the heart cycle. The two transducers were excited alternately to avoid interference between the resulting ultrasonic signals. Thus backscatter measurements could be obtained from the transducer angled at 30°, while the perpendicular transducer was used to ensure the desired orientation of the pair relative to the epicardial surface.

We employed a real-time integrated backscatter system described initially and in detail by Thomas *et al.*[28] In brief, a 3-μs portion of the backscattered signal emanating from the middle segment of the myocardial wall was gated from the rf signal and fed into the real-time backscatter system. The real-time backscatter system produced an analog signal proportional to the received rf power and, therefore, approximately proportional to the ultrasonic energy backscattered from the portion of the myocardial tissue of interest. This signal was integrated and peak detected to provide a voltage proportional to the integrated backscatter. The system was calibrated by measuring its response to a signal reflected from a steel plate. The output of the real-time integrated backscatter system was recorded with a transient waveform recorder at a sampling rate of 200 Hz. At this sampling rate, the recorder could record data from about five full cardiac cycles in each 1024-point trace. The digitized record was analyzed later on a PDP 11/23 computer.

As the heart contracts and relaxes, the thickness of the myocardial wall varies. In order to restrict our investigation to the middle segment of the myocardial wall that contains predominantly circumferentially oriented fibers,[9] circuitry was constructed to produce a gating signal that would track the motion of the midmyocardium. Synchronization with the cardiac cycle was accomplished with the signal from the left ventricular pressure monitor. This signal was low-pass filtered and amplified, with gain and offset adjusted until the resulting electrical signal was observed to follow accurately the ventricular wall motion depicted on the M-mode display. The resulting voltage controlled a timer that triggered the gate so that the gate remained within the middle segment of the ventricular wall at all times. The gate-control voltage was recorded along with the integrated backscatter signal on a second channel of the waveform recorder.

The time delay (and, therefore, the depth within the tissue) that corresponded to a particular voltage was calibrated by applying dc voltages at levels that shifted the gate in small increments and fitting a straight line to the resultant points. The recorded voltages for the gate's position were interpolated to units of time from this fit. The gate time delay was transformed to a depth in the myocardium, based on the assumption that the speed of sound in myocardium was approximately constant throughout the cardiac cycle.

Wall thickness was determined directly from the perpendicular transducer M-mode display. For the angled transducer, wall thickness could be reliably measured only at end diastole. Wall thickness at other intervals during the cardiac cycle were estimated from thickness measured directly at end diastole and fractional wall thickening measured with the perpendicular transducer. Wall thickening was typically of the order of 30%–50%, consistent with published measurements for open-chest dogs.[29]

C. Measurement protocol

For these studies, we defined a coordinate system based on the externally visible anatomical features of the exposed heart shown in Fig. 3. The axis of alignment was defined by a line from the apex of the heart to the region of the bifurcation of the left coronary artery into the anterior descending and circumflex vessels, a readily detectable visual marker. This axis is approximately perpendicular to the predominant fiber orientation in the middle segment of the myocardium, according to Streeter *et al.*[9] To be consistent with the definition of fiber axes in our previous work,[6,7] we denoted this as the 90° and 270° axis of the azimuthal angle ϕ. Thus fibers were oriented approximately along the 0° and 180° axis as depicted in Fig. 3(a). The angle Γ between the incident ultrasonic wave and the muscle fiber axes is given by the formula in the preceding article,[30]

$$\Gamma = \cos^{-1}[|\cos(\phi)|\sin(\theta)]. \quad (1)$$

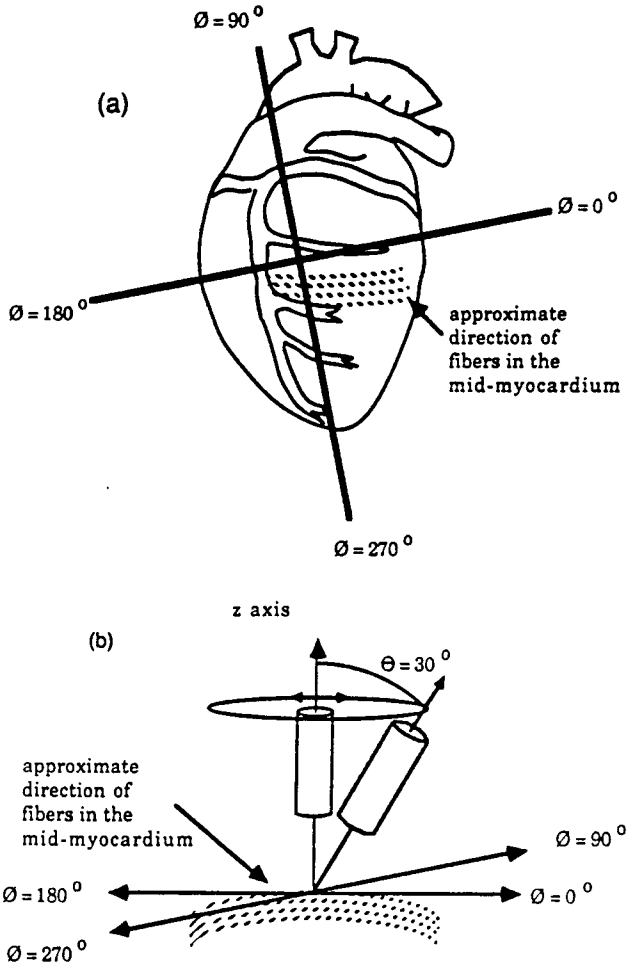

FIG. 3. (a) Line drawing of the canine heart, showing major landmarks, with the coordinate axes used in defining azimuthal angle (ϕ) superimposed. (b) Orientation of the transducers with respect to the coordinate axes shown.

As illustrated in Figs. 1–3, θ was either 0°($\sin\theta = 0$) or 30°($\sin\theta = 0.5$), depending on which transducer was excited. A set of backscatter measurements from the region of interest was obtained with the plane of incidence oriented initially along the $\phi = 90°$ axis. Measurements were then obtained at increments of 30° in azimuthal angle through a full 360°. The series was completed with repeat 90° measurements to verify consistency. In addition, backscatter measured with the fixed, perpendicular transducer and calibration measurements were obtained at the beginning and at the end of the azimuthal series.

A set of measurements consisted of ten sites over the left ventricular wall for each animal. The region of the left ventricle characterized encompassed a zone from near the apex to near the base and from the locus of the left descending coronary artery to that of the left posterior descending. Each trace included data from approximately five cardiac cycles. Any traces in which the integrated backscatter exceeded the linear range of our instrumentation or in which each heart cycle was not properly paced were excluded prospectively from processing.

After compensation for attenuation had been performed on each trace as described below, each cardiac cycle was divided into 32 equally spaced time windows, and backscatter measurements within each of the windows averaged together to provide 32 equally spaced samples of backscatter over a cardiac cycle. Subsequently, measurements within each window were averaged with data from other cardiac cycles and from sites measured at the same orientation in the same animal. The result was a set of average integrated backscatter curves for each animal as a function of both the interval within the cardiac cycle and the azimuthal angle of insonification.

It was necessary to compensate backscatter measurements for the attenuation resulting from the varying thickness of tissue overlying the fibers insonified. Unfortunately, the relationship between the contractile state of cardiac tissue and attenuation *in vivo* has not been delineated. Wear *et al.* observed no significant change in attenuation between rest and contraction in isolated perfused cardiac muscles.[27] Attenuation of frog skeletal muscle[7,31,32] *in vitro* varies with contraction. However, the change in backscatter with contraction in frog skeletal muscle differs in direction from the corresponding change in cardiac tissue. Furthermore, the overall magnitude of the backscatter is much greater in the skeletal muscle (by approximately 10 dB). Thus extrapolation from skeletal to cardiac muscle is likely to be misleading.

We assumed that the attenuation of canine myocardium does not vary significantly throughout the cardiac cycle. For ultrasound incident perpendicular to the fibers, we assumed a value for the slope of attenuation of 0.072 $(\text{cm MHz})^{-1}$ based on results from canine myocardium *in vitro*.[33] Using this value, taking 5 MHz as the center frequency, and assuming a linear dependence of the attenuation coefficient on frequency, we obtained a compensation term of 3.1 dB/cm.

We have previously shown[6,7] that the attenuation of canine myocardium *in vitro* is minimum for ultrasound propagating perpendicular to the fibers and maximum for ultrasound propagating parallel to the fibers, with a ratio of maximum to minimum of approximately 2. In the studies reported here, the range of angles of incidence ranged from 60° to 90°. Therefore, we would expect that the attenuation would be 20% greater with the beam directed 60° from the fiber axis than with propagation at 90°. Because the predominant axis of myocardial fiber direction varies as a function of the depth of the fibers within the ventricular wall,[9] the ultrasonic beam in our studies passed through tissue layers oriented at azimuthal angles spanning a range of approximately 90°. We modeled the depth dependence of myocardial fiber direction to first order as a linear function of depth into the myocardial tissue, i.e., the azimuthal angle (ϕ) of the fiber axis at depth d is given by

$$\text{azimuthal angle} = 90°(1 - d/d_0), \tag{2}$$

where d_0 is the depth of the gate within the wall. Based on our results for anisotropy of attenuation[6,7] and with averaging over the appropriate range of angles, we determined an attenuation correction for backscatter measured using the transducer fixed at 30° from the perpendicular. This term was approximately constant with azimuthal angle. Its averaged value of 3.5 dB/cm was 11% greater than the correction applied to data acquired with the perpendicular transducer. The extreme condition of having all the fibers' axes at 60° from the transducer would lead to a worst case, 20% shift in the attenuation correction. Thus the correction of 11% seems reasonable, despite the simple assumption of linear variation of fiber direction with depth.

II. RESULTS

Cyclic variation of integrated backscatter throughout the cardiac cycle was evident in each animal and at each azimuthal orientation. The cyclic variation of backscatter exhibited consistent phase, reaching a maximum at end diastole and a minimum at end systole in agreement with previous reports.[7,14–19] Integrated backscatter throughout the cardiac cycle averaged for all eleven dogs at each of four aximuthal angles ($\phi = 0°, 90°, 180°, 270°$) is presented in Fig. 4, in which measurements from individual dogs are all aligned at end diastole. Thus the point at which end systole occurs is blurred because of animal-to-animal variation in the fraction of the cardiac cycle comprising systole. It is evident in the figure that the $\phi = 0°$ and $\phi = 180°$ azimuthal angles, i.e., when the angle to the fiber axes Γ is 60°, exhibit a lower magnitude for backscatter compared with backscatter from the $\phi = 90°$ and $\phi = 270°$ azimuthal angles of insonification, when the angle Γ is 90°.

Figure 5(a) depicts the fiber direction of interest and three insonification directions. Figure 5(b) and Table I depict integrated backscatter obtained at end diastole and at end systole for each of the three orientations. The results obtained at perpendicular incidence (i.e., at $\theta = 0°$ and at $\theta = 30°, \phi = 90°$) are essentially identical. Although in both of these orientations the transducer insonifies the tissue perpendicular to the predominant axis of the myocardial fibers ($\Gamma = 90°$), compensation for effects arising from attenuation differs in the two cases. Thus the concordance illustrated in Fig. 5(b) supports the validity of our approach for

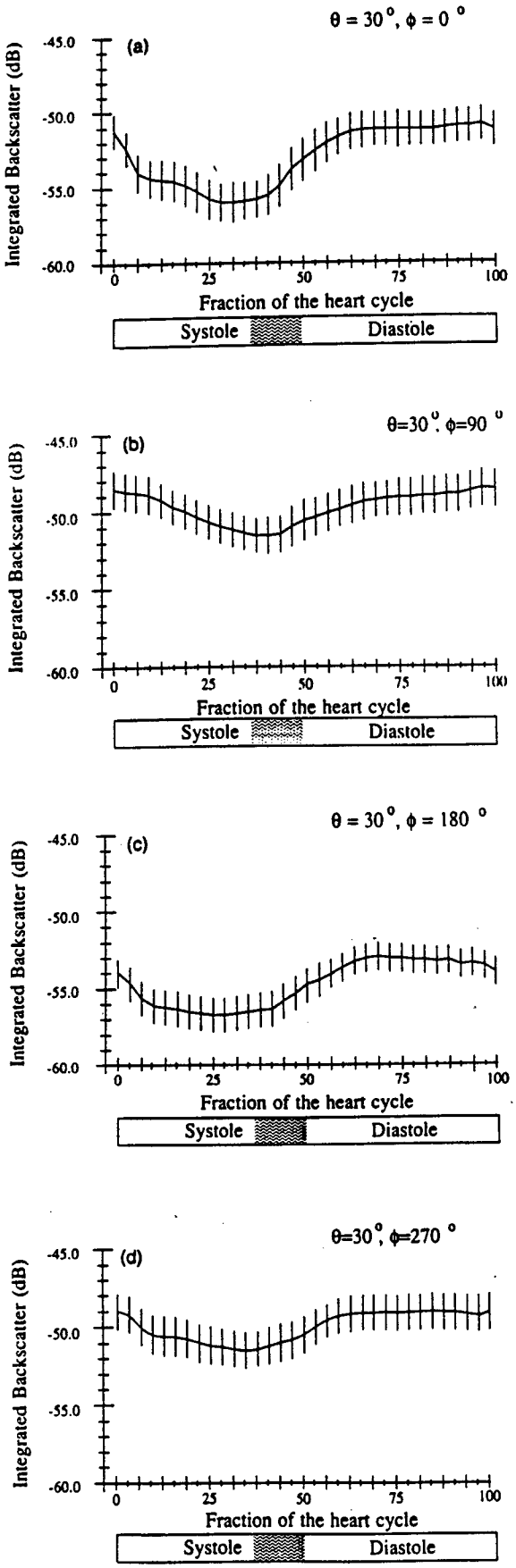

FIG. 4. Integrated backscatter, averaged for all animals, measured throughout the cardiac cycle with polar angle $\theta = 30°$ in four cardinal azimuthal directions, $\phi = 0°$, 90°, 180°, and 270°.

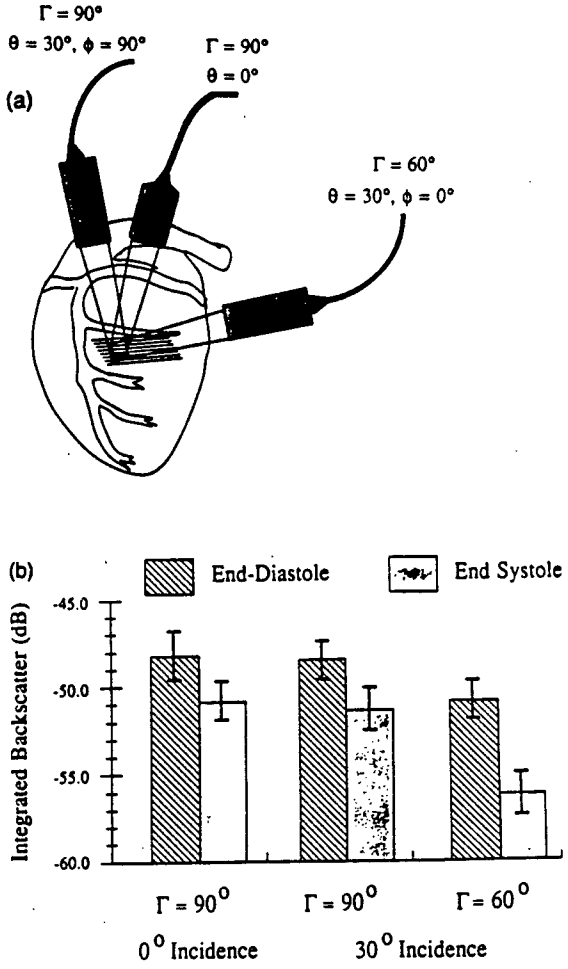

FIG. 5. (a) Three special directions of insonification at which measurements were carried out. In (b), the integrated backscatter at end diastole and end systole is presented at these three directions: perpendicular to fiber axes ($\Gamma = 90°$) both at normal incidence ($\theta = 0°$) and non-normal incidence (the average of $\theta = 30°$, $\phi = 90°$ and 270°), and at the minimum angle of 60° to the fiber axes (the average of $\theta = 30°$, $\phi = 0°$, 180°, and 360°).

TABLE I. Values of integrated backscatter measured *in vivo* from canine myocardium at three angles of incidence. Polar angles (θ) were 0°, 30°, and 30° and azimuthal angles (ϕ) were undefined, 90°, and 0°, with resultant angles relative to the fiber axes (Γ) of 90°, 90°, and 60°.

	Backscatter (dB)	
Conditions	End systole	End diastole
0° Polar angle ($\Gamma = 90°$)	-50.8 ± 1.1	-48.2 ± 1.4
30° Polar angle ($\Gamma = 90°$)	-51.3 ± 1.1	-48.5 ± 1.2
30° Polar angle ($\Gamma = 60°$)	-56.2 ± 1.2	-50.9 ± 1.1

compensation for the effects of attenuation. The remaining insonification direction shown in Fig. 5(a) ($\theta = 30°, \phi = 0°$) represents the other extreme in which the tissue was insonified at the minimum angle ($\Gamma = 60°$) with respect to the predominant axis of the fibers. The integrated backscatter at both end systole and end diastole is lower for the orientation $\Gamma = 60°$ than for the orientations in which $\Gamma = 90°$.

In Figs. 4 and 5(b), animal-to-animal variations in absolute values of integrated backscatter result in relatively large standard errors of the means. Consequently, angular variations can be delineated more directly by expressing the backscatter at any angle relative to that measured at perpendicular incidence ($\Gamma = 90°$) at end diastole. Subtracting this baseline backscatter expressed in dB from each value yields the results presented in Fig. 6. At end diastole, the backscatter shows anisotropy with an excursion of 3.2 dB. Insonification perpendicular to the fibers ($\phi = 90°$ or 270° and, hence, $\Gamma = 90°$) yields a maximum and insonification at a 0° azimuthal angle ($\phi = 0°$ or 180°, hence, $\Gamma = 60°$) a minimum value. Values at end systole exhibit qualitatively similar differences, with lower average value, but greater variation as a function of azimuthal angle.

The data were fit to curves of the form $A + B \times \cos(2\phi + \delta)$, where A is the average value of integrated backscatter, B is the relative amplitude of variation, ϕ is the azimuthal angle, and δ is a phase shift. A least-squares-fitting procedure yields values of $B = 1.6 \pm 0.2$ dB (mean $\pm$ SEM) at end diastole and $B = 2.5 \pm 0.2$ dB (mean $\pm$ SEM) at end systole, corresponding to peak-to-peak variations of 3.2 dB at end diastole and 5.0 dB at end systole. These results are significantly different from $B = 0$, expected in an isotropic medium ($p < 0.001$ for both end diastole and end systole, Student t test modified by Bonferroni's procedure[34] for multiple comparisons). The predicted angle of maximum backscatter is 90°. Based on the fits to the data, the angular maxima occur at $105.4° \pm 9.1°$ (mean $\pm$ SEM) for end diastole and $81.1° \pm 5.8°$ (mean $\pm$ SEM) for end systole, values that are not significantly different from 90° at the 0.05 level (Student t test modified by Bonferroni's procedure for multiple comparisons).[34]

III. DISCUSSION

This study was performed with open-chest dogs so that a specific layer of myocardium could be utilized for systematic backscatter measurements by applying the transducer directly to the epicardial surface of the heart. The transducer holder was applied with modest pressure to assure contact, and this allowed the device to conform to the heart's surface without unduly flattening the surface. Because the curvature of the heart's surface is modest in the region investigated, the angle of incidence of the $\theta = 30°$ transducer remained at approximately 30° for all azimuthal angles. The interface losses due to reflection do not differ substantially from those for the perpendicular transducer case, and the mode conversion losses are very small (estimated at 1% or so) because of the small difference in velocity between the heart tissue and the water in the delay line and the small shear velocities of tissue.[35] Hence, no corrections for the effects of refraction, reflection losses, or mode conversion were applied. Possible effects on the measurements arising from tissue motion cannot be ignored. The most significant motion arises because of the thickening of the myocardial wall during systole. The use of the time-varying gate substantially reduces effects arising from this source. Some lateral motion of the heart wall also accompanies systole. Although compensation for effects due to this motion was not feasible, measurements were carried out in a region of the left ventricular wall in which this lateral motion is relatively modest. The attenuation coefficient was assumed to remain constant throughout the cardiac cycle. Small variations in the attenuation correction with azimuthal angle were neglected. The validity of this approach is supported by the concordance of the backscatter results obtained at orientations ($\theta = 0°$) and ($\theta = 30°, \phi = 90°$), shown in Fig. 5(b) and Table I. The results in Figs. 5 and 6 indicate that the ultrasound is backscattered more efficiently

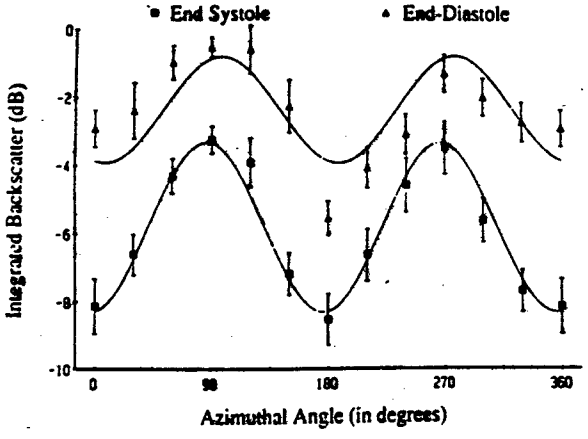

FIG. 6. The average integrated backscatter at end diastole and end systole as a function of azimuthal angle (ϕ) normalized to the values obtained at end diastole with the $\theta = 30°$ transducer at perpendicular incidence, $\Gamma = 90°$ (i.e., $\phi = 90°$).

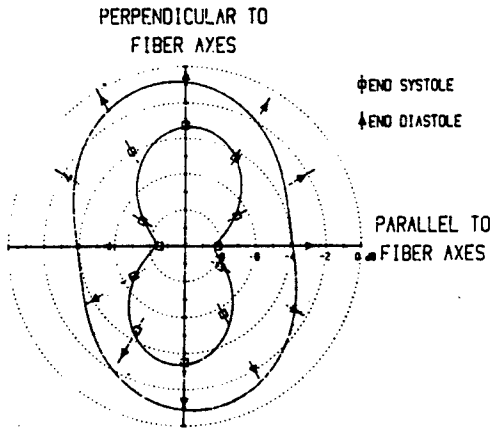

FIG. 7. Polar plot (based on the coordinate axes shown in Fig. 3) of the average integrated backscatter at end diastole and end systole as a function of azimuthal angle (ϕ) normalized to the values obtained at end diastole with the $\theta = 30°$ transducer at perpendicular incidence, $\Gamma = 90°$ (i.e., $\phi = 90°$).

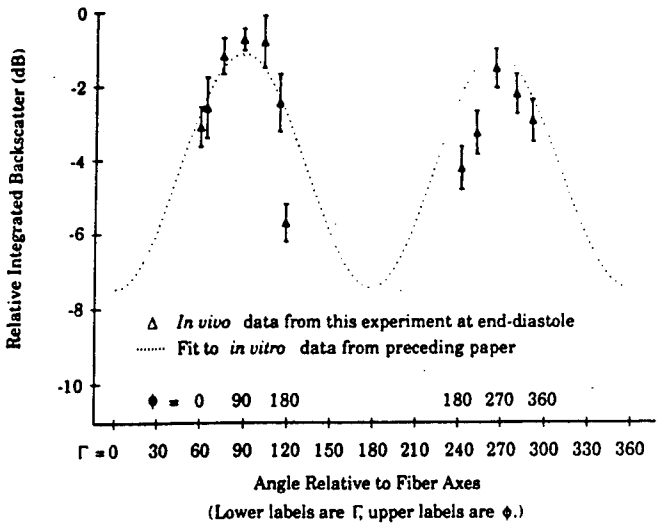

FIG. 8. The average integrated backscatter measured at end diastole as a function of the angle (Γ) relative to the fiber axes, illustrated with the fit to the data *in vitro* by Mottley and Miller.[30] Values of the angle ϕ corresponding to specific values of the angle Γ are indicated.

when the incident beam is perpendicular to the axis of the fibers, in agreement with theoretical considerations and with results *in vitro* described in the preceding article.[30]

The results of the present study are pertinent to cardiac imaging with ultrasound. Based on the coordinate axes depicted overlying the heart in Fig. 3(a), the polar plot of Fig. 7 shows the extent of anisotropy observed at specific azimuthal angles. If the myocardium were isotropic in its ultrasonic backscatter, then the data display on the polar plot would be circular. The solid lines are fits to the data shown in Fig. 6. Deviations from circular symmetry reflect the extent of anisotropy of myocardium.

In Fig. 8, we compare the results of this study with fits to data acquired *in vitro*, presented in the preceding article,[30] with the assumption that characteristics of myocardium *in vitro* are most similar to those of tissue *in vivo* at end diastole. Angular variables have been converted to angles relative to the fiber axes Γ. Accordingly, data from this experiment are plotted over a limited range. (For reference, the corresponding angles of ϕ are also indicated on the figure.) We assume the same form for the angular dependence of the backscatter $[A + B\cos(2\Gamma)]$ as that described previously.[30] By taking the amplitude of angular variation of the fit to measurements obtained *in vitro* and aligning the fit such that maxima conform to the average of the 90° and 270° *in vivo* data, we obtain the curve shown. Thus data collected under quite disparate conditions are generally consistent with the angular variation measured *in vitro*.

With two-dimensional echocardiography performed in intact, closed-chest animals or patients, the ultrasonic beam follows paths corresponding to varying fiber directions. Thus anisotropy of backscatter can lead to errors in estimates of the cyclic variations during the cardiac cycle. Rotation of the heart when it contracts will alter insonification angles with respect to fiber axes even though the transducer does not move with reference to the chest wall. Thus spurious patterns of cyclic variation of backscatter can arise because of changing angles of insonification. Cyclic variation might be magnified, attenuated, or even reversed in phase if anisotropic effects were not properly identified. Conversely, the accuracy of myocardial tissue characterization can be enhanced if the anisotropy effects delineated here are incorporated in the analysis of backscattered signals.

ACKNOWLEDGMENTS

This research was supported by NIH Grants HL17646 and RR01362. We wish to acknowledge the expert technical assistance of Dèlbert Macgraw. Contributions by Mark R. Kaufmann are appreciated.

[1]R. C. Chivers, R. C. Hill, and D. Nicholas, "Frequency dependence of ultrasonic backscattering cross-section, an indicator of tissue structure characteristics," in *Proceedings of the 2nd World Congress on Ultrasonic Medicine*, 1973, p. 300.
[2]D. Nicholas, "Ultrasonic diffraction analysis in the investigation of liver disease," Br. J. Radiol., **52**, 949–961 (1979).
[3]D. K. Nassiri, D. Nicholas, and C. R. Hill, "Attenuation of ultrasound in skeletal muscle," Ultrasonics **17**, 230–232 (1979).
[4]D. Nicholas, A. W. Nicholas, and R. Greenbaum, "An ultrasonic determination of cardiac muscle structures," in *Acoustical Imaging* (Plenum, New York, 1982), Vol. 11, pp. 95–108.
[5]E. Shapiro, D. L. Marier, M. G. St. John Sutton, and D. G. Gibson, "Regional non-uniformity of wall dynamics in normal left ventricle," Br. Heart J. **45**, 264–270 (1981).
[6]J. G. Mottley and J. G. Miller, "Anisotropy of ultrasonic attenuation in canine heart and liver," Ultrason. Imag. **4**, 180 (abstract) (1982).
[7]J. G. Mottley, "Physical principles of the ultrasonic attenuation and backscatter of soft tissues: Dependence on the angle of propagation and the physiologic state," Ph. D. thesis, Washington University, St. Louis, MO (1985).
[8]J. R. Klepper, G. H. Brandenburger, J. W. Mimbs, B. E. Sobel, and J. G. Miller, "Application of phase insensitive detection and frequency dependent measurements to computed ultrasonic attenuation tomography," IEEE Trans. Biomed. Eng. **BME-28**, 186–201 (1981).
[9]D. D. Streeter, Jr., H. M. Spotnitz, D. P. Patel, J. Ross, Jr., and E. H. Sonnenblick, "Fiber orientation in the canine left ventricle during diastole and systole," Circ. Res. **XXIV**, 339–347 (1969).
[10]R. A. Greenbaum, S. Y. Ho, D. G. Gibson, A. E. Becker, and R. H. Anderson, "Left ventricular fibre architecture in man," Br. Heart J. **45**, 248–263 (1981).
[11]D. Shore, M. O. Woods, and C. A. Miles, "Attenuation of ultrasound in *post rigor* bovine skeletal muscle," Ultrasonics **24**, 81–87 (1986).
[12]G. H. Brandenburger, J. R. Klepper, J. G. Miller, and D. L. Snyder, "Effects of anisotropy in the ultrasonic attenuation of tissue on computed tomography," Ultrason. Imag. **3**, 113–143 (1981).
[13]G. H. Brandenburger, "Simulation of ultrasound in tomographic imaging: Theory and methods based on geometrical acoustics," D.Sc. thesis, Washington University, St. Louis, MO (1981).
[14]E. I. Madaras, B. Barzilai, J. E. Perez, B. E. Sobel, and J. G. Miller, "Changes in myocardial backscatter throughout the cardiac cycle," Ultrason. Imag. **5**, 229–239 (1983).
[15]B. Barzilai, E. I. Madaras, B. E. Sobel, J. G. Miller, and J. E. Perez, "Effects of myocardial contraction on ultrasonic backscatter before and after ischemia," Am. J. Physiol. Soc. **247** (Heart Circ. Physiol **16**) H478–H483 (1984).
[16]J. G. Mottley, R. M. Glueck, J. E. Perez, B. E. Sobel, and J. G. Miller, "Regional differences in the cyclic variation of myocardial backscatter that parallel regional differences in contractile performance," J. Acoust. Soc. Am. **76**, 1617–1623 (1984).
[17]B. Olshansky, S. M. Collins, D. J. Skorton, and N. V. Prasad, "Variation of left ventricular myocardial gray level on two-dimensional echocardiograms as a result of cardiac contraction," Circulation **70**, 972–977 (1984).
[18]S. A. Wickline, L. J. Thomas, III, J. G. Miller, B. E. Sobel, and J. E. Perez, "A relationship between ultrasonic integrated backscatter and myocardial contractile function," J. Clin. Invest. **76**, 2151–2160 (1985).

[19]S. A. Wickline, L. J. Thomas, III, J. G. Miller, B. E. Sobel, and J. E. Perez, "The dependence of myocardial ultrasonic integrated backscatter on contractile performance," Circulation 72, 183–192 (1985).
[20]A. F. Brown, "Materials testing by ultrasonic spectroscopy," Ultrasonics 11, 202–210 (1973).
[21]Y. Bar-Cohen and R. L. Crane, "Acoustic-backscattering imaging of subcritical flaws in composites," Mater. Eval. 40, 970–975 (1982).
[22]L. J. Thomas, III, E. I. Madaras, and J. G. Miller, "Two-dimensional imaging of selected ply orientations in quasi-isotropic composite laminates using polar backscattering," *Proceedings of the 1982 IEEE Ultrasonics Symposium*, IEEE Cat. No. 82 CH1823-4 (IEEE, New York, 1982), pp. 965–970.
[23]E. D. Blodgett, L. J. Thomas, III, and J. G. Miller, "Effects of porosity on polar backscatter from fiber reinforced composites," Rev. Prog. Quant. Nondestr. Eval. 5B, 1267–1274 (1986).
[24]E. D. Blodgett, S. M. Freeman, and J. G. Miller, "Correlation of ultrasonic polar backscatter with the Deply technique for assessment of impact damage in composite laminates," Rev. Prog. Quant. Nondestr. Eval. 5B, 1227–1238 (1986).
[25]S. A. Wickline, L. J. Thomas, III, J. G. Miller, B. E. Sobel, and J. E. Perez, "Ultrasonic tissue characterization detects favorable effects of reperfusion on myocardium," Circulation 72, III–450 (1985).
[26]M. O'Donnell, J. W. Mimbs, B. E. Sobel, and J. G. Miller, "Collagen as a determinant of ultrasonic attenuation in myocardial infarcts," Ultrasound Med. 4, 503–513 (1978).
[27]K. A. Wear, T. A. Shoup, and R. L. Popp, "Ultrasonic characterization of canine myocardium contraction," IEEE Trans. Ultrason. Ferroelectr. Frequency Control UFFC-33, 347–353 (1986).
[28]L. J. Thomas, III, S. A. Wickline, J. E. Perez, B. E. Sobel, and J. G. Miller, "A real-time integrated backscatter measurement system for quantitative cardiac tissue characterization," IEEE Trans. Ultrason. Ferroelectr. Frequency Control UFFC-33, 27–32 (1986).
[29]J. H. Myers, M. C. Stirling, M. Choy, A. J. Buda, and K. P. Gallagher, "Direct measurement of inner and outer wall thickening dynamics with epicardial echocardiography," Circulation 74, 164–172 (1986).
[30]J. G. Mottley and J. G. Miller, "Anisotropy of the ultrasonic backscatter of myocardial tissue: I. Theory and measurements *in vitro*," J. Acoust. Soc. Am. 83, 755–761 (1988).
[31]J. G. Mottley, R. M. Glueck, J. E. Perez, B. E. Sobel, and J. G. Miller, "Changes in attenuation and backscatter of frog skeletal muscle between rest and tetanic contraction," Ultrason. Imag. 6, 221 (abstract) (1984).
[32]R. M. Glueck, J. G. Mottley, B. E. Sobel, J. G. Miller, and J. E. Perez, "Changes in ultrasonic attenuation and backscatter of muscle with state of contraction," Ultrasound Med. Biol. 11, 605–610 (1985).
[33]M. O'Donnell, J. W. Mimbs, and J. G. Miller, "The relationship between collagen and ultrasonic attenuation in myocardial tissue," J. Acoust. Soc. Am. 65, 512–517 (1979).
[34]S. Wallenstein, C. L. Zucker, and J. L. Fleiss, "Some statistical methods useful in circulation research," Circ. Res. 47, 1–9 (1980).
[35]E. L. Madsen, H. J. Sathoff, and J. A. Zagzebski, "Ultrasonic shear wave properties of soft tissues and tissuelike materials," J. Acoust. Soc. Am. 74, 1346–1355 (1983).

☆U.S. GPO: 1989—629-336